SEAFLOOR MAPPING OF THE ATLANTIC OCEAN

EDITED BY: Pål Buhl-Mortensen, Vincent Lecours and Craig John Brown
PUBLISHED IN: Frontiers in Marine Science

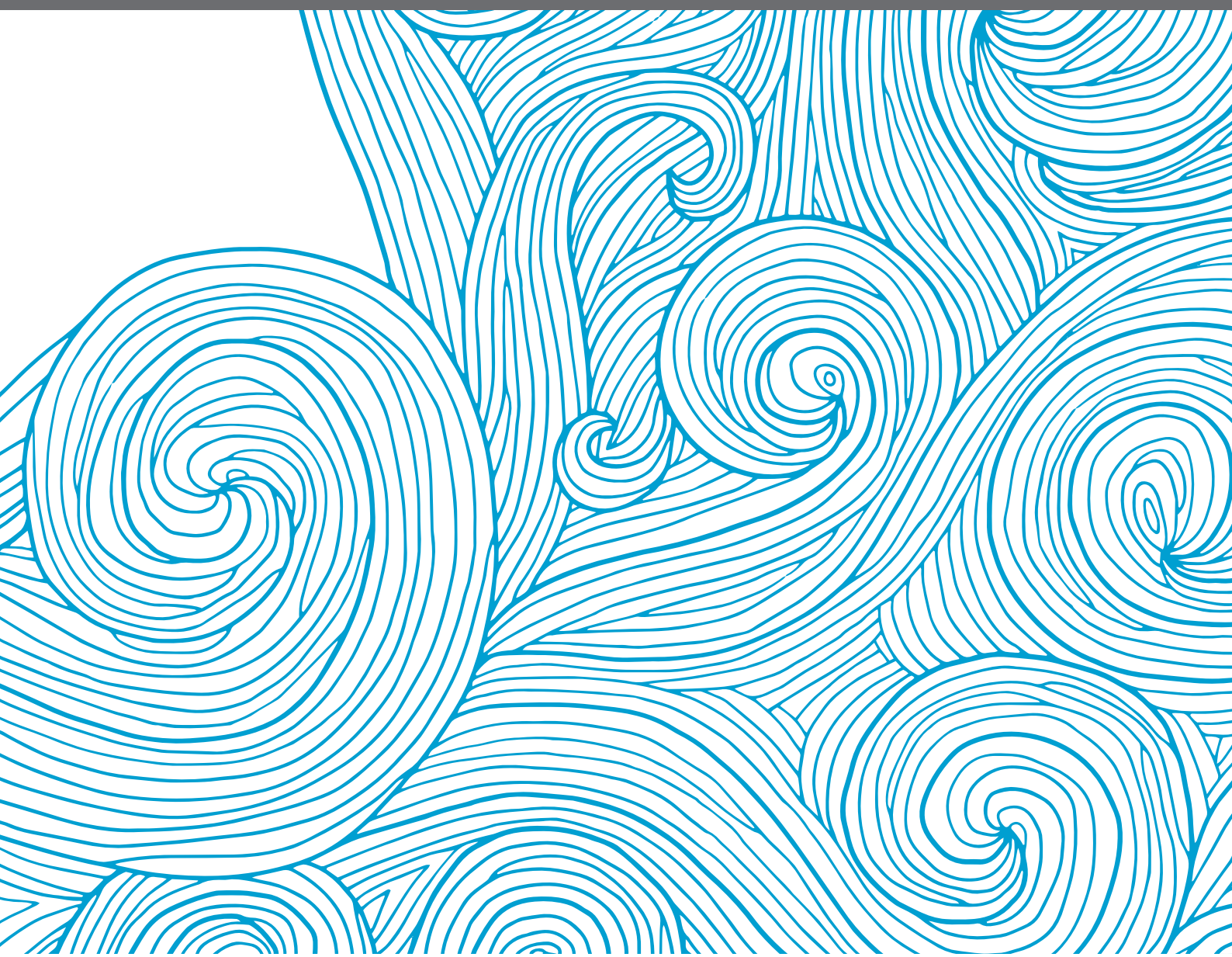

frontiers Research Topics

frontiers

ISSN 1664-8714
ISBN 978-2-88971-390-5
DOI 10.3389/978-2-88971-390-5

About Frontiers

Frontiers is more than just an open-access publisher of scholarly articles: it is a pioneering approach to the world of academia, radically improving the way scholarly research is managed. The grand vision of Frontiers is a world where all people have an equal opportunity to seek, share and generate knowledge. Frontiers provides immediate and permanent online open access to all its publications, but this alone is not enough to realize our grand goals.

Frontiers Journal Series

The Frontiers Journal Series is a multi-tier and interdisciplinary set of open-access, online journals, promising a paradigm shift from the current review, selection and dissemination processes in academic publishing. All Frontiers journals are driven by researchers for researchers; therefore, they constitute a service to the scholarly community. At the same time, the Frontiers Journal Series operates on a revolutionary invention, the tiered publishing system, initially addressing specific communities of scholars, and gradually climbing up to broader public understanding, thus serving the interests of the lay society, too.

Dedication to Quality

Each Frontiers article is a landmark of the highest quality, thanks to genuinely collaborative interactions between authors and review editors, who include some of the world's best academicians. Research must be certified by peers before entering a stream of knowledge that may eventually reach the public - and shape society; therefore, Frontiers only applies the most rigorous and unbiased reviews.
Frontiers revolutionizes research publishing by freely delivering the most outstanding research, evaluated with no bias from both the academic and social point of view. By applying the most advanced information technologies, Frontiers is catapulting scholarly publishing into a new generation.

What are Frontiers Research Topics?

Frontiers Research Topics are very popular trademarks of the Frontiers Journals Series: they are collections of at least ten articles, all centered on a particular subject. With their unique mix of varied contributions from Original Research to Review Articles, Frontiers Research Topics unify the most influential researchers, the latest key findings and historical advances in a hot research area! Find out more on how to host your own Frontiers Research Topic or contribute to one as an author by contacting the Frontiers Editorial Office: frontiersin.org/about/contact

SEAFLOOR MAPPING OF THE ATLANTIC OCEAN

Topic Editors:
Pål Buhl-Mortensen, Norwegian Institute of Marine Research (IMR), Norway
Vincent Lecours, University of Florida, United States
Craig John Brown, Dalhousie University, Canada

Citation: Buhl-Mortensen, P., Lecours, V., Brown, C. J., eds. (2021). Seafloor Mapping of the Atlantic Ocean. Lausanne: Frontiers Media SA. doi: 10.3389/978-2-88971-390-5

Table of Contents

frontiers in Marine Science

EDITORIAL
published: 27 July 2021
doi: 10.3389/fmars.2021.721602

Editorial: Seafloor Mapping of the Atlantic Ocean

Pål Buhl-Mortensen[1]*, *Vincent Lecours*[2] and *Craig J. Brown*[3]

[1] Benthic Communities and Coastal Interactions Research Group, Institute of Marine Research (IMR), Bergen, Norway, [2] School of Forest, Fisheries, and Geomatics Sciences, University of Florida, Gainesville, FL, United States, [3] Department of Oceanography, Dalhousie University, Halifax, NS, Canada

Keywords: seafloor bathymetry, seafloor mapping, benthic habitats, seascape ecology, habitat mapping, marine geology, marine geomorphology

Editorial on the Research Topic

Seafloor Mapping of the Atlantic Ocean

THE IMPORTANCE OF SEAFLOOR MAPPING

Patricio Bernal, the Coordinator of the International Union for Conservation of Nature High Seas Initiative, once wrote: "We know more about the surface of the Moon and about Mars than we do about the deep seafloor, despite the fact that we have yet to extract a gram of food, a breath of oxygen or a drop of water from those bodies" (Snelgrove, 2010). Often referred to as the last frontier on Earth, the deep seafloor is thought to shelter both critical ecosystems and exploitable resources (i.e., minerals, bio-active natural products, and genetic material, in addition to food resources already being harvested by the fishing industry). These resources are said to have enormous potential to contribute to the growth of the blue economy, potential that will be realized only with an increased understanding of deep-sea environments (Glover et al., 2018). However, knowledge of deep-sea environments and the anthropogenic impacts on them lags in comparison to other marine environments. To address this issue, several cooperative international agreements have been signed. For instance, the Galway Statement (signed by the European Union, United States, and Canada) and the Belém Statement (also signed by Brazil and South Africa) were endorsed to launch an All-Atlantic Ocean Research Alliance. This alliance aims to increase our understanding of the Atlantic Ocean and its systems and promote the sustainable management of its resources. In addition, activities and programs associated with the United Nations Decade of Ocean Science for Sustainable Development (2021–2030), such as The Nippon Foundation-GEBCO Seabed 2030 Project, Challenger 150, and the One Ocean Network for Deep Observation, will likely help increase awareness of the importance of seafloor mapping.

The efforts involved in mapping the seafloor, its habitats, and its resources require the adoption of an interdisciplinary perspective, working across fields such as marine geology, geomorphology, oceanography, biology, ecology, underwater acoustics, geomatics, and more. While the technologies to map the physical and biological components of the deep seafloor exist, the financial, human, and material resources required to collect data at a spatial resolution that is adequate for conservation and management purposes are currently limiting the scope of the work that could be achieved (Danovaro et al., 2020). There have been significant technological and methodological developments in recent years, some of which are presented in this Research Topic.

This Research Topic showcases contributions addressing all aspects of the marine sciences that introduce new knowledge and new approaches to improve our understanding of the characteristics of the Atlantic Ocean. Three themes central to seafloor mapping are covered: (1) the spatial settings of the environment (e.g., bathymetry, geomorphology, marine landscapes); (2) the abiotic

OPEN ACCESS

Edited and reviewed by:
Eva Ramirez-Llodra, REV Ocean, Norway

***Correspondence:**
Pål Buhl-Mortensen
paal.buhl.mortensen@HI.no

Specialty section:
This article was submitted to Deep-Sea Environments and Ecology, a section of the journal Frontiers in Marine Science

Received: *07 June 2021*
Accepted: *29 June 2021*
Published: *27 July 2021*

Citation:
Buhl-Mortensen P, Lecours V and Brown CJ (2021) Editorial: Seafloor Mapping of the Atlantic Ocean. Front. Mar. Sci. 8:721602. doi: 10.3389/fmars.2021.721602

environment (e.g., seafloor geology, oceanography, hydrodynamics, water chemistry); and (3) the biotic environment (e.g., benthic biodiversity, communities, habitats).

STATE OF THE ART MAPPING APPROACHES

Despite continued growth in marine habitat mapping technologies and methods, development is still needed to further our understanding of marine habitats and how they are explored; there is still no "standard recipe" for seafloor mapping studies. Seafloor mapping efforts can be categorized into different themes depending on their primary objective. The management and exploitation of living resources including fisheries, petroleum and mineral explorations, ecosystem conservation and restoration, navigation and maritime safety, and academic knowledge gathering are examples where different perspectives define the focus of what information is most relevant. A holistic description of the seafloor would require enormous efforts involving a multitude of equipment. Nonetheless, many studies now collect comprehensive suites of interdisciplinary data, as demonstrated in several studies presented in this Research Topic (e.g., Jovane et al.; Buhl-Mortensen et al.).

Multibeam echosounders are widely used for seafloor mapping, as reflected in this collection of articles; seven out of twelve articles used data collected with such instrument (e.g., Buhl-Mortensen et al.; Jovane et al.; Masetti et al.). Half of the contributions used at least one compiled dataset (e.g., GEBCO or EMODnet bathymetry) (e.g., Burgos et al.; Gonzales-Mirelis et al.; Ross et al.; Sundahl et al.), highlighting the importance of seafloor data compilation and integration efforts and making data available to increase their use and the potential for new scientific discoveries. This relates to the spatial scale of the research that is performed; six of the study areas presented in this Research Topic covered a broad geographic extent with broader-scale seafloor data (up to km-scale resolution) (e.g., Burgos et al.; Gonzales-Mirelis et al.), and the remaining contributions used finer-scale data (down to cm-scale resolution) over smaller extents (e.g., Thorsnes et al.). There is also an interest in sub-seafloor geology; four articles (Alves et al.; Jovane et al.; Meredyk et al.; Thorsnes et al.) used instruments such as sub-bottom profilers or magnetometers to integrate structural elements of the seafloor.

Visual information about the seafloor has been gathered from remotely-operated vehicles (ROVs) (e.g., Meredyk et al.), towed video (e.g., Buhl-Mortensen et al.; Gonzalez-Mirelis et al.; Sundahl et al.), and Autonomous Underwater Vehicles (AUVs) (e.g., Thorsnes et al.). These observation platforms have their benefits and limitations where time consumption (cost), visual quality, and purpose of the survey are governing elements. Thorsnes et al. used an AUV as a platform for a multibeam echosounder, a synthetic aperture sonar, and digital photography. Over the last 20 years, the development of AUVs has increased their applications in local high-resolution bathymetry mapping and visual ground-truthing. However, due to limitations in battery power and steady maneuvering close to the bottom in rugged terrain, the quality of imagery collected with AUVs is still limited compared to imagery collected with ROVs.

To fully understand benthic ecosystems, studying the physio-chemical properties of the water near the seafloor is essential. Many of the papers in the Research Topic have integrated chemical data (e.g., salinity and aragonite saturation) (e.g., Burgos et al.), near-bottom currents (e.g., Ross et al.), and temperature data (e.g., Sundahl et al.) with bathymetric and biological data. Even though these data are generally only available at a coarser resolution than the acoustic mapping and optical ground validation data, they are nonetheless valuable additional information for understanding benthic ecosystems and increasing the performance of species distribution models and habitat maps.

CHALLENGES AND FUTURE DIRECTIONS

The diversity of work done in habitat mapping strongly depends upon funding sources and funding opportunities. A comprehensive survey of seafloor habitats requires agencies or organizations willing to dedicate significant funds toward seafloor mapping. Most contributions (10 out of 12 papers) cover study areas within the Exclusive Economic Zones (EEZ) of countries in the North Atlantic, where several well-funded seafloor mapping initiatives are active [e.g., Norway's MAREANO programme (Buhl-Mortensen et al., 2015; Bøe et al., 2020)]. This highlights a geographic bias in resource allocation toward EEZs, even though international waters account for about two-thirds of the global ocean. Only two papers represent the South Atlantic (Alves et al.; Jovane et al.). The North Atlantic studies are divided among the Caribbean Sea (Lavagnino et al.), North West Atlantic (Masetti et al.; Meredyk et al.; Sowers et al.), North East Atlantic (Buhl-Mortensen et al.; Sundahl et al.; Ross et al.; Burgos et al.; Gonzales-Mirelis et al.), and the Arctic Ocean (Buhl-Mortensen et al.; Burgos et al.; Gonzales-Mirelis et al.; Thorsnes et al.). Mapping efforts that cannot count on well-funded initiatives must rely on existing datasets rather than new data acquisition. Initiatives like The Nippon Foundation-GEBCO Seabed 2030 Project (Mayer et al., 2018; Wölfl et al., 2019), an international effort to create a bathymetric map of the oceans by 2030, are helping to raise awareness about the importance of mapping waters beyond EEZs. Seafloor mapping in international waters is a global responsibility, and progress is being made as the number of initiatives and funding for such efforts is increasing.

Mapping the deep sea is time-consuming and costly as it covers vast areas that are challenging to sample. Thus, there is a strong motivation to develop new technologies and approaches to facilitate mapping and exploration. Crowd-sourced bathymetric data (e.g., Novaczek et al., 2019) and bycatch registration of invertebrates and fish are examples of alternative ways to collect data outside dedicated surveys. Commercial vessels may be equipped with relevant instruments and towed sensors that can increase data collection rate. Many existing datasets are not shared open access but are stored on local servers or as printed material, which hampers the progression of knowledge

gathering for broader seafloor areas. The inclusion of such data in international data repositories is therefore critical.

Matching different spatial scales is a challenge for producing composite maps or understanding benthic ecosystems. While ground-truthing data are very fine-scale, acoustic data (bathymetry and backscatter) and other environmental data are usually collected at a coarser resolution. How we integrate such multiscale information remains unclear and is an active field of research (e.g., Misiuk et al., 2021). There is a tradeoff between the comprehensiveness of the environmental characterization and the level of detail provided: the inclusion of a broader-scale environmental dataset may constrain the analysis to a coarser resolution, potentially losing important information. By not including broader-scale datasets, analyses can be performed at higher spatial resolutions, but important patterns and processes may not be captured (Lecours et al., 2015).

Visual observations are commonly used to gather geological and biological seafloor information. Visual seafloor observations must be conducted within a visible range using subsea cameras, and increased efficiency of seafloor observation instruments like cameras and lights is needed. For AUVs to address this challenge, their maneuvering autonomy and optical quality must improve. Nevertheless, even with high-quality image, there remain limitations of visual data. For example, taxonomic identification of benthic fauna and accurate quantification of sediment grain size compositions remain challenging. For confident species identification, the sampling of specimens or material for genetic analysis is still needed. Analysis of subsea optical imagery and biological samples is also very time-consuming. The early applications of artificial intelligence are promising to support biological and geological data extraction from subsea imagery, interpreting geological and biological patterns, and modeling the spatial distribution of habitats and communities. As the field of seafloor mapping continues to grow, we look forward to the continued technical and methodological innovations that will result from these efforts.

AUTHOR CONTRIBUTIONS

PB-M introduced the idea for the Research Topic Seafloor Mapping of the Atlantic Ocean. PB-M, VL, and CB have revised and edited contributions to the Research Topic and contributed to the writing of this editorial. All authors contributed to the article and approved the submitted version.

FUNDING

This work was supported by AORA-CSA, Grant agreement ID: 652677.

ACKNOWLEDGMENTS

Thanks to colleagues in the Atlantic Ocean Research Alliance (EU project AORA-CSA). Also, thanks to Dr. Margaret Dolan at the Geological Survey of Norway (NGU), and Thomas Furey at the Marine Institute in Ireland for useful comments on this paper.

REFERENCES

Bøe, R., Bjarnadóttir, L. R., Elvenes, S., Dolan, M., Bellec, V., Thorsnes, T., et al. (2020). "Revealing the secrets of Norway's seafloor – geological mapping within the MAREANO programme and in coastal areas," in *From Continental Shelf to Slope: Mapping the Oceanic Realm,* eds K. Asch, H. Kitazato, and H. Vallius. *Geological Society* (London: Special Publications), 505. doi: 10.1144/SP505-2019-82

Buhl-Mortensen, L., Buhl-Mortensen, P., Dolan, M. F. J., and Holte, B. (2015). The MAREANO programme – a full coverage mapping of the Norwegian off-shore benthic environment and fauna. *Mar. Biol. Res.* 11, 4–17. doi: 10.1080/17451000.2014.952312

Danovaro, R., Fanelli, E., Aguzzi, J., Billet, D., Carugati, L., Corinaldesi, C., et al. (2020). Ecological variables for developing a global deep-ocean monitoring and conservation strategy. *Nat. Ecol. Evol.* 4, 181–192. doi: 10.1038/s41559-019-1091-z

Glover, A. G., Wiklund, H., Chen, C., and Dahlgren, T. G. (2018). Point of view: managing a sustainable deep-sea 'blue economy' requires knowledge of what actually lives there. *eLife* 7:e41319. doi: 10.7554/eLife.41319

Lecours, V., Devillers, R., Schneider, D. C., Lucieer, V. L., Brown, C. J., and Edinger, E. N. (2015). Spatial scale and geographic context in benthic habitat mapping: review and future directions. *Mar. Ecol. Prog. Ser.* 535, 259–284. doi: 10.3354/meps11378

Mayer, L., Jakobsson, M., Allen, G., Dorschel, B., Falconer, R., Ferrini, V., et al. (2018). The Nippon Foundation—GEBCO seabed 2030 project: the quest to see the world's oceans completely mapped by 2030. *Geosciences* 8:63. doi: 10.3390/geosciences8020063

Misiuk, B., Lecours, V., Dolan, M. F. J., and Robert, K. (2021). Evaluating the suitability of multi-scale terrain attribute calculation approaches for seabed mapping applications. *Mar. Geodesy.* 44, 327–385. doi: 10.1080/01490419.2021.1925789

Novaczek, E., Devillers, R., and Edinger, E. (2019). Generating higher resolution regional seafloor maps from crowd-sourced bathymetry. *PLoS ONE* 14:e0216792. doi: 10.1371/journal.pone.0216792

Snelgrove, P. V. R. (2010). *Discoveries of The Census of Marine Life: Making Ocean Life Count.* New York, NY: Cambridge University Press, 270.

Wölfl, A.-C., Snaith, H., Amirebrahimi, S., Devey, C. W., Dorschel, B., Ferrini, V., et al. (2019). Seafloor mapping – the challenge of a truly global ocean bathymetry. *Front. Mar. Sci.* 6:283. doi: 10.3389/fmars.2019.00283

Conflict of Interest: The authors declare that the research was conducted in the absence of any commercial or financial relationships that could be construed as a potential conflict of interest.

frontiers in Marine Science

DATA REPORT
published: 24 May 2019
doi: 10.3389/fmars.2019.00252

Multidisciplinary Scientific Cruise to the Rio Grande Rise

Luigi Jovane[1], James R. Hein[2], Isobel A. Yeo[3,4], Mariana Benites[1], Natascha M. Bergo[1], Paulo V. F. Corrêa[1], Daniel M. Couto[1], Ayrton D. Guimarães[1], Sarah A. Howarth[3], Henrique R. Miguel[1], Kira L. Mizell[2], Denise S. Moura[1], Francisco L. Vicentini Neto[1], Mayza Pompeu[1], Ianco M. M. Rodrigues[1], Frederico R. Santana[1], Pedro F. Serrao[1], Tomas E. Silva[1], Pedro M. Tura[1], Carolina L. Viscarra[1], Mateus G. Chuqui[1], Vivian H. Pellizari[1], Camila N. Signori[1], Ilson C. A. Da Silveira[1], Paulo Y. G. Sumida[1], Bramley J. Murton[3] and Frederico P. Brandini[1]*

[1] Instituto Oceanográfico, Universidade de São Paulo, São Paulo, Brazil, [2] United States Geological Survey, Santa Cruz, CA, United States, [3] National Oceanographic Centre, Southampton, United Kingdom, [4] Department of Geography, Geology and the Environment, Kingston University London, London, United Kingdom

Keywords: Rio Grande Rise, South Atlantic Ocean, multidisciplinary cruise, Fe-Mn crusts and nodules, benthic fauna

OPEN ACCESS

Edited by:
Craig John Brown, Nova Scotia Community College, Canada

Reviewed by:
Helena Passeri Lavrado, Federal University of Rio de Janeiro, Brazil
Akkur Vasudevan Raman, Andhra University, India

****Correspondence:***
Luigi Jovane
jovane@usp.br

Specialty section:
This article was submitted to Deep-Sea Environments and Ecology, a section of the journal Frontiers in Marine Science

Received: *09 November 2018*
Accepted: *25 April 2019*
Published: *24 May 2019*

Citation:
Jovane L, Hein JR, Yeo IA, Benites M, Bergo NM, Corrêa PVF, Couto DM, Guimarães AD, Howarth SA, Miguel HR, Mizell KL, Moura DS, Vicentini Neto FL, Pompeu M, Rodrigues IMM, Santana FR, Serrao PF, Silva TE, Tura PM, Viscarra CL, Chuqui MG, Pellizari VH, Signori CN, Da Silveira ICA, Sumida PYG, Murton BJ and Brandini FP (2019) Multidisciplinary Scientific Cruise to the Rio Grande Rise. Front. Mar. Sci. 6:252. doi: 10.3389/fmars.2019.00252

INTRODUCTION

The western Rio Grande Rise (RGR), where this research took place, is an extensive oceanic rise (~150,000 km^2) in the South Atlantic Ocean, located ~1,000 km to the east of the Brazil and Argentine basins (Cavalcanti et al., 2015). The RGR has gained special attention from scientists and governments worldwide due to its marine mineral deposits and, as yet, the controversial origin of the rise itself (Montserrat et al., 2019). In 2015, the International Seabed Authority (ISA) and the state-owned Companhia de Pesquisa de Recursos Minerais (CPRM) of Brazil signed a 15-year contract for exploration of Co-rich ferromanganese crusts in the RGR, accentuating the need for baseline environmental studies in the area. Co-rich ferromanganese crusts are of interest as potential resources for critical and rare metals such as Co, Ni, Mn, Bi, Mo, Nb, Pt, REEs, Te, Th, Ti, W, Y, and Zr, most of which are essential for high- and green-technology industries (Hein et al., 2013). The supply of these rare metals is becoming critical as global consumption increases, hence deep-ocean mineral deposits may present an additional resource for these raw materials.

Extensive geophysical surveys in the 1970s and 1980s aimed to characterize the geological structure and morphology of the RGR and surrounding areas. Seismic refraction and reflection surveys by Leyden et al. (1971) covered the SE Brazilian margin. The Deep-Sea Drilling Project (DSDP) contributed significantly to the understanding of the geological history of the region (Barker et al., 1981; Barker, 1983), with DSDP borehole data enabling interpretation of seismic-reflection profiles (Gamboa and Rabinowitz, 1984). This work led to the recognition of the RGR as an aseismic ridge, but has a negative Bouguer anomaly across the summit. This anomaly implies a relative mass deficit for the aseismic ridge relative to the surrounding regions. Gamboa and Rabinowitz (1984) separated the RGR into two distinct geomorphological units with different geological histories; the western (WRGR) and eastern (ERGR) units. The WRGR has an average summit depth of 2,000 m, and widespread Eocene volcanism is thought to have driven the formation of numerous seamounts and later uplift. The ERGR is less well-characterized and consists of two segments bound to the north and south by fracture zones (Gamboa and Rabinowitz, 1981). Both the WRGR and ERGR are cut by NW-SE trending troughs. Recent extensive hull-mounted multibeam surveys by CPRM were carried out as part of a campaign focused on the Fe-Mn crust resources of the RGR (CPRM, 2018). However, detailed and high-resolution geophysical surveys are still scarce for the area. Regarding RGR mineral deposit formation, even greater scarcity exists concerning published scientific studies, except for the work of Benites et al. (2018), in which geochemical results of a single Fe-Mn oxide-coated pebble indicates a hydrogenetic origin—precipitation of Fe and Mn oxyhydroxides directly from the cold seawater.

In this cruise report, we detail the geophysical, hydrographic, geological, oceanographic, and ecological surveys carried out on board the N/Oc Alpha Crucis of the Instituto Oceanográfico da Universidade de São Paulo (**Figure 4C**) during 22 days (28 January 2018 to 19 February 2018). The goal of the RGR cruise (RGR1) was to gather multidisciplinary data to supplement and expand previous environmental studies of RGR, to serve as baseline data on understanding Fe-Mn deposit formation, and environmental assessments for possible future mining activities on the RGR.

METHODS

Areas of Interest

The surveys were conducted over four (4) areas of interest (A1, A2, B1, and B2) (**Figure 1**), determined based on the likelihood of encountering Fe-Mn crusts on the flanks of the central rift and thicker sediment packages for coring along the plateaus. Areas A and B, as well as the subsections 1 and 2 on opposite sides of the central rift, were chosen in order to compare different locations on the RGR.

Benthic Organisms

Sediment at RGR was collected by using a BX-650 box corer manufactured by Ocean Instruments. The sample box is 50 x 50 cm in area (0.25 m^2) and 60 cm deep. Eight attempts at box coring were made, from which six were successful and retrieved sediment from 935 m to 1,566 m water depths (**Supplementary Table 4**). The box cores collected the first 5 to 15 cm of sediment layer, which was mainly composed of sand, foraminifera, and pteropod ooze. Once on deck, small sediment cores were retrieved from the material collected by the box core for geomicrobiology analysis. Afterwards, the top 5 cm of sediments were sieved through a 300 μm mesh screen and fixed in 96% alcohol for the preservation of macrofauna for shore-based analyses. A total of 39 L of sediment were retained in the sieve from the six box cores.

Biota attached to the rocks collected via dredgings were photographed, removed from the rocks, and fixed in 96% ethanol. Larger individuals had a small piece of tissue cut and frozen at −80°C for molecular biology. Future activity will involve sorting the specimens according to morphotypes and identification to the lowest taxonomic level possible, based on morphological features and DNA barcode. In general, we collected a low number of morphotypes with a few numbers of specimens each (usually one to three individuals). By the end of the cruise, we counted 60 morphotypes, but this number is expected to increase with further analysis, as part of the material could not be sorted during the cruise. Because of the mesh size of the dredges (2 and 2.5 cm), only benthic megafauna organisms have been collected. Nevertheless, a few interesting organisms were collected, including the demersal fish *Chaunax* sp. (**Figure 2E**), starfish, sea urchins, barnacles, and black corals, but the most common organisms were corals (**Figures 2F, H**), small tube-dwelling annelids, and sponges (**Figure 2G**). We expect the new records will help to determine the biodiversity and ecological patterns of RGR. Besides, it is likely that some of the organisms are new to science. A summary of benthic organisms collected in each dredge is provided in **Supplementary Table 5**.

Geophysics

The geophysical survey was designed to obtain: (1) full bathymetric and backscatter coverage over the study areas for use in understanding the morphological and hydrographical setting of Fe-Mn crusts on RGR and for use in planning other operations; (2) chirp sub-bottom profiler data along the lengths of tracks to define the sedimentary cover and to aid selection of gravity and box corer sampling sites; (3) extensive magnetic dataset in order to recognize magnetic inversions, characterize the oceanic crust surrounding the RGR, and to identify the principle anomalies on the RGR and interpret them with regard to the geological and tectonic evolution of the area.

Multibeam bathymetric data were acquired using a Reson 7160 multibeam echosounder (MBES) operating at 41 kHz. The Reson 7160 MBES collected bathymetric, backscatter, and snippet data (**Figure 3**). Surveys were conducted over areas A1, A2, B1, and B2 (**Figures 1**, **3**; **Supplementary Figures 1, 2**). Bathymetric data were not collected on the transits to and from the working area as the speed of the ship (8 kn) and water depth (>2,000 m) would have compromised data quality. Data acquisition was achieved using the acquisition module of PDS2000 alongside the Reson Seabat sensor software to modify settings (power, pulse length, range, gain, beam width) during surveys. Raw multibeam files were generated in.s7k format which were automatically time and date stamped in the filename. The surveys were conducted at a relatively slow speed of 4–4.5 kn and aligned as much as possible with the prevailing wave direction as close as possible to the bathymetric contours. Prevailing south-westerly waves caused degradation of data quality because of roll movement of the ship. Lines were planned with a NE-SW orientation and 2.1 km spacing, perpendicular to the main slope. Spacing between acquisition lines (1–2.1 km) was calculated in order to optimize the beam coverage, while beam width was modified dynamically during the survey to attempt to maintain good data quality. The footprint of the sonar operating at 44 kHz and with a beam angle of 1.5° at a slant-range of 30° at 1,000 m water depth was calculated to be around 30 m, slightly better at shallower depths. The sonar was predominantly operated in maximum coverage mode, meaning an equi-distance beam spacing was maintained, rather than an equi-angular one.

Sound Velocity Profiles (SVPs) were collected at least every other day during surveys and at least once per survey to full water depth. A patch test was carried out in area B later and the results were applied retrospectively to data already collected.

Single beam bathymetric tracks were collected using an EA600 echosounder along almost all tracks to calibrate the magnetometer data. The data were recorded in *.xyz format. No further processing was done on this data.

The seismic survey was performed using a Knudsen sub-bottom profiler (SBP) CHIRP 3260, which operated at a frequency of 3.5 kHz and power 2 kW. We used the software SoundeSuite EchoControl from Knudsen for data acquisition. SBP data was used to give information on sediment coverage on the seabed and help select sites for box core and

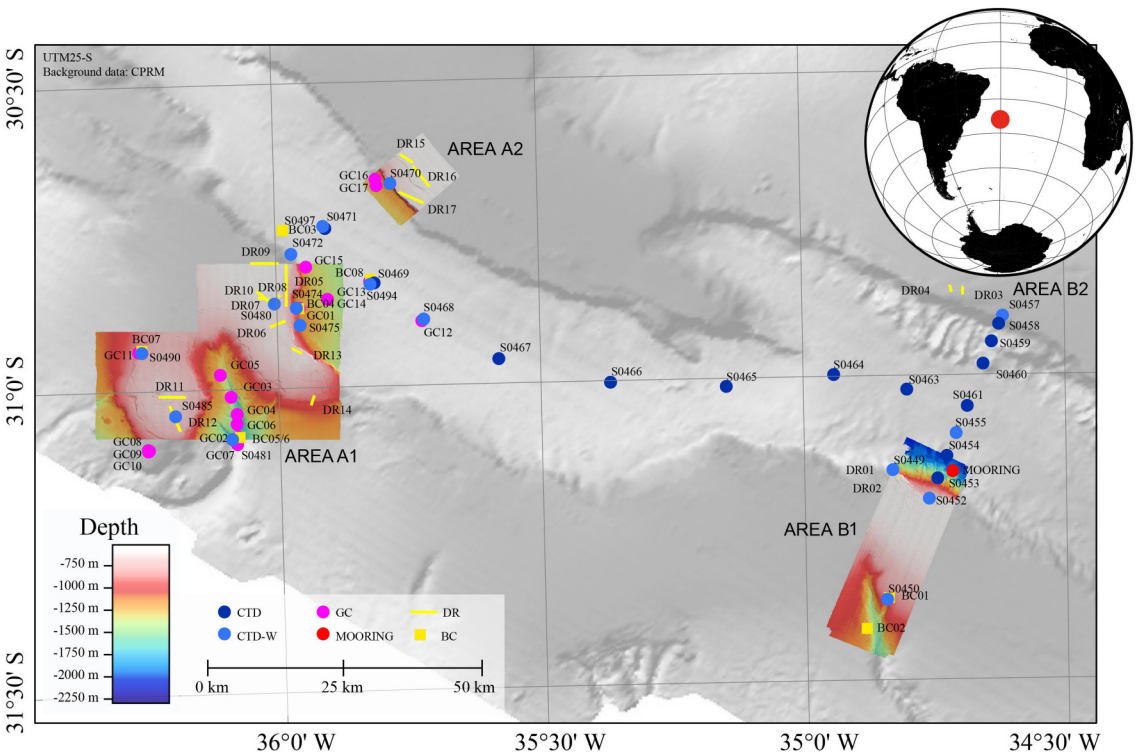

FIGURE 1 | Location map of the operations performed during the oceanographic expedition RGR1 to Rio Grande Rise on board the research vessel Alpha Crucis (Universidade de São Paulo). High resolution bathymetry was performed during the cruise. GC, gravity corer; DR, dredge; BC, box-corer.

gravity core operations (**Figure 3B**). We used the following procedure for data processing with software SeisPrho 2.0, following the procedure: (1) Data reading; (2) Geometrical analysis; (3) Filtering and Gain; (4) Deconvolution; and (5) Seismic interpretation.

Finally, a magnetometry survey was performed (**Figure 3D**) using a SeaSPY magnetometer with an Overhauser sensor produced by Marine Magnetics. During multibeam surveys the magnetometer was towed 250 m behind the ship so survey lines were deliberately overshot by a few hundred meters with wide turning circles to keep the magnetometer at as constant a water depth as possible. The SeaSPY is a total field magnetometer, so it measures only the intensity or magnitude of the magnetic field vector, independent of its direction. The resolution is 0.001 nT and the absolute accuracy is 0.1 nT. There is no heading error, temperature drift, or dead zone associated with the measurements.

For all geophysical surveys, the GPS positioning was provided by an Applanix Wave Master DGPS with spatial resolution of 17 m.

Hydrography

The goals of the hydrographic survey were to: (1) measure current velocities to unravel local small-scale circulation features generated by topography; (2) measure the current close to the seabed to determine the nature of the benthic nepheloid layer; (3) map the main hydrographic features and; (4) infer possible interactions between secondary circulation generated by bathymetric gradients and regional current flow. Measurements of currents, temperature, salinity, dissolved oxygen, and fluorescence were carried out with unprecedented spatial resolution for the RGR area.

The hydrographical stations consisted of conductivity-temperature-depth (CTD) profiles collected using a Sea-Bird Electronics 9plus equipped with pressure, conductivity, dissolved oxygen, turbidity, and a-chlorophyll and picoerythrin fluorescence sensors (**Figures 4A,D** and **Supplementary Table 7**). The stations were taken along three transects, two perpendicular to the RGR central rift and 120 km distant from each other, and the third one along the central rift. Besides these stations, additional CTD stations were carried out at places where biological material was collected.

Vertical profiles of current velocity through the water column were acquired, including the benthic nepheloid layer, using a downward-facing lowered acoustic doppler current profiler (LADCP) WorkHorse 300 kHz from Teledyne RDI with 2 m resolution coupled to the rosette. Finally, a hull-mounted ADCP Ocean Surveyor 75 kHz from Teledyne RDI continuously acquired velocity profiles from 16 to 400 m depth with horizontal resolution of 8 m. Data acquired by CTD, LADCP, and hull-mounted ADCP will be processed using the codes provided by the producer (SBE). The data are corrected using these codes, mainly for the relative delay on sensors response and removal of oscillations due to waves. Afterwards, the pre-processed data

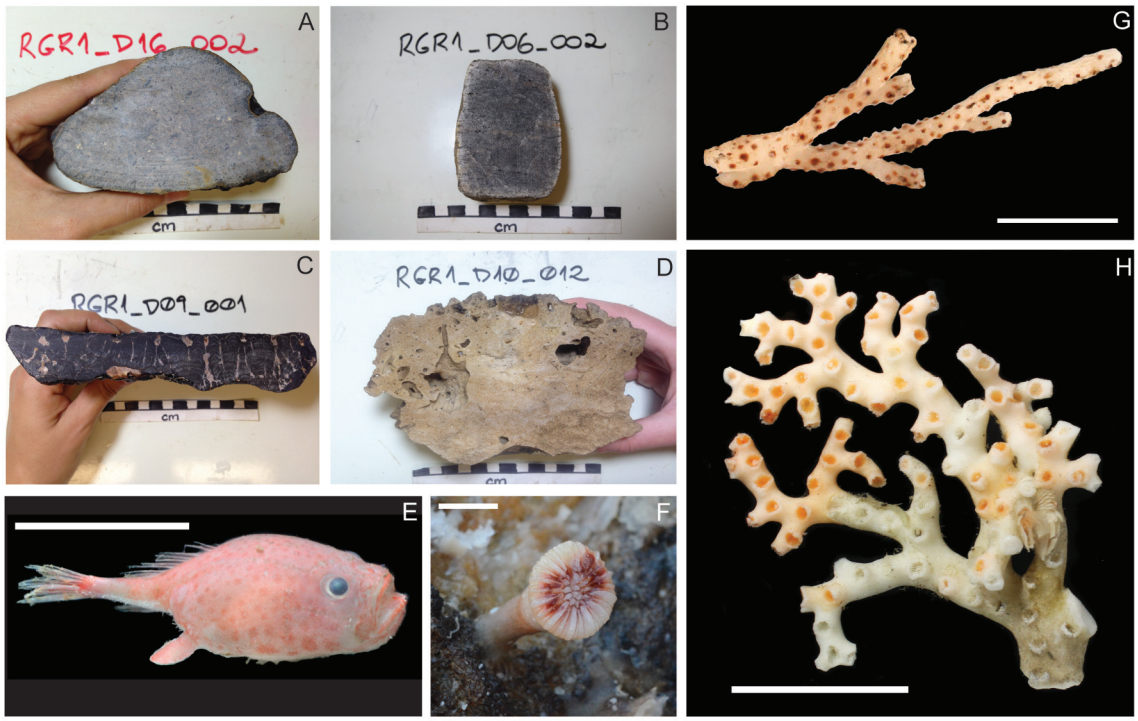

FIGURE 2 | Representative samples of **(A)** volcanic rock collected in dredge 16, **(B)** crystalline rock collected in dredge 06, **(C)** Fe-Mn crusts collected in dredge 09, **(D)** and calcareous sedimentary rock collected in dredge 10, **(E)** a dermersal fish *Chaunax* sp. from dredge 03 (scale represents 50 mm), **(F)** a solitary coral *Caryophyllia diomedeae* attached to a rock from dredge 17 (scale: 10 mm), **(G)** a branch of sponge *Sarostegia oculata* from dredge 13 (scale: 32 mm), and **(H)** a branch of coral *Enallopsammia rostrata* from dredge 03 (scale: 35 mm).

are exported as ASCII files and processed in MATLAB for removal of biased values, smoothing, and windowing. Figures will be generated based on the processed data. ADCP data are processed by using the Common Ocean Data Access System (CODAS) package (developed by University of Hawaii), in which the data are corrected for vessel height and georeferenced using GPS from the vessel. Biased data are removed manually and the processed data are exported to MATLAB. The hydrographic stations summary is in **Supplementary Table 1**.

Geological Sampling

Three different dredge types were used for dredge operations during the cruise. For Dredgings 1–3 sampling, the dredge used had a 1 m diameter circular opening encapsulated by a metal chain bag of 2 cm mesh size. For Dredging 4 sampling, a 0.5 m diameter opening steel cyclinder with 2.5 cm mesh-size dredge was used. For Dredgings 5–17 sampling, a 0.5 m wide rectangular dredge of 2.5 cm mesh-size was used. The rectangular dredge was favorable for the majority of dredge sites because it had the largest contact with the seafloor, increasing the probability of recovery on flat surfaces.

Dredge operations typically occurred by placing the dredge in the water and letting out wire until equal to the water depth (dredge on bottom). Next, additional wire equal to 30–50% of the water depth was let out while the ship held position. Then, the ship followed the planned dredge line while holding 1–2 knots and dredge bites (strikes) were recorded. Once the ship reached the end of the line and/or enough bites were recorded to ensure rock recovery, the ship held position and the winch was used to retrieve wire; the "off bottom" latitude/longitude/depth was recorded once the wire out was equal to the water depth below the ship. "On bottom" and "Off bottom" latitude/longitude/depth records should be taken as good estimates rather than exact locations. Dredging operations typically lasted for several hours.

A total of 17 dredging operations were completed during the cruise (**Figure 1**): two in area B1, two in area B2, ten in area A1, and three in area A2. From these operations, more than 300 rock samples were recovered and 254 of them were cut and described onboard. The major rock types recovered included volcanic rocks, limestones, and Fe-Mn crusts (**Figure 2**). In a few dredges some rare rocks were recovered including rounded pebbles/cobbles of metamorphic rocks, mudstone, siltstone, pyroclastic rocks, and a pegmatitic rock. Overall, more rocks recovered appeared to be talus material than those that showed evidence of being broken from outcrop. Dredge stations and a summary of recovered rocks are in **Supplementary Table 3**.

In addition, gravity core operations were carried out, however, from 17 attempts at coring only three were successful on recovering sediments: GC04 (1.90 m) and GC05 (0.4 m) from the canyon in south Area A1; and GC13 (2 m) from the central rift valley between areas A1 and A2. These cores will

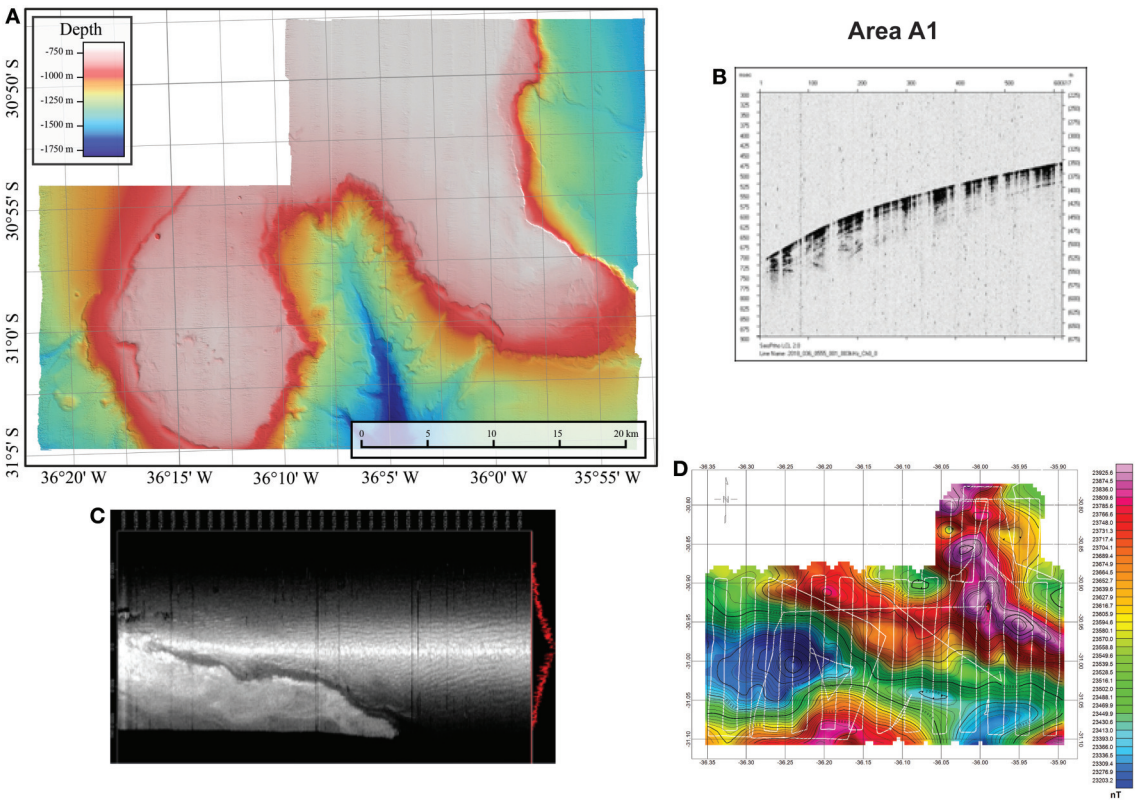

FIGURE 3 | Geophysical survey acquired at Rio Grande Rise: **(A)** Multibeam bathymetry map, **(B)** example of a chirp record, **(C)** example of multibeam backscatter record and **(D)** total magnetic field (observed raw data with spike removed) from area A1.

be used for grain size, mineralogy, chemical composition, and micropaleontological analyses.

Biogeochemistry

The biogeochemical program of the RGR1 cruise aimed to collect biological material and perform a variety of experiments to understand the biological processes that take place in the water column, sediments, and Fe-Mn crusts. The potential relationships between the microbiota to Fe-Mn crust formation will be determined based on four main activities: (1) determination of primary production and export of particulate organic matter, Chemosynthetic Primary Production *in situ* Experiment, and Molecular Biology; (2) quantification of the incorporated ^{14}C by the autotrophic organisms, dissolved organic matter, dissolved organic carbon, and nutrients in the water column along the RGR; (3) quantification of the incorporated ^{14}C by the chemolithotrophic microorganisms in different habitats (water column, sediments, and crusts) along RGR; (4) determination of the microbial taxonomy, diversity, and metabolism in different habitats (water column, sediments, and crusts) along RGR by the combination of complementary high-throughput techniques, 16S rRNA sequencing, metagenomics, and metatranscriptomics. Each of the experiments conducted during the RGR1 cruise are described below.

Primary Production Experiment

A Profiler of Natural Fluorescence (PNF) was deployed to calculate light attenuation coefficient, following the light attenuation model:

$$I(z) = I(0) * e - kz$$

Where k is the attenuation coefficient, I(0) is the surface radiance, and I(z) is radiance in the z depth. The depths of 100, 67, 30, 20, 14, 10, 6, 4, 2, 0.56% of incident light were calculated along the water column in order to be incubated in an *in-situ* simulated experiment. Water samples were collected using the CTD-Rosette system. 500 μL of ^{14}C (duplicates) were inoculated in the water samples and incubated in the respective light filter. A single bottle was reserved as control, and was incubated in the dark and covered in aluminum foil. All incubations were made up to 6 h to simulate the photosynthetic processes in the water column (**Figure 4B**). One to two liters of water was filtered in a vacuum pump with a GFF membrane filters (Millipore, MA) to analyze photosynthetic pigments of abundant autotrophic groups. Membranes were stored at −80°C until transport to the Instituto Oceanográfico for High Performance Liquid Chromatographic analysis. After incubation, the samples were filtered in a vacuum pump with 0.22 μm pore-size membrane filters (Millipore, MA) and stored at −4°C for further analyses at the Instituto Oceanográfico. The samples collected for primary

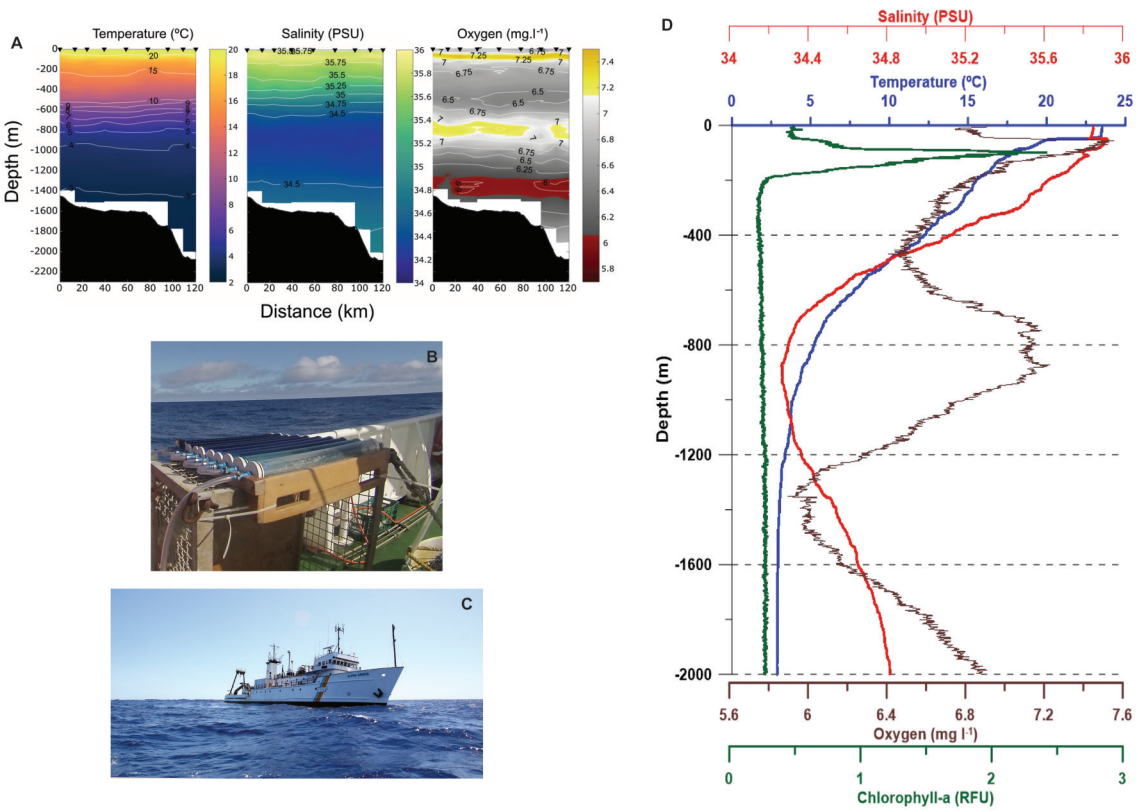

FIGURE 4 | (A) Water column temperature (°C), Salinity (PSU), and Dissolved Oxygen (mg L^{-1}) section for the CTD transect along the central rift, **(B)** *In-situ* simulated primary production experiment, **(C)** RV Alpha Crucis from the Instituto Oceanográfico da Universidade de São Paulo, and **(D)** CTD water column profiles of salinity (PSU), temperature (°C), dissolved oxygen (mg L^{-1}), and chlorophyll-a (RFU).

production are described in **Supplementary Table 2**. Samples for nitrate, nitrite, phosphate (10 mL), ammonium (60 mL), colored—Dissolved Organic Matter (cDOM), fluorescence—Dissolved Organic Matter (fDOM) (150 mL), and Dissolved Organic Carbon (DOC) (45 mL) analyses were collected using 0.22 μm pore-size filtered water. Samples for nitrate, nitrite, phosphate, ammonium and DOC were frozen at −4°C.

Chemosynthetic Primary Production *in situ* Experiment

Once water, sediment, and Fe-Mn crusts samples were collected, subsamples were made in triplicate as follows: 60 mL of water, 10 g of sediment and 10 g of Fe-Mn crusts, and a control composed of formaldehyde (37%)—to avoid microbial growth. In all triplicates, 5 μL of ^{14}C were added. Samples were incubated in darkness at 4°C for 12 h for water samples, 24 h for sediment samples, and for 20 h for Fe-Mn crusts. Afterwards, the water samples were filtered using a vacuum pump and 0.22 μm pore-size membrane filters (Millipore, MA). The filters were then kept frozen at −80°C until further analysis. The sediments and Fe-Mn crust incubations were interrupted by adding 200 μl of formaldehyde (37%) and stored at 4°C. All steps were made inside a glove box. The samples were transported from the vessel to the laboratory facilities at Instituto Oceanográfico, at 4°C for further analyses at the Radioisotopes Laboratory. The samples collected for the chemosynthesis experiment are described in **Supplementary Table 2**.

Molecular Biology

Fe-Mn crusts collected by dredging were aseptically taken from the dredge and transferred to a DNA/RNA-free plastic bag. The sediment collected by box corer and subsamples were prepared aseptically. RNA latter was added to the sediments and Fe-Mn crusts samples, which were stored at −80°C until transported to the Instituto Oceanográfico, for DNA and RNA extraction at the Laboratório de Ecologia Microbiana (LECOM). Water samples were collected using a CTD-Rosette (Sea-bird 911 Plus) equipped with 24 Niskin bottles of 5 L each. Water was collected at five or six discrete depths within the water column and center of water masses: 5 m—surface; 100 m—Tropical Water and Deep Chlorophyll Maximum Layer; 400 m—South Atlantic Central Water; 900 m—Antarctic Intermediate Water; 1,600 m—Upper Circumpolar Deep Water; 2,400 m—North Atlantic Deep Water. Triplicate samples of water (1.5 mL) were transferred into cryotubes for flow cytometry, to which 0.1% glutaraldehyde (final concentrations) was added. After 20 min to guarantee fixation, the tubes were flash-frozen in liquid nitrogen and stored at −80°C. Water samples were filtered

for 20 min using a peristaltic pump and 0.22 μm pore-size membrane filters (Sterivex, Millipore, MA) for RNA. Nine liters of water were also filtered for DNA analyses. Latter, RNA was added to the filters, which were stored at −80°C until transport to the Instituto Oceanográfico, Universidade de São Paulo (Brazil), for DNA and RNA extraction at LECOM Laboratory. The samples collected for biological molecular analyses are described in **Supplementary Table 2**. The 0.22 μm pore-size filters were stored to analyze nutrients, cDOM and fDOM, and DOC at the Instituto Oceanográfico. The samples collected for geomicrobiology are described in **Supplementary Table 6**.

CONCLUSIONS

Multidisciplinary data were collected during the Rio Grande Rise cruise (RGR1), including geophysical (using multibeam, sonar, backscatter, chirp, magnetometer), geological (using dredges, box corer, gravity corer), benthic ecology, hydrographic (using CTD, ADCP, L-ADCP), biogeochemical, and geomicrobiological. These data supplement and expand previous environmental studies based on data collected from RGR, and provide essential baseline information needed to understand the geological, tectonic, and oceanographic evolution of the region, the genesis and evolution of the Fe-Mn deposits, and the interactions of ecosystems with the geological and oceanographic parameters measured at RGR, all of which are required for assessments of possible future mining activities. We detected different sediments with particular distribution and unique bottom features such us deep canyons and a main central rift defined by steep scarps. On the Rio Grande Rise, we found crusts pavements and calcarenitic mounds characterized by depressions, stripes, and features similar to terraces.

AUTHOR CONTRIBUTIONS

LJ: Chief Scientist of the Cruise, writing and overall organization. JRH: Co-chief (Geology) and writing. IAY: Co-chief (Geophysics) and writing. MB and KLM: geology and writing. NMB, PVFC, MP, PMT, CLV, MGC, and DMC: biology and writing. SAH, DSM, PFS, and IMMR: geophysics and writing. ADG, HRM, FLN, FRS, and TES: technician support and writing. VHP, CNS, ICAS, PYGS, BJM, and FPB: conceptualization and editing.

ACKNOWLEDGMENTS

We are grateful to the Captain, Officers, and Crew of the NOc Alpha Crucis for their professionalism and dedication to data acquisition. The RGR1 cruise was funded by Fundação de Amparo a Pesquisa do Estado de São Paulo (FAPESP) grant number 14/50820-7 project Marine ferromanganese deposits: a major resource of E-tech elements which is an international collaboration between NERC (UK) and FAPESP (Brazil). Rio Grande Rise was in International Waters at the time of the cruise, so no permission is required to distribute the samples.

SUPPLEMENTARY MATERIAL

The Supplementary Material for this article can be found online at: https://www.frontiersin.org/articles/10.3389/fmars.2019.00252/full#supplementary-material

REFERENCES

Barker, P. F. (1983). Tectonic evolution and subsidence history of the Rio-Grande Rise. *Initial Rep. Deep Sea Drill Project* 72, 953–976. doi: 10.2973/dsdp.proc.72.151.1983

Barker, P. F., Carlson, R. L., Johnson, D. A., Cepek, P., Coulbourn, W., Gambôa, L. A., et al. (1981). Deep sea drilling project leg 72: Southwest Atlantic paleocirculation and Rio Grande Rise tectonics. *Geol. Soc. Am. Bull.* 92, 294–309. doi: 10.1130/0016-7606(1981)92<294:DSDPLS>2.0.CO;2

Benites, M., Millo, C., Hein, J., Nath, B., Murton, B., Galante, D., et al. (2018). Integrated geochemical and morphological data provide insights into the genesis of ferromanganese nodules. *Minerials* 8:488. doi: 10.3390/min8110488

Cavalcanti, J. A. D., Santos, R. V., Lacasse, C. M., Rojas, J. N. L., and Nobrega, M. (2015). "Potential mineral resources of phosphates and trace elements on the Rio Grande Rise, South Atlantic Ocean," in *Nearshore Underwater Mining: Critical Commodities for the Future UMC 2015* (Tampa Bay, FL).

CPRM (2018). Available online at: https://www.cprm.gov.br/publique/Noticias/Brasil-realiza-expedicao-inedita-no-Atlantico-Sul-5027.html (accessed May 8, 2019).

Gamboa, L. A., and Rabinowitz, P. D. (1981). The Rio Grande fracture zone in the western South Atlantic and its tectonic implications. *Earth Planet. Sci. Lett.* 52, 410–418. doi: 10.1016/0012-821X(81)90193-X

Gamboa, L. A., and Rabinowitz, P. D. (1984). The evolution of the Rio Grande Rise in the southwest Atlantic Ocean. *Mar. Geol.* 58, 35–58. doi: 10.1016/0025-3227(84)90115-4

Hein, J. R., Mizell, K., Koschinsky, A., and Conrad, T. A. (2013). Deep-ocean mineral deposits as a source of critical metals for high- and green-technology applications: comparison with land-based resources. *Ore Geol. Rev.* 51, 1–14. doi: 10.1016/j.oregeorev.2012.12.001

Leyden, R., Ludwig, W. J., and Ewing, M. (1971). Structure of continental margin off Punta del Este, Uruguay, and Rio de Janeiro, Brazil. *AAPG Bull.* 55, 2161–2173. doi: 10.1306/819A3E2A-16C5-11D7-8645000102C1865D

Montserrat, F., Guilhon, M., Corrêa, P. V. F., Bergo, N. M., Signori, C. N., Tura, P. M., et al. (2019). Deep-sea mining on the Rio Grande Rise (Southwestern Atlantic): a review on environmental baseline, ecosystem services and potential impacts. *Deep Sea Res. I Oceanogr. Res. Pap.* 145, 31–58. doi: 10.1016/j.dsr.2018.12.007

Conflict of Interest Statement: The authors declare that the research was conducted in the absence of any commercial or financial relationships that could be construed as a potential conflict of interest.

frontiers in Marine Science

ORIGINAL RESEARCH
published: 18 September 2019
doi: 10.3389/fmars.2019.00574

Combining Distribution and Dispersal Models to Identify a Particularly Vulnerable Marine Ecosystem

Rebecca E. Ross[1,2], Edward J. G. Wort[2,3] and Kerry L. Howell[2]*

[1] Institute of Marine Research, Bergen, Norway, [2] School of Biological and Marine Science, University of Plymouth, Plymouth, United Kingdom, [3] Gardline Ltd., Great Yarmouth, United Kingdom

Habitat suitability models are being used worldwide to help map and manage marine areas of conservation importance and scientific interest. With groundtruthing, these models may be found to successfully predict patches of occurrence, but whether all patches are part of a larger interbreeding metapopulation is much harder to assert. Here we use a North Atlantic deep-sea case study to demonstrate how dispersal models may help to complete the picture. *Pheronema carpenteri* is a deep-sea sponge that, in aggregation, forms a vulnerable marine ecosystem in the Atlantic Ocean. Published predictive distribution models from United Kingdom and Irish waters have now gained some support from targeted groundtruthing, but known aggregations are distantly fragmented with little predicted habitat available in-between. Dispersal models were used to provide spatial predictions of the potential connectivity between these patches. As little is known of *P. carpenteri*'s reproductive methods, twenty-four model set-ups with different dispersal assumptions were simulated to present a large range of potential dispersal patterns. The results suggest that up to 53.1% of the total predicted habitat may be reachable in one generation of dispersal from known populations. Yet, even in the most dispersive scenario, the known populations in the North (Hatton-Rockall Basin) and the South (Porcupine Sea Bight) are predicted to be unconnected, resulting in the relative isolation of these patches across multiple generations. This has implications for Ireland's future conservation efforts as they may have to conserve patches from more than one metapopulation. This means that conserving one patch may not demographically support the other, requiring additional attentions to ensure that marine protected areas are ecologically coherent and sustainable. This example serves as a demonstration of a combined modeling approach where the comparison between predicted distribution and dispersal maps can highlight areas with higher conservation needs.

Keywords: *Pheronema carpenteri*, deep sea sponge aggregations, dispersal model, habitat suitability model, vulnerable marine ecosystem, connectivity, metapopulation

OPEN ACCESS

Edited by:
Vincent Lecours, University of Florida, United States

Reviewed by:
Lisa Ann Levin, University of California, San Diego, United States
Erik Simon-Lledó, University of Southampton, United Kingdom

****Correspondence:***
Rebecca E. Ross
Rebecca.Ross@hi.no

Specialty section:
This article was submitted to Deep-Sea Environments and Ecology, a section of the journal Frontiers in Marine Science

Received: *14 June 2019*
Accepted: *29 August 2019*
Published: *18 September 2019*

Citation:
Ross RE, Wort EJG and Howell KL (2019) Combining Distribution and Dispersal Models to Identify a Particularly Vulnerable Marine Ecosystem. Front. Mar. Sci. 6:574. doi: 10.3389/fmars.2019.00574

INTRODUCTION

Habitat suitability models (HSMs) are have growing utility in marine ecology and management (Guisan and Zimmermann, 2000). These models relate species or habitat occurrence data to geographically referenced environmental conditions, providing a means to fill in observational gaps with an occurrence prediction where environmental conditions are known and found to be

similar (Elith and Leathwick, 2009). Such maps can be useful in, for example, the planning of marine protected area (MPA) networks and fishery management (Ross and Howell, 2013), targeting sampling efforts (Martin et al., 2014), and understanding marine ecology (Skov et al., 2008).

While HSMs can perform well, one downfall is their failure to account for animal movement. These correlative models are built on wide-coverage abiotic variables, often derived from satellite data, but usually necessarily omit species interactions and dispersal information due to the lack of available data on relevant scales (Elith and Leathwick, 2009; Thuiller et al., 2015; Yates et al., 2018). Without knowledge of species dispersal abilities or the positioning of potential dispersal barriers, it is impossible to know whether fragmented areas of predicted suitable habitat can be reached by animals from known patches. If known patches are far apart then it is possible that they are not part of the same interbreeding metapopulation [*sensu* Hanski and Gilpin (1991) after Levins (1969)].

Accounting for animal movement is important for sustainable marine management (Cowen and Sponaugle, 2009). The MPA concept relies upon protecting enough of the population to be sustainable, reseeding patches both outside and within the MPAs and allowing the population to persist despite potential destructive activities occurring in surrounding areas (Jones et al., 2007; Ross et al., 2017). If MPAs are positioned across an area thought to represent one metapopulation when in fact there are two, then one or both metapopulations may be insufficiently supported resulting in demographic decline despite best efforts to protect them (Kritzer and Sale, 2004; Sale et al., 2005; Agardy et al., 2011). Consequently, it is wise to reassess any previous distribution predictions, should appropriate animal movement data become available in the future.

Population dynamics attributed to animal movement can be assessed in multiple ways. Classical animal tracking methods may be appropriate for larger motile species, but benthic invertebrates, which are especially suited to HSMs due to having a sessile or limited-mobility adult life stage, are more complex to track due to dispersal predominantly occurring during a larval phase (Levin, 2006; Cowen and Sponaugle, 2009). Population genetics can provide a connectivity assessment showing the relatedness of faunal patches where suitable markers can be identified, but this requires expensive and difficult sampling to collect and process multiple organisms within each patch (Hedgecock et al., 2007). Geochemical tracers are appropriate for animals with calcified structures that persist from their dispersive life stage to adulthood, but again require both physical samples and a means to interpret the geochemical markers that are discovered (Thorrold et al., 2007). Biophysical dispersal models (DMs) integrate known species occurrence and life history data with numerical models of ocean currents to predict the possible pathways of dispersal and infer spatially explicit population connectivity patterns (Werner et al., 2007; Metaxas and Saunders, 2009). As a benefit, these models can be made without physical samples, but ultimately predictions remain unverified, necessitating later groundtruthing using one of the sampling-dependent methods (Cowen and Sponaugle, 2009; Ross et al., 2019).

Cautiously, DMs are gaining popularity in marine ecology. Together with the increase of accessible computational power, the ability to try out multiple scenarios and provide a low-cost best guess, prior to intensive sampling programs, is an attractive proposition (particularly in the deep sea where physical sampling is especially expensive and difficult). For example, simulating dispersal has facilitated the analysis of coral bleaching recovery potential (Bode et al., 2018), the effects of dispersal barriers (Wood et al., 2016), the effects of larval behavior on dispersal potential (North et al., 2008), the discovery of likely larval behaviors (James et al., 2019), and the location of undiscovered populations (Yearsley and Sigwart, 2011).

Given the abilities of both HSMs and DMs, it is now possible to consider habitat distribution and dispersal patterns together. Such studies can highlight the potential for invasive species spread (Inglis et al., 2006; Sullivan et al., 2012), site restoration success (Elsäßer et al., 2013), and identifying spawning sites (Hinrichsen et al., 2016). Although only theoretical until groundtruthing can be completed, this form of combined modeling assessment can also offer some insights into potential metapopulation structure.

This study considers both habitat distribution and dispersal patterns to investigate the potential metapopulation structure of a vulnerable marine ecosystem (VME) found in the deep North Atlantic. VMEs are defined by the international Food and Agriculture Organization (FAO) as communities with attributes which may be considered unique or rare, functionally significant, fragile, having limited recovery potential, or providing structural complexity to the benefit of biodiversity (FAO, 2009). In the Northeast Atlantic, OSPAR (the OSlo PARis commission for the Protection of the Marine Environment of the North-East Atlantic) has defined deep sea sponge aggregations as one such VME (OSPAR, 2010), with this study focusing on aggregations of the hexactinellid sponge *Pheronema carpenteri* (Wyville Thomson, 1869) in United Kingdom and Irish waters (which are themselves explicitly listed as a type of deep sea sponge aggregation VME (OSPAR, 2010)). *Pheronema carpenteri* occurs in high densities (up to 1.5 m^2) at known patches in the Porcupine Seabight (Rice et al., 1990) and the Hatton Rockall Basin (Howell et al., 2014; Neat et al., 2019), with historical records of additional aggregations ("the *Holtenia* grounds," referring to their original name *Holtenia carpenteri*) in the Northern Rockall Trough (Wyville Thomson, 1874). The sponges themselves seem to provide some elevation and shelter to other megabenthic invertebrates, but their presence notably may promote increased abundance and diversity in macrobenthos within their spicule mats (Bett and Rice, 1992). As hexactinellids, these aggregations may also play an important part as a sink in the marine silicon cycle which is thought to influence primary productivity and the carbon cycle (Maldonado et al., 2005; Hendry et al., 2019). Presently aggregations are found between 950 and 1350 m in the study area, beyond the 800 m legal depth limit for EU deep-sea trawl fisheries but, as they occur on gently sloping soft sediment, they could be impacted if this limit were to change. Currently only one MPA is designated for their protection (the Hatton-Rockall Basin Nature Conservation MPA).

Almost nothing is known about the life history of this VME's umbrella species, *P. carpenteri*, but there are some observations which can be used to frame dispersal simulations. Generally, Hexactinellids are currently assumed to be viviparous with lecithotrophic larvae and short planktonic larval durations (PLDs, <24 h), but these assumptions are based on limited observations of only a few species (Leys and Ereskovsky, 2006). The short PLD is only known from one shallow water cave-dwelling species (*Oopsacas minuta* Topsent, 1927; Boury-Esnault et al., 1999) which is unlikely to be representative of these deep-water taxa: deep-sea species are thought to have longer PLDs than their shallow water counterparts (Hilário et al., 2015). Records of "wandering populations" of *P. carpenteri* with juveniles found on the edge of patches (Barthel et al., 1996) may suggest very limited dispersal capabilities, but we have also observed solitary *P. carpenteri* distant from any known patch, suggesting that another more dispersive mode may also be possible. This could be explained by also employing asexual reproduction which is thought to be less common in sponges but is known from some hexactinellids and may even be the dominant form of reproduction for some species (Teixidó et al., 2006). Asexual reproduction takes the form of budding or fragmentation of the adult (Teixidó et al., 2006) which may be less dispersive, but buds have also been collected from the water column (Dayton et al., 2013). Two early texts (Wyville Thomson, 1869; Kent, 1870) on the species (where it is referred to as *Holtenia carpenteri* or *Pheronema greyi*) suggest that *P. carpenteri* may produce gemmules, a method more common in freshwater sponges where a small coated cluster of cells are released (Simpson and Fell, 1974). If this is true, then a more dispersive asexual mode may be possible.

Our previously published HSM in the region shows a potential separation of major *P. carpenteri* aggregation habitat patches in the north and south (Ross and Howell, 2013), posing questions of metapopulation structure and population connectivity. This study utilizes the published HSM and combines it with new DMs to explore:

(a) Whether the predicted habitat patches in the north and south are likely to be connected,
(b) The dispersal considerations for designing sponge VME protection efforts in the region.

MATERIALS AND METHODS

The Study Area and the HSM

In 2013, we published a habitat suitability model for *Pheronema carpenteri* aggregation habitats in United Kingdom and Irish waters, centered around the Rockall Trough (**Figure 1**, Ross and Howell, 2013). The HSM was built in Maxent (version 3.3.3, Phillips et al., 2004, 2006) and based on aggregation [not species, see Howell et al. (2011)] presence data from 222 research transects collected between 1977–2000 (photographic and trawl) and 2005–2011 (photographic and video). The model was driven by topographic variables derived from the General Bathymetric Chart of the Oceans (GEBCO, 2008) at a resolution of 30 arc-seconds (roughly 750 m at this latitude). The HSM was internally evaluated using presence/absence data (repeat splits of 75% training, 25% test data) with an Area Under the Curve of 0.99, and sensitivity 0.96, specificity 0.95, and percent correctly classified 0.95 (the latter three being threshold-dependent metrics based on the best performing threshold that maximizes sensitivity and specificity, 0.19). All assessment metric values were considered to be "excellent" (above 0.9). As a consequence, to the best of our knowledge, and prior to extensive validation, this model is adequate for the purposes of this study [but see other studies on issues with HSM performance metrics and the potential for artificially good performance ratings (Liu et al., 2005; Lobo et al., 2008; Gregr et al., 2019)]. For more information see Ross and Howell (2013).

A subsequent HSM based on high resolution bathymetry (200 m multibeam) tested worse than the GEBCO-based model and predicted a distribution over an area that was 53% larger (Ross et al., 2015). It is possible that the coarser resolution GEBCO model may better reflect the scales of oceanographic drivers that influence these aggregations: Rice et al. (1990) posit that *P. carpenteri* aggregations may be situated proximate to, but not within, areas of enhanced near-bottom velocities that may resuspend organic matter to the sponges feeding advantage. Until further validation data can be collected it remains unknown which prediction is closest to reality, but for the purposes of this study the precautionary principle advises testing the most spatially restricted prediction.

Pheronema carpenteri aggregations were predominantly predicted to occur in the Hatton Rockall Basin (HRB) and the Northern Rockall Trough ("the northern patch"), and around the upper slopes of the Porcupine Seabight (PSB) ("the southern patch", Ross and Howell, 2013, **Figure 1**). The nearest intermediate areas between the southern and northern patches are on the south-eastern slopes of Rockall Bank to the northwest and on the continental slope beside the Hebrides Terrace Seamount to the northeast. The habitat gap is formed by the topographic high of Porcupine Bank, and the topographic lows of the Porcupine Abyssal Plain and the Rockall Trough (**Figure 1**).

The DMs

Dispersal simulations require three components:

- Biological data to parameterize simulations [e.g., release locations, planktonic larval duration, larval growth, behavior in the water column, etc, see Metaxas and Saunders (2009)],
- A hydrodynamic model that supplies current velocity instructions,
- A dispersal simulator that follows the hydrodynamic instructions whilst integrating time and biological parameters.

Biological Parameters

Due to the lack of life history data available for *P. carpenteri*, a suite of biological parameters were used to bracket simulations

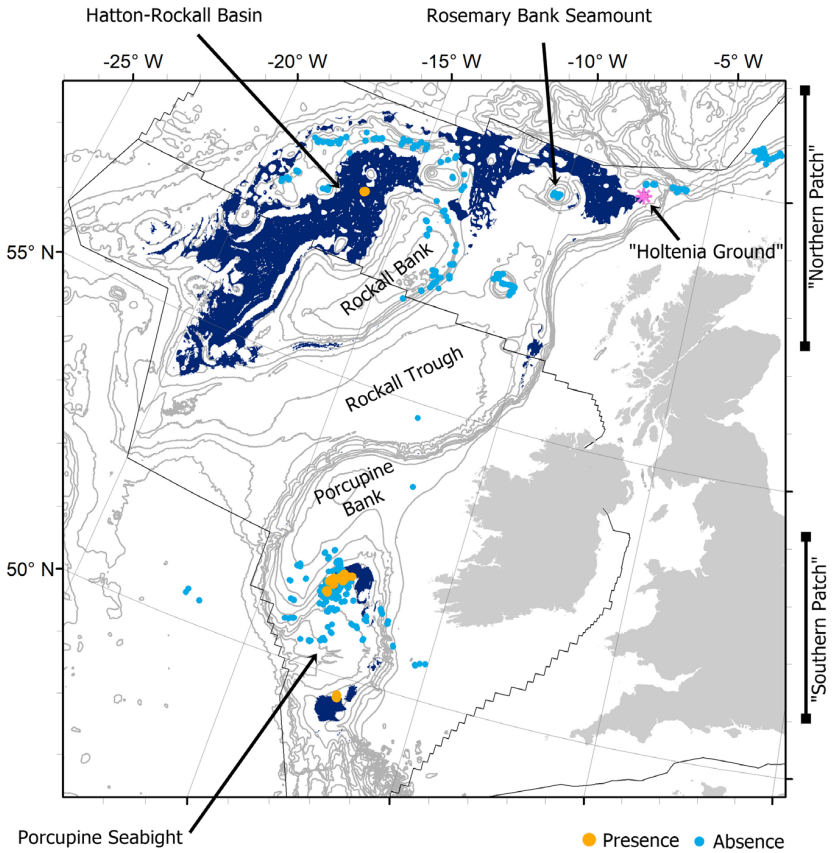

FIGURE 1 | A map of the study area showing the predicted distribution of *Pheronema carpenteri* aggregations in United Kingdom and Irish waters (after Ross and Howell, 2013). The prediction shows all areas where the likelihood of *P. carpenteri* aggregation presence is above 0.19 (a threshold selected to maximize the sensitivity and specificity metrics of assessment). Presence and absence data used to train the HSM (after Ross and Howell, 2013) are shown to contextualize known aggregations. Names of locations mentioned in the text are labeled. Background bathymetry contours from GEBCO show every 200–1000 m depth, then every 500 m. Black lines show the current extent of the United Kingdom and Irish continental shelves within the study area.

into four different potential scenarios (S1–S4) that could be relevant to this species and the habitat it creates:

- S1 – The most retentive simulation (with respect to achievable dispersal distance): Assumed a terrain-hugging dispersal of either an asexual bud or fragment, or a passive cloud of larvae traveling together as released from observed locations. This may be the case if buds, fragments, or larvae are trapped in the bottom boundary layer, are negatively buoyant, or have a positive geotaxis. This may represent the mechanism for the observed wandering populations.
- S2 – Moderate retentive: Assumed a passive non-terrain hugging individual larvae or bud with limited random diffusion away from their cohort, as released from observed locations. The diffusive component is a proxy for either limited random swimming behavior or oceanographic mixing.
- S3 – Moderate dispersive: Echoed the second but parameterized with strong random diffusion away from the cohort. This would represent larvae that swim actively, have a phototaxis, have positive buoyancy, or encounter turbulent oceanographic mixing.
- S4 – The most dispersive: Echoed the high diffusion scenario (S3), but simulated release is from across all predicted suitable habitat (not just releasing from observed locations).

It is possible that there may be very specific active swimming behavior in *P. carpenteri* larvae, e.g., specific times spent at specific depths, but this is impossible to represent without *a priori* information. The random diffusive kicks of different severity in S2 and S3/4 can capture some of this potential and may allow at least the possibility of traversing major topographic barriers to dispersal which is potentially the main dispersive advantage of a vertical migration strategy (Ross et al., 2017). Alternatively, active swimming may have a retentive effect (Cowen et al., 2006), in which case the dispersive predicted dispersal patterns from this study may be more dispersive than is realistic. Either way the bracketed scenarios should capture a realistic range of dispersal patterns given the knowledge that is currently available.

For the purposes of this study two different dispersal simulators were used in order to capture different biological assumptions. The Marine Geospatial Ecology Tools simulator

(MGET) tracks the expansion of a footprint of dispersal so is suited for passive dispersal or consideration of an area of influence (used in S1). The Connectivity Modeling Tools simulator (CMS) is closer to an individual based model tracking each particle independently and allowing the integration of behaviors and random walk patterns (used in S2–S4). The dispersal simulators are explained in more detail in section "The Dispersal Simulators."

Dispersal model release locations were based on both observational data and the HSM. The observations of *P. carpenteri* aggregations that were used to build the HSM were used in S1–S3 as release locations optimized to reflect the horizontal sensitivity of the dispersal simulator (3 km separation). For S4, a regular grid of release locations, spaced at the resolution of the hydrodynamic model (1/12°, see section "The Hydrodynamic Model"), was created to span all predicted areas of suitable habitat according to the HSM. For all release locations see **Supplementary Data**.

It is unknown what temporal pattern may be found in *P. carpenteri* reproduction: whether spawning is possible year-round or follows a seasonal pattern. Both have been observed in hexactinellids (Leys and Ereskovsky, 2006). It therefore seemed prudent to adopt a year-round release frequency, allowing the full range of seasonal variability in dispersal patterns to be captured in predictions. To reduce computational load this was represented as a monthly release of larvae.

A range of PLDs was used to time the simulations in each of the four scenarios. The observed 24 h PLD of the shallow water hexactinellid *Oopsacas minuta* (Boury-Esnault et al., 1999) was considered to be the minimum potential PLD for *P. carpenteri* which is a deep-water species and is therefore likely to spend longer in the water column (Hilário et al., 2015). Simulations within each of the four scenarios were therefore run for 1, 5, 10, 20, 30, and 50 days to capture a range of potential PLDs (totaling 24 model set-ups). Hilário et al. (2015) calculated that the average known PLD of a deep sea organism is 35 days so the range used in this study should span the majority of likely scenarios.

Due to the different natures of the dispersal simulators used the number of larvae released is different for S1 and S2–S4. While in reality the number of larvae released could range anywhere from tens to millions, model simulations are better treated as statistical representations with numbers chosen to capture the range of predicted dispersal directions available in the model. In S1 an initial density of 10 000 particles (theoretical larvae) per km^2 was used as recommended by Treml et al. (2008). In S2–S4, as a balance of computational power and ease of interpretation, 100 particles were released and tracked individually to provide a proportional representation of likely dispersal pathways.

Table 1 shows a summary of the parameterization of each of the four scenarios.

The Hydrodynamic Model

For this study the hydrodynamic model was the freely available Hybrid Coordinate Ocean Model (HYCOM, Chassignet et al., 2007). This is a global model gridded at 1/12° (approx. 8 km), with daily outputs available online spanning 40 depth layers down to 5000 m. Simulations were run using outputs from three selected years (2003, 2007, 2010) to capture extremes of the North Atlantic Oscillation (neutral, positive, and negative, respectively) which may differently affect dispersal predictions (Fox et al., 2016; Ross et al., 2016) and allowed a reduced computational demand.

HYCOM has been tested locally for DM applications with sensitivity testing (Ross et al., 2016) and a model comparison (Ross et al., 2019). Tests showed a broad agreement with dominant current directions and speeds, but a tendency to give over-dispersive predictions due to the absence of tides (typical in large scale models) and the type of algorithm it uses to handle horizontal pressure gradient errors (Ross et al., 2016, 2019). The results are therefore interpreted assuming dispersal is likely to be more restrictive in reality.

The Dispersal Simulators

Two different dispersal simulators were used together with the HYCOM outputs. Each simulator utilizes different assumptions and algorithms. The life history traits of the simulated species should be used to decide what type of simulator is likely to be

TABLE 1 | A parameterization summary of each of the four scenarios (S1–S4) simulated in this study.

	S1	S2	S3	S4
Prediction Level	Retentive	Moderate Retentive	Moderate Dispersive	Dispersive
Short Description	Terrain-hugging, passive, known locations	Escapes BBL, passive, known locations	Escapes BBL, turbulent/active, known locations	Escapes BBL, turbulent/active, predicted locations
Dispersal Simulator	MGET	CMS	CMS	CMS
Release Locations	Observed locations, 3 km separation	Observed locations, 500 m separation	Observed locations, 500 m separation	HSM locations, 8 km separation
No. Particles	10,000/km^2	100	100	100
Diffusivity	1 m^2/s	7 m^2/s horizontal 0 m^2/s vertical	15 m^2/s horiz. 0.05 m^2/s vert.	15 m^2/s horiz. 0.05 m^2/s vert.
Vertical velocities	Excluded	Included	Included	Included
PLD	1, 5, 10, 20, 30 and 50 days			
Release Frequency	Monthly			

Acronyms used are as follows: Marine Geospatial Ecology Tools (MGET), Connectivity Modeling System (CMS), benthic boundary layer (BBL). For more information on dispersal simulators see section "The Dispersal Simulators."

relevant, but in this case a lack of life history data necessitates testing different scenarios to capture a range of possible predicted dispersal abilities.

The Coral Reef Larval Connectivity Model available in the Marine Geospatial Ecology Tools (MGET, Roberts et al., 2010; which is based on Treml et al., 2008) package (version 0.8a52), attached to ArcGIS version 9.3 was used to simulate dispersal within the benthic boundary layer, with particles moving as a spreading cloud or as aggregated chunks (the retentive scenario, S1). Only the HYCOM depth rasters (obtained through MGET) over which the adults have been found in the study area (900–1400 m) were selected. These were then converted into a single terrain-following (sigma) raster using a python batch script which instructed the ArcGIS spatial analyst extension to mosaic the HYCOM rasters ordered from the deepest to shallowest (retaining only the deepest velocity values). Consequently, depths shallower than 900 m were treated as 'land' by the model. Simulations were run in a polar stereographic projection with data gaps filled using ArcGIS's inverse distance weighting interpolation. The MGET simulator has been successfully applied to dispersal predictions of reef fish (Mora et al., 2011), sargassum (Mattio et al., 2013) and an assessment of MPA connectivity (Crochelet et al., 2016) among other studies.

The connectivity modeling system (CMS, Paris et al., 2013) is a standalone Linux-based simulator which was used to statistically represent individual larvae dispersing above the benthic boundary layer (in the three moderate/dispersive scenarios). These simulations, hosted by the University of Plymouth High Performance Computing cluster, were driven by HYCOM z-level outputs. Although HYCOM outputs are not supplied with vertical velocities as standard, these simulations incorporated vertical velocities computed using the continuity equation, allowing some vertical movement in the water column, supplemented by random diffusivity kicks every hour. Among other studies, the CMS simulator has recently been used to: estimate the connectivity of shrimp between management units (Le Corre et al., 2019), track oil spills (Ainsworth et al., 2018) and water masses (Ypma et al., 2019), and assess the deep refugia hypothesis in mesophotic coral ecosystems (Sponaugle and Cowen, 2019).

Analysis

The results of all simulations were visualized in ArcGIS 10.3 for qualitative and semi-quantitative evaluation. S1 daily output rasters were summed to show the predicted dispersal footprint for each of the six PLDs. Matlab was used to convert S2–S4 netcdf outputs into rasters of larval density comparable to the outputs from S1. Raster footprints of dispersal per PLD per scenario were compared with the footprint of suitable habitat from the Ross and Howell (2013) HSM. All rasters were compared at a resolution of 4 km (∼1/2 HYCOM resolution) and projected in Albers Equal Area Conic with modified standard parallels (parallel 1 = 50.2°, parallel 2 = 58.5°).

The percentage overlap between footprints of dispersal and the HSM predicted suitable habitat was calculated as a measure of how much habitat was within reach of one individual (or one generation if considering gene flow from the release location).

The most dispersive scenario, S4, was then evaluated further with the footprints of dispersal from northern and southern populations visualized separately and considered together with predicted larval densities which operates as a proxy for likelihood of connectivity potential.

RESULTS

Maps of predicted larval dispersal under the four scenarios, each with six PLDs, are visualized in **Figure 2** (24 dispersal footprints in total). As expected, scenarios S1–S4 show progressively greater potential distances of dispersal. After 50 days of dispersal the maximum straight-line distance traveled was 140 km (S1, terrain-hugging/passive), 470 km (S2, escape BBL/low diffusion), 695 km (S3, escape BBL/high diffusion), and >700 km (S4, escape BBL/high diffusive/HSM releases; particles exit the model domain).

Table 2 shows the proportions of habitat that could be reached by each dispersal footprint launched from observed populations (S1–S3). While S1 generally predicted a reduced dispersal potential, this terrain hugging strategy may allow a greater proportion of habitat to be reached in 1 day (1.6% as compared to 0.3%) than a dispersal strategy that escapes the benthic boundary layer. After 5 days S2–S3 are consistently more dispersive.

All PLDs in S1 resulted in isolated patches to the north and south of the Rockall Trough, but also within the Porcupine Seabight. If this scenario is realistic then none of the known habitat patches are likely to be connected, potentially representing at least three separate metapopulations.

S2 allowed a more diffuse dispersal, but under this scenario larvae cannot vertically migrate far enough to overcome dispersal barriers such as Rockall Bank and Porcupine Bank. This scenario suggests that all patches in the Porcupine Seabight could be part of the same metapopulation if *P. carpenteri* has a PLD of 20 days or more.

S3 with the added diffusion, permits dispersal over Rockall Bank and Porcupine Bank, suggesting that propagules may possibly be found in shallower shelf and coastal waters at approximately 200m depth (see S1 and S2, **Figure 2**). Under S3 a maximum of 53.1% of habitat can be reached by larvae from known extant populations (**Table 2**), but there is no potential connection either between the north and south patches, nor between the observed Hatton Rockall Basin aggregations and the historic 'Holtenia grounds' in the north-eastern Rockall Trough.

S4 looks positive from the visualization of the dispersal footprints shown in **Figure 2**: where there are clearly larvae with the potential to cross the Rockall Trough and maybe even connect the north and south patches. However, S4 can be re-visualized as shown in **Figure 3**: separating the releases from across predicted suitable habitat in the northern and southern patches and showing densities of larvae that highlight the areas with highest likelihood of connection. From this perspective there is still a strong separation of northern and southern patches. From the southern releases there may be a very low chance of some larvae reaching the southernmost predicted suitable

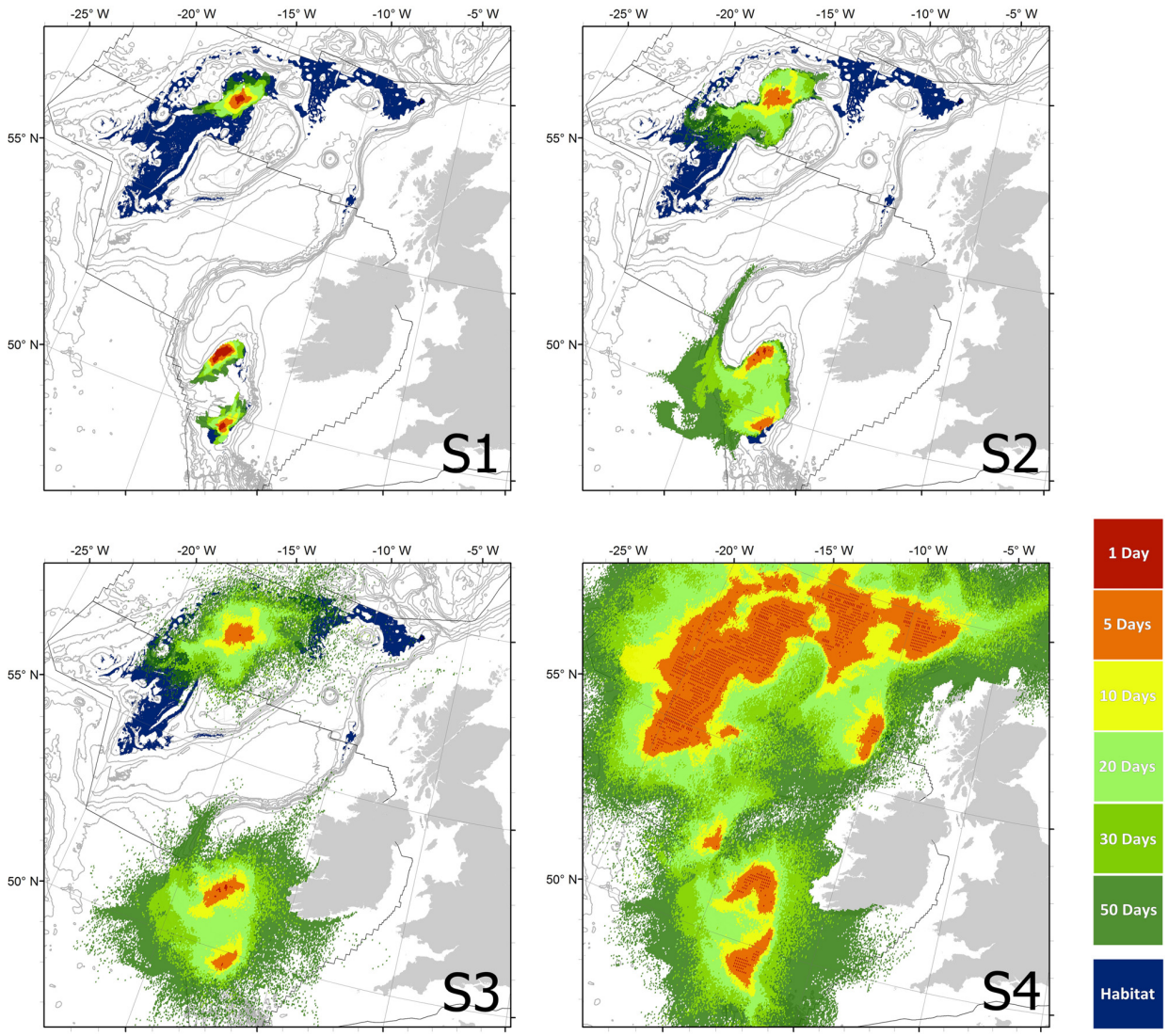

FIGURE 2 | Maps of the four scenarios showing the habitat suitability model (Ross and Howell, 2013) predicted habitat overlaid with the footprints of each of the six Planktonic Larval Durations (PLDs). Background bathymetry contours from GEBCO show every 200–1000 m depth, then every 500 m. Black lines show the current extent of the United Kingdom and Irish continental shelves within the study area.

habitat in the northern patch, but the fact that these appear as isolated pixels of low larval density suggests a high likelihood of error in this prediction. Furthermore, these sparse connections are to ungroundtruthed predicted habitat which may yet be proven unsuitable.

DISCUSSION

Are Predicted Habitat Patches in the North and South Likely to Be Connected?

Dispersal predictions from DMs can help to refine and interpret predictions of suitable habitat. This study shows that the observed aggregations of *Pheronema carpenteri* in the Hatton Rockall Basin and the Porcupine Seabight may be members of separate metapopulations that are unable to support each other with new recruits, even if all predicted habitat is found to be accurate.

While models are by definition imperfect simplifications of reality, the combined issues of these models (DM and HSM) suggest that these predictions are more likely to be overestimates, predicting both more expansive dispersal than is likely, due to lack of tides and diffusive numerical handling of pressure gradient errors within HYCOM (Müller et al., 2010; Ross et al., 2017, 2019), and more suitable habitat than is actually available (Ross and Howell, 2013; Ross et al., 2015).

More recent observations can begin the process of groundtruthing the HSM used in this study. Presence has been confirmed at another location in the northern Hatton

TABLE 2 | The percentage of predicted suitable habitat (after Ross and Howell, 2013) that is overlapped by the dispersal footprint (from **Figure 2**) of each scenario and planktonic larval duration simulated when released from known aggregations.

PLD	S1. Terrain hugging	S2. Low diffusion	S3. High diffusion
1	1.6%	0.3%	0.3%
5	3.8%	5.3%	7.5%
10	6.6%	16.3%	16.5%
20	10.6%	22.5%	29.3%
30	14.1%	31.5%	37.0%
50	17.9%	41.7%	53.1%

S4 is excluded as releases occurred from across the entire habitat suitability model and all PLDs would therefore have 100% overlap.

Rockall Basin (Neat et al., 2019), in line with model predictions. However, a recent survey (RV Celtic Explorer CE15011, 2015, Authors pers. comm) undertook three video transects (of <1 km) in the southern Hatton Rockall Basin finding no *P. carpenteri* where it was predicted, although some associated fauna were present. This limited evidence is insufficient to properly groundtruth the HSM, but notably the bottom temperatures recorded in this southern region (∼4.1°C) were lower than at the known *P. carpenteri* aggregations (5.07–6.41°C; Howell et al., 2014, Authors pers. comm). Therefore, it may be that a minimum temperature around 5°C is necessary to present optimal conditions for aggregation formation in this region. If so, then the sparse predicted connections from southern releases into the northern patch (see **Figure 3**) are even less probable as they would attempt to settle within this too-cold region (see **Supplementary Figure S1** with 5°C isobath approximation). The presence of *P. carpenteri* aggregations has also recently been confirmed on Rosemary Bank Seamount, albeit together with other sponge species (McIntyre et al., 2016); an area not captured by the prediction of the Ross and Howell (2013) HSM. However, the historic Holtenia ground (Wyville Thomson, 1874), which is the type locality for this species (formerly named *Holtenia greyi*), is predicted by the HSM as an area of suitable habitat (but has not been confirmed as an extant presence locality, to our knowledge). A higher resolution model based on multibeam bathymetry and oceanographic layers including temperature is currently in development with the hope of improving upon the existing published HSMs (Ross and Howell, 2013; Ross et al., 2015; Howell et al., 2016).

The DMs will also require groundtruthing in the future. Population genetic sampling of *P. carpenteri* is ongoing in the region and hopefully will eventually be able to confirm whether the predicted isolation of the southern metapopulation is indeed the case. The results of population genetics when compared to these DMs may also help discern more about the likely reproductive modes and timings of *P. carpenteri* and the role of dispersal in any genetic structuring. In the absence of more traditional observation methods, such a comparison can provide information that will better refine future DMs for this VME in other areas.

Notably the HSM and the bathymetry it is based upon are hugely important to the process of targeting new sampling areas, increasing the number of observations of this VME, and informing management decisions. Offshore and deep-water studies, such as this one, remain limited by the expense and difficulty of obtaining samples and observing the seafloor at great depths. Without seafloor mapping, this study, and much of this field of research, would not be possible.

What Are the Implications for Conservation Management in the Region?

The predicted separation of metapopulations in the north (predominantly United Kingdom) and south (predominantly

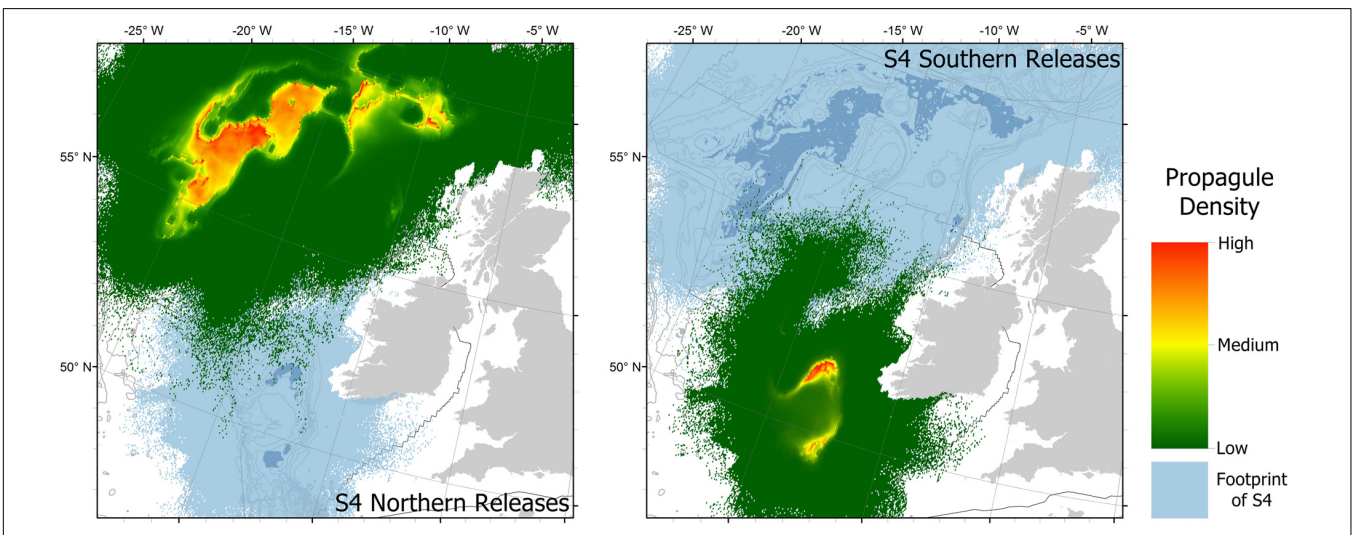

FIGURE 3 | The scenario 4, 50 day Planktonic Larval Duration (PLD) simulations re-visualized showing the full footprint of scenario 4 broken down into those released from the north, and those released from the south. Colors now show densities of larvae rather than PLDs. Background bathymetry contours from GEBCO show every 200–1000 m depth, then every 500 m. Black lines show the current extent of the United Kingdom and Irish continental shelves within the study area.

Ireland) could greatly affect conservation efforts for this species. To ensure that MPA networks are sustainable and ecologically coherent, ideally MPAs should protect a healthy portion of each metapopulation, such that, should the unprotected areas be destroyed, the species will persist and be able to reseed the area. This is made more complicated by national jurisdictions, with the study area spanning the extended exclusive economic zones of both the United Kingdom and Ireland.

In United Kingdom waters there is clear intention to make efforts to conserve this VME in line with OSPAR advice. Currently only one Scottish MPA is designated specifically for the protection of *P. carpenteri* aggregations in the study region [the Hatton Rockall Basin Nature Conservation MPA (NCMPA)], with Rosemary Bank Seamount NCMPA also acknowledging the presence of similar aggregations among other VMEs (McIntyre et al., 2016).

Ireland is yet to protect this VME but has also committed to doing so, as a signatory to OSPAR, and is currently undertaking a major baseline survey effort to inform conservation planning and management ("SeaRover", funded by the European Maritime and Fisheries Fund). When future MPAs are planned for the protection of this VME, Ireland will be faced with the possibility of encountering two separate metapopulations in Irish waters. Should aggregations be found in the Irish Hatton Rockall Basin, their protection cannot be assumed to be supportive of conservation efforts in the southern patch spanning the Porcupine Seabight.

It is possible that the southern metapopulation extends southwards into the Bay of Biscay. The next nearest currently designated MPA containing *P. carpenteri* aggregations is currently Le Danois Bank in the Spanish El Cachucho MPA (Le Danois, 1948; García-Alegre et al., 2014), with the geographic population extending as far south as Morocco if not further. Nearer patches in French waters have been recorded (Guillaumont et al., 2011, 2012) but are also yet to be protected, leaving the Porcupine Seabight population particularly sensitive to future impact without a protected larval supply.

A new EU regulation has banned bottom trawling below 800 m (Regulation (EU) 2016/2336) potentially resulting in the incidental protection of this VME, but the regulation is still being approved at the national level, could be subject to change in the future, and is difficult to enforce over such a large area. Bottom trawling arguably poses the biggest threat to *P. carpenteri* aggregations, which favor gently sloping soft sediment bottoms at continental slope depths (900–1300 m) which can be found proximate to land. The porcupine seabight aggregations already show evidence of bottom trawling through some patches in the past (Vieira, 2017) and have continued proximity to bottom fishing activities (Gerritsen and Lordan, 2011, 2014). It is therefore paramount that bottom trawling remains restricted in areas where this VME is found, with the Porcupine Seabight metapopulation being the most vulnerable to destruction.

Beyond the Case Study

While this study was designed to investigate the implications of habitat fragmentation for one VME in the North Atlantic, it also serves to highlight the need to investigate HSM predictions more closely in general. In datapoor situations HSMs can provide a best guess at species or habitat distribution and extent, but without investigating dispersal or connectivity it can be impossible to know how many interbreeding populations are present across a fragmented habitat. This case study demonstrates that, on occasion, an assumed larger metapopulation can turn out to be more than one, with critical implications for conservation decisions in the future.

DATA AVAILABILITY

All datasets generated for this study are included in the manuscript and/or the **Supplementary Files**.

AUTHOR CONTRIBUTIONS

All authors conceived and developed the idea, and wrote the manuscript. RR and EW carried out the modeling. KH provided the supervision and obtained the funding.

FUNDING

The majority of the work was funded by the University of Plymouth. KH and RR had additional support from the NERC funded DeepLinks project and the EU Seventh Framework Programme EUROFLEETS2. Gardline Ltd. supported EW during writing. The Norwegian Institute of Marine Research supported the writing of this article, and the IMR library covered open access publication fees.

ACKNOWLEDGMENTS

The authors would like to thank their current institutes (RR, Institute of Marine Research; EW, Gardline Ltd.; and KH, University of Plymouth) for supporting the writing of this manuscript, and the University of Plymouth for the rest of the work. The authors would also like to thank Peter Mills at the University of Plymouth High Performance Computing Centre, and the other members of the Deep Sea Conservation Research Unit (CRU) for valuable discussion and support.

SUPPLEMENTARY MATERIAL

The Supplementary Material for this article can be found online at: https://www.frontiersin.org/articles/10.3389/fmars.2019.00574/full#supplementary-material

REFERENCES

Agardy, T., Notarbartolo di Sciara, G., and Christie, P. (2011). Mind the gap: addressing the shortcomings of marine protected areas through large scale marine spatial planning. *Mar. Policy* 35, 226–232. doi: 10.1016/j.marpol.2010.10.006

Ainsworth, C. H., Paris, C. B., Perlin, N., Dornberger, L. N., Patterson, W. F. III, Chancellor, E., et al. (2018). Impacts of the deepwater horizon oil spill evaluated using an end-to-end ecosystem model. *PLoS One* 13:e0190840. doi: 10.1371/journal.pone.0190840

Barthel, D., Tendal, O. S., and Thiel, H. (1996). A wandering population of the hexactineliid sponge pheronema carpenteri on the continental slope off morocco, Northwest Africa. *Mar. Ecol.* 17, 603–616. doi: 10.1111/j.1439-0485.1996.tb00420.x

Bett, B. J., and Rice, A. L. (1992). The influence of hexactinellid sponge (Pheronema carpenteri) spicules on the patchy distribution of macrobenthos in the porcupine seabight (bathyal NE Atlantic). *Ophelia* 36, 217–226. doi: 10.1080/00785326.1992.10430372

Bode, M., Bode, L., Choukroun, S., James, M. K., and Mason, L. B. (2018). Resilient reefs may exist, but can larval dispersal models find them? *PLoS Biol.* 16:e2005964. doi: 10.1371/journal.pbio.2005964

Boury-Esnault, N., Efremova, S., Bézac, C., and Vacelet, J. (1999). Reproduction of a hexactinellid sponge: first description of gastrulation by cellular delamination in the Porifera. *Invertebr. Reprod. Devl.* 35, 187–201. doi: 10.1080/07924259.1999.9652385

Chassignet, E. P., Hurlburt, H. E., Martin Smedstad, O., Halliwell, G. R., Patrick, J. H., Wallcraft, A. J., et al. (2007). The HYCOM (HYbrid coordinate ocean model) data assimilative system. *J. Mar. Syst.* 65, 60–83. doi: 10.1016/j.jmarsys.2005.09.016

Cowen, R. K., Paris, C. B., and Srinivasan, A. (2006). Scaling of connectivity in marine populations. *Science* 311, 522–527. doi: 10.1126/science.1122039

Cowen, R. K., and Sponaugle, S. (2009). Larval dispersal and marine population connectivity. *Annu. Rev. Mar. Sci.* 1, 443–466. doi: 10.1146/annurev.marine.010908.163757

Crochelet, E., Roberts, J., Lagabrielle, E., Obura, D., Petit, M., and Chabanet, P. (2016). A model-based assessment of reef larvae dispersal in the Western Indian Ocean reveals regional connectivity patterns — potential implications for conservation policies. *Reg. Stud. Mar. Sci.* 7, 159–167. doi: 10.1016/j.rsma.2016.06.007

Dayton, P. K., Kim, S., Jarrell, S. C., Oliver, J. S., Hammerstrom, K., Fisher, J. L., et al. (2013). Recruitment, growth and mortality of an antarctic hexactinellid sponge, anoxycalyx joubini. *PLoS One* 8:e56939. doi: 10.1371/journal.pone.0056939

Elith, J., and Leathwick, J. R. (2009). Species distribution models: ecological explanation and prediction across space and time. *Ann. Rev. Ecol. Evol. Syst.* 40, 677–697. doi: 10.1146/annurev.ecolsys.110308.120159

Elsäßer, B., Fariñas-Franco, J. M., Wilson, C. D., Kregting, L., and Roberts, D. (2013). Identifying optimal sites for natural recovery and restoration of impacted biogenic habitats in a special area of conservation using hydrodynamic and habitat suitability modelling. *J. Sea Res.* 77, 11–21. doi: 10.1016/j.seares.2012.12.006

FAO, (2009). *). Paragraph 42. International Guidelines for the Management of Deep-sea Fisheries in the High Seas*. Rome: FAO, 9–10.

Fox, A. D., Henry, L. A., Corne, D. W., and Roberts, J. M. (2016). Sensitivity of marine protected area network connectivity to atmospheric variability. *R. Soc. Open Sci.* 3:160494. doi: 10.1098/rsos.160494

García-Alegre, A., Sánchez, F., Gómez-Ballesteros, M., Hinz, H., Serrano, A., and Parra, S. (2014). Modelling and mapping the local distribution of representative species on the Le Danois Bank, El cachucho marine protected area (Cantabrian Sea). *Dee -Sea Res.* 106, 151–164. doi: 10.1016/j.dsr2.2013.12.012

GEBCO (2008). *General Bathymetric Chart of the Oceans (GEBCO): The GEBCO_08 Grid*. Available at: https://www.gebco.net/data_and_products/gridded_bathymetry_data/documents/gebco_08.pdf (accessed September, 2019).

Gerritsen, H., and Lordan, C. (2011). Integrating vessel monitoring systems (VMS) data with daily catch data from logbooks to explore the spatial distribution of catch and effort at high resolution. *ICES J. Mar. Sci.* 68, 245–252. doi: 10.1093/icesjms/fsq137

Gerritsen, H. D., and Lordan, C. (2014). *Atlas of Commercial Fisheries Around Ireland,* 2 Edn, Ireland: Marine Institute, 59.

Gregr, E. J., Palacios, D. M., Thompson, A., and Chan, K. M. A. (2019). Why less complexity produces better forecasts: an independent data evaluation of kelp habitat models. *Ecography* 42, 428–443. doi: 10.1111/ecog.03470

Guillaumont, B., Van Den Beld, I., Davies, J., and Bayle, C. (2012). *Habitats particuliers des biocénoses du bathyal et de l'abyssal. Sous-région marine Golfe de Gascogne. Evaluation Initiale DCSMM. MEDDE, AAMP, Ifremer, Ref. DCSMM/EI/EE/GDG/29/2012*. 10. Available at: https://www.academia.edu/1864493/Habitats_particuliers_des_bioc%C3%A9noses_du_bathyal_et_de_labyssal_SRM_GDG (accessed September, 2019).

Guillaumont, B., Van den Beld, I. M. J., Davies, J. S., Bayle, C., Bourillet, J.-F., and De Mol, L. (2011). *Vulnerable Marine Ecosystems of the Bay of Biscay (NE Atlantic). The Geohab 2011 conference, Marine Geological and Biological Habitat Mapping, 3-6 May. Special Issue 1 Bulletin of the Geological Society of Finland. Espoo: Geological Survey of Finland*. 46. Available at: http://www.geologinenseura.fi/bulletin/Special_Issue_1_2011/Bulletin_Abstrakt2011_netti.pdf (accessed September, 2019).

Guisan, A., and Zimmermann, N. E. (2000). Predictive habitat distribution models in ecology. *Ecol. Model.* 135, 147–186. doi: 10.1016/S0304-3800(00)00354-9

Hanski, I., and Gilpin, M. (1991). Metapopulation dynamics: brief history and conceptual domain. *Biol. J. Linnean Soc.* 42, 3–16. doi: 10.1111/j.1095-8312.1991.tb00548.x

Hedgecock, D., Barber, P. H., and Edmands, S. (2007). Genetic approaches to measuring connectivity. *Oceanography* 20, 70–79. doi: 10.5670/oceanog.2007.30

Hendry, K. R., Cassarino, L., Bates, S. L., Culwick, T., Frost, M., Goodwin, C., et al. (2019). Silicon isotopic systematics of deep-sea sponge grounds in the North Atlantic. *Q. Sci. Rev.* 210, 1–14. doi: 10.1016/j.quascirev.2019.02.017

Hilário, A., Metaxas, A., Gaudron, S. M., Howell, K. L., Mercier, A., Mestre, N. C., et al. (2015). Estimating dispersal distance in the deep sea: challenges and applications to marine reserves. *Front. Mar. Sci.* 2:6. doi: 10.3389/fmars.2015.00006

Hinrichsen, H.-H., Lehmann, A., Petereit, C., Nissling, A., Ustups, D., Bergström, U., et al. (2016). Spawning areas of eastern baltic cod revisited: using hydrodynamic modelling to reveal spawning habitat suitability, egg survival probability, and connectivity patterns. *Prog. Oceanog.* 143, 13–25. doi: 10.1016/j.pocean.2016.02.004

Howell, K. L., Holt, R., Pulido Endrino, I., and Stewart, H. (2011). When the species is also a habitat: comparing the predictively modelled distributions of Lophelia pertusa and the reef habitat it forms. *Biol. Conserv.* 144, 2656–2665. doi: 10.1016/j.biocon.2011.07.025

Howell, K. L., Huvenne, V., Piechaud, N., Robert, K., and Ross, R. E. (2014). *Analysis of Biological Data From the JC060 Survey of Areas of Conservation Interest in Deep Waters off North and West Scotland*. JNCC Report No. 528. Peterborough: JNCC.

Howell, K. L., Piechaud, N., Downie, A. L., and Kenny, A. (2016). The distribution of deep-sea sponge aggregations in the North Atlantic and implications for their effective spatial management. *Deep Sea Res. Part I Oceanogr. Res. Pap.* 115, 309–320. doi: 10.1016/j.dsr.2016.07.005

Inglis, G. J., Hurren, H., Oldman, J., and Haskew, R. (2006). Using habitat suitability index and particle dispersion models for early detection of marine invaders. *Ecol. Appl.* 16, 1377–1390. doi: 10.1890/1051-0761(2006)016%5B1377:uhsiap%5D2.0.co;2

James, M., Polton, J., Brereton, A., Howell, K., Nimmo-Smith, A., and Knights, A. (2019). Reverse-engineering field-derived vertical distribution profiles to infer larval swimming behaviours. *Proc. Natl. Acad. Sci. U.S.A.* 116, 11818–11823. doi: 10.1073/pnas.1900238116

Jones, G. P., Srinivasan, M., and Almany, G. R. (2007). Population connectivity and conservation of marine biodiversity. *Oceanography* 20, 100–111. doi: 10.5670/oceanog.2007.33

Kent, W. S. (1870). On the "HEXACTINELLIDÆ", or hexradiate spiculed siliceous sponges taken in the 'Norna' expedition off the coast of spain and portugal. with description of new species, and revision of the order. *Mon. Micros. J.* 4, 241–252. doi: 10.1111/j.1365-2818.1870.tb01123.x

Kritzer, J. P., and Sale, P. F. (2004). Metapopulation ecology in the sea: from Levins' model to marine ecology and fisheries science. *Fish Fish.* 5, 131–140. doi: 10.1111/j.1467-2979.2004.00131.x

Le Corre, N., Pepin, P., Han, G., Ma, Z., and Snelgrove, P. V. R. (2019). Assessing connectivity patterns among management units of the newfoundland and labrador shrimp population. *FIrsheries Oceanogr.* 28, 183–202. doi: 10.1111/fog.12401

Le Danois, E. (ed.) (1948). *Les Profondeurs de la mer*. Paris: Payot, 303.

Levin, L. A. (2006). Recent progress in understanding larval dispersal: new directions and digressions. *Integr. Comp. Biol.* 46, 282–297. doi: 10.1093/icb/icj024

Levins, R. (1969). Some demographic and genetic consequences of environmental heterogeneity for biological control. *Bull. Entomol. Soc. Am.* 15, 237–240. doi: 10.1093/besa/15.3.237

Leys, S. P., and Ereskovsky, A. V. (2006). Embryogenesis and larval differentiation in sponges. *Can. J. Zool.* 84, 262–287. doi: 10.1139/Z05-170

Liu, C., Berry, P. M., Dawson, T. P., and Pearson, R. G. (2005). Selecting thresholds of occurrence in the prediction of species distributions. *Ecography* 28, 385–393. doi: 10.1111/j.0906-7590.2005.03957.x

Lobo, J. M., Jiménez-Valverde, A., and Real, R. (2008). AUC: a misleading measure of the performance of predictive distribution models. *Global Ecol. Biogeogr.* 17, 145–151. doi: 10.1111/j.1466-8238.2007.00358.x

Maldonado, M., Carmona, M. C., Velásquez, Z., Puig, A., Cruzado, A., López, A., et al. (2005). Siliceous sponges as a silicon sink: an overlooked aspect of benthopelagic coupling in the marine silicon cycle. *Limnol. Oceanogr.* 50, 799–809. doi: 10.4319/lo.2005.50.3.0799

Martin, C. S., Giannoulaki, M., De Leo, F., Scardi, M., Salomidi, M., Knittweis, L., et al. (2014). Coralligenous and maërl habitats: predictive modelling to identify their spatial distributions across the Mediterranean Sea. *Sci. Rep.* 4:5073. doi: 10.1038/srep05073

Mattio, L., Zubia, M., Loveday, B., Crochelet, E., Duong, N., Payri, C. E., et al. (2013). Sargassum (*Fucales*, *Phaeophyceae*) in mauritius and réunion, western Indian Ocean: taxonomic revision and biogeography using hydrodynamic dispersal models. *Phycologia* 52, 578–594. doi: 10.2216/13-150.1

McIntyre, F. D., Drewery, J., Eerkes-Medrano, D., and Neat, F. C. (2016). Distribution and diversity of deep-sea sponge grounds on the Rosemary Bank Seamount, NE Atlantic. *Mar. Biol.* 163:143. doi: 10.1007/s00227-016-2913-z

Metaxas, A., and Saunders, M. (2009). Quantifying the "bio-" components in biophysical models of larval transport in marine benthic invertebrates: advances and pitfalls. *Biol. Bull.* 216, 257–272. doi: 10.1086/BBLv216n3p257

Mora, C., Treml, E. A., Roberts, J., Crosby, K., Roy, D., and Tittensor, D. P. (2011). High connectivity among habitats precludes the relationship between dispersal and range size in tropical reef fishes. *Ecography* 35, 89–96. doi: 10.1111/j.1600-0587.2011.06874.x

Müller, M., Haak, H., Jungclaus, J. H., Sündermann, J., and Thomas, M. (2010). The effect of ocean tides on a climate model simulation. *Ocean Model.* 35, 304–313. doi: 10.1016/j.ocemod.2010.09.001

Neat, F. C., Jamieson, A. J., Stewart, H. A., Narayanaswamy, B. E., Collie, N., Stewart, M., et al. (2019). Visual evidence of reduced seafloor conditions and indications of a cold-seep ecosystem from the Hatton–Rockall basin (NE Atlantic). *J. Mar. Biol. Assoc. U.K.* 99, 271–277. doi: 10.1017/S0025315418000115

North, E. W., Schlag, Z., Hood, R. R., Li, M., Zhong, L., Gross, T., et al. (2008). Vertical swimming behavior influences the dispersal of simulated oyster larvae in a coupled particle-tracking and hydrodynamic model of Chesapeake Bay. *Mar. Ecol. Progress Series* 359, 99–115. doi: 10.3354/meps07317

OSPAR, (2010). *Background Document for Deep-Sea Sponge Aggregations. OSPAR Biodiversity and Ecosystems Series 47*. Available at: https://www.ospar.org/documents?d=7234 (accessed August 2019).

Paris, C. B., Helgers, J., van Sebille, E., and Srinivasan, A. (2013). Connectivity modeling system: a probabilistic modeling tool for the multi-scale tracking of biotic and abiotic variability in the ocean. *Environ. Mod. Softw.* 42, 47–54. doi: 10.1016/j.envsoft.2012.12.006

Phillips, S. J., Anderson, R. P., and Shapire, R. E. (2006). Maximum entropy modeling of species geographic distributions. *Ecol. Mod.* 190, 231–259. doi: 10.1016/j.ecolmodel.2005.03.026

Phillips, S. J., Dudík, M., and Schapire, R. E. (2004). "A Maximum Entropy Approach to Species Distribution Modeling," in *Proceedings of the Twenty-First International Conference on Machine Learning*, (New York, NY: ACM), 655–662.

Rice, A. L., Thurston, M. H., and New, A. L. (1990). Dense aggregations of a hexactinellid sponge, Pheronema carpenteri, in the Porcupine Seabight (northeast Atlantic Ocean), and possible causes. *Prog. Oceanog.* 24, 179–196. doi: 10.1016/0079-6611(90)90029-2

Roberts, J. J., Best, B. D., Dunn, D. C., Treml, E. A., and Halpin, P. N. (2010). Marine geospatial ecology tools: an integrated framework for ecological geoprocessing with ArcGIS, Python, R, MATLAB, and C++. *Environ. Mod. and Softw.* 25, 1197–1207. doi: 10.1016/j.envsoft.2010.03.029

Ross, R. E., and Howell, K. L. (2013). Use of predictive habitat modelling to assess the distribution and extent of the current protection of 'listed' deep-sea habitats. *Divers. Distrib.* 19, 433–445. doi: 10.1111/ddi.12010

Ross, R. E., Nimmo-Smith, W. A. M., and Howell, K. L. (2016). Increasing the depth of current understanding: sensitivity testing of deep-sea larval dispersal models for ecologists. *PLoS One* 11:e0161220. doi: 10.1371/journal.pone.0161220

Ross, R. E., Nimmo-Smith, W. A. M., and Howell, K. L. (2017). Towards 'ecological coherence': assessing larval dispersal within a network of existing marine protected areas. *Deep Sea Res. Part I* 126, 128–138. doi: 10.1016/j.dsr.2017.06.004

Ross, R. E., Nimmo-Smith, W. A. M., Torres, R., and Howell, K. L. (2019). Modelling marine larval dispersal: a cautionary deep-sea tale for ecology and conservation. *Boirxiv*

Ross, L. K., Ross, R. E., Stewart, H. A., and Howell, K. L. (2015). The influence of data resolution on predicted distribution and estimates of extent of current protection of three 'listed' deep-sea habitats. *PLoS One* 10:e0140061. doi: 10.1371/journal.pone.0140061

Sale, P. F., Cowen, R. K., Danilowicz, B. S., Jones, G. P., Kritzer, J. P., Lindeman, K. C., et al. (2005). Critical science gaps impede use of no-take fishery reserves. *Trends Ecol. Evol.* 20, 74–80. doi: 10.1016/j.tree.2004.11.007

Simpson, T. L., and Fell, P. E. (1974). Dormancy among the porifera: gemmule formation and germination in fresh-water and marine sponges. *Trans. Am. Microsc. Soc.* 93, 544–577. doi: 10.2307/3225157

Skov, H., Humphreys, E., Garthe, S., Geitner, K., Grémillet, D., Hamer, K. C., et al. (2008). Application of habitat suitability modelling to trackingdata of marine animals as a means of analysing their feeding habitats. *Ecol. Mod.* 212, 504–512. doi: 10.1016/j.ecolmodel.2007.11.006

Sponaugle, S., and Cowen, R. K. (2019). "Coral Ecosystem Connectivity Between Pulley Ridge and the Florida Keys," in *Mesophotic Coral Ecosystems. Coral Reefs of the World*, Vol. 12, eds Y. Loya, K. Puglise, and T. Bridge, (Switzerland: Springer), 897–907. doi: 10.1007/978-3-319-92735-0_46

Sullivan, M. J. P., Davies, R. G., Reino, L., and Franco, A. M. A. (2012). Using dispersal information to model the species–environment relationship of spreading non-native species. *Methods Ecol. Evol.* 3, 870–879. doi: 10.1111/j.2041-210X.2012.00219.x

Teixidó, N., Gili, J.-M., Uriz, M.-J., Gutt, J., and Arntz, W. E. (2006). Observations of asexual reproductive strategies in Antarctic hexactinellid sponges from ROV video records. *Deep Sea Res. II* 53, 972–984. doi: 10.1016/j.dsr2.2006.02.008

Thorrold, S. R., Zacherl, D. C., and Levin, L. A. (2007). Population connectivity and larval dispersal using geochemical signatures in calcified structures. *Oceanography* 20, 80–89. doi: 10.5670/oceanog.2007.31

Thuiller, W., Pollock, L. J., Gueguen, M., and Münkemüller, T. (2015). From species distributions to meta-communities. *Ecol. Lett.* 18, 1321–1328. doi: 10.1111/ele.12526

Treml, E. A., Halpin, P. N., Urban, D. L., and Pratson, L. F. (2008). Modeling population connectivity by ocean currents, a graph-theoretic approach for marine conservation. *Landsc. Ecol.* 23, 19–36. doi: 10.1007/s10980-007-9138-y

Vieira, R. P. (2017). *Functioning and vulnerability of continental slope ecosystems: combining stable isotope and visual survey approaches*. Ph.D. Thesis, University of Southampton: Southampton, 158.

Werner, F. E., Cowen, R. K., and Paris, C. B. (2007). Coupled biological and physical models: present capabilities and necessary developments for future studies of population connectivity. *Oceanography* 20, 54–69. doi: 10.5670/oceanog.2007.29

Wood, S., Baums, I. B., Paris, C. B., Ridgwell, A., Kessler, W. S., and Hendy, E. J. (2016). El Niño and coral larval dispersal across the eastern pacific marine barrier. *Nat. Commun.* 7:12571. doi: 10.1038/ncomms12571

Wyville Thomson, C. (1869). On holtenia, a genus of vitreous sponges. *Proc. R. Soc. Lond.* 18, 114–122. doi: 10.1098/rspl.1869.0010

Wyville Thomson, C. (1874). *Depths of the Sea*. London: Macmillan and co, 527.

Yates, K. L., Bouchet, P. J., Caley, M. J., Mengersen, K., Randing, C. F., Parnell, S., et al. (2018). Outstanding challenges in the transferability of ecological models. *Tends Ecol. Evol.* 33, 790–802. doi: 10.1016/j.tree.2018.08.001

Yearsley, J. M., and Sigwart, J. D. (2011). Larval transport modeling of deep-sea invertebrates can aid the search for undiscovered populations. *PLoS One* 6:e23063. doi: 10.1371/journal.pone.0023063

Ypma, S. L., Brüggemann, N., Georgiou, S., Spence, P., Dijkstra, H. A., Pietrzak, J. D., et al. (2019). Pathways and watermass transformation of Atlantic water entering the nordic seas through denmark strait in two high resolution ocean models. *Deep Sea Res. Part I* 145, 59–72. doi: 10.1016/j.dsr.2019.02.002

Conflict of Interest Statement: EW was employed by the company Gardline Ltd. at the time of writing, but Gardline Ltd. did not have any influence on the undertaking of this study.

The remaining authors declare that the research was conducted in the absence of any commercial or financial relationships that could be construed as a potential conflict of interest.

frontiers in Marine Science

ORIGINAL RESEARCH
published: 26 November 2019
doi: 10.3389/fmars.2019.00708

Strategy for Detection and High-Resolution Characterization of Authigenic Carbonate Cold Seep Habitats Using Ships and Autonomous Underwater Vehicles on Glacially Influenced Terrain

Terje Thorsnes[1,2], Shyam Chand[1,2], Harald Brunstad[3], Aivo Lepland[1,2] and Petter Lågstad[4]*

[1] Marine Geology, Geological Survey of Norway, Trondheim, Norway, [2] Centre for Arctic Gas Hydrate, Environment and Climate, University of Tromsø, Tromsø, Norway, [3] Lundin Norway AS, Oslo, Norway, [4] Norwegian Defence Research Establishment, Kjeller, Norway

OPEN ACCESS

Edited by:
Vincent Lecours, University of Florida, United States

Reviewed by:
Garrett Mitchell, Fugro, United States
Veerle Ann Ida Huvenne, National Oceanography Centre, United Kingdom

***Correspondence:**
Terje Thorsnes
terje.thorsnes@ngu.no

Specialty section:
This article was submitted to Deep-Sea Environments and Ecology, a section of the journal Frontiers in Marine Science

Received: *16 June 2019*
Accepted: *04 November 2019*
Published: *26 November 2019*

Citation:
Thorsnes T, Chand S, Brunstad H, Lepland A and Lågstad P (2019) Strategy for Detection and High-Resolution Characterization of Authigenic Carbonate Cold Seep Habitats Using Ships and Autonomous Underwater Vehicles on Glacially Influenced Terrain. Front. Mar. Sci. 6:708. doi: 10.3389/fmars.2019.00708

Cold seep habitats with authigenic carbonates and associated chemosynthetic communities in glacially influenced terrains constitute an important part of the benthic ecosystems, but they are difficult to detect in large-scale seabed surveys. The areas they occupy are normally small, and survey platforms and sensors allowing high-resolution spatial characterization are necessary. We have developed a cold seep habitat mapping strategy that involves both ship and autonomous underwater vehicle (AUV) as platforms for multibeam echosounder, synthetic aperture sonar (SAS) and a digital photo system. Water column data from the shipborne multibeam echosounder data are initially used to detect gas flares resulting from fluid flow from the seabed. The next phase involves mapping of flare areas by SAS, mounted on an AUV. This yields an acoustic image with a resolution up to 2 cm over a swath of c. 350 m, allowing detection of seep-related features on the seabed. The last phase involves digital photographing of the seabed, with the AUV moving close to the seabed, allowing recognition of bubble streams, seep-related features and giving a first order documentation of the fauna. The strategy was applied to a 3775 km^2 large area on the continental shelf, northern Norway. This is a passive continental margin, with thick deposits of oil- and gas-bearing sedimentary rocks. Extensive faulting and tilting of layers provide potential conduits for fluid flow. The seabed is glacially influenced with a highly variable backscatter reflectivity. More than 200 gas flares have been identified, and a similar number of cold seep habitats have been characterized in high spatial detail. Two case studies are shown. In the first area, there is a close spatial relation between active gas seepage and carbonate crust fields. The second case study shows that carbonate crust fields are not necessarily spatially associated with currently active seeps, but represent dormant or formerly active gas

expulsion. An important finding is that the bathymetric resolution of shipborne multibeam echosounders will often be too low to detect cold seep habitats. This means that a nested multi-resolution approach involving a multitude of platforms and sensors is required to provide the full picture.

Keywords: cold seep habitat, authigenic carbonate crusts, high-resolution, autonomous underwater vehicle, synthetic aperture sonar, water column backscatter data, gas flares

INTRODUCTION

Cold seeps are found ubiquitously at oceanic margins and are characterized by the transport of fluids including dissolved compounds to the ocean through sediments (Campbell, 2006; Hovland, 2007; Suess, 2014). The compounds provide the bioactive reductants sulfide, methane and hydrogen, sustaining ecosystems (Suess, 2014). The surficial expression of cold seeps at the seafloor varies considerably, reflecting differences in mechanisms generating the fluids, the fluid migration pathways, and sedimentary and hydrodynamic conditions at the seafloor (Naudts et al., 2006; Klaucke et al., 2008, 2010). Cold seeps are commonly associated with areas with sub-seafloor hydrocarbon reservoirs (Hovland et al., 1993; Milkov and Sassen, 2003). Numerous cold seeps occur on the Norwegian continental shelf (Bünz et al., 2012; Crémière et al., 2016; Andreassen et al., 2017; Chand et al., 2017; Panieri et al., 2017). Pockmarks, mud diapirs, bacterial mats and methane-derived carbonates are commonly associated with cold seeps (Hovland and Judd, 1988). Pockmark formation depends on the fluid flow to be sufficiently strong through a sufficiently fine-grained sediment (Cathles et al., 2010). Precipitation of methane-derived authigenic carbonates is caused by elevated carbonate alkalinity due to anaerobic oxidation of methane (Aloisi et al., 2002; Naehr et al., 2007). The authigenic carbonates form at or near the surface (Greinert et al., 2001), and are exposed due to subsequent erosion. They may form three-dimensional rock structures, creating a unique habitat (Levin et al., 2015).

Acoustic characteristics of cold seeps and methods for mapping have been described by e.g., Orange et al., 2002; Johnson et al., 2003; Naudts et al., 2008; Wagner et al., 2013; Mitchell et al., 2018, and Paull et al., 2015. These studies are from non-glaciated areas where relatively fine-grained sediments with low backscatter reflectivity surround seep-related features with either high backscatter reflectivity or topographically rough seabed. This is in contrast to this study, where the seabed is characterized by highly variable backscatter reflectivity and rough topography.

Many studies rely upon surface-based single beam or multibeam bathymetry/backscatter in combination with side-scan sonars, and ROVs or video sleds for finding and studying cold seep habitats. In this paper, we want to demonstrate that the combination of shipborne bathymetry, backscatter and water column data, in combination with AUV-mounted very high resolution synthetic aperture sonar (SAS) data and optical sensors provide unprecedented possibilities to screen large areas, find objects of interest, and give a detailed characterization of cold seep habitats in an effective way.

GEOLOGICAL SETTING

The study area (northern part of Nordvestbanken, the Håkjerringdjupet glacial trough and the southern part of Fugløybanken – **Figure 1**) is located in the southwestern part of the Barents Sea (Eldholm et al., 1984). Mesozoic and Cenozoic sedimentary rocks, hydrocarbon-bearing in some strata, accumulated in intracratonic basins, with deposition shifting to the continental margin in the west following the early Eocene opening of the Norwegian Sea (Spencer et al., 1984). The seafloor morphology of the Barents Sea is shaped by repeated glaciations since the late Pliocene and during the Pleistocene. The thickness of the ice sheet has been modeled to be 750–1000 m during the Last Glacial Maximum (Siegert et al., 2001). The ice sheet retreated from the region c. 18,000–20,000 years ago. The ice sheets have extended beyond the shelf edge in the south western Barents Sea several times (Vorren et al., 1991; Laberg et al., 2010, 2012) and formed many erosional channels.

The Håkjerringdjupet trough is one of these large channels (**Figure 1**). The trough is c. 100 km long, 20–40 km wide, average depth is c. 300 m and the deepest part is c. 410 m. The trough is located between two major banks – the Nordvestbanken bank in the south, and the Fugløybanken bank in the northwest. Extensive glacitectonism occurred during glacial advances in the Håkjerringdjupet trough (Winsborrow et al., 2016).

Jurassic to Eocene sedimentary rocks subcrop under the Quaternary deposits in the central parts of the trough, while Precambrian basement rocks, and Paleozoic to Triassic sedimentary rocks subcrop in the eastern, innermost parts, and Pliocene sedimentary rocks subcrop in the western, outermost parts (Sigmond, 1992). Oil and gas reservoirs have been found in these sequences north of this area. The Troms-Finnmark Fault Complex crosses the area, separating the structural domains of Harstad Basin in the west and the Finnmark Platform in the east. The fault systems in combination with dipping sedimentary strata provide conduits for gas leaking from underlying gas bearing sedimentary rocks (Crémière et al., 2018). Gas flares fueled from these conduits are abundant. Dating of methane-derived carbonate crusts associated with these flares shows ages between 13.8 $\pm$ 0.8 and 0.99 $\pm$ 0.3 kyr, with an apparent clustering between 7 and 13 kyr (Crémière et al., 2018). These ages are consistent with the model proposed by Crémière et al. (2016), where crust formation is associated with gradual dissociation of

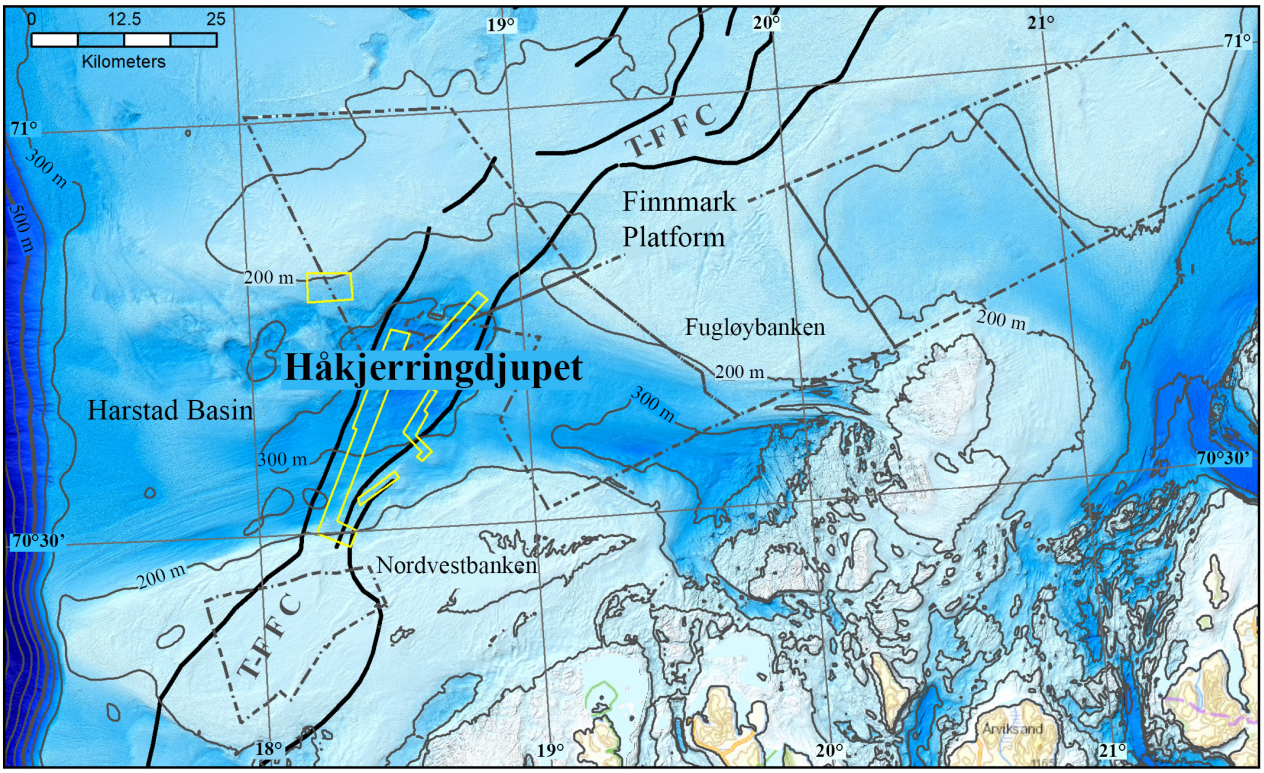

FIGURE 1 | The Håkjerringdjupet study area. Black lines – faults within the Troms-Finnmark Fault Complex (T-F F C). Stippled gray lines – extent of MAREANO multibeam data. Yellow lines – extent of other multibeam data.

methane hydrates following the deglaciation after the collapse of the Scandinavian Ice Sheet at around 16–17 kyr BP.

MATERIALS AND METHODS

This study benefited from data sets collected by the MAREANO programme[1] in 2010 and data sets collected in a cooperation project between Lundin Norway, the Geological Survey of Norway, and the Norwegian Defence Research Establishment during two cruises in 2013 and 2014 (Chand et al., 2015). Ships, an AUV and a remotely operated vehicle (ROV) were used as platforms for a variety of acoustic, optical and chemical sensors in different cruises. The results from the ROV investigations have been reported by Crémière et al. (2018).

The majority of the shipborne multibeam echosounder data (bathymetry, backscatter, water column) were collected by the MAREANO programme (see text footnote 1), while smaller data sets were collected later by the Norwegian Defence Research Establishment. Prior to the acquisition of the MAREANO dataset (performed by the company FOSAE) a patch test was performed which fulfilled the technical specifications of the Norwegian Hydrographic Service (responsible within the MAREANO programme for bathymetry, backscatter, water column and sub bottom profiler data acquisition). Sound velocity profiles were taken regularly. As an example, 85 SVPs were collected from one of the survey areas, where a total of 323 line segments were collected to cover 567 km^2. No backscatter calibration was performed. During all surveys the Kongsberg Maritime EM710 multibeam echosounder was used. This echosounder has an operating frequency of 70–100 kHz. The bathymetry data was processed to a grid size of 2 m, and the backscatter data was processed to a grid size of 0.9 m. Water column data was processed using Fledermaus Midwater software. Available echosounder data with water column registrations are shown in **Figure 1**, covering an area of 3775 km^2.

Additional data sets were collected with the HUGIN HUS AUV, produced by Kongsberg Maritime[2]. The deployed one-of-a-kind experimental research AUV was equipped with non-standard sensors and has the possibility to change the angle of the HiSAS 1030 RX array (see below for description of the HiSAS 1030). The AUV is 5.6 m long, with a diameter of 0.75 m, a dry weight of 1000 kg and can operate down to 3000 m water depth. The AUV is normally launched from the stern of the ship (**Figure 2**), where it is stored and maintained in a dedicated container. It is equipped with inertial navigation and HiPap positioning (an USBL system from Kongsberg Maritime) from the mothership.

[1]www.mareano.no

[2]www.kongsberg.com/maritime/

FIGURE 2 | Launch of the HUGIN HUS AUV from the aft of the ship.

The HUGIN AUV was equipped with the following payloads: (1) An EdgeTech 2200 high resolution 2–12 kHz chirp sub-bottom profiler (SBP), (2) high-resolution interferometric SAS (HiSAS 1030), (3) Methane Sniffer, (4) Temperature, turbidity and salinity sensors, (5) B&W digital photo camera.

The HISAS 1030 is a high resolution interferometric SAS system capable of providing very high-resolution imagery and detailed micro-bathymetry of the seabed. The sensor is a wideband SAS sonar with frequency range of 70–100 kHz with 30 kHz bandwidth. The system has a range-independent resolution of approximately 3 × 3 cm out to a distance of 200 m from both sides of the AUV at a speed of 2 m/s (see text footnote 2). The flight height was typically 40 ± 10 m. The SAS data were processed onboard using the Kongsberg FOCUS software, with a grid size of 20 cm for the bathymetry, and 5 cm for the imagery. For an overview of principles and processing steps for the SAS data, please see Ødegård et al. (2018), who used the same equipment for archeological investigations in the North Sea. Onboard processed high-resolution mosaics in geotiff format were available for inspection in the Kongsberg Reflection and/or ESRI ArcMap softwares within 10 h of HUGIN recovery. Micro-bathymetry data from Area 1 was available after 24 h.

The TFish B&W camera provided very high resolution images (pixel size 6–8 mm) and photo mosaics (pixel size 10 mm) of the seafloor. The flight height for the AUV was typically 5–7 m, with photos taken every second. The TFish images were available co-registered with the SAS data within hours through the Reflection software system on-board HU Sverdrup. A georeferenced photomosaic was also available.

RESULTS

Interpretation of the water column data from a total of 3775 km^2 resulted in identification of 210 gas flares (Chand et al., 2017; Crémière et al., 2018). **Figure 3A** shows a subsection of this area, with 103 flare observations in an area of 370 km^2. In some of the locations, there are several gas flares grouped together as a cluster, so the number of 210 is a minimum estimate. The distinction between single gas flares and gas flare clusters is based on the distance between individual flares. If gas flares occur within a distance of c. 30 m or less of each other, they are considered to form a cluster (**Figure 3B**). The average density is about 55 gas flares pr. 1.000 km^2, but the distribution is uneven, and groups of gas flares and/or gas flare clusters are commonly found (**Figure 3A**). Some of the flare groups tend to be aligned with

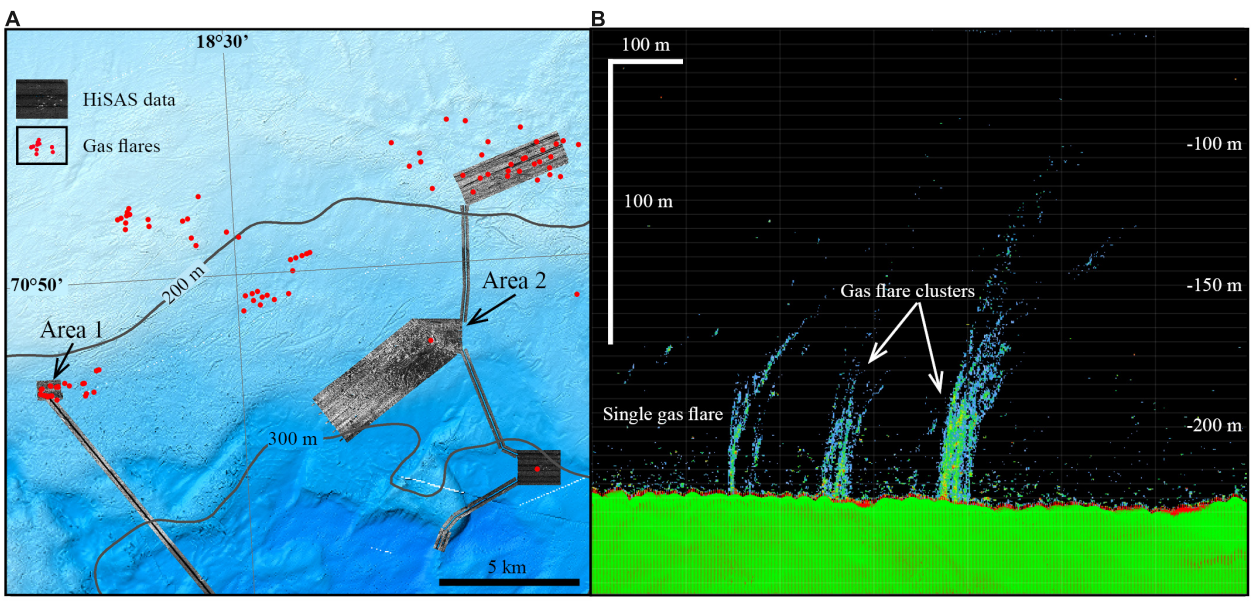

FIGURE 3 | (A) Gas flares and synthetic aperture sonar data. **(B)** Side view of multibeam echosounder line showing a single gas flare and two gas flare clusters. The gas flare clusters correspond to the two carbonate crust fields shown in **Figure 5**.

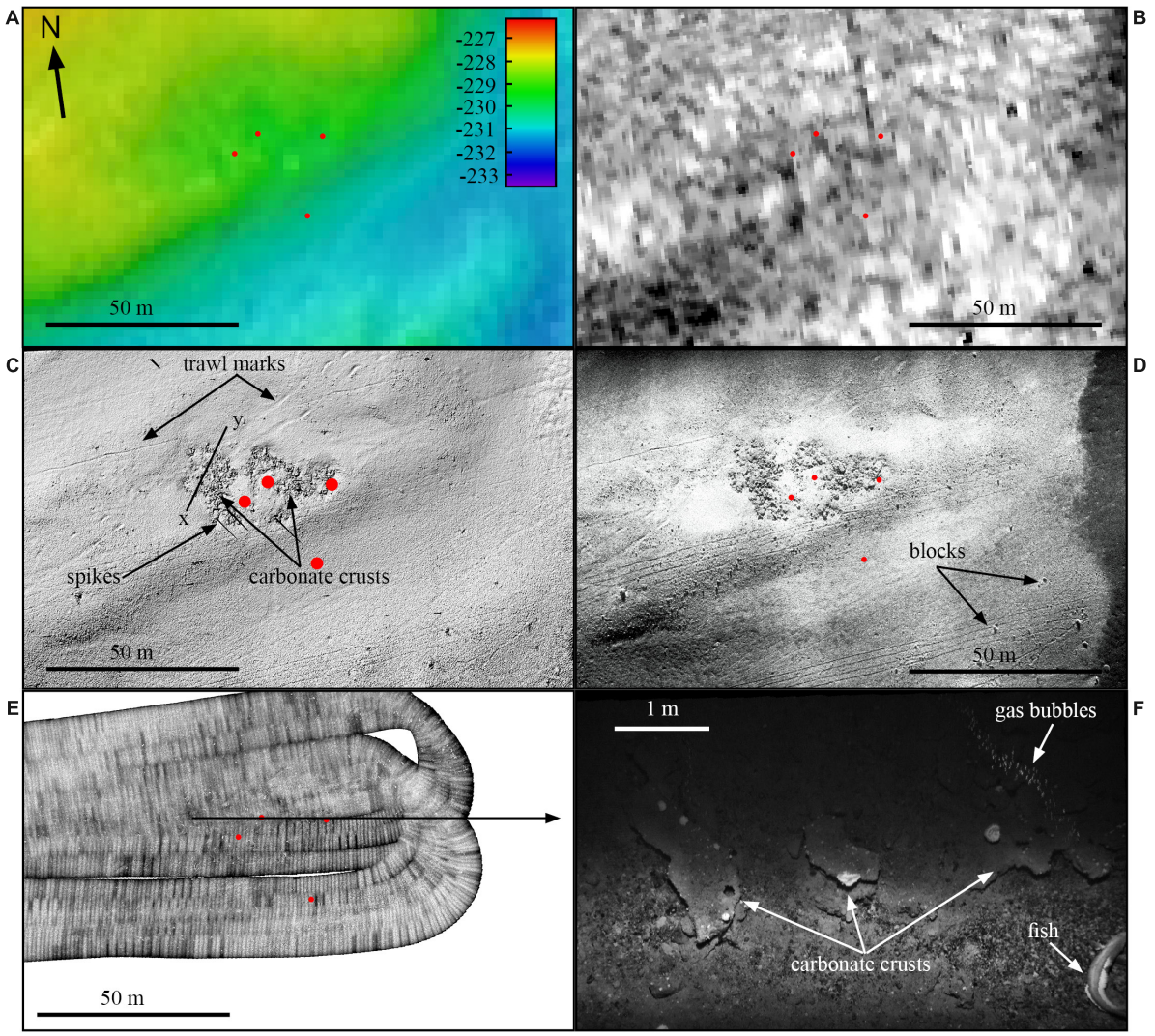

FIGURE 4 | Examples of different sensors from a subsection in Area 1 – see **Figure 5** for location. **(A)** Ship-based multibeam bathymetry. Red dots show gas flares. **(B)** Ship-based backscatter. High backscatter – lighter tones, low backscatter – darker tones. **(C)** Hillshade image, based on AUV SAS micro-bathymetry, with profile line (x–y) for **Figure 6**. **(D)** AUV-based SAS imagery. **(E)** AUV-based photo mosaic. Striping is due to level differences between individual photos. **(F)** Single photo from AUV. Note carbonate crusts and gas bubbles.

the direction of the regional faults in the Troms-Finnmark Fault Complex, while other flares do not show such alignment.

Selection of areas for surveying the seabed with SAS was guided by the distribution of the gas flares. An example of this is shown in **Figure 3A**, where four sites with a total area of 20.2 km^2 were surveyed. Data were also collected from the connection lines, giving an additional 9.2 km^2 sonar coverage. The following description focusses on Area 1 and Area 2, highlighting different aspects of how authigenic carbonate cold seep habitats occur.

Area 1 – Carbonate Crust Fields Associated With Numerous Gas Flares

Area 1 is located north of the Håkjerringdjupet trough (**Figure 3A**) at a water depth c. 230 m. The shipborne bathymetry data from Area 1 and the surrounding area shows an irregular seabed, with numerous iceberg ploughmarks. The ploughmarks are up to 100 m wide, and at least 3 km long. Numerous semi-circular to elongated depressions up to 200 m long and 10 m deep occur. These were probably formed when icebergs tipped over and indented the seabed (Chand et al., 2016). The backscatter data from the multibeam echosounder show highly variable reflectivity, with low reflectivity in the bottom of the iceberg ploughmarks, and the highest reflectivity associated with the berms of the ploughmarks. The overall reflectivity in the area is medium to high, indicating the presence of coarse seabed sediments. This is in line with the interpretation of Bellec et al. (2012) who mapped this area as "gravelly sand."

Step one in the search for cold seep habitats associated with authigenic carbonate crust pavements was to analyze the water

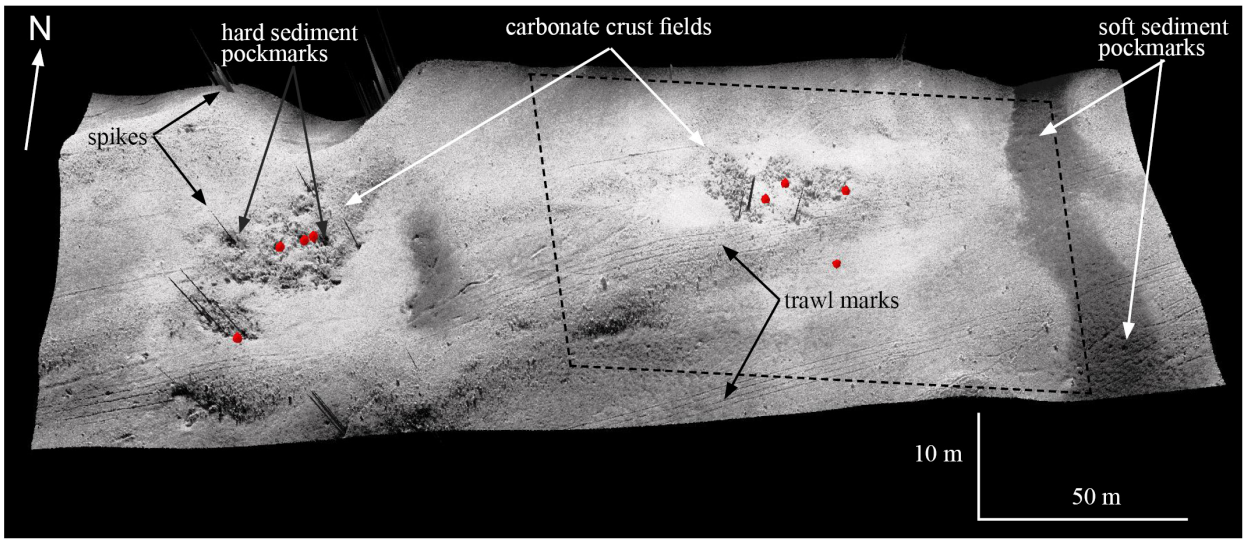

FIGURE 5 | 3D model of a subsection from Area 1, with SAS imagery (high backscatter – lighter tones, low backscatter – darker tones) draped over SAS micro-bathymetry. Carbonate crust fields, gas flares (red dots), trawl marks and pockmarks are evident. Stippled lines show the extent of **Figures 4A–E**. Vertical exaggeration 5×. Water depth –233 to –227 m.

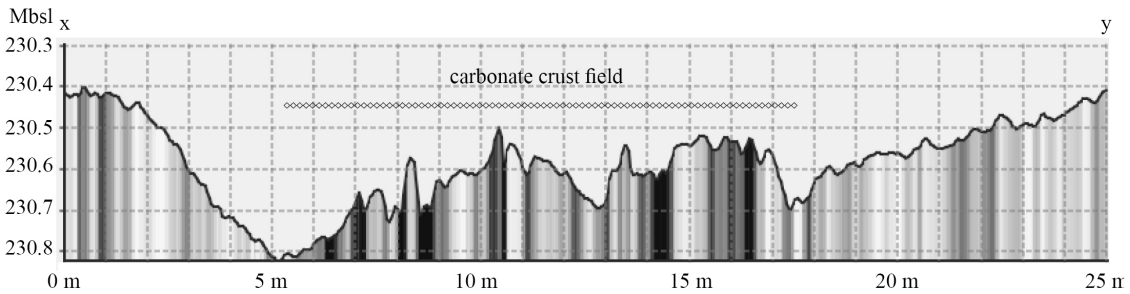

FIGURE 6 | Bathymetric profile across the eastern carbonate crust field in subsection of Area 1 (profile line x–y is shown in **Figure 4C**). Vertical exaggeration: 10×.

column data, showing that there were eight gas flares, grouped in two clusters which were c. 130 m apart.

Step two involved inspection of the shipborne bathymetry data and backscatter data. No anomalies could be detected in the bathymetry or backscatter data (**Figures 4A,B**).

Step three involved collection and inspection of SAS data with the HUGIN HUS AUV. The SAS micro-bathymetry revealed two areas with irregular relief (**Figure 5**), where the easternmost area overlaps with the cluster of three flares (**Figure 4C**). The size of the area was c. 25 m × 50 m. Close inspection of the micro-bathymetry shows that the carbonate field is located in a depression which is up to 40 cm deep, and forms a broad, irregular pockmark (**Figure 6**). Integration of the micro-bathymetry and the imagery data shows that the irregular relief is caused by uneven flat-lying slabs, being up to 2 m in diameter and with a local relief in the order of 10–20 cm. The western (left) crust field also forms a broad pockmark (depression), and has several small pockmarks within it, forming a composite pockmark (**Figure 5**). Small circular to slightly elongated pockmarks (less than 5 m wide, and less than 1 m deep) are found in the low-reflectivity soft sediments filling in an iceberg ploughmark (**Figure 5**, right).

Linear depressions which are more than 150 m long, up to 1 m wide and 15 cm deep can be observed, and are attributed to trawl marks (**Figure 4C**). Some of the trawl marks are only 2–3 cm deep, but can still be visualized using shaded relief techniques.

The SAS imagery (**Figure 4D**) shows the authigenic carbonate crust field and the trawl marks, but with a considerably sharper appearance. Individual blocks with a diameter down to 20–30 cm can be observed. An area of low reflectivity can be seen in the right part of the panel, considered to be fine-grained sediments having accumulated in an iceberg ploughmark.

The final stage involved collection of black and white photos using the TFish system, and a mosaic of all photos is shown in **Figure 4E**. The photos (e.g., **Figure 4F**) allowed identification of seabed sediments, authigenic carbonate crusts, gas bubbles and fauna (fish, benthic/sessile macrofauna, i.e., sea anemones etc.). Bacteria mats encrusting rocks, and pipe-shaped stones likely representing past fluid flow conduits that have been filled

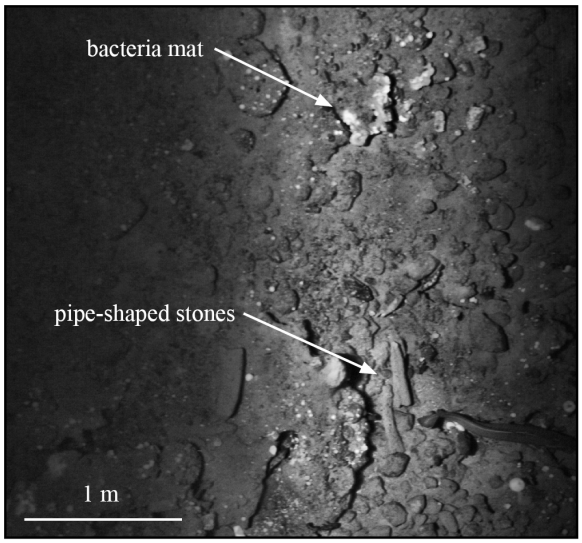

FIGURE 7 | TFish photo showing bacteria mats and pipe-shaped stones likely representing past fluid flow conduits.

and lithified by authigenic carbonates (Campbell, 2006) were observed in a several places (**Figure 7**).

Area 2 – Carbonate Crust Fields With Nearly No Gas Flares

Area 2 is located north of the Håkjerringdjupet trough (**Figure 3**) at water depths between 245 and 305 m. The shipborne bathymetry data from Area 2 and the surrounding area shows an irregular seabed, with numerous iceberg ploughmarks. The ploughmarks are up to 150 m wide, and at least 4 km long. As in Area 1, numerous semi-circular to elongated depressions, up to 200 m long, and 10 m deep were found. These were probably formed when icebergs tipped over and indented the seabed. The backscatter data show highly variable reflectivity, with low reflectivity in the bottom of the iceberg ploughmarks, and the highest reflectivity associated with the berms of the ploughmarks. The overall reflectivity in the area is medium to high, except for an area in the central part, where the reflectivity is low (**Figure 8A**). According to Bellec et al. (2012), the areas with high reflectivity are dominated by sandy gravel to gravelly sand, while the low reflectivity area is dominated by muddy sand and sandy mud.

Only one gas flare was observed in Area 2, while in excess of 100 carbonate crust fields are identified from the SAS imagery (**Figure 8A**). These fields occur along a WSW-ENE belt which is nearly 3 km long, and up to 500 m wide. The appearance of the carbonate crust fields varies according to the seabed sediments surrounding them. In some places, the carbonate crust fields are developed where soft (muddy) sediments with low reflectivity overlie coarser sediments with high reflectivity, thus forming broad, irregular pockmarks (**Figure 8C**). Smaller pockmarks developed in hard, high-reflectivity sediments are present. In such places, characteristic sub-circular to irregular high reflectivity zones up to 50–100 m in diameter occur around the carbonate crusts (**Figures 8B,C**). Soft sediment pockmarks up to 10 m in diameter are commonly found in the soft, low-reflectivity sediments surrounding the carbonate crust fields (**Figure 8C**). Photos of the seabed (**Figure 8D**) verify that the interpretation of the occurrence of carbonate crusts is correct.

In areas where the substrate is more coarse-grained and the reflectivity is higher, there is little or no acoustic contrast between areas with crusts, and areas without crusts. This is e.g., the case in the northern part of Area 2 (**Figure 8A**).

The photos from the TFish system reveal that there is locally a high abundance of fish in association with carbonate crusts. Particularly ling cod was abundant, with sizes up to 1.4 m (**Figure 9**). A number of deep-sea corals were observed, possibly Paragorgia. Sponges and sea anemones were abundant, while no bacteria mats could be identified with certainty. Nor were gas bubbles observed.

DISCUSSION

Cold seeps may form distinct geomorphic features on the seabed, and may modify their physical environment by supporting chemosynthetic communities, forming methane-derived authigenic carbonate crusts and displacing sediment due to fluid expulsion (Fisher et al., 2007; León et al., 2007; Paull et al., 2015).

The cold seeps are often associated with a distinctive, anomalous backscatter 'fingerprint' on multibeam echosounder data (Johnson et al., 2003), with medium to high backscatter areas often coinciding with pockmarks (Naudts et al., 2008). Similar patterns were recognized by Mitchell et al., 2018, noting that seafloor seeps often appear as anomalous bright red "bloodspots" surrounded by relatively lower backscatter. This "classic" kind of signature is often explained by the occurrence of hard carbonate crusts and/or chemosynthetic fauna, surrounded by fine-grained seafloor sediments (Orange et al., 2002).

This "classic" acoustic signature is not fully representative for the cold seeps reported in this study. In both Area 1 and 2, we noted that the seeps did not make up geomorphic features that could be detected using shipborne multibeam echosounders. Nor was it possible to observe the bright spots commonly observed in deeper waters with muddy sediments. This can be explained by the higher backscatter variation commonly found in areas where the seabed has been sculptured by glacial processes, and partly covered by hemipelagic sediments in post-glacial times.

Pockmarks are abundant in both areas. Relatively small pockmarks, less than 10 m wide, are found in low-reflectivity soft sediments. This kind of pockmark is commonly found in the Barents Sea (Chand et al., 2016). Pockmarks developed in hard, high-reflectivity sediments are far less common. We observe them in conjunction with the carbonate crust fields, forming broad irregular depressions, with smaller pockmarks inside them. These composite pockmarks are interpreted to indicate substantial gas expulsion.

Micro-bathymetry from Area 1 indicates that substantial volumes of sediments have been removed since the formation

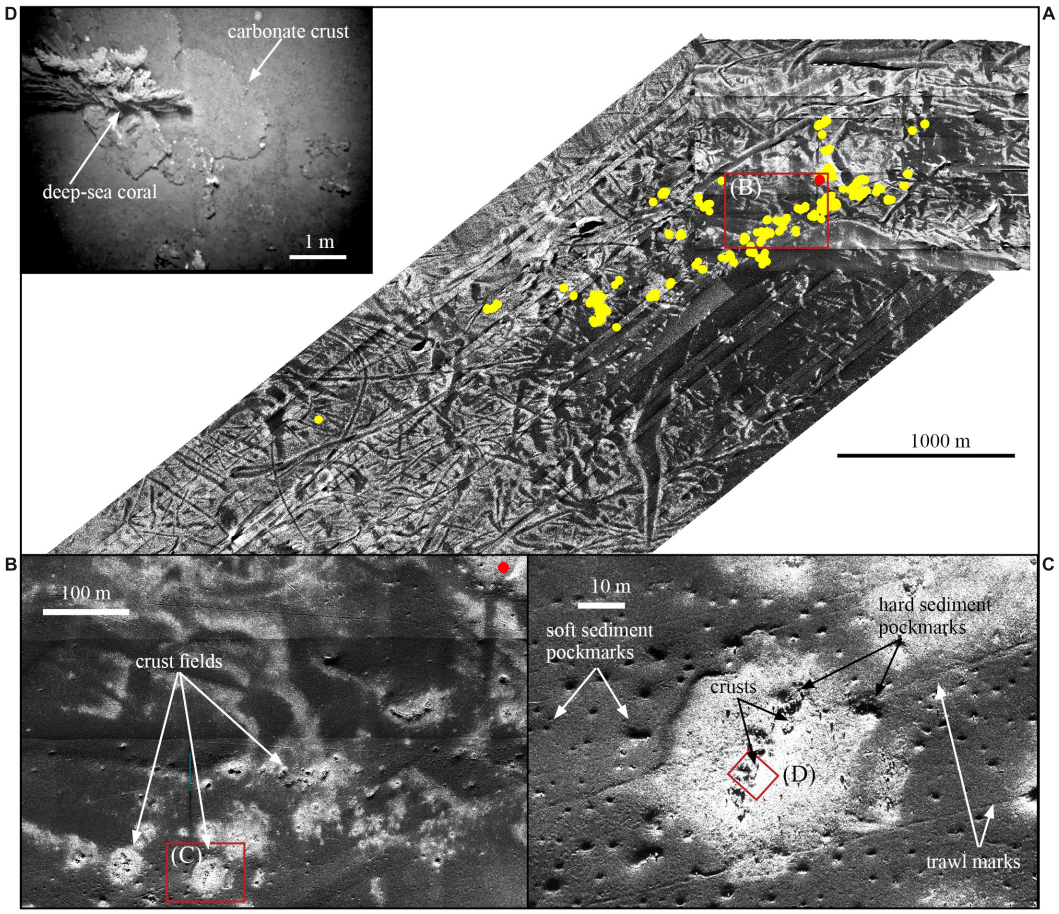

FIGURE 8 | (A) SAS imagery of Area 2 with one gas flare (red dot), carbonate crust fields (yellow dots). High backscatter – light tones, low backscatter – darker tones. Red rectangle shows inset map B. **(B)** SAS imagery showing carbonate crust fields. Red rectangle shows inset map C. **(C)** Zoomed in map showing individual crusts, pockmarks and trawl marks. Red rectangle shows photo D. **(D)** TFish photo of carbonate crusts and a deep-sea coral (possibly Paragorgia).

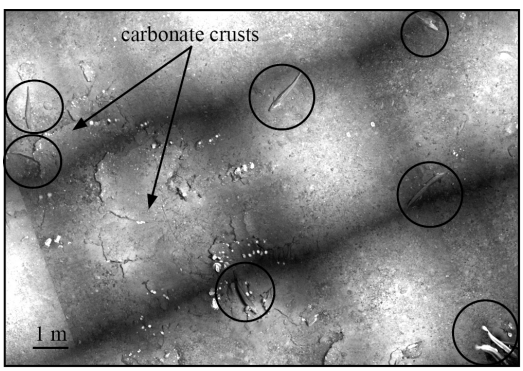

FIGURE 9 | TFish photo mosaic showing carbonate crusts and ling cod up to 1.4 m (in circles).

of the crusts. The SAS imagery shows a 0–20 m wide zone of higher reflectivity around the carbonate crusts. We interpret this to indicate that diffuse flow occurred and removed the more fine-grained part of the sediment, increasing the reflectivity of the sediment. Alternatively, it could be due to cementation of the sediment caused by a diffuse flow which was not sufficiently strong to produce discrete carbonate crusts. The occurrence of pipe-shaped stones in the crust field, interpreted to represent mineralized fluid conduits in the uppermost plumbing system (e.g., Campbell, 2006; Zwicker et al., 2015), indicates a focused fluid flow regime.

In Area 2, we observe two acoustic signatures associated with the carbonate crusts. In the first case, carbonate crusts are found in the central parts of pockmarks surrounded by sub-circular to irregular high reflectivity zones, with a sharp or gradual transition to surrounding fine-grained low reflectivity sediments. In this case no crusts have been observed in this high-reflectivity zone outside the central parts, and the reflectivity is equivalent to or slightly higher than the coarse-grained sediments not associated with carbonate crusts. We interpret this mainly to be a result of focused fluid flow in the central parts, and diffuse fluid flow in the remaining part, removing a thin layer of fine-grained low reflectivity sediments. Removal of finer sediment particles and/or cementation as in

Area 1 may also have contributed to this signature. The second case is found in the northern parts of Area 2 where there are little or no fine-grained sediments. There is hardly any contrast with respect to reflectivity between the crusts and the surrounding sediments. Since the crusts and the surrounding sediments have nearly the same reflectivity, backscatter cannot be used as a guide for locating the carbonate crusts.

Whitish mats of putative sulfide oxidizing bacteria are frequently observed on the TFish photos from Area 1, indicating that seepage is a continuous or at least semi-continuous process. Furthermore, four gas flares were detected overlapping or in close vicinity of the small carbonate crust field. In contrast, only one gas flare was detected in Area 2 where over 100 carbonate crust fields in a comparable size are found. This can be result of diurnal seepage variations since the area was surveyed only once. However, no bacteria mats were observed in the TFish photos from Area 2, suggesting that seepage has largely ceased in this area.

Seabed with high rugosity and hard grounds associated with cold seeps is known to influence the habitat suitability for sessile fauna (Wilson et al., 2007; Barrie et al., 2011; Levin et al., 2015). Abundant ling cod, anemones, sponges and deep-sea corals are found in both areas. We have not done a systematic recording of the fauna within and outside the crust fields. However, our impression is that the abundance is significantly higher within the crust fields. Furthermore, we do not observe any obvious difference in terms of fauna abundance between Area 1 and 2 except for the bacteria mats present in Area 1, and absent in Area 2. This indicates that the 3D hard ground structure provided by the carbonate crusts plays an important role as habitat, and has an important ecological function, regardless of the fluid flow.

CONCLUSION

A nested approach for detecting and describing cold seep habitats associated with authigenic carbonate crusts has been successfully applied in the Håkjerringdjupet region on the continental shelf in the southwestern part of the Barents Sea. More than 210 gas flares from an area of 3775 km^2 were identified from analysis of water column data using a shipborne multibeam echosounder. Application of the HiSAS 1030 SAS mounted on a HUGIN AUV yielded imagery and micro-bathymetry data sets which allowed detection of carbonate crust fields based on expert pattern recognition. The presence of carbonate crust was verified by TFish photos from selected locations.

The study demonstrates that cold seep habitats with carbonate crusts may be associated with active gas flares as in Area 1, or may represent extinct or dormant gas seepage fields as in Area 2. In both cases, the main phase of crust formation likely took place shortly after the last deglaciation.

The "classic" acoustic signature of cold seeps reported from many previous studies is not fully representative for the cold seeps considered here. It is evident that the nature of the sediments hosting the carbonate crusts have a strong influence on the acoustic signature. In regions where the seabed has been formed by a complex interplay between glacial processes and hemipelagic sedimentation, the resulting seabed will often have a highly variable backscatter intensity and irregular morphology. In such areas, it is necessary to combine shipborne water column data with very high-resolution sensors on autonomous or remotely operated vehicles to detect and to provide a spatial documentation of cold seep carbonate crust habitats.

DATA AVAILABILITY STATEMENT

The datasets generated for this study are available upon request to the corresponding author, with the exception of data collected by AUV for the PL 695 area (eastern part of Area 2).

AUTHOR CONTRIBUTIONS

TT wrote the article and participated in data collection and interpretation. SC, HB, and AL participated in data collection and interpretation, and have contributed to the manuscript. PL was in charge of data collection and processing, and has contributed to the manuscript.

FUNDING

This work was supported by the Research Council of Norway through its Centre of Excellence funding scheme for CAGE (grant number 223259). The data used for this publication comes from a cooperative project between the Geological Survey of Norway, Lundin Norway AS and the Norwegian Defence Research Establishment. The project was co-funded by Lundin Norway AS and the Geological Survey of Norway.

ACKNOWLEDGMENTS

The Norwegian Mapping Authority is thanked for making the multibeam echosounder data available through the MAREANO programme. The reviewers are thanked for their constructive comments.

REFERENCES

Aloisi, G., Bouloubassi, I., Heijs, S. K., Pancost, R. D., Pierre, C., Sinninghe Damsté, J. S., et al. (2002). CH4-consuming microorganisms and the formation of carbonate crusts at cold seeps. *Earth Planet. Sci. Lett.* 203, 195–203. doi: 10.1016/S0012-821X(02)00878-6

Andreassen, K., Hubbard, A., Winsborrow, M., Patton, H., Vadakkepuliyambatta, S., Plaza-Faverola, A., et al. (2017). Massive blow-out craters formed by hydrate-controlled methane expulsion from the arctic seafloor. *Science* 356, 948–953. doi: 10.1126/science.aal4500

Barrie, J. V., Cook, S., and Conway, K. (2011). Cold seeps and benthic habitat on the Pacific margin of Canada. *Cont. Shelf Res.* 31, S85–S92. doi: 10.1016/j.csr.2010.02.013

Bellec, V., Picard, K., Bøe, R., Thorsnes, T., Rise, L., Dolan, M., et al. (2012). *Geologisk havbunnskart, Kart 70301800*. Trondheim: Norges geologiske.

Bünz, S., Polyanov, S., Vadakkepuliyambatta, S., Consolaro, C., and Mienert, J. (2012). Active gas venting through hydrate-bearing sediments on the vestnesa ridge, offshore w-svalbard. *Mar. Geol.* 33, 189–197. doi: 10.1016/j.margeo.2012.09.012

Campbell, K. A. (2006). Hydrocarbon seep and hydrothermal vent paleoenvironments and paleontology: past developments and future research directions. *Palaeogeogr. Palaeoclimatol. Palaeoecol.* 232, 362–407. doi: 10.1016/j.palaeo.2005.06.018

Cathles, L. M., Su, Z., and Chen, D. (2010). The physics of gas chimney and pockmark formation, with implications for assessment of seafloor hazards and gas sequestration. *Mar. Pet. Geol.* 27, 82–91. doi: 10.1016/j.marpetgeo.2009.09.010

Chand, S., Crémière, A., Lepland, A., Thorsnes, T., Brunstad, H., and Stoddart, D. (2017). Long-term fluid expulsion revealed by carbonate crusts and pockmarks connected to subsurface gas anomalies and palaeo-channels in the central North Sea. *Geo-Mar. Lett.* 37, 215–227. doi: 10.1007/s00367-016-0487-x

Chand, S., Thorsnes, T., Lepland, A., and Crémière, A. (2015). *Pockmarks, gas flares and carbonate crusts and their relation to the tectonic and stratigraphic evolution of the Alvheim and Utsira High areas (North Sea) and the Harstad Basin (SW Barents Sea)*. NGU Report. 2015 024. Patan: NGU.

Chand, S., Thorsnes, T., Rise, L., Brunstad, H., and Stoddart, D. (2016). "Pockmarks in the SW Barents Sea and their links with iceberg ploughmarks," in *Atlas of Submarine Glacial Landforms:Modern, Quaternary and Ancient*, Vol. 46, eds J. A. Dowdeswell, M. Canals, M. Jakobsson, B. J. Todd, E. K. Dowdeswell, and K. A. Hogan (London: Geological Society), 295–296. doi: 10.1144/M46.23

Crémière, A., Chand, S., Sahy, D., Thorsnes, T., Martma, T., Noble, S. R., et al. (2018). Structural controls on seepage of thermogenic and microbial methane since the last glacial maximum in the harstad basin, southwest barents sea, mar. *Pet. Geol.* 98, 569–581. doi: 10.1016/j.marpetgeo.2018.07.010

Crémière, A., Lepland, A., Chand, S., Sahy, D., Condon, D. J., Noble, S. R., et al. (2016). Timescales of methane seepage on the norwegian margin following collapse of the scandinavian ice sheet. *Nat. Commun.* 7:11509. doi: 10.1038/ncomms11509

Eldholm, O., Sundvor, E., Myhre, A. M., and Faleide, J. I. (1984). "Cenozoic evolution of the continental margin off Norway and western Svalbard," in *Petroleum Geology of the North European Margin*, ed. A. M. Spencer (Berlin: Springer), 3–18. doi: 10.1007/978-94-009-5626-1_2

Fisher, C., Roberts, H., Cordes, E., and Bernard, B. (2007). Cold seeps and associated communities of the gulf of mexico. *Oceanography* 20, 69–79. doi: 10.5670/ocean

Greinert, J., Bohrmann, G., Suess, E., Paull, C. K., and Dillon, P. W. (2001). "Gas hydrate-associated carbonates and methane-venting at hydrate ridge: classification, distribution and origin of authigenic lithologies," in *Natural Gas Hydrates Occurrence, Distribution and Detection. Geophys. Monogr*, Vol. 124, (Washington, DC: AGU), 99–113. doi: 10.1029/gm124p0099

Hovland, M. (2007). Discovery of prolific natural methane seeps at Gullfaks, northern North Sea. *Geo-Mar. Lett.* 27, 197–201. doi: 10.1007/s00367-007-0070-6

Hovland, M., and Judd, A. (1988). *Seabed Pockmarks and Seepages: Impact on Geology, Biology, and the Marine Environment*. London: Graham and Trotman.

Hovland, M., Judd, A. G., and Burke, R. A. (1993). The global flux of methane from shallow submarine sediments. *Chemosphere* 26, 559–578. doi: 10.1016/0045-6535(93)90442-8

Johnson, J. E., Goldfinger, C., and Suess, E. (2003). Geophysical constraints on the surface distribution of authigenic carbonates across the hydrate ridge region. Cascadia Margin. *Mar. Geol.* 202, 79–120. doi: 10.1016/s0025-3227(03)00268-8

Klaucke, I., Masson, D. G., Petersen, C. J., Weinrebe, W., and Ranero, C. R. (2008). Multifrequency geoacoustic imaging of fluid escape structures offshore costa rica: implications for the quantification of seep processes. *Geochem. Geophys. Geosyst.* 9:Q04010. doi: 10.1029/2007GC001708

Klaucke, I., Weinrebe, W., Petersen, C. J., and Bowden, D. (2010). Temporal variability of gas seeps offshore New Zealand: multi-frequency geoacoustic imaging of the wairarapa area. Hikurangi margin. *Mar. Geol.* 272, 49–58. doi: 10.1016/j.margeo.2009.02.009

Laberg, J. S., Andreassen, K., Knies, J., Vorren, T. O., and Winsborrow, M. (2010). Late pliocene–pleistocene development of the barents sea ice sheet. *Geologica* 38, 107–110. doi: 10.1130/G30193.1

Laberg, J. S., Andreassen, K., and Vorren, T. O. (2012). Late cenozoic erosion of the high-latitude southwestern barents sea shelf revisited. *Geol. Soc. Am. Bull.* 124, 77–88. doi: 10.1130/b30340.1

León, R., Somoza, L., Medialdea, T., González, F. J., Díaz-del-Río, V., Fernández-Puga, M. C., et al. (2007). Sea-floor features related to hydrocarbon seeps in deepwater carbonate-mud mounds of the Gulf of Cádiz: from mud flows to carbonate precipitates. *Geo-Mar. Lett.* 27, 237–247. doi: 10.1007/s00367-007-0074-2

Levin, L. A., Mendoza, G. F., Grupe, B. M., Gonzalez, J. P., Jellison, B., Rouse, G., et al. (2015). Biodiversity on the rocks: macrofauna inhabiting authigenic carbonate at costa rica methane seeps. *PLoS One* 10:e0131080. doi: 10.1371/journal.pone.0131080

Milkov, A. V., and Sassen, R. (2003). Two-dimensional modeling of gas hydrate decomposition in the northwestern gulf of Mexico: significance to global change assessment. *Glob. Planet. Change* 36, 31–46. doi: 10.1016/s0921-8181(02)00162-5

Mitchell, G. A., Orange, D. L., Gharib, J. J., and Kennedy, P. (2018). Improved detection and mapping of deepwater hydrocarbons seeps: optimizing multibeam echosounder seafloor backscatter acquisition and processing techniques. *Mar. Geophys. Res.* 39, 323–347. doi: 10.1007/s11001-018-9345-8

Naehr, T. H., Eichhubl, P., Orphan, V. J., Hovland, M., Paull, C. K., Ussler, W. III. et al. (2007). Authigenic carbonate formation at hydrocarbon seeps in continental margin sediments: a comparative study: *Deep Sea Res. Part II: Top. Stud. Oceanogr.* 54, 1268–1291. doi: 10.1016/j.dsr2.2007.04.010

Naudts, L., Greinert, J., Artemov, Y., Beaubien, S. E., Borowski, C., and De Batist, M. (2008). Anomalous sea-floor backscatter patterns in methane venting areas. Dnepr paleodelta, NW Black Sea. *Mar. Geol.* 251, 253–267. doi: 10.1016/j.margeo.2008.03.002

Naudts, L., Greinert, J., Artemov, Y., Staelens, P., Poort, J., Van Rensbergen, P., et al. (2006). Geological and morphological setting of 2778 methane seeps in the Dnepr paleo-delta, northwestern Black Sea. *Mar. Geol.* 227, 177–199. doi: 10.1016/j.margeo.2005.10.005

Ødegård, Ø, Hansen, R. E., Singh, H., and Maarleveld, T. J. (2018). Archaeological use of synthetic aperture sonar on deepwater wreck sites in skagerrak. *J. Archaeol. Sci.* 89, 1–13. doi: 10.1016/j.jas.2017.10.005

Orange, D. L., Yuna, Y., Maher, N., Barry, J., and Greene, G. (2002). Tracking California seafloor seeps with bathymetry. *Cont. Shelf Res.* 22, 2273–2290. doi: 10.1016/S0278-4343(02)00054-7

Panieri, G., Bünz, S., Fornari, D. J., Escartin, J., Serov, P., Jansson, P., et al. (2017). An integrated view of the methane system in the pockmarks at vestnesa ridge, 79°N. *Mar. Geol.* 390, 282–300. doi: 10.1016/j.margeo.2017.06.006

Paull, C. K., Caress, D. W., Thomas, H., Lundsten, E., Anderson, K., Gwiazda, R., et al. (2015). Seafloor geomorphic manifestations of gas venting and shallow subbottom gas hydrate occurrences. *Geosphere* 11, 491–513. doi: 10.1130/GES01 012.1 doi: 10.1130/ges01012.1

Siegert, M. J., Dowdeswell, J. A., Hald, M., and Svendsen, J. I. (2001). Modelling the eurasian ice sheet through a full (Weichselian) glacial cycle. *Glob. Planet. Change* 31, 367–385. doi: 10.1016/s0921-8181(01)00130-8

Sigmond, E. M. O. (1992). *Bedrock Map. Norway and Adjacent Ocean Areas. Scale 1: 3 Mill*. Trondheim: Norges geologiske undersøkelse.

Spencer, A. M., Home, P. C., and Berglund, L. T. (1984). "Tertiary structural development of western barents shelf: troms to svalbard," in *Petroleum Geology of the North European Margin*, ed. A. M. Spencer (London: Graham and Trotman), 199–210. doi: 10.1007/978-94-009-5626-1_14

Suess, E. (2014). Marine cold seeps and their manifestations: geological control, biogeochemical criteria and environmental conditions. *Int. J. Earth Sci.* 103, 1889–1916. doi: 10.1007/s00531-014-1010-0

Vorren, T. O., Richardsen, G., Knutsen, S. M., and Henriksen, E. (1991). Cenozoic erosion and sedimentation in the western Barents Sea. *Mar. Pet. Geol.* 8, 317–340. doi: 10.1016/0264-8172(91)90086-g

Wagner, J. K. S., McEntee, M. H., Brothers, L. L., German, C. R., Kaiser, C. L., Yoerger, D. R., et al. (2013). Cold-seep habitat mapping: high-resolution spatial characterization of the blake ridge diapir seep field. *Top. Stud. Oceanogr.* 92, 183–188. doi: 10.1016/j.dsr2.2013.02.008

Wilson, M. F. J., O'Connell, B., Brown, C., Guinan, J. C., and Grehan, A. J. (2007). Multiscale terrain analysis of multibeam bathymetry data for habitat mapping on the continental slope. *Mar. Geol.* 30, 3–35. doi: 10.1080/01490410701295962

Winsborrow, M., Andreassen, K., Hubbard, A., Plaza-Faverola, A., Gudlaugsson, E., and Patton, H. (2016). Regulation of ice stream flow through subglacial formation of gas hydrates. *Nat. Geosci.* 9, 370–374. doi: 10.1038/ngeo2696

Zwicker, J., Smrzka, D., Gier, S., Goedert, J. L., and Peckmann, J. (2015). Mineralized conduits are part of the uppermost plumbing system of oligocene methane-seep deposits. Washington State (USA). *Mar. Pet. Geol.* 66, 616–630. doi: 10.1016/j.marpetgeo.2015.05.035

Conflict of Interest: HB was employed by company Lundin Norway AS.

The remaining authors declare that the research was conducted in the absence of any commercial or financial relationships that could be construed as a potential conflict of interest.

frontiers in Marine Science

ORIGINAL RESEARCH
published: 14 January 2020
doi: 10.3389/fmars.2019.00804

Applications of the Gulf of Maine Operational Forecast System to Enhance Spatio-Temporal Oceanographic Awareness for Ocean Mapping

Giuseppe Masetti[1], Michael J. Smith[1], Larry A. Mayer[1] and John G. W. Kelley[2]*

[1] Center for Coastal and Ocean Mapping/NOAA-UNH Joint Hydrographic Center, School of Marine Science and Ocean Engineering, University of New Hampshire, Durham, NH, United States, [2] NOAA, National Ocean Service, Coastal Marine Modeling Branch, Durham, NH, United States

Despite recent technological advances in seafloor mapping systems, the resulting products and the overall operational efficiency of surveys are often affected by poor awareness of the oceanographic environment in which the surveys are conducted. Increasingly reliable ocean nowcast and forecast model predictions of key environmental variables – from local to global scales – are publicly available, but they are often not used by ocean mappers. With the intention of rectifying this situation, this work evaluates some possible ocean mapping applications for commonly available oceanographic predictions by focusing on one of the available regional models: NOAA's Gulf of Maine Operational Forecast System. The study explores two main use cases: the use of predicted oceanographic variability in the water column to enhance and extend (or even substitute) the data collected on-site by sound speed profilers during survey data acquisition; and, the uncertainty estimation of oceanographic variability as a meaningful input to estimate the optimal time between sound speed casts. After having described the techniques adopted for each use case and their implementation as an extension of publicly available ocean mapping tools, this work provides evidence that the adoption of these techniques has the potential to improve efficiency in survey operations as well as the quality of the resulting ocean mapping products.

Keywords: ocean mapping, underwater acoustics applications, oceanographic modeling, operational forecast models, surveying accuracy

OPEN ACCESS

Edited by:
Craig John Brown, Dalhousie University, Canada

Reviewed by:
Anand Hiroji, The University of Southern Mississippi, United States
Mary Alida Young, Deakin University, Australia

****Correspondence:***
Giuseppe Masetti
gmasetti@ccom.unh.edu;
giuseppemasetti@gmail.com

Specialty section:
This article was submitted to Deep-Sea Environments and Ecology, a section of the journal Frontiers in Marine Science

Received: *19 August 2019*
Accepted: *13 December 2019*
Published: *14 January 2020*

Citation:
Masetti G, Smith MJ, Mayer LA and Kelley JGW (2020) Applications of the Gulf of Maine Operational Forecast System to Enhance Spatio-Temporal Oceanographic Awareness for Ocean Mapping. Front. Mar. Sci. 6:804. doi: 10.3389/fmars.2019.00804

INTRODUCTION

Recent technological advances in seafloor mapping systems have greatly improved the quality and the efficiency of data acquisition (Mayer, 2014; Hughes Clarke, 2018; Lamarche and Lurton, 2018). Nevertheless, the resulting products (e.g., bathymetric grids, acoustic backscatter mosaics) and the overall operational efficiency of surveys are often affected by the poor awareness of the oceanographic environment in which the surveys are conducted (Lurton et al., 2015; Hughes Clarke et al., 2017; Mayer et al., 2018).

If the timing of sound speed casts does not properly capture the spatio-temporal variability of the ocean environment, the under-sampled water column produces refraction-induced depth biases in the collected soundings (Beaudoin, 2010; Wilson et al., 2013; Lucieer et al., 2016). Such refraction-induced depth biases can quickly cause the survey to exceed the allowable error tolerances prescribed by best practices and by international and national survey specifications (UKHO, 2004; IHO, 2011; NOAA, 2019a). Along with the sound speed profile, which is critical for ray-tracing, knowledge of the temperature and the salinity variability is crucial in the calculation of appropriate absorption coefficients for acoustic backscatter processing (Masetti et al., 2017; Malik et al., 2018; Montereale-Gavazzi et al., 2019). To summarize, a poor understanding of the oceanographic environment will inevitably lead to increased processing time and effort and may even lead to the need to acquire additional data (Hughes Clarke, 2012; Lecours et al., 2015; Weber et al., 2018). The cautious surveyor will often adopt an approach that overestimates the effects of oceanographic variability by either reducing the sonar swath aperture (and thus affecting the survey efficiency due to the reduced swath coverage) or over-sampling the water column using underway profilers, with the associated wear and tear related costs (Masetti et al., 2018).

Given the current level of predictability of the oceanographic environment, the situation described above can be easily addressed. Increasingly reliable nowcast and forecast guidance from operational oceanographic forecast modeling systems – from local to global scales – are publicly available for key environmental variables (e.g., water temperature and salinity), but they are often not used by ocean mappers (Dudhia, 2014; Bauer et al., 2015; Tonani et al., 2015; Powers et al., 2017; Masetti et al., 2018). This is likely due to the limited awareness of these predictions and the lack of tools that easily allow surveyors to transform model predictions into the estimated effects on the survey data as well as the limited number of studies that have shown the potential benefits incorporating modeled data (Beaudoin et al., 2013; Ros, 2018; Sowers et al., 2019). With the intent of bridging this gap, this study evaluates possible ocean mapping applications for publicly available oceanographic predictions by focusing on one of the available regional models: NOAA National Ocean Service's Gulf of Maine Operational Forecast System (GoMOFS) (Yang et al., 2016). The GoMOFS was selected because the Gulf of Maine, a semi-enclosed coastal basin along the United States east coast, has a wide variety of physical oceanographic phenomena (from a complex circulation system to strong tidal currents) varying both spatially and seasonally (more details on the model are provided in section "The NOAA's Gulf of Maine Operational Forecast System"). Thus, a good part of the study's outcomes should be applicable to other forecast modeling systems of similar (or less) complexity.

The traditional approach to characterizing the water column for ocean mapping aims has been to deploy instruments from a stationary vessel (i.e., performing a hydrocast). Such an approach requires the cessation of mapping for the duration of the cast, directly impacting survey efficiency. With this traditional approach, the ocean mapper is called upon to maintain a balance between the loss in survey efficiency from each new cast and the benefits in terms of improved water column characterization (Beaudoin, 2010; Lucieer et al., 2016; Ros, 2018). The advent of expendable probes has not substantially changed this challenge since the reduced loss of profiling time is offset by the decreased accuracy of the probes relative to a traditional hydrocast, the cost of each expendable probe (combined with the environmental impact of abandoning the used probe on the ocean seafloor). Modern ocean mapping surveys are increasingly adopting underway profilers that can sample the water column at very high rates with the vessel in motion (Furlong et al., 2006; Rudnick and Klinke, 2007). Although those profilers may considerably improve the survey efficiency, the identification of the proper balance between the desired spatio-temporal knowledge of the water column and the working load of the profilers (with associated higher risk of losing the towed probe) is also required (Hughes Clarke et al., 2000; Beaudoin, 2010).

By leveraging predictions from GoMOFS, this study explores two main use cases: the use of predicted oceanographic variability in the water column to enhance and extend (or even substitute) the data collected on-site by sound speed profilers during the survey data acquisition; and, the use of uncertainty estimation of oceanographic variability as a meaningful input to estimate the optimal time between sound speed casts. An analysis of ray-tracing uncertainty is used to evaluate the adequacy level of a given sampling interval ranging from under-sampling to over-sampling the spatio-temporal variability of the water column. With the intention to removing subjectivity in the determination of the cast interval and improving the overall sounding accuracy, Wilson et al. (2013) proposed a method, called *CastTime*, that estimates the optimal sampling interval by reacting to the observed variability. This work proposes a new method, called *ForeCast*, that combines the *CastTime* reactive approach with the predicted spatio-temporal variability provided by an oceanographic forecast modeling system (i.e., the GoMOFS).

After describing the techniques adopted for each use case as well as the related code provided as an extension of publicly available ocean mapping tools (Masetti et al., 2017; Masetti et al., 2018), this paper provides evidence that the adoption of these techniques has the potential to improve efficiency in survey operation as well as the quality of the resulting ocean mapping products. Finally, several possible future improvements are discussed and additional tests to validate such techniques are proposed.

MATERIALS AND METHODS

The NOAA's Gulf of Maine Operational Forecast System

The GoMOFS is an operational nowcast/forecast system for the Gulf of Maine developed by the National Ocean Service (NOS) of the National Oceanic and Atmospheric Administration (Yang et al., 2016). The GoMOFS uses the Regional Ocean Modeling System (ROMS) as its core hydrodynamic prediction model. The model domain is centered on the Gulf of Maine and extends from Rhode Island coast to the mid-coast of Nova Scotia, Canada (**Figure 1**), with its open ocean boundary extending

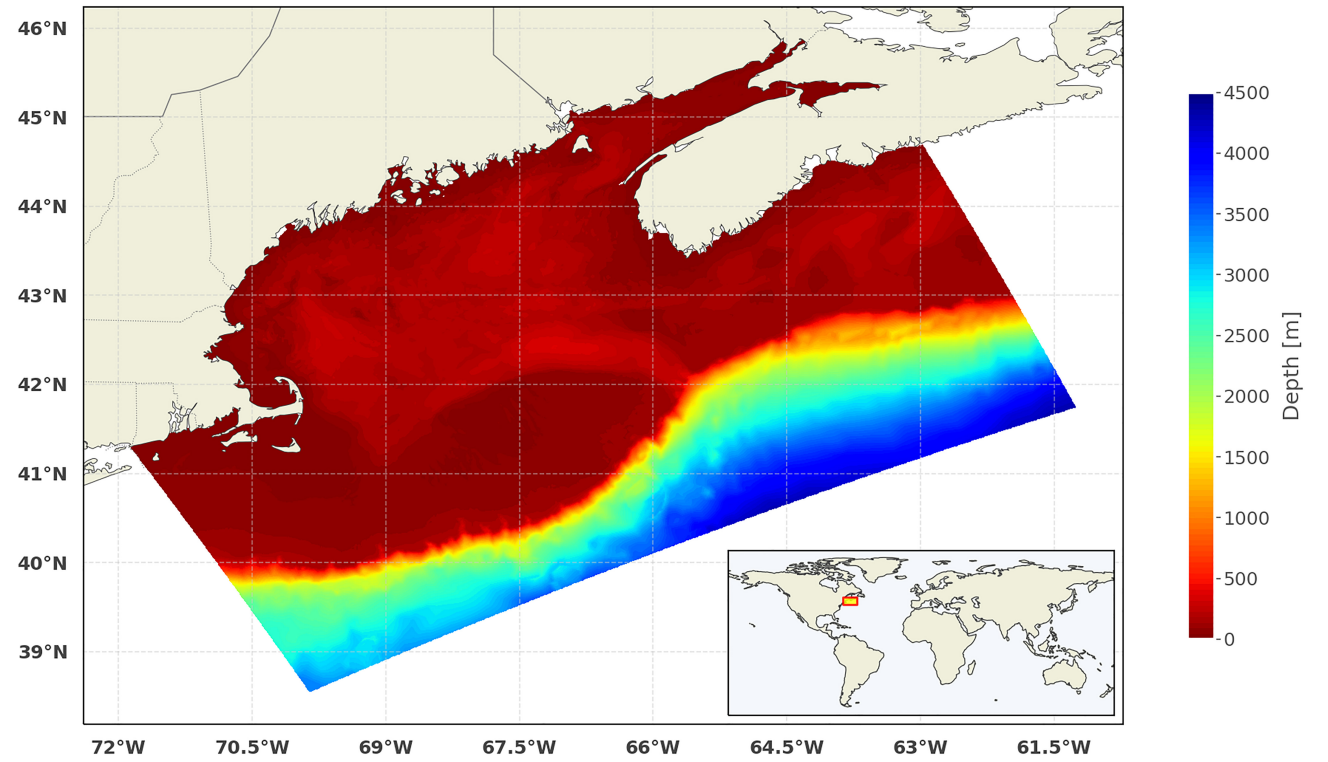

FIGURE 1 | Map of the Gulf of Maine region with the GoMOFS model domain represented using its bathymetric coverage (in meters). The inset shows (with a red-framed yellow rectangle) the location of the model in the world.

past the shelf break south of Georges Bank. The model grid has a horizontal resolution of about 700 meters and has thirty vertical sigma layers. This region, located along the NE seacoast of the United States, includes a range of physiographic features (e.g., shoals, banks, channels) as well as intense tidal, circulatory, and meteorological phenomena that are modulated in intensity both spatially and seasonally (Greenberg, 1979; Xue et al., 2000; Yang et al., 2016). Thus, the outcomes of this study are likely to be applicable to predictions from forecast modeling systems of similar (or less) complexity.

Before becoming operational in 2018, the GoMOFS outputs were compared against observations (for the year of 2012) at various depths, and the results demonstrated that the hindcast performance meets the NOS standard criteria (Hess et al., 2003; Zhang et al., 2006). Based on Yang et al. (2016), the following root-mean-squared errors were estimated: less than 1.5°C for temperature, and less than 1.5 psu for salinity. Furthermore, the model successfully reproduced both the magnitude and the annual cycle of the temperature, while it was noted that it tends to overestimate the salinity (Yang et al., 2016).

GoMOFS is run four times per day at 0, 6, 12, and 18 Coordinated Universal Time (UTC) and consists of both a now cast cycle and a forecast cycle. GoMOFS' nowcast cycle is forced by very-short-range meteorological forecast guidance from the National Weather Service's (NWS) North American Mesoscale (NAM) weather prediction forecast modeling system (NOS, 2017). GoMOFS' lateral open ocean boundary conditions for water temperatures, salinity, baroclinic velocity, and subtidal water levels are based on predictions from NWS' Global Real-Time Ocean Forecast System (Global RTOFS) (Peng et al., 2018). Tidal forcing is provided by the ADCIRC Tidal Database (Luettich et al., 1992). Freshwater water inputs, as represented by discharge rates are specified for nine rivers based on the latest observations from United States Geological Survey (USGS) river gages. Each nowcast cycle uses the nowcast from the previous cycle as its initial conditions. There is no data assimilation by GoMOFS (NOAA, 2019b). GoMOFS' forecast cycle is forced by forecast guidance out to 72 h from the NAM forecast modeling system and Global RTOFS along with tidal forcing from the ADCIRC Tidal Database (NOS, 2017). River discharge rates at the nine river gages for the 72-hour duration of the forecast cycle are not presently based on forecast guidance from a river model forecast modeling system. Instead, the most recent discharge observations at the gages are persisted for the duration of the forecast cycle (Peng et al., 2018). The forecast cycle uses the most recent nowcast to provide its initial conditions (NOAA, 2019b). GoMOFS is run on NOAA Weather and Climate Operational Supercomputer System.

The two GoMOFS variables used in this study are water temperature and salinity. They represent the key components in calculating "synthetic" sound speed profiles from the GoMOFS products. Specifically, the variation of sound speed with depths was calculated – with the related limitations and accuracy – using the dependences of temperature, salinity, and pressure on depth

as defined by the United Nations Educational, Scientific and Cultural Organization (UNESCO) adopted equation of Chen and Millero (1977).

Study Area and Input Dataset

The input dataset for this study was collected as ancillary data from a high-resolution hydrographic survey completed during June 2019. The primary objective of the survey was to meet the academic requirements of the Hydrographic Field Course, part of the Ocean Mapping curricula at the University of New Hampshire's (UNH) Center for Coastal and Ocean Mapping (CCOM). The survey data were collected (and the deliverables were prepared) following the requirements of the *NOAA NOS Hydrographic Survey Specifications and Deliverables 2019* (HSSD) manual (NOAA, 2019a). Two distinct areas were surveyed: a main area (hereafter, "A") that was north of Gerrish Island, ME and south of the Cape Neddick lighthouse; and an offshore area (hereafter, "B") south east of the coastline around York Harbor (see **Figure 2**). As shown in the inset of **Figure 2**, the study area is located in the middle of the western area of the GoMOFS domain region.

During the survey, water column properties were measured using an AML Oceanographic MVP30 underway profiler installed onboard the *R/V Gulf Surveyor*. The towed body was equipped with an AML Sound Velocity, Pressure, and Temperature (SVPT) sensor. At the survey speed of 6–8 knots, the underway profiler can collect profiles up to a depth of about 60 meters, with cycles between 2.0 and 1.8 min. Accordingly, the sampling intervals adopted during the survey were of the order of a few minutes. Such high-rate datasets are useful for the near-continuous evaluation of the structure of the water column below the survey vessel. A data set of 329 casts was acquired during the survey (**Figure 2**). For the purpose of this study, three subsets where extracted from the whole dataset: the "A" and "B" subsets corresponds to the two distinct surveyed areas, the "C" subset was collected during an offshore-sailing transect (**Figure 2**). Additional details about the subsets are provided in **Table 1** and, graphically, in **Figure 3**.

The Sound Speed Manager Application

Jointly developed by the NOAA Office of Coast Survey (OCS) and the UNH's COM, Sound Speed Manager (SSM) is an open-source application (and software library) designed to perform accurate processing and management of sound speed profiles (HydrOffice, 2019b). Since its inception, the main aim has been to support the surveyors in fulfilling the accuracy and validity requirements of a modern survey workflow (Masetti et al., 2017). After its official deployment during the 2017 NOAA OCS field season, SSM has been adopted by several NOAA and UNOLS vessels, as well as by a number of professionals around the world (Johnson et al., 2018; Masetti et al., 2019; Sowers et al., 2019).

SSM supports cast data collected from various types of devices (e.g., CTDs, velocimeters, expendable bathythermographs (XBT), underway profilers), and formats. Once imported (or received from the network), the user is able to enhance/extend the profile (e.g., based on oceanographic atlases) and then export the validated data in a number of formats commonly recognized by acquisition and processing applications. Through SSM, the surveyor may also retrieve synthetic profiles from oceanographic databases (e.g., the NOAA World Ocean Atlas 2013) and forecast modeling systems (e.g., the NCEP Global Real-Time Forecast System) (Mehra and Rivin, 2010; Levitus et al., 2013). As part of the research efforts presented in this study, SSM was extended to support predictions from NOAA NOS regional operational forecast modeling systems and, specifically, the GoMOFS (Yang et al., 2016). The synthetic profiles from the model forecasts can be used to complement collected profiles with environment variables that have not been directly measured (e.g., the salinity for XBT profiles), extend them to a deeper depth, and/or perform a visual comparison to confirm their reliability.

SSM stores the processed profiles in a per-project SQLite database and provides several analysis functions and tools to manage the database-stored profiles (Masetti et al., 2017). Among those functionalities, the surveyor also has access to a software implementation of the previously cited *CastTime* algorithm designed to estimate the time when performing the next cast (Wilson et al., 2013).

SmartMap

SmartMap is a tool that estimates the ray-traced refraction component of the surveyed depth uncertainty based on a spatial variability analysis of publicly available oceanographic environmental data (Masetti et al., 2018). First, the SmartMap analysis estimates the uncertainty up to the minimum common depth among the retrieved synthetic profiles. Then, based on the consideration that the largest sound speed variability is commonly observed in the uppermost area of the water column (Medwin and Clay, 1998; Kinsler et al., 2000), the results are provided as a percentage of ray-tracing depth uncertainty ($PDU^{rt}_{r,c}$) as a function of the calculated uncertainty ($\delta^{rt}_{r,c}$) scaled to the 95% confidence level and the full depth ($d_{r,c}$) at each grid location (r, c):

$$PDU^{rt}_{r,c} = \frac{2\delta^{rt}_{r,c}}{d_{r,c}} * 100.0 \quad (1)$$

Finally, a logarithmic transformation is applied (due to the large range of the resulting ray-tracing uncertainty values), and the resulting map is stored in the GeoTIFF format (Ritter and Ruth, 1997). SmartMap maps are made available daily (and stored) through Open Geospatial Consortium (OGC) web services and a Web GIS[1] (Michaelis and Ames, 2012; HydrOffice, 2019a).

SmartMap outputs can be used in all the phases of a survey: planning (e.g., by accessing the output based on the model forecasts), execution (by providing a synoptic representation of the water column variability during the data acquisition), and processing (by retrieving the analysis from past dates) (de Moustier, 2001; Hughes Clarke, 2003; Beaudoin et al., 2004).

The original implementation of SmartMap provides maps based on the predictions from Global RTOFS and data from NOAA World Ocean Atlas 2013 (Mehra and Rivin, 2010; Levitus et al., 2013). Support for GoMOFS forecasts (Yang et al., 2016) has been added to SmartMap (see **Figure 4**) to underpin the

[1]https://www.hydroffice.org/smartmap/

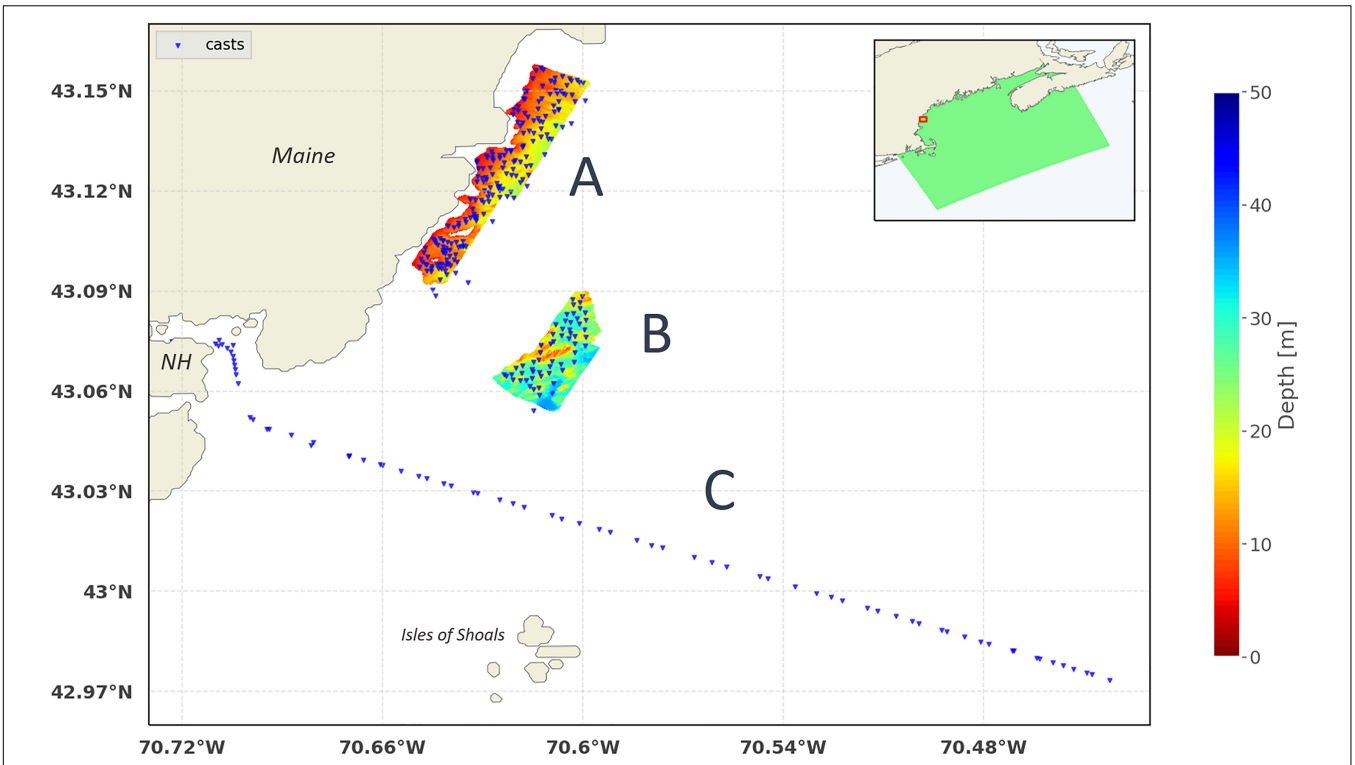

FIGURE 2 | Bathymetric coverage completed by the UNH Hydrographic Field Course 2019. The collected casts (in blue) were grouped into three subsets: the "A" and "B" subsets corresponds to the two distinct surveyed areas, the "C" subset was collected during an offshore-sailing transect. The inset shows the locations of the survey area (red-framed yellow rectangle) and the GoMOFS domain (green tilted rectangle) in the Gulf of Maine.

TABLE 1 | Information about the adopted cast subsets.

Subset Name	Collection Time	Number of Casts
A	13–14, 17–20 June 2019	174
B	24 June 2019	59
C	26 June 2019	58

predictive component of the *ForeCast* algorithm (more details on the algorithm are provided in section "The ForeCast *A*lgorithm"), and ease its potential future transition to operations.

The ForeCast Algorithm

The *ForeCast* algorithm estimates the optimal cast timing by combining a reactive component based on the observed variability and the predicted spatio-temporal variability provided by the predictions of an oceanographic forecast modeling system (i.e., the GoMOFS).

The main processing steps of the algorithm are:

- Application of a constant-gradient ray-tracing algorithm for each newly acquired sound speed profile.
- Using uncertainty analysis, comparison of each newly collected cast with the latest acquired profiles.
- Retrieval of the local GoMOFS-derived spatio-temporal depth bias from the SmartMap WCS.
- Estimation of a new sampling interval based on previous intervals, the GoMOFS-derived spatio-temporal depth bias, and a specified maximum allowable tolerance.

Figure 5 provides a flowchart outlining the main algorithmic steps, data inputs, user parameter, and processing outputs. All the processing steps have been implemented in the Python 3 programming language (van Rossum, 2018).

Constant-Gradient Ray-Tracing

Normally, a multibeam echosounder (MBES) repeatedly emits acoustic pulses that are much broader in the across-track direction than along track. After having traveled through the water column, those pulses insonify a seafloor area that usually has a width of several times the measured depth and are then scattered back in multiple directions (Lurton, 2010). The component of each pulse returned to the MBES is processed through electronic beam steering to determine the travel time at each beam angle (Burdic, 1991). Finally, those pairs of travel time and beam angles (β) are combined with the sound speed profile to obtain seafloor depth measurements (z) or the range of mid-water targets within the swath (Medwin and Clay, 1998).

Ray-tracing is one of the most popular methods for obtaining the swath measurements through modeling of underwater sound propagation (Huang, 2012). Ray-tracing is performed by splitting the sound speed profile, $c(z)$, into a set (N) of finite layers (with indices $n = 0, \ldots, N$), and then calculating the refraction of a

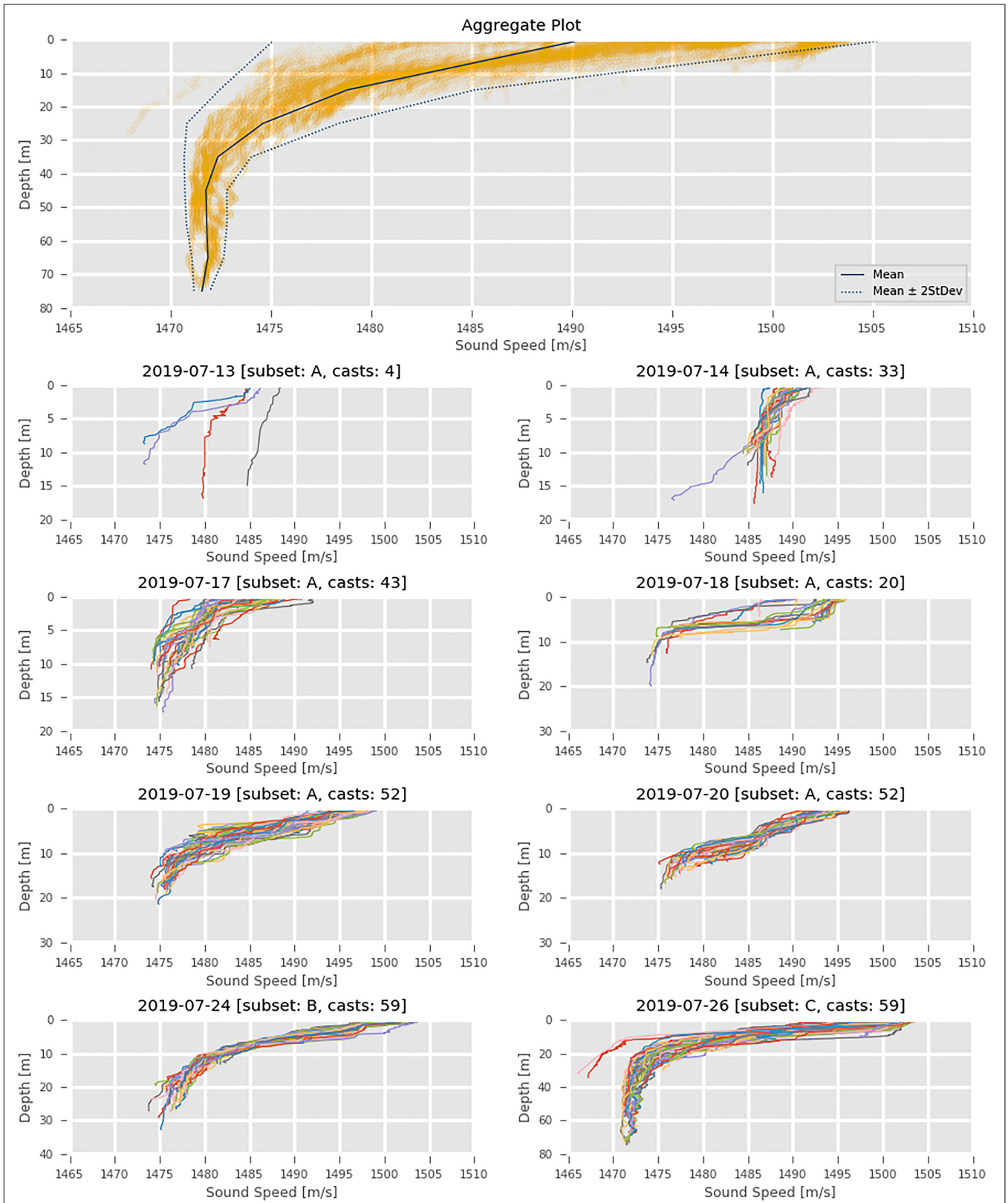

FIGURE 3 | The **upper panel** shows the aggregate plot based on all the available casts (with the resulting average profile in blue). The **other panels** show the casts by subset and day of acquisition.

ray path across the layer (Medwin and Clay, 1998). With the constant-gradient approach, the ray-tracing algorithm assumes linear variation of sound speed between each subsequent pair of samples in a profile (Medwin and Clay, 1998). For each of the $N-1$ finite layers, a constant gradient of sound speed (g_n) is estimated:

$$g_n = \frac{c_n - c_{n-1}}{z_n - z_{n-1}} \tag{2}$$

The algorithm then applies the Snell-Descartes law for isotropic media to trace the ray (a is a constant known as the ray parameter):

$$\frac{\cos\beta_n}{c_n} = \frac{\cos\beta_{n-1}}{c_{n-1}} = a \tag{3}$$

The resulting path through the finite layer draws an arc of a circle (see **Figure 6**) whose center lies at a baseline depth calculated by extrapolating the layer sound speed to zero (Medwin and Clay, 1998). After having calculated the local radius of curvature (R_n), the circular refraction formulae for changes in depths and horizontal ranges (r) can be derived (Lurton, 2010):

$$R_n = \frac{c_{n-1}}{g_n \cos\beta_{n-1}} \tag{4}$$

$$\begin{cases} r_n - r_{n-1} = \frac{c_{n-1}}{g_n \cos\beta_{n-1}} (\sin\beta_{n-1} - \sin\beta_n) \\ z_n - z_{n-1} = \frac{c_{n-1}}{g_n \cos\beta_{n-1}} (\cos\beta_n - \cos\beta_{n-1}) \end{cases} \tag{5}$$

Finally, the total travel time can be obtained by integration of the travel times along the layers. **Figure 7** shows an example of the described ray-tracing algorithm in action, at different initial beam angles.

Uncertainty Analysis on Acquired Profiles

The uncertainty analysis adopted by *ForeCast* is based on pairs of ray-traced profiles (**Figure 5**). For each profile, the ray-tracing algorithm is iteratively executed until the desired end-point is reached. The depth and launch angle of each individual ray-trace have to be adjusted based on the current sonar configuration: the dynamic draft of the sonar head, the sound speed values measured at the transducer, and the adopted angular swath aperture. The results are interpolated to a decimetric resolution by applying a spline interpolation of third order and stored into a look-up table (Ferguson, 1964). Because sound speed measurements within a given profile are likely collected at depths distinct from another profile, the interpolated values are used to

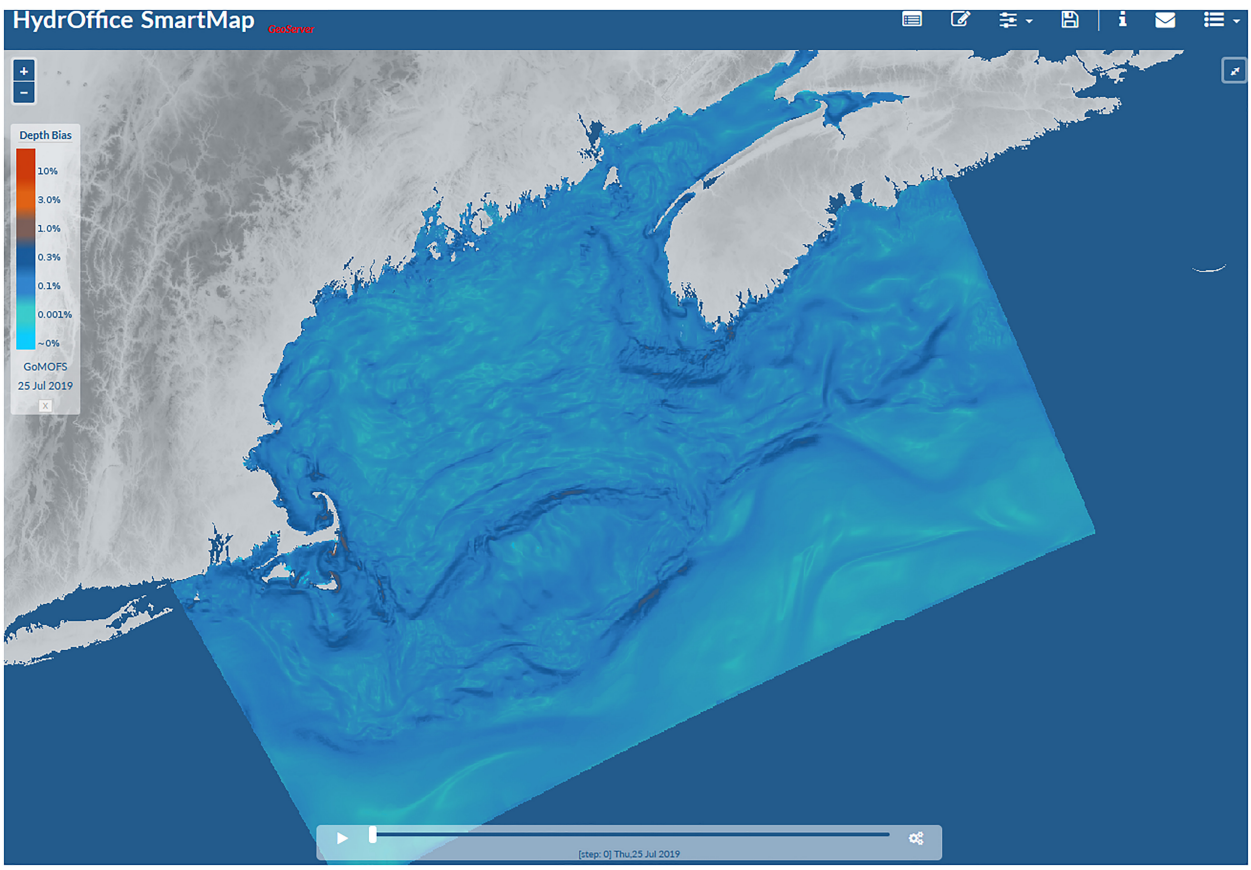

FIGURE 4 | Visualization on the SmartMap Web GIS (https://www.hydroffice.org/smartmap/) of the GoMOFS-based 24-hr forecast map of estimated ray-tracing depth bias as percentage of water depth (valid on July 25, 2019).

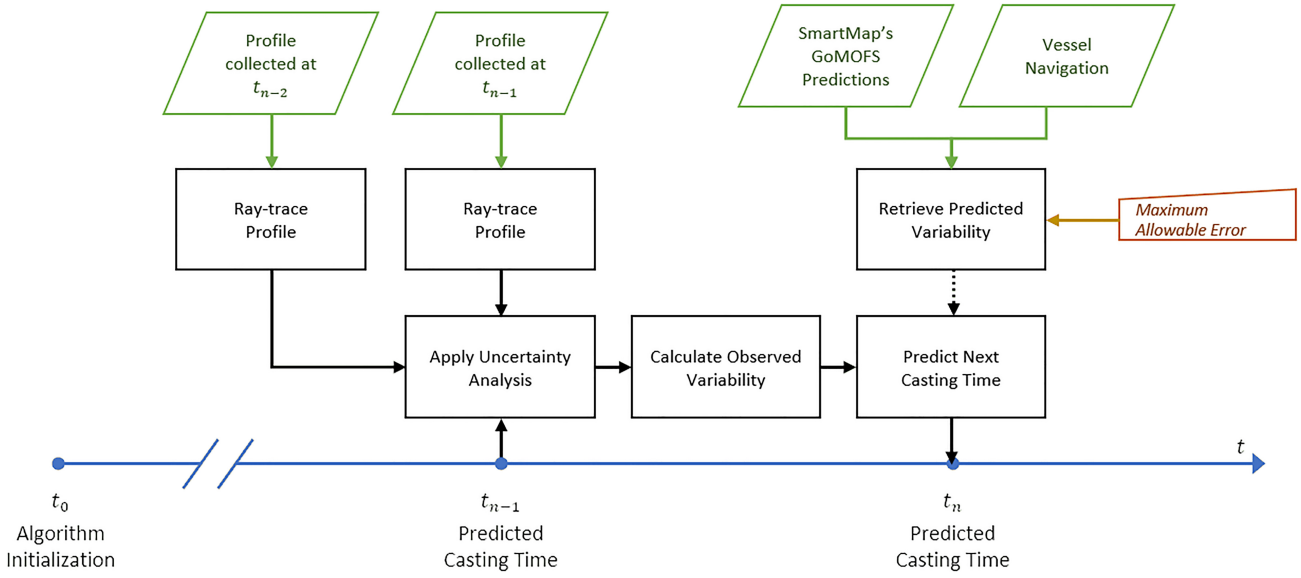

FIGURE 5 | The flowchart shows, in black, the main steps of the *ForeCast* algorithm with a dashed connector when optional (i.e., the predictive component based on SmartMap's GoMOFS maps). The inputs are represented in green, the user parameter in orange, and the timeline in blue.

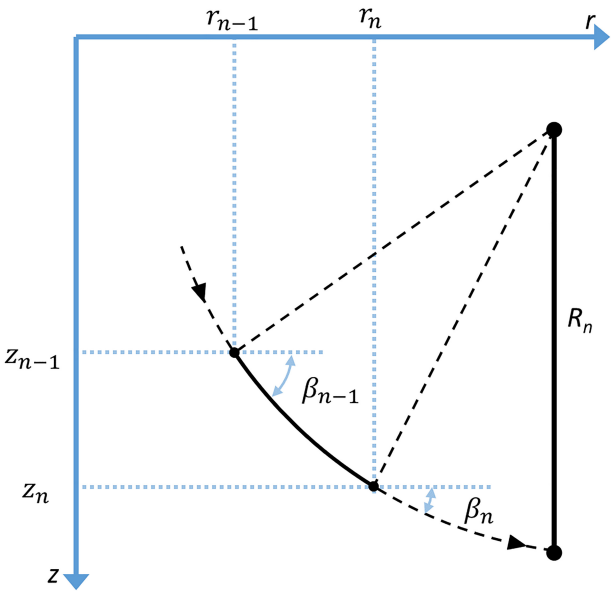

FIGURE 6 | Geometry and symbols used in the constant gradient ray-tracing algorithm for a given ray in a finite layer.

obtain a consistent comparison between pairs of ray-traced sound speed profiles. Since the results of the ray-tracing are symmetrical about the sonar nadir, the computation is only necessary on one side of the sonar swath.

Any bias in the environmental characterization in one or more of the profile layers directly affects the quality of the resulting sonar solutions. As such, by ray-tracing subsequent profiles, it is possible to compare the outdated water column characterization with a newer (and likely better) representation. The ray-tracing outputs can be used to perform a quantitative comparison between pairs of sound speed profiles to estimate the sounding uncertainty due to water column variability. Such an evaluation does not require actual sounding data, and can be performed at any desired depth that is covered by both the profiles (Beaudoin, 2010; Wilson et al., 2013).

Figure 8A shows an example of applying the described uncertainty analysis on two acquired profiles. When profile *b* is acquired, it is assumed to provide a better representation of the water column conditions than profile *a*. While profile *a* was showing quite well-mixed conditions (i.e., water temperature and salinity have limited variations), profile *b* has generally higher sound speed values as well as the presence of a thermocline. An assessment of the biases that would have been introduced by the continued use profile *a* is performed and shown in the **Figure 8B**. This assessment is obtained by first calculating, based on profile *b*, the travel time required by a ray (with a given initial β) to reach a simulated flat seafloor, then retrieving the corresponding *r* and *z* values in the ray-traced profile *a*. The differences between those values and the corresponding ones in profile *b* provide the absolute (vertical and horizontal) bias (δz and δr). In other words, the rays based on profile *a* will no longer end at the assumed flat seafloor because the travel times are derived from the ray-tracing of the (assumed) more correct profile *b*. The resulting artificial curvature of the seafloor is commonly known as refraction smile, and it is usually used by surveyors to qualitatively evaluate the presence of refraction issues. As shown in both the bias plots in **Figure 8**, the highest values tend to be associated with beam angles larger than 65° (visualized as a red dotted line). Although possible in ideal conditions to acquire MBES data with a swath aperture larger than 65°, such a value will be adopted as a reference value for this

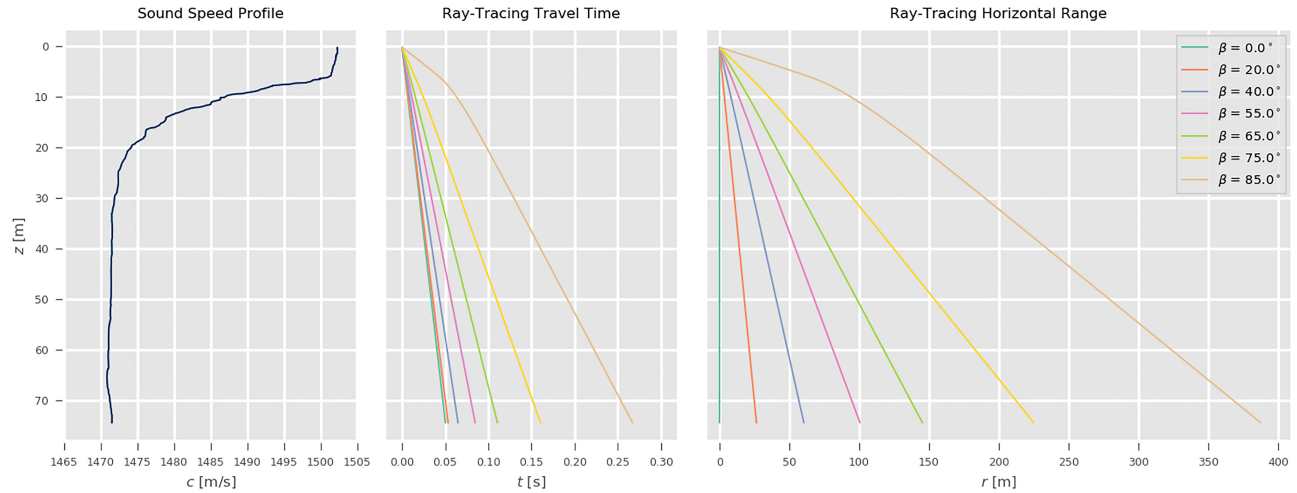

FIGURE 7 | An example of application of the constant gradient ray-tracing algorithm. The **left panel** shows the sound speed samples (in blues) from one of the collected survey profiles. The **middle panel** and the **right panel,** respectively provide the resulting travel time (*t*) and horizontal range (*r*) at different initial beam angle (β).

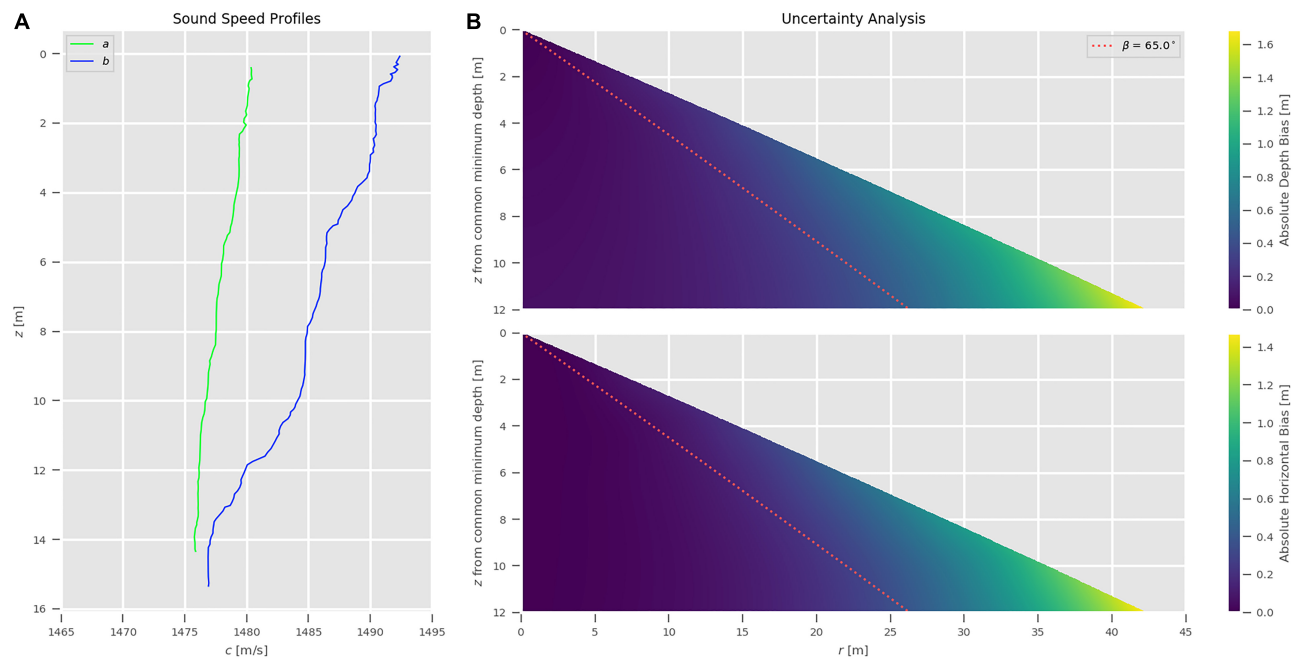

FIGURE 8 | Outcomes from the uncertainty analysis applied to the pair of profiles on the panel **(A)**. The two panels on the right **(B)** show the absolute depth bias and the absolute horizontal bias, respectively. The initial beam angle of 65° is provided as a reference in dotted red.

work (Hughes Clarke, 2012; Masetti et al., 2018). For example, given the scenario shown in **Figure 8**, the depth bias using 65° as initial beam angle would be ∼0.38 m at the deepest common depth between the profiles.

Retrieval of the Predicted Spatio-Temporal Variability

The predicted spatio-temporal depth bias for the study area is retrieved through the SmartMap server. As noted in section "SmartMap," the support for GoMOFS predictions has been added as part of the research efforts of the present study. The main advantage of such a solution is that the download of the large NetCDF files storing the GoMOFS nowcasts and the computationally demanding spatial variability analysis are performed on the remote server (Yang et al., 2016; Masetti et al., 2018). Then, a subset of the map (limited to the survey area, thus usually just a few kilobytes) can be accessed through the GeoServer-provided implementation of the OGC Web Coverage Service (WCS) (Deoliveira, 2008).

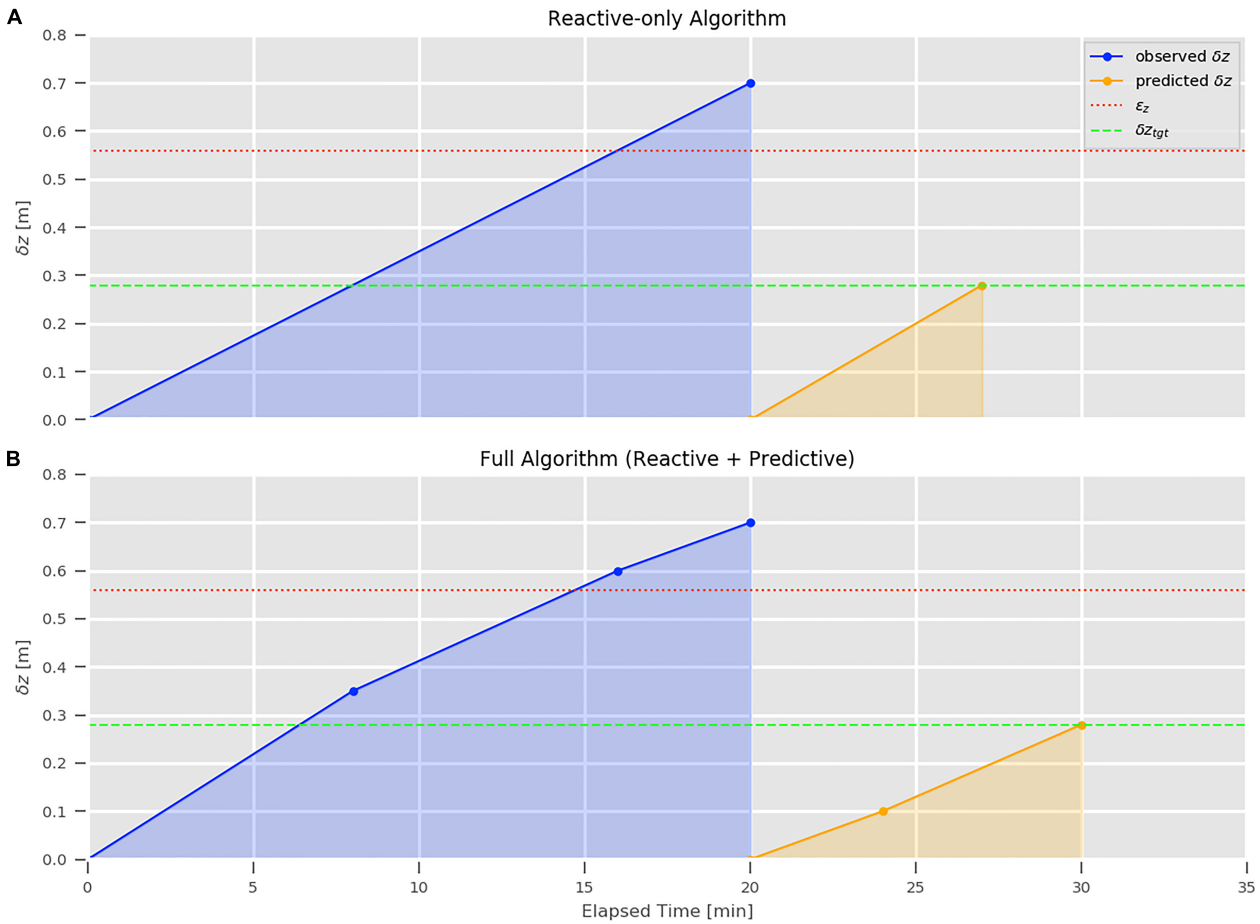

FIGURE 9 | An example of observed variability exceeding the maximum allowable error (red dotted line). When a model forecast is not available, the ForeCast algorithm assumes linear increase in depth bias between observed profile **(A)**. **(B)** Shows an example application for the full algorithm where the predictive component (based on GoMOFS SmartMap maps) is calibrated using the observed spatial variability at different model locations along the track (in blue) and applied to predict the time interval (in orange) when the target depth bias (green dashed line) is reached.

Estimation of Future Casting Intervals

The estimation of a new sampling interval is based on a user-specified maximum allowable tolerance that is evaluated against previous intervals and combined with the GoMOFS-derived spatio-temporal depth bias.

Although any error tolerance can be potentially adopted in order to follow agency-specific survey requirements, the default parameters of the *ForeCast* algorithm are based on the NOAA OCS's refraction error tolerance (ε_z) for MBES surveys as defined in the HSSD manual (NOAA, 2019a). The ε_z, is given in meters by combining a fixed component and a variable part that is a function of the water depth (*wd*):

$$\varepsilon_z = 0.3 + 0.005 \times wd \tag{6}$$

The calculated ε_z is useful to provide a baseline (i.e., an upper and a lower limit) of accepted variability surrounding the assumed-correct answer that is derived from ray-tracing the latest profile. Whether the tolerance limits have been exceeded is evaluated at a user-defined β that has to be modified to match the adopted MBES settings. For such an angle, the *ForeCast* algorithm has a default value of 65° (the assumed outermost beams used and thus the worst-case) that is adopted for the analysis presented in the reminder of this work.

The algorithm logic in estimating the future casting time is based on a target depth bias (δz_{tgt}) calculated as a percentage of ε_z. The adopted formula for δz_{tgt} uses the following default value:

$$\delta z_{tgt} = 0.5 \times \varepsilon_z \tag{7}$$

If the analysis is limited to information that can be retrieved from the collected profiles, the solution proposed by Wilson et al. (2013) of assuming that the depth bias linearly increases with the elapsed time between pairs of subsequent profiles would represent an acceptable strategy. However, given that the GoMOFS-based SmartMap maps provide a representation of the oceanographic variability in the survey area, those values are used to derive a spatial component (e.g., a calibration factor) for the *ForeCast* algorithm, thus potentially improving its forecasting capability (**Figure 5**). Specifically, the predicted rate of change

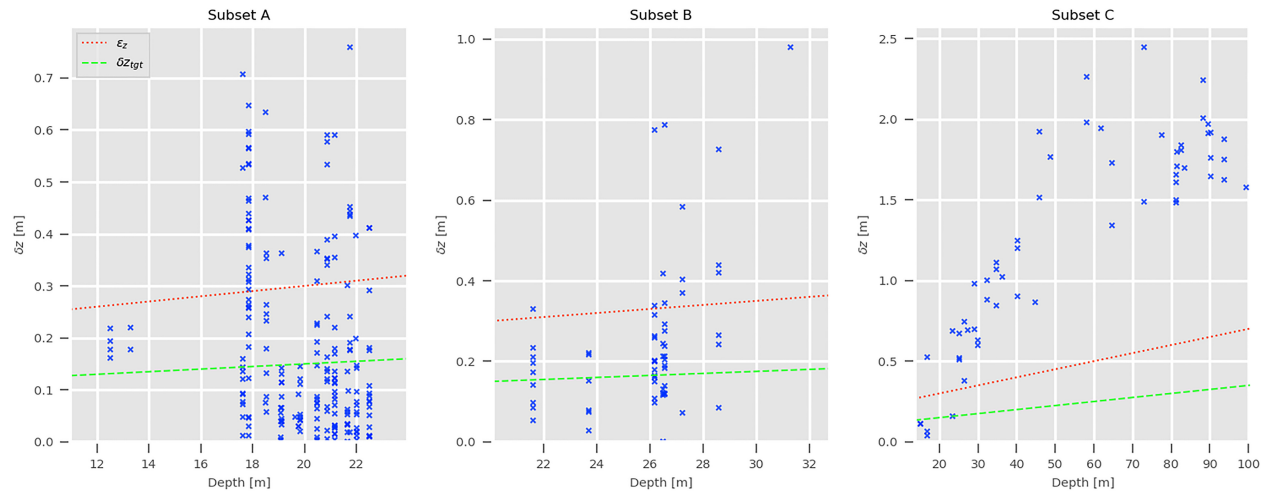

FIGURE 10 | Each collected profile is compared against a synthetic profile retrieved from the GoMOFS predictions. The resulting depth bias (δz) is shown with a blue cross, while the refraction error tolerance (ε_z) and the target depth bias (δz_{tgt}) are represented by a red dotted line and a green dashed line, respectively.

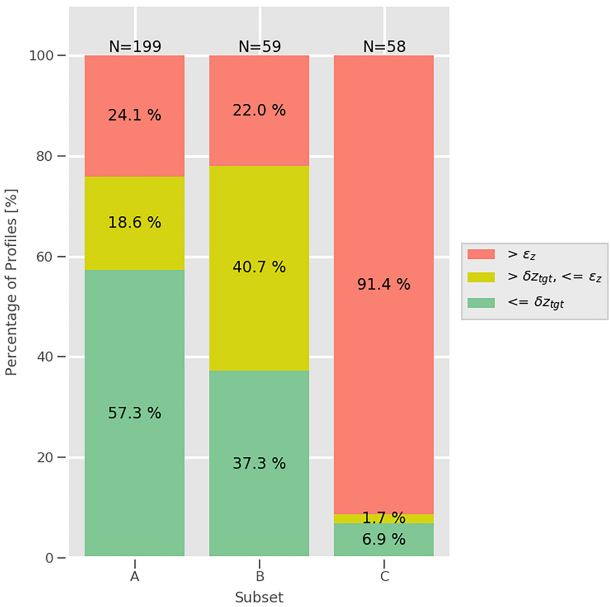

FIGURE 11 | Percentages of GoMOFS-derived profiles per subset that have δz exceeding ε_z (in red), within ε_z and δz_{tgt} (in yellow), and fulfilling this latter requirements (in green).

obtained from the SmartMap analysis is first calibrated using the variability observed in the collected profiles (initialization phase), then the obtained calibration value is used to predict the optimal timing interval based on the δz_{tgt} (**Figure 9**). The adoption of such an approach requires the addition of the vessel route and speed over ground to the algorithm's input parameters that are not required in the *CastTime* algorithm (Wilson et al., 2013). However, when a model forecast is not available, the *ForeCast* algorithm reverts back to the reactive-only method (see **Figure 9B**).

RESULTS

The testing was conducted using the three subsets ("A", "B", and "C") of profiles described in section "Study Area and Input Dataset." The profiles, collected in the "s21" variant of the Kongsberg Maritime SSP datagram, have been loaded in SSM, assessed for quality assurance, and then stored in the application's project SQLite-based database (Kongsberg, 2015).

For each subset, the profiles were used to evaluate the use of the synthetic values derived from the GoMOFS nowcasts in place of the observed data (**Figure 10**). The percentages of profiles that fulfill the refraction error tolerance (ε_z) and the target depth bias (δz_{tgt}) are summarized in **Figure 11**. The maps in **Figure 12** are provided to spatially locate the calculated depth biases.

Due to the higher variability in depth bias, the profiles in subset C were selected to evaluate the ForeCast algorithm. The profiles were analyzed separately based on the vessel heading during the data acquisition: seaward (**Figure 13**) and shoreward (**Figure 14**).

In **Figures 13A**, **14A** shows the evolution of δz in the worst-case scenario that only a single cast would have been collected at the beginning of the transect. In **Figures 13B**, **14B**, an optimal cast timing solution is presented. Specifically, based on the assumption that the high-density subset represents an over-sampled water column, the addition of a new cast is triggered each time that δz exceeds the locally estimated δz_{tgt}. The first obtained cast time is used to define the initialization time (in yellow) of the *ForeCast* algorithm. The predicted casting times in **Figures 13C,D**, **14C,D** are obtained from the *ForeCast* algorithm in two different ways: by only using its reactive component (thus, with a logic similar to the *CastTime* algorithm) in **Figures 13C**, **14C**, and with its full version (thus,

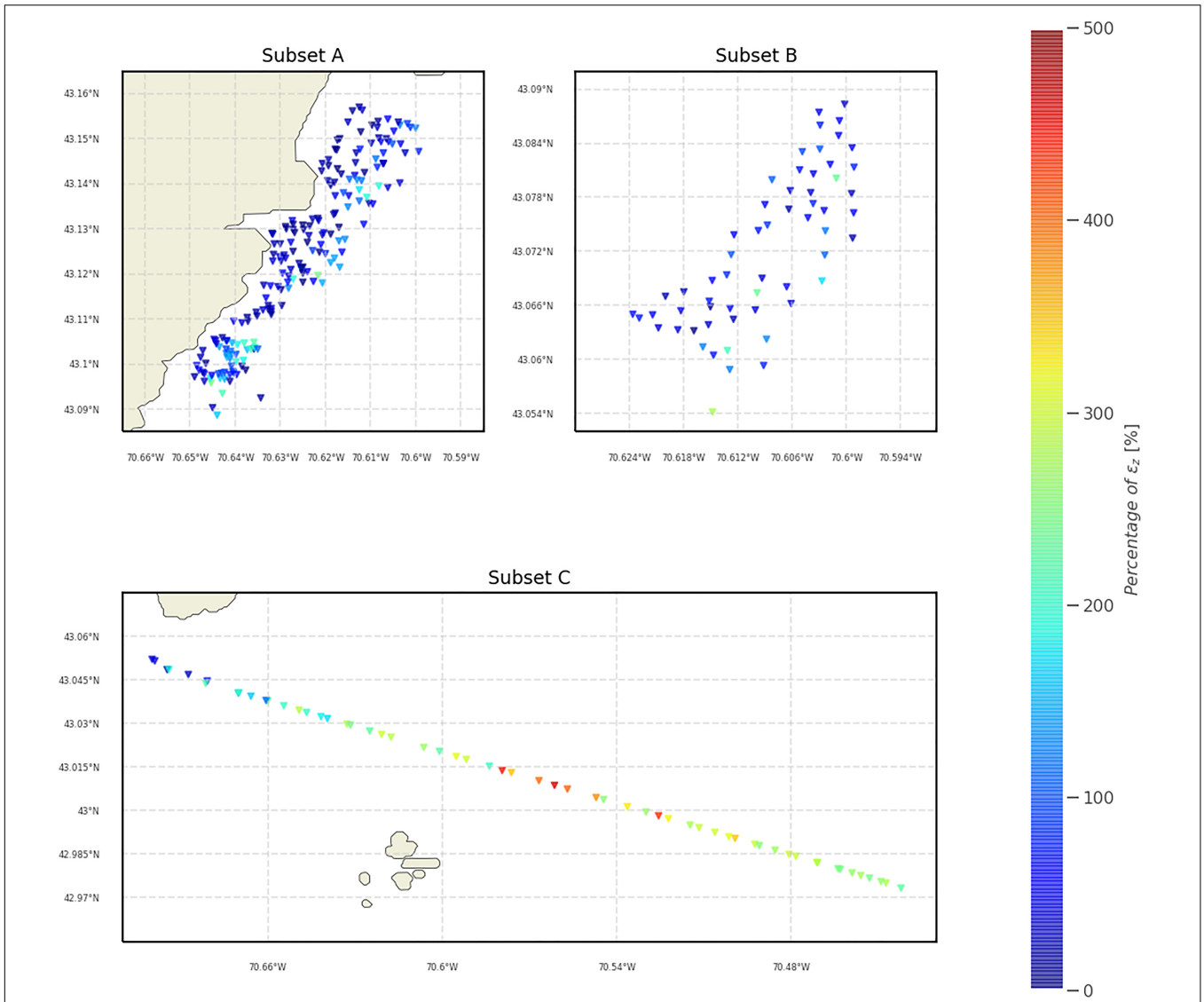

FIGURE 12 | Georeferenced δz derived from comparing observations and GoMOFS-derived synthetic profiles. The values are represented as percentage of ε_z.

adjusting the estimated times based on the spatial component provided by the SmartMap analysis of GoMOFS predictions) in **Figures 13D**, **14D**. The actual δz is the depth bias computed using the full high-density series of profiles (blue markers in **Figures 13**, **14**). The observed δz is the depth bias that would be observed following the cast times suggested by the algorithm (orange markers in **Figures 13C,D**, **14C,D**). For the full *ForeCast* algorithm, **Figures 13D**, **14D** also shows the intermediate estimated observed δz (i.e., adjusted based on the GoMOFS SmartMap output) as orange dots between cast times (see **Figure 9**).

The algorithm performances may be assessed by both evaluating the survey efficiency and the mitigation of the resulting refraction-driven depth bias in the acquired soundings. This latter is based on the comparison between the observed δz (in orange) and the actual δz (in blue). δz For instance, in **Figure 13D**, both the observed δz and the actual δz are assumed zero at the 80-minute epoch; then, the observed δz is increased with time in function of the underline spatial variability predicted by the GoMOFS model. The algorithm triggers the collection of a new profile at the 100-minute epoch, when the observed δz overcomes the target depth bias (δz_{tgt}) of 0.37 m. The actual δz between the casts suggested by the algorithm are not used in the algorithm computation, but they are provided for evaluation of the uncaptured variability. For instance, there are ∼0.2 m of uncaptured depth bias at the 84-minute epoch in **Figure 13D**.

DISCUSSION

The use of the GoMOFS-predicted oceanographic variability in the water column in place of the observed profiles was

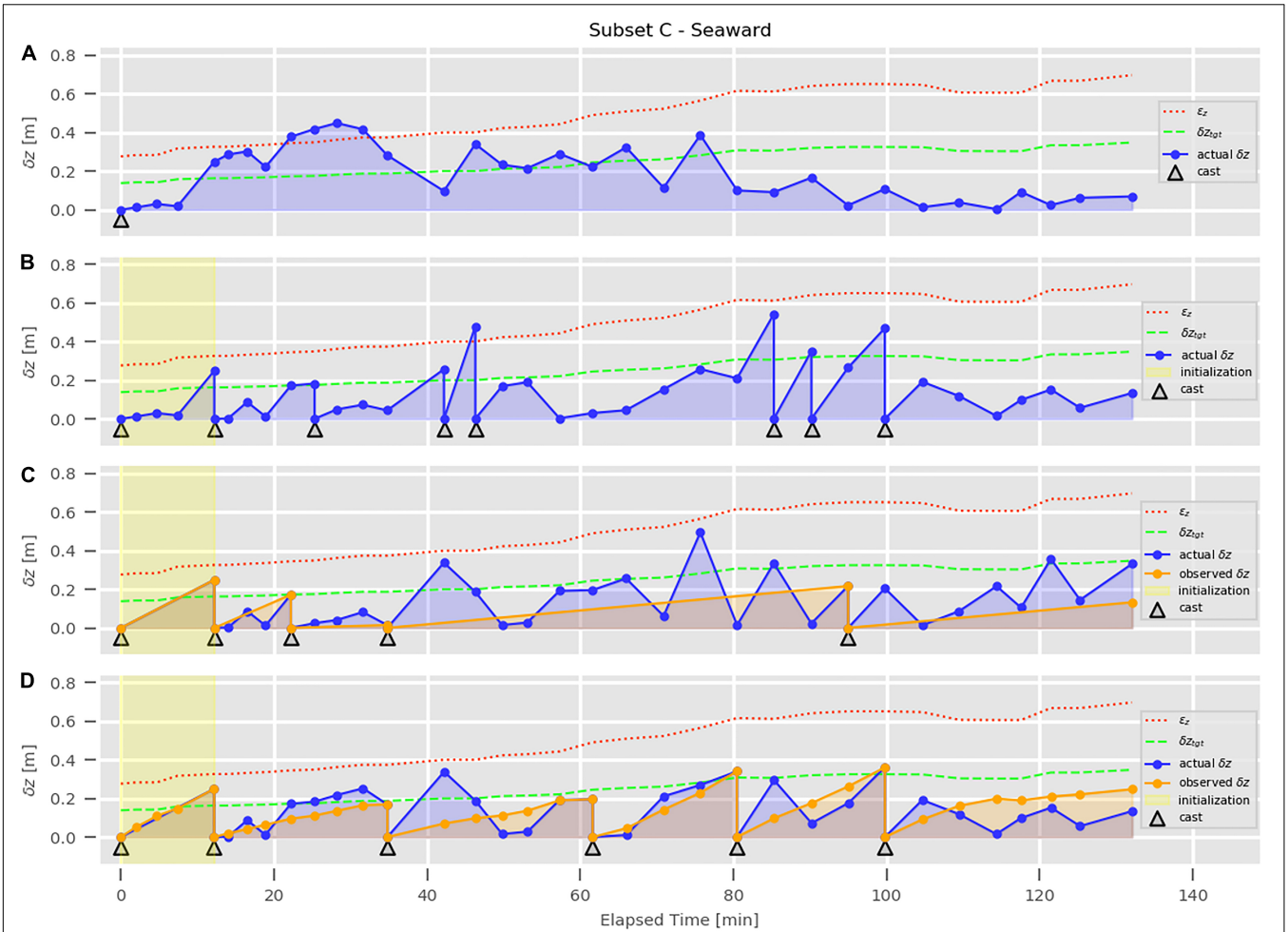

FIGURE 13 | Worst-case scenario **(A)**, optimal solution **(B)**, solutions from the reactive-only **(C)** and the full **(D)** *ForeCast* algorithm for profiles from Subset C collected in the seaward direction.

evaluated in **Figure 10** for each of the three input subsets. Although the results are quite satisfactory for subsets A and B – with 74.4 and 76.3% of profiles fulfilling the allowable ε_z, respectively (**Figure 11**) –, the large number of profiles (63.8%) in subset C exceeding ε_z and their values in percentage of ε_z (**Figure 12**) demonstrate reliability concerns in adopting the model-derived synthetic profiles to fully substitute the profile collection during a regular survey. Indeed, the critical hydrographic practice of collecting hydrocasts should never be abandoned. Nevertheless, the GoMOFS-derived synthetic profiles (in conjunction with synthetic profiles derived from climatological atlases such as WOA) provide a useful reference to evaluate the quality of newly collected data (e.g., identifying a malfunctioning device). Furthermore, they offer acceptable estimates to be used to enhance and extend the data collected on-site by sound speed profilers. The accuracy of nowcasts from NOS' regional oceanographic forecast modeling systems are expected to improve as they are upgraded to assimilate *in situ* and satellite-based observations. Based on such considerations, both capabilities (visual comparison and profile enhancement) were added to SSM to facilitate the transition from research to operations of some of the outcomes of this study.

The second part of the results presented in this work evaluates whether the uncertainty estimation of the oceanographic variability can be used as a meaningful input to estimate the optimal casting time. The predictive component of the *ForeCast* algorithm required the addition of a GoMOFS layer to SmartMap (**Figure 4**). Such an addition does not only represent a required step toward a potential future transition to operations of the *ForeCast* algorithm, but also provides surveyors mapping in the Gulf of Maine with a tool to synoptically evaluate the spatio-temporal variability of the oceanographic conditions in the survey area.

Figures 13, **14** show the evolution of δz in different scenarios, using the analysis of ray-tracing uncertainty to evaluate the adequacy level at different profiling times. The worst-case scenarios represented in **Figures 13A**, **14A** clearly show the need to perform additional casts after the collection of the first profile. The optimal solutions, represented in **Figures 13B**,

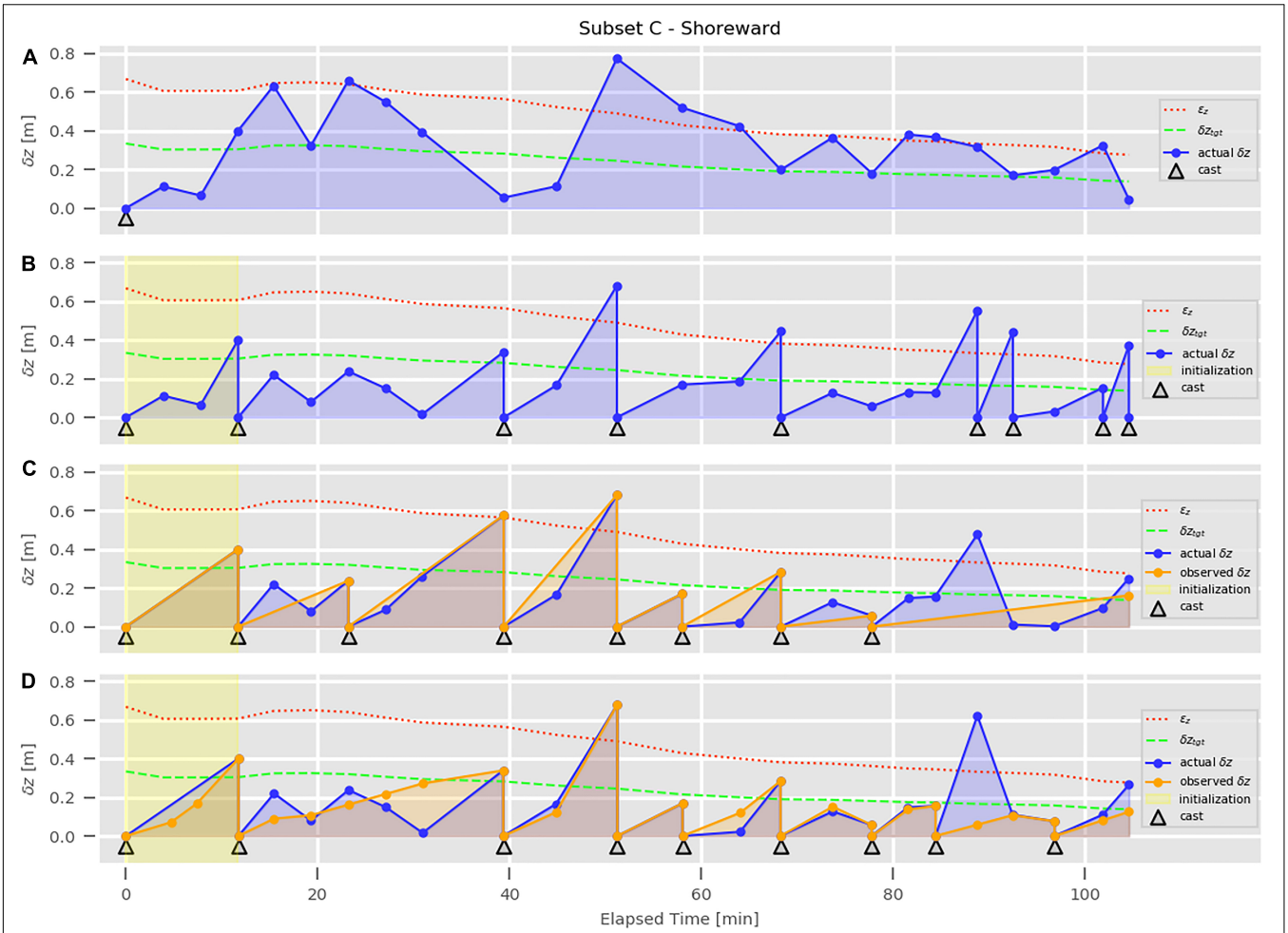

FIGURE 14 | Worst-case scenario **(A)**, optimal solution **(B)**, solutions from the reactive-only **(C)** and the full **(D)** *ForeCast* algorithm for profiles from Subset C collected in the shoreward direction.

14B, provide a baseline to evaluate the performance of the reactive-only (**Figures 13C**, **14C**) and the full (**Figures 13D**, **14D**) *ForeCast* algorithm. The full algorithm estimates cast times whose actual δz values are generally lower than the ones provided by the reactive-only algorithm. Furthermore, a surveyor following the full algorithm would have exceeded the threshold for ε_z in only one case (shoreward case, **Figure 14D**), while it happens a few times in **Figures 14C,D**. Based on such considerations, the proposed method seems to alleviate the subjectivity in the determination of the casting interval and improve the overall sounding accuracy for effect of the predicted spatio-temporal variability provided by GoMOFS. However, more extensive test datasets need to be collected to confirm these results, and new data acquisition are planned for the UNH CCOM's Hydrographic Field Course in 2020. Among others, a relevant possible future improvement to the current algorithm would be in the definition of the initialization time that is currently estimated based on the first obtained cast time from the optimal solution. From a speculative point of view, a relation between the initialization time and the SmartMap-provided $PDU^{rt}_{r,c}$ could be identified. Another improvement could be manifested by integrating the values of sound speed continuously measured at the MBES transducer. The weight given to such point measurements is an open research question.

Although a general evaluation of the survey environment can potentially be retrieved directly from the available climatological atlases and forecast modeling systems, the applications presented in this work digest the large amount of information contained in four-dimensional oceanographic variables and present it in a way most relevant to the ocean mapper. A more accurate knowledge of the oceanographic variability in the survey area has several potential implications. For instance, during the planning phase, surveying directions may be oriented to limit the number of crossings of large uncertainty fronts. In case that the estimated uncertainty for the outmost swath depths is too large based on the targeted specifications, the time of survey execution may be modified, or the estimated swath coverage can be reduced accordingly. Other possible uses are the selection of a calibration site with limited environmental variability and the identification

of the appropriated device to sample the water column (e.g., a survey area with high environmental variability should suggest the adoption of an underway profiler).

This work presents a shift in awareness from the traditional method of monitoring the sound speed at the transducer – a point measurement of sound speed (at ∼1-Hz temporal resolution) that has a critical role in beam forming – and performing profiles measurements at fixed intervals (with additional casts as needed). The combination of these two types of measurements provide a limited awareness of the surrounding oceanographic variability that the methods presented in this work try to overcome. The adoption of the proposed methods has the potential to improve efficiency in survey operations as well as the quality of resulting ocean mapping products.

DATA AVAILABILITY STATEMENT

The GoMOFS-derived datasets analyzed for this study can be downloaded from the SmartMap server (https://smartmap.ccom.unh.edu/geoserver/web/). The original GoMOFS outputs were retrieved from the NOAA CO-OPS THREDDS server (https://opendap.co-ops.nos.noaa.gov/thredds/catalog.html).

AUTHOR CONTRIBUTIONS

GM, MS, and LM: conceptualization and project administration. GM and JK: formal analysis. GM, MS, LM, and JK: methodology. GM: writing the original draft. MS, LM, and JK: writing, review, and editing. GM and MS: analyzed the data.

FUNDING

This work was supported by the National Oceanic and Atmospheric Administration (NOAA) Grant NA15NOS4000200 and the National Science Foundation (NSF) Grant 1524585.

ACKNOWLEDGMENTS

The authors would like to acknowledge the contribution of Semme Dijkstra, Andrew Armstrong, and the students of the UNH CCOM's Hydrographic Field Course 2019, for the collected environmental data analyzed in this study; Jason Greenlaw (Earth Resources Technology, NOAA nowCOAST project) and Erin Nagel (University Corporation for Atmospheric Research, NOAA nowCOAST project), for assisting in the retrieval of the regional operational forecast model outputs.

REFERENCES

Bauer, P., Thorpe, A., and Brunet, G. (2015). The quiet revolution of numerical weather prediction. *Nature* 525, 47–55. doi: 10.1038/nature14956

Beaudoin, J. (2010). Real-time monitoring of uncertainty due to refraction in multibeam echo sounding. *Hydrogr. J.* 134, 3–13.

Beaudoin, J., Hughes Clarke, J., and Bartlett, J. (2004). Application of surface sound speed measurements in post-processing for multi-sector multibeam echosounders. *Int. Hydrogr. Rev.* 5, 26–31.

Beaudoin, J., Kelley, J. G., Greenlaw, J., Beduhn, T., and Greenaway, S. F. (2013). "Oceanographic weather maps: using oceanographic models to improve seabed mapping planning and acquisition," in *US Hydro 2013* (New Orleans, LA).

Burdic, W. S. (1991). *Underwater Acoustic System Analysis*. New Jersey: Prentice Hall.

Chen, C. T., and Millero, F. J. (1977). Speed of sound in seawater at high pressures. *J. Acoust. Soc. Am.* 62, 1129–1135. doi: 10.1121/1.381646

de Moustier, C. (2001). "Field evaluation of sounding accuracy in deep water multibeam swath bathymetry," in *OCEANS, 2001. MTS/IEEE Conference and Exhibition* (Piscataway, NJ: : IEEE), 1761–1765.

Deoliveira, J. (2008). "GeoServer: uniting the GeoWeb and spatial data infrastructures," in *10th International Conference for Spatial Data Infrastructure*, (St. Augustine).

Dudhia, J. (2014). A history of mesoscale model development. *AsiaPacific. J. Atmos. Sci.* 50, 121–131. doi: 10.1007/s13143-014-0031-8

Ferguson, J. (1964). Multivariable curve interpolation. *J. ACM* 11, 221–228. doi: 10.1145/321217.321225

Furlong, A., Osler, J., Christian, H., Cunningham, D., and Pecknold, S. (2006). "The moving vessel profiler (MVP)-a rapid environmental assessment tool for the collection of water column profiles and sediment classification," in *Proceedings of the Undersea Defence Technology Pacific Conference 2006* (San Diego, CA), 1–13.

Greenberg, D. A. (1979). A numerical model investigation of tidal phenomena in the bay of fundy and gulf of maine. *Mar. Geod.* 2, 161–187. doi: 10.1080/15210607909379345

Hess, K. W., Gross, T. F., Schmalz, R. A., Kelley, J. G. W., Aikman, F., Wei, E., et al. (2003). *NOAA Technical Report NOS CS 17: NOS Standards for Evaluating Operational Nowcast and Forecast Hydrodynamic Model Systems*. Silver Spring, MD: National Oceanic and Atmospheric Administration.

Huang, X. (2012). A comprehensive study of the Bellhop algorithm for underwater acoustic channel modelings. *J. t Acous. Soc. Am.* 132, 1942–1942. doi: 10.1121/1.4755149

Hughes Clarke, J., Lamplugh, M., and Kammerer, E. (2000). "Integration of near-continuous sound speed profile information," in *Proceedings of Canadian Hydrographic Conference 2000* (Canada).

Hughes Clarke, J. E. (2003). Dynamic motion residuals in swatch sonar data: ironing out the creases. *Int. Hydrogr. Rev.* 4, 6–23.

Hughes Clarke, J. E. (2012). "Optimal use of multibeam technology in the study of shelf morphodynamics," in *Sediments, Morphology and Sedimentary Processes on Continental Shelves: Advances in Technologies, Research and Applications*, eds M. Z. Li, C. R. Sherwood, and P. R. Hill (Hoboken, NJ: John Wiley & Sons), 440.

Hughes Clarke, J. E. (2018). The impact of acoustic imaging geometry on the fidelity of seabed bathymetric models. *Geosciences* 8:109. doi: 10.3390/geosciences8040109

Hughes Clarke, J. E., Hiroji, A., Rice, G., Sacchetti, F., and Quinlan, V. (2017). Regional seabed backscatter mapping using multiple frequencies. *J. Acous,. Soc. Am.* 141, 3948–3948. doi: 10.1121/1.4988963

HydrOffice, (2019a). *SmartMap. Smart map the world!*. Available: https://www.hydroffice.org/smartmap/main (accessed 24 July 2019).

HydrOffice, (2019b). *Sound Speed Manager. Ease the management of your profiles!*. Available: https://www.hydroffice.org/soundspeed (accessed 24 July 2019).

IHO (2011). *C-13: Manual Of Hydrography*, 1.04 Edn. Monaco: International Hydrographic Organization.

Johnson, P., Ferrini, V. L., Jerram, K., and Masetti, G. (2018). "Multibeam advisory committee: looking back on seven years of multibeam echosounder system acceptance and quality assurance testing for the ships of the U.S. Academic Fleet," in *Femme 2018* (Bordeaux).

Kinsler, L. E., Frey, A. R., Coppens, A. B., and Sanders, J. V. (2000). *Fundamentals of Acoustics*. New York, NY: Wiley.

Kongsberg. (2015). *EM Series Datagram Formats - Instruction Manual - rev.U*. Norway: Kongsberg Maritime AS.

Lamarche, G., and Lurton, X. (2018). Recommendations for improved and coherent acquisition and processing of backscatter data from seafloor-mapping sonars. *Mar. Geophys. Res.* 39, 5–22. doi: 10.1007/s11001-017-9315-6

Lecours, V., Devillers, R., Schneider, D. C., Lucieer, V. L., Brown, C. J., and Edinger, E. N. (2015). Spatial scale and geographic context in benthic habitat mapping: review and future directions. *Mar,. Ecol. Progr. Ser.* 535, 259–284. doi: 10.3354/meps11378

Levitus, S., Antonov, J., Baranova, O. K., Boyer, T., Coleman, C., Garcia, H., et al. (2013). The world ocean database. *Data Sci. J.* 12, WDS229–WDS234. doi: 10.2481/dsj.WDS-041

Lucieer, V., Huang, Z., and Siwabessy, J. (2016). Analyzing uncertainty in multibeam bathymetric data and the impact on derived seafloor attributes. *Mar. Geod.* 39, 32–52. doi: 10.1080/01490419.2015.1121173

Luettich, R. A. Jr., Westerink, J. J., and Scheffner, N. W. (1992). "ADCIRC: an advanced three-dimensional circulation model for shelves, coasts, and estuaries," in *Report 1. Theory and Methodology of ADCIRC-2DDI and ADCIRC-3DL* (Vicksburg, MS: Coastal engineering research center).

Lurton, X. (2010). *An Introduction to Underwater Acoustics : Principles and Applications*. New York, NY: Springer.

Lurton, X., Lamarche, G., Brown, C., Lucieer, V., Rice, G., Schimel, A., et al. (2015). "Backscatter measurements by seafloor—mapping sonars: guidelines and recommendations,"in *A Collective Report by Members of the GeoHab Backscatter Working Group*. (New Zealand) 1–200.

Malik, M., Lurton, X., and Mayer, L. A. (2018). A framework to quantify uncertainties of seafloor backscatter from swath mapping echosounders. *Mar. Geophys. Res.* 39, 151–168. doi: 10.1007/s11001-018-9346-7

Masetti, G., Faulkes, T., and Calder, B. R. (2019). "Opening the black boxes in ocean mapping: design and implementation of the hydroffice framework," in *AMSA 2019* (Freemantle, WA).

Masetti, G., Gallagher, B., Calder, B. R., Zhang, C., and Wilson, M. (2017). Sound speed manager: an open-source application to manage sound speed profiles. *Int. Hydrogr. Rev.* 17, 31–40.

Masetti, G., Kelley, J. G. W., Johnson, P., and Beaudoin, J. (2018). A Ray-Tracing Uncertainty Estimation Tool For Ocean Mapping. *IEEE Access* 6, 2136–2144. doi: 10.1109/ACCESS.2017.2781801

Mayer, L., Jakobsson, M., Allen, G., Dorschel, B., Falconer, R., Ferrini, V., et al. (2018). The nippon foundation—GEBCO Seabed 2030 Project: the quest to see the world's oceans completely mapped by 2030. *Geosciences* 8, 63. doi: 10.3390/geosciences8020063

Mayer, L. A. (2014). Ocean mapping. *J. Ocean Technol.* 9, 13–18.

Medwin, H., and Clay, C. (1998). *Fundamentals of Acoustical Oceanography*. Cambridge, MA: Academic Press.

Mehra, A., and Rivin, I. (2010). A Real Time Ocean Forecast System for the North Atlantic Ocean. *Terr. Atmos. Ocean. Sci.* 21, 211–218.

Michaelis, C. D., and Ames, D. P. (2012). Considerations for Implementing OGC WMS and WFS Specifications in a Desktop GIS. *J. Geogr. Inform. Syst.* 4, 161. doi: 10.4236/jgis.2012.42021

Montereale-Gavazzi, G., Roche, M., Degrendele, K., Lurton, X., Terseleer, N., Baeye, M., et al. (2019). Insights into the Short-Term Tidal Variability of Multibeam Backscatter from Field Experiments on Different Seafloor Types. *Geosciences* 9:34. doi: 10.3390/geosciences9010034

NOAA (2019a). *Hydrographic Surveys Specifications and Deliverables*. Silver Spring, MD: National Oceanic and Atmospheric Administration, National Ocean Service.

NOAA (2019b). *The Gulf of Maine Operational Forecast System (GoMOFS) NOAA Tides and Currents*. Silver Spring, MD: NOAA.

NOS (2017). Updated: Implementation of New Oceanographic Forecast Modeling System for the Gulf of Maine Effective January 3, 2018. NOS Service Change Notice 17-108. Available: https://www.weather.gov/media/notification/pdfs/scn17-108nos_gomofsaaa.pdf (accessed December 4, 2017).

Peng, M., Zhang, A., and Yang, Z. (2018). "Implementation of the gulf of maine operational forecast system (GOMOFS) and the semioperational nowcast/forecast skill assessment,"in *NOAA Technical Report NOS CO-OPS 088*. Washington, DC: U.S. Department of Commerce.

Powers, J. G., Klemp, J. B., Skamarock, W. C., Davis, C. A., Dudhia, J., Gill, D. O., et al. (2017). The weather research and forecasting model: overview, system efforts, and future directions. *Bull. Am. Meteorol. Soc.* 98, 1717–1737. doi: 10.1175/bams-d-15-00308.1

Ritter, N., and Ruth, M. (1997). The GeoTiff data interchange standard for raster geographic images. *Int. J. Remote Sens.* 18, 1637–1647. doi: 10.1080/014311697218340

Ros, J. M. C. (2018). *Improved Sound Speed Control Through Remotely Detecting Strong Changes in the Thermocline*. Ph.D. Thesis University of New Hampshire , St, Durham, NH..

Rudnick, D. L., and Klinke, J. (2007). The underway conductivity–temperature–depth instrument. *J Atmos. Ocean. Technol.* 24, 1910–1923. doi: 10.1175/JTECH2100.1

Sowers, D., White, M. P., Malik, M., Lobecker, E., Hoy, S., and Wilkins, C. (2019). "NOAA ship okeanos explorer 2018: ocean mapping achievements," in *New Frontiers in Ocean Exploration: The E/V Nautilus, NOAA Ship Okeanos Explorer, and R/V Falkor 2018 Field Season*, eds N. A. Raineault, and J. Flanders (Rockville, MD: The Oceanographic Society), 92–95. doi: 10.5670/oceanog.2019.supplement.01

Tonani, M., Balmaseda, M., Bertino, L., Blockley, E., Brassington, G., Davidson, F., et al. (2015). Status and future of global and regional ocean prediction systems. *J Operat. Oceanogr.* 8, s201–s220. doi: 10.1080/1755876X.2015.1049892

UKHO, (2004). *Hydrographic Quality Assurance Instructions for Admiralty Surveys*. Taunton: United Kingdom Hydrographic Office.

van Rossum, G. (2018). *The Python Language Reference: Release 3.6.4*. Suwanee, GA: 12th Media Services.

Weber, T. C., Rice, G., and Smith, M. (2018). Toward a standard line for use in multibeam echo sounder calibration. *Mar. Geophys. Res.* 39, 75–87. doi: 10.1007/s11001-017-9334-3

Wilson, M., Beaudoin, J., and Smyth, S. (2013). "Water-column variability assessment for underway profilers to improve efficiency and accuracy of multibeam surveys," in *U.S. Hydrographic Conference* (New Orleans, LA).

Xue, H., Chai, F., and Pettigrew, N. R. (2000). A model study of the seasonal circulation in the gulf of maine. *J. Phys. Oceanogr.* 30, 1111–1135. doi: 10.1175/1520-0485(2000)030<1111:amsots>2.0.co;2

Yang, Z., Richardson, P., Chen, Y., Kelley, J. G. W., Myers, E., Aikman, F., et al. (2016). Model development and hindcast simulations of NOAA's gulf of maine operational forecast system. *J. Mar. Sci. Eng.* 4:77. doi: 10.3390/jmse4040077

Zhang, A., Hess, K. W., Wei, E., and Myers, E. (2006). *NOAA Technical Report NOS CS 24: Implementation of Model Skill Assessment Software for Water Level and Current in Tidal Regions*. Silver Spring, MA: U.S. Department of Commerce.

Conflict of Interest: The authors declare that the research was conducted in the absence of any commercial or financial relationships that could be construed as a potential conflict of interest.

frontiers in Marine Science

ORIGINAL RESEARCH
published: 28 January 2020
doi: 10.3389/fmars.2020.00009

Standardized Geomorphic Classification of Seafloor Within the United States Atlantic Canyons and Continental Margin

Derek C. Sowers[1,2], Giuseppe Masetti[1], Larry A. Mayer[1], Paul Johnson[1], James V. Gardner[1] and Andrew A. Armstrong[1,3]*

[1] Center for Coastal and Ocean Mapping – Joint Hydrographic Center, School of Marine Science and Ocean Engineering, University of New Hampshire, Durham, NH, United States, [2] CNSP at Office of Ocean Exploration and Research, National Oceanic and Atmospheric Administration, Silver Spring, MD, United States, [3] Office of Coast Survey, National Oceanic and Atmospheric Administration, Silver Spring, MD, United States

Accurate seafloor maps serve as a critical component for understanding marine ecosystems and guiding informed ocean management decisions. From 2004 to 2015, the Atlantic Ocean continental margin offshore of the United States has been systematically mapped using multibeam sonars. This work was done in support of the U.S. Extended Continental Shelf (ECS) Project and for baseline characterization of the Atlantic canyons, but the question remains as to the relevance of these margin-wide data sets for conservation and management decisions pertaining to these areas. This study utilized an automatic segmentation approach to initially identify landform features from the bathymetry of the region, then translated these results into complete coverage geomorphology maps of the region utilizing the coastal and marine ecological classification standard (CMECS) to define geoforms. Abyssal flats make up more than half of the area (53%), with the continental slope flat class making up another 30% of the total area. Flats of any geoform class (including continental shelf flats and guyot flats) make up 83.06% of the study area. Slopes of any geoform class make up a cumulative total of 13.26% of the study region (8.27% abyssal slopes, 3.73% continental slopes, and 1.25% seamount slopes). While ridge features comprise only 1.82% of the total study area (1.03% abyssal ridges, 0.63 continental slope ridge, and 0.16% seamount ridges). Key benefits of the study's semi-automated approach include computational efficiency for large datasets, and the ability to apply the same methods to large regions with consistent results.

Keywords: geomorphology, seafloor, classification, coastal and marine ecological classification standard, Atlantic, bathymorphon, geomorphometry, geoform

OPEN ACCESS

Edited by:
Pål Buhl-Mortensen, Norwegian Institute of Marine Research (IMR), Norway

Reviewed by:
Jason Chaytor, United States Geological Survey (USGS), United States
Peter Townsend Harris, Grid-Arendal, Norway

****Correspondence:***
Derek C. Sowers
derek.sowers@noaa.gov

Specialty section:
This article was submitted to Deep-Sea Environments and Ecology, a section of the journal Frontiers in Marine Science

Received: *17 June 2019*
Accepted: *09 January 2020*
Published: *28 January 2020*

Citation:
Sowers DC, Masetti G, Mayer LA, Johnson P, Gardner JV and Armstrong AA (2020) Standardized Geomorphic Classification of Seafloor Within the United States Atlantic Canyons and Continental Margin. Front. Mar. Sci. 7:9. doi: 10.3389/fmars.2020.00009

INTRODUCTION

Between 2004 and 2015, a vast region of the Atlantic Ocean margin adjacent to the east coast of the United States – from the continental shelf break to the abyssal ocean, from Canada to Florida – was systematically mapped using multibeam sonars, collecting both bathymetry and backscatter data (Gardner, 2004; Cartwright and Gardner, 2005; Calder and Gardner, 2008;

Lobecker et al., 2011, 2012, 2014, 2015a,b, 2017a,b, 2019; Armstrong et al., 2012; Malik et al., 2012; Lamplugh et al., 2013; Calder, 2015; Eakins et al., 2015; McKenna and Kennedy, 2015; Sowers et al., 2015; Lobecker, 2019a,b,c; Lobecker and Malik, 2019a,b; Lobecker and Sowers, 2019; Sowers and Lobecker, 2019). This work was done in support of the U.S. Extended Continental Shelf (ECS) Project (U. S. Extended Continental Shelf Project, 2011) and for baseline characterization of the submarine canyons in this region.

The unprecedented detail and complete coverage of these multibeam sonar data sets has enabled new insights into the distribution of submarine landslides (Twichell et al., 2009), the tsunami hazard potential of the Atlantic Margin (ten Brink et al., 2014), submarine canyon morphology (Brothers et al., 2013a), and the apparent relationship between canyon catchment area and sediment flow dynamics (Brothers et al., 2013b). However, the question remains as to the relevance of these margin-wide bathymetry and backscatter data sets for conservation and management decisions pertaining to these areas. This study utilizes one aspect of these data (bathymetry) to generate broad scale continuous coverage geomorphology maps as a key component of marine habitat characterization in support of ecosystem-based management of the ocean.

Broadly speaking, geomorphology is the study of the physical features of the surface of the earth (or other planets) and their relation to its geological structures (Stevenson, 2010). Seafloor geomorphology is a first-order expression of geologic processes that create benthic habitats. Harris (2012b) insightfully articulated three broad categories of spatial seafloor classification (geomorphology, seascapes, and predictive habitats), representing a continuum of characterization as managers move from data-poor to data-rich circumstances. Therefore classifying geomorphology serves as a fundamental step in translating bathymetry into value-added spatial data of use for ocean managers, and a primary basis for generating seascape maps and informing predictive habitat models. Maps of seafloor geomorphology directly support marine spatial planning, including applications in protected area designation, offshore infrastructure siting, geohazard assessment, habitat research, and environmental monitoring (Micallef et al., 2018).

Evaluating the usefulness of seafloor geomorphology as a proxy for characterization of complex benthic biological communities is an active area of global marine research effort (Harris and Baker, 2011; Althaus et al., 2012). While many useful studies have been completed on this topic, methods applied in one study area are typically challenging for other researchers to replicate in other regions of interest. When the delineation and classification of geomorphology is based solely on subjective expert opinion, results are difficult to duplicate by other scientists and the classification rules may only be readily applicable to specific regions. Thus, an important trend in this field of research is the development of approaches that take advantage of the computational power and the objectivity and reproducibility of automated digital terrain analysis tools (e.g., Verfaillie et al., 2007; Walbridge et al., 2018). With proper documentation, these tools also provide the benefit of reproducible analytical workflows and the generation of comparable results over large regions. This is becoming even more important as the global ocean exploration community is making commitments toward mapping the entirety of the Earth's deep sea by 2030 (Mayer et al., 2018), and interpreting the results in support of sustainable ocean management. Harris et al. (2014) produced the first digital global geomorphology map of the ocean generated using a combination of automated and expert judgment methods applied to the SRTM30_PLUS global bathymetry grid (Becker et al., 2009) reduced to a uniform grid spacing of about 1 km. The present study utilizes a terrain analysis approach based on the identification of bathymorphons (Jasiewicz and Stepinski, 2013; Masetti et al., 2018) in order to semi-automate the classification of landforms from a bathymetric terrain model with 100 m grid resolution covering a vast expanse of deep ocean seafloor off the east coast of the United States and Canada.

An emerging trend in the field of marine habitat characterization is the development and application of standardized classification schemes (e.g., European Environment Agency [EEA], 2004; Weaver et al., 2013). A "common language" of terminology in describing seabed features is necessary if spatial datasets from a variety of sources are to be synthesized into coherent products useful to ocean managers, researchers, and policy makers. The benefits of standardized classification schemes become particularly important when synthesizing marine habitat information at the regional level covering many marine datasets and management jurisdictions. Harris (2012a) provided a review of standardized hierarchical marine classification schemes utilized by different nations, and noted that direct comparisons among them are difficult given that they have been derived from varying information sources and intended for application to different environments. In the United States, the Coastal and Marine Ecological Classification Standard (CMECS) was developed as a framework for organizing data about the marine environment so that ecosystems can be identified, characterized, and mapped in a standard way across regional and national boundaries (Federal Geographic Data Committee [FGDC], 2012). The purpose of this study was not to evaluate the merits of different classification schemes, but rather to test and refine the application specifically of the CMECS standard to a deep sea environment largely within U.S. management jurisdiction.

CMECS is a hierarchical classification scheme that enables the user to characterize the marine environment utilizing separate "components" – major topical themes that describe the water column (water column component), the geomorphology of the seafloor (geoform component), the substrate of the seafloor (substrate component), and the biology of an area (biotic component). Each of these components has its own hierarchical structure and catalog of defined classification units. Thus thoroughly characterizing a cube of the three-dimensional marine environment could involve all four components. Each of these components can also be utilized independently of each other and used to generate separate spatial datasets. This paper focuses solely on the application of the CMECS geoform component. This work is envisioned as a fundamental piece of the larger holistic characterization of the marine seascape for the Atlantic Margin offshore of the United States.

Application of CMECS to deep sea habitats is still in the early phases of testing and adoption. As a dynamic content standard, CMECS incorporates the use of provisional units, which allow researchers to add proposed new units to the standard as they are discovered. This flexibility is especially valuable in the deep sea, where knowledge is increasing rapidly and new discoveries are commonplace in these poorly studied habitats. The current study developed methods to map the CMECS geoform component (geomorphology) in a repeatable way that could also be applied to other regions. This study demonstrates the application of both a semi-automated approach to delineating and classifying seafloor geomorphologies, and the application of a standardized terminology to describe these "geoforms" as consistent with the framework provided by CMECS.

The study region was selected to examine how broad scale multibeam sonar data specifically collected to support extended continental shelf studies can be further interpreted to provide value for ecosystem-based management purposes. It is important to note that within this paper, the terms continental shelf, continental slope, and continental rise and distinctions between them, are not being used in the context of Article 76 of the United Nations Convention of the Law of the Sea (UNCLOS) and thus should not be taken as representative of any U.S. position on the location of these boundaries. UNCLOS specifies the formulas a nation must use to delineate the continental shelf beyond 200 nautical miles for juridical purposes, unrelated to ecological processes or classification. This study used different criteria, based on professional judgement that met the study purpose of segmentation of the seafloor for application of an ecological classification scheme (CMECS) that has different classification decision rules from those applied under UNCLOS.

MATERIALS AND METHODS

Study Area and Input Datasets

The study area covered by this analysis includes the continental slope/rise and abyssal plain of the Atlantic Ocean east of the continental shelf of the east coast of the United States and Canada. Depths in the study area range from 72 m near the edge of the continental shelf break to a maximum depth of 5435 m in the abyssal plains. Mapped areas included in the study extend beyond the existing 200 nm maritime limit of the U.S. Exclusive Economic Zone (EEZ). The northern limits of the study area are at latitude 43° 47.8N offshore of Canada, and the southern limits of the area are at latitude 28°18.8N offshore from the U.S. state of Florida. The mapped area is approximately 959,875 km^2 (well over twice the size of the state of California).

The primary input dataset for the analysis was a digital terrain model generated via synthesis of the highest quality bathymetric data publicly available within the study region. The synthesis incorporates the best bathymetric data from 28 separate cruises (Johnson, 2018). All of the source data used in the analysis is available via the NOAA National Centers for Environmental Information multibeam archives (National Centers for Environmental Information [NCEI], 2004). The synthesis bathymetry grid specifically used in the study was created as part of the ECS effort and is available on a public internet map server hosted by the University of New Hampshire's Center for Coastal and Ocean Mapping/Joint Hydrographic Center (CCOM/JHC) (Johnson, 2018). The vast majority of bathymetry data used in the synthesis grid originated from extended continental shelf expeditions led by CCOM/JHC on several research vessels and on ocean exploration expeditions led by NOAA's Office of Ocean Exploration and Research on the NOAA vessel *Okeanos Explorer*. Data were also incorporated from mapping surveys conducted by other vessels.

Data were synthesized into a grid using WGS84 spatial reference and projected with the Lambert Conformal Conic projection. The bathymetric terrain model used for this study has a grid resolution of 100m and is shown in **Figure 1**. The bathymetric grid was generated using the weighted moving average gridding option in QPS Qimera software with a 3 × 3 moving window algorithm that fills small holes in the bathymetry and slightly smooths the overall surface. However, the underlying bathymetric data is very close to 100% full coverage at the 100 m resolution of the grid, and interpolated depth values are essentially negligible as a percentage of the study area mapped.

Data quality was validated for the mapping cruises that generated the data used in the synthesis by the calibration of multibeam mapping systems, professional ocean mapping experts overseeing all aspects of the surveys, regular frequent sound velocity profiles of the water column, rigorous cleaning of noise and erroneous soundings following raw data collection, and cross-line validation analysis of survey areas. The synthesis of multibeam sonar data was compiled and quality controlled by an expert from the UNOLS Multibeam Advisory Committee (Johnson, 2018; Multibeam Advisory Committee, 2019). Specifics on data quality control and validation can be found in the individual publicly available cruise reports for each cruise.

Bathymetry for the deeper regions of the study area (generally deeper than 2000 m) were collected as part of the ECS Project by CCOM/JHC. Data were collected on eight different cruises between 2004 and 2015, using 12-kHz, Kongsberg EM120 or EM122 multibeam sonars. Data were acquired with the initial purpose of supporting the determination of the outer limits of the U.S. juridical continental shelf consistent with international law.

Shallower bathymetry data that cover the shelf break and Atlantic canyons out to depths of the coverage of ECS cruises were collected for the National Oceanic and Atmospheric Administration (NOAA) Atlantic Canyons Undersea Mapping Expeditions (ACUMEN) Project using NOAA vessel *Okeanos Explorer*. Data were collected during nine different cruises using a 30-kHz Kongsberg EM302 multibeam sonar on the Okeanos Explorer between 2011 and 2014.

Interpretation of Seafloor Landforms

The analysis of the bathymetric terrain model of the study area utilized the bathymetry- and reflectivity-based estimator for seafloor segmentation (BRESS) method developed by Masetti et al. (2018). This tool is a free stand-alone application available at https://www.hydroffice.org/bress/main (Hydroffice, 2019). The BRESS analytical approach implements principles of topographic

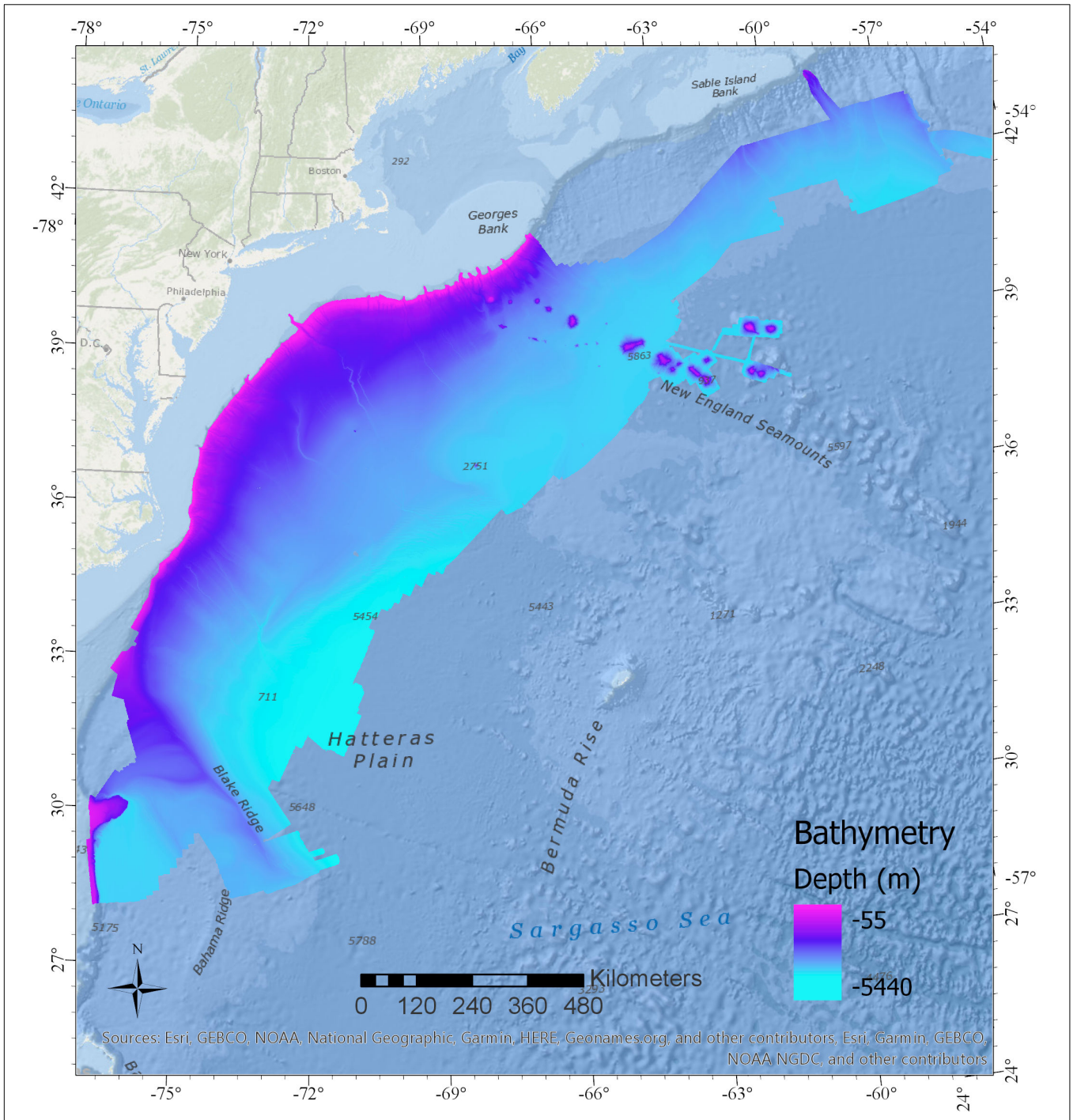

FIGURE 1 | Bathymetric synthesis terrain model grid of the U.S. Atlantic Margin study region used as the primary data source input into the study.

openness and pattern recognition to identify terrain features that can be classified into easily recognizable landform types such as valleys, slopes, ridges, and flats. These "bathymorphon" architypes represent the relative landscape relationships between a single grid node and surrounding grid nodes as assessed in eight directions around the node. The position of a grid node relative to others in the terrain are determined via a line-of-sight method looking out in each direction by a user defined search annulus specified by an inner and outer search radius. Details on this approach to geomorphic terrain analysis can be found in Jasiewicz and Stepinski (2013).

An important distinction between this method and many other terrain analysis algorithms is that the identification of landform elements between a grid node and eight directions

around it self-scales to adjacent features, whereas many terrain analysis algorithms work using a fixed neighborhood "moving window" approach (Jasiewicz and Stepinski, 2013). The grid neighborhood approach will identify fine features with a small cell window frame, and larger features with a bigger window, while the geomorphon approach has the capacity to capture both scales to some extent (within the limits of a defined search annulus). This is because it calculates elevation values (using both zenith and nadir angles) between the grid node and the maximum change in height of surrounding features (positive or negative) via a "line-of-sight" approach.

The bathymetry- and reflectivity-based estimator for seafloor segmentation algorithm was used to identify bathymorphon patterns in the bathymetric surface, generate area kernels (aggregations of the same bathymorphon type) and then utilizing a look-up classification table, these patterns were translated into landform types. The original geomorphon work (Jasiewicz and Stepinski, 2013) proposed a ten-type landform classification: flat, peak, ridge, shoulder, spur, slope, pit, valley, footslope, and hollow. BRESS introduced a simplified six-type landform classification (flat, ridge, shoulder, slope, valley, and footslope) and, recently, a minimalistic classification (flat, ridge, slope, and valley). The most simplistic classification was determined to be the best choice for the extremely large study area in this case, resulting in the creation of a continuous landform map of the Atlantic Margin region comprised of four classes: flat, slope, ridge, and valley.

Key user defined parameters in the landforms analysis tool within BRESS are the inner and outer radius of the search annulus and the flatness parameter. If the inner radius is set too small results can be negatively impacted by noise near the grid node (e.g., multibeam sonar surveying sound velocity offsets or outer beam "striping" artifacts in the bathymetry grid). The search annulus units are grid nodes, so the length of this is dependent directly on the resolution of the input raster grid. Alternatively, the user may specify the search radius parameters in meters. Reasonable values for the search annulus are fairly intuitive to a skilled analyst and are informed primarily by the scale of the features one is seeking to detect and the resolution of the bathymetric grid. The default parameters of inner/outer radii of 5/10 grid nodes, respectively, work well for many terrains. For this study extensive testing of the parameters on different regions of the grid revealed that an inner radius of 3 grid nodes and an outer radius of 15 grid nodes resulted in the delineation of landform features most comparable to what would be manually classified by a skilled analyst. This was determined by varying the inner and outer radius parameters of the model and draping the automatically classified landform spatial layers over the bathymetry for examination within 3D visualization software (QPS Fledermaus). The results were then evaluated to determine if delineations among landforms aligned with logical topographic feature breaks and to assess if the key morphologies of interest in the terrain (in this case ridges, slopes, valleys, and flats) were identified. Separate manual landform classification maps were not generated in this study for direct comparison with the automatic classification results, as they would be as equally subjective as the methodology used and therefore offer limited additional insights. The bathymetric grid used in this study was 100 m resolution, so the inner search radius was equal to 300 m and the outer radius was equal to 1500 m.

Results of the landforms analysis are sensitive to the choice of flatness parameter. Too large a flatness number will result in low to moderate relief seafloor features being classified as "flat," and too small a number will result in excessive "slope" results. This parameter was tested extensively in both the steep terrains (continental canyons and seamounts) and low relief terrains (e.g., abyssal plain) found in the study region. Testing results determined that one flatness parameter could not yield useful results for the entire region. It was determined that the extremely steep seamounts needed a flatness parameter of 5.0 degrees, the continental slope region of the margin needed a flatness parameter of 3.0 degrees, and the low gradient regions of the Blake Ridge and abyssal plains needed a flatness parameter of 1.0 degree. In order to apply the necessary variable flatness terrain values to the bathymetry, a separate spatial layer mask was created using the masking tool in BRESS, then applied to compute landforms (**Figure 2**). This flatness angle mask spatial layer was generated manually via interpretation of the logical bathymetric breaks among the continental slope, abyss, and seamount features.

The initial output of the landforms classification identified most of the prominent landform features of interest in both high and low relief areas of the study region. However, within low relief areas, a limited number of linear artifacts from the outer beam striping typical of multibeam sonar mapping systems were visible and easily discernible from real seafloor features. These small artifacts were minor and typical of the increased uncertainty of soundings in the outer beams of multibeam sonars, and were not the result of any interpolation of the original underlying dataset. Given the low flatness parameter applied to abyssal areas, the larger bumps in the outer swath sectors of multibeam in a few isolated areas were classified by BRESS as small landforms other than flats. These classification artifacts occurred in small select regions of the overall abyssal region of the grid, and were manually reclassified to flats via the application of a user-generated mask. This targeted manual quality control of the landform classification output was completed via visual inspection of the landforms draped on the bathymetric grid, and areas were corrected by encircling in a polygon using the masking tool within the BRESS software. While not an automated process, this tool provides a quick and effective quality check to improve the appearance and quantitative results of the analysis over survey areas subject to limited systematic artifacts from multibeam sonar surveys.

The output from the BRESS landform tool is either an ASCII Grid file or a geotiff image that can be imported into any spatial analysis or visualization software that can read these formats. The resolution of the output ASCII exactly matches the resolution of the input bathymetry file, in this case 100 m. The ASCII file consists of raster cells with code values that represent the landform designation of the nodes in the grid. In this case there were four code values representing each of the four landform

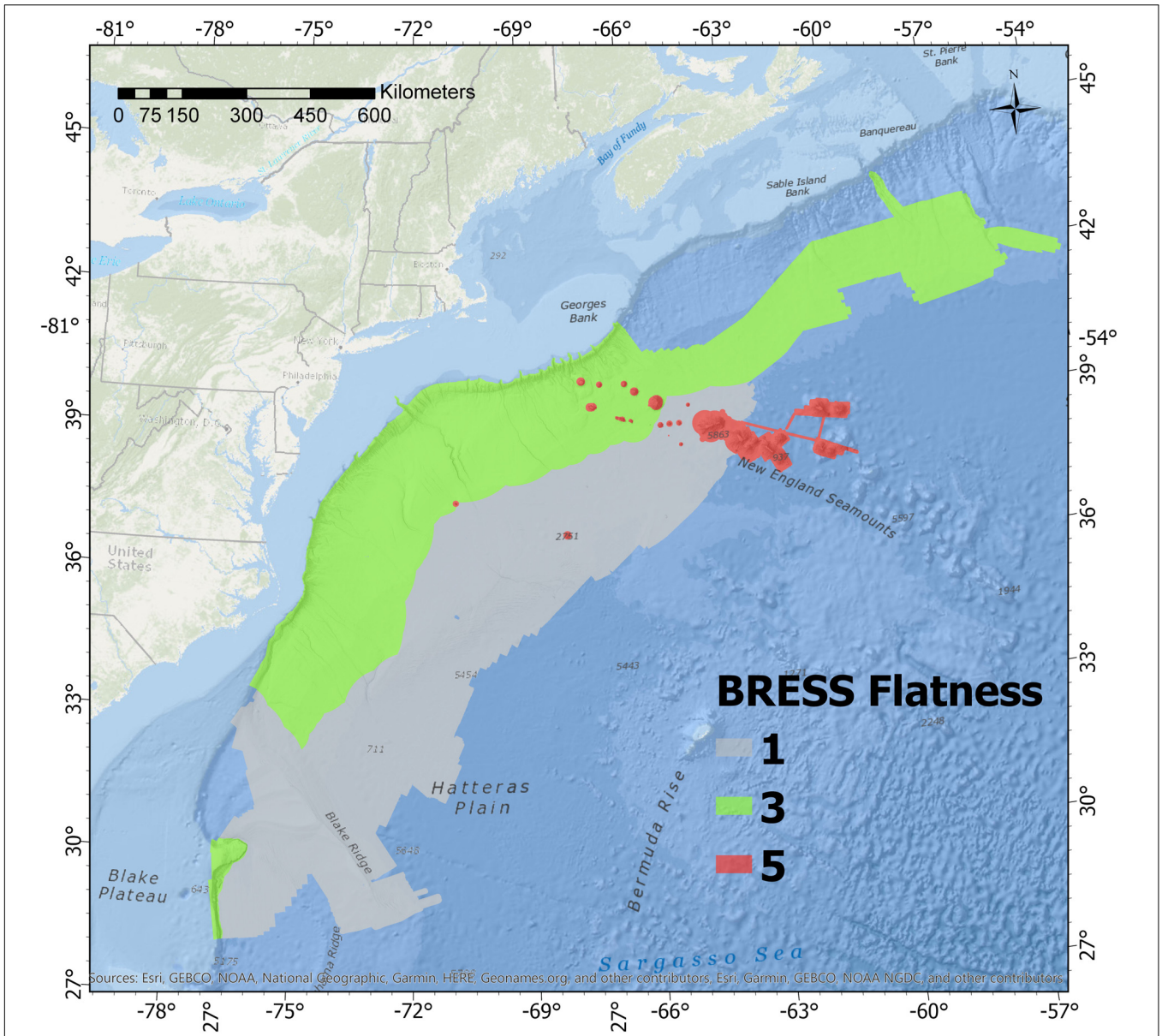

FIGURE 2 | Flatness parameter mask used to apply different flatness values of the BRESS landform algorithm to different regions of the Atlantic Margin study area. Parameter of 5.0 degrees (red) applied to the seamounts, 3.0 degrees (green) applied to the continental slope, and 1 degrees (gray) applied to abyssal areas. Bathymetry data shown in the background for context.

classes derived from the lookup table in BRESS: 1 for flats, 3 for ridges, 6 for slopes, and 9 for valleys.

Conversion of Landform Units to Coastal and Marine Ecological Classification Standard Geoform Units

The landform raster output from BRESS (a grid file in ASCII Grid format) was imported into ArcGIS Pro version 3.2 for additional analysis and conversion of landform units into CMECS geoform units. Landform units were modified to delineate CMECS geoforms using decision rules based on existing CMECs standard definitions of units. CMECS provides a catalog of units for geoform classification, along with definitions of each unit class in the standard document (Federal Geographic Data Committee [FGDC], 2012). Since CMECS is intended to be a dynamic content standard, the user is able to propose "provisional units" if the existing units do not adequately meet classification needs. This study proposes one new geoform called "valley" (not to be confused with the existing CMECS term "submarine canyon" which is a specific type of valley as explained further later) and six new geoform types that are intended to describe specific types of geoforms unique to deep sea features (**Table 1**).

TABLE 1 | CMECS geoform classes mapped within the Atlantic Margin study area.

	Tectonic setting	Physiographic setting	Geoform origin	Geoform	Geoform type (mapped unit name shown in study maps)
Shelf	Passive continental margin	Continental shelf	Geologic	Flat	Continental shelf flat
Continental Slope	Passive continental margin	Continental slope	Geologic	Flat	Continental slope flat
				Ridge	Continental slope ridge
				Slope	Continental slope
				Provisional: Valley	Continental slope valley
Abyssal plain	Abyssal plain	Marine basin floor	Geologic	Flat	Abyssal flat
				Ridge	Abyssal ridge
				Slope	Abyssal slope
				Provisional: Valley	Provisional: Abyssal valley
Seamount	Abyssal plain	Marine basin floor	Geologic	Seamount	Guyot/pinnacle seamount
				Flat	Provisional: Guyot flat
				Ridge	Provisional: Seamount ridge
				Slope	Provisional: Seamount slope
				Provisional: valley	Provisional: Seamount valley

CMECS classification hierarchy moves toward smaller sized features moving to the right within the columns. Classes noted as "provisional" (gray) are not yet part of the CMECS standard, but were used in this study and are recommended for adoption. A map of the final geoform types from this table is shown in ***Figure 11****. Units in column 6 show the names of the classification units assigned to the geoform maps presented in this study (mapped units). Most of the units in column 6 are not defined specifically in the Geoform Type hierarchy level of CMECS, but are implicit in the upper level classification (for instance a ridge geoform located on a continental slope is mapped as a continental slope ridge as the geoform type). The term "abyssal" was used in this column instead of "marine basin floor" as it was deemed more descriptive.*

Landform classes were converted to CMECS geoforms primarily by re-naming them as appropriate for the marine setting in which the units occurred throughout the extent of the Atlantic Margin. While landform units can be thought of as the primary building blocks for the identification of larger geomorphic seafloor features (e.g., canyon complexes and sand wave fields) it is proposed here that they also have value in many cases for direct translation into classified geomorphic features. This assertion is based on the fact that the landform features identified for the study area largely fit well within the existing geomorphic classification scheme being applied (CMECS). As apparent from **Table 1**, the landform types "flat," "ridge," and "slope" are also existing geoform units within CMECS. So a direct translation from landforms to geoforms for these cases was logical.

Although existing CMECS units worked well for direct translation of some landforms, other terms that are useful are not yet part of the standard. For instance, valley features were evident in all of the major study regions evaluated (continental slope, abyssal plain, and seamounts), but the concept of a valley feature in the deep sea is absent from CMECS. CMECS currently has Submarine Canyons (Physiographic Setting), Shelf Valleys (Level 1 geoform), and Channels (Level 1 and 2 geoforms). None of these classification terms are adequate descriptors for all of the valleys observed in deep sea environments. While certainly some of the valley features on the continental slope and on seamounts and guyots could be called "submarine canyons," there are many valley features in these areas identified as valleys in the landform analysis which are not submarine canyons. Fortunately, CMECS was designed to be a dynamic content standard subject to user refinement and open to proposals for formal future modifications. Users are advised to designate "provisional units" for classes that are deemed useful but absent from the current version of the standard. Therefore, this study designated the term "valley" as a provisional geoform unit for now (column 5 in **Table 1**), and then defined provisional geoform type units (another step down in the classification hierarchy, column 6 in **Table 1**) to describe the specific types of valleys occurring within the context of different features in the deep ocean (continental slopes, abyssal areas, and seamounts).

CMECS currently lacks geoform terms that adequately describe the geomorphology of features found within seamount features. Seamounts as entire features are covered by the standard, as there is a Seamount geoform unit and both Guyot and Pinnacle Seamount geoform types defined. It is proposed that adding Guyot Flat, Seamount Ridge, Seamount Slope, and Seamount Valley would all be useful unit additions to the standard. These units are shown as provisional units in **Table 1**. Seamounts have been demonstrated to be hotspots of biological diversity in the deep sea. Ocean exploration ROV dives on seamounts have found that ridge features and the edges of guyots can support dense and diverse aggregations of deep sea corals and sponges, where sessile attached fauna take advantage of the combination of exposed hard substrates and food-supplying currents that can occur in these relatively rare topographic areas (see for example NOAA CAPSTONE expedition results in Raineault et al., 2018).

It is important to note that this study did not classify and map geoforms that are comprised of a complex aggregation of landforms. For instance, a submarine canyon is an important feature to map and identify along continental margins, and a CMECS geoform descriptor exists for this feature. However, a typical manual delineation encircling a complete canyon system would encompass the following separate landform types: a channel at the bottom of the valley (thalweg), the steep valley walls, and the ridges on the tops of the slopes. Therefore this

single geomorphological unit is comprised of valley, slope, and ridge landforms [refer to Harris et al. (2014) for example]. Complex submarine canyon systems contain many of these features, as well as flats and more complex landforms not part of the current scheme (e.g., pits, peaks, and shoulders, etc.). Also, since the purpose of this study was to demonstrate what can be done via semi-automated terrain analysis tools over very large regions manual delineation of these more complex morphologies was not attempted.

CMECS is structured with physiographic setting high up in the hierarchy in order to discriminate between continental shelf, continental slope, abyssal plain, and seamount features. Therefore it was necessary to spatially delineate the study region into these categories. This was done by using the flatness mask ASCII grid which was already developed during landform modeling, as it was driven directly by the need to apply different flatness parameters to the continental slope, abyssal plain, and seamount regions. The mask was modified for the region offshore of Canada, as this region was mostly deep abyssal plain for the purposes of geoform classification, but was originally given the flatness parameter applied to the continental shelf due to the need to minimize classification of significant multibeam artifacts.

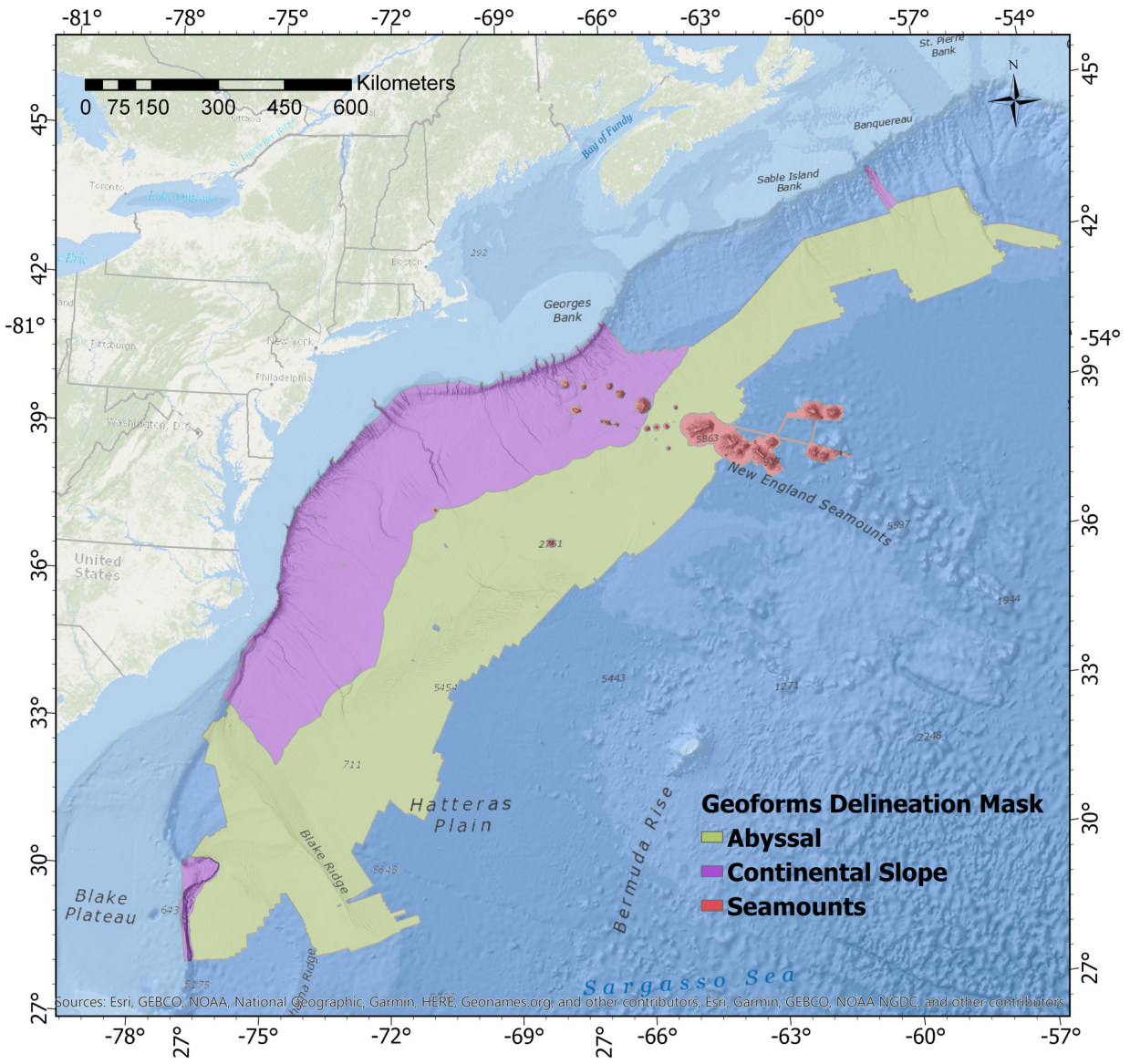

FIGURE 3 | Regional mask applied to the study region in order to provide approximate CMECS classification boundaries between continental slope areas (purple shading) seamounts (red shading), and abyssal regions (green shading). Bathymetry data is shown in the background for context. The key difference with the **Figure 2** (flatness parameter) mask is that the deep areas offshore of Canada are included with the abyssal (i.e., deep and low gradient) areas, whereas in **Figure 2** that area was masked differently because it had low relief features that were hard to discriminate from multibeam mapping artifacts in the bathymetry and thus needed a larger flatness parameter value.

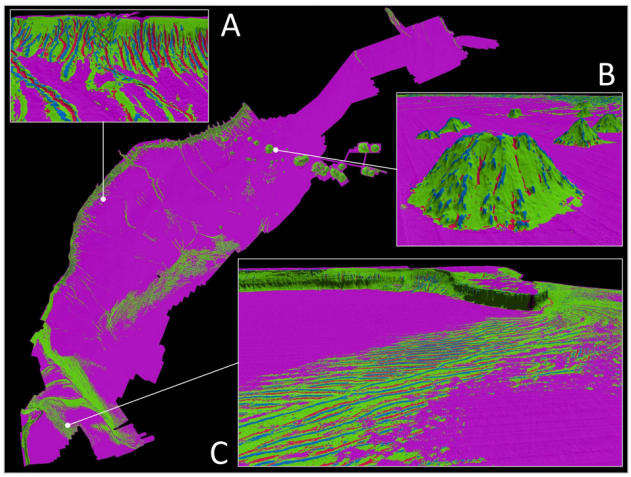

FIGURE 4 | Continuous coverage landform map of the Atlantic Margin study region classified into four landform types: flats (purple), slopes (green), ridges (blue), and valleys (red). Oblique 3-D inset views of landform type draped on bathymetry provided to show details. Note the clear delineation of canyon ridges, valleys, and steep slopes on the continental slope **(A)**. Seamount features are dominated by very steep slopes with occasional ridge and valley features **(B)**. Several large regions of the abyssal plains exhibit bedform features that follow a distinct pattern of repeating crest and trough (slope and ridge landform) combinations. Bottom right inset highlights one of these bedform fields east of the prominent Blake Spur feature **(C)**. Figure made with QPS Fledermaus software version 7.7.9. with vertical exaggeration of 4×.

While the term "continental rise" is a physiographic setting term in CMECS, it was not used in the study. This was because the Atlantic Margin has a gradual slope in many areas that makes it challenging to discriminate between a continental slope and a continental rise, and if present, a flattening out in gradient did not appear to occur until depths of 4000 m at the shallowest. In these settings, it was logical to refer to the area deeper than this as part of the abyssal plain. The global geomorphology classification study by Harris et al. (2014) did define a continental rise along the U.S. Atlantic continental margin, but the resolution of the data and methods for that study were different, and the results were therefore not applied to this study.

Delineation of seamounts from abyssal plain was straightforward, with clear topographic breaks between the two. The mask provides a more subjective delineation of continental slope and abyssal plain regions based on professional judgment of the approximate transition zone between the two. This was done visually based on the bathymetry grid and the approximate location of where the gradient flattened out. Using the depth contour lines was another option as a way to distinguish between continental slope and abyssal landforms, but this was not selected because it was a poor fit for the actual feature breaks along the entire length of the margin. Based on examining the changes in gradient along the margin, the demarcation mask between continental slope and abyssal areas was established generally between 4000 and 5000 m in depth along most of the margin, except for the southern region which

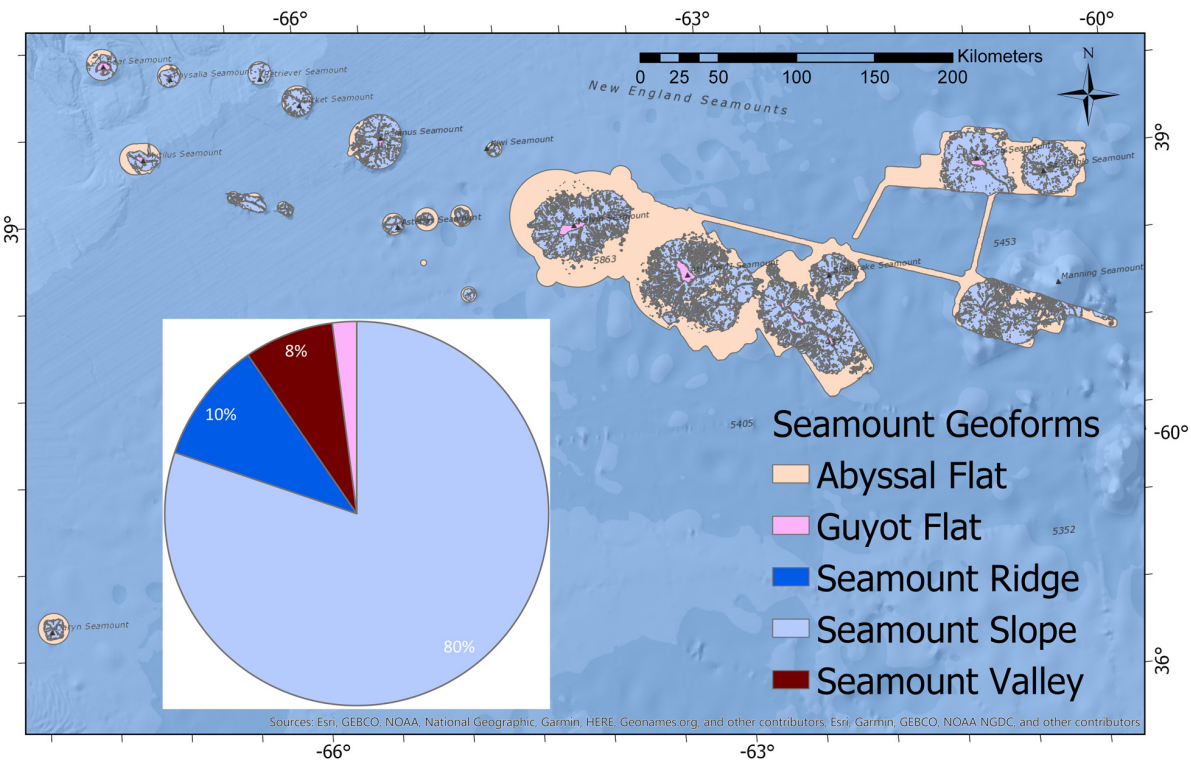

FIGURE 5 | CMECS geoform classifications specific to seamounts. The tan area shown in the figure met the definition of the "abyssal flat" class and was added to that class for calculating overall study region summary statistics and for the map shown in **Figure 11** of all geoform classes for the whole region.

has the dramatically different features of Blake Ridge and Blake Escarpment. Because of its character in relation to CMECS concepts, all of Blake Ridge was included in the abyssal marine basin floor category even though it gets shallower than 3000 m for a small portion in the study area. The logical topographic break on the Blake Escarpment was at the base of the escarpment at a depth contour of approximately 5000 m.

Although depths greater than 3000 m in the ocean are commonly referred to as abyssal depths, along the Atlantic Margin in many areas the actual depth where the continental slope flattens out onto an abyssal plain is substantially deeper. Alternatively, using a smoothed (generalized) gradient map of the margin was also evaluated, but was also not deemed an effective delineation approach in this case. Although the U.S. ECS Program refers to the continental slope and determines foot of the slope for juridical purposes, those delineations are a special use case unrelated to ecological processes or classification. The mask used to delineate among seamounts, continental slope, and abyssal regions for this study's specific purpose of classifying CMECS geoforms is shown in **Figure 3**. This mask was created manually via expert interpretation, and was a modification of the flatness parameter mask used in BRESS software for the landforms analysis.

For visualization purposes the raster grid output of landforms from BRESS was imported into QPS Fledermaus software (version 7.7.9) and draped onto the bathymetric grid. This provided for effective three-dimensional exploration of the landform interpretation directly on top of the bathymetry from which is was derived (see **Figure 4** in section "Results"). This method was utilized to evaluate the results of testing various search annulus and flatness parameter settings from the BRESS landforms tool, as well as for visualization of the final output prior to further geoprocessing in ArcGIS Pro.

Raster grids of the seafloor geoforms were converted in ArcGIS Pro to vector files for the creation of plots showing square kilometers within each geoform classification. These spatial files were also used to select polygons on the continental shelf to reclassify the geoform type as "continental shelf flats," and to select the flat tops of some of the seamounts (guyots) to reclassify these areas to geoform type "guyot flats." CMECS classifies guyots as a type of seamount, as the "seamount" unit is at the geoform level of the hierarchy,

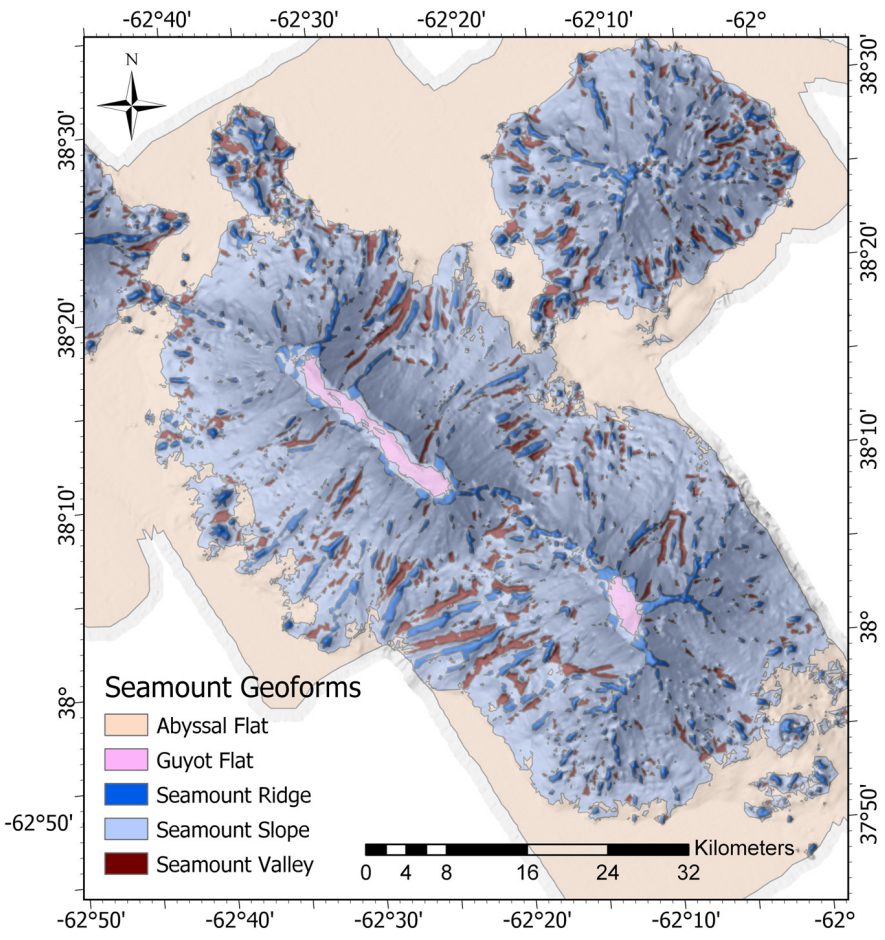

FIGURE 6 | Geoform classes of Gosnold Seamount. A hillshade layer was computed from the bathymetry and is shown with partial transparency to provide depth and context to the figure.

and "guyot" and "pinnacle seamount" are nested within this class at the geoform type level. This reclassification was done using manual selections in ArcGIS Pro software, but was limited to a small subset of the data given the small spatial extent of these geoform units relative to the size of the study region.

RESULTS

Seafloor Geomorphology Maps: Landforms

The results of the landform analysis are shown in **Figure 4**, showing flats in purple, slopes in green, ridges in blue, and valleys in red. It is immediately notable (and expected) that the dominant landform class in the region is flats. The classification of flat doesn't mean an area lacks any slope, it is classified as such in relation to the surrounding terrain and subject to the flatness parameter defined in BRESS. Slope landforms are the second-most dominant class, and together with flats show the dominant relief features of the Atlantic Margin even at the broad scale of the entire study region. Ridge and valley features provide insightful details into the structure and complexity of the continental slope canyons, abyssal bedform fields, and seamount features (see insets in **Figure 4**). Overall the landform results exhibit logical topographic breaks when draped over the bathymetry data, and the automated classification process from BRESS clearly works well for this purpose.

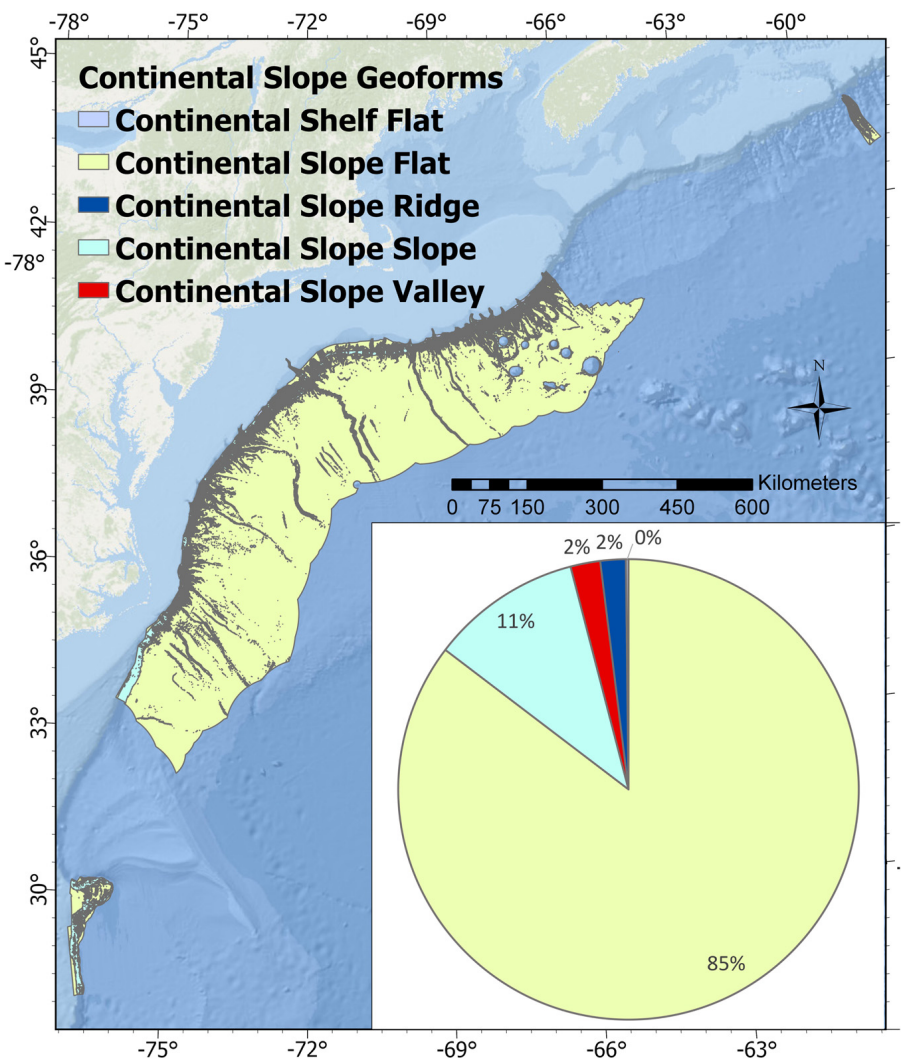

FIGURE 7 | CMECS geoform classifications specific to the continental slope region of the study area. 85% of the area is classified as flats, followed by 11% slopes. Ridges and valleys both comprised 2% each. A very small portion of the mapped area in the study (0.2%) was classified as continental shelf flat (in the shallow areas above the heads of the canyons). These results highlight the fact the continental slope drops off dramatically within a relatively short distance down the steep Atlantic canyons region of the margin, then exhibits a mild gradient down to abyssal depths. While the "continental slope flat" geoform type (yellow green) occurs on the continental slope, it is classified as a flat relative to the steepness of the canyons region, and due to the fact that slopes in these areas are nearly uniformly gradual and tend to range from about 0.1–1.5 degrees.

Seafloor Geomorphology Maps: Geoforms

CMECS geoform maps derived from the landform maps are shown in **Figures 5–11**. Results are shown separately for seamounts (**Figures 5**, **6**), continental slope features (**Figures 7**, **8**), and abyssal features (**Figure 9**). For each of these regions the area of each geoform unit class, and percent contribution of each class to the whole area, were calculated. Area is report in square kilometers. The relative dominance or rarity of geoform types has ramifications for the potential habitat role of these areas, and can inform management decisions pertaining to regional marine spatial planning.

Seamount geoforms are dominated by seamount slopes (80% by area). The second most notable features are seamount ridges (10%), followed by seamount valleys (8%). The uniform steepness of the seamounts on all sides and scarcity of consistent prominent ridge features as visible from the maps is consistent with these numbers. The rarity of the guyot flat class (2%) highlights how small these features truly are by area, even though their visual interest in bathymetric maps immediately makes an impression on the interpreter. Only 9 out of the 28 seamounts within the study region have flats at their tops (guyot flats).

In the abyssal region 84% of the area is classified as flats, 13% as slopes, 2% as ridges, and about 1% as valleys. Notable geoform characteristics of this region include the dominance of flats, the major contribution of the Blake Ridge feature to the slope class, and the importance of the bedform sediment wave formations in the U.S. Mid- and South-Atlantic regions to the slope, ridge, and valley classes. Bedform features and broad shallow submarine channels offshore of the Canadian margin do exist, but were not picked up by the methods used in this study given their smaller extent and vertical relief.

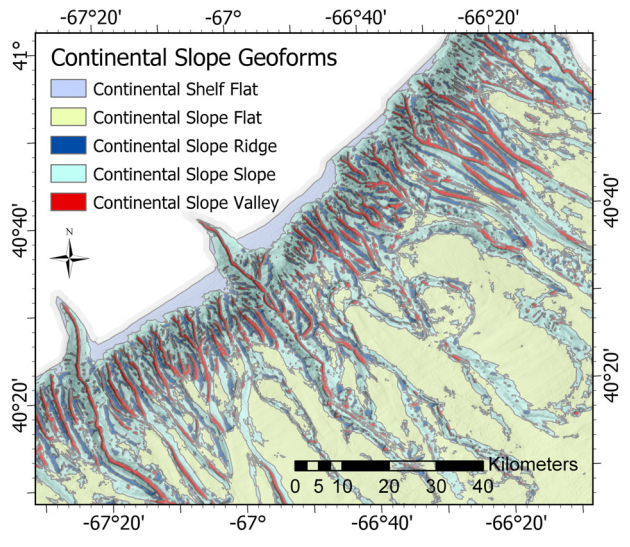

FIGURE 8 | Prominent submarine canyon features on the continental slope in the Mid-Atlantic as classified by CMECS geoforms. This geoform map clearly highlights the extensive network of gullies and submarine canyons that are a signature feature of the region. A hillshade layer was computed from the bathymetry and is shown with partial transparency to provide depth and context to the figure.

Figure 10 shows a complex region of the study area encompassing portions of Blake Escarpment, Blake Spur, and Blake Ridge. The figure provides mapped geoforms in both the continental shelf and abyssal portions of the study area. The bedform features in the right corner of the figure are striking, with crest-to-crest distances between about 2000–3000 meters.

Figure 11 illustrates the results for all geoform classes across the entire Atlantic Margin study area. Abyssal flats make up more than half of the area (53%), with the continental slope flat class making up another 30% of the total area. Flats of any geoform class (including continental shelf flats and guyot flats) make up 83.06% of the study area. Slope classes make up a cumulative total of 13.26% of the study region (8.27% abyssal slopes, 3.73% continental slopes, and 1.25% seamount slopes). While ridge features comprise only 1.82% of the total study area (1.03% abyssal ridges, 0.63 continental slope ridge, and 0.16% seamount ridges). The area (in square kilometers) and percentage calculations for each geoform class are shown in **Table 2**.

DISCUSSION

Advantages of the Semi-Automated Standardized Geomorphic Classification

This study tested the application of semi-automated terrain analysis methods and a standardized geomorphic classification scheme to a diverse region of the deep sea. The BRESS terrain analysis algorithm was effective at generating meaningful landform maps that could be readily translated to existing and proposed CMECS geoform units. Benefits of the tested methods include the following:

- The generation of landform results is repeatable and documented. The BRESS tool is based on a published mathematical terrain modeling approach, and is therefore not a "black box" tool. While improvements and refinements can be made to the algorithm, the methods are transparent.
- The semi-automated approach provides high speed classification of terrain over very large areas and complex terrain. The study area encompassed 959,875 km^2. The classification work presented in this paper represents several months of focused full time analytical effort (not including initial pilot studies, refinement of study analysis methods, and improvements to software interfaces). Full coverage manual interpretation of landforms and geoforms by a skilled analyst to a comparable level of detail is estimated to take 3–5× longer.
- The classification of landforms using the study methods involve far less subjectivity than classification methods conducted manually via expert interpretation.
- The line-of-sight analytical approach to terrain analysis employed in BRESS provides benefits in its ability to

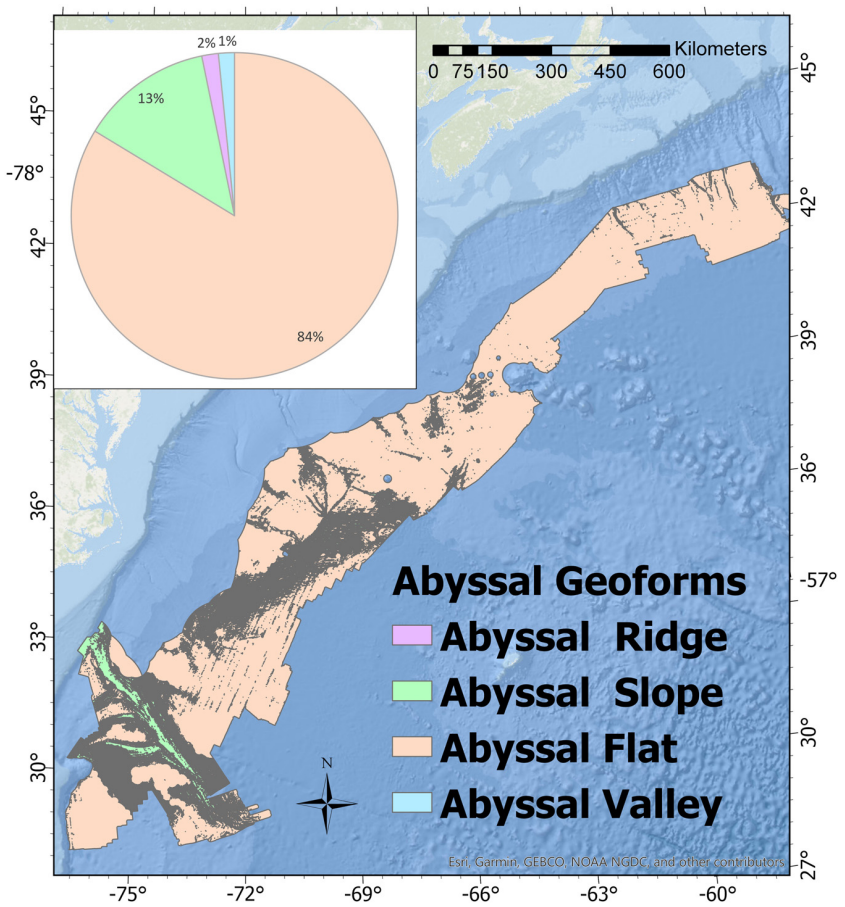

FIGURE 9 | CMECS geoform classifications for the abyssal region of the Atlantic Margin.

self-scale to features in the terrain as versus fixed neighborhood moving window algorithms.

- The methods are adaptable to data collected with different sensors and resolutions. The BRESS landform analysis tool can utilize bathymetry data independent of the technology used to generate the data. CMECS is also designed to be data agnostic. Both of these tools can be utilized to perform similar processing workflows that remain useful with emerging seafloor mapping technology and higher resolution maps.
- The methods are scalable to very large ocean regions, making them promising tools for interpreting data collected at regional scales and in international waters.
- Due to standardized processing methods and terminology this approach can enable integration of data sets from a variety of sources and provide outputs useable across a variety of ocean governance boundaries.

Limitations of the Approach

This approach is subject to limitations typical for studies employing methods to describe and map marine habitat, including the fact that all interpretation of remotely sensed information about the marine environment is constrained by issues of spatial and temporal scale and resolution of measurement data. This study was effective at classifying broad scale features discernible from a 100m resolution bathymetric grid generated from full coverage multibeam sonar data. Smaller geomorphic pattern detection is always limited by resolution and scale considerations. The BRESS tool used in this study currently requires several trial-and-error cycles to get the parameters fine-tuned to the study area. In addition, manually generated mask spatial layers based on subjective expert interpretation were still needed to adjust the flatness parameter across the terrain, to generally delineate among continental slope, abyss, and seamount regions, and to quality control a small subset of the landform classification output. The current study is one of several other applications of the landform modeling tool aimed at improving use guidelines and best practices.

As described in the methods section, the analysis results are fairly sensitive to the selection of an appropriate flatness angle parameter. Common artifacts in multibeam mapping data result from greater uncertainty in the seafloor bottom detections of the outer beams even for fully calibrated systems with regular sound velocity measurements being taken while surveying. In several thousand meters of water

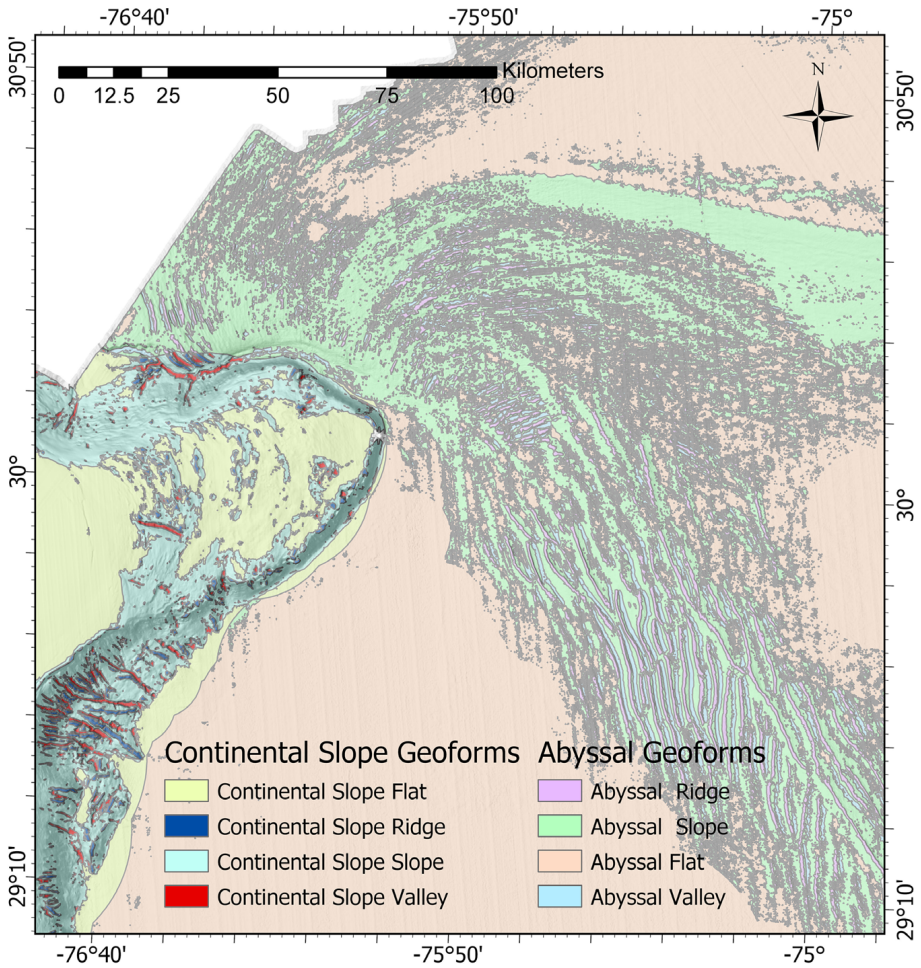

FIGURE 10 | Geoform view of part of the Blake Escarpment and Blake Ridge.

depth these striping artifacts in the mapping swath can result in bathymetric grid artifacts that can partially mask seafloor features of interest. In this setting, choosing a low flatness angle in BRESS can classify low relief features like the channels shown in **Figure 12**. However, that is often at the expense of also classifying the striping artifacts that are also embedded into the bathymetric grid (which are not real geomorphic features). In this case, choosing a higher value for the flatness parameter ignores the classification of undesired artifacts, but also loses the ability to classify features of interest like the abyssal channels in **Figure 12**. This area was ultimately assigned a higher flatness parameter of 3.0 degrees in the BRESS tool in order to avoid identifying the multibeam striping artifacts as landform features.

Complex combinations of landform elements that together aggregate into larger geomorphic features of interest were not identified in this study. A good example is the bedform features found in the abyssal plains of the study area. While the study effectively classified the slope, ridge, and valley combinations that comprise the components of larger geoforms such as a "sediment wave field," the ability to automatically classify these aggregate geoforms is the subject of future research.

Potential Applications of Coastal and Marine Ecological Classification Standard Geomorphic Maps

Coastal and Marine Ecological Classification Standard geoform maps for the Atlantic Margin provide insights useful for informing additional characterization of the region, and for informing current management decisions. The clear delineation of channels (i.e., the red continental slope valley features shown in **Figure 8**) for the Atlantic canyons makes it easy to see the low points and gain insights into the potential pathways of sediment transport out onto the abyssal basins. Their delineation from the surrounding terrain makes it easy to identify and enumerate the number of distinct canyon channels and continental shelf gullies more easily than by examining the bathymetry directly. This facilitates a better assessment of the nature and number of gully and submarine canyon features on this margin, and provides a quantitative

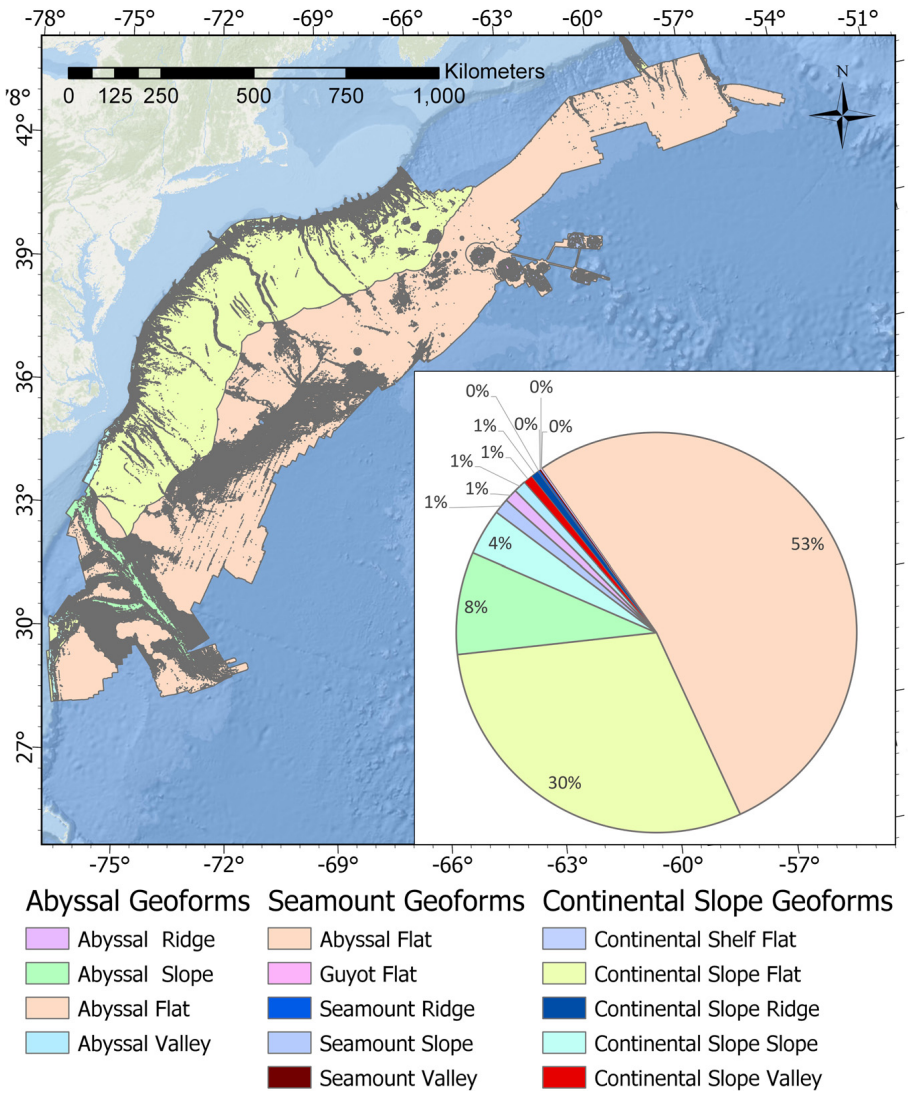

FIGURE 11 | CMECS geoform classifications for the entire Atlantic Margin region in the study.

methodical basis by which to compare these attributes to the same type of features on other continental margins. Similarly, the ability to automatically delineate significant ridge features within canyons has implications for assessing the habitat associations of organisms that may utilize these features.

The relative rarity of steep slopes (i.e., >3 degree angle from surrounding terrain) and ridges in the continental slope (11 and 2%, respectively) is striking. These areas have proven to be some of the highest likelihood places capable of supporting deep sea coral and sponge communities that often attach to steep exposed hard surfaces (Quattrini et al., 2015). The canyons area is clearly a hotspot of geodiversity, and has been recognized as a hotspot for biological diversity as well. The delineation of the canyon systems into flat, slope, ridge, and valley geoforms enables simple calculations of the relative number and area of these features within a given area of interest. This type of quantitative data on marine seascapes supports more informed marine resource management decisions, including strategic planning of marine protected area designations.

The extreme rarity of the guyot flat class (0.03% of the total area of the study region) make them a potentially vulnerable habitat. Extractive fishing pressure (Clark, 2010), seafloor mining activities (Miller et al., 2018), and potential impacts from climate change (Levin, 2019) could impact these relatively small areas in different ways than more abundant geoforms and a precautionary approach to management is appropriate given their relative scarcity in the marine environment. Limited exploration of seamounts to date has revealed that many of these features also serve as hotspots of biological diversity and habitat for deep sea coral and sponge communities (Lamplugh et al., 2013).

The ability to quickly automatically classify features such as steep slopes and ridges, generate accurate spatial datasets of these features, and calculate the area encompassed within them, should be of great interest to marine predictive habitat modelers. While

TABLE 2 | Geoform classes of the Atlantic Margin study region by area and percentage.

Mapped geoform classification unit	Area (square km)	Percent of margin
Abyssal flat	507,354.97	52.86
Continental slope flat	289,047.2	30.11
Abyssal slope	79,427.9	8.27
Continental slope	35,851.2	3.73
Seamount slope	11,978.5	1.25
Abyssal ridge	9,929.6	1.03
Abyssal valley	9,602.9	1.00
Continental slope valley	7,065	0.74
Continental slope ridge	6,047.7	0.63
Seamount ridge	1,531.8	0.16
Seamount valley	1,125.5	0.12
Continental shelf flat	606.8	0.06
Guyot flat	306.3	0.03

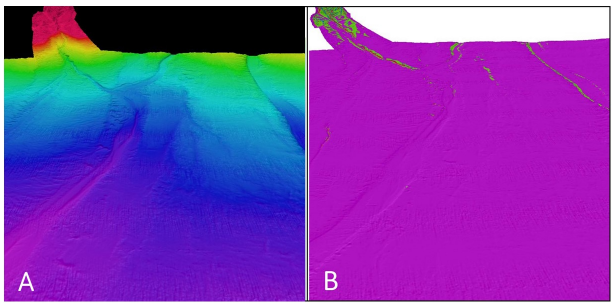

FIGURE 12 | Perspective view comparison of bathymetry data **(A)** with the classified landform results as draped on bathymetry **(B)**. Note the presence of channel features in the bathymetry that could not be resolved as geoforms using the landform parameters applied (they were classified as flats as represented by the purple color).

depth (bathymetry) is a common variable in habitat suitability modeling, having spatial layers of geoforms that are known to be strongly correlated with the presence of certain species or communities of biotic importance could support more powerful and accurate predictive models (e.g., Savini et al., 2014).

Conclusion

Our results provide a characterization of the marine landscape that serves as an inventory of the cumulative area and abundance of geoforms and the spatial relationships among them. The derived maps and associated databases can be used for a broad range of spatial analyses defined by other end users to inform management decisions. Geoform summary statistics were calculated over the study region to quantify the area of each geoform type. These analyses represent a first step in identifying regions of consistent morphology within which the consistency of the backscatter can then be determined (Masetti et al., 2018).

The approach developed through this work provides a model of how to consistently classify ecological marine units using CMECS as an organizing framework across large continental margin regions nationally or globally. Given that many nations have already invested heavily in gathering bathymetric data for these areas, this approach can be adopted to obtain a standardized interpretation to inform baseline marine habitat characterization in support of ecosystem-based management.

DATA AVAILABILITY STATEMENT

The datasets generated supporting the conclusions of this article will be made available by the authors, without undue reservation, to any qualified researcher. The primary input bathymetry dataset used by this study is publicly available and located at the following website URL: https://maps.ccom.unh.edu/portal/apps/webappviewer/index.html?id=375a12ced0e242bbbb83958069bbae2d. Source datasets for each cruise that were used as part of the synthesis grid are accessible at https://maps.ngdc.noaa.gov/viewers/bathymetry/.

AUTHOR CONTRIBUTIONS

DS and LM developed the conceptual ideas for the study as part of a larger investigation into utilizing data from the ECS Program for marine habitat characterization. DS completed the analysis of geomorphology and translation to proposed geoforms within the CMECS framework. GM created and refined the BRESS software utilized for automated identification of geomorphic landforms, and contributed substantially to the analysis and interpretation of the data. JG was Chief Scientist on 5 of the ECS cruises and processed and gridded all of the Atlantic ECS data. PJ analyzed and synthesized the regional bathymetric terrain model used as the primary data source for the study. DS, LM, and AA provided the critical revisions of the manuscript with respect to relevance to the field of seafloor characterization and ocean exploration.

FUNDING

Support for this research was provided by the NOAA grant NA15NOS4000200, Principal Investigator LM.

ACKNOWLEDGMENTS

The authors wish to acknowledge the contribution of the following collaborators to this study. Dr. Larry Ward for discussions and refinement of ideas on refining the BRESS software tool and converting landform classes to geoforms, JG for conceptualization of value-added uses for ECS datasets and leadership completing bathymetric surveys of the study area, Mark Finkbeiner for expert advice and guidance on the application of CMECS and development of this dynamic content standard, and the captains and crews of all of the oceanographic vessels involved in gathering the bathymetric data for the study.

REFERENCES

Althaus, F., Williams, A., Kloser, R. J., Seiler, J., and Bax, N. J. (2012). "Evaluating geomorphic features as surrogates for benthic biodiversity on australia's western continental margin," in *Mapping the Seafloor for Habitat Characterization*, eds B. J. Todd, and H. G. Greene, (Canada: Geological Association of Canada), 665–679. doi: 10.1016/b978-0-12-385140-6.00048-7

Armstrong, A. A., Calder, B. R., Smith, S. M., and Gardner, J. V. (2012). *U.S. Law of the Sea Cruise to Map the Foot of the Slope of the Northeast U.S. Atlantic Continental Margin: Leg 7*. Durham, NH: University of New Hampshire.

Becker, J. J., Sandwell, D. T., Smith, W. H. F., Braud, J., Binder, B., Depner, J., et al. (2009). Global bathymetry and elevation data at 30 arc seconds resolution: SRTM30_PLUS. *Mar. Geodesy* 32, 355–371. doi: 10.1080/01490410903297766

Brothers, D. S., ten Brink, U. S., Andrews, B. D., and Chaytor, J. D. (2013a). Geomorphic characterization of the U.S Atlantic continental margin. *Mar. Geol.* 338, 46–53.

Brothers, D. S., ten Brink, U. S., Andrews, B. D., Chaytor, J. D., and Twichell, D. C. (2013b). Geomorphic process fingerprints in submarine canyons. *Mar. Geol.* 337, 53–66. doi: 10.1016/j.margeo.2013.01.005

Calder, B. R. (2015). *U.S. Law of the Sea Cruise to Map the Foot of the Slope of the Northeast U.S. Atlantic Continental Margin: Leg 8*. Durham, NH: University of New Hampshire.

Calder, B. R., and Gardner, J. V. (2008). *U.S. Law of the Sea Cruise to Map the Foot of the Slope of the Northeast U.S. Atlantic Continental Margin: Leg 6*. Durham, NH: University of New Hampshire.

Cartwright, D., and Gardner, J. V. (2005). *U.S. Law of the Sea Cruise to Map the Foot of the Slope and 2500-m Isobath of the Northeast U.S. Atlantic Continental Margin: Legs 4 and 5*. Durham, NH: University of New Hampshire.

Clark, M. (2010). Effects of trawling on seamounts. *Oceanography* 23:1.

Eakins, B. W., Bohan, M. L., Armstrong, A. A., Westington, M., Jencks, J., Lim, E., et al. (2015). NOAA's role in defining the U.S. Extended Continental Shelf. *Mar. Technol. Soc. J.* 49, 204–210. doi: 10.4031/MTSJ.49.2.17

European Environment Agency [EEA] (2004). *European Nature Information System (EUNIS)*. Copenhagen, DK: European Environment Agency.

Federal Geographic Data Committee [FGDC] (2012). *FGDC-STD-018-2012. Coastal and Marine Ecological Classification Standard*. Reston, VA: Federal Geographic Data Committee.

Gardner, J. V. (2004). *U.S. Law of the Sea Cruise to Map the Foot of the Slope and 2500-m Isobath of the Northeast U.S. Atlantic Continental Margin: Cruises HO4-1,2, and 3*. Durham, NH: Center for Coastal and Ocean Mapping / Joint Hydrographic Center.

Harris, P. T. (2012a). "Biogeography, benthic ecology and habitat classification schemes," in *Seafloor Geomorphology as Benthic Habitat: GeoHab Atlas of Seafloor Geomorphic Features and Benthic Habitats*, eds P. T. Harris, and E. K. Baker (Amsterdam: Elsevier), 61–91. doi: 10.1016/b978-0-12-385140-6.00004-9

Harris, P. T. (2012b). *From Seafloor Geomorphology to Predictive Habitat Mapping: Progress in Applications of Biophysical Data to Ocean Management*. Canberra: Geoscience Australia.

Harris, P. T., and Baker, E. K. (eds) (2011). *Seafloor Geomorphology as Benthic Habitat: GeoHab Atlas of Seafloor Geomorphic Features and Benthic Habitats*. Amsterdam: Elsevier.

Harris, P. T., MacMillan-Lawler, M., Rupp, J., and Baker, E. K. (2014). Geomorphology of the oceans. *Mar. Geol.* 352, 4–24. doi: 10.1016/j.margeo.2014.01.011

Hydroffice (2019). *Bathymetric- and Reflectivity-Based Estimator of Seafloor Segments (BRESS)*. Available at: https://www.hydroffice.org/bress/main (accessed May 6, 2019).

Jasiewicz, J., and Stepinski, T. F. (2013). Geomorphons - A pattern recognition approach to classification and mapping of landforms. *Geomorphology* 182, 147–156. doi: 10.1016/j.geomorph.2012.11.005

Johnson, P. (2018). *Atlantic Margin Bathymetry and Backscatter Map Viewer*. Available at: https://maps.ccom.unh.edu/portal/apps/webappviewer/index.html?id=b130c6b32d9d4273af0ae1733ce19905 (accessed June 15, 2019).

Kennedy, B. R. C., Cantwell, K., Malik, M., Kelley, C., Potter, J., Elliott, K., et al. (2019). The unknown and the unexplored: insights into the Pacific Deep-Sea following NOAA CAPSTONE expeditions. *Front. Mar. Sci.* 6:480. doi: 10.3389/fmars.2019.00480

Lamplugh, M., Forbes, S., and Armstrong, A. A. (2013). *Joint Canada -U.S. Mapping Cruise in Support of Extending Territorial Claim Under the United Nations Convention on the Law of the Sea: Canadian Scotian Shelf. Final Field Report #2600352*. Ottawa: Canadian Hydrographic Service.

Levin, L. A. (2019). Sustainability in deep water: the challenges of climate change, human pressures, and biodiversity conservation. *Oceanography* 32, 170–180. doi: 10.1002/2017WR020970

Lobecker, E. (2019a). Mapping Data Acquisition and Processing Summary Report: Cruise EX-12-04 Exploration: Northeast Canyon and Continental Margins Mapping (Mapping). Silver Spring, MD: NOAA. doi: 10.5670/oceanog.2019.224

Lobecker, E. (2019b). *Mapping Data Acquisition and Processing Summary Report: Cruise EX-13-03, New England Seamount Chain Exploration (Mapping)*. Silver Spring, MD: NOAA.

Lobecker, E. (2019c). *Mapping Data Acquisition and Processing Summary Report: Cruise EX-13-04 Leg 2 Northeast United States Canyons Exploration*. Silver Spring, MD: NOAA.

Lobecker, E., Cantelas, F., Skarke, A., Peters, C., Stuart, L., Harris, A., et al. (2011). *Mapping Data Report: Cruise EX-11-06 Exploration Mapping, Pascagoula, Mississippi to Davisville, Rhode Island*. Silver Spring, MD: NOAA.

Lobecker, E., Doroba, J., Pinero, C., Smithee, T., Kok, T., Kennedy, B., et al. (2017a). *Mapping data acquisition and processing report, cruise EX1202 Leg 2: Exploration: Gulf of Mexico, March 19 - April 7, 2012 Tampa, FL to Pascagoula, MS*. Silver Spring, MD: NOAA.

Lobecker, E., Elliott, K., Gallant, L., James, J., Conway, R., and Raymond, A. (2015a). *Mapping Data Acquisition and Processing Report, Cruise EX-13-04 Leg 1, Exploration, NE Canyons, July 8 - 25, 2013*. Silver Spring, MD: NOAA.

Lobecker, E., Gray, L. M., and Skarke, A. (2019). *Mapping Data Acquisition and Processing Summary Report: Cruise EX-12-06 Northeast and Mid-Atlantic Canyons Exploration (Mapping)*. Silver Spring, MD: NOAA.

Lobecker, E., and Malik, M. (2019a). *Mapping Data Acquisition and Processing Summary Report: Cruise EX-12-01 Ship Shakedown and Patch Test Canyons and Continental Margin Exploration (Mapping)*. Silver Spring, MD: NOAA.

Lobecker, E., and Malik, M. (2019b). *Mapping Data Acquisition and Processing Summary Report: Cruise EX-12-05 Leg 2 Canyons and Continental Margin Exploration (Mapping)*. Silver Spring, MD: NOAA.

Lobecker, E., and Sowers, D. (2019). *Mapping Data Acquisition and Processing Summary Report: Cruise EX-14-01 Mission Systems Shakedown and Patch Test (Mapping)*. Silver Spring, MD: NOAA.

Lobecker, E., Malik, M., Gallant, L., Stuart, L., James, J., Conway, R., et al. (2015b). *Mapping Data Acquisition and Processing Report, Cruise EX-13-02 : Ship Shakedown & Multibeam Patch Test, ROV Shakedown & Field Trials, NE Canyons Exploration, May 13 - June 6, 2013, Charleston, South Carolina to North Kingstown, Rhode Island*. Silver Spring, MD: NOAA.

Lobecker, E., Malik, M., Gallant, L., Stuart, L., James, J., Nadeau, R., et al. (2014). *Mapping Data Acquisition and Processing Report, Cruise EX-13-01: Ship Shakedown & Patch Test & Exploration, Northeast Canyons (Mapping), March 28 - April 5, 2013 N. Kingston, RI - N. Kingston, RI*. Silver Spring, MD: NOAA.

Lobecker, E., Skarke, A., Nadeau, M., Brothers, L., Bingham, B., Stuart, L., et al. (2012). *Mapping Data Acquisition and Processing Report : Cruise EX1205 Leg 1, Exploration Blake Plateau, July 5 - 24, 2012*. Silver Spring, MD: NOAA.

Lobecker, E., Sowers, D., McKenna, L., Rose, E., James, J., Weller, E., et al. (2017b). *Mapping Data Acquisition and Processing Report, Cruise EX-14-02 Leg 1: Mission System Shakedown and Patch Test, February 24 - March 15, 2014 N. Kingstown, RI - N. Kingstown, RI*. Silver Spring, MD: NOAA.

Malik, M., Stuart, L., Argento, A., Denney, S., Flinders, A., Whitesell, D., et al. (2012). *Mapping Data Report. Cruise EX1203, Exploration Mapping, Gulf of Mexico, May 5 - May 23, 2012, Galveston, TX to Norfolk, VA*. Silver Spring, MD: NOAA.

Masetti, G., Mayer, L. A., and Ward, L. G. (2018). A bathymetry- and reflectivity-based approach for seafloor segmentation. *Geosciences* 8:14. doi: 10.3390/geosciences8010014

Mayer, L., Jakobsson, M., Allen, G., Dorschel, B., Falconer, R., Ferrini, V., et al. (2018). The Nippon Foundation - GEBCO seabed 2030 project: the quest to see the World's Oceans Completely Mapped by 2030. *Geosciences* 8:63. doi: 10.3390/geosciences8020063

McKenna, L., and Kennedy, B. (2015). *Mapping Data Acquisition and Processing Report, Cruise EX-14-04 Leg III : Exploring Atlantic Canyons and Seamounts (ROV and Mapping), September 16 to October 7, 2014 Baltimore, MD - N. Kingstown, RI*. Silver Spring, MD: NOAA.

Micallef, A., Krastel, S., and Savini, A. (eds) (2018). *Submarine Geomorphology*. Cham: Springer.

Miller, K. A., Thompson, K. F., Johnston, P., and Santillo, D. (2018). An overview of seabed mining including the current state of development, environmental impacts, and knowledge gaps. *Front. Mar. Sci.* 4:418. doi: 10.3389/fmars.2017.00418

Multibeam Advisory Committee (2019). Available at: http://mac.unols.org/ (accessed June 6, 2019).

National Centers for Environmental Information [NCEI], (2004). *Multibeam Bathymetry Database (MBBDB)*. Silver Spring, MD: NOAA.

Quattrini, A. M., Nizinski, M. S., Chaytor, J. D., Demopoulos, A. W. J., Roark, E. B., France, S. C., et al. (2015). Exploration of the canyon-incised continental margin of the Northeastern United States Reveals dynamic habitats and diverse communities. *PLoS One* 10:e0139904. doi: 10.1371/journal.pone.0139904

Raineault, N. A., Flanders, J., and Bowman, A. (eds) (2018). New frontiers in ocean exploration: the E/V Nautilus, NOAA Ship Okeanos Explorer, and R/V Falkor 2017 field season. *Oceanography* 31, 1–94. doi: 10.5670/oceanog.2017.supplement.01

Savini, A., Vertino, A., Marchese, F., Beuck, L., and Freiwald, A. (2014). Mapping cold-water coral habitats at different scales within the Northern Ionian Sea (Central Mediterranean): an assessment of coral coverage and associated vulnerability. *PLoS One* 9:e87108. doi: 10.1371/journal.pone.0087108

Sowers, D., and Lobecker, E. (2019). *Mapping Data Acquisition and Processing Summary Report: Cruise EX-14-03 Exploration, East Coast (Mapping)*. Silver Spring, MD: NOAA.

Sowers, D., Lobecker, E., McKenna, L., Rose, E., James, J., and Malik, M. (2015). *Mapping data acquisition and processing report, cruise EX-14-04 Leg 1 : Ship shakedown & patch test & exploration, New England Seamounts (mapping), August 9 - August 29, 2014 N. Kingstown, RI - N. Kingstown, RI*. Silver Spring, MD: NOAA.

Stevenson, A. (2010). *Oxford Dictionary of English*. Oxford: Oxford University Press.

ten Brink, U. S., Chaytor, J. D., Geist, E. L., Brothers, D. S., and Andrews, B. D. (2014). Assessment of tsunami hazard to the U.S. Atlantic margin. *Mar. Geol.* 353, 31–54. doi: 10.1016/j.margeo.2014.02.011

Twichell, D. C., Chaytor, J. D., ten Brink, U. S., and Buczkowski, B. (2009). Morphology of late Quaternary submarine landslides along the U.S. Atlantic continental margin. *Mar. Geol.* 264, 4–15. doi: 10.1016/j.margeo.2009.01.009

U. S. Extended Continental Shelf Project (2011). Available at: https://www.state.gov/u-s-extended-continental-shelf-project/ (accessed June 15, 2019).

Verfaillie, E., Doornenbal, P., Mitchell, A. J., White, J., and Van Lancker, V. (2007). *The Bathymetric Position Index (BPI) as a Support Tool for Habitat Mapping. Worked example for the MESH Final Guidance*, 14.

Walbridge, S., Slocum, N., Pobuda, M., and Wright, D. J. (2018). Unified geomorphological analysis workflows with benthic terrain modeler. *Geosciences* 8:94. doi: 10.3390/geosciences8030094

Weaver, K. J., Shumchenia, E. J., Ford, K. H., Rousseau, M. A., Greene, J. K., Anderson, M. G., et al. (2013). *Application of the Coastal and Marine Ecological Classification Standard (CMECS) to the Northwest Atlantic*. Boston, MA: The Nature Conservancy.

Conflict of Interest: The authors declare that the research was conducted in the absence of any commercial or financial relationships that could be construed as a potential conflict of interest.

frontiers in Marine Science

ORIGINAL RESEARCH
published: 30 January 2020
doi: 10.3389/fmars.2019.00744

Enigmatic Deep-Water Mounds on the Orphan Knoll, Labrador Sea

Shawn P. Meredyk[1†], Evan Edinger[1,2], David J. W. Piper[3], Veerle A. I. Huvenne[4], Shannon Hoy[5,6] and Alan Ruffman[7,8]*

[1] Environmental Science Program, Memorial University of Newfoundland, St. John's, NL, Canada, [2] Department of Geography, Department of Biology, and Department of Earth Sciences, Memorial University of Newfoundland, St. John's, NL, Canada, [3] Natural Resources Canada, Geological Survey of Canada – Atlantic, Dartmouth, NS, Canada, [4] National Oceanography Centre, University of Southampton Waterfront Campus, Southampton, United Kingdom, [5] School of Earth Sciences, University of Bristol, Bristol, United Kingdom, [6] Department of Earth Science, University of New Hampshire, Durham, NH, United States, [7] Geomarine Associates, Ltd., Halifax, NS, Canada, [8] Department of Earth Sciences, Dalhousie University, Halifax, NS, Canada

OPEN ACCESS

Edited by:
Vincent Lecours, University of Florida, United States

Reviewed by:
Autun Purser, Alfred Wegener Institute Helmholtz Centre for Polar and Marine Research (AWI), Germany
Andrea Gori, University of Salento, Italy

***Correspondence:**
Evan Edinger
eedinger@mun.ca

†Present address:
Shawn P. Meredyk, Amundsen Science, Quebec City, QC, Canada

Specialty section:
This article was submitted to Deep-Sea Environments and Ecology, a section of the journal Frontiers in Marine Science

Received: *15 June 2019*
Accepted: *14 November 2019*
Published: *30 January 2020*

Citation:
Meredyk SP, Edinger E, Piper DJW, Huvenne VAI, Hoy S and Ruffman A (2020) Enigmatic Deep-Water Mounds on the Orphan Knoll, Labrador Sea. Front. Mar. Sci. 6:744. doi: 10.3389/fmars.2019.00744

Deep-sea mounds can have a variety of origins and may provide hard-substrate features in depths that are normally dominated by mud. Orphan Knoll, a 2 km high bedrock horst off northeast Newfoundland, hosts more than 200 mounds, or mound complexes, of unknown composition, in water depths of 1720–2500 m. Most mounds are 10–600 m high, with average mound height 187 m, and 1–3 km wide. The study objective was to characterize the size, shape, orientation, and composition of the enigmatic Orphan Knoll mounds, in order to determine their age and origin. Archival ship-based side-scan sonar, multibeam sonar, airgun, high-resolution sparker and 3.5 kHz acoustic sub-bottom profiling, and newly acquired ship-based multibeam sonar, video transects by remotely operated vehicle (ROV), rock samples, and near-bottom multibeam sonar data were analyzed. Four mounds were studied during two ROV dives. Archival sidescan sonar data show > 200 mounds. Sparker profiles show that the mound crests are covered by condensed stratified Quaternary sediment and airgun seismic data show faults reaching near the seafloor. New multibeam sonar data show mounds are dominantly conical to elliptical in shape, but without preferred orientation or alignment. Remotely operated vehicle (ROV) transects and near-bottom multibeam showed that three mounds were rounded and symmetrically arranged, while a fourth was more asymmetrical, with steep faces on the southwestern and southeastern flanks, where finely bedded to massive sedimentary bedrock outcropped dipping 15–45°SW. Rock samples from the mounds include Eocene calcareous ooze and mid-Miocene bedded pelagic limestone. Thick ferromanganese crusts were found on many surfaces, obscuring possible outcrops from physical sampling. Polymetallic nodules were found on the slope of one mound. Ice-rafted detritus, including igneous and metamorphic rocks and Paleozoic limestone and dolostone, was common in the sediments immediately surrounding the mounds. Quaternary sub-fossil solitary scleractinian corals accumulated over a span of at least 0.18 Ma at the base of one mound. The presence of uplifted condensed Eocene-Miocene rocks on the mounds and faulting in seismic profiles suggest uplift during

reactivation of old rift-related faults during the Neogene, with seabed mass wasting creating residual mounds, which were then draped by Quaternary proglacial muds. Sculpting of hemipelagic Quaternary sediment by bottom currents probably contributed to mound morphology.

Keywords: Orphan Knoll, deep-sea, mound, multibeam sonar, Northwest Atlantic, cold-water corals

INTRODUCTION

Deep-water mounds are intermediate-scale bathymetric features found in bathyal to abyssal settings, with a wide variety of possible origins. Deep-water mounds are typically 10s to 100s of meters in height above the surrounding sea floor, and may have lateral dimensions of 100s of meters to kilometers, rarely 10s of kilometers. Mounds are larger than sedimentary structures, but smaller than volcanic seamounts, whose definition includes an elevation of 1000 m above the surrounding sea floor, and a conical shape with length/width ratios < 2 (Harris et al., 2014). Deep-water mounds can provide important hard-substrate habitats in environments that are otherwise dominated by soft sediment, hence hosting higher levels of biodiversity, particularly epifaunal and fish biodiversity, than surrounding level-bottom seafloor. In the past 1–2 decades, deep-water mounds built by biogenic processes, especially carbonate mounds, have received greater attention (e.g., Huvenne et al., 2003). Bathyal carbonate mounds were also investigated particularly as a possible modern analog for carbonate mud-mounds in the fossil record (e.g., Henriet et al., 2011, reviewed by Lo Iacono et al., 2018).

The range of biogenic and abiogenic processes responsible for mound formation is considerable. Some examples of the more common abiotic processes of mound formation, include tectonism and block-faulting (e.g., Laughton et al., 1972; Sibuet, 1992; Moscardelli et al., 2013, reviewed by Cormier and Sloan, 2018); magmatic volcanism (e.g., Wiles et al., 2014, reviewed by Casalbore, 2018), and diapirism (e.g., Laughton et al., 1972), often associated with rifting or failed rifts; salt diapirs (e.g., Laughton et al., 1972; Parson et al., 1984), mud volcanoes and similar structures related to fluid escape (e.g., Barrett et al., 1988; Bolton et al., 1988; Enachescu, 2004; Burton-Ferguson et al., 2006, reviewed by Mazzini and Etiope, 2017); cold-seeps and authigenic carbonate precipitation (reviewed by Ceramicola et al., 2018); some types of contourite drifts (reviewed by Esentia et al., 2018) and submerged subaerial erosion features such as karst (Hart, 1977; Parson et al., 1984; Dronov, 1993; Immenhauser and Rameil, 2011; Taviani et al., 2012). Biogenic mounds in the deep sea include, a variety of types of biogenic carbonate mound formation including cold-water coral reefs and mounds (e.g., Hovland et al., 1994; Huvenne et al., 2003; Roberts et al., 2003, 2006, reviewed by Lo Iacono et al., 2018), and siliciclastic-dominated sponge reefs (e.g., Conway et al., 2005; Howell et al., 2016) and microbial mounds (e.g., Riding and Awramik, 2000). The different origins of mounds may or may not yield distinctive morphologies that can be used to interpret the geological origins of the mound features. As is typical for the deep sea, far more mound features have been mapped using acoustic remote sensing than have been directly investigated and sampled.

This paper examines deep-sea mounds of indeterminate origin on Orphan Knoll. The Orphan Knoll mounds were first detected in 1970 (Laughton et al., 1972). Parson et al. (1984) provided a first map and description of the mounds based on side-scan sonar, and analysis of rock dredge samples, and considered various hypotheses for their origin. Interest in Orphan Knoll and the Orphan Knoll mounds re-emerged in the late 1990s and early 2000s when late Pleistocene and Holocene solitary scleractinian corals collected in the 1978 Geological Survey of Canada exploration of Orphan Knoll (Keen, 1978) were re-analyzed for paleoceanographic investigations (e.g., Smith et al., 1997). The cold-water coral research on the Orphan Knoll, combined with previous studies on carbonate rock samples from the Knoll (Legault, 1982; Parson et al., 1984; van Hinte et al., 1995) raised the possibility that the Orphan Knoll mounds were biogenic carbonate mounds (Enachescu, 2004). Accordingly, Orphan Knoll was eventually protected from deep-water fishing activity by a Northwest Atlantic Fisheries Organization (NAFO) closure (Thompson and Campanis, 2007), despite the fact that the nature of the mounds, and the nature of the coral fauna, were not yet well-understood.

In this paper, we report on acoustic mapping and sub-bottom profiling, combined with limited *in situ* investigations, of continental slope-depth seafloor mounds on Orphan Knoll. We combine use of archival and new acoustic mapping of these mounds with the results of ROV dives aimed partly at deciphering the origin of these mounds. We also present preliminary results on the living and sub-fossil cold-water coral species present on the mounds. In addition to describing the mounds and exploring the nature and origin of these features, our results chronicle the evolution of submarine surficial geological survey techniques and geomorphological data collection over half a century. The history of the exploration of these features testifies to the evolution of the disciplines of seafloor mapping and submarine geomorphology.

MATERIALS AND METHODS

Study Area

History of Discovery and Exploration of Orphan Knoll

Prior to the Fall of 1969 Orphan Knoll was not a known feature on the ocean floor off Canada's east coast. It first shows as a single 970 fathom sounding on British Admiralty Chart 2060A in 1917 (British Admiralty, 1917). In the 1960s the International Hydrographic Office (IHO) in Monaco initiated the General Bathymetric Chart of the Oceans (GEBCO). Canada took on the compilation of the bathymetry of the Northwest Atlantic which in the 1960s comprised mainly plotting sheets of raw soundings that

were provided voluntarily by vessels passing through the area. These soundings were initially contoured by an undergraduate student at Dalhousie University, resulting in an oblique view of the whole east coast of North America from 50° N southward to Florida. Canada had not yet charted, or compiled, the bathymetry north of about 49° N and it was necessary to use the raw and unedited data on the GEBCO collected soundings sheet #27 (Deutschen Hydrographischen Institut, 1964). These data yielded severely distorted contours that reflected the NE to SW orientation of the Europe to Canada vessel tracks rather than what might be the true shape of the ocean floor.

A reassessment of the GEBCO lines was undertaken, including the removal of certain vessels' data and the deliberate smoothing of the contours. A large feature emerged as an area of shallower depths some 550 km northeast of the island of Newfoundland. It was in the order of 100 km in size, was rather flat-topped and stood over 1250 m proud at a depth of about 3000 to 1720 m. It was hypothesized that this topographic feature was a continental fragment that had become detached from the European plate as the process of continental drift began to open up the northwest Atlantic and the Labrador Sea. The feature was named Orphan Knoll because it had been left behind, and a brief nomination was sent to the embryonic Deep Sea Drilling Project (DSDP) as a proposed drilling site to prove that it was a continental fragment.

The nomination was successful, in part because 1969 magnetometer data from the French vessel *N/O Jean Charcot V* showed that it was not just a very large igneous plateau, and Orphan Knoll was selected as a DSDP Leg 12 drilling site for the mid-1970 voyage of the *Glomar Challenger* despite there being no pre-drilling site survey available. To aid in site selection, the drilling vessel trailed a 20 cubic inch airgun and ran a continuous sub-bottom and magnetic profile whenever it was underway. On the vessel's initial WNW to ESE traverse across the flat top of Orphan Knoll it quite unexpectedly crossed what appeared to be very narrow 'peaks' of up to 300 m in height at the northeast edge of the Knoll. The selected Site 111 was chosen to be approximately 8 km SW of the 'peaks.' When the Site 111 drill hole was completed the vessel moved to the southwest of the drill hole, streamed the survey gear, and then ran a SW to NE survey line across the Site 111 and on off the Knoll into deep water. Once again the vessel mapped a narrow zone of significant 'peaks' at the northeast edge of Orphan Knoll. The 'peaks' came to be called "narrow ridge-like structures" by the scientific team on board the *Glomar Challenger*. The use of the term 'peaks' was misnomer, in 1970, and today they are now more appropriately called 'mounds.' They were first called 'mounds' by Parson et al. (1984) and then the "Enigmatic Mounds" in Ruffman (2011), as their origin has continued to defy geoscientists.

The final core of DSDP Leg 12, Site 111, took an hour to drill and the bedrock core recovered was only 1 m in length, because the diamond bit was almost worn out. The lowermost recovered bedrock was determined to be a non-marine fluvial sandstone with spores that gave it a Bajocian (middle Jurassic) age. This core confirmed that Orphan Knoll was a foundered continental fragment (Laughton et al., 1972; Ruffman and van Hinte, 1973). The Leg 12 Initial Report contained as its **Figure 2** a newly-compiled bathymetry map covering the whole of the feature from 49°30′ to 52°30′ North and 48°52′ to 48°00′ West. The mid-1971 compilation by Ruffman (Laughton et al., 1972) at a contour interval of 200 m then served science in the area for 29 years prior to the first multibeam bathymetry being gathered over the southeast part of the Knoll in 2000. The 'peaks' found along the northeast side of the Knoll were contoured to indicate that they formed a series of prominent sub-parallel NW-SE "narrow ridge-like structures" – probably bedrock in the (then) view of Ruffman. By the time the Leg 12 report was issued, Ruffman and van Hinte, as members of the Leg 12 shipboard scientific party, were permitted to add an 'Addendum' on p. 80 stating that: "The ridges now appear to be erosional remanants[*sic*] of steeply dipping massive limestone beds" based on their interpretation of the contents of a biologic dredge haul in 1971 from the *USNS Lynch* (Ruffman, 1971; Laughton et al., 1972).

With the completion of the Leg 12 scientific Initial Report (Laughton et al., 1972) Canada's interest in Orphan Knoll seemed to stagnate. However the British Institute of Oceanographic Sciences in 1979 ran a single test line over Orphan Knoll on board the MV *Starella,* and in 1981, on board the MV *Farnella,* ran four more E–W lines (400 km *in toto*) of their Geological LOng Range Inclined Asdic (GLORIA) that produced side-scan sonograms of up to 30 km width. These records were somewhat difficult to interpret but served very well in two papers to demonstrate "that the mounds have a random distribution in an elongate northwesterly trending belt" (Parson et al., 1984, 1985). The British survey found that the mounds ranged in height above the seafloor from 115 to 320 m with their flanks sloping at 15 to 20°. "Almost 250 individual mounds have been identified on top of Orphan Knoll. There is no evidence for a northwest–southeast linear fabric in the disposition of the mounds. Although the overall area of distribution of these features is slightly elongated in a northwest–southeast direction, parallel to the continental margin" (Parson et al., 1984, p. 62).

Parson et al. (1984) dismissed all the suggested origins of the mounds to date and instead suggested: "an interpretation based on an irregular, partially buried palaeolandscape best fits the available evidence." A paragraph later they hedged their bets by adding "Alternatively, the mounds might be erosional remnants of original depositional features of sedimentary rocks" and gave an example, "of reef knolls, [in] the Spanish Sahara. Here, circular reef knolls, preserved due to their greater resistance to erosion than the marls in which they occur, form topographic features up to 2 km in diameter and 100 m in height. Aerial photographs of the reef-knoll terrain. bear a striking resemblance to the GLORIA sonographs of Orphan Knoll" (Parson et al., 1984, p. 66). The Spanish Sahara reef knolls, or *kes-kes*, have been attributed to both shallow- and deep-water corals and carbonate mound formation (Henriet et al., 2014), and were part of the later interest in the Orphan Knoll mounds as possible biogenic carbonate mounds.

A year later Parson et al. (1985) gathered together their thoughts on the regional structural development of the eastern Grand Banks including normal faulting at the ocean-continental transition (OCT). The fault-bounded basin that contains the Middle Jurassic non-marine rocks in a half-graben on top of

Orphan Knoll is interpreted to be probably related to "a tensional episode with graben formation during the Late Triassic and Early Jurassic, rifting and erosion began in the Late Jurassic and continued until the Aptian" (Parson et al., 1985, p. 700). The work of the British in 1979 and 1981 using the towed GLORIA tool to gather seafloor sonograms and sub-bottom profiling data was the last mound-specific survey work done by any research cruise for 23 years.

In 1978 a team from the Bedford Institute of Oceanography (BIO) attempted two rock dredge hauls on one of the mounds located using the 1970 DSDP Leg 12 drill ship echosounder data during the *Hudson* 78-020 expedition. One dredge did not obtain any material that clearly reflected nearby bedrock. The other, however, brought up over 200 pieces of dead, lightly-Mn-coated, *Desmophyllum cristagalli* (now synonimzed to *Desmophyllum dianthus*). The preferred habitat of this azooxanthellate, cold water, solitary to pseudocolonial scleractinian coral is a vertical to slightly over-hanging rock face (Keen, 1978; Ruffman and van Hinte, 1989; Forsterra et al., 2005). No one at BIO was interested in the samples, and the coral remained unstudied and mis-identified for a decade. Eventually the dredge haul was fully examined and Stephen D. Cairns of the Smithsonian Institution in Washington identified the coral recovered as *D. cristagalli*. We concluded that the rock dredge had dragged through a *Desmophyllum* 'graveyard' below a bedrock face hosting living examples of the coral (Ruffman and van Hinte, 1989). This coral collection ultimately was the topic of a B.Sc. Honours and eventually a portion of a Ph.D. thesis at McMaster University, focusing on Quaternary paleoceanographic reconstructions of the Labrador Sea based on the coral skeleton stable isotope geochemistry (Smith, 1993, 1997; Smith et al., 1997, 2013).

The first multibeam sonar data acquired over any part of Orphan Knoll and the Orphan Seamount was obtained almost by accident. The Americans had built the new ice-capable *USCGC Healy,* which was equipped with a 12 kHz Seabeam multi-beam sonar. The vessel was to transit from the Atlantic Ocean to its area of operations in the Beaufort Sea via the Northwest Passage. A testing area for the multibeam sonar was chosen without much thought about the underlying geology of the ocean floor that was to be mapped. The equipment testing cruise covered only the southeastern edge of Orphan Knoll and mainly the abyssal depths of the bordering Labrador Abyssal Plain (Toews and Piper, 2002). Six years later Canada still had no deep-sea vessels in the Atlantic with a multi-beam bathymetry system and in 2006 chartered Fugro's *Kommandor Jack* with its 12 kHz multibeam bathymetry system to run a zig-zag series of check lines along Canada's eastern continental margin, including the Orphan Knoll area (Pe-Piper et al., 2013, 2014). These data were collected to fortify Canada's claim for extended jurisdiction under Article 76 of the United Nations Convention on the Law of the Sea (UNCLOS). Canada finally added a multi-beam sonar system to one of its Arctic-capable icebreakers, *CCGS Amundsen,* in 2003. Despite extensive mapping in the Canadian Arctic and the northern Labrador sea, the vessel has not yet been used to map the bathymetry of Orphan Knoll. To date, the modest amount of *Kommandor Jack* multi-beam data from 2006 comprise the only 'Canadian' swath bathymetry data over any part of Orphan Knoll.

Michael Enachescu (2004) re-examined two commercial Husky Oil deep seismic profiles run in Orphan Basin to the west of Orphan Knoll. These 2000–2003 2D multi-channel seismic lines crossed the western flanks of Orphan Knoll and ran partway onto the flatter top of the feature to the east. Enachescu (2004) identified two features that he called "geo-mounds," which appeared to have possibly grown up through the ca. 150 m of Quaternary hemipelagic sediment cover, and were visible as small "geo-mounds" in the present-day bathymetry. He suggested that these might be bioherms of cold-water corals, and as such Enachescu prompted us all to consider cold water bioherms as the origin of the mounds on the northeast part of Orphan Knoll. In 2004 a brief visit over the top of Orphan Knoll was made by the *CCGS Hudson* 2004-024 cruise. A dredge attempt was made on one of the mounds without any bedrock recovery but a Huntec sparker profile over the mound showed ca. 10 m of stratified sediment draped over the mound crest (as reported in this paper).

In the period 2007–2008 the North Atlantic Fisheries Organization (NAFO) was being challenged to consider the possible need for regulation of fishing effort on any seamounts within its jurisdiction of the Northwest Atlantic (Thompson and Campanis, 2007). The maximum economic depth of possible fishing was considered to be 2000 m. Thus seamounts in the New England Seamount Chain off Nova Scotia and New England, in the Fogo Seamount Group on the southern edge of the Grand Banks and seamounts in the Newfoundland Seamount Group to the east of the southern Grand Banks were all targeted for assessment by NAFO. To NAFO the whole of the top of Orphan Knoll rose above 2000 m – *ergo* Orphan Knoll must be a 'seamount' and it has been mis-named by NAFO ever since. In 2008 NAFO closed the four seamount areas to all fishing (Thompson and Campanis, 2007). This closure and the ensuing Canadian Department of Fisheries and Oceans (DFO) assessment led to a comprehensive measurement and documentation of the physical oceanographic parameters over Orphan Knoll (Greenan et al., 2010), and spurred the biological aspects of the 2010 ROV survey of Orphan Knoll, some of which are reported on in this paper.

There was no further work on the Enigmatic Mounds themselves until the 2010 Bedford Institute of Oceanography and Memorial University *CCGS Hudson*-2010-029 cruise using the tethered *ROPOS* ROV which examined two mounds with video, rock and coral sampling, and a ROV-mounted multi-beam system. Edinger and Sherwood (2012) and Blénet (2016), examine the taphonomy of the corals in this time-averaged assemblage. The 2010 cruise was followed by the 2017 British ICY-LAB Cruise DY081 on *RRS Discovery* which recorded a multibeam sonar survey over the mounds on the northeast portion of Orphan Knoll. The data ROV video observations, rock samples, and near-bottom multibeam bathymetry data from the *Hudson* 2010-029 cruise and the ship-based multibeam data from the 2017 *Discovery* cruise to Orphan Knoll are reported on in this paper.

Geological Background

Orphan Knoll is a flat-topped (∼1700 m) basement high of continental crust separated from the eastern Canadian

continental shelf by the Orphan Basin (2500–3000 m). The Knoll rises 2 km above the adjacent Labrador Sea ocean basin. Orphan Basin was affected by several phases of Mesozoic rifting culminating in the Late Jurassic-Early Cretaceous hyperextension (Enachescu et al., 2005; Dafoe et al., 2017). Continental breakup east of Orphan Knoll followed during the Mid-to Late Cretaceous, with the oldest definite magnetic anomaly on the seaward side of Orphan Knoll being C34n (84 Ma, Santonian, Srivastava et al., 1988). A major fault scarp on the eastern side of Orphan Knoll bounds 40 km of thinned continental crust (Chian et al., 2001; Welford et al., 2012) before oceanic crust is reached. Flemish Cap, 100 km to the south, is an analogous but shallower basement high seaward of the Grand Banks of Newfoundland.

The geological history of Orphan Knoll is known principally from Deep Sea Drilling Project Site 111 drilled in 1970 on the crest of the Knoll (Laughton et al., 1972). Sparsely cored intervals sampled a 150 m thick hemipelagic Quaternary interval (seismic unit 6 in **Figure 4**) overlying very thin Miocene chalk and 30 m of Paleogene zeolitic clays (unit 5) resting on latest Cretaceous chalk (upper part of unit 4). This deeper water succession overlies 50 m of shallow water limestones, of Aptian–Cenomanian (mid Cretaceous) age (lower unit 4), unconformably overlying middle Jurassic (Bajocian) terrestrial sandstones and shales. In seismic profiles these Jurassic strata overlie Appalachian crystalline basement (Enachescu, 2004).

Late Quaternary sedimentation on Orphan Knoll is known from studies of piston cores and from the nearby deeper water Ocean Drilling Program Sites U1302/3 (Channell et al., 2012). Sediments of the last glacial cycle on the crest of the Knoll are about 5 m thick and are predominantly of proglacial origin, including Heinrich layers rich in detrital carbonate rocks derived from Hudson Bay. Ice-rafted detritus is thus rich in Lower Paleozoic rocks and previous accounts of Ordovician and Devonian rocks are probably from icre-rafted boulders.

Mapping

Compilation and Analysis of Archival Mapping Data

Archival acoustic and seismic data sources available for studying the Orphan Knoll mounds included extensive low-resolution GLORIA side-scan sonar data (Parson et al., 1984), Geological Survey of Canada air gun and Huntec sparker seismic data, and isolated swaths of multibeam sonar data covering the Orphan Knoll (**Figure 1** and **Supplementary Material** for individual data layers).

Historical acoustic imagery

Raw survey data (seismic reflection profiles, side-scan sonar and multibeam sonar) from historical cruises were compiled into an ArcGIS project to aid in planning the *Hudson* 2010-029 survey and data interpretation.

Seismic profiles. Hull-mounted Knudsen 3.5 kHz seismic profiles were collected from cruises: 78-020, 86-013, 90-007, 2001-043, 2003-033, 2004-024; 3.5 kHz Knudsen and 3.5 kHz Huntec® sparker profiles were collected from CCGS *Hudson* cruises: 2003-033, 2004-024, and 2010-029; 3.5 kHz airgun seismic profiles were collected from CSS *Hudson* cruise 69-041; LITHOPROBE deep seismic data from line FGP 84-3D, TGS line 107 and GSI lines ORO-111 and ORO-129 were examined and new enigmatic mounds [high slope (>45°)] were recorded and plotted in a ArcGIS project (see **Supplementary Figure 4**).

Side scan imagery. GLORIA (Geological Long Range Inclined Asdic) 6.5 kHz side-scan imagery collected on the *MV Starella* and *MV Farnella* cruises covered ∼40% of the Orphan Knoll, focused on the northern section of the Orphan Knoll (Parson et al., 1984, see **Supplementary Material**). Ridge and mound features were created by geopositioning GLORIA imagery and manually digitizing the mounds and ridges seen in the imagery. See **Supplementary Figures 1**, **2**.

Multibeam bathymetry. In 2000, the United States Coast Guard Cutter (USCGC) *Healy* used a Seabeam 2112 multibeam sonar (12 kHz) and collected bathymetry (gridded to 100 m res.) over the SE-W Orphan Knoll; these data were made available by the Geological Survey of Canada (GSC). See **Supplementary Figure 3**.

In 2006, the Fugro vessel *Kommandor Jack* (*Kmdr. Jack*) was commissioned by Natural Resources Canada to collect data for Canada's claim for extended jurisdiction under the United Nations Convention on the Law of the Sea 's (UNCLOS) Commission on the Limits of the Continental Shelf (CLCS), re-defining areas of the Canadian continental shelf. The *Kmdr. Jack* used a Kongsberg EM 120 12 kHz multibeam unit and collected bathymetry gridded to 100 m resolution over the southeast Orphan Knoll (see **Supplementary Figure 4**). The *Kmdr. Jack* multibeam raster was overlain by *Healy* multibeam raster, due to raster merging inaccuracies [the *Kmdr. Jack* data was less 'clean' (increased interpolation variance) than the *Healy* data] within ArcGIS (inaccuracies were visualized in 3D, using GlobalMapper ver. 11); therefore, rather than merging the rasters, the *Healy* data was overlaid the *Kmdr. Jack* data, to get the most accurate raster for point-sampling statistical purposes.

Acquisition of New Ship-Based Multibeam Bathymetry

In the summer of 2017, approximately 3400 square kilometers of Orphan Knoll were mapped (bathymetry and backscatter intensity) with Kongsberg's EM122 12 kHz multibeam echosounder (MBES) aboard the RRS Discovery (Cruise DY081). These data were collected in support of the first fieldwork component of Isotope CYcling in the LABrador sea (ICY-LAB) project, led by Dr. K. Hendry from the University of Bristol to study nutrient cycling in the North Atlantic. These data were processed during the expedition (using CARIS HIPS and SIPS v8) and gridded to a 25 m × 25 m resolution. The data (both raw multibeam data and gridded products) and further details can be found in the associated Pangaea data release (Hoy et al., 2018).

ROV Dives and *in situ* Observations

Six ROV dives were carried out on Orphan Knoll during the *CCGS Hudson* Cruise 2010-029 in July 2010 (**Figure 1**

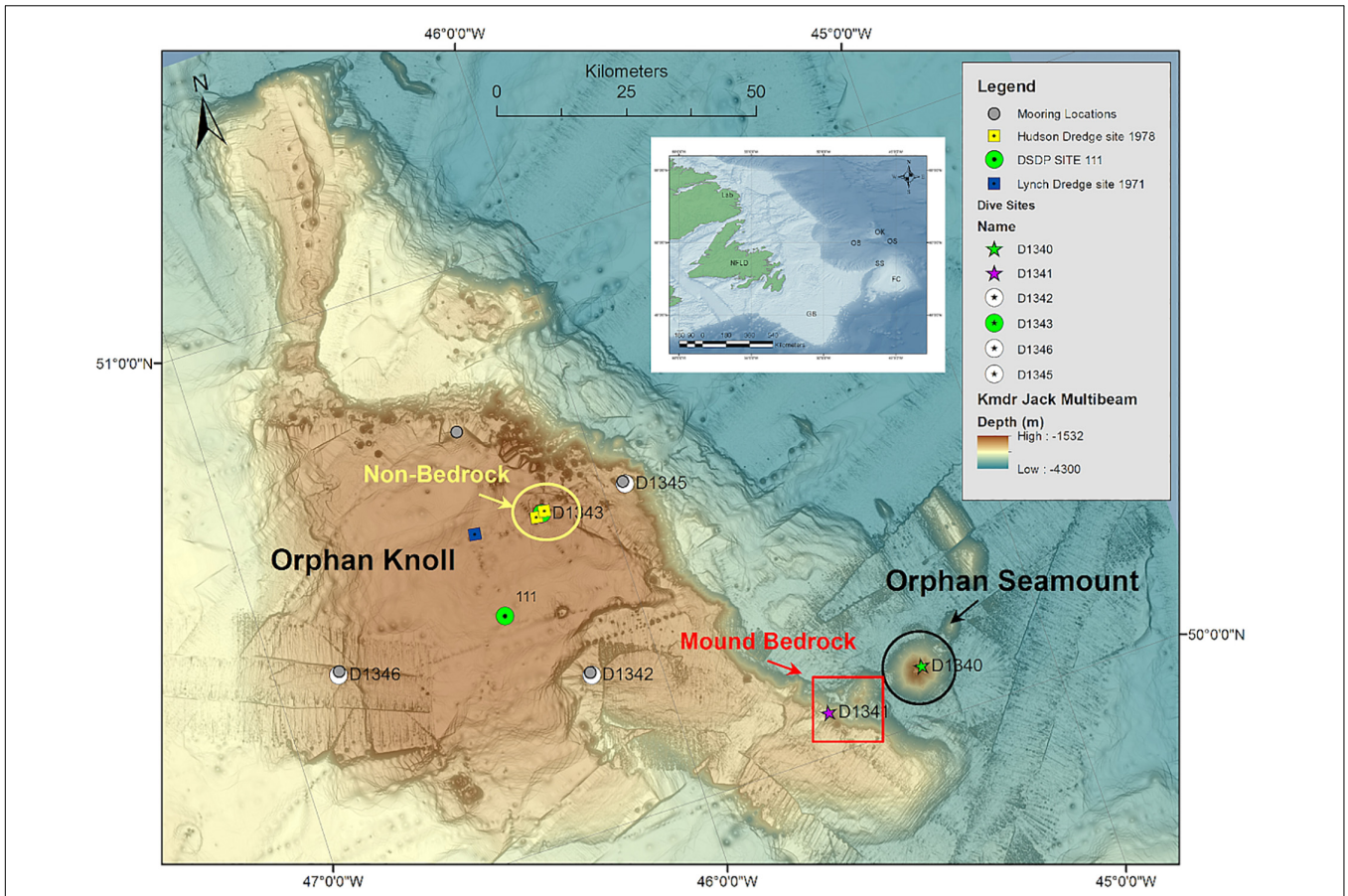

FIGURE 1 | Location of Orphan Knoll and of features studied in detail. Inset map: NFLD, Island of Newfoundland; Lab, Labrador; GB, Grand Banks of Newfoundland; OK, Orphan Knoll; OS, Orphan Seamount; OB, Orphan Basin; FC, Flemish Cap; SS, Sackville Spur. Main figure: Bathymetry is a mosaic of archival multibeam sonar from *USCGC Healy* and *MV Kommandor Jack* data (see **Supplementary Material**) with GEBCO bathymetry for region. Positions of previous drilling (DSDP site 111) and rock dredge sampling (*USNS Lynch*, 1971, *CCGS Hudson*, 1978) also shown, as well as locations or remotely operated vehicle (ROV) dives completed during *CCGS Hudson* 2010-029 mission.

TABLE 1 | ROPOS dives during the *Hudson* 2010-029 mission.

Dive #	Date	Start lat	Start long	Max depth (m)	Min depth (m)	Duration (h:m)	Distance surveyed (km)	Principal objectives
R1341	20 July 2010	N50° 04.5695′	W45° 37.301′	2895	2344	15:25	3.8	Survey SE Orphan Knoll mounds
R1342	21 July 2010	N50° 15.8704′	W46° 11.1371′	2195	2150	9:00	Not linear survey	Search for lost current meter mooring, collect sediment cores
R1343	22 July 2010	N50° 33.8078′	W46° 10.3591′	1852	1682	15:51	5.35	Survey NE Orphan Knoll mounds, collect fossil corals
R1344	23 July 2010	N50° 34.1167′	W45° 54.164′	n/a	n/a	3:35	0	Bottom type and biological survey of NE Orphan Knoll curremt meter location.
R1345	23 July 2010	N50° 33.4792′	W45° 55.6297′	2370	2240	7:34	3.5	Bottom type and biological survey of NE Orphan Knoll curremt meter location
R1346	24 July 2010	N50° 23.8483′	W46° 50.7028′	2270	2162	9:34	4.65	Bottom type and biological survey of SW Orphan Knoll curremt meter location

Remotely operated vehicle dives on the Orphan Knoll during the 2010 CCGS Hudson cruise. Depth minima and maxima refer to bottom depths, as opposed to water column observerations, Dive R1344 aborted due to ROV technical issues. Only dives R1341 and R1343 are important for understanding the geology of the Orphan Knoll mounds.

and **Table 1**). Dives R1341 and R1343 were planned in order to investigate and sample mound features on Orphan Knoll. Dives R1342, R1344, 1345, and 1346 were planned to describe bottom type and benthic fauna in the vicinity of four current meters that had been deployed on Orphan Knoll by Fisheries & Oceans Canada in 2009 (Greenan et al., 2010). Three of

these current meters were recovered during the cruise; the current meter at site R1342 was not located. The start and end positions, bottom depth ranges, and durations of the six ROV dives are indicated in **Table 1**. Results relating to the Orphan Knoll mounds relate mostly to dives R1341 and R1343. Dive R1344 was aborted due to ROV malfunction, and yielded no scientific results.

During the *CCGS Hudson* 2010-029 expedition, ROPOS was equipped with two high-definition (HD) (forward facing 1080p HD camera and a downward facing 1080i HD camera) and one 5 Megapixel (MP) digital still camera. Both HD cameras had zooming capabilities with green laser sights 10 cm apart to provide scale at variable zoom distances. The forward facing camera had pan and tilt capabilities while the downward facing camera was affixed to the frame with only tilt functionality, but provided a quantitative view of bottom composition and benthos. Unfortunately, after dive R1340 on the Orphan Seamount (see Pe-Piper et al., 2013), moisture was observed inside the forward-looking HD camera. Therefore the forward-looking HD camera was replaced with the old 3-CCD camera aboard ROPOS, recording data in standard definition, for the remainder of the cruise. The high-definition downward-looking camera remained in operation for the duration of the cruise.

Rock Sample Collection

Ice-rafted debris (IRD) has accumulated on the OK since the initiation of glaciations in the North Atlantic Ocean [Piacenzian (∼3 Ma)] (Hiscott et al., 1989); therefore, positive discrimination of bedrock from ice-rafted boulders could only be verified through *in situ* video, photographs and substrate samples.

Bedrock samples were collected by ROPOS when bedrock outcrops were physically accessible to the ROV and when there was enough room for rock storage within the collection boxes on ROPOS. A CH-15 Stanley underwater chipping hammer clamped to spring-loaded metal rods was installed onto ROPOS for the purpose of chipping sections of bedrock without over-stressing the manipulating arms of ROPOS and to allow ROPOS to collect the sample with its restricted manipulator arm gape (cobble sized rock samples) (**Figure 2A**).

Unfortunately, the shaking of the manipulator arm caused by the chipping hammer limited its use, out of concern for the safety of the manipulator arms and the ability to proceed with other ROV dive objectives. Therefore most of the rock samples were collected by using the ROV manipulator arms to break pieces of bedrock outcrop (**Figure 2B**). Rock samples collected were analyzed by thin-section analysis and x-ray diffraction to study mineralogy, as appropriate.

Bedrock Composition and Structural Observations

The position of ROPOS was plotted within GlobalMapper ver. 11 software by inputting the position data (decoded audio signal from the HD video) from a Geostamp® decoder. Strike measurements were made by observing the heading, pitch and roll of ROPOS, allowing the observer to identify the bedding strike. Dip measurements were made by observing a feature in multiple directions (forward and downward camera perspectives) while being mindful of ROPOS's heading, pitch and roll.

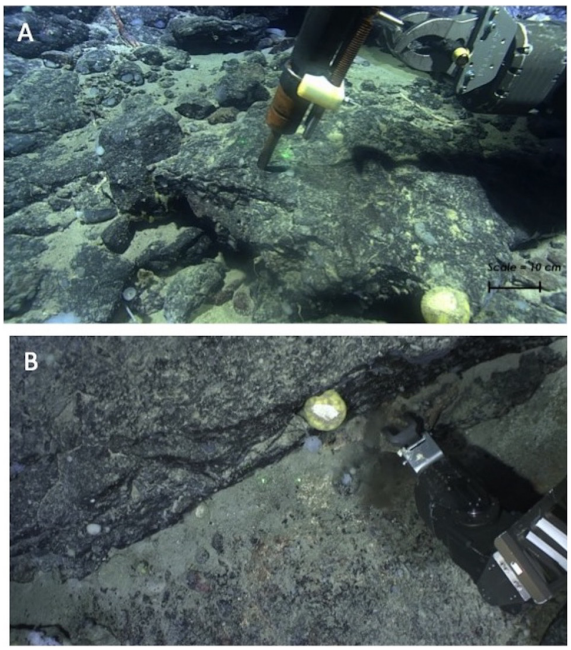

FIGURE 2 | Bedrock sampling from the ROPOS ROV. **(A)** Stanley CH15 hydraulic chipping hammer installed on ROPOS, sampling basalt bedrock on Orphan Seamount (ROPOS dive R1340, Pe-Piper et al., 2013). **(B)** Collecting a rock sample with the ROV manipulator arm, ROPOS dive R1341, SE Orphan Knoll. Note that because the rock samples were picked, rather than broken directly from exposed bedrock, there was greater risk of either collecting ice-rafted debris mistaken for bedrock, or of collecting Fe–Mn oxide crusts from the surface of bedrock exposures.

ROV-Based Near-Bottom Multibeam Sonar Acquisition and Processing

An Imagenex model 837A "Delta T" multibeam unit using 120 beams (3°) at 260 kHz with 0.2% spatial range resolution (res.) (e.g., 2 mm res. at 1 m altitude to 30 mm res. at 15 m altitude) was forward mounted on the ROPOS ROV and calibrated by the Canadian Hydrographic Service (CHS) and the ROPOS engineering team. In addition to measuring small-scale bathymetry along the path of video transects (reported in Lecours et al., 2019), high-resolution maps of two mound features were recorded using the Imagenex Delta T with the ROV at 20 m off bottom. These features were recorded on the second mound observed on dive R1341, and on the principal mound targeted by dive R1343 (see **Table 1**). The Imagenex multibeam data was preliminarily processed on-board and then extensively post-processed (beam and angle elimination were used to 'clean-up' the data; ∼5% beam rejection) using CARIS HIPS & SIPS version 7 (service pack 3). The multibeam unit recorded backscatter data as well; however, due to the ROV flying close to the ground with a high output signal, there was too much acoustic energy ('washed out') to create a color gradient. CARIS image exports were created using 25 cm spatial resolution to smooth fine-scale artificial features within the data, to have the most accurate

bathymetry capable. The raster exports, of the exposed enigmatic OK mounds, were exported from CARIS (ASCII format) and converted by ArcGIS 3D Analyst extension, into an ArcGIS raster grid at 25 cm grid size. In order to visually highlight the small-scale topographic features on these mounds, the bathymetric raster was converted to a slope raster, and the bathymetric raster was draped over the slope raster.

Biological Observations of Cold-Water Corals

The primary goal of biological observations of cold-water corals in this study was to investigate the role of bedrock and surficial geology in influencing benthic faunal distributions. Biological analysis of Orphan Knoll fauna was focused on sessile and sedentary benthic invertebrates, especially cold-water corals and sponges, due to their importance as Vulnerable Marine Ecosystem indicator taxa. Corals and sponges were identified visually where possible, using regional coral identification guides (Kenchington et al., 2009; Wareham, 2009), to the highest taxonomic level possible. The video acquisition and annotation team at sea always included two scientists familiar with coral identification on each watch. In cases where the scientists at sea were uncertain about the identity of a coral, a sample was collected for skeletal or sclerite analysis.

Taxa were identified mostly from the forward-looking camera, and were quantified using the downward-looking camera.

ROV Video Post-processing and Analysis

The HD video was geo-referenced using a Geostamp® device, which audio-encoded the geographic position into the HD video signal\stream. The time-stamped geo-referenced HD video allowed for accurate (1 m spatial resolution) positioning of species relative to surficial geology percentages *in situ* and during re-processing of the HD video. The video annotation program ClassActMapper (CAM) was used during the cruise and in the post-processing of the HD video data to collect geospatial positioning of species relative to surficial geology percentages *in situ* and during re-processing of the HD video. CAM is a graphical user-interface (GUI), whereby the user pressed custom-made species labeled buttons for each instance that a species was seen within the video. The resulting MS Access database contained when and where a species was observed relative to the surficial geology percentages *in situ* and during re-processing of the HD video.

The collective (totaling 100% coverage) surficial geology was recorded every second by CAM using visual estimates and a slider bar of the following sediment size classes, based on the Wentworth scale: bedrock, boulders, cobbles, pebbles, granules, and fine-grained sediment (Sand-Mud). Sand and mud were undistinguishable by eye and were therefore grouped as fine-grained sediment.

The annotations were stored in a MS Access® 97-2003 database and are linked through a post-processing field (JDayGMT) that combines Julian Day and Universal Coordinated Time (UCT). A secondary post-processing of the HD video was performed by a single user to eliminate multi-person estimation variation. The user performed a self-calibration (10 random frame grabs were analyzed using area sampling within ImageJ and compared to the user's estimates to ensure accuracy and precision of their estimates) to determine the offset between the computer calculated percentage and the user's estimate.

Coral Distribution in Relation to Bedrock and Surficial Geology

The location that each coral was observed was noted in the dive log, and was linked via timestamp to the bedrock and surficial geology observations in Class-Act Mapper. The distributions of corals in relation to mounds and bottom type are presented in map form. Quantitative analysis of the relationship between benthic fauna and surficial geology will be published separately.

Geomorphological Analysis of 2017 Bathymetry Data

The 2017 MBES survey carried out during the ICY-LAB expedition covered ca. 3430 km^2 of the Orphan Knoll and Orphan Seamount complex, and mapped out a large number of the enigmatic mounds in great detail. In order to summarize their morphological characteristics, mounds were extracted automatically from the bathymetry (**Supplementary Figure 5**). All data operations and analysis were carried out in ArcGIS v10.5. We used a top-hat transformation (as discussed by Huvenne et al., 2003) with a circular kernel of 40 pixels to single out the mounds. Following the closing operation, mounds were separated from their background at a threshold of 35 m. An additional erosion (3 × 3 pixels) and dilation (5 × 5 pixels) operation was applied to remove fine-scale noise. The resulting binary mask was used to extract the basic metrics of the mounds. Only mound features associated with the main plateau of the Orphan Knoll were retained for further analysis. Mound length and width were defined as the two horizontal dimensions of their bounding rectangles.

Mound orientation was measured according to the azimuth of the longer of the two bounding rectanges, and a histogram of mound orientations constructed on a 180°N–S half-rose diagram. No automated detection of mound alignment was attempted. Instead, possible (speculative) mound alignments were identified visually, as cases where a minimum of four mounds were observed to be aligned following approximately linear trends.

RESULTS

Compilation and Analysis of Archival Acoustic Data

The compiled and mosaicked archival multibeam sonar data from the *USCG Healy* and *Kommandor Jack*, mosaicked with GEBCO bathymetry, revealed the general bathymetry of the Orphan Knoll, and the location of some of the mounds, but provided limited details about the morphology of most mounds, due to the 100 m pixel size in both multibeam data sources (**Figure 1**). Furthermore, the multibeam data were collected in

isolated swaths (see **Supplementary Material**), with more detail on the Northeast edge of the Knoll, and more interpolated data in the center of the Knoll, smoothing the small- to intermediate-scale bathymetric variation necessary for describing the morphology and morphometry of the mounds.

Compilation and Mapping of Mounds in Multibeam Sonar, Side-Scan Sonar, and Sub-Bottom Profile Data for Mound Detection

The compiled data sources detected over 200 mounds (**Figure 3**). The resolution of the archival data, particularly the archival GLORIA side-scan sonar data, allowed for identification of the mounds, and to a much lesser extent, shape. The archival sub-bottom profile data generally allowed for detection of positive relief features that included mounds, but likely also included other unrelated relief features. Most importantly, the sub-bottom profile data allowed for interpretation of mound structure, but not for shape analysis.

Analysis of Mounds in Sub-Bottom Profile for Mound Structure

A few of the mounds on northeast Orphan Knoll are crossed by airgun and sparker single-channel seismic profiles (**Figure 4**). Mounds have steep sides that are masked by hyperbolic diffractions and seismic profiles are cluttered by side-echos from mounds. One mound crossed directly by the ship shows at least 10 m of stratified parallel reflections over its flat crest (**Figure 4A**). In the airgun seismic profiles (**Figure 4C**), interpretation of seismic stratigraphy is difficult, but the most westerly mound imaged appears to have a condensed Quaternary and Cenozoic section over basement, based on seismic character compared to the vicinity of DSDP Site 111. Between the mounds, particularly on the E–W track segment, subvertical faults cut the stratified Cenozoic and Quaternary section between the mounds, and the mounds themselves appear to be fault bounded (**Figure 4C**).

New Multibeam Sonar of Northeast Orphan Knoll Mounds From DY081

The automated mapping exercise based on the ICY-LAB bathymetry data revealed 198 positive bathymetric features (**Figures 5A,B**). Their main morphological characteristics are presented in **Figure 5C**, and summarized in **Table 2**. There was no preferred orientation of mounds, nor was any large-scale alignment of mounds apparent, except where mounds have apparently coalesced near the northern edge of Orphan Knoll (**Figure 5B**). At a smaller spatial scale, visual interpretation suggested that mounds may be aligned following dominantly N–S trends in the southern end of the area mapped (**Figure 5D**).

Overall, mounds are conical to only slightly elliptic (length/width ratios ∼1.5), with an elongation either in roughly N–S or E–W direction (**Figure 5C**). The morphological distributions are strongly skewed, with a lot of small mounds and fewer large features. Based on length and height values, the OK mounds are typically quite steep.

Detailed bathymetry and bathymetric profiles of several mounds close to the zones of ROV exploration are shown in **Figures 6**, **7**. The mounds profiled are clustered, and are broadly conical in shape (**Figures 6A**, **7A**), and had slightly concave to slightly convex curvature (**Figures 6B**, **7B**).

Near-Bottom Multibeam Sonar Records of Mounds and Ridges

Near-bottom (20 m altitude) mapping of a mound on the southeast tongue of Orphan Knoll found the summit of one knoll to be roughly conical to dome-shaped on dive R1341 (**Figure 6**). Mounds on northeast Orphan Knoll were domal to conical in 25 m grid bathymetry, but detailed near-bottom bathymetry revealed more complex features (**Figure 7**).

Southeast tongue of Orphan Knoll, R1341

Near-bottom (20 m altitude) mapping of the mound at the end of dive R1341 showed the summit of this mound to be symmetrical and domal in shape, despite uncorrectable artifacts in the data, probably related to the relatively low frequency of ROV navigation data (0.2 Hz) compared to the MBES acquisition (**Figure 6**). The approximately dome-shaped bedrock outcrop on this mound did not provide clear exposures of stratification within the bedrock of which this mound is composed. The near-bottom bathymetric profile across the mound was measured parallel to ROV motion in order to avoid influence of artifacts on the profile data.

Northeast Orphan Knoll mounds, R1343

The zone investigated by dive R1343 had several large mounds (**Figure 7A**), of which two were surveyed. Detailed near-bottom mapping of the southern end of a large mound surveyed at the end of dive R1343 focused on the area of the coral graveyard collection. The flank of the mound portion mapped at low altitude was generally ridge-shaped (**Figure 7C**). The portion of the mound mapped included extensive stratified bedrock exposure on both the SW and SE flanks of the mound ridge (**Figures 8A–C**). The strike and dip of these bedrock exposures are indicated (see section "Bedrock Structure and Orientation," below). The southern portion of this mound was found to be asymmetrical, with a steeper, concave, face to the southwest, and gentler, linear or convex, bathymetric profiles to the southeast and north (**Figures 7C,D**). Depressions and erosionally accentuated limestone beds were observed within the ROPOS HD video, on and around the OK NE mound, and were also recorded within the ROPOS collected multibeam imagery (**Figures 8A–C**). The concave faces of the mound flank may be attributable to small slope failures, of which three are suggested in the near-bottom multibeam bathymetry, two on the SW side of the mound and one on the southeast side (**Figure 7C**). An approximately north-south oriented linear trough was observed near the crest of this ridge.

ROV Dives and *in situ* Observations

Bedrock Structure and Orientation

Mound bedrock was observed in several locations during dive R1341, most notably in segments A–A, B–C, C′–D′, and G′–H (**Figure 9A**). Despite the extent of these bedrock exposures, none of these outcrops revealed three-dimensional exposures that allowed for examination of bedrock structure.

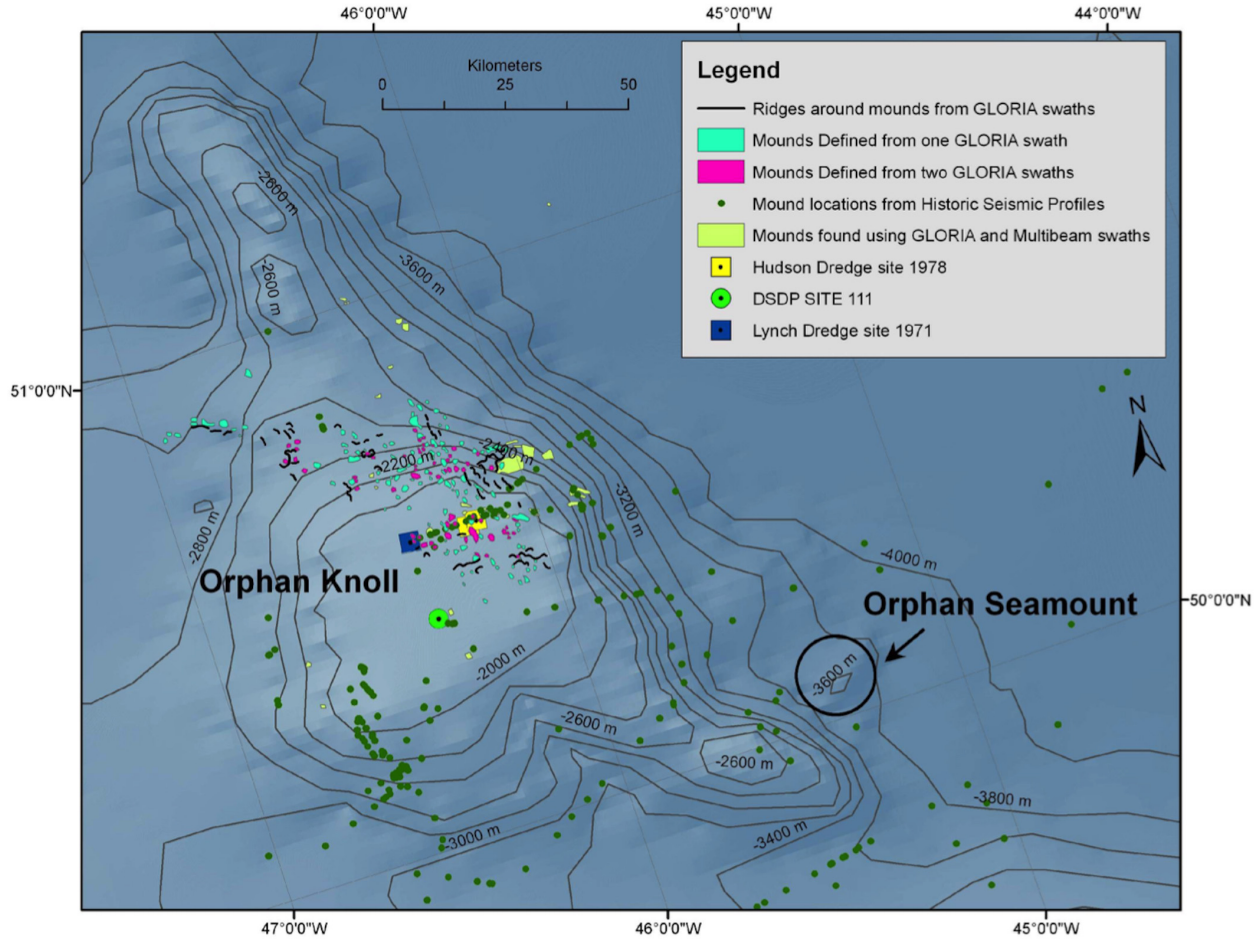

FIGURE 3 | Compilation of mound occurrences from GLORIA side-scan sonar, *USCG Healy* and *Kommandor Jack* multibeam sonar. Green dots represent positive relief features from various legacy Geological Survey of Canada sub-bottom profile data. The apparent alignment of positive relief features from historical seismic profiles is an artifact of linear data acquisition. Orientation and distribution of the various datasets contributing to this figure are presented in **Supplementary Material**.

The bedrock in segments A–A′ consisted of soft carbonate ooze, and polymetallic nodules were observed and collected at the base of this outcrop. The ooze at this outcrop was soft and easily collected with the ROV manipulator arms, in contrast to all other bedrock exposures, which were well-indurated bedrock.

The most extensive ROV observations of Orphan Knoll mound bedrock structure and composition were made during ROV dive R1343 on the northeast Orphan Knoll mounds. **Figure 9B** shows the distribution of bedrock exposures along the track of dive R1343. Along the track of dive R1343, zones with extensive bedrock exposure were found in segments A′–B and E–E′ of the dive. The clearest exposure of stratigraphy within bedrock was found around the SE and SW sides of the mound in segment E–E′ of the dive, near the site from which subfossil corals were dredged in 1978, and collected again in 2010.

Two extensive (250 m long) bedrock outcrops, approximately 250 and 500 m long (**Figure 9B**, surficial geology unit (SGU) A′–B and E–E′) were observed on dive R1343. These were thought to be two mound structures seen in legacy seismic-reflection and side scan imagery (see **Figure 4** and **Supplementary Figures 1**, **2**). Video analysis from SGU E-E' identified exposed bedrock walls on the NW and SE sides of the exposed bedrock outcrop (**Figures 7C**, **10**). The wall feature on the NW side was overlain by fine-grained sediment, while the SE side of the mound consisted primarily of bedrock and granules. The stepped nature of the sedimentary bedrock walls indicated differential erosion, most likely by near-bottom currents.

The most detailed description of stratigraphy and bedrock structure within a mound was possible in segment E–E′ of the mound in dive R1343 (**Figures 7C**, **10**). An unconformity was seen in the larger bedrock outcrop (NE OK mound) between units 2 and 3 (**Figure 10**). The upper bedrock layers (layers 1 and 2) dipped 25–45° with a strike of 135° (SW-NE) (**Figures 7C**, **10**). Unit 1 had thinner bedding than unit 2, while unit 2 had thinner bedding than unit 3. Unit 3 had a different strike and dip than units 1 and 2, probably indicating an unconformity; however, the horizon of the unconformity was covered by overlying IRD, talus and fine grained sediment (**Figure 9**).

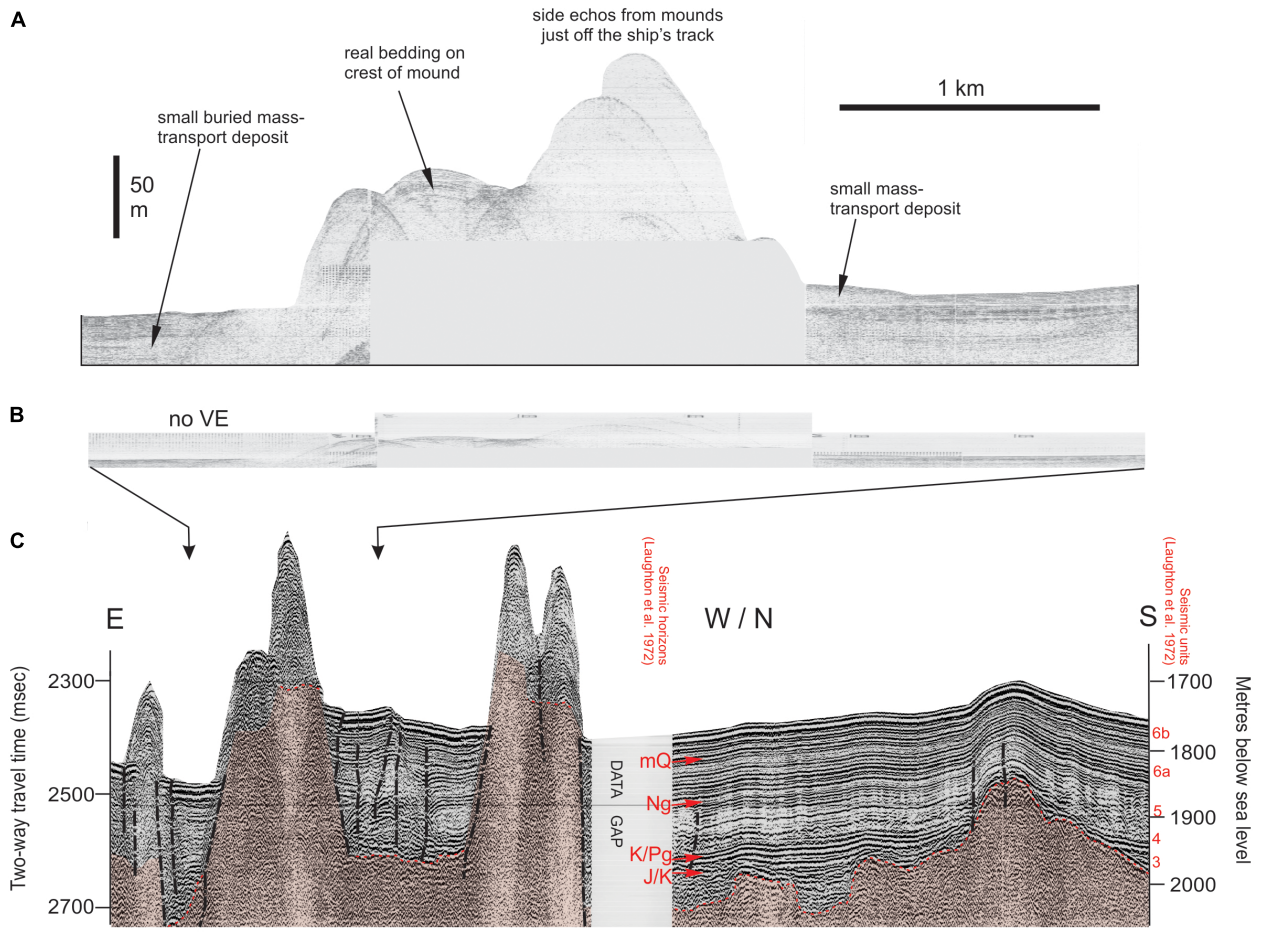

FIGURE 4 | Seismic profiles across mounds on northeast Orphan Knoll (**A**, top panel). Huntec sparker profile across a cluster of mounds showing > 10 m stratified sediment on one mound crest and small mass-transport deposits on the mound flanks **(B,** middle panel). The above profile shown with no vertical exaggeration (**C**, lower panel). 40 cu in GI gun seismic profile showing several mounds, with faulting in stratified section between the mounds. S end of the profile is 5 km north of DSDP Site 111. 3, 4, 5, 6a, 6b are seismic units from Laughton et al. (1972). mQ, mid Quaternary marker (?ca. 1Ma); Ng, thin Neogene (Miocene) unit; K/Pg, Cretaceous-Paleogene boundary; J/K, Jurassic-Cretaceous unconformity. All images from CCGS *Hudson* cruise 2004-024. See **Figure 5B** and **Supplementary Figure 4** for location of seismic profiles shown.

Mound bedrock dips varied between 0 and 45°, accompanied by a general strike of 325° (SW-NE) (**Figure 7C**). However, three strike and dip measurements at the NE OK mound indicated a general strike of 225 and a 0–20° dip. This change in strike and dip possibly indicates an undetected unconformity above unit 3 (**Figure 12**).

Rock Sampling

Due to the intense vibrations induced in the ROV manipulator arm by the hydraulic jackhammer, efforts to sample the bedrock composing the Orphan Knoll mounds were largely unsuccessful. Although we attempted to break off pieces of bedrock with the ROV manipulator arms, most samples collected from bedrock outcrops were thick Fe–Mn crusts, often interbedded with pelagic limestones (see **Supplementary Table 1**). Ice-rafted debris of all size classes was common on all ROV dives. The exceptions to this pattern were the collection of weakly lithified calcareous ooze at the deeper of the two mounds sampled on dive R1341, and collection of pelagic limestones on the shallower of the two mounds studied on dive R1341. Other rock samples included ice-rafted debris collected with sub-fossil deep-sea corals from the sides of the mound studied in dive R1343.

Calcareous ooze with polymetallic nodules

At the beginning of dive 1341, weakly indurated calcareous ooze (R1341-4) and round Fe–Mn nodules (samples R1341-3 and -5) were recovered at the base of an ∼7 m high calcareous ooze outcrop (**Figure 8D**) on a 6° slope near the base of one of two mounds studied on dive R1341. The calcareous ooze sample R1341-4, contained nannofossils *Discoaster sublodoensis, Nannotetrina fulgens*, *Discoaster kuepperi,* and *Discoaster lodoensi* (**Figure 8F**). Nannofossil recovery was good but preservation was poor with extensive etching (central structure of most coccoliths were missing). Some hydrodynamic sorting was evident as only medium to large sized nannofossils were found, though smaller fossils could be absent due to dissolution. No definite recent

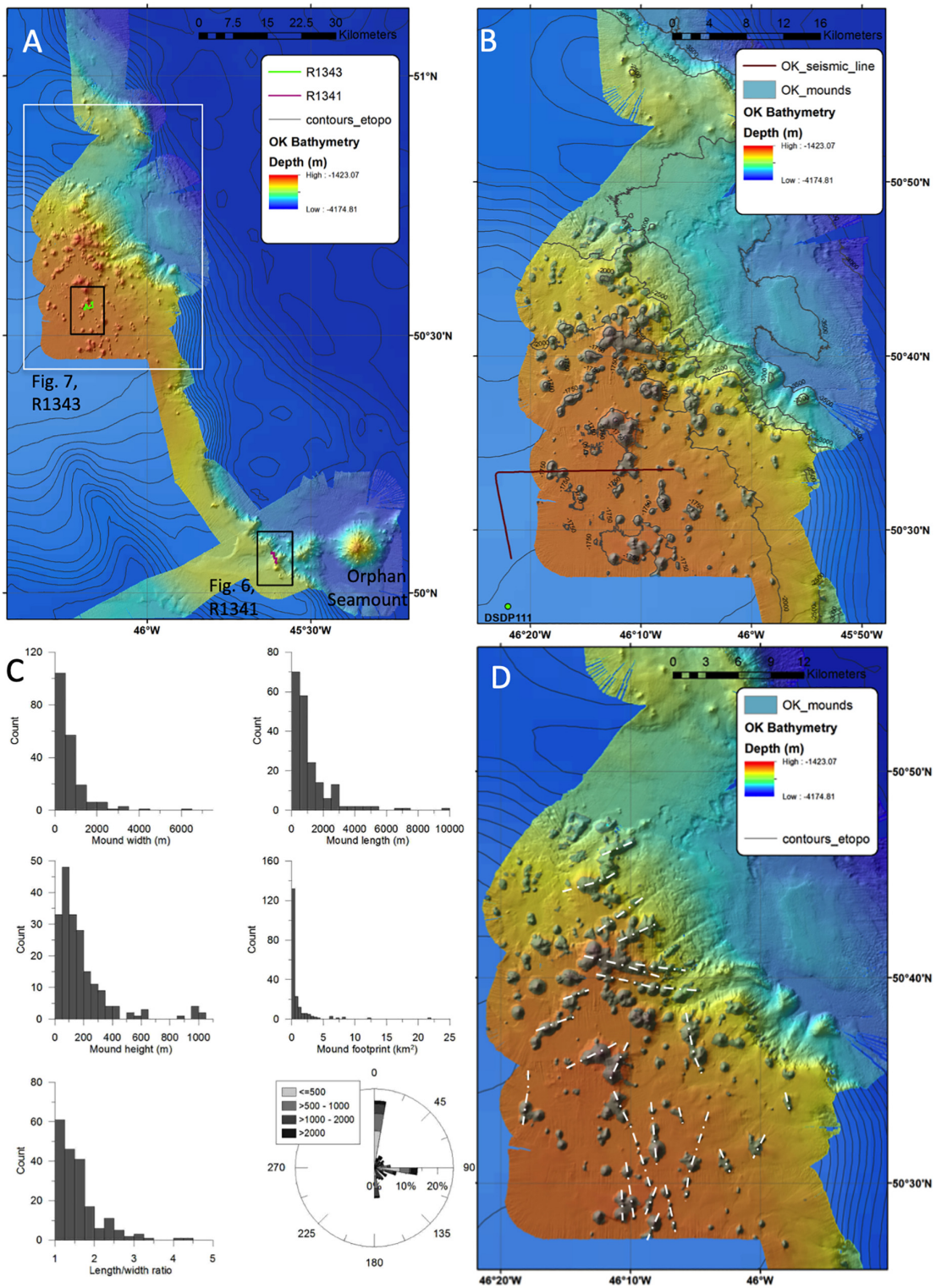

FIGURE 5 | (A) Overview map of the ICY-LAB bathymetry data set over Orphan Knoll. White box indicates are enclosed in right-hand panel **(B)**. Two dark boxes indicate close-up bathymetry shown in **Figures 6A**, 7A. **(B)** Zoom on the central part of the map, illustrating the results of the automated mound mapping exercise over northeast Orphan Knoll. Also shown are the locations of the sub-bottom profile line in **Figure 4**, and the location of DSDP site 111. **(C)** Mound characteristics: histograms of mound width, length, height, footprint area, and length/width ratio. The rose diagram illustrates the orientation of mound elongation, grayscale-coded by mound length in m. **(D)** Speculative linear trends exhibited by groups of mounds. Trends in the southern part of the data set are parallel to the orientation of faults interpreted from seismic reflection profiles.

TABLE 2 | Main morphological characteristics of the 198 Orphan Knoll mounds, measured from the DY081 multibeam sonar survey.

	Width (m)	Length (m)	L/W ratio	Area (km^2)	Height (m)	Depth (m)
Mean	719	1168	1.58	0.96	183.2	2127.1
Median	463	710	1.44	0.26	124.6	2051.1
Standard deviation	759	1329	0.55	2.19	195.7	369.3
Minimum	125	125	1.0	0.02	3.3	1622.0
Maximum	6368	9732	4.31	21.71	1032.7	3160.7

nannofossils were identified; however evidence of reworking of early Eocene zones NP14a- NP12 nannofossils, *Discoaster kuepperi* and *Discoaster lodoensis*, was observed (Kevin Cooper, personal communication 2011).

Pelagic limestone

More indurated limestone (R1341-7) was pulled out of a bedrock outcrop (2914 m) on a 14° slope. Limestone (R1341-10) was collected from the top of a bedrock outcrop (2888 m) on a 30° slope. Microfossils *Globigerina* spp. and *Orbulina* spp. (Mid-Miocene to present) were found in both limestone samples (R1341-7 and R1341-10).

Bedded sedimentary rock covered with Fe–Mn oxide crusts

The most common type of bedrock observed on ROV dive R1343 was bedded sedimentary rock (**Figures 8A–C**), for example, as exposed on the SW and SE flanks of the second mound surveyed on that dive. Attempts to collect pieces of this bedrock yielded only the Fe–Mn oxide crusts, without the underlying bedrock. Therefore its age and composition remains unknown.

Biological Observations of Cold-Water Coral Distributions

Cold-water corals, including a variety of octocorals and three species of solitary scleractinian corals, were observed on the Orphan Knoll mounds, and on soft sediments between mounds. The coral morphotypes observed on the ROV dives are shown in **Figure 11**.

Figures 12A,B summarize the distribution of cold-water coral observations on dive R1341, and dive R1343, respectively. Contrary to expectations, coral morphotypes that normally require hard substrates were commonly observed in areas with dominantly fine sediment, but growing on isolated cobbles and boulders, presumably ice-rafted. Quantitative analysis of coral distributions in relation to surficial geology will be published separately.

One of the principal objectives of the Orphan Knoll cruise in 2010 was to collect sub-fossil solitary scleractinian corals, *D. dianthus*, from the coral graveyard discovered on the Northeast OK mounds in 1978. This coral graveyard was observed, and sampled again using the ROV during ROPOS dive R1343. The corals in this time-averaged accumulation were partially buried in mixed gravelly muddy sediment, in which the transported gravel component was polymictic, and sub-rounded to angular in shape. Some basalt samples were observed within the rock samples recovered. These basalt samples were subangular clasts within the sediment at the coral graveyard, co-occurring with granites, limestones, and other lithologies as well as the sub-fossil corals (**Supplementary Table 1**), and were most likely sourced from ice-rafted debris. The exposed portions of the coral skeletons were heavily encrusted with Fe–Mn oxides.

DISCUSSION

Mound Form, Distribution, and Probable Origin

Previous hypotheses for the origin of the mounds have been of two main types: those that emphasize the positive relief of the mounds and those that focus on the depressions around the mounds. In this contribution we attempt to interpret the mounds with horizontal dimensions of generally less than 1.5 km and elevations of less than 300 m that have been investigated in the 2017 *Discovery* multibeam data and the ROV dives. The large isolated mounds on southwestern Orphan Knoll, 2 km wide and 400 m high, were not investigated in this study and may have a quite different origin (Enachescu, 2004).

An early interpretation that involved the depressions between the mounds was the concept of a submerged karst plateau of Paleozoic limestone (Parson et al., 1984). This explanation predates modern seismic and multibeam sonar coverage and seems unlikely, given the thick Mesozoic–Cenozoic succession in the area of the mounds (**Figure 4**) and the resulting generally flat sea floor between the mounds (**Figure 5**). No submerged dolines or other clearly karst-related geomorphic features (e.g., Taviani et al., 2012) were observed in the seismic or multibeam data or in ROV observations. Small-scale depressions and possible erosional or dissolutional scour features are seen in layers 1 and 2 on the top of the NE Orphan Knoll mound (**Figures 8**, **9**, **12**). The depressions might have an origin in subaerial dissolution in the Cenomanian to Maastrichtian unconformity (Dafoe et al., 2017), similar to the dissolution of Cretaceous chalks of the Wyandot Formation on the Scotian Shelf (Wielens et al., 2002). Alternatively, depressions might result from submarine fluid escape (Land et al., 1995; Wielens et al., 2002). However, neither seismic profiles (**Figure 4**) nor the new multibeam bathymetry provide support for any of these interpretations.

The possibility of strong erosional bottom currents forming the observed curved depressions (**Figures 7B,C**) cannot be ruled out. The high-velocity core of the Deep Western Boundary Undercurrent (WBUC) is known to pass along the NE edge of Orphan Knoll. Current meter data from Orphan Knoll indicate that the Knoll as a whole induces a Taylor column, with cyclonic water circulation around the Knoll (Greenan et al., 2010). The small size of most of the mounds visible

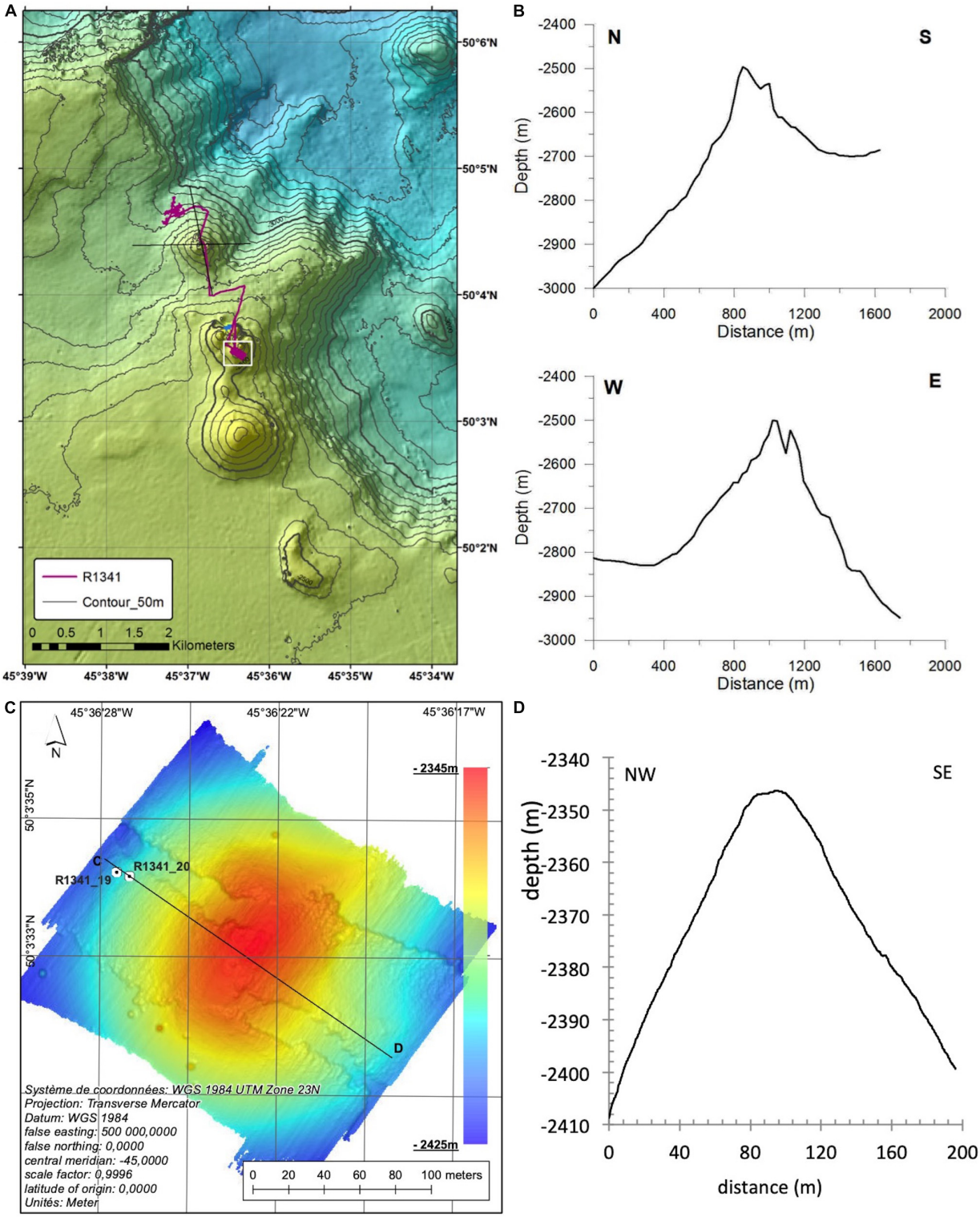

FIGURE 6 | Detailed bathymetry of mounds on the SE tongue of Orphan Knoll. **(A)** ICY_LAB multibeam sonar of mounds surveyed on ROPOS dive R1341. Multibeam sonar gridded to 26 m resolution. **(B)** Bathymetric profiles of the first mound encountered on dive R1341, based on 2017 ICY-LAB multibeam data. Full mound profiles are slightly concave, consistent with conical shape in 3D. **(C)** Near-bottom ROV-based bathymetry of SE Orphan Knoll mound mapped during ROV dive R1341, at 25 cm grid. The domal shape of the mound is evident despite the swath/navigation artifacts that we were unable to remove from the sonar data. These artifacts are likely related to the maximum 5 Hz navigation data available for ROV position. **(D)** Bathymetric profile C–D across mound, based on near-bottom ROV-based multibeam sonar parallel to multibeam acquisition swaths to minimize influence of position and swath artifacts.

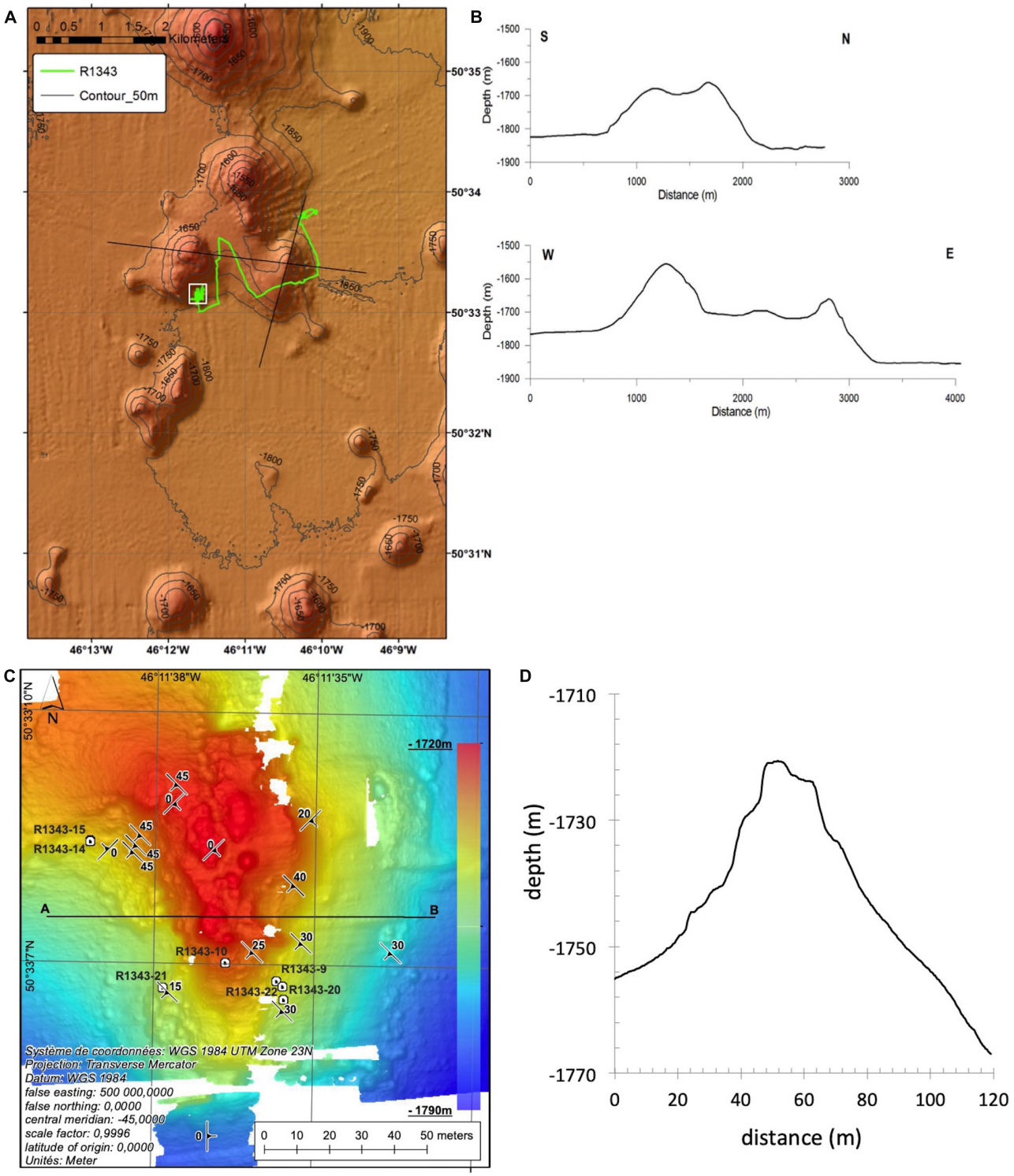

FIGURE 7 | Detailed bathymetry of the mound complex on NE Orphan Knoll, including the site of the coral graveyard collection. **(A)** ICY-LAB multibeam sonar of mounds,including mounds surveyed on ROPOS dive R1343. Multibeam bathymetry gridded to 25 m. **(B)** Bathymetric profiles across one (N–S) and two (W–E profile) mounds in 25 m grid bathymetry. The West-to East profile line crosses both mounds surveyed on dive R1343. VE = 2. **(C)** Detailed of bathymetry of the mound sampled in ROPOS dive R1343, also showing strike and dip measurements and locations of rock sample collections (see **Supplementary Table 1**). **(D)** Bathymetric profile A–B across ridge-shaped portion of mound surveyed with near-bottom multibeam sonar. VE = 2.

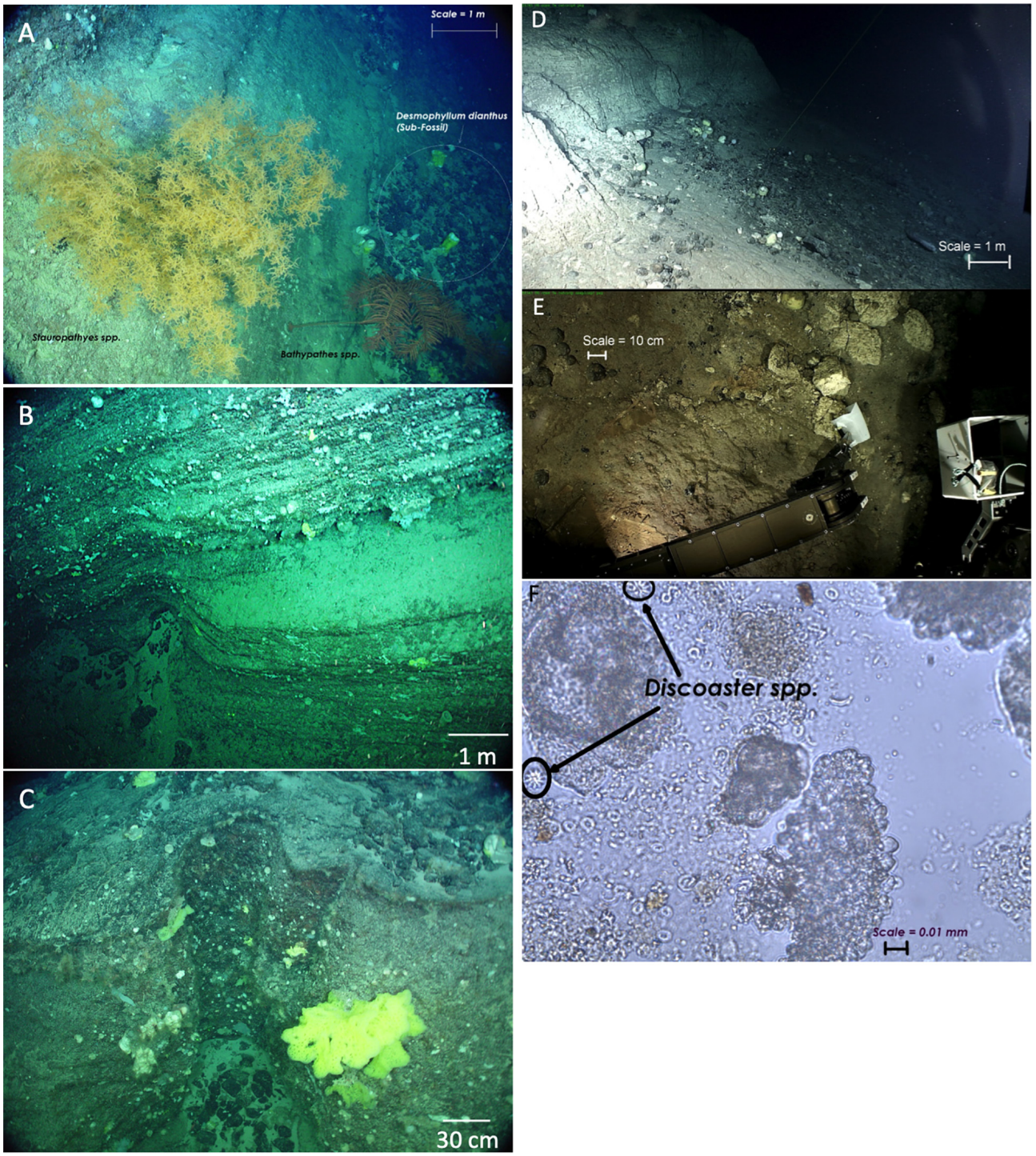

FIGURE 8 | Remotely operated vehicle bottom photos. **(A–C)** Bottom photos of stratified sedimentary bedrock at Orphan Knoll northeast mounds, ROV dive R1343. **(A)** View of bedrock wall above the coral graveyard collection site, with two large antipatharian corals growing on the wall. **(B)** Scour feature and bedded sedimentary rock along the base of the bedrock wall. **(C)** Another scour feature along the base of the bedrock wall. Scale bar for **(C)** is approximate, because laser pointers were on a curved portion of the bedrock wall. **(D–F)** ROV photos of calcareous ooze and polylmetallic nodules in segment A–A′ of ROV dive R1341. **(D)** Weakly indurated calcareous ooze outcrop. **(E)** Polymetallic nodules eroding form the calcareous ooze. Polymetallic nodules collected from this site were estimated as Eocene in age, based upon Re/Os dating (Poirier et al., 2011). **(F)** Smear microphotograph of calcareous ooze. Analysis of microfossils within the ooze suggested Eocene age. The ooze probably post-dates the indurated bedrock exposures observed on the other mounds of the southeast tongue of Orphan Knoll.

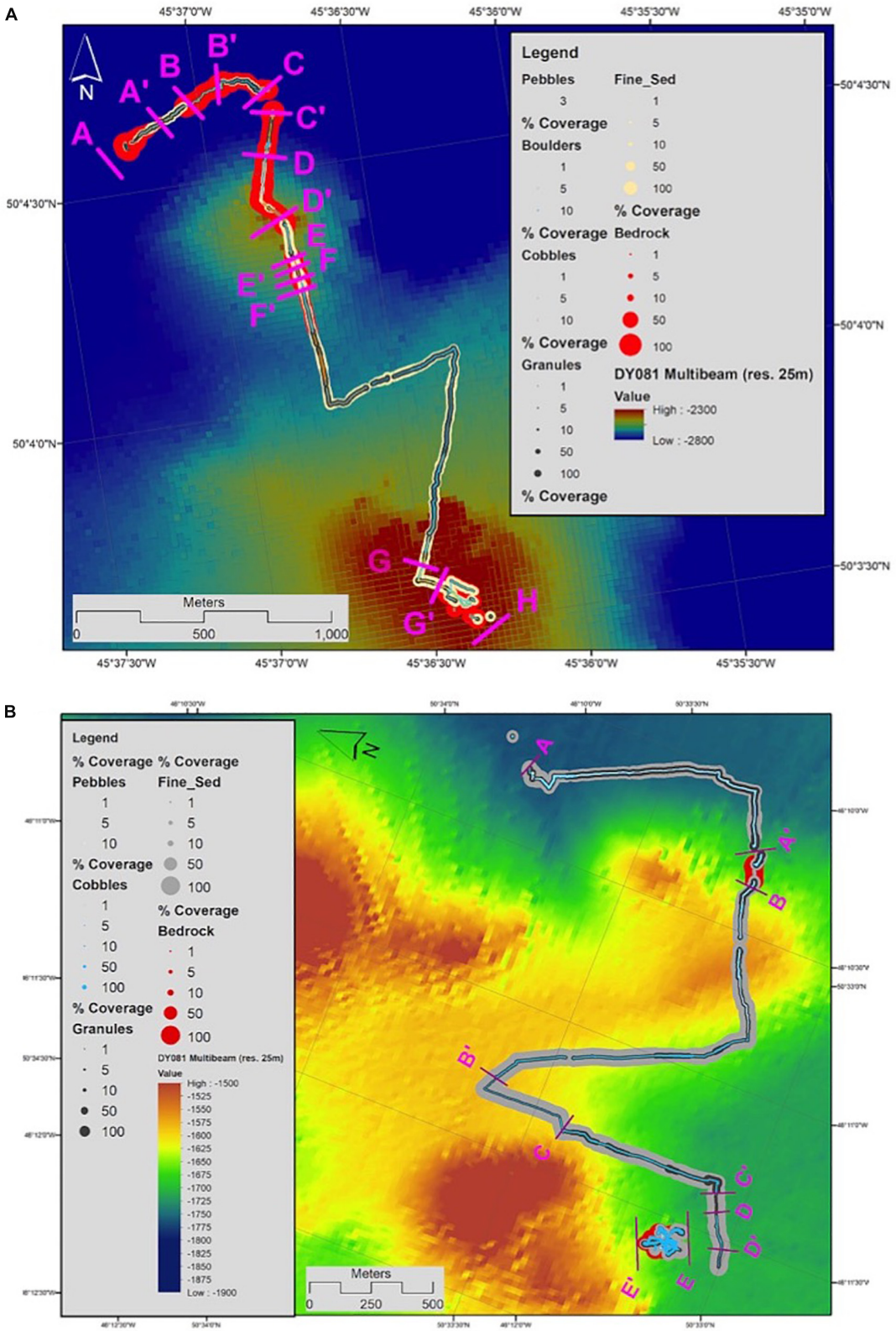

FIGURE 9 | Track of ROV dives, annotated for surficial geology. Bedrock exposure areas are indicated in red. **(A)** Dive R1341, SE Orphan Knoll. Bedrock areas were found most extensively in segments A–A′, B–C, C′–D′, and G′–H. **(B)** R1343, NE Orphan Knoll. Observations in **Figures 8**, **10** are from segment E–E′, which was the most carefully mapped segment of bedrock exposure, and was also the site of the subfossil coral graveyard.

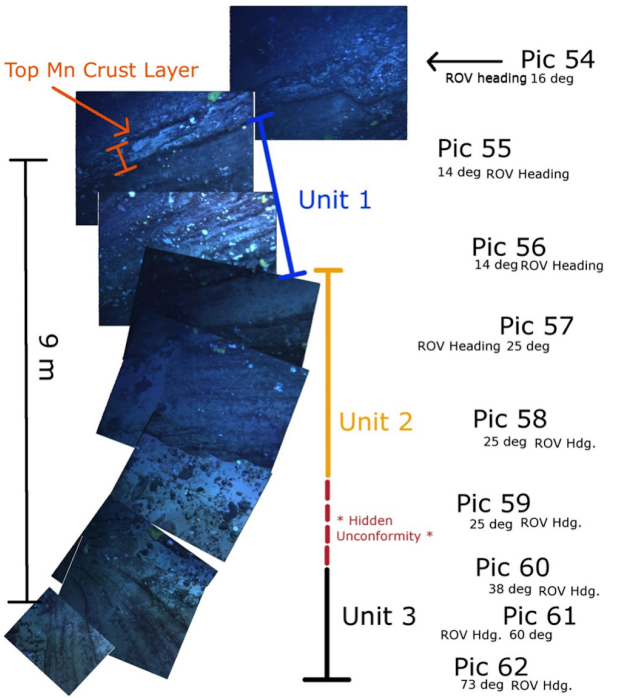

FIGURE 10 | Video frame grabs as ROPOS traveled down the exposed SW side of the NE OK mound in dive R1343. The picture ID is labeled 'Pic' and the heading of ROPOS is shown below the picture ID. Units 1 and 2 are of the same strike and dip; however Unit 2 has thicker bedded layers than Unit 1. Unit 3 is of a different strike than Units 1 and 2, and has no apparent dip. The summary of all strike and dip observations on the mound are presented in **Figure 7C**.

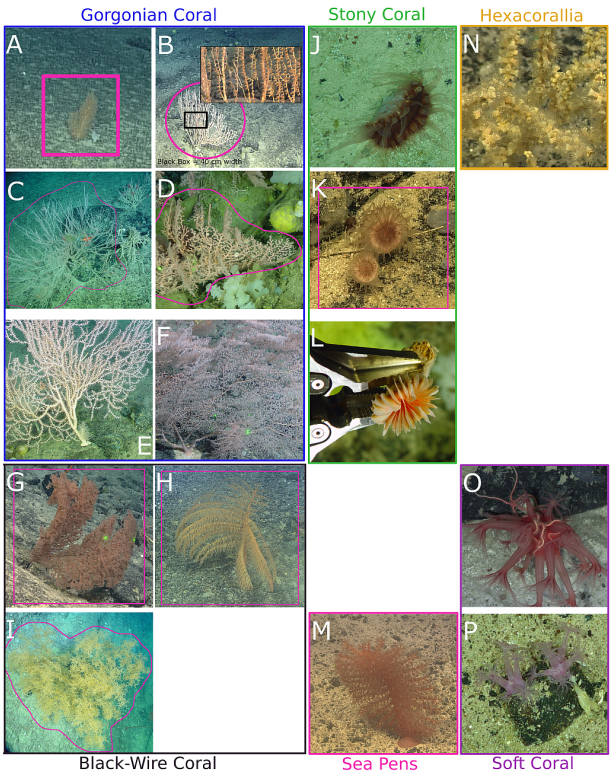

FIGURE 11 | Cold-water corals observed on the Orphan Seamount and Orphan Knoll. 'Gorgonian' corals: (top left): **(A)** *Acanella arbuscula*. **(B)** Isididae. **(C)** Keratoisidinae. **(D)** *Corallium* sp., probably *C. niobe* **(E)** *Paramuricea* sp. **(F)** *Chrysogorgia* sp. Black-wire coral (bottom-left): **(G)** Antipatharia indet., **(H)** *Bathypathes* sp., **(I)** *Stauropathes* sp., Stony coral (green box): **(J)** *Flabellum* sp., **(K)** *Caryophyllia ambrosia*, **(L)** *Desmophyllum dianthus*. Sea Pens (pink box): **(M)** various sea pen species, the most common was *Pennatula* spp., as shown here, Hexacorallia (top right): **(N)** Zoantharia, and Soft corals (bottom-right): **(O)** *Anthomastus* spp., **(P)** Nephtheidae. All corals identified visually, hence morphospecies, except for corals shown in **(C,D,F,H–L)**, for which voucher specimens were collected.

in the multibeam, however, suggests that the mounds are too small to have induced cyclonic currents surrounding them from small Taylor columns. They may, however, experience inertial currents moving around the mounds, perhaps under the influence of unusually strong winter storms (cf. Li et al., 2017). Variations in sediment accumulation rates in piston cores from Orphan Knoll (Piper, unpublished data) suggest that there are local effects of near-bottom currents. Bottom currents were likely stronger in the Holocene than in the glacial Pleistocene (Mao et al., 2018). The very thin Miocene section in DSDP 111 suggests particularly erosional bottom water conditions as the Oligocene-Mid Miocene abyssal circulation changed in the western North Atlantic Ocean (Miller and Fairbanks, 1983). The ROV observations and samples of bedrock mostly indicated thinly bedded to massive sedimentary rock with extensive Fe–Mn encrustation, suggesting a long duration of submarine exposure. Corals collected from the coral graveyard at R1343 included samples as old as 181 ka, from Marine Isotope Stage (MIS) 7 (Ménabréaz et al., 2015; Maccali et al., in review). Osmium isotope studies of the polymetallic nodules from R1341 suggested an Eocene origin, with a hiatus in accretion during the Miocene (Poirier et al., 2011). Geochemical evidence on the subfossil corals collected from the graveyard site at R1343 suggests that the corals were buried and later exhumed by Holocene current scour (Maccali et al., in review). Strong Holocene current winnowing of hemipelagic sediments from the corals in the coral graveyard are suggested as a taphonomic mechanism causing degradation of the coral samples, and perhaps concentration of the coral samples by removal of intervening fine sediments. Such current winnowing would also help explain the abundance of polymictic gravels containing Paleozoic limestone derived from Arctic Canada within the coral graveyard deposit, consistent with ice-rafted debris supplied during Heinrich events. The bottom type observations during ROV dives R1341 and R1343 found sloping areas of mud and mixed lithic clasts surrounding the exposed bedrock core of mounds. These apparent hemipelagic sediments could be affected by current winnowing and sediment drift, but no diagnostic features were observed. We therefore conclude that locally in the Holocene and perhaps during other full interglacials near bottom currents were strong enough to modify the sea floor. On the other hand, clear current scour moats or other features typically associated with prolonged formation of contourite drifts (van Rooij et al., 2007; Esentia et al., 2018) were

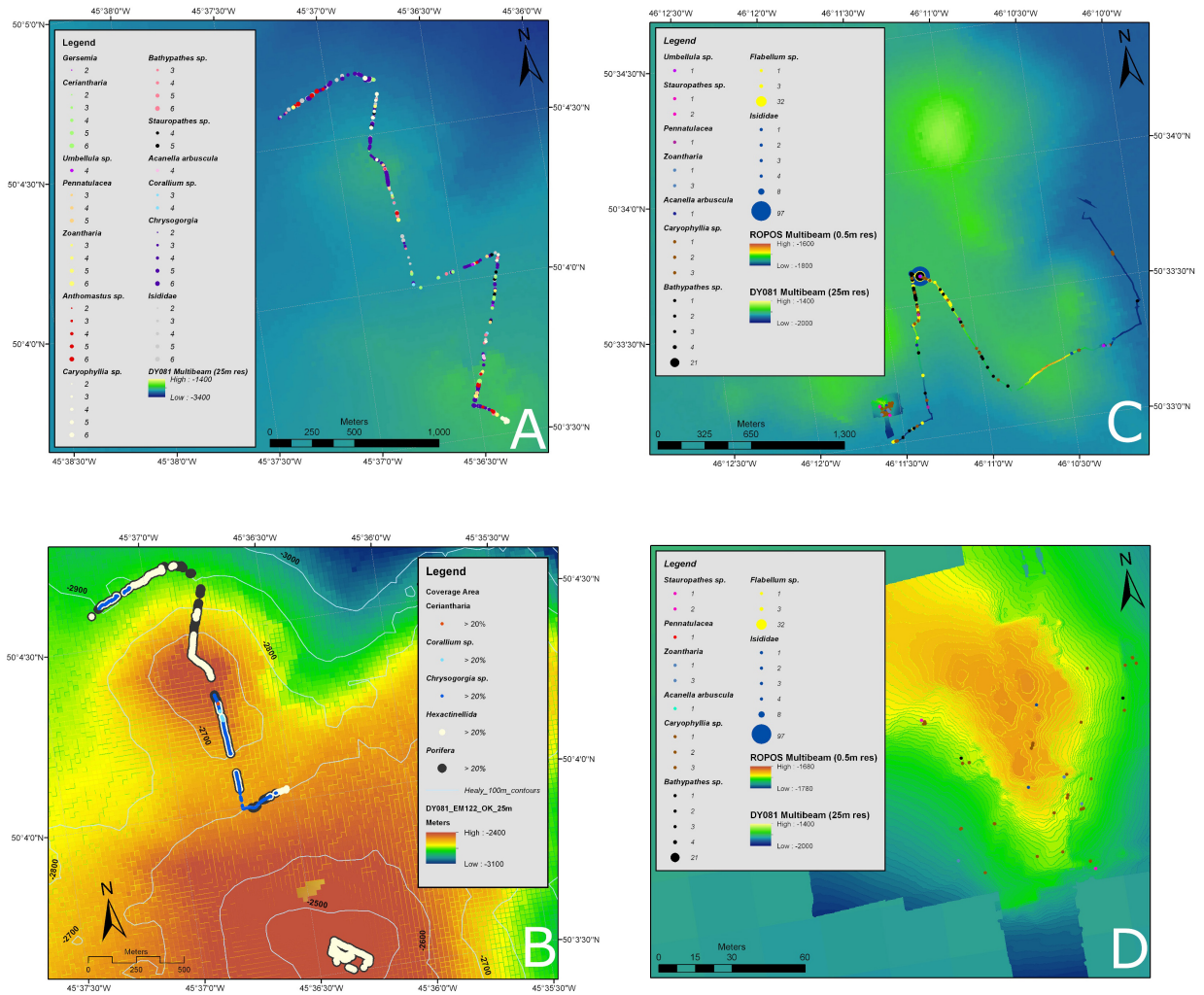

FIGURE 12 | Distribution of cold-water coral observations along ROPOS dives. **(A,B)** Coral observations on SE Orphan Knoll dive R1341. **(A)** Coral observations. **(B)** Locations of faunal concentrations of corals and sponges > 20% cover. See **Figure 9A** for surficial geology layer. **(C,D)** Coral observations on NE Orphan Knoll dive R1343. **(C)** Coral distributions throughout dive R1343. See **Figure 9B** for the surficial geology layer. The track of the ROV showing coral occurrences is overlaid over DY081 bathymetry. Coral abundances not adjusted for area observed. White box indicates location of **(D)**. **(D)** Coral observations surrounding bedrock outcrop mapped in **Figure 8C**, including *Desmophyllum dianthus* coral graveyard. See **Figure 9B** for surficial geology layer, and see **Figure 7C** for underlying ROV-derived bathymetry below **(D)**.

not observed around any of the mounds in the 2017 *Discovery* multibeam data (**Figure 5**), nor in seismic profiles (**Figure 4**).

A striking morphological features of the mounds revealed in the 2017 Discovery multibeam data is their approximately conical shape. This morphology is superficially similar to the shape of subaerial cinder cones or submarine volcanic seamounts (Casalbore, 2018), though at a smaller than normal scale than seamounts as usually defined (e.g., Harris et al., 2014). A volcanic origin can be excluded based on the seismic profiles through the mounds (**Figure 4**), complete lack of evidence in ROV observations and the lack of magnetic anomaly detected in several magnetometer surveys across the Knoll, starting with the 1969 Charcot survey, and magnetometer surveys associated with the DSDP expedition (Laughton et al., 1972).

Visual observations using the ROV likewise uncovered no evidence for a biogenic origin of the mounds, i.e., cold-water coral carbonate mounds (Huvenne et al., 2003; Roberts et al., 2006). The mounds were clearly colonized by cold-water corals, mostly octocorals, with a few antipatharians, and by sponges, but the mounds were not composed of coral skeletons. Stratified late Pleistocene sediment imaged by seismic profile on a mound crest (**Figure 4A**) is inconsistent with a biogenic mound origin. Our lack of observation of biogenic mounds does not preclude the presence of biogenic mounds, formed by corals or sponges, elsewhere on the Orphan Knoll or adjacent regions such as the Sackville Spur (Campbell, personal communication). Nor does it preclude the possibility of buried biogenic mounds of pre-mid Quaternary age forming a substrate for proglacial hemipelagic deposition in the later Quaternary.

One of the early proposed origins of the mounds on Orphan Knoll was the presence of (aligned) bedrock ridges. Laughton et al. (1972) proposed apparently aligned mounds, but on the basis of single-beam sonar data on hand-drawn maps. Higher resolution seismic profiles (**Figure 4C**) show faulting of Mesozoic-Cenozoic bedrock, with some faults extending upwards to near the seabed. The 2017 *Discovery* mapping of the mounds on NE Orphan Knoll shows local alignment of series of several mounds, for example ESE–WNW at 50°40′ N near the eastern edge of the Knoll, and almost N–S at around 50°30′ N (**Figure 5D**), extending northward to the mounds in **Figure 4A**. Thus although the overall data shows no statistical preferred orientation, the patterns of mound distribution are consistent with alignment along relatively short fault segments (<5 km in length).

Bedrock orientation observed from dive R1343, with generally westward to southwestward dip angles, is consistent with the concept that mounds are fault bounded and experienced some tilting. So too are the gentle dips in fault-bound blocks of Cenozoic-Quaternary strata visible in seismic profiles (**Figure 4C**). The seismic profiles suggest that some of the mounds could expose Mesozoic strata at their base. The Eocene age of the calcareous ooze sampled at the beginning of dive R1341 is consistent with this interpretation. The Quaternary section over the mounds appears condensed compared with that in flat areas of the crest of Orphan Knoll (**Figure 4**), not unexpected given the regional southward flowing currents (Hall et al., 2013).

With available data, it is difficult to further characterize the faulting style. They may represent normal, possibly listric faults, structurally similar to the extensional faulting within the Orphan Basin (Dafoe et al., 2017). Alternatively, the faults may be parallel to the NNW-trending fault-bound northeastern face of Orphan Knoll, although this is not supported by orientations of groups of mounds in the bathymetry (**Figure 5D**). Quaternary neotectonic faulting has been demonstrated farther south on Flemish Cap (Normandeau et al., 2019) but is not apparent in Orphan Basin.

The available data suggest that the short linear groups of mounds represent tilted fault blocks of uplifted Mesozoic-Cenozoic bedrock on Orphan Knoll. A highly condensed section in Oligocene and Miocene pelagic sediments with hiatuses was intersected by DSDP 111 and the seismic signature is irregular, suggestive of bottom current winnowing. At that time, fault uplift may have exceeded burial by accumulated sediment, and the resulting fault scarps would have been susceptible to mass wasting, similar to that seen at the seabed today on the NE face of Orphan Knoll. Localized submarine landsliding and winnowing by bottom currents broke up the short fault scarps into a series of residual erosional highs, as evidenced by the Eocene sediment recovered on dive 1341. With increased sediment supply in the Pliocene and particularly the Quaternary, this erosional landscape was blanketed by distal proglacial hemipelagic sediment. Sculpting of this hemipelagic sediment by bottom currents, particularly when sedimentation rates were a little lower in the early Pleistocene and Pliocene, probably contributed to mound morphology, as sediment was swept off the crests of the mounds and accumulated on the flanks, and small landslides also developed on the steep flanks.

Despite a long but scattered history of study, ROV observations and rock collections, and an extensive new multibeam dataset, the origin and composition of the enigmatic Orphan Knoll mounds remains unclear. The hypothesis of a fault-based origin of the mounds is supported, but not confirmed, by the data in this study. The juxtaposition of the new multibeam data demonstrating approximately conical shape and no strong systematic alignment of mounds, with the ROV observations suggesting block-faulted sedimentary bedrock composition for at least one of the mounds observed, serves to reinforce the necessity of sub-bottom or seismic data, *in situ* direct observations, and ROV-based bedrock collections, to complement interpretations of seafloor mounds origins based on mound shape revealed in remotely sensed bathymetry. It is possible that a 1–2 days of dedicated high-resolution deep-towed seismic surveys around some of the larger and more isolated mounds could detect faults surrounding more of the mounds on Orphan Knoll.

Significance of Biological Observations, Particularly Deep-Sea Corals

The coral fauna observed on Orphan Knoll was generally similar to the fauna observed elsewhere in the Newfoundland and Labrador region, with the exception of two species. First, the gorgonian coral, *Corallium? niobe*, was observed on the SE Orphan Knoll mounds (R1341). Further samples of *C. niobe* were collected during the DY081 cruise ROV dives on Orphan Knoll in 2017 (Hendry, 2017).

The small-scale distribution of hard-substrate dependent species on the Orphan Knoll was not limited to mound bedrock. All types of hard-substrate dependent corals and sponges were also observed growing on ice-rafted debris, on clasts ranging in size from small cobbles to large boulders (Meredyk, 2017). The abundant ice-rafted debris in the Northwest Atlantic may weaken apparent substrate limitations for cold-water coral species that require hard-substrate attachment surfaces (Miles, 2018).

The solitary scleractinian coral *Caryophyllia ambrosia* was observed in muddy sediments between the mounds on Orphan Knoll, on dives R1345 and R1346. While this species is well-known from deep-water environments elsewhere, it has not previously been recorded in the Newfoundand and Labrador region.

Overall our data suggest that the mounds were not built by scleractinian corals, as has been reported for mounds in the Porcupine Seabight or Rockall Trough, for example (NE Atlantic, Mienis et al., 2006; Kano et al., 2007), nor authigenic carbonates colonized by cold-water corals. Although evidence was found for moderate densities of *D. dianthus* in some locations, the mounds were also not covered by extensive scleractinian reefs, which was one of the underlying hypotheses that supported the 2008 NAFO decision to close the area to bottom-contact fisheries. However, the evidence provided here shows that the hard substratum and habitat complexity provided by the mounds support a diverse fauna that includes a large number of other cold-water coral and benthic species, which are protected from fisheries impacts by the NAFO closure. Independent of their origin and development mechanism, deep-sea mounds often

provide an attractive environment for benthic communities that warrant conservation.

CONCLUSION

The 'Enigmatic Mounds' on Orphan Knoll remain enigmatic. The majority of mounds surveyed to date are less than 1 km^2 in area and < 100 m in height above the surrounding portions of Orphan Knoll. The mounds surveyed in new multibeam data are mostly conical in form, without a clear preferred orientation or apparent alignment.

Remotely operated vehicle observations of the Orphan Knoll mounds including near-bottom ROV-based multibeam surveys suggested domal to ridge-shaped mounds, some with potential collapse features around some edges. The *in situ* camera observations on one mound suggested that the mound bedrock was composed of bedded sedimentary rock, probably siliciclastic, with a prevailing, but not uniform, dip direction to the southwest. These observations are consistent with a block-faulted origin of the observed mounds. No direct evidence of former subaerial processes, submarine volcanic rocks, mud-volcanoes, karst dissolution, or cold-water coral bioherms was observed.

Our results emphasize the importance of *in situ* observations and rock sample collections to complement remotely-sensed bathymetric datasets, and the need for improved techniques of ROV-based submarine bedrock collection and submarine bedrock structural analysis.

DATA AVAILABILITY STATEMENT

The *USCGC Healy* and *Kommandor Jack* multibeam sonar and Geological Survey of Canada seismic data are available through the Canadian Hydrographic Service and the Geological Survey of Canada, but with some confidentiality limitations applied to the *Kommandor Jack* data compiled for the Canadian UNCLOS claim. The UNCLOS Atlantic Ocean multibeam data reside with CHS and are available through a request sent to: CHS ATL Data Centre/Centre de Données CHS ATL. DFO.CHSATLDataCentre-CentreDeDonneesCHSATL.MPO@dfo-mpo.gc.ca. HUDSON 2010-029 mission data and ROPOS multibeam data are archived at the Geological Survey of Canada and at Memorial University, and are available upon request from the authors. The ICY-LAB multibeam bathymetry data are archived at the National Oceanography Centre, Southampton, United Kingdom. ICY-LAB EM-122 multibeam swath bathymetry datasets are now published on PANGAEA (doi: 10.1594/PANGAEA.892825) and are free to access.

AUTHOR CONTRIBUTIONS

SM compiled the archival multibeam, side-scan, and sub-bottom profile data, participated in the field work aboard *CCGS Hudson* Cruise 2010-029, processed the video, identified the rock samples, identified the corals and sponges in video, and contributed to the writing. EE and DP directed the thesis of SM. EE participated in the field work aboard *CCGS Hudson* cruise 2010-029, guided the interpretations, and contributed to the writing. DP provided archival multibeam, side-scan, and sub-bottom profile data, guided the interpretations, and contributed to the writing. VH and SH collected, processed, and analyzed the multibeam sonar data on cruise DY081, and contributed to the writing. AR guided the interpretations and contributed to the writing, particularly with detailing the history of geological exploration and mapping of Orphan Knoll.

FUNDING

This research was supported by NSERC Discovery Grants to EE and DP. *CCGS Hudson* ship-time and ROV support was funded by an NSERC ship time grant to EE and co-applicants, and by Fisheries and Oceans Canada (DFO) International Governance Strategy (IGS) grants to K. Gilkinson and E. Kenchington, and DFO ship time allocated to E. Kenchington. Support for SM studies was provided by funding from the Memorial University, NSERC Discovery Grants to EE and DP, and the Geological Survey of Canada. 2017 ship time aboard *RRS Discovery* was funded by a NERC (United Kingdom) ship-time grant to ICY-LAB Principal Investigator Kate Hendry. Additional support was received from a Memorial University 2018-19 sabbatical research grant to EE and by European Research Council Starting grant # 678371.

ACKNOWLEDGMENTS

The authors would like to thank the captain and crew of *CCGS Hudson* and the Canadian Scientific Submersible Facility (CSSF) ROV team, for support during the *Hudson* 2010-029 mission. The authors would also like to thank the Principal Investigator Kate Hendry, together with the captain, crew, and scientific party of the ICY-LAB expedition DY081. R. Devillers (MUN) guided the collection and processing of near-bottom multibeam data during and after *CCGS Hudson* 2010-029 cruise. S. Bermell (IFREMER) reprocessed the near-bottom multibeam rasters to highlight geomorphic features, and generated high-resolution bathymetric profiles of two mounds. This manuscript was completed while EE was on sabbatical leave at IFREMER Centre Bretagne, France. EE thanks IFREMER for cartographic and computational support. Dedicated to the memories of Edgar Edinger (1919–2018), Anthony Laughton (1927–2019), Jan E. van Hinte (1935–2019), and Callum Mireault (1991–2018).

SUPPLEMENTARY MATERIAL

The Supplementary Material for this article can be found online at: https://www.frontiersin.org/articles/10.3389/fmars.2019.00744/full#supplementary-material

REFERENCES

Barrett, T. J., Jarvis, I., Longstaffe, F. J., and Farquhar, R. (1988). Geochemical aspects of hydrothermal sediments in the eastern Pacific Ocean; an update. *Can. Mineral.* 26, 841–858.

Blénet, A. (2016). *La Taphonomie des Coraux Profonds des Cimetirères sous-marins d'Orphan Knoll et de Flemish Cap, Une Étude Préliminaire aux Analyses Géochimiques*. M.Sc. thesis, Université du Québec à Montréal, Montreal.

Bolton, B. R., Both, R., Exon, N. F., Hamilton, T. F., Ostwald, J., and Smith, J. D. (1988). Geochemistry and mineralogy of seafloor hydrothermal and hydrogenetic Mn oxide deposits from the Manus Basin and Bismarck Archipelago region of the southwest Pacific Ocean. *Mar. Geol.* 85, 65–87. doi: 10.1016/0025-3227(88)90084-9

British Admiralty (1917). *North Atlantic Ocean, Eastern Portion*. London: British Admiralty.

Burton-Ferguson, R., Enachescu, M. E., and Hiscott, R. (2006). *Preliminary seismic interpretation and maps for the Paleogene-Neogene (Tertiary) Succession, Orphan Basin* (Canada: Memorial University of Newfoundland), 28–32.

Casalbore, D. (2018). "Volcanic islands and seamounts," in *Submarine Geomorphology*, eds A. Micallef, S. Krastel, and A. Savini, (Berlin: Springer), 333–347. doi: 10.1007/978-3-319-57852-1_17

Ceramicola, S., Dupre, S., Somoza, L., and Woodside, J. (2018). "Cold seep systems," in *Submarine Geomorphology*, eds A. Micallef, S. Krastel, A. Savini, (Berlin: Springer), 367–387. doi: 10.1007/978-3-319-57852-1_19

Channell, J. E. T., Hodell, D. A., Romero, O., Hillaire-Marcel, C., De Vernal, A., Stoner, J. S., et al. (2012). A 750-kyr detrital-layer stratigraphy for the North Atlantic (IODP Sites U1302–U1303. Orphan Knoll, Labrador Sea). *Earth Planet. Sci. Lett.* 317, 218–230. doi: 10.1016/j.epsl.2011.11.029

Chian, D., Reid, I. D., and Jackson, H. R. (2001). Crustal structure beneath Orphan Basin and implications for nonvolcanic continental rifting. *J. Geophys. Res.* 106, 923–940.

Conway, K., Barrie, J. V., and Krautter, M. (2005). Geomorphology of unique reefs on the western Canadian shelf: sponge reefs mapped by multibeam bathymetry. *Geol. Mar. Lett.* 25, 205–213. doi: 10.1007/s00367-004-0204-z

Cormier, M.-H., and Sloan, H. (2018). "Abyssal hills and abyssal plains," in *Submarine Geomorphology*, eds A. Micallef, S. Krastel, and A. Savini, (Berlin: Springer), 389–408. doi: 10.1007/978-3-319-57852-1_20

Dafoe, L. T., Keen, C. E., Dickie, K., and Williams, G. L. (2017). Regional stratigraphy and subsidence of Orphan Basin near the time of breakup and implications for rifting processes. *Basin Res.* 29, 233–254. doi: 10.1111/bre.12147

Deutschen Hydrographischen Institut (1964). *General Bathymetric Chart of the Oceans (GEBCO), Deut. Hydro*. Hamburg: Deutschen Hydrographischen Institut.

Dronov, A. (1993). Middle paleozoic waulsortian-type mud mounds in Southern Fergana (Southern Tien-Shan, commonwealth of independent states): the shallow-water atoll model. *Facies* 28, 169–180. doi: 10.1007/bf02539735

Edinger, E. N., and Sherwood, O. A. (2012). Applied taphonomy of gorgonian and antipatharian corals in Atlantic Canada: experimental decay rates, field observations, and implications for assessing fisheries damage to deep-sea coral habitats. *Neues Jahrb. Geol. Paläontol.* 265, 199–218. doi: 10.1127/0077-7749/2012/0255

Enachescu, M., Kearsey, S., Hardy, V., Sibuet, J.-C., Hogg, J., Srivastava, S., et al. (2005). "Evolution and petroleum potential of Orphan Basin, offshore Newfoundland, and its relation to the movement and rotation of Flemish Cap based on plate kinematics of the North Atlantic," in *Petroleum Systems of Divergent Continental Margin Basins*, eds N. Rosen, D. Olsen, S. L. Palmes, K. T. Lyons, and G. B. Newton, (Houston, TX: GCSSEPM), 75–131. doi: 10.5724/gcs.05.25.0075

Enachescu, M. E. (2004). Conspicuous deepwater submarine mounds in the northeastern Orphan Basin and on the Orphan Knoll, offshore Newfoundland. *Lead. Edge* 23, 1290–1294. doi: 10.1190/leedff.23.1290_1

Esentia, I., Stow, D., and Smillie, Z. (2018). "Contourite drifts and associated bedforms," in *Submarine Geomorphology*, eds A. Micallef, S. Krastel, and A. Savini, (Berlin: Springer), 301–331. doi: 10.1007/978-3-319-57852-1_16

Forsterra, G., Beuck, L., Häussermann, V., and Freiwald, A. (2005). "Shallow-water *Desmophyllum dianthus* (Scleractinia) from Chile: characteristics of the biocoenoses, the bioeroding community, heterotrophic interactions and (paleo)-bathymetric implications," in *Cold-Water Corals and Ecosystems. Erlangen Earth Conference Series*, eds A. Freiwald, and J. M. Roberts, (Berlin: Springer), 937–977. doi: 10.1007/3-540-27673-4_48

Greenan, B. J. W., Yashayaev, I., Head, E. J. H., Harrison, W. G., Azetsu-Scott, K., Li, W. K. W., et al. (2010). *Interdisciplinary Oceanographic Observations of Orphan Knoll*. Dartmouth: Northwest Atlantic Fisheries Organization.

Hall, M. M., Torres, D. J., and Yashayaev, I. (2013). Absolute velocity along the AR7W section in the Labrador Sea. *Deep Sea Res.* 72, 72–87. doi: 10.1016/j.dsr.2012.11.005

Harris, T., Macmillan-Lawler, M., Rupp, J., and Baker, E. K. (2014). Geomorphology of the Oceans. *Mar. Geol.* 352, 4–24. doi: 10.1016/j.margeo.2014.01.011

Hart, B. (1977). The mid-Cretaceous succession of Orphan Knoll (northwest Atlantic): micropaleontology and palaeo-oceanographic implications. *Deep Sea Res.* 24, 272–272.

Hendry, K. (2017). *RRS Discovery Cruise DY081 cruise report: ICY-LAB (Isotope sampling in the Labrador Sea)*. Fort Lauderdale, FL: National Marine Facilities.

Henriet, J., Hamoumi, N., Da Silva, A. C., Foubert, A., Lauridsen, B. W., Ruggeberg, A., et al. (2014). Carbonate mounds: from paradox to World Heritage. *Mar. Geol.* 352, 89–110. doi: 10.1016/j.margeo.2014.01.008

Henriet, J., Spezzaferri, S., Samankassou, E., Foubert, A., van Rooij, D., and Ruggeberg, A. (2011). Carbonate mounds in shallow and deep time. *Mar. Geol.* 282, 1–4. doi: 10.1016/j.margeo.2011.02.010

Hiscott, R. N., Aksu, A. E., and Nielsen, O. B. (1989). Provenance and dispersal patterns, Pliocene-Pleistocene section at site 645, Baffin Bay. *Proc. Ocean Drill. Prog. Sci. Results* 105, 31–52.

Hovland, M., Croker, P. F., and Martin, M. (1994). Fault-associated seabed mounds(carbonate knolls?) off western Ireland and north-west Australia. *Mar. Pet. Geol.* 11, 232–246. doi: 10.1016/0264-8172(94)90099-x

Howell, K.-L., Piechaud, N., Downie, A.-L., and Kenny, A. (2016). The distribution of deep-sea sponge aggregations in the North Atlantic and implications for their effective spatial management. *Deep Sea Res.* 115, 309–320. doi: 10.1016/j.dsr.2016.07.005

Hoy, S. K., Hendry, K. R., and Huvenne, V. A. I. (2018). *North Atlantic EM-122 Multibeam Swath Bathymetry Collected During RRS Discovery Cruise DY081 (Links to Raw Files and Gridded Data)*. Los Angeles: PANGAEA.

Huvenne, V. A. I., de Mol, B., and Henriet, J. (2003). A 3D seismic study of the morphology and spatial distribution of buried coral banks in the Porcupine Basin, SW of Ireland. *Mar. Geol.* 198, 5–25. doi: 10.1016/s0025-3227(03)00092-6

Immenhauser, A., and Rameil, N. (2011). Interpretation of ancient epikarst features in carbonate successions — A note of caution. *Sediment. Geol.* 239, 1–9. doi: 10.1016/j.sedgeo.2011.05.006

Kano, A., Ferdelman, T. G., Williams, T., Henriet, J., Ishikawa, T., Kawagoe, N., et al. (2007). Age constraints on the origin and growth history of a deep-water coral mound in the northeast Atlantic drilled during integrated ocean drilling program expedition 307. *Geology* 35, 1051–1054.

Keen, C. E. (1978). *Cruise Report C.S.S.* Hudson: Bedford Institute of Oceanography.

Kenchington, E., Best, M., Cogswell, A., MacIsaac, K., Murillo-Perez, F. J., MacDonald, B., et al. (2009). *Accurate Identification of Deep-Water Coral Harvested in the NAFO Regulatory Area*. Dartmouth: Northwest Atlantic Fisheries Organization.

Land, L., Paull, C., and Hobson, B. (1995). Genesis of a submarine sinkhole without subaerial exposure: Straits of Florida. *Geology* 23, 949–951.

Laughton, A. S., Berggren, W. A., Benson, R. N., Davies, T. A., Franz, U., Musich, L. F., et al. (1972). *Site 111, Initial Reports of the Deep-Sea Drilling Project* (Washington, DC: U. S. Government Printing Office), 133–159.

Lecours, V., Gabor, L., Edinger, E., and Devillers, R. (2019). "Fine-scale cold-water coral habitat characterization of The Gully, the Flemish Cap and the Orphan Knoll, Northwest Atlantic," in *GEOHAB Atlas: Seafloor Geomorphology as Benthic Habitat, 2nd Edition*, eds T. Harris, and E. K. Baker, (Amsterdam: Elsevier).

Legault, J. (1982). First report of Ordovician (Caradoc-Ashgill) palynomorphs from Orphan Knoll, Labrador Sea. *Can. J. Earth Sci.* 19, 1851–1856. doi: 10.1139/e82-163

Li, M. Z., Wu, Y., Han, G., Prescott, R. H., and Tang, C. C. L. (2017). A modeling study of the impact of major storms on seabed shear stress and sediment transport on the Grand Banks of Newfoundland. *J. Geophys. Res.* 122, 4183–4216. doi: 10.1002/2016JC012215

Lo Iacono, C., Savini, A., and Basso, D. (2018). "Cold-water carbonate bioconstructions," in *Submarine Geomorphology*, eds A. Micallef, S. Krastel, A. Savini, (Berlin: Springer), 425–455. doi: 10.1007/978-3-319-57852-1_22

Maccali, J., Hillaire-Marcel, C., Ghaleb, B., Menabreaz, L., Blenet, A., Edinger, E., et al. (in review). Quaternary sporadic development of *Desmophyllum dianthus* deep-sea coral populations in the southern Labrador Sea with specific attention to their ^{14}C and ^{230}Th-dating. *Mar. Chem.*

Mao, L., Piper, D. J., Saint-Ange, F., and Andrews, J. T. (2018). Labrador Current fluctuation during the last glacial cycle. *Mar. Geol.* 395, 234–246. doi: 10.1016/j.margeo.2017.10.012

Mazzini, A., and Etiope, G. (2017). Mud volcanism: an updated review. *Earth Sci. Rev.* 168, 81–112. doi: 10.1016/j.earscirev.2017.03.001

Ménabréaz, L., Maccali, J., Blénet, A., Ghaleb, B., Poirier, A., Edinger, E., et al. (2015). *Neodymium Isotopic Composition of Deep-Sea Corals from the Labrador Sea: Implications for NW Atlantic Deep-Water Masses Circulation During the Holocene, MIS 5 and 7*. Montreal: AGU.

Meredyk, S. (2017). *Physical characterization and benthic megafauna distribution and species composition on Orphan Knoll and Orphan Seamount, NW Atlantic*. M.Sc. thesis, Memorial University of Newfoundland, Canada.

Mienis, F., van Weering, T., de Haas, H., de Stigter, H., Huvenne, V., and Wheeler, A. (2006). Carbonate mound development at the SW Rockall Trough margin based on high resolution TOBI and seismic recording. *Mar. Geol.* 233, 1–19. doi: 10.1016/j.margeo.2006.08.003

Miles, L. L. (2018). *Cold-Water Coral Distribution and Surficial Geology on the Flemish Cap, Northwest Atlantic*. M.Sc. thesis, Memorial University of Newfoundland, Canada.

Miller, K. G., and Fairbanks, R. G. (1983). Evidence for Oligocene–middle miocene abyssal circulation changes in the western North Atlantic. *Nature* 306:250. doi: 10.1038/306250a0

Moscardelli, L., Ramnarine, S. K., Wood, L., and Dunlap, D. B. (2013). Seismic geomorphological analysis and hydrocarbon potential of the lower cretaceous Cromer Knoll Group, Heidrun field, Norway. *AAPG Bull.* 97, 1227–1248. doi: 10.1306/02081312155

Normandeau, A., Piper, D. J. W., Shaw, J., Todd, B. J., Campbell, D. C., and Mosher, D. C. (2019). "Chapter 20: the seafloor of Southeastern Canada," in *Landscapes and Landforms of Eastern Canada*, eds O. Slaymaker, and N. Catto, (Berlin: Springer).

Parson, L. M., Masson, D. G., Pelton, C. D., and Grant, A. C. (1985). Seismic stratigraphy and structure of the east Canadian continental margin between 41 and 52° N. *Can. J. Earth Sci.* 22, 686–703. doi: 10.1139/e85-075

Parson, L. M., Masson, D. G., Rothwell, R. G., and Grant, A. C. (1984). Remnants of a submerged pre-Jurassic (Devonian?) landscape on Orphan Knoll, offshore eastern Canada. *Can. J. Earth Sci.* 21, 61–66. doi: 10.1139/e84-007

Pe-Piper, G., Meredyk, S., Zhang, Y., Piper, D. J. W., and Edinger, E. N. (2013). Petrology and tectonic significance of seamounts within transitional crust east of Orphan Knoll, offshore eastern Canada. *Geo-Mar. Lett.* 33, 433–447. doi: 10.1007/s00367-013-0342-2

Pe-Piper, G., Meredyk, S., Zhang, Y., Piper, D. J. W., and Edinger, E. N. (2014). Erratum to: petrology and tectonic signficance of seamounts within transitional crust east of Orphan Knoll, offshore eastern Canada. *Geo-Mar. Lett.* 34, 567–568.

Poirier, A., Hillaire-Marcel, C., Meredyk, S., and Edinger, E. (2011). Osmium isotopes in manganese nodules from the Labrador Sea. *Mineral. Mag.* 75:1653.

Riding, R., and Awramik, S. M. (2000). *Microbial Sediments*. Berlin: Springer.

Roberts, M., Long, D., Wilson, J. B., Mortensen, B., and Gage, J. D. (2003). The cold-water coral *Lophelia pertusa* (Scleractinia) and enigmatic seabed mounds along the north-east Atlantic margin: are they related? *Mar. Pollut. Bull.* 46, 7–20. doi: 10.1016/s0025-326x(02)00259-x

Roberts, M., Wheeler, A., and Freiwald, A. (2006). Reefs of the deep: the biology and geology of cold-water coral ecosystems. *Science* 312, 543–547. doi: 10.1126/science.1119861

Ruffman, A. (1971). *A Report on the Participation of A. Ruffman on the USNS LYNCH Cruise 7/11/71 in the North Atlantic*. Bedford Institute of Oceanography.

Ruffman, A. (2011). *Orphan Knoll as a Window on the Palaeozoic; Seemingly Ignored by the Petroleum Industry for 40 Years*. Calgary: Canadian Society of Petroleum Geology.

Ruffman, A., and van Hinte, J. E. (1973). "Orphan Knoll - A 'Chip' off the North American 'Plate'," in *Earth Science Symposium on Offshore Eastern Canada*, ed. J. Hood, (Ottawa: Geological Survey of Canada), 407–449.

Ruffman, A., and van Hinte, J. E. (1989). *Devonian Shelf-Depth Limestone Dredged from Orphan Knoll: A 1971 Discovery and a Reassessment of the HUDSON 78-020 Dredge Hauls from Orphan Knoll*. Ottawa: Geological Survey of Canada.

Sibuet, J.-C. (1992). New constraints on the formation of the non-volcanic continental Galicia-Flemish Cap conjugate margins. *Geol. Soc.* 149, 829–840. doi: 10.1144/gsjgs.149.5.0829

Smith, J. (1997). *The Use of Deep-Sea Corals in Paleooceanographic Monitors*. Ph.D. thesis, Department of Geology, McMaster University, Hamilton.

Smith, J. E. (1993). *Late Quaternary Climatic Reconstruction using the Deep-Water Coral Desmophyllum Cristigalli [sic]*. B.Sc. Honours thesis, Department of Geology, McMaster University, Hamilton.

Smith, J. E., Risk, M. J., Schwarcz, H., and McConnaughey, T. A. (1997). Rapid climate change in the North Atlantic during the younger dryas recorded by deep-sea corals. *Nature* 386, 818–820. doi: 10.1038/386818a0

Smith, J. E., Risk, M. J., Schwarcz, H., and McConnaughey, T. A. (2013). Corrigendum. *Nature* 502:258.

Srivastava, S., Verhoef, J., and Macnab, R. (1988). Results from a detailed aeromagnetic survey across the northeast Newfoundland margin. Part I: spreading anomalies and relationship between magnetic anomalies and the ocean-continent boundary. *Mar. Pet. Geol.* 5, 306–323. doi: 10.1016/0264-8172(88)90025-6

Taviani, M., Angeletti, L., Campiani, E., Ceregato, A., Foglini, F., Maselli, V., et al. (2012). Drowned karst landscape offshore the Apulian margin (southern Adriatic Sea, Italy). *J. Cave Karst Stud.* 74, 197–212. doi: 10.4311/2011jcks0204

Thompson, A. B., and Campanis, G. M. (2007). *Information on Fishing On and Around the Four Closed Seamount Areas in the NRA*. Dartmouth: North Atlantic Fisheries Organization.

Toews, M., and Piper, D. J. W. (2002). *Recurrence Interval of Seismically Triggered Mass-Transport Deposition at Orphan Knoll, Continental Margin off Newfoundland and Labrador*. Ottawa: Geological Survey of Canada Current Research.

van Hinte, J., Ruffman, A., van den Boogaard, M., Jansonius, J., van Kempen, T. M. G., Melchin, M. J., et al. (1995). Palaeozoic microfossils from Orphan Knoll, NW Atlantic Ocean. *Scr. Geol.* 109, 1–63.

van Rooij, D., Blamart, D., Kozachenko, M., and Henriet, J. (2007). "Small mounded contourite drifts associated with deep-water coral banks, Porcupine Seabight, NE Atlantic Ocean," in *Economic and Palaeoceanographic Significance of Contourite Deposits*, eds A. R. Viana, and M. Rebesco, (Geological Society: London), 225–244. doi: 10.1144/gsl.sp.2007.276.01.11

Wareham, V. E. (2009). *Identification guide to deep-sea corals: Newfoundland, Labrador and Baffin island, Canada*. Ottawa: Fisheries and Oceans Canada.

Welford, J. K., Shannon, M., O'Reilly, B. M., and Hall, J. (2012). Comparison of lithosphere structure across the Orphan Basin-Flemish Cap and Irish Atlantic conjugate continental margins from constrained 3D gravity inversions. *J. Geol. Soc.* 169, 405–420. doi: 10.1144/0016-76492011-114

Wielens, H., MacRae, A., and Shimield, J. (2002). Geochemistry and sequence stratigraphy of regional Upper Cretaceous limestone units, offshore eastern Canada. *Org. Geochem.* 33, 1559–1569. doi: 10.1016/s0146-6380(02)00103-1

Wiles, E., Green, A., Watkeys, M., Jokat, W., and Krocker, R. (2014). Anomalous seafloor mounds in the northern Natal Valley, southwest Indian Ocean: implications for the East African rift system. *Tectonophysics* 630, 300–312. doi: 10.1016/j.tecto.2014.05.030

Conflict of Interest: AR is owner and President of Geomarine Associates, Ltd., and declares no conflict of interest.

The remaining authors declare that the research was conducted in the absence of any commercial or financial relationships that could be construed as a potential conflict of interest.

frontiers in Marine Science

ORIGINAL RESEARCH
published: 10 March 2020
doi: 10.3389/fmars.2020.00131

Predicting the Distribution of Indicator Taxa of Vulnerable Marine Ecosystems in the Arctic and Sub-arctic Waters of the Nordic Seas

Julian M. Burgos[1], Lene Buhl-Mortensen[2], Pål Buhl-Mortensen[3], Steinunn H. Ólafsdóttir[1], Petur Steingrund[4], Stefán Á. Ragnarsson[1] and Øystein Skagseth[5]*

[1] Demersal Division, Marine and Freshwater Research Institute, Reykjavik, Iceland, [2] Department of Marine Research in Developing Countries, Institute of Marine Research, Bergen, Norway, [3] Research Group on Bethic Communities, Institute of Marine Research, Bergen, Norway, [4] Demersal Division, Faroe Marine Research Institute, Tórshavn, Faroe Islands, [5] Department of Oceanography, Institute of Marine Research, Bergen, Norway

OPEN ACCESS

Edited by:
Anthony Grehan, National University of Ireland Galway, Ireland

Reviewed by:
Michael Vecchione, National Oceanic and Atmospheric Administration (NOAA), United States
Ian David Tuck, National Institute of Water and Atmospheric Research (NIWA), New Zealand

***Correspondence:**
Julian M. Burgos
julian.burgos@hafogvatn.is

Specialty section:
This article was submitted to Deep-Sea Environments and Ecology, a section of the journal Frontiers in Marine Science

Received: *08 September 2019*
Accepted: *18 February 2020*
Published: *10 March 2020*

Citation:
Burgos JM, Buhl-Mortensen L, Buhl-Mortensen P, Ólafsdóttir SH, Steingrund P, Ragnarsson SÁ and Skagseth Ø (2020) Predicting the Distribution of Indicator Taxa of Vulnerable Marine Ecosystems in the Arctic and Sub-arctic Waters of the Nordic Seas. Front. Mar. Sci. 7:131. doi: 10.3389/fmars.2020.00131

In the deep waters of the Nordic Seas and adjacent areas, several benthic habitats such as cold-water coral reefs, coral gardens, and deep-sea sponge aggregations have been classified as vulnerable marine ecosystems (VMEs), due to their uniqueness, limited spatial extent, physical fragility, and slow recovery rate. In the last decade observations carried out by habitat mapping programmes in Norway, Iceland, and more recently in the Faroe Islands have substantially increased knowledge on the distribution of VMEs in the Nordic Seas. Nevertheless, large areas have not been explored due to the cost and logistics of obtaining observations in the deep-sea. Species distribution models can be used to predict the distribution of VMEs and their indicator species. Here we present the predicted distribution of 44 VME indicator taxa including 20 sponges, 17 cold-water corals, and 7 seapens in the Nordic Seas based on data compiled and models developed by the NovasArc project (2016–2018). Models for 44 VME indicator species were developed using the maximum entropy algorithm MaxEnt, using an extensive database compiled from habitat mapping surveys, by-catch data from bottom fish surveys, and records from reports and peer reviewed publications. Modeled distributions showed good agreement with observations. Niche overlap measures were used to identify seven groups and four subgroups of VME indicator taxa that co-occur. These were consistent with the species composition of known biotopes in the study area. A VME Index that combine the predictions for all VME indicator species was computed to identify particularly valuable and vulnerable ecosystems that should be targets of further exploration and conservation efforts. Such areas were identified at shelf break and slope off Iceland, the Faroe Islands, and central Norway, and the continental shelf off southern Greenland. The predicted distribution of VMEs in Arctic and sub-Arctic waters allows for the evaluation of interactions with fisheries and other anthropogenic activities and provides an important input for managers.

Keywords: vulnerable marine ecosystems, indicator taxa, cold-water corals, sponge aggregations, species distribution models, Nordic Seas

1. INTRODUCTION

In the deep sea, bottom trawling is the main source of anthropogenic impacts (Benn et al., 2010; Ramirez-Llodra et al., 2011). Of particular concern are the effects of bottom trawling on Vulnerable Marine Ecosytems (VMEs), ecosystems dominated by large epibenthic organisms (e.g., corals or sponges) which are likely to experience substantial alterations, and where recovery occurs very slowly (Wheeler et al., 2005; Clark et al., 2010; Williams et al., 2010; Buhl-Mortensen et al., 2013). In addition, VMEs are increasingly being threatened by pollution (Fisher et al., 2014) and by the effects of climate change including increasing water temperatures and ocean acidification (Guinotte et al., 2006; Levin and Le Bris, 2015).

The recognition that some deep-sea ecosystems are particularly susceptible to bottom trawling led the United Nations General Assembly (UNGA) to adopt resolutions 59/25, 61/105, and 64/72, calling for member states and regional fisheries management organisations (RFMOs) to identify areas beyond national jurisdiction (ABNJ) where VMEs occur, or are likely to occur, and to prevent significant negative impacts from damaging fishing practices. The Food and Agriculture Organisation of the United Nations (FAO) defined a set of criteria to identify VMEs, including their uniqueness or rarity, the functional significance of the habitat they form, structural complexity, fragility, and life history traits that make recovery difficult (e.g., slow growth, limited mobility; FAO, 2009). In general VMEs are identified by the presence of indicator taxa (e.g., stony corals, sponges), although merely detecting the presence of a VME element (species, habitats or features) is not sufficient to identify a VME (FAO, 2009). In the north-east Atlantic several benthic habitats have been classified by the Convention for the Protection of the Marine Environment of the North East Atlantic (OSPAR) and by the North East Atlantic Fisheries Commission (NEAFC) as vulnerable to human impacts (VMEs). In the sub-Arctic waters of the Nordic seas these habitats include seapen fields, cold-water coral reefs, coral gardens, and deep-sea sponge aggregations.

Vulnerable marine ecosystems are by definition susceptible to low levels of fishing pressure, and some types of spatial management have been shown to be effective to protect VMEs in the deep-sea (Clark and Dunn, 2012; Schlacher et al., 2014). These include confining the bottom trawling effort to already established footprints and establishing spatial closures to protect vulnerable species and habitats (Hourigan, 2014; Clark et al., 2015). In the North East Atlantic several closures have been established by NEAFC and OSPAR in areas beyond national jurisdiction (NEAFC, 2014). In addition, spatial closures to protect VMEs from fishery impacts have been established within the territorial waters of Norway (Fossåand Skjoldal, 2010), Iceland (Ólafsdóttir and Burgos, 2012), and the Faroe Islands (Anonymous, 2014).

A fundamental requirement for spatial management is detailed information on the distribution of VMEs. The optimal and non-destructive methodology to identify the occurrence of VMEs is through the use of underwater imagery, which allows an accurate description of the species composition and the abundance or density of organisms (e.g., Fabri et al., 2014; Anderson et al., 2016a; Beisiegel et al., 2017; Buhl-Mortensen et al., 2017). Nevertheless, the collection of underwater images in deep-sea environments is an expensive and complex endeavor, and therefore in most areas only a limited proportion of the seabed has been mapped visually. Often, the only available information is from the occurrence of VME indicator species in by-catch from fishery surveys and commercial trawls (Murillo et al., 2011; Durán Muñoz et al., 2012; Jørgensen et al., 2014). The lack of information on the distribution of VMEs in the deep sea is hampering the development and application of measures to protect these habitats from impacts of anthropogenic activities (Weaver et al., 2011).

Given the lack of extensive biological data on VMEs in most offshore environments and their presumed wide distribution, species distribution models (SDMs), also known as habitat suitability models or environmental niche models, are increasingly recognized as an effective way to obtain knowledge on the likely distribution of VMEs (Hourigan, 2014; Vierod et al., 2014; Clark et al., 2015). SDMs are models that predict the potential distribution of a species or a group of species in a given area using environmental variables as suitability predictors. Several studies have used SDMs to predict the distribution of VMEs (Howell et al., 2011, 2016) and of VME indicator species (e.g., Rengstorf et al., 2013; Ross and Howell, 2013; Guinotte and Davies, 2014; Anderson et al., 2016b). The use of these models has been recommended for designing management plans to protect VMEs from fishing impacts (Ardron et al., 2014; Vierod et al., 2014). This includes the evaluation of the risk of fishing impacts (Penney and Guinotte, 2013) and the selection of areas for spatial closures (Lagasse et al., 2015; Rowden et al., 2019).

Within the Nordic Seas, the presence of VMEs has been documented by visual habitat mapping programmes in Norway and Iceland (Ólafsdóttir and Burgos, 2012; Buhl-Mortensen et al., 2015b), and records of VME indicator taxa have been obtained from commercial fisheries and scientific surveys. But predictive models of the distribution of VMEs and VME indicator taxa have not been developed in this area, except for Howell et al. (2016), who modeled the distribution of deep-sea sponge aggregations, and the predicted distribution of biotopes produced by the MAREANO programme in several regions in Norwegian waters (Elvenes et al., 2014; Buhl-Mortensen et al., 2015b; Gonzalez-Mirelis and Buhl-Mortensen, 2015). Here we present predictive models for a suite of indicator taxa of the most important VMEs in the Nordic Seas and adjacent areas.

2. MATERIALS AND METHODS

2.1. Study Area

The study area ranged between 56°N and 80°N and was centered in the Nordic Seas, including the Norway Sea, the Greenland Sea, and the Icelandic Sea, and a portion of the Barents Sea west of 38°E (**Figure 1**). The area includes the Exclusive Economic Zone (EEZ) of Iceland and Norway, most of Svalbard's Fisheries Protection Zone, part of the EEZ of Greenland, the United Kingdom, and Ireland, and the Exclusive

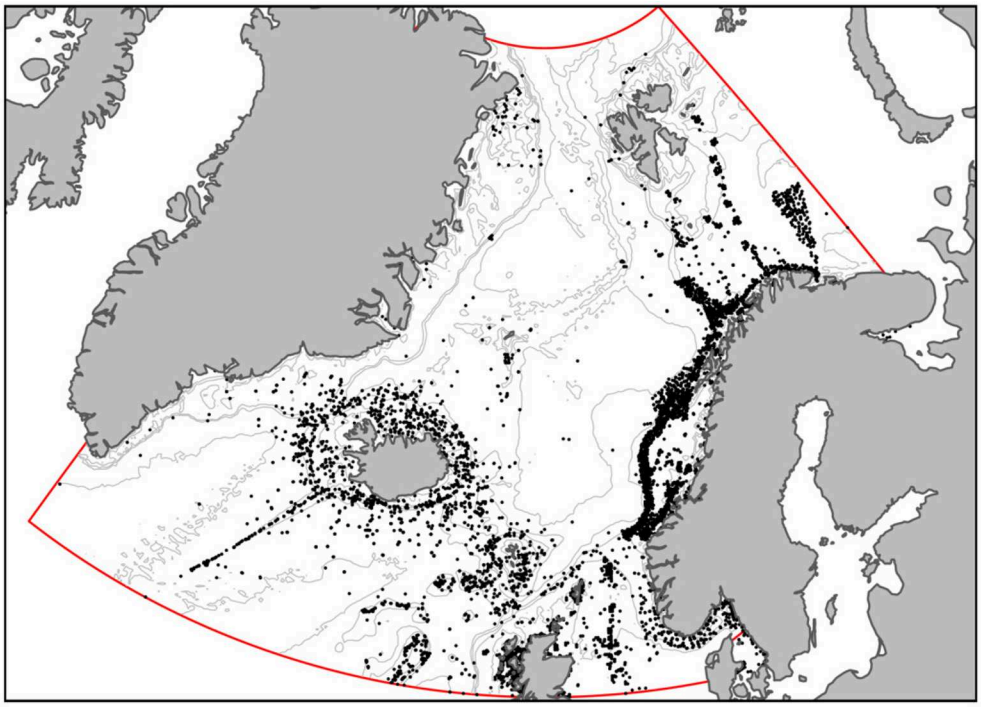

FIGURE 1 | Map of the study area, indicated by the red line. Black dots indicate the location of records of VME indicator taxa. Gray lines are the 100, 500, 1,000, and 2,500 m depth contours.

Fisheries Zone of the Faroe Islands. The study area also includes the entire NEAFC's Regulatory Area 2 (known as the "Banana Hole") and part of Regulatory Area 1. The study area is encompassed mostly in region I of OSPAR (e.g., the Arctic), but includes also small proportions of regions II, III, and V.

This area can be divided into three main basins separated by the northern extension of the mid Atlantic Ridge and the Greenland-Iceland-Scotland Ridge (GISR). The oceanography of the area is characterized by relatively warm surface water supplied from the south by the North Atlantic Drift, an extension of the Gulf Stream, overlying colder water masses (Norwegian Sea Deep Water, Arctic Intermediate Water) supplied from deep-water formation in Arctic areas (Buhl-Mortensen et al., 2015c). In coastal areas, the water is influenced by run-off from land. The seasonal variation is much less in the deeper waters than in the upper layers. Current velocities are controlled by the flow of the water masses and the tide, modified by the seabed topography. The GISR has a major impact on the distribution of water masses. The main pathway of water crossing this ridge is through the Wyville-Thomson Ridge between the Faroe Islands and Scotland. Here, the warm NAD passes into the Norwegian Sea above a sill of approximately 500 m. South of the Wyville-Thomson Ridge, the NAD water extends deeper and overlies a watermass characterized by water from the Mediterranean Ocean (the Mediterranean Outflow Water). The ridge system from Greenland to Scotland represents a major geographic barrier with great implications for distribution of marine species (Brix and Svavarsson, 2010; Dauvin et al., 2012; Omarsdottir et al., 2013).

2.2. Biological Data

Records of VME indicator species in the Nordic Seas were compiled from an extensive set of sources. Data were extracted from several databases in Norway, Iceland, and the Faroe Islands, including data from the Benthic Invertebrates of Icelandic waters (BIOICE) and the Marine Benthic Fauna of the Faroe Islands (BIOFAR) projects, and the Institute of Marine Research (IMR) coral database. In addition we used unpublished data from habitat mapping surveys by the Marine and Freshwater Research Institute (MFRI) in Iceland (Ólafsdóttir and Burgos, 2012) and the MAREANO project in Norway (Buhl-Mortensen et al., 2015b), and recent video observations carried out in the Faroe Islands (Buhl-Mortensen et al., 2019). We included by-catch data from the Joint Annual Norwegian-Russian Ecosystem Surveys in the Barents Sea (Jørgensen et al., 2015), and from the MFRI autumn surveys. We also extracted data from the ICES VME database (Morato et al., 2018), and the Ocean Biogeographic Information System (OBIS, Grassle, 2000). Finally, records were extracted from the literature including published data from the early expeditions, and the more recent work by Copley et al. (1996), Klitgaard and Tendal (2004), Mortensen et al. (1995, 2001), Cárdenas and Rapp (2015), and Hestetun et al. (2017). A complete list of the publications used to obtain records of VME indicator species can be found in Buhl-Mortensen et al. (2015b) and as an appendix in Buhl-Mortensen et al. (2019).

2.3. Selection of VMEs and Indicator Species

For the selection of the relevant vulnerable marine ecosystems and their indicator species for the Arctic and sub-Arctic area of

this study, we considered: the VME classifications made by the Convention for the Protection of the Marine Environment of the North East Atlantic (OSPAR, 2010b); the list of VMEs compiled by the North East Atlantic Fisheries Commission (NEAFC, 2014) and the Northwest Atlantic Fisheries Organization (NAFO, Fuller et al., 2008); and the revised list of deep-water VMEs with characteristic taxa for ICES/NAFO waters by the ICES Workshop on Vulnerable Marine Ecosystem Database (WKVME, ICES, 2016). In addition we used recent experience gathered by national mapping projects in the study region. We selected 44 indicator taxa of 11 VME types and sub-types in the study area (**Table 1**). In total, 21 models were at the species level (e.g., *Acanella arbusculla*). The remaining 23 models were fitted at the genus level, either because most of the compiled record originated from video observations and the species could not be identified (e.g., *Stryphnus* sp.), or because there were several species of the same genus and the number of records was too low to allow modeling of individual species (e.g., *Cladorhiza* sp.). The VME types included in this study are the following:

2.3.1. Soft Bottom Sponge Aggregationse

In the Nordic Seas, demosponges of the order Tetractinellida form dense aggregations commonly known as "ostur" or "cheese bottom." These species can occur at depths between 150 and 1,700 m, on gravel and coarse-sand bottoms (Klitgaard and Tendal, 2004; Murillo et al., 2012; Maldonado et al., 2015). Two main types of ostur assemblages were recognized by Klitgaard and Tendal (2004) : the boreal "ostur" and the cold water "ostur." The boreal "ostur" is, according to Klitgaard and Tendal (2004), characterized by *Geodia barretti*, *G. macandrewii*, *G. phlegraei*, *G. atlantica*, *Stelletta normaini*, and *Strypnhus ponderosus*, although more recently it has been suggested that the latter species correspond to *Strypnhus fortis* (Cárdenas and Rapp, 2015; Maldonado et al., 2015). Boreal "ostur" assemblages were observed on some areas of the western Barents Sea, the Norwegian shelf (Kutti et al., 2013; Gonzalez-Mirelis and Buhl-Mortensen, 2015) and Faroese shelf (Klitgaard et al., 1997; Davison et al., 2019), and off southern Iceland (Klitgaard and Tendal, 2004). The cold water "ostur" is characterized by *G. hentscheli*, *G. parva*, and *Stelletta raphidiophora*, and it is found off northern Iceland, the Denmark Strait, off East Greenland, and north of Spitzbergen (Klitgaard and Tendal, 2004). The models of the distribution of species of the genus *Geodia* in the North Atlantic made by Howell et al. (2016) agreed with the observed distribution patterns. We fitted eight models of sponges considered indicators of soft bottom sponge aggregations: six models based on the *Geodia* species, and two models for sponges of the genera *Stryphnus* and *Stelletta*.

2.3.2. Hard Bottom Sponge Aggregations

A range of medium- to large-sized sponges occur on hard substrates including bedrock, lithified crust, and rocks. In the study area these include various axinellid sponges from the genera *Axinella* and *Phakellia*, and the demosponges *Antho dichotoma* and *Mycale lingua*. Off northern Norway, hard bottom demospongiae represents a single community (Gonzalez-Mirelis

TABLE 1 | List of the 44 VME indicator taxa selected for modeling using SDMs.

VME type and subtype	Indicator taxa	Number of records
Soft bottom sponge aggregations	*Geodia atlantica*	527
	Geodia barretti	3,265
	Geodia macandrewi	432
	Geodia phlegraei	92
	Geodia hentscheli	79
	Geodia parva	50
	Strypnhus sp., *S. fortis*, *S. ponderosus*	601
	Stelletta sp., *S. normani*, *S. rhaphidiophora*	889
Hard bottom sponge aggregations	*Axinella* sp., *A. infundibuliformis*	1,755
	Phakelia sp., *P. robusta*, *P. ventilabrum*	3,997
	Anto (Antho) dichotoma	793
	Tethya sp., *T. aurantium*, *T. cintrina*	480
	Mycale (Mycale) lingua	2,133
	Polymastia sp., *Polymastia cf. uberrima*	841
	Craniella sp., *C. cranium*, *C. zetlandia*, *Tetilla* sp.	646
Deep arctic sponge aggregations	*Caulophacus (Caulophacus) arcticus*	119
	Cladorhiza sp., *C. abyssicola*, *C. corticocancellata*, *C. gelida*, *C. oxeata*	88
	Chondrocladia (Chondrocladia) grandis	205
	Asconema sp.	237
	Lycopodina sp., *L. tendali*, *L.pressiformis*	45
Scleractinean reefs and colonies	*Lophelia pertusa*	6,725
	Madrepora oculata	364
	Solenosmilia variabilis	47
Soft bottom gorgonian gardens	*Radicipes* sp., *R. gracilis*	707
	Acanella arbuscula	339
	Isidella lofotensis	162
Cup coral fields	*Flabellum* sp., *F. (Ulocyathus) alabastrum*, *F. (Ulocyathus) angulare*, *F. (Ulocyathus) macadrewi*	281
	Caryophylla (Caryophyllia) smithii	2,849
Hard bottom gorgonian gardens	*Paragorgia arborea*	1,169
	Paramuricea sp., *P. placomus*	420
	Primnoa resedaeformis	682
	Anthomastus sp., *A. grandiflorus*, *A. purpureus*	149
	Anthothela grandiflora	59
Stylasterid corals on hard bottom	Stylasteridae, *Stylaster* sp., *S. norvegicus*, *S. gemmascens*	398
Cauliflower coral fields	*Drifa glomerata*	1,418
	Duva florida	300
	Gersemia sp., *G. fruticosa*, *G. rubiformis*	1,085
Shallow sea pen communities	*Funiculina sp.*, *Funiculina quadrangularis*	976
	Virgularia sp., *V. glacialis*, *V. mirabilis*, *V. tuberculata*	2,543
	Kophobelemnon sp., *Kophobelemnon stelliferum*	2,580
	Pennatula sp., *P. phosphorea*	2,259
	Halipteris sp.	315
Deep-sea sea pen communities	*Anthoptilum* sp., *A. murrayi*, *A. grandiflorum*	66
	Umbellula sp., *U. ecrinus*	516

and Buhl-Mortensen, 2015). In addition to these four taxa, the ICES WGDEC (ICES, 2016) considered the family Tetillidae (genera *Crainella* and *Tetilla*), as well as sponges of the genera *Polymastia* and *Tethya* also to be indicators of hard bottom sponge aggregations, and these are frequently recorded in the Nordic seas (Buhl-Mortensen et al., 2012, 2015b). Models were fitted to seven indicator taxa of this VME.

2.3.3. Deep Arctic Sponge Aggregations

Several species of hexactinellid sponges are found in relatively high densities in deep cold (<0 °C) waters. One of the most common species in the Norwegian Sea is *Caulophacus arcticus*, which is generally found on hard bottoms at the lower part of the continental slope (Tendal and Barthel, 1993; Buhl-Mortensen et al., 2015b), and has been observed on the base of the Schultz Massif Seamount, at depths below 1,400 m (Roberts et al., 2018). Hexactinellid sponges of the genus *Asconema* can also constitute sponge grounds, although in restricted geographical settings (ICES, 2008). *Asconema foliata* has been observed on seamounts (Roberts et al., 2018), and is considered as a main habitat builder associated to cold water "ostur" habitats (Maldonado et al., 2015). In addition, poecilosclerid demosponges of the family Cladorhizidae become numerous at depths below 400 m, and at greater depths they constitute a large fraction of the sponge fauna (Hestetun et al., 2017). Several species of these carnivorous sponges of the genera *Chrondocladia*, *Cladorhiza*, and *Lycopodina* have been reported in the Nordic Seas (Hestetun et al., 2017). They are usually found in low densities, although aggregations of *Chondrocladia grandis* and *Cladorhiza* sp. have been observed off northern Iceland. Models were fitted to five indicator taxa of this VME.

2.3.4. Soft Bottom Coral Gardens

The term "coral garden" refers to relatively dense aggregations of colonies or individuals of one or several coral species (OSPAR, 2010a). They can be classified by substrate type (soft and hard bottoms) and the main representative taxa (ICES, 2016). Soft bottom coral gardens can be comprised by gorgonians of the families Isididae and Chrysogorgiidae, which can form dense aggregations on sandy mud (Buhl-Mortensen et al., 2015d). Among these, *Isidella lofotensis* is found almost exclusively off Norway (Buhl-Mortensen et al., 2015c), although it has been reported off east Greenland (Mayer and Piepenburg, 1996). *Radicipes* sp. aggregations have been observed off Norway only on the area known as the Bjørnøya slide, but it seems to be more widely distributed south of Iceland (Buhl-Mortensen et al., 2015c). In the warmer waters off southern Iceland the bamboo coral *Acanella arbuscula* is also relatively common. Soft-bottom coral gardens can also be comprised of solitary scleractinean corals of the genus *Caryophyllia* and *Flabellum* aggregated in relatively high densities forming what is known as "cup coral fields" (Baker et al., 2012; Buhl-Mortensen et al., 2015d). Models were produced for six indicator taxa of this VME.

2.3.5. Hard Bottom Coral Gardens

Hard-bottom coral gardens often occur in locations with strong currents. In the study area three of the subtypes from the ICES VME classification (ICES, 2016) are relevant: hard bottom gorgonian gardens, stylasterid corals on hard bottom, and cauliflower coral fields. In the Nordic Seas, the main indicator taxa of gorgonian gardens are *Paragorgia arborea*, *Paramuricea* sp., and *Primnoa resedaeformis*. In addition, *Anthomastus* sp. is also frequent south of Iceland. Hydrocorals from the family Stylasteridae are not commonly observed in large aggregations but form part of mixed coral communities. Cauliflower corals of the family Nephtheidae (*Duva florida*, *Drifa glomerata*, and *Gersemia* sp.) are widely distributed and dense aggregations have been observed in video surveys off NW and SE of Iceland at 500–600 m (Buhl-Mortensen et al., 2019), and off northern Norway (ICES, 2011).

2.3.6. Reef-Forming Scleractineans

In Nordic waters only three species of scleractinean corals are reef building: *Lophelia pertussa*, *Madrepora oculata*, and *Solenosmilia variabilis*. Among them, *L. pertusa* is the most common and has been recorded frequently on the Norwegian shelf, around the Faroe Islands and off southern Iceland. *M. oculata* is less abundant, has a more limited framework-building capacity, and it often co-occurs with *L. pertusa* (Roberts et al., 2009). In our study area, *S. variabilis* has been observed deep on the Reykjanes Ridge south of Iceland (Copley et al., 1996). Reef forming scleractineans do not always form reefs. For example, on vertical solid substrates coral debris cannot aggregate and reefs do not develop (Buhl-Mortensen et al., 2015d). In the North Atlantic reef-forming scleractineans can also form densely-packed "thickets," as part of hard bottom coral gardens, or as isolated colonies (Mortensen and Buhl-Mortensen, 2004, 2005; Davies et al., 2017). These growth forms are usually considered to represent different habitats. For example, the ICES VME classification distinguishes between cold-water coral reefs, non-reefal scleractineans, and colonial scleractineans on rocky outcrops (ICES, 2016). Because the growth form is seldom known or reported all observations of each taxon were grouped under a single VME type. Three models were fitted using presence data of each of the three reef-forming scleractineans.

2.3.7. Shallow Sea Pen Communities

Sea pen communities are usually defined as areas of bioturbated fine sediments with relatively high densities of sea pens. In OSPAR's list of threatened and/or declining habitats, this biotope is termed "sea-pens and burrowing megafauna communities" (Curd, 2010). This biotope is found in the relatively warm Atlantic water shallower than 700 m. The most common sea pen species are *Funiculina quadrangularis*, *Virgularia mirabilis*, *Pennatula phosphorea*, and *Kophobelemnon stelliferum*. Here we fitted four models based on records of these four species.

2.3.8. Deep-Sea Sea Pen Communities

The sea pen species *Umbellula* spp. and *Anthoptilum* spp. occur in deep waters (below 700 m) in an environment with colder temperatures and less anthropogenic activities than shallow water sea pens, and therefore should be regarded as a separate sea pen VME or at least a distinct sub-type (Buhl-Mortensen et al., 2019). High densities of *Umbellula encrinus* are found in deep waters

north of Iceland and on the Norwegian slope, at depths below 800 m in the Norwegian Sea-Arctic Intermediate water. This large sea pen can reach a height of three meters. Off southern Iceland, sea pens of the genus *Anthoptilum* are also found in deep, albeit warmer waters. Models were fitted for both species.

2.4. Environmental Predictors

Bathymetry data for the study area was obtained from the General Bathymetric Chart of the Oceans (GEBCO version 20150318, Weatherall et al., 2015), a global relief model with a resolution of 30 arc-seconds. The data was projected using a Lamberts Equal Area projection centered at 69°N and 4°W and bilinearly interpolated to obtain a grid with a resolution of 500 m. All other environmental data sets were adjusted to match the same projection and resolution using bilinear interpolation.

The seabed morphology was characterized following Lecours et al. (2017), using the following parameters derived from the 500 m bathymetry grid: local mean depth, slope, aspect (divided into northness and eastness), bathymetric position index (BPI), and vector roughness. The BPI indicates if a particular pixel forms part of a positive or negative feature of the surrounding terrain (Wilson et al., 2007). Vector roughness on the other hand measures the topographic surface roughness by quantifying the local variability in slope and aspect (McKean and Roering, 2004). Terrain analysis variables were calculated using a moving window of 3 cells, corresponding to a scale of 1,500 m, by fitting a bivariate quadratic polynomial to each window size using least squares. In addition BPI and vector roughness were also calculated using a moving window of 21 cells, corresponding to a scale of 10,500 m.

Temperature and salinity profiles for the study area were obtained from the NISE project (Norwegian Iceland Seas Experiment; Nilsen, 2008). Near-bottom temperature and salinity gridded fields were estimated following the methodology described in Jochumsen et al. (2016). The data going into the gridding corresponded to the deepest observation point. To avoid including shallow profiles, we only used observations obtained deeper than 80 % and within 80 m of the bottom depth. The gridding was then performed on a spatial resolution of 0.2° longitudinal by 0.1° latitudinal using an objective analysis and with an influence radius of 50 km. Minimum and maximum temperature, temperature difference (the difference between the lowest and highest temperature values), and mean salinity were calculated by interpolating along topography following Davis (1998) using a topography length scale of 300 km (Voet et al., 2010; Skagseth and Mork, 2012).

The aragonite saturation state for the study area was obtained from data provided by Jiang et al. (2015), and interpolated using a similar methodology to the temperature and salinity. Since the aragonite data is much more limited, the criteria for data to be included in the gridding was relaxed. We only required the observation depth to be within 80% of the bottom depth, and further we increased the influence radius to 200 km.

Monthly averages of mean net primary productivity (mg C m^{-2} day^{-1}, NPP) estimated from MODIS data using the carbon-based Production Model (CbPM) (Behrenfeld et al., 2005; Westberry et al., 2008) were obtained from the Ocean Productivity site[1]. Data was downloaded for the period 2006-2015 with a resolution of 5 arc min. Particulate organic carbon flux to the sea bottom (POC flux; g C m^{-2} $year^{-1}$) was estimated from the bottom depth and the seasonal variation in NPP, defined as the ratio between the standard deviation and the mean of monthly NPP values (Lutz et al., 2002, 2007).

Data on near-bottom average current speed and concentrations of nitrate, phosphate, and silicate were obtained from the Bio-ORACLE v2.0 database using the package "sdmpredictors" (Assis et al., 2018) in the R statistical environment (R Core Team, 2019), which provides layers of near-bottom physical and chemical parameters. Current velocity data ($m.s^{-1}$) was produced by the Global Ocean Physics Reanalysis (ECMWF) using the OCEAN5 system at a native resolution of 0.25° in the horizontal and 75 levels in the vertical, with the separation between vertical levels increasing with depth. Nutrient concentrations ($mmol.m^{-3}$) were derived from the Global Ocean Biogeochemistry Non-assimilative Hindcast (PISCES). In both cases, data was obtained from the E.U. Copernicus Marine Service Information[2], and statistically downscaled to a resolution of 5 arcmin using a kriging model (Assis et al., 2018).

Collinearity among environmental layers was explored by computing the Variance Inflation Factor (VIF) (Dormann et al., 2013). Variables with high collinearity were eliminated through a stepwise procedure in which the VIF was calculated for all variables, the variable with highest VIF was removed, and VIFs were recalculated until all variables had a VIF value lower than 10 (Naimi et al., 2014). This procedure selected maximum temperature, nitrate and phosphate as variables causing collinearity, therefore these parameters were not included as predictors. The correlation among remaining variables is shown in **Figure 2**. In the case of MaxEnt, it has been suggested that variables should be selected based on previous knowledge on the biology and ecology of the modeled species, but that stricter selection of variables is unlikely to improve models (Elith and Graham, 2009; Elith et al., 2011). Therefore we did not attempted to select particular sets of predictor variables for individual taxa, and all models were constructed using all available variables.

2.5. Modeling Approach

In this study, rather than modeling the distribution of a VME by using the combined records of all indicator taxa (as done e.g., by Buhl-Mortensen et al., 2019), we opted to model each taxon individually. The rationale for this approach is that some of the VMEs include indicator taxa with different environmental requirements. For example, the corals *Isidella lofotensis* and *Radicipes* sp. are both considered indicators of soft-bottom coral gardens, but *I. lofotensis* is almost exclusively found on the Norwegian shelf, while *Raicipes* sp. is much more common off southern Iceland (Buhl-Mortensen et al., 2015c). A single model with records of both taxa will overestimate their distribution because a wider range of environmental settings would be

[1]http://www.science.oregonstate.edu/ocean.productivity/index.php
[2]http://marine.copernicus.eu

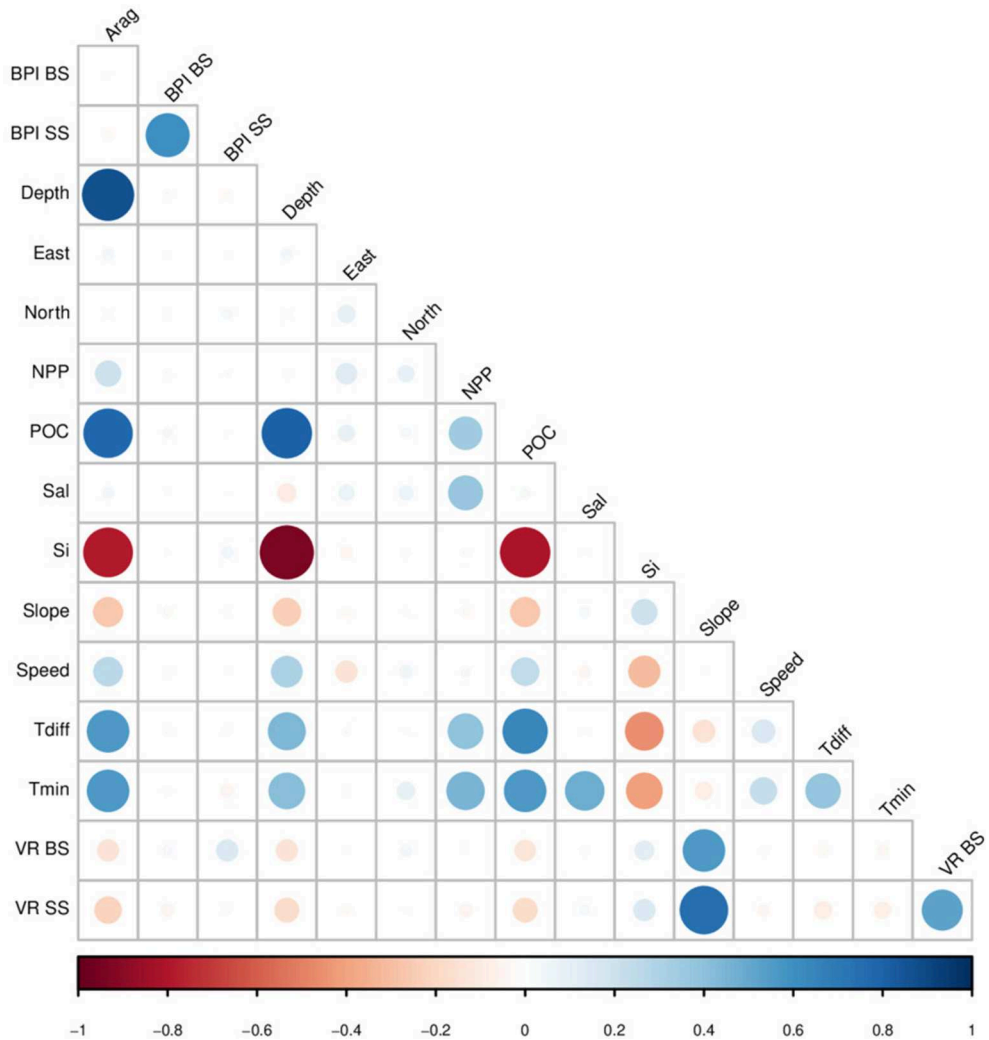

FIGURE 2 | Correlation matrix among the environmental variables used as predictor for the species distribution models: Aragonite saturation state (Arag), broad-scale bathimetric position index (BPI BS), small-scale bathimetric position index (BPI SS), bottom depth (Depth), eastness (East), northness (North), mean net primary productivity (NPP), particulate organic carbon (POC), mean salinity (Sal), silica concentration (Si), bottom slope (Slope), near-bottom current speed (Speed), temperature difference (Tdiff), minimum temperature (Tmin), broad-scale vector roughness, and small-scale vector roughness. Colors and size of circles indicate correlation values, from 1 (blue) to –1 (red).

considered suitable. To avoid this, we choose to (a) model individually each of the 44 taxon, (b) measure the similarity among the predicted distributions using the "I" similarity statistic (Warren et al., 2008), (c) use cluster analysis to identify groups of taxa with similar predicted distributions, and (d) combine the predictions of the taxa of each group using a stacked species distribution approach in order to obtain a predictive map of the distribution of each group. Finally, a VME index was computed to map the distribution and relative vulnerability of VMEs in the Nordic Seas.

2.6. Models of Individual Taxa

The distribution of VME indicator taxa was predicted using species distribution models (SDMs), which predict the geographic distribution of a species by identifying the combinations of environmental variables where they are observed to be more prevalent and then mapping that combination of variables into geographic space. We predicted the distribution of suitable habitats for VME indicator taxa using the maximum entropy algorithm MaxEnt (version 3.4.1). MaxEnt is a machine learning model that uses a presence-only approach to quantify the relationship between environmental variables at locations where a species has been observed vs. background locations in the study region (Phillips et al., 2006). MaxEnt uses transformations of the original environmental variables named "feature classes" (FC), namely the linear, product, quadratic, hinge, threshold, and categorical feature classes (Elith et al., 2011). Different combinations of feature classes allow the construction of very flexible models. By default, MaxEnt selects the number of feature classes based on the

number of presence observations, increasing the number of feature classes with the number of records. To avoid overfitting, MaxEnt uses regularization, which penalizes the inclusion of parameters that produce small improvements in the model (Merow et al., 2013). Regularization is controlled by a parameter termed regularization multiplier (RM, default value = 1). Higher RM values reduce the flexibility in the relationships between species presence and environmental predictor variables. The performance of SDM models is sensible to model specifications (Elith et al., 2011; Merow et al., 2013; Warren et al., 2014). Recent studies have shown that the default MaxEnt options (i.e., the RM value and feature classes used) can produce models that perform poorly (Radosavljevic and Anderson, 2014). To select model settings that approximate optimal levels of model complexity, models were fitted to each VME indicator taxon using different combinations of feature classes and regularization multiplier values using the "ENMeval" (Muscarella et al., 2014) and "dismo" (Hijmans et al., 2017) packages in the R statistical environment (R Core Team, 2019). Each model was fitted using k-fold validation with five bins. To predict the distribution of each VME indicator taxon we selected the model with the highest average test AUC (area under the curve of the receiver operating characteristic plot), averaged across the 5-folds. This was the model with the best capability to successfully discriminate occurrence from background localities (Muscarella et al., 2014). In addition, we evaluated the Symmetric Extremal Dependence Index (SEDI, Wunderlich et al., 2019). SEDI is analogous to the widely used True Skill Statistic (TSS, Allouche et al., 2006) but better behaved in presence-background models because its error weighting reflects the low confidence in the pseudo-absence data, in particular in models with low prevalence and a high number of background points as the models in this study (Wunderlich et al., 2019). The SEDI for each model was estimated using a confusion matrix obtained after converting the model prediction into a binary presence-absence raster using the threshold that maximizes the sum of sensitivity and specificity (maxSSS), minimizing commission and omission errors (Liu et al., 2016). This threshold is commonly used to transform the output of SDMs into a binary output (Liu et al., 2005; Elith et al., 2006).

To evaluate if the models were overfitting we examined two metrics. The first is the difference between training and testing AUC, averaged across the 5 random folds (Warren and Seifert, 2011). This metric is expected to be high if models are overfitting the data (Muscarella et al., 2014). The second is the values of the 10% training omission rate (OR10). This is a threshold-dependent metric equivalent to the proportion of test localities with predicted suitability values lower than excluding the 10% of training localities with the lowest predicted suitability. Omission rates higher that the expected value of 10% typically indicate model overfitting (Muscarella et al., 2014; Radosavljevic and Anderson, 2014). Higher values are sometimes used to distinguish between degrees of overfitting. Here we followed Kivlin et al. (2017) by considering values below 0.2 as indicators of models with relatively low degrees of overfitting.

The model selected was used to indicate the distribution of VME indicator taxa in the study area based on the predicted occurrence of suitable habitat. Predictions were obtained for each cell in the same 500 m grid used for the environmental predictors. Model predictions were exported in the cloglog scale, which under specific conditions can be approximated to a probability of presence (Phillips et al., 2017). In each model we computed the permutation importance of each predictor variable, which is the drop in AUC resulting from randomly permuting the values of the predictor variable on the training and background data sets and reevaluating the model (Phillips et al., 2006). Finally, models were examined visually to evaluate that high suitability areas corresponded to the locations of the majority of observations (Radosavljevic and Anderson, 2014).

2.7. Target Group Background

The spatial distribution of the available records of VME indicator species showed a strong sampling bias within the study area. In some areas the sampling intensity was high, in particular on areas of the Norwegian shelf and in the Barents Sea that have been mapped by the MAREANO programme (Buhl-Mortensen et al., 2015b), but also to some degree the Icelandic and Faroese shelves. In other areas like the eastern Greenland shelf and the deep basins the sampling effort has been very low or non-existent, or existing data is unavailable. Sampling bias can strongly influence the reliability of predictions of presence-background modeling. One way to reduce the effect of sampling bias in presence-only models is to use a set of background points with the same bias as the sampling effort (Phillips et al., 2009; Fourcade et al., 2014). To do this we modeled the sampling effort in the study area by fitting a kernel density estimate (KDE) to the locations of all indicator taxa compiled in the database, an approach known as target-group sampling (Elith et al., 2011; Merow et al., 2013). The KDE produced an estimation of the density of samples in each cell of the 500 m grid. These estimates were normalized so the sum of all cells was equal to one. These values were used to select 50,000 background points using the normalized kernel density values as a probability grid.

2.8. Niche Similarity

Niche overlap among all VME indicator taxa was estimated using the "I" similarity statistic (Warren et al., 2008), which ranges between 0 (no overlap) and 1 (niches are identical). To verify if VME classes currently used (e.g., ICES, 2016) consisted of indicator taxa with similar predicted distribution we carried out a cluster analysis using the Ward method, which defines groups by minimizing the within-group sum of squares (Legendre and Legendre, 1998). As a measure of dissimilarity between predicted distributions we used the complement of the "I" similarity statistic (1 - I). Groups of VME indicator taxa with similar distributions were identified from a dendrogram using a dissimilarity cutoff value of 0.4. This value was selected to produce groups roughly similar to known VME classifications.

2.9. Stacked Species Distribution Models

To map patterns of environmental suitability for VMEs, we merged the predicted distribution of VME indicator taxa to form stacked species distribution models (S-SDMs, Ferrier and Guisan, 2006; D'Amen et al., 2017; Wiltshire et al., 2018). S-SDMs is an approach that follows the "predict first,

assemble latter" strategy in which the distribution of each individual taxon is modeled first, and then the predictions are combined (or "stacked") to produce a community prediction (D'Amen et al., 2017). This approach allows for the use of presence-only data where the presence records originated from different sources and where records of species of the same community or habitat are not usually collected at the same location. This is important when modeling deep-sea benthic megafauna in areas where the majority of records originated from fisheries by-catch and from scientific surveys using gear with relatively low sampling efficiency like dredges or bottom trawls (as opposed to underwater video surveys, which provide a more complete description of the benthic megafauna in a particular location). The S-SDMs approach also provides the flexibility of letting different environmental variables influence the distribution of individual species with distinct species-environment relationships (Ferrier and Guisan, 2006).

Here we produced S-SDMs for groups of VME indicator taxa with similar predicted habitat suitability, as defined by the cluster analysis of the "I" similarity statistic. SDMs were produced by averaging the predictions of individual VME indicator taxa (Calabrese et al., 2014; D'Amen et al., 2015; Wiltshire et al., 2018), and scaling the resulting average to a range of values between 0 and 1.

In the absence of knowledge on species prevalence, the output of presence-only models like MaxEnt is monotonically, but not proportionally, related to the relative probability of presence (Elith et al., 2011; Wiltshire et al., 2018), and cannot be interpreted as a measure of abundance or compared between species (Elith et al., 2011; Merow et al., 2013). As a result, the average suitability in each cell is likely to be related to the relative species richness in that location, although the relationship is not necessarily directly proportional (Aranda and Lobo, 2011; Guillera-Arroita et al., 2015; Wiltshire et al., 2018). Therefore, rather than attempting to predict species richness or community composition, we considered the average suitability as a tool to examine patterns of habitat suitability in each VME and to highlight areas of high average suitability that should be examined more closely and targeted for conservation measurements.

2.10. VME Index

To obtain a general overview of the distribution and relative vulnerability of the VMEs in the Nordic Seas, we computed a SDM-based VME Index analogous to the VME index developed for the ICES VME database (Morato et al., 2018). This index is a combination of a set of indicator scores, which quantifies in very broad terms the vulnerability of a taxa or group of taxa to anthropogenic impacts, and abundance scores based on abundance data of each taxon usually obtained from by-catch.

The indicator scores in Morato et al. (2018) were based on the vulnerability criteria defined by FAO (2009): uniqueness or rareness, functional significance, fragility, life-history that makes recovery difficult, and structural complexity. The degree to which each group fit each of the five criteria were scored using a scale between 1 (low) and 5 (high) by a group of experts (Morato et al., 2018). As the five indicators are considered to be approximately orthogonal, an indicator score was computed for each group using the quadratic mean (Morato et al., 2018). We used the indicator scores of the seven VME indicator groups present in our study area (**Table 2**). Each of the 44 VME indicator taxon in our study were assigned to one of the seven VME indicator groups. Following Morato et al. (2018), sponges of the genera *Asconema*, *Craniella*, *Geodia*, *Polymastia*, *Strypnhus*, *Tetilla*, and *Thenea* were included in the "large sponges" group, while the remaining genera were considered as "generic sponges."

TABLE 2 | Indicator scores for VME taxa groups, based on the degree to which each group fits the FAO VME criteria (FAO, 2009): uniqueness or rareness, functional significance, fragility, life-history that makes recovery difficult, and structural complexity.

VME Indicator group	Unique.	Funct.	Fragility	Life history	Structural	Indicator score
Stony coral	3	4	5	5	5	4.47
Large sponge	2	5	4	4	3	3.74
Generic sponges	2	3	3	3	2	2.65
Gorgonian	4	3	3	5	2.5	3.61
Stylasterid	4	1	4	2.5	2	2.94
Cup coral	2	1	2	4	1	2.28
Soft coral	1	1	2	2	2	1.67

Adapted from Morato et al. (2018).

The ICES VME index combines the indicator scores with an abundance score where by-catch weights are classified into a 1-5 scale based on current encounter threshold for live corals and live sponges established by NEAFC and the European Union (Morato et al., 2018). In an analogous manner, we scaled the predicted habitat suitability of each VME indicator taxon to a scale of 1-5 by computing the maxSSS threshold (Liu et al., 2016). Cells with values below this threshold received an abundance score of zero. Suitability values above the threshold were linearly scaled into a 1-5 scale, where 1 corresponds to the presence threshold and 5 corresponds to 1 (the maximum possible suitability value). The final SMD-based VME index was calculated by thresholding and scaling each of the predicted suitability for the 44 SDMs into a 1-5 scale, and multiplying by the corresponding VME indicator score. As opposed to Morato et al. (2018) we opted to average the VME index among the 44 indicator taxa, in order to highlight areas suitable for multiple VME indicator taxa.

3. RESULTS

3.1. Model Performance

All models had average test AUC values above 0.85, with 30 models having AUC values above 0.9, which indicates good model performances and capacity to distinguish between observation and background points (**Table 3**). In addition, all models had relatively high SEDI values which indicate good model performance and a balance of omission and comission errors. In most cases (n = 33) the model with the highest AUC included all four feature classes (linear, quadratic, hinge, and product). This is the default behavior of MaxEnt,

TABLE 3 | Performance of the models selected for the 44 VME indicator taxa.

Indicator taxa	AUC	SEDI	FC	RM	AUC diff	OR10
Geodia atlantica	0.8935	0.911	LQHP	1	0.046	0.146
Geodia barretti	0.8818	0.893	LQHP	1	0.016	0.12
Geodia macandrewi	0.8723	0.88	LQHP	1.5	0.036	0.15
Geodia phlegraei	0.8787	0.834	H	1	0.122	0.252
Geodia parva	0.9719	0.94	LQHP	3	0.026	0.202
Geodia hentscheli	0.9734	0.864	H	3	0.025	0.2
Stryphnus sp.	0.8991	0.921	LQHP	1	0.036	0.159
Stelletta sp.	0.8784	0.845	LQHP	2.5	0.026	0.143
Axinellida sp.	0.8876	0.934	LQHP	1	0.014	0.121
Phakellia sp.	0.858	0.906	LQHP	1	0.012	0.112
Anto (A.) dichotoma	0.9046	0.953	LQHP	1	0.02	0.137
Thetya sp.	0.9152	0.911	LQHP	1	0.028	0.135
Mycale (M.) lingua	0.8729	0.906	LQHP	1	0.017	0.125
Polymastia sp.	0.8595	0.822	LQHP	1	0.026	0.146
Tetillidae	0.8647	0.873	LQHP	1	0.037	0.152
Caulophacus (C.) arcticus	0.9676	0.772	LQH	4.5	0.011	0.119
Cladorrhiza sp.	0.8935	0.647	LQHP	4	0.037	0.145
Chrondocladia (C.) grandis	0.9638	0.952	H	2.5	0.01	0.128
Asconema sp.	0.9128	0.903	LQHP	1.5	0.041	0.163
Lycopodina sp.	0.9631	0.848	LQHP	2	0.043	0.3
Lophelia pertussa	0.9123	0.926	LQHP	1	0.006	0.107
Madrepora oculata	0.9644	0.958	LQHP	2.5	0.011	0.127
Solenosmilia variabilis	0.9772	0.826	H	5	0.019	0.15
Isidella lophotensis	0.9625	0.965	LQH	1	0.043	0.25
Radicipes sp.	0.9801	0.972	H	2.5	0.009	0.12
Acanella arbuscula	0.9879	0.948	LQHP	1	0.012	0.266
Flabellum sp.	0.9146	0.755	LQHP	1	0.047	0.2
Caryopyllia (C.) smithii	0.9799	0.974	LQH	1.5	0.005	0.133
Paragorgia arborea	0.945	0.964	LQHP	3	0.011	0.131
Paramuricea sp.	0.9181	0.918	LQHP	1	0.032	0.113
Primnoa resedaeformis	0.9186	0.928	LQHP	1	0.024	0.148
Anthomastus sp.	0.9673	0.863	LQHP	1	0.031	0.231
Anthotella grandiflora	0.9691	0.987	H	2.5	0.032	0.5
Stylasteridae	0.934	0.944	LQHP	1	0.031	0.17
Gersemia sp.	0.9294	0.851	LQHP	1	0.015	0.141
Drifa glomerata	0.9184	0.892	LQHP	1	0.025	0.168
Duva florida	0.9109	0.867	LQHP	1.5	0.049	0.189
Anthoptylum sp.	0.9868	0.936	LQHP	1	0.02	0.198
Umbellula sp.	0.958	0.938	LQHP	1	0.017	0.178
Funiculina sp.	0.8939	0.862	LQH	1	0.022	0.149
Vigularia sp.	0.8537	0.779	LQHP	1	0.028	0.124
Kophobelemnon sp.	0.919	0.854	LQHP	1	0.018	0.15
Pennatula sp.	0.9215	0.829	LQH	2	0.013	0.12
Halipteris sp.	0.9571	0.887	LQHP	1	0.074	0.265

AUC indicates the average test AUC (area under the curve of the receiver operating characteristic plot). SEDI is the Symmetric Extremal Dependence Index computed using a maxSSS threshold. FC indicates the feature classes selected (L, Linear; Q, quadratic; H, hinge; P, product). RM is the value of the regularization multplier parameter. AUC diff is the difference between training and testing AUC, averaged across 5 random folds. OR10 is the value that excludes the 10% of training localities with the lowest value (i.e., the values of the 10% training omission rate), averaged across 5 random folds.

which selects the number of feature classes depending on the number of presence records. A total of 17 models had a regularization parameter (RM) of more than 1, which is the default in MaxEnt.

In general, models had a relatively low degree of overfitting, with an average OR10 (10% training omission rate) of 0.17. Only six models had OR10 values equal or above 0.25, which we took as indicator of high overfitting. The models with higher levels of

overfitting were *Anthothela grandiflora* (OR10=0.50, **Figure S6**), *Lycopodina* sp. (OR10 = 0.30, **Figure S7**), *Halipteris* sp. (OR10 = 0.27, **Figure S5**) *Radicipes* sp. (OR10 = 0.26, **Figure S6**), *Geodia phlegraei* (OR10 = 0.25, **Figure S2**), and *Isidella lophotensis* (OR10 = 0.25, **Figure S10**). In addition to these, the models of *Geodia atlantica* (**Figure S2**), *Asconema* sp. (**Figure S9**), and *Duva florida* (**Figure S9**) produced relatively high values of AUC diff (the mean difference between training and testing AUC) also suggesting overfitting.

3.2. Importance of Environmental Variables

There was high variability in the explanatory power of the 16 predictor variables, as measured by their permutation importance, on the 44 MaxEnt models (**Table 4**). Minimum temperature was the most important predictor across all models, with an average permutation importance of 27.4% and explaining more than 10% of the variability in 40 of the 44 models. In individual models the importance of temperature reached up to 78.7% and it was particularly high for cold-water sponges (*Caulophacus*, *Cladorrhiza*, *Chrondocladia Geodia phlegraei*), but also for some cold-water corals (*Lophelia pertusa*, *Madrepora oculata*, *Flabellum Gersemia*), and gorgonians (*Paragorgia arborea*, *Paramuricea*, *Primnoa resedaeformis*, and *Anthomastus*). In addition, temperature difference had an average importance of 4.8%.

Depth was the second most important predictor, with an average importance of 20.2% and reaching up to 67.4%. Variables describing the morphology of the seafloor (small and large scale BPI and roughness, slope, northness, eastness) did not have high average importance by themselves (0.13–3.6%), but their averaged combined contribution was relatively large (11.86%) and reached up to 26.3%.

The combined effect of variables related to seawater chemistry (salinity, aragonite saturation state and silica concentration) was also relatively large (average importance 21.9%). Aragonite saturation state had an average importance of 6.5%, but had higher importance on some taxa including *Caryophyllia* (52.0%), *Geodia phlegraei* (20.21%), Stylasterids (32.9%), *Drifa glomerata* (14.6%), and *Madrepora oculata* (12.5%). In general salinity had a low explanatory power, with an average importance of 4.4%. For two *Geodia* species, *G. parva* and *G. hentschelli* salinity explained a large proportion of the variance.

3.3. Predicted Distributions and Niche Similarity

Predicted distributions of individual taxa are shown in **Figures S1–S10**. Pairwise niche similarity, measured by the "I" similarity statistic, ranged between 0.03 and 0.95, indicating a wide range of similarities among the predicted distribution of the VME indicator taxa. The cluster dendrogram shows seven groups (1–7) of VME indicator taxa at a dissimilarity level of 0.4 (**Figure 3**). Three of the groups can be divided into two subgroups each based on their dissimilarity value and the similarity of the spatial patterns of the predicted distribution. These groups represents VME indicator taxa with similar habitat suitability as predicted by the models. The following groups were identified:

3.3.1. Group 1

The first group includes the reef-forming corals *Lophelia pertusa* and *Madrepora oculata*, the gorgonians *Parmuricea sp.*, *Primnoa resedaeformis*, and *Pargorgia arborea*, as well as corals of the family Stylasteridae. These species are often found in close proximity (Buhl-Mortensen et al., 2015c). Depending on local conditions, *L. pertusa* and *M. oculata* may be the dominant species and form coral reefs or coral thickets, or they can be found as isolated colonies forming part of hard-bottom coral gardens together with the other species in this group. This group of VME taxa is predicted to be distributed in narrow areas on the southern and western Icelandic shelf, around the Faroe Islands, off southern Greenland, and broadly on the central Norwegian shelf (**Figure 4A**).

3.3.2. Group 2

The second group includes three *Geodia* species (*G. atlantica*, *G. macandrewi*, and *G. phlegraei*) considered characteristic of the boreal "ostur" community (Klitgaard and Tendal, 2004), as well as the sponges *Stelletta* sp. and *Strypnhus* sp. Klitgaard and Tendal (2004) included *Stelletta normani* and *Strypnhus ponderosus* as part of the boreal "ostur," while *Stelletta raphidiophora* was considered associated to the cold "ostur" community. Although we modeled *Stelletta* sp. and *Strypnhus* sp. at the genus level, given the geographic distribution of our samples it is likely that the majority of our records correspond to the species associated boreal "ostur" (**Figure S2**). High suitability for this group was observed off western Iceland, the Denmark strait, and the southern Greenlandic shelf, off the Faroe Islands, and in broad areas of the central and northern Norway shelf (**Figure 4B**).

3.3.3. Group 3

The next group includes a number of sponge taxa usually associated to hard bottoms. Two subgroups can be recognized here. Subgroup 3A included *Axinella* sp., *Phakellia* sp., *Antho (Antho) dichotoma*, and *Mycale (Mycale) lingua*. Areas of high suitability for this group includes the central Norwegian shelf, the western and southern Icelandic shelf, and off the Faroe Islands (**Figure 4C**). Subgroup 3B included *Thetya* sp., *Polymastia* sp. and Tetillidae, and also *Geodia baretti*, which is one of the *Geodia* species usually considered as part of the boreal "ostur" community (Klitgaard and Tendal, 2004). This group was associated to the colder waters of the Barents Sea, the Greenlandic shelf and off north Iceland, and to the shelf break off Norway (**Figure 4D**).

3.3.4. Group 4

This group includes four indicator taxa of the shallow sea pen VME: *Funiculina* sp., *Pennatula* sp., *Kophobelemnon* sp., and *Halipteris* sp. Individual models for these taxa suggest that the four taxa have areas of high suitability south of the GISR, on the Skagerrak and in the North Sea, while only *Funiculina* sp. and *Kophobelemnon* sp. have relatively high suitability on the Norwegian shelf. The SSDM of these four taxa indicate some areas of high combined suitability on the southern Icelandic shelf and on the Skagerrak strait (**Figure 5A**).

TABLE 4 | Permutation importance of environmental predictors: Minimum temperature (Tmin), temperature difference (Tdiff), bottom depth (depth), combined importance of terrain parameters (Terr), aragonite saturation state (Arag), mean net primary productivity (NPP), particulate organic carbon (POC), salinity (Sal), silica concentration (Si), and near-bottom current speed (Speed).

Indicator taxa	Tmin	Tdiff	Depth	Terr	Arag	NPP	POC	Sal	Si	Speed
Geodia atlantica	14.04	1.28	23.03	26.3	7.38	9.59	0.96	4.02	5.95	7.46
Geodia barretti	23.62	4.75	15.79	13.83	5.09	1.98	6.73	5.59	15.93	6.68
Geodia macandrewi	16.67	10.31	18.41	7.56	3.62	3.22	23.2	10.03	0.57	6.4
Geodia phlegraei	6.68	0	17.78	15.42	20.21	16.1	13.57	0.54	8.28	1.44
Geodia parva	39.57	17.72	4.14	3.92	0	0.49	0.48	30.56	0	3.11
Geodia hentscheli	8.57	6.74	2.65	4.08	0.06	3.36	0	52.37	16.4	5.77
Stryphnus sp.	20.25	6.85	14.39	17.59	1.04	0.34	4.88	7.26	18.61	8.79
Stelletta sp.	22.72	4.64	24.6	6.95	2.17	8.72	0	1.17	17.99	11.04
Axinellida sp.	18.08	4.44	11.96	14.76	1.92	0.79	12.21	5.55	24.67	5.62
Phakellia sp.	16.86	2.2	12.28	12.54	5.03	1.32	13.74	8.62	21.95	5.49
Anto (A.) dichotoma	16.17	0.73	10.17	10.28	6.43	4.9	13.75	3.94	30.77	2.85
Thetya sp.	15.47	2.99	34.44	7.33	5.01	1.05	3.22	1.74	21.48	7.27
Mycale (M.) lingua	3.39	3.34	33.13	15.5	4.36	2.19	5.86	5.43	22.11	4.68
Polymastia sp.	20.81	2.73	27.08	5.5	4.13	4.27	6.66	8.48	16.4	3.96
Tetillidae	19.01	4.2	11.15	14.47	5.9	2.32	19.41	3.48	17.9	2.16
Caulophacus (C.) arcticus	59.17	0	23.8	12.45	0	3.36	1.21	0	0	0
Cladorrhiza sp.	73.74	0	17.43	6.57	0	0	0.08	0	2.01	0.17
Chrondocladia (C.) grandis	68.27	0	18.12	2.25	1.67	0.02	2.47	4.08	0	3.12
Asconema sp.	24.68	7.69	31.67	14.66	1.66	1.12	7.35	1.29	7.57	2.34
Lycopodina sp.	26.78	10.02	8.91	11.52	3.5	1.39	5.47	0	31.13	1.27
Lophelia pertussa	38.58	1.34	17.41	15.1	4.08	5.66	13.1	2.32	0.33	2.07
Madrepora oculata	44.76	0.24	11.99	16.63	12.5	0.75	0.92	3.02	7.91	1.27
Solenosmilia variabilis	21.04	0.33	63.27	3.8	0	0	0	0	4.1	7.45
Isidella lophotensis	28.22	0.4	21.89	10.07	2.1	8.29	0	0.84	26.46	1.72
Radicipes sp.	22.7	0	66.97	1.27	0.45	8.61	0	0	0	0
Acanella arbuscula	18.1	31.72	6.3	6.41	2.8	0.32	9.62	1.48	15.99	7.26
Flabellum sp.	40.76	4.3	25.04	12.74	2.24	0.92	1.25	4.66	5.06	3.01
Caryopyllia (C.) smithii	10.98	7.72	9.86	7.2	52.03	0.78	0.99	6.96	0.1	3.37
Paragorgia arborea	24.59	0.99	28.36	19	1.65	3.31	1.38	4.19	16.54	0
Paramuricea sp.	30.82	3.11	6.6	22.87	20.3	0.98	3.3	5.05	4.08	2.89
Primnoa resedaeformis	27.58	2.55	18.96	15.65	6.44	1.49	24.65	0.71	1.75	0.21
Anthomastus sp.	41.03	0.11	3.96	12.56	11.75	3.54	0.32	0.11	22.96	3.66
Anthotella grandiflora	7.11	0	67.43	21.68	0	0	0	0	0	3.78
Stylasteridae	20.1	5.73	4.01	17.97	32.9	3.89	9.65	0.13	0.86	4.76
Gersemia sp.	78.71	1.85	1.88	5.21	1.62	4.45	2.31	0.81	0.13	3.05
Drifa glomerata	23.82	1.37	17.72	10.12	14.58	9.37	10.72	0.3	9.91	2.09
Duva florida	19.36	5.82	35.68	20.36	8.37	0.8	1.58	0	2.77	5.27
Anthoptylum sp.	38.5	18.24	5.02	21.89	1.06	0.69	0	0	13.33	1.27
Umbellula sp.	27.46	4.83	15.54	11.97	1.72	3.62	1.62	3.7	23.82	5.72
Funiculina sp.	32.44	12.26	12.8	11.95	7.79	6.99	7.17	0	5.54	3.05
Vigularia sp.	18.64	3.3	33.78	10.52	10.71	1.05	4.69	0.59	6.79	9.95
Kophobelemnon sp.	25.22	3.79	21.4	8.66	6.2	7.47	13.9	3.95	1.53	7.88
Pennatula sp.	35.33	7.04	6.27	4.62	6.23	4.32	1.83	0.2	20.69	13.47
Halipteris sp.	19.08	4.64	25.08	9.92	0	14.36	1.75	0.01	15.31	9.85

Only predictors with permutation importance >5 in at least one model were included.

3.3.5. Group 5

This group incorporates a mixture of taxa with predicted suitability mostly south of the GISR including the gorgonians *Radicipes* sp., *Anthotella grandiflora*, and *Anthomastus* sp., the deep-water sea pen *Anthoptilum* sp., the cup coral *Flabellum* sp., and the reef-forming coral *Solenosmilia variabilis* (**Figure 5B**).

3.3.6. Group 6

This group consists of two subgroups of sponge taxa associated to cold waters. Subgroup 6A included *Geodia parva* and *G. hentschelli*, two species characteristic of the cold "ostur" assemblage (Klitgaard and Tendal, 2004). This group showed high suitability on the Greenlandic shelf (**Figure 5C**). Subgroup

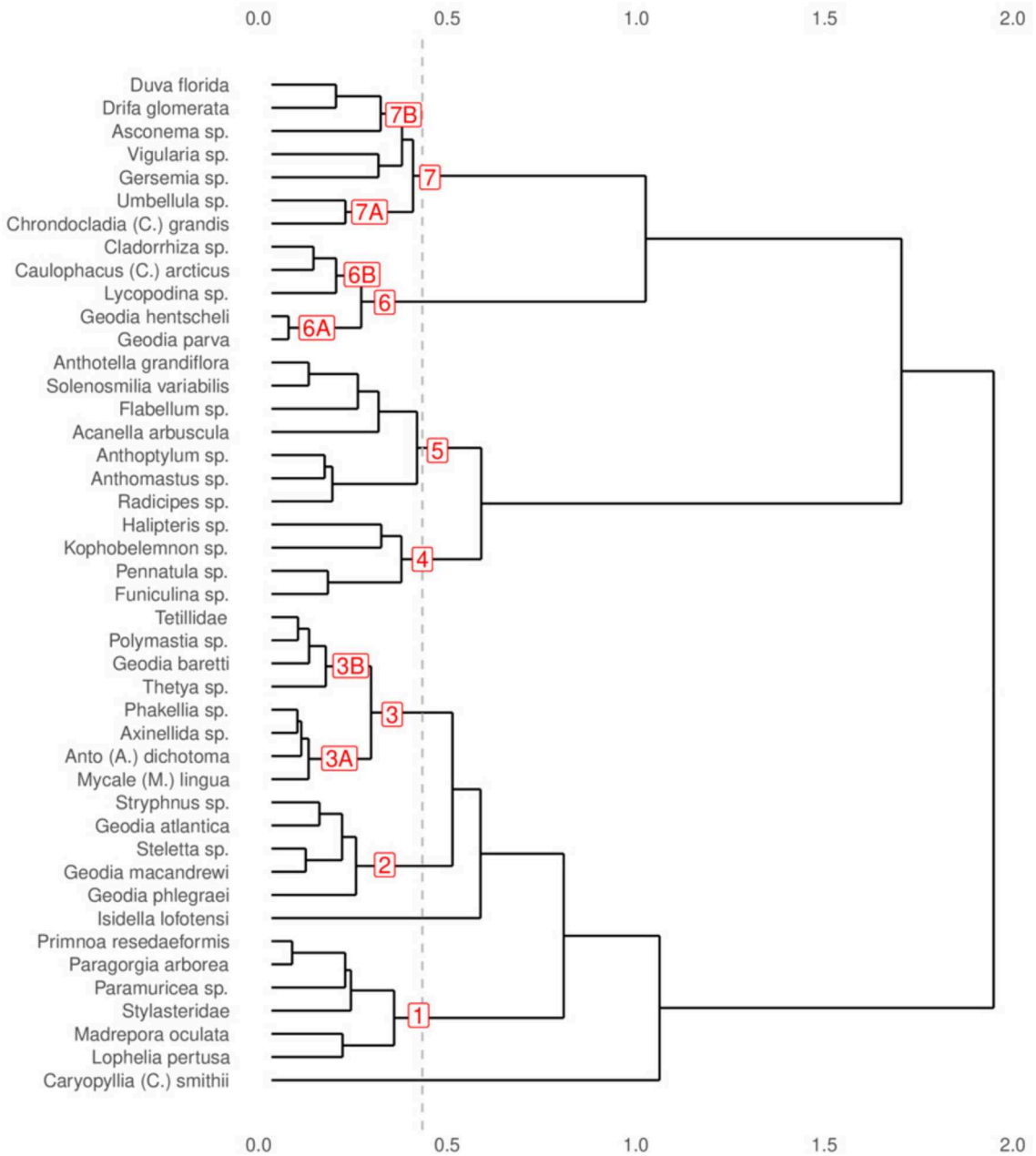

FIGURE 3 | Dendrogram of the predicted distribution of 44 VME indicator taxa, based on a cluster analysis (Ward method) of the complement of the "I" similarity statistic computed among all predicted distributions. Red labels indicate the seven groups identified at the 0.4 dissimilarity value, and the six sub-groups identified by examining the distribution patterns of taxa in each group.

6B included three taxa of carnivorous sponges *Caulophacus (C.) arcticus*, *Chladorhiza* sp., and *Lycopodina* sp., and is predicted to be present mostly on the deep basins on the Norway and Greenland seas (**Figure 5D**).

3.3.7. Group 7

This group incorporates VME indicator species mostly associated to the continental slopes north of the GISR. Two subgroups can be identified in this group. Subgroup 7A included the deep-water sea pen *Umbellula* sp. and the carnivorous sponge *Chrondocladia (C.) grandis*, with predicted distribution mainly restricted to the deep continental slopes (**Figure 6A**). Subgroup 7B consisted of the VME cauliflower coral fields indicator species *Duva florida*, *Drifa glomerata*, and *Gersemia* sp., together with the sea pen *Virgularia* sp. and the carnivorous sponge *Asconema* sp. Its predicted distribution included the continental slope but also on broader areas of the shelves off Greenland, northern Iceland and the Faroe Islands, and on the Barents Sea (**Figure 6B**).

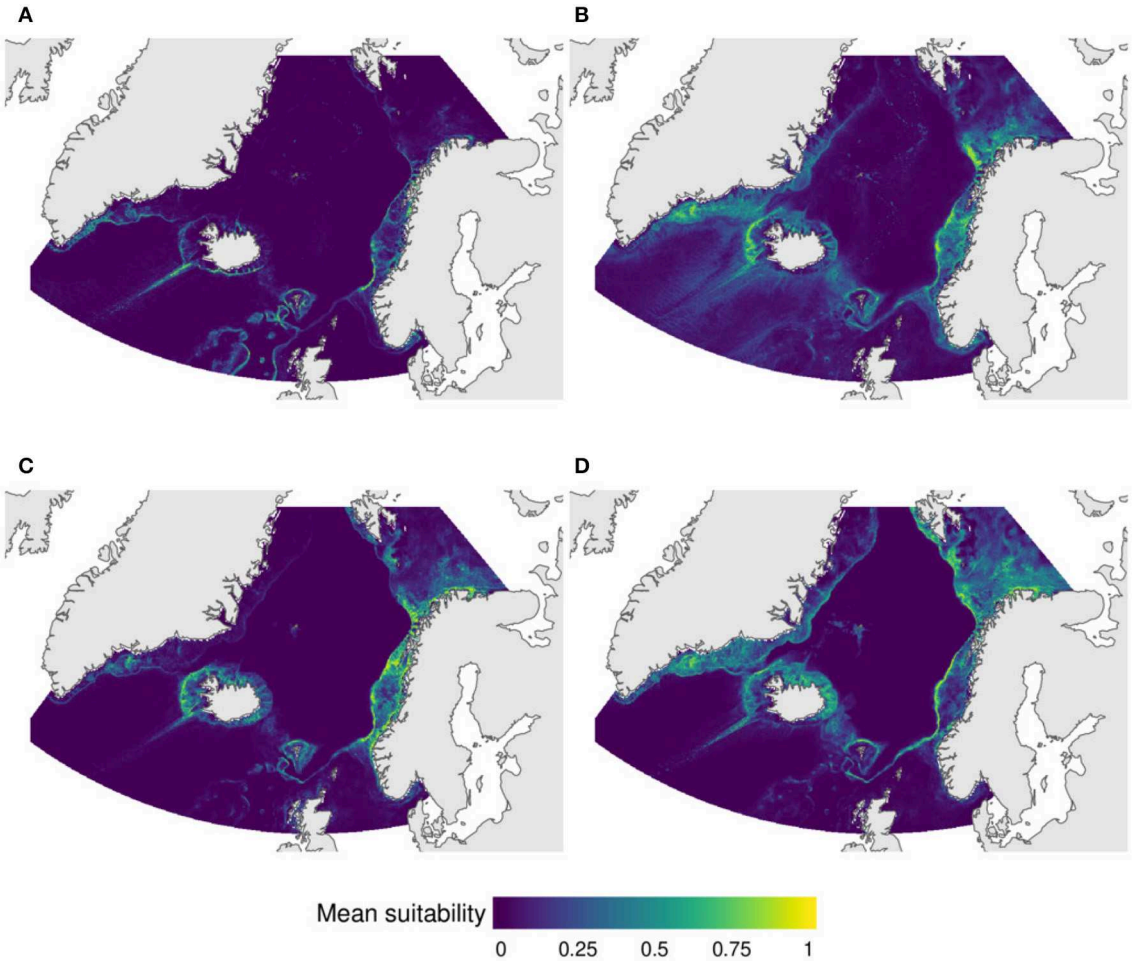

FIGURE 4 | Predicted distribution of VMEs based on stacked species distribution model (SSMD) of **(A)** the reef-forming corals *Lophelia pertusa* and *Madrepora oculata*, the gorgonians *Paragorgia arborea*, *Primnoa resedaeformis*, and *Paramuricea* sp., and Stylasterid corals, **(B)** ssponges of the taxa *Geodia atlantica*, *G. macandrewi*, *G. phlegraei*, *Stryphnus* sp., and *Stelletta* sp., **(C)** sponges of the taxa *Mycale* sp., Axinellidae, *Phakellia*, and *Antho (Antho) dichotoma*, and **(D)** sponges of the taxa *Thethya* sp., *Geodia baretti*, *Polymastia* sp., and *Tetillidae*.

The two VME indicator taxa *Isidella lofotensis* and *Caryophylla smithii* had predicted distributions distinctly different from the others and were not part of any cluster. The gorgonian *I. lofotensis* is mainly restricted to Norwegian waters, but has been reported off northern Greenland (Mayer and Piepenburg, 1996; Buhl-Mortensen et al., 2015c), with a predicted distribution also including some areas around the Jan Mayen archipelago (**Figure S10**). The observed and predicted distributions of the cup coral *C. (C.) smithii* was restricted to some areas between the Shetland Islands and Norway, and within the North Sea.

3.4. VME Index

Values for the computed VME index ranged between 0 and 8.4 (**Figure 7**). Areas with high VME index values indicate locations where multiple VMEs are expected to be present, and/or where the VMEs present had high values in the indicator scores quantifying the vulnerability criteria defined by FAO (2009). The VME index suggest that even though some VME indicator taxa are predicted to have broad distributions, areas with high VME index values are more restricted. These areas include most of the Norwegian continental slope between 62°N and 71°N, coastal areas in the Barents Sea, the shelf break off the Faroe Islands and on the Faroe Bank, the southern and western Icelandic shelves, areas in the Reykjanes Ridge and the Kolbeinseyn Ridge, and some areas in the southern Greenlandic shelf and slope.

4. DISCUSSION

Here we presented the first comprehensive broad-scale modeling effort for VME indicator taxa on the Nordic Seas, including Icelandic and Faroese waters. Models of VME indicator taxa have been produced at more local scales within this area, in particular off Norway (Gonzalez-Mirelis and Buhl-Mortensen, 2015; Sundahl, 2017). Previous efforts in broad-scale models for cold-water corals (e.g., Davies and Guinotte, 2011; Yesson et al.,

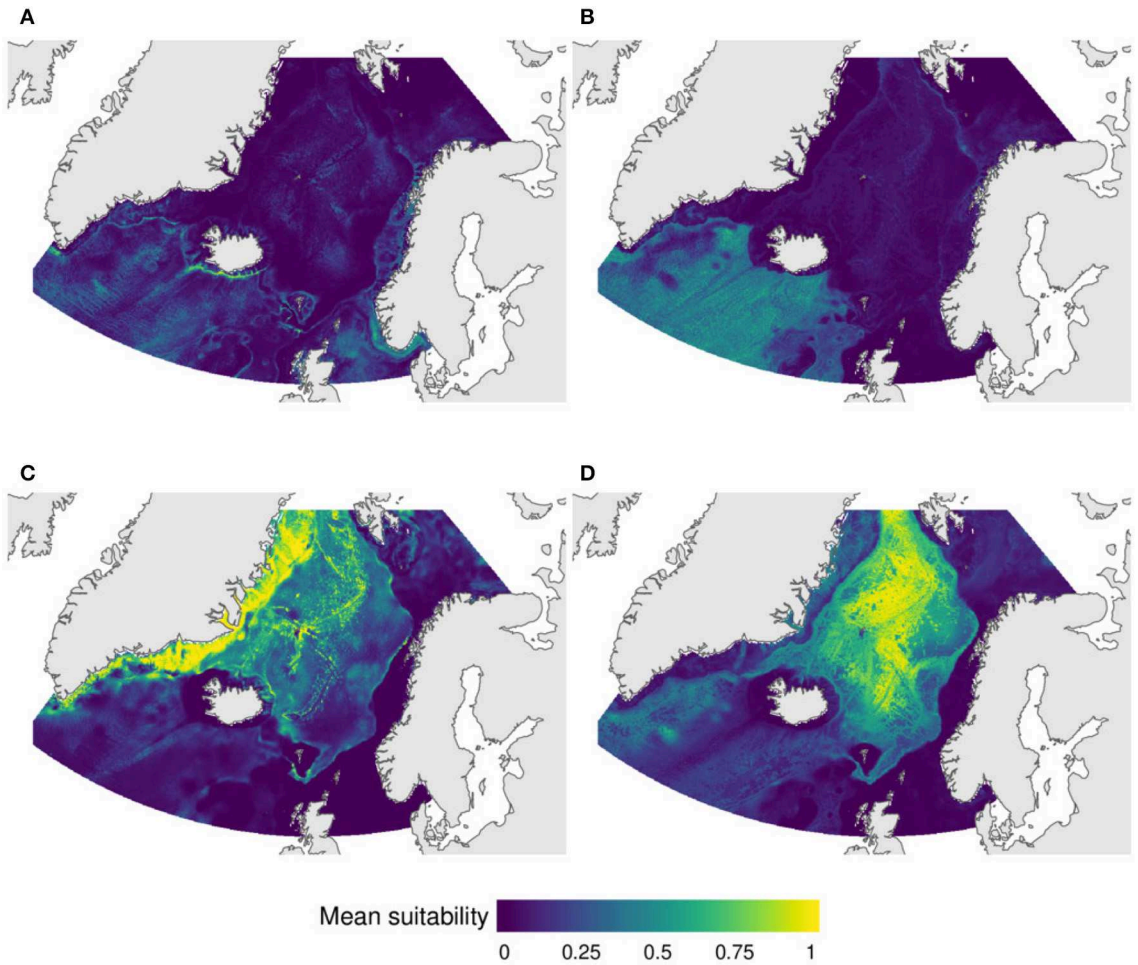

FIGURE 5 | Predicted distribution of VMEs based on stacked species distribution model (SSMD) of **(A)** the sea pens *Funiculina* sp., *Pennatula* sp., *Kophobelemnon* sp., and *Halipteris* sp., **(B)** the gorgonians *Anthotella grandiflora*,/Radicipes/ sp. and *Anthomastus* sp., the deep-water sea pen *Anthoptilum* sp., the cup coral *Flabellum* sp., and the reef-forming coral *Solenosmilia variabilis*, **(C)** the sponges *Geodia parva* and *G. hentschelli*, and **(D)** the sponges *Caulophacus (C.) arcticus*, *Chladorhiza* sp., and *Lycopodina* sp.

2012) did not include our study area, and with the exception of Howell et al. (2016), who focused on *Geodia* sp., no broad scale models have been produced for VME indicator taxa for this area. The models presented in this study significantly expand the knowledge on the potential distribution of VME indicator taxa in Arctic and sub-Arctic waters, and provide a baseline for the evaluation of the presence of VMEs in the Nordic Seas.

4.1. Limitations of the Modeling Approach

SDMs are subjected to an array of sources of uncertainty (Vierod et al., 2014). Some degree of uncertainty is introduced by the observations of the taxa modeled. Positional uncertainty (Moudrý and Šímová, 2012; Naimi et al., 2014) and imperfect detection (Monk, 2014) are issues when using historical records, and data from fisheries by-catch and bottom trawl surveys. Sampling bias (Beck et al., 2014; Fourcade et al., 2014) is an important factor in our study, given that in some areas the number of observations is high (i.e., the Norwegian shelf, and to a lesser degree the Icelandic and Faroese shelves), while much lower in other locations (the Greenlandic shelf and the deep basins). Methods like the target group background approach used in this study can reduce the effects of sampling bias in the model prediction but cannot eliminate it completely. Additional sources of uncertainty arise from the environmental predictors. Oceanographic parameters are derived from databases like the World Ocean Atlas (Locarnini et al., 2013) or from physical ocean models (e.g., Logemann et al., 2013), often at relatively coarse resolutions. Estimates from both sources have their own uncertainty, but modeling approaches like MaxEnt do not incorporate this uncertainty in the predictions. Finally, the selection of the modeling approach itself can introduce biases in the prediction (Piechaud et al., 2015). In our study we utilized a single modeling framework, although some authors have suggested the use of ensemble models, averaging predictions from different models (Georgian et al., 2019). Given all the potential sources of the uncertainty, we echo Piechaud et al.

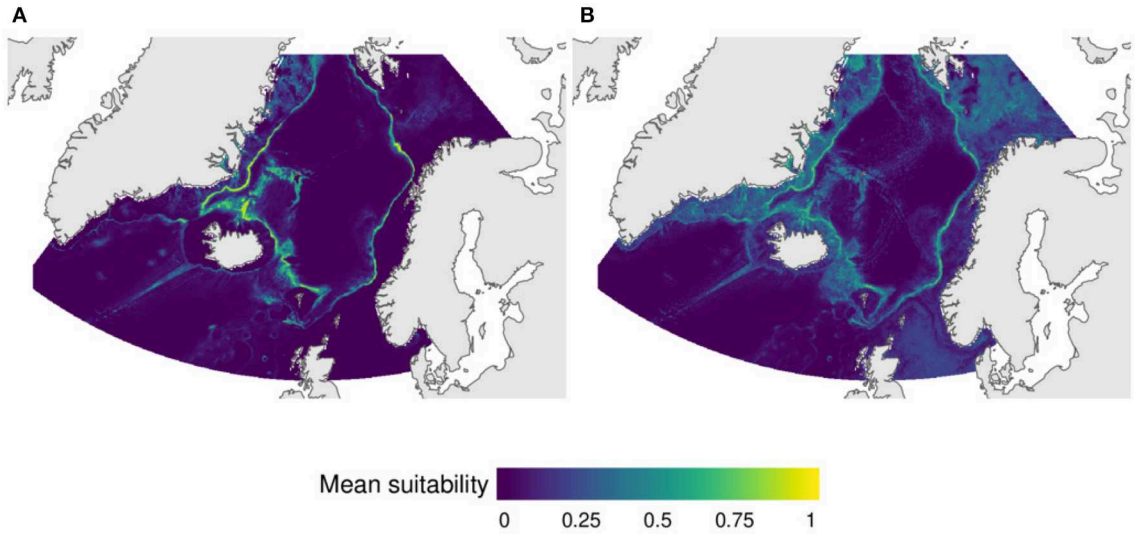

FIGURE 6 | Predicted distribution of VMEs based on a stacked species distribution model (SSMD) of **(A)** the deep-water sea pen *Umbellula* sp. and the carnivorous sponge *Chrondocladia (C.) grandis*, and **(B)** the cauliflower corals *Duva florida*, *Drifa glomerata*, and *Gersemia* sp., the sea pen *Virgularia* sp. and the carnivorous sponge *Asconema* sp.

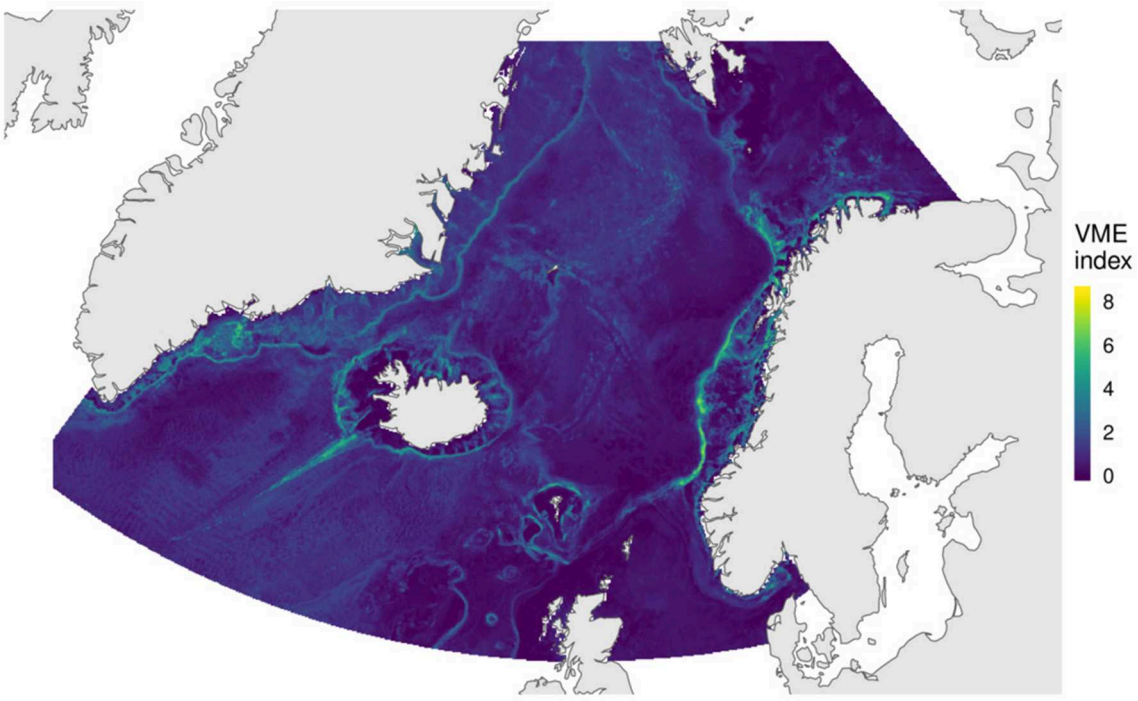

FIGURE 7 | VME index combining indicator scores by Morato et al. (2018), and abundance scores from the species distribution models of 44 indicator taxa.

(2015) and urge caution when using the output of these models for management purposes. Modeled distributions should be used not as evidence of the presence of VMEs, but rather as a data-driven approach to identify areas where the presence of these habitats is likely (Hourigan, 2014).

In this study we have not produced uncertainty estimates for the predicted distribution of VMEs. Before predicted VME distributions can be used for management applications, it is necessary to quantify their uncertainty and to develop methods to incorporate the uncertainty in management decisions (Guisan

et al., 2013). Although the internal uncertainty of MaxEnt models is difficult to quantify, bootstrap methods have been used to quantify some aspects of the uncertainty of MaxEnt predictions (Anderson et al., 2016b). For example, if planning tools like Zonation (Lehtomäki and Moilanen, 2013) or Marxan (Watts et al., 2017) would be used to prioritize areas for protection, it would be possible to prioritize locations with high conservation value (i.e., with high VME suitability and low uncertainty, Anderson et al., 2016b). Locations with confirmed VME presence, for example from underwater video surveys, would have no uncertainty and receive the highest priority for conservation. Uncertainty maps could also inform which areas should be targeted by future surveys, by highlighting locations where VMEs are predicted to occur and where the predictions are uncertain because of the lack of samples. An analysis of this type should follow this study.

We need to perform independent validation of the models (Elith et al., 2006; Davies and Guinotte, 2011) which can confirm model predictions (e.g., Rooper et al., 2018) or can highlight limitations of the predicted distributions. One form of validation is to compare model predictions with new observations. For example, recent observations in the Schultz Massif Seamount indicated the presence of *Geodia parva*, *G. hentscheli*, *Stelleta* sp., *Caulophacus articus* (Roberts et al., 2018), in agreement with our predicted suitability for these taxa. A comparison between predicted distributions and independent observations can provide useful information about the performance of the models. In an illustrative example, Anderson et al. (2016a) validated models for four reef-forming corals in the South Pacific Ocean using data from photographic surveys collected independently from the data used to fit the model. They found that the observed frequency of corals was much lower than predicted and that the correlation between observed and predicted coral distribution was not particularly high. The poor performance of the models was attributed to the low precision of the global bathymetry data, and to the lack of data on geomorphology and substrate data at the scale appropriate to the taxa modeled (Anderson et al., 2016a). These factors may be also relevant for the models in our study. An inspection of high-resolution bathymetry derived from multibeam data available for the Norwegian shelf and some regions on the Icelandic shelf indicates that the GEBCO global bathymetry models are much less detailed and do not resolve small geomorphic features that may be important for the distribution of VMEs (Davies et al., 2009; Henry et al., 2010; Rengstorf et al., 2012). The lack of information describing substrates is also likely to affect the results of our models, as sediment composition is highly variable and is known to influence the distribution of epibenthic sessile organisms (Davies and Guinotte, 2011; Tracey et al., 2011). The effect of the lack of substrate data in our models can be illustrated by the fact that the cold-water coral model predicts high suitability in regions of the Skagerrak known to be dominated by soft sediments and where cold-water corals are usually not observed. The effect of the lack of sediment data is accentuated by the low resolution of the bathymetry model, because terrain variables derived from high-resolution bathymetry can play a better role serving as proxy variables for sediment composition (Dunn and Halpin, 2009). Given these factors, there is a need to produce SDMs at finer scales, incorporating high resolution bathymetry and sediment distribution data, if available.

When estimating the present distribution of VMEs and VME indicator taxa, depending on the goal of a study, it can be argued that the effect of historical fishing should be included (Ross et al., 2012). Some areas may have high predicted VME suitability, but if these areas are continuously being trawled, they may not have high concentrations of VME indicator species because of the cumulative effect of fishing-induced mortality. Penney and Guinotte (2013) suggested computing a "discounted suitability", where the suitability of each cell is reduced proportionally to the swept-area ratio. This method assumes that VME indicator species do not survive the impact of a single trawling event, and therefore in cells that are fished more than once per year the suitability is reduced to zero. This assumption can be adjusted to incorporate differences in the vulnerability of each VME to bottom trawling. An analysis of historical fishing patterns may highlight relatively pristine areas with high suitability for VME indicator taxa. These areas should be targeted for exploration and conservation.

4.2. Environmental Factors Influencing the Distribution of VME Indicator Species

Temperature is an important factor determining the distribution of cold-water corals (Davies and Guinotte, 2011; Yesson et al., 2012; Buhl-Mortensen et al., 2015c) and sponges (Klitgaard and Tendal, 2004; Howell et al., 2016). Given the strong bottom temperature gradients in the study area, it is no surprise that this parameter explained a large proportion of the predicted distribution patterns of the VME indicator taxa. In our study, minimum temperature was the most important factor with a permutation importance higher than 10% in 42 of the 44 taxa modeled. It was particularly high for species associated with cold waters including the sponges *Geodia parva*, *Caulophacus (C.) arcticus*, *Cladorrhiza* sp., *Chrondocladia (C.) grandis*, and the Neptheidae coral *Gersemia* sp. Temperature was also an important predictor for the scleractinean corals *Lophelia pertusa*, *Madrepora oculata*, and for taxa with predominantly southern distributions like *Flabellum* sp., *Anthomastus* sp., and *Anthoptylum* sp.

Next to temperature, depth was the next most predominant factor predicting the distribution of the VME indicator taxa in this study. Depth had a permutation importance higher than 10% in 33 of the 44 models. Similar to temperature, our study area included a wide depth range (Buhl-Mortensen et al., 2015c). Depth is not considered a direct explanatory variable, as hydrostatic pressure does not limit the distribution of VME indicator species. Instead it acts as a surrogate for other environmental parameters that are usually correlated with depth (Thresher et al., 2014; Howell et al., 2016). In our study there was some correlation between bottom depth and aragonite saturation state, particulate organic carbon and silica concentration. In addition, the environmental data sets used in this study had relatively low spatial resolution. In these conditions depth can

act as a proxy explaining some proportion of the spatial patterns controlled by more direct explanatory variables.

Although the permutation importance of individual variables describing the morphology (i.e., terrain variables) of the seafloor was relatively low, their combined contribution was considerable in most of the models. This is consistent with previous modeling efforts for cold-water corals and sponges in which terrain variables have been important predictors (e.g., Rengstorf et al., 2013; Gullage et al., 2017; Rowden et al., 2017). It is well-known that the topography of the seafloor has a strong influence on the distribution patterns of filter feeders like cold-water corals and sponges, which are often associated with complex and elevated topographic features where locally accelerated currents increase the provision of food particles (Thiem et al., 2006; Duineveld et al., 2007; Navas et al., 2014) and influence the transport of larvae (Piepenburg and Müller, 2004; Dullo et al., 2008). The permutation importance of near-bottom current speed as a predictor variable was higher than 5% in 17 of the 44 models. These include four of the six models of sponges of the genus *Geodia*, and in the models of *Stryphnus* sp. and *Steletta* sp, taxa considered indicators of soft bottom sponge aggregations. Current speed had also an importance >5% in five of the seven models of sea pens (Pennatulacea). On the other hand, the importance of current speed was below 5% for most other taxa including reef-forming scleractinean corals, gorgonians, and sponges associated to hard bottoms. This is likely the result of the relatively low resolution of the near-bottom current speed data, which helped to predict the distribution of species with relatively broad distributions associated to soft sediments, but could not resolve more localized effects to predict the distribution of species associated with more complex terrain features. In the later cases, and similar to previous models for VME indicator taxa, the terrain descriptor variables act as proxies of near-bottom current speed. When the output of high-resolution oceanographic models is used as a predictor of the distribution of scleractinean corals like *Lophelia pertussa* or *Madrepora oculata*, near-bottom current speed do explain much of the observed patterns (Mohn et al., 2014; Bargain et al., 2018). In addition to acting as proxies of near-bottom current speed, terrain variables can also explain some of the spatial patterns associated to substrate type, which is another factor that strongly influence the distribution of benthic megafauna including corals and sponges (Gass and Roberts, 2006; Greathead et al., 2014; Baker et al., 2019). For example, hard bottom habitats are associated with complex topographies (Dunn and Halpin, 2009) where sediments are less likely to accumulate.

As expected, silicate was an important variable explaining the distribution of several sponge taxa. The permutation importance of silicate was higher than 10% in 12 of the 20 models for sponges. It was particularly high in the models of sponges associated to hard bottoms, including *Axinellida* sp., *Phakellia* sp., *Antho (A.) dichotoma*, and *Mycale (M.) lingua*. Silicate is required by sponges that form siliceous spicules, and its concentration may be a factor limiting the spatial distribution of sponge habitats (Leys et al., 2004; Howell et al., 2016). Silicate was also an important predictor for the distribution of some corals and sea pens, i.e., *Isidella lophotensis*, *Anthomastus* sp., *Umbellula* sp., and *Pennatula* sp. It is likely that for these taxa the concentration of silicate is not a direct limiting factor but rather is acting as an indicator of water masses. In the case of corals and sea pens, aragonite saturation had a lower importance than expected with only seven of 24 models having a permutation importance above 10%.

Geodia parva and *G. hentscheli* are the only two species for which salinity was an important predictor (permutation importances of 30.6 and 52.8% respectively). Both species are considered indicators of the cold "ostur" assemblage, with their distribution restricted to the Greenland shelf and Denmark strait. Here it is likely that salinity is a proxy for water masses (Yesson et al., 2012) rather than being a direct physiological constraint, acting as an indicator of the waters on the Greenland shelf characterized by the low temperatures and low salinity due to the input of glacial meltwater. This is supported by the fact that for *G. hentscheli* the permutation importance of temperature is lower, and the permutation importance of salinity is higher than for *G. parva*, but the combined importance of both parameters is similar for both species (70.1 and 60.9%, respectively).

4.3. Spatial Distribution of Predicted Taxa and Taxa Groups

As expected, there was a good agreement between the observed locations of VME indicator species and the areas of predicted high suitability, in particular for taxa distributed along a narrow range of environmental variables like *Lophelia pertusa* and the other taxa in cluster group 1 (**Figure S1**), *Umbellula* sp., and for taxa with rather limited geographic distributions like *Isidella* sp. and *Caryophila*. For other taxa the prediction appears less precise, the models tended to predict broad areas of high suitability. Some examples are the models for *Geodia phlegraei*, *Anthothela gradiflora*, *Anthomastus* sp., *Flabellum* sp., and *Lycopodina* sp. This could be because the taxa modeled are generalist species with a broad distribution, or could be an artifact due to low sample sizes or the lack of environmental predictors that limit their distribution.

Our predicted distributions for *Lophelia pertusa*, *Paragorgia arborea*, and *Primnoa resedaeformis* are very similar to those obtained by Sundahl (2017) in Norwegian waters using mostly data from the MAREANO programme (Buhl-Mortensen et al., 2015a,b). This is reassuring, given that Sundahl (2017) produced models at a higher spatial resolution (176 m) and included environmental predictors that were not available for our models, including sediment type and the output of a high-resolution ocean model. In addition, our areas of predicted high suitability for *Lophelia pertusa* in the territorial waters of the United Kingdom and Ireland are similar to the areas identified by Ross and Howell (2013) as having medium and high probability of reef presence.

In general, the predicted distributions for sponges of the genus *Geodia* were comparable to those predicted by Howell et al. (2016) in our study area. In particular, the predicted presence of *G. mandrewi* were very similar to the areas of high suitability predicted by our model. Our predictions for *G. parva* and *G. hentschelli* were also similar,

TABLE 5 | Biotopes identified in the Norwegian shelf by Elvenes et al. (2014) and Gonzalez-Mirelis and Buhl-Mortensen (2015) with associated VME indicator taxa, and the cluster dendrogram groups in which those taxa were assigned in our study.

Habitat name or biotope number	Associated VME indicator taxa	Cluster group
Umbellula stands	*Umbellula ecrinus*	7A
Radicipes meadow	*Radicipes cf. gracialis*	5
Hard bottom demosponges	*Axinella*, *Phakellia*, *Antho dichotoma*, *Tethya* spp., *Mycale*	3A, 3B
Soft bottom demosponges	*Geodia* spp.,/Stryphnus/, *Steletta*	2
Deep sea sponges	*Caulophacus articus*,/Cladorhizidae/ spp., *Hexactinellida* spp.	6B, 7B
Sea Pens and burrowing megafauna	*Funiculina quadrangularis*, *Kophobelemnon stelliferum*, *Pennatula* sp.. *Virgularia* spp.	4, 7B
Hard bottom coral gardens	*Paragorgia arborea*, *Paramuricea placomus*, *Primnoa resedaformis*	1
Biotope class 2	*Caulophacus*	6B
Biotope class 3	*Chrondocladia*, *Umbellula*	7A
Biotope class 4	*Funiculina*, *Flabellum*	4, 5
Biotope class 6	*Phakelia*, *Craniella*, *Geodia* spp., *Stryphnus*, *Mycale*	2, 3A, 3B
Biotope class 8	*Paragorgia*, *Gersemia*, *Drifa*	1, 7B
Biotope class 9	*Kophobelemnon*, *Virgularia*, *Stelletta*	2, 4, 7B
Biotope class 10	*Lophelia*, *Axinella*, *Primnoa*	1, 3A

with the caveat that Howell et al. (2016) did not predicted distributions at depths <200 m, with includes most of the eastern Greenland shelf north of 66°N where our models predict high suitability. On the other hand, our predictions for *G. phlegraei*, *G. atlantica*, and *G. baretti* were more restricted than those in Howell et al. (2016), whose predicted areas with presence included the deep basins of the Norwegian Sea and off southern Iceland where our models predicted low suitability.

The cluster analysis of the "I" similarity statistic computed among the predicted distributions of VME indicator taxa produced 7 groups and 6 subgroups. These groups are not biotopes or communities in the strict sense, as they are not the result of direct observations of species living in close proximity, but rather are groups of taxa with similar predicted distributions. Predictions from the broad-scale models in our study are not expected to agree with the species composition and distribution of biotopes identified from high-resolution local predictions, but reveal similarities at large scales relevant for the management of large marine ecosystems. Nevertheless, in several instances the groups identified were analogous to known VMEs in the study area, and in some cases to biotopes identified on the Norwegian shelf by the MAREANO programme (**Table 5**).

Group 1 included the gorgonians *Paramuricea* sp., *Paragorgia arborea*, and *Primnoa resadaeformis*, which are indicators of hard-bottom coral gardens (ICES, 2016) and were identified as an homogeneous community in the Norwegian shelf (Gonzalez-Mirelis and Buhl-Mortensen, 2015). Group 1 also included the scleractinean corals *Lophelia pertusa* and *Madrepora oculata*, which are the most important reef-forming corals in the study area. These two species are indicator taxa of cold-water coral reefs, but also of two types of hard-bottom coral gardens: colonial scleractineans on rocky outcrops, and non-reefal scleractinean aggregations (ICES, 2016). In our study we could not distinguish between *L. pertusa* and *M. oculata* records originating from different VMEs, and therefore we consider them indicators of a single VME termed reef-forming scleractineans. In addition, in the study area the taxa in this group are often found in close proximity (Buhl-Mortensen et al., 2015c), and therefore their predicted broad-scale distribution was similar. At local scales, it is likely that there are differences in the distribution patterns among the taxa in the groups identified in this study. For example, Elvenes et al. (2014) identified ten biotopes on the Norwegian shelf off the Lofoten and Vesterålen archipelagos (Elvenes et al., 2014), seven of which included VME indicator taxa. *Lophelia* and *Primnoa* were assigned to the same biotope (biotope class 10, **Table 5**), while *Paragorgia* was included in biotope class 8. These differences are expected when comparing predicted distributions at relatively large scales with biotopes identified at more local scales.

Five of the groups identified in our analysis were dominated by sponges and corresponded well to sponge VMEs within the study area. Our groups 2 and 6A include indicator species of soft-bottom sponge aggregations (ICES, 2016) and are analogous to the boreal and cold "ostur" assemblages described by Klitgaard and Tendal (2004), respectively. The stacked distribution models for groups 2 and 6a suggest that "ostur" habitats are widely distributed on the continental shelves and slopes of eastern Greenland, Denmark Strait, Iceland, the Faroe Islands, the Norwegian shelf, and the Bartents Sea. This agrees with previous studies by Klitgaard and Tendal (2004), Christiansen (2010), Howell et al. (2016). *Geodia* aggregations have been observed at depths between 150 and 1,700 m (Maldonado et al., 2015), which correspond well to the depth ranges of predicted high suitability for group 2 (boreal "ostur"). Areas of predicted high suitability for group 6a (cold "ostur") includes areas in the Norwegian and Greenland seas at depths below 1,500 m. The sampling effort at these depths is very low and no *Geodia* aggregations have been previously reported. Group 3 included indicator taxa for hard-bottom sponge aggregations (ICES, 2016). The fact that these taxa form a distinct group from sponges associated to soft-bottoms supports the notion that deep-sea sponge aggregations form distinct habitats depending on their bottom type preferences as proposed by Gonzalez-Mirelis and Buhl-Mortensen (2015).

The list of indicator taxa for ICES/NAFO waters (ICES, 2016) also includes *Caulophacus articus* as an indicator for soft-sponge aggregations. In an analysis of community structure, Gonzalez-Mirelis and Buhl-Mortensen (2015) concluded that Hexactinellid

and other sponges associated to deep, cold waters constitute a distinct habitat separated from soft-bottom and hard-bottom sponge aggregations. Our analysis placed *C. articus*, together with *Cladorrhiza* sp. and *Lycopodina* sp. into group 6B, which can be considered analogous to the deep sea sponges habitat defined by Gonzalez-Mirelis and Buhl-Mortensen (2015). This supports the need to define a distinct VME type for taxa in deep, cold waters, as suggested by Buhl-Mortensen et al. (2019). *Caulophacus* was associated to a distinct biotope (biotope class 2) by Elvenes et al. (2014), and our predicted distribution for *Caulophacus* sp. shows high suitability at depths below 1,500 m, which agrees with the predicted distribution of biotope 2 (Elvenes et al., 2014).

Group 4 included four sea pens considered indicators of the VME type "sea-pen fields" in the list of indicator taxa for ICES/NAFO waters (ICES, 2016): *Funiculina* sp., *Pennatula* sp., *Kophobelemnon* sp. and *Haliperis* sp., and it is analogous to the biotope "sea pen and burrowing megafauna communities" identified by Gonzalez-Mirelis and Buhl-Mortensen (2015) on the Norwegian shelf. The ICES/NAFO list also includes deep-sea sea pens *Umbellula* sp. and *Anthoptilum* sp., which our analysis did not included in group 4 given the differences in their predicted distributions. Similarly, Gonzalez-Mirelis and Buhl-Mortensen (2015) concluded that the sea pens *Funiculina cuadrangularis*, *Kophobelemnon stelliferum*, *Pennatula* sp., and *Virgularia* spp. formed an homogeneous community on the Norwegian shelf distinct from the *Umbellula* stands (e.g., areas with high densities of *Umbellula* sp). This supports the definition of two separate VME types which include shallow and deep-sea sea pen species (Buhl-Mortensen et al., 2019). Gonzalez-Mirelis and Buhl-Mortensen (2015) predicted the distribution of *Umbellula* sp. stands in two regions in the continental slope at depths below 500m roughly off the Lofoten and Vesterålen archipelagos, and in the Eggakanten north of 71°N. Our model for this taxa predicts very high suitability values in similar locations (**Figure S8**). In our analysis *Umbellula* spp. clustered together with the sponge *Chrondocladia (C.) grandis*, as both species have a distinct predicted distribution in the slopes north of the GISR. A biotope comprised by both species was also identified on the slopes of the Norwegian shelf (biotope class 3, Elvenes et al., 2014). Our models for both species and our stacked model for group 7a predicted high suitability along the continental slope between 800 and 1,500 m, which agrees well with the predicted distribution biotope class 3.

As opposed to most other groups, groups 5 is formed by taxa indicators of different VMEs characterized by a predicted distribution mostly in the deep basins south of the GISR. Among the taxa in this group are indicators of soft bottom coral gardens, including the gorgonians *Radicipes* sp., *Acanella arbuscula*, and the cup coral *Flabellum*, and indicators of hard bottom coral gardens including the gorgonians *Anthomastus* sp., *Anthotella grandiflora*. *A. arbuscula* has been reported to co-occur with *Flabellum alabastrum* (Buhl-Mortensen and Buhl-Mortensen, 2018). Our model for *Radicipes* sp. correctly predicted high suitability in the Bjørnøya slide area, which is the only area in Norwegian waters where *Radicipes* meadows have been observed (Buhl-Mortensen et al., 2015c; Gonzalez-Mirelis and Buhl-Mortensen, 2015, **Figure S6**). The group also includes *Solenosmilia variabilis*, a reef-forming scleractinean coral than in our study area was recorded south of the GISR, and the deep-sea sea pen *Anthoptilum* sp. This group includes taxa reported in the Mid-Atlantic ridge at a relatively wide depth range (800–2,400 m, Mortensen et al., 2008).

Group 7B includes mostly corals of the family Nephtheidae family that are indicator taxa of the VME subtype cauliflower coral fields (ICES, 2016; Buhl-Mortensen et al., 2019). These corals are found over a wide range of substrates including semiconsolidated mudstone (Buhl-Mortensen and Buhl-Mortensen, 2018), sometimes in relatively high densities as observed off the Westfjords in Iceland. On the Norwegian shelf, Elvenes et al. (2014) identified a biotope (biotope 8) that included *Gersemia* and *Drifa*, but also *Paragorgia* (**Table 5**).

Our VME Index provides a summary of the distribution of all 44 taxa, giving more weight to taxa that are considered to more closely fulfill the FAO criteria for VME identification (FAO, 2009). Areas with high VME Index include much of the shelf break and slope off Norway and the Barent Sea, Iceland, and the Faroe Islands, the shelf off southern Greenland, and the areas in the Reykjanes Ridge and the Kolbeinseyn Ridge. Several of these areas are being targeted by the MAREANO programme in Norway, and by the habitat mapping efforts by the Marine and Freshwater Research Institute (MFRI) in Iceland. Recent video observations carried out in the Faroe Islands are providing new information on the distribution of VME indicator species (Buhl-Mortensen et al., 2019). Nevertheless, there are vast areas where the number of observations is very low and should be the target of new research efforts. The continental shelf off southern Greenland is of particular interest because the predicted suitability of several VME indicator taxa is high in this region, and the area has not been subjected to intense fishing effort which increases the probability of finding pristine VMEs. Recent mapping efforts have been producing information off the west coast off Greenland (Yesson et al., 2016), but little is know off the eastern coast. Also there is a lack of data on the fauna on the deep basins of the Norwegian and Greenland sea.

DATA AVAILABILITY STATEMENT

The datasets generated for this study are available on request to the corresponding author.

AUTHOR CONTRIBUTIONS

LB-M, PB-M, JB, SÓ, SR, and PS conceived the study. LB-M secured funding. LB-M, PB-M, SÓ, PS, and SR compiled the database with records of VME indicator taxa. ØR provided data on temperature and salinity and performed spatial interpolations. JB compiled the remaining environmental predictors and carried out species distribution models and other analysis. The manuscript was written by JB, and was contributed to and edited by LB-M, PB-M, SÓ, SR, and ØR.

FUNDING

This article is a product of the Nordic Project On Vulnerable Marine Ecosystems And Anthropogenic Activities In Arctic And Sub-Arctic Waters (NovasArc, 2016-2018), a collaboration between the Institute of Marine Research (Norway), the Marine and Freshwater Research Institute (Iceland) and the Faroe Marine Research Institute (Faroe Islands). NovasArc was supported by the Marine Group (HAV) and the Working Group for Fisheries (AG-Fisk) of the Nordic Counsel of Ministers.

ACKNOWLEDGMENTS

L. Q. Jiang provided aragonite saturation data. Two reviewers and the journal editor provided useful comments that improved the quality of this article.

SUPPLEMENTARY MATERIAL

The Supplementary Material for this article can be found online at: https://www.frontiersin.org/articles/10.3389/fmars.2020.00131/full#supplementary-material

REFERENCES

Allouche, O., Tsoar, A., and Kadmon, R. (2006). Assessing the accuracy of species distribution models: prevalence, kappa and the true skill statistic (tss). *J. Appl. Ecol.* 43, 1223–1232. doi: 10.1111/j.1365-2664.2006.01214.x

Anderson, O., Guinotte, J., Rowden, A., Clark, M., Mormede, S., Davies, A., et al. (2016a). Field validation of habitat suitability models for vulnerable marine ecosystems in the South Pacific Ocean: implications for the use of broad-scale models in fisheries management. *Ocean Coast. Manage.* 120, 110–126. doi: 10.1016/j.ocecoaman.2015.11.025

Anderson, O., Guinotte, J., Rowden, A., Tracey, D., Mackay, K., and Clark, M. (2016b). Habitat suitability models for predicting the occurrence of vulnerable marine ecosystems in the seas around New Zealand. *Deep Sea Res. Part I Oceanogr. Res. Pap.* 115, 265–292. doi: 10.1016/j.dsr.2016.07.006

Anonymous (2014). *Meting av Fri?a?um og Stongdum ϕkjum (Evaluation of Protected and Closed Areas)*. Report to the Faroese Fisheries Ministry. Faroe Marine Research Institute, 41.

Aranda, S., and Lobo, J. (2011). How well does presence-only-based species distribution modelling predict assemblage diversity? A case study of the Tenerife flora. *Ecography* 34, 31–38. doi: 10.1111/j.1600-0587.2010.06134.x

Ardron, J. A., Clark, M. R., Penney, A. J., Hourigan, T. F., Rowden, A. A., Dunstan, P. K., et al. (2014). A systematic approach towards the identification and protection of vulnerable marine ecosystems. *Mar. Policy* 49, 146–154. doi: 10.1016/j.marpol.2013.11.017

Assis, J., Tyberghein, L., Bosch, S., Verbruggen, H., Serrão, E. A., and De Clerck, O. (2018). Bio-oracle v2. 0: extending marine data layers for bioclimatic modelling. *Global Ecol. Biogeogr.* 27, 277–284. doi: 10.1111/geb.12693

Baker, K. D., Snelgrove, P. V., Fifield, D. A., Edinger, E. N., Wareham-Hayes, V. E., Haedrich, R. L., et al. (2019). Small-scale patterns in the distribution and condition of bamboo coral, *Keratoisis grayi*, in submarine canyons on the grand banks, Newfoundland. *Front. Mar. Sci.* 6:374. doi: 10.3389/fmars.2019.00374

Baker, K. D., Wareham, V. E., Snelgrove, P. V., Haedrich, R. L., Fifield, D. A., Edinger, E. N., et al. (2012). Distributional patterns of deep-sea coral assemblages in three submarine canyons off Newfoundland, Canada. *Mar. Ecol. Prog. Ser.* 445, 235–249. doi: 10.3354/meps09448

Bargain, A., Foglini, F., Pairaud, I., Bonaldo, D., Carniel, S., Angele+tti, L., Taviani, M., Rochette, S., and Fabri, M. (2018). Predictive habitat modeling in two mediterranean canyons including hydrodynamic variables. *Prog. Oceanogr.* 169, 151–168. doi: 10.1016/j.pocean.2018.02.015

Beck, J., Böller, M., Erhardt, A., and Schwanghart, W. (2014). Spatial bias in the gbif database and its effect on modeling species' geographic distributions. *Ecol. Inform.* 19, 10–15. doi: 10.1016/j.ecoinf.2013.11.002

Behrenfeld, M. J., Boss, E., Siegel, D. A., and Shea, D. M. (2005). Carbon-based ocean productivity and phytoplankton physiology from space. *Glob. Biogeochem. Cycles* 19:1. doi: 10.1029/2004GB002299

Beisiegel, K., Darr, A., Gogina, M., and Zettler, M. L. (2017). Benefits and shortcomings of non-destructive benthic imagery for monitoring hard-bottom habitats. *Mar. Pollut. Bull.* 121, 5–15. doi: 10.1016/j.marpolbul.2017.04.009

Benn, A., Weaver, P., Billet, D., van den Hove, S., Murdock, A., Doneghan, G., and Le Bas, T. (2010). Human activities on the deep seafloor in the north east atlantic: an assessment of spatial extent. *PLoS ONE* 5:e12730. doi: 10.1371/journal.pone.0012730

Brix, S., and Svavarsson, J. (2010). Distribution and diversity of desmosomatid and nannoniscid isopods (crustacea) on the greenland–iceland–faeroe ridge. *Polar Biol.* 33, 515–530. doi: 10.1007/s00300-009-0729-8

Buhl-Mortensen, L., Aglen, A., Breen, M., Buhl-Mortensen, P., Ervik, A., Husa, V., et al. (2013). *Impacts of Fisheries and Aquaculture on Sediments and Benthic Fauna: Suggestions for New Management Approaches*. Fisken of havet 2/2013. Institute of Marine Research, 69.

Buhl-Mortensen, L., and Buhl-Mortensen, P. (2018). "Cold temperate coral habitats," in *Corals in a Changing World*, eds C. Duque Beltran and E. Tello Camach (InTech), 9–27. doi: 10.5772/65203

Buhl-Mortensen, L., Buhl-Mortensen, P., Dolan, M., Dannheim, J., Bellec, V., and Holte, B. (2012). Habitat complexity and bottom fauna composition at different scales on the continental shelf and slope of Northern Norway. *Hydrobiologia* 685, 191–219. doi: 10.1007/s10750-011-0988-6.

Buhl-Mortensen, L., Buhl-Mortensen, P., Dolan, M., and Gonzalez-Mirelis, G. (2015a). Habitat mapping as a tool for conservation and sustainable use of marine resources: some perspectives from the mareano programme, Norway. *J. Sea Res.* 100, 6–61. doi: 10.1016/j.seares.2014.10.014

Buhl-Mortensen, L., Buhl-Mortensen, P., Dolan, M. F., and Holte, B. (2015b). The mareano programme–a full coverage mapping of the norwegian off-shore benthic environment and fauna. *Mar. Biol. Res.* 11, 4–17. doi: 10.1080/17451000.2014.952312

Buhl-Mortensen, L., Burgos, J., Steingrund, P., Buhl-Mortensen, P., Ólafsdóttir, S., and Ragnarsson, S. (2019). *Vulnerable Marine Ecosystems (VME) Coral and Sponge VMEs in Arctic and Sub-Arctic Waters-Distribution and Threats*. TemaNord 2019:519. Nordic Council of Ministers, 144.

Buhl-Mortensen, L., Ólafsdóttir, S., Buhl-Mortensen, P., Burgos, J., and Ragnarsson, S. (2015c). Distribution of nine cold-water coral species (scleractinia and gorgonacea) in the cold temperate North Atlantic: effects of bathymetry and hydrography. *Hydrobiologia* 759, 39–61. doi: 10.1007/s10750-014-2116-x

Buhl-Mortensen, L., Serigstad, B., Buhl-Mortensen, P., Olsen, M., Ostrowski, M., Błażewicz-Paszkowycz, M., et al. (2017). First observations of the structure and megafaunal community of a large *Lophelia* reef on the ghanaian shelf (the Gulf of Guinea). *Deep Sea Res. II Top. Stud. Oceanogr.* 137, 148–156. doi: 10.1016/j.dsr2.2016.06.007

Buhl-Mortensen, P., Buhl-Mortensen, L., and Purser, A. (2015d). "Trophic ecology and habitat provision in cold-water coral ecosystems," in *Marine Animal Forests: The Ecology of Benthic Biodiversity Hotspots*, eds S. Rossi, L. Bramanti, A. Gori, and C. Orejas (Cham: Springer International Publishing), 919–944.

Calabrese, J. M., Certain, G., Kraan, C., and Dormann, C. F. (2014). Stacking species distribution models and adjusting bias by linking them to macroecological models. *Glob. Ecol. Biogeogr.* 23, 99–112. doi: 10.1111/geb.12102

Cárdenas, P., and Rapp, H. T. (2015). Demosponges from the northern mid-atlantic ridge shed more light on the diversity and biogeography of north atlantic deep-sea sponges. *J. Mar. Biol. Assoc. U.K.* 95, 1475–1516. doi: 10.1017/S0025315415000983

Christiansen, S. (2010). *Background Document for Deep-Sea Sponge Aggregations*. Biodiversity Series. OSPAR Comission, 47.

Clark, M., Althaus, F., Schlacher, T., Williams, A., Bowden, D., and Rowden, A. (2015). The impacts of deep-sea fisheries on benthic communities: a review. *ICES J. Mar. Sci. J. Conseil* 73(Suppl. 1), i51–i69. doi: 10.1093/icesjms/fsv123

Clark, M., Bowden, D., Baird, S., and Stewart, R. (2010). *Effects of Fishing on the Benthic Biodiversity of Seamounts of the" Graveyard" Complex, Northern Chatham Rise*. New Zealand Aquatic Environment and Biodiversity Report 46, 40.

Clark, M. R., and Dunn, M. R. (2012). Spatial management of deep-sea seamount fisheries: balancing sustainable exploitation and habitat conservation. *Environ. Conserv.* 39, 204–214. doi: 10.1017/S0376892912000021

Copley, J., Tyler, P., Sheader, M., Murton, B., and German, C. (1996). Megafauna from sublittoral to abyssal depths along the mid-atlantic ridge south of Iceland. *Oceanol. Acta* 19, 549–559.

Curd, A. (2010). *Background Dcument for Seapen and Burrowing Megafauna Communities*. Biodiversity Series. OSPAR Comission, 27.

D'Amen, M., Dubuis, A., Fernandes, R. F., Pottier, J., Pellissier, L., and Guisan, A. (2015). Using species richness and functional traits predictions to constrain assemblage predictions from stacked species distribution models. *J. Biogeogr.* 7, 1255–1266. doi: 10.1111/jbi.12485

D'Amen, M., Rahbek, C., Zimmermann, N. E., and Guisan, A. (2017). Spatial predictions at the community level: from current approaches to future frameworks. *Biol. Rev.* 92, 169–187. doi: 10.1111/brv.12222

Dauvin, J., Alizier, S., Weppe, A., and Gu?mundsson, G. (2012). Diversity and zoogeography of icelandic deep-sea ampeliscidae (crustacea: Amphipoda). *Deep Sea Res. Part I Oceanogr. Res. Pap.* 68, 12–23. doi: 10.1016/j.dsr.2012.04.013

Davies, A., Duineveld, G., Lavaleye, M., Bergman, M., Van Haren, H., and Roberts, J. (2009). Downwelling and deep-water bottom currents as food supply mechanisms to the cold-water coral *Lophelia pertusa* (scleractinia) at the mingulay reef complex. *Limnol. Oceanogr.* 54, 620–629. doi: 10.4319/lo.2009.54.2.0620

Davies, A. A. J. and Guinotte, J. M. J. (2011). Global habitat suitability for framework-forming cold-water corals. *PLoS ONE* 6:e18483. doi: 10.1371/journal.pone.0018483

Davies, J., Guillaumont, B., Tempera, F., Vertino, A., Beuck, L., Ólafsdóttir, S., et al. (2017). A new classification scheme of European cold-water coral habitats: implications for ecosystem-based management of the deep sea. *Deep Sea Res. Part II Top. Stud. Oceanogr.* 145, 102–109. doi: 10.1016/j.dsr2.2017.04.014

Davis, R. E. (1998). Preliminary results from directly measuring middepth circulation in the tropical and south pacific. *J. Geophys. Res. Oceans* 103, 24619–24639. doi: 10.1029/98JC01913

Davison, J. J., van Haren, H., Hosegood, P., Piechaud, N., and Howell, K. L. (2019). The distribution of deep-sea sponge aggregations (porifera) in relation to oceanographic processes in the faroe-shetland channel. *Deep Sea Res. Part I Oceanogr. Res. Pap.* 146, 55–61. doi: 10.1016/j.dsr.2019.03.005

Dormann, C. F., Elith, J., Bacher, S., Buchmann, C., Carl, G., Carré, G., et al. (2013). Collinearity: a review of methods to deal with it and a simulation study evaluating their performance. *Ecography* 36, 27–46. doi: 10.1111/j.1600-0587.2012.07348.x.

Duineveld, G. C., Lavaleye, M. S., Bergman, M. J., De Stigter, H., and Mienis, F. (2007). Trophic structure of a cold-water coral mound community (rockall bank, ne atlantic) in relation to the near-bottom particle supply and current regime. *Bull. Mar. Sci.* 81, 449–467.

Dullo, W.-C., Flögel, S., and Rüggeberg, A. (2008). Cold-water coral growth in relation to the hydrography of the celtic and nordic european continental margin. *Mar. Ecol. Prog. Ser.* 371, 165–176. doi: 10.3354/meps07623

Dunn, D. and Halpin, P. (2009). Rugosity-based regional modeling of hard-bottom habitat. *Mar. Ecol. Prog. Ser.* 377, 1–11. doi: 10.3354/meps07839

Durán Muñoz, P., Sayago-Gil, M., Murillo, F., Del Río, J., López-Abellán, L., Sacau, M., et al. (2012). Actions taken by fishing nations towards identification and protection of vulnerable marine ecosystems in the high seas: The spanish case (Atlantic Ocean). *Mar. Policy* 36, 536–543. doi: 10.1016/j.marpol.2011.09.005

Elith, J., and Graham, C. (2009). Do they? how do they? why do they differ? on finding reasons for differing performances of species distribution models. *Ecography* 32, 66–77. doi: 10.1111/j.1600-0587.2008.05505.x

Elith, J., Graham, C., Anderson, R., Dudik, M., Ferrier, S., Guisan, A., et al. (2006). Novel methods improve prediction of species' distributions from occurrence data. *Ecography* 29, 129–151. doi: 10.1111/j.2006.0906-7590.04596.x

Elith, J., Phillips, S., Hastie, T., Dudík, M., Chee, Y., and Yates, C. (2011). A statistical explanation of maxent for ecologists. *Divers. Distrib.* 17, 43–57. doi: 10.1111/j.1472-4642.2010.00725.x

Elvenes, S., Dolan, M. F., Buhl-Mortensen, P., and Bellec, V. K. (2014). An evaluation of compiled single-beam bathymetry data as a basis for regional sediment and biotope mapping. *ICES J. Mar. Sci. J. Conseil* 71, 867–881. doi: 10.1093/icesjms/fst154

Fabri, M., Pedel, L., Beuck, L., Galgani, F., Hebbeln, D., and Freiwald, A. (2014). Megafauna of vulnerable marine ecosystems in french mediterranean submarine canyons: spatial distribution and anthropogenic impacts. *Deep Sea Res. Part II Top. Stud. Oceanogr.* 104, 184–207. doi: 10.1016/j.dsr2.2013.06.016

FAO (2009). *International Guidelines for the Management of Deep-Sea Fisheries in the High Seas*. Rome: Food and Agriculture Organization of the United Nations, 73.

Ferrier, S., and Guisan, A. (2006). Spatial modelling of biodiversity at the community level. *J. Applied Ecol.* 43, 393–404. doi: 10.1111/j.1365-2664.2006.01149.x

Fisher, C. R., Hsing, P.-Y., Kaiser, C. L., Yoerger, D. R., Roberts, H. H., Shedd, W. W., et al. (2014). Footprint of deepwater horizon blowout impact to deep-water coral communities. *Proc. Natl. Acad. Sci. U.S.A.* 111, 11744–11749. doi: 10.1073/pnas.1403492111

Fossså, J., and Skjoldal, H. (2010). "Chapter 16: Conservation of cold-water coral reefs in norway," in *Handbook of Marine Fisheries Conservation and Management*, eds R. Grafon, R. Hilborn, D. Squires, M. Tait, and M. Williams (Oxford: Oxford University Press), 215–230.

Fourcade, Y., Engler, J. O., Rödder, D., and Secondi, J. (2014). Mapping species distributions with maxent using a geographically biased sample of presence data: a performance assessment of methods for correcting sampling bias. *PLoS ONE* 9:e97122. doi: 10.1371/journal.pone.0097122

Fuller, S., Murillo, F., Wareham, V., and Kenchington, E. (2008). *Vulnerable Marine Ecosystems Dominated by Deep-Water Corals and Sponges in the NAFO Convention Area*. NAFO SCR Doc. 08/22 Serial No.N5524. Northwest Atlantic Fisheries Organization, 24.

Gass, S. E., and Roberts, J. M. (2006). The occurrence of the cold-water coral *Lophelia pertusa* (scleractinia) on oil and gas platforms in the North Sea: colony growth, recruitment and environmental controls on distribution. *Mar. Pollut. Bull.* 52, 549–559. doi: 10.1016/j.marpolbul.2005.10.002

Georgian, S. E., Anderson, O. F., and Rowden, A. A. (2019). Ensemble habitat suitability modeling of vulnerable marine ecosystem indicator taxa to inform deep-sea fisheries management in the South Pacific Ocean. *Fish. Res.* 211, 256–274. doi: 10.1016/j.fishres.2018.11.020

Gonzalez-Mirelis, G., and Buhl-Mortensen, P. (2015). Modelling benthic habitats and biotopes off the coast of norway to support spatial management. *Ecol. Inform.* 30, 284–292. doi: 10.1016/j.ecoinf.2015.06.005

Grassle, J. F. (2000). The ocean biogeographic information system (obis): an on-line, worldwide atlas for accessing, modeling and mapping marine biological data in a multidimensional geographic context. *Oceanography* 13, 5–7. doi: 10.5670/oceanog.2000.01

Greathead, C., González-Irusta, J., Clarke, J., Boulcott, P., Blackadder, L., Weetman, A., and Wright, P. (2014). Environmental requirements for three sea pen species: relevance to distribution and conservation. *ICES J. Mar. Sci.* 72, 576–586. doi: 10.1093/icesjms/fsu129

Guillera-Arroita, G., Lahoz-Monfort, J. J., Elith, J., Gordon, A., Kujala, H., Lentini, P. E., et al. (2015). Is my species distribution model fit for purpose? Matching data and models to applications. *Glob. Ecol. Biogeogr.* 24, 276–292. doi: 10.1111/geb.12268

Guinotte, J., Orr, J., Cairns, S., Freiwald, A., Morgan, L., and George, R. (2006). Will human-induced changes in seawater chemistry alter the distribution of deep-sea scleractinian corals? *Front. Ecol. Environ.* 4, 141–146. doi: 10.1890/1540-9295(2006)004[0141:WHCISC]2.0.CO;2

Guinotte, J. M., and Davies, A. J. (2014). Predicted deep-sea coral habitat suitability for the US West Coast. *PLoS ONE* 9:e93918. doi: 10.1371/journal.pone.0093918

Guisan, A., Tingley, R., Baumgartner, J. B., Naujokaitis-Lewis, I., Sutcliffe, P. R., Tulloch, A. I., et al. (2013). Predicting species distributions for conservation decisions. *Ecol. Lett.* 16, 1424–1435. doi: 10.1111/ele.12189

Gullage, L., Devillers, R., and Edinger, E. (2017). Predictive distribution modelling of cold-water corals in the Newfoundland and Labrador Region. *Mar. Ecol. Prog. Ser.* 582, 57–77. doi: 10.3354/meps12307

Henry, L.-A., Davies, A. J., and Roberts, J. M. (2010). Beta diversity of cold-water coral reef communities off Western Scotland. *Coral Reefs* 29, 427–436. doi: 10.1007/s00338-009-0577-6

Hestetun, J. T., Tompkins-Macdonald, G., and Rapp, H. T. (2017). A review of carnivorous sponges (porifera: Cladorhizidae) from the boreal North Atlantic and Arctic. *Zool. J. Linnean Soc.* 181, 1–69. doi: 10.1093/zoolinnean/zlw022

Hijmans, R. J., Phillips, S., Leathwick, J., and Elith, J. (2017). *dismo: Species Distribution Modeling*. R package version 1.1-4. Available online at: https://CRAN.R-project.org/package=dismo

Hourigan, T. (2014). "A Strategic Approach to Address Fisheries Impacts on Deep-Sea Coral Ecosystems," in *Interrelationships Between Corals and Fisheries*, ed S. Bortone (CRS Press), 127–145.

Howell, K.-L., Piechaud, N., Downie, A.-L., and Kenny, A. (2016). The distribution of deep-sea sponge aggregations in the north atlantic and implications for their effective spatial management. *Deep Sea Res. Part I Oceanogr. Res. Pap.* 115, 309–320. doi: 10.1016/j.dsr.2016.07.005

Howell, K. L., Holt, R., Endrino, I. P., and Stewart, H. (2011). When the species is also a habitat: comparing the predictively modelled distributions of *Lophelia pertusa* and the reef habitat it forms. *Biol. Conserv.* 144, 2656–2665. doi: 10.1016/j.biocon.2011.07.025

ICES (2008). *Report of the ICES-NAFO Joint Working Group on Deep-water Ecology (WGDEC)*. ICES CM 2008/ACOM:45. Technical Report. ICES 126.

ICES (2011). *Report of the ICES/NAFO Joint Working Group on Deep-water Ecology (WGDEC)*. ICES CM 2011/ACOM:27, Copenhagen.

ICES (2016). *Report of the Workshop on Vulnerable Marine Ecosystem Database (WKVME)*. ICES CM 2015/ACOM:62, Report. ICES 42. Peterborough.

Jiang, L.-Q., Feely, R. A., Carter, B. R., Greeley, D. J., Gledhill, D. K., and Arzayus, K. M. (2015). Climatological distribution of aragonite saturation state in the global oceans. *Global Biogeochem. Cycles* 29, 1656–1673. doi: 10.1002/2015GB005198

Jochumsen, K., Schnurr, S. M., and Quadfasel, D. (2016). Bottom temperature and salinity distribution and its variability around Iceland. *Deep Sea Res. Part I Oceanogr. Res. Pap.* 111, 79–90. doi: 10.1016/j.dsr.2016.02.009

Jørgensen, L. L., Ljubin, P., Skjoldal, H. R., Ingvaldsen, R. B., Anisimova, N., and Manushin, I. (2014). Distribution of benthic megafauna in the barents sea: baseline for an ecosystem approach to management. *ICES J. Mar. Sci.* 72, 595?-613. doi: 10.1093/icesjms/fsu106 fsu106.

Jørgensen, L. L., Planque, B., Thangstad, T. H., and Certain, G. (2015). Vulnerability of megabenthic species to trawling in the Barents Sea. *ICES J. Mar. Sci.* 73, i84?-i97. doi: 10.1093/icesjms/fsv107

Kivlin, S. N., Muscarella, R., Hawkes, C. V., and Treseder, K. K. (2017). "The predictive power of ecological niche modeling for global arbuscular mycorrhizal fungal biogeography," in *Biogeography of Mycorrhizal Symbiosis* eds E, Tedersoo (Springer), 143–158. doi: 10.1007/978-3-319-56363-3_7

Klitgaard, A., Tendal, O., and Westerberg, H. (1997). "Mass occurrences of large sponges (Porifera) in Faroe Island (NE Atlantic) Shelf and slope areas: characteristics, distribution and possible causes," in *The Responses of Marine Organisms to Their Enviroments* eds L. Hawkins and S. Hutchinson (Southampton Ocenography Centre), 129–142.

Klitgaard, A. B., and Tendal, O. S. (2004). Distribution and species composition of mass occurrences of large-sized sponges in the Northeast Atlantic. *Prog. Oceanogr.* 61, 57–98. doi: 10.1016/j.pocean.2004.06.002

Kutti, T., Bannister, R., and Fosså, J. H. (2013). Community structure and ecological function of deep-water sponge grounds in the traenadypet MPA-northern Norwegian continental shelf. *Contin. Shelf Res.* 69, 21–30. doi: 10.1016/j.csr.2013.09.011

Lagasse, C. R., Knudby, A., Curtis, J., Finney, J. L., and Cox, S. P. (2015). Spatial analyses reveal conservation benefits for cold-water corals and sponges from small changes in a trawl fishery footprint. *MEPS* 528, 161–172. doi: 10.3354/meps11271

Lecours, V., Devillers, R., Simms, A. E., Lucieer, V. L., and Brown, C. J. (2017). Towards a framework for terrain attribute selection in environmental studies. *Environ. Model. Softw.* 89, 19–30. doi: 10.1016/j.envsoft.2016.11.027

Legendre, P., and Legendre, L. (1998). *Numerical Ecology, 2nd Edition. Developments in Environmental Modelling 20*. Amsterdam: Elsevier Science, 852.

Lehtomäki, J., and Moilanen, A. (2013). Methods and workflow for spatial conservation prioritization using zonation. *Environ. Model. Softw.* 47, 128–137. doi: 10.1016/j.envsoft.2013

Levin, L., and Le Bris, N. (2015). The deep ocean under climate change. *Science* 350, 766–768. doi: 10.1126/science.aad0126

Leys, S., Wilson, K., Holeton, C., Reiswig, H., Austin, W., and Tunnicliffe, V. (2004). Patterns of glass sponge (porifera, hexactinellida) distribution in coastal waters of British Columbia, Canada. *Mar. Ecol. Prog. Ser.* 283, 133–149. doi: 10.3354/meps283133

Liu, C., Newell, G., and White, M. (2016). On the selection of thresholds for predicting species occurrence with presence-only data. *Ecol. Evol.* 6, 337–348. doi: 10.1002/ece3.1878

Liu, C., P.M., B., Dawson, T., and Pearson, R. (2005). Selecting thresholds of occurrence in the prediction of species distributions. *Ecography* 28, 385–393. doi: 10.1111/j.0906-7590.2005.03957.x

Locarnini, R., Mishonov, A., Antonov, J., Boyer, T., Garcia, H. Zweng, M. M., et al. (2013). *Temperature*. NOAA Atlas NESDIS: 73, ed S. Levitus and A. Mishonov, 40.

Logemann, K., Ólafsson, J., Snorrason, Á., Valdimarsson, H., and Marteinsdóttir, G. (2013). The circulation of icelandic waters–a modelling study. *Ocean Sci. Discuss.* 10, 763–824. doi: 10.5194/os-9-931-2013

Lutz, M., Dunbar, R., and Caldeira, K. (2002). Regional variability in the vertical flux of particulate organic carbon in the ocean interior. *Global Biogeochem. Cycles* 16:3. doi: 10.1029/2000GB001383

Lutz, M. J., Caldeira, K., Dunbar, R. B., and Behrenfeld, M. J. (2007). Seasonal rhythms of net primary production and particulate organic carbon flux to depth describe the efficiency of biological pump in the global ocean. *J. Geophys. Res. Oceans* 112:C10. doi: 10.1029/2006JC003706

Maldonado, M., Aguilar, R., Bannister, R. J., Bell, J. J., Conway, K. W., Dayton, P. K., et al. (2015). "Sponge grounds as key marine habitats: a synthetic review of types, structure, functional roles, and conservation concerns," in *Marine Animal Forests: The Ecology of Benthic Biodiversity Hotspots* (Cham: Springer International Publishing), 1–39.

Mayer, M., and Piepenburg, D. (1996). Epibenthic community patterns on the continental slope off east greenland at 75° N. *Mar. Ecol. Prog. Ser.* 143, 151–164. doi: 10.3354/meps143151

McKean, J., and Roering, J. (2004). Objective landslide detection and surface morphology mapping using high-resolution airborne laser altimetry. *Geomorphology* 57, 331–351. doi: 10.1016/S0169-555X(03)00164-8

Merow, C., Smith, M. J., and Silander, J. A. (2013). A practical guide to maxent for modeling species' distributions: what it does, and why inputs and settings matter. *Ecography* 36, 1058–1069. doi: 10.1111/j.1600-0587.2013.07872.x

Mohn, C., Rengstorf, A., White, M., Duineveld, G., Mienis, F., Soetaert, K., et al. (2014). Linking benthic hydrodynamics and cold-water coral occurrences: a high-resolution model study at three cold-water coral provinces in the ne atlantic. *Prog. Oceanogr.* 122, 92–104. doi: 10.1016/j.pocean.2013.12.003

Monk, J. (2014). How long should we ignore imperfect detection of species in the marine environment when modelling their distribution? *Fish Fish.* 15, 352–358. doi: 10.1111/faf.12039

Morato, T., Pham, C. K., Pinto, C., Golding, N., Ardron, J. A., Muñoz, P. D., et al. (2018). A multi criteria assessment method for identifying vulnerable marine ecosystems in the North-East Atlantic. *Front. Mar. Sci.* 5:460. doi: 10.3389/fmars.2018.00460

Mortensen, P., and Buhl-Mortensen, L. (2004). Distribution of deep-water gorgonian corals in relation to benthic habitat features in the northeast channel (Atlantic Canada). *Mar. Biol.* 144, 1223–1238. doi: 10.1007/s00227-003-1280-8

Mortensen, P., Buhl-Mortensen, L., Gebruk, A., and Krylova, E. (2008). Occurrence of deep-water corals on the mid-atlantic ridge based on mar-eco data. *Deep Sea Res. Part II Top. Stud. Oceanogr.* 55, 142–152. doi: 10.1016/j.dsr2.2007.09.018

Mortensen, P., Hovland, M., Brattegard, T., and Farestveit, R. (1995). Deep water bioherms of the scleractinian coral lophelia pertusa (l.) at 64° N on the norwegian shelf: structure and associated megafauna. *Sarsia* 80, 145–158. doi: 10.1080/00364827.1995.10413586

Mortensen, P., Hovland, M., Fosså, J., and Furevik, D. (2001). Distribution, abundance and size of *Lophelia pertusa* coral reefs in mid-norway in relation to seabed characteristics. *J. Mar. Biol. Assoc. U.K.* 81, 581–597. doi: 10.1017/S002531540100426X

Mortensen, P. B., and Buhl-Mortensen, L. (2005). "Deep-water corals and their habitats in the gully, a submarine canyon off Atlantic Canada," in *Cold-Water Corals and Ecosystems* eds A. Freiwald and J. Murray Roberts (Springer), 247–277. doi: 10.1007/3-540-27673-4_12

Moudrý, V., and Šímová, P. (2012). Influence of positional accuracy, sample size and scale on modelling species distributions: a review. *Int. J. Geogr. Inform. Sci.* 26, 2083–2095. doi: 10.1080/13658816.2012.721553

Murillo, F., Wareham, V., Sacau, M., Román, E., and Durán-Muñoz, P. (2011). *New data on deep-water corals and sponges from Spanish/EU and Canadian bottom trawl groundfish surveys in the NAFO Regulatory Area (Divs. 3LMNO): 2008-2010 period*. Serial No. N6004 NAFO SCR Doc. 11/074. NAFO.

Murillo, F. J., Muñoz, P. D., Cristobo, J., Ríos, P., González, C., Kenchington, E., et al. (2012). Deep-sea sponge grounds of the flemish cap, flemish pass and the grand banks of newfoundland (Northwest Atlantic ocean): distribution and species composition. *Mar. Biol. Res.* 8, 842–854. doi: 10.1080/17451000.2012.682583

Muscarella, R., Galante, P. J., Soley-Guardia, M., Boria, R. A., Kass, J. M., Uriarte, M., et al. (2014). Enmeval: an R package for conducting spatially independent evaluations and estimating optimal model complexity for maxent ecological niche models. *Methods Ecol. Evol.* 5, 1198–1205. doi: 10.1111/2041-210X.12261

Naimi, B., Hamm, N. A., Groen, T. A., Skidmore, A. K., and Toxopeus, A. G. (2014). Where is positional uncertainty a problem for species distribution modelling? *Ecography* 37, 191–203. doi: 10.1111/j.1600-0587.2013.00205.x.

Navas, J. M., Miller, P. L., Henry, L.-A., Hennige, S. J., and Roberts, J. M. (2014). Ecohydrodynamics of cold-water coral reefs: a case study of the mingulay reef complex (Western Scotland). *PLoS ONE* 9:e98218. doi: 10.1371/journal.pone.0098218

NEAFC (2014). *Recommendation 19:2014. Article 2(g) and Annex 5.* North-East Atlantic Fisheries Comission, 24.

Nilsen, J. E. ?., H?t?n, H., Mork, K. A., and Valdimarsson, H. (2008). *The NISE Dataset*. Technical Report. The Faroese Fisheries Laboratory - Fiskiranns?knarstovan, 20.

Ólafsdóttir, S., and Burgos, J. (2012). "Fir?un kóralsvæ?a vi? Ísland og í nor?ur atlantshafi (cold water coral conservation in iceland and the North Atlantic)," in *?ættir úr vistfræ?i sjávar 2011 (Environmental Conditions in Icelandic Waters 2011)*, number 162 in Hafranns?knir nr. 162, 30–35.

Omarsdottir, S., Einarsdottir, E., Ögmundsdottir, H., Freysdottir, J., Olafsdottir, E., Molinski, T., et al. (2013). Biodiversity of benthic invertebrates and bioprospecting in icelandic waters. *Phytochem. Rev.* 12, 517–529. doi: 10.1007/s11101-012-9243-7

OSPAR (2010a). *Descriptions of Habitats on the OSPAR List of Threatened and/or Declining Species and Habitats. OSPAR Agreeement 2008-07*. Ospar Comission.

OSPAR (2010b). *OSPAR List of Threatened and/or Declining Species and Habitas. OSPAR Agreement 2008-6*. Ospar Comission.

Penney, A. J. and Guinotte, J. M. (2013). Evaluation of New Zealand's high-seas bottom trawl closures using predictive habitat models and quantitative risk assessment. *PLoS ONE* 8:e82273. doi: 10.1371/journal.pone.0082273

Phillips, S., Anderson, R., and Schapire, R. (2006). Maximum entropy modeling of species geographic distributions. *Ecol. Model.* 190, 231–259. doi: 10.1016/j.ecolmodel.2005.03.026

Phillips, S., Dudík, M., Elith, J., Graham, C., Lehmann, A., Leathwick, J., et al. (2009). Sample selection bias and presence-only distribution models: implications for background and pseudo-absence data. *Ecol. Appl.* 19, 181–197. doi: 10.1890/07-2153.1

Phillips, S. J., Anderson, R. P., Dudík, M., Schapire, R. E., and Blair, M. E. (2017). Opening the black box: an open-source release of maxent. *Ecography* 40, 1–7. doi: 10.1111/ecog.03049

Piechaud, N., Downie, A., Stewart, H. A., and Howell, K. L. (2015). The impact of modelling method selection on predicted extent and distribution of deep-sea benthic assemblages. *Earth Environ. Sci. Trans. R. Soc. Edinburgh* 105, 251–261. doi: 10.1017/S1755691015000122

Piepenburg, D., and Müller, B. (2004). Distribution of epibenthic communities on the great meteor seamount (North-East Atlantic) mirrors pelagic processes. *Arch. Fish. Mar. Res.* 51, 55–70.

R Core Team (2019). *R: A Language and Environment for Statistical Computing*. Vienna: R Foundation for Statistical Computing.

Radosavljevic, A., and Anderson, R. P. (2014). Making better maxent models of species distributions: complexity, overfitting and evaluation. *J. Biogeogr.* 41, 629–643. doi: 10.1111/jbi.12227

Ramirez-Llodra, E., Tyler, P., Baker, M., Bergstad, O., Clark, M., Escobar, E., et al. (2011). Man and the last great wilderness: human impact on the deep sea. *PLoS ONE* 6:e22588. doi: 10.1371/journal.pone.0022588

Rengstorf, A. M., Grehan, A., Yesson, C., and Brown, C. (2012). Towards high-resolution habitat suitability modeling of vulnerable marine ecosystems in the deep-sea: resolving terrain attribute dependencies. *Mar. Geodesy* 35, 343–361. doi: 10.1080/01490419.2012.699020

Rengstorf, A. M., Yesson, C., Brown, C., and Grehan, A. J. (2013). High-resolution habitat suitability modelling can improve conservation of vulnerable marine ecosystems in the deep sea. *J. Biogeogr.* 40, 1702–1714. doi: 10.1111/jbi.12123

Roberts, E., Mienis, F., Rapp, H., Hanz, U., Meyer, H., and Davies, A. (2018). Oceanographic setting and short-timescale environmental variability at an arctic seamount sponge ground. *Deep Sea Res. Part I Oceanogr. Res. Pap.* 138, 98–113. doi: 10.1016/j.dsr.2018.06.007

Roberts, J., Wheeler, A., Freiwald, A., and Cairns, S. (2009) *Cold-Water Corals. The Biology and Geology of Deep-Sea Coral Habitats*. Cambridge: Cambridge University Press, 334.

Rooper, C. N., Wilborn, R., Goddard, P., Williams, K., Towler, R., and Hoff, G. R. (2018). Validation of deep-sea coral and sponge distribution models in the Aleutian Islands, Alaska. *ICES J. Mar. Sci.* 75, 199–209. doi: 10.1093/icesjms/fsx087

Ross, R. E., and Howell, K. L. (2013). Use of predictive habitat modelling to assess the distribution and extent of the current protection of 'listed' deep-sea habitats. *Divers. Distrib.* 19, 433–445. doi: 10.1111/ddi.12010

Ross, S. W., Carlson, M. C., and Quattrini, A. M. (2012). The utility of museum records for documenting distributions of deep-sea corals off the Southeastern United States. *Mar. Biol. Res.* 8, 101–114.

Rowden, A., Stephenson, F., Clark, M., Anderson, O., Guinotte, J., Baird, S., et al. (2019). Examining the utility of a decision-support tool to develop spatial management options for the protection of vulnerable marine ecosystems on the high seas around New Zealand. *Ocean Coast. Manage.* 170, 1–16. doi: 10.1016/j.ocecoaman.2018.12.033

Rowden, A. A., Anderson, O. F., Georgian, S. E., Bowden, D. A., Clark, M. R., Pallentin, A., and Miller, A. (2017). High-resolution habitat suitability models for the conservation and management of vulnerable marine ecosystems on the louisville seamount chain, South Pacific Ocean. *Front. Mar. Sci.* 4:335. doi: 10.3389/fmars.2017.00335

Schlacher, T. A., Baco, A. R., Rowden, A. A., O'Hara, T. D., Clark, M. R., Kelley, C., et al. (2014). Seamount benthos in a cobalt-rich crust region of the central pacific: conservation challenges for future seabed mining. *Divers. Distrib.* 20, 491–502. doi: 10.1111/ddi.12142

Skagseth, Ø., and Mork, K. A. (2012). Heat content in the norwegian sea, 1995–2010. *ICES J. Mar. Sci.* 69, 826–832. doi: 10.1093/icesjms/fss026

Sundahl, H. (2017). *Driving forces in the distributions of the three most common deep-water coral species in Norway: Lophelia pertusa, Paragorgia arborea, and Primnoa resedaeformis* (Master?s Thesis). University of Bergen, Bergen, Norway.

Tendal, O. S., and Barthel, D. (1993). Chondrocladia gigantea (demospongiae)-the giant clubsponge of the northeast atlantic. *Deep Sea Newslett.* 20, 12–15.

Thiem, Ø., Ravagnan, E., Fosså, J., and Berntsen, J. (2006). Food supply mechanisms for cold-water corals along a continental shelf edge. *J. Mar. Syst.* 60, 207–219. doi: 10.1016/j.jmarsys.2005.12.004

Thresher, R., Althaus, F., Adkins, J., Gowlett-Holmes, K., Alderslade, P., Dowdney, J., et al. (2014). Strong depth-related zonation of megabenthos on a rocky continental margin (700–4000 m) off Southern Tasmania, Australia. *PLoS ONE* 9:e85872. doi: 10.1371/journal.pone.0085872

Tracey, D., Rowden, A., Mackay, K., and Compton, T. (2011). Habitat-forming cold-water corals show affinity for seamounts in the New Zealand region. *Mar. Ecol. Prog. Ser.* 430, 1–22. doi: 10.3354/meps09164

Vierod, A. D., Guinotte, J. M., and Davies, A. J. (2014). Predicting the distribution of vulnerable marine ecosystems in the deep sea using presence-background models. *Deep Sea Res. Part II Top. Stud. Oceanogr.* 99, 6–18. doi: 10.1016/j.dsr2.2013.06.010

Voet, G., Quadfasel, D., Mork, K. A., and Søiland, H. (2010). The mid-depth circulation of the nordic seas derived from profiling float observations. *Tellus A Dyn. Meteorol. Oceanogr.* 62, 516–529. doi: 10.1111/j.1600-0870.2010.00444.x

Warren, D. L., Glor, R. E., and Turelli, M. (2008). Environmental niche equivalency versus conservatism: quantitative approaches to niche evolution. *Evolution* 62, 2868–2883. doi: 10.1111/j.1558-5646.2008.00482.x

Warren, D. L. and Seifert, S. N. (2011). Ecological niche modeling in maxent: the importance of model complexity and the performance of model selection criteria. *Ecol. Appl.* 21, 335–342. doi: 10.1890/10-1171.1

Warren, D. L., Wright, A. N., Seifert, S. N., and Shaffer, H. B. (2014). Incorporating model complexity and spatial sampling bias into ecological niche models of climate change risks faced by 90 California vertebrate species of concern. *Divers. Distrib.* 20, 334–343. doi: 10.1111/ddi.12160

Watts, M. E., Stewart, R. R., Martin, T. G., Klein, C. J., Carwardine, J., and Possingham, H. P. (2017). "Systematic conservation planning with marxan," in *Learning Landscape Ecology* eds S. Gergel and M. Turner (New York, NY: Springer), 211–227.

Weatherall, P., Marks, K. M., Jakobsson, M., Schmitt, T., Tani, S., Arndt, J. E.,et al. (2015). A new digital bathymetric model of the world's oceans. *Earth Space Sci.* 2, 331–345. doi: 10.1002/2015EA000107

Weaver, P., Benn, A., Arana, P., Ardron, J., Bailey, D., Baker, K., et al. (2011). *The impact of deep-sea fisheries and implementation of the UNGA Resolutions 61/105 and 64/72.* Report of an international scientific Workshop, National Oceanography Centre, Southampton.

Westberry, T., Behrenfeld, M., Siegel, D., and Boss, E. (2008). Carbon-based primary productivity modeling with vertically resolved photoacclimation. *Global Biogeochem. Cycles* 22. doi: 10.1029/2007GB003078

Wheeler, A., Bett, B. J., Billett, D. S. M., Masson, D. G., and Mayor, D. (2005). "The impact of demersal trawling on Northeast Atlantic deepwater coral habitats: The case of the Darwin Mounds, United Kingdom," in *Benthic Habitats and the Effects of Fishing*, eds P. Barnes and J. Thomas (Bethesda, MD: American Fisheries Society), 890.

Williams, A., Schlacher, T. A., Rowden, A. A., Althaus, F., Clark, M. R., Bowden, D. A., et al. (2010). Seamount megabenthic assemblages fail to recover from trawling impacts. *Mar. Ecol.* 31, 183–199. doi: 10.1111/j.1439-0485.2010.00385.x

Wilson, M. F. J., O'Connell, B., Brown, C., Guinan, J. C., and Grehan, A. J. (2007). Multiscale terrain analysis of multibeam bathymetry data for habitat mapping on the continental slope. *Mar. Geodesy* 30, 3–35. doi: 10.1080/01490410701295962

Wiltshire, K. H., Tanner, J. E., Althaus, F., Sorokin, S. J., and Williams, A. (2018). Predicting environmental suitability for key benthic species in an ecologically and economically important deep-sea environment. *Deep Sea Res. Part II Top. Stud. Oceanogr.* 157, 121–133. doi: 10.1016/j.dsr2.2018.06.011

Wunderlich, R. F., Lin, Y.-P., Anthony, J., and Petway, J. R. (2019). Two alternative evaluation metrics to replace the true skill statistic in the assessment of species distribution models. *Nat. Conserv.* 35:97. doi: 10.3897/natureconservation.35.33918

Yesson, C., Fisher, J., Gorham, T., Turner, C. J., Hammeken Arboe, N., Blicher, M. E., et al. (2016). The impact of trawling on the epibenthic megafauna of the west greenland shelf. *ICES J. Mar. Sci.* 74, 866–876. doi: 10.1093/icesjms/fsw206.

Yesson, C., Taylor, M. L., Tittensor, D. P., Davies, A. J., Guinotte, J., Baco, A., et al. (2012). Global habitat suitability of cold-water octocorals. *J. Biogeogr.* 39, 1278–1292. doi: 10.1111/j.1365-2699.2011.02681.x

Conflict of Interest: The authors declare that the research was conducted in the absence of any commercial or financial relationships that could be construed as a potential conflict of interest.

frontiers in Marine Science

ORIGINAL RESEARCH
published: 16 April 2020
doi: 10.3389/fmars.2020.00190

Geomorphometric Seabed Classification and Potential Megahabitat Distribution in the Amazon Continental Margin

Ana Carolina Lavagnino[1], Alex Cardoso Bastos[1], Gilberto Menezes Amado Filho[2†], Fernando Coreixas de Moraes[2], Lais Silva Araujo[3] and Rodrigo Leão de Moura[3]*

[1] Marine Geoscience Laboratory, Departamento de Oceanografia, Universidade Federal do Espírito Santo, Vitória, Brazil, [2] Instituto de Pesquisas Jardim Botânico do Rio de Janeiro, Rio de Janeiro, Brazil, [3] Instituto de Biologia and SAGE-COPPE, Universidade Federal do Rio de Janeiro, Rio de Janeiro, Brazil

OPEN ACCESS

Edited by:
Vincent Lecours, University of Florida, United States

Reviewed by:
Ian David Tuck, National Institute of Water and Atmospheric Research (NIWA), New Zealand
Fantina Madricardo, Italian National Research Council, Italy

***Correspondence:**
Alex Cardoso Bastos
alex.bastos@ufes.br

† Deceased

Specialty section:
This article was submitted to Deep-Sea Environments and Ecology, a section of the journal Frontiers in Marine Science

Received: *12 June 2019*
Accepted: *11 March 2020*
Published: *16 April 2020*

Citation:
Lavagnino AC, Bastos AC, Amado Filho GM, de Moraes FC, Araujo LS and de Moura RL (2020) Geomorphometric Seabed Classification and Potential Megahabitat Distribution in the Amazon Continental Margin. Front. Mar. Sci. 7:190. doi: 10.3389/fmars.2020.00190

The geomorphometry of the northeast portion of the Amazon Shelf, along the Brazilian Equatorial Margin (BEM), off the Amazonas River mouth, was analyzed using the Benthic Terrain Modeler, a spatial analysis technique that defines physical megahabitat classes based on seafloor relief heterogeneities. A compilation of bathymetric data was used to explore a regional level model, and novel high-resolution multibeam data were used to detail specific portions of the region, with emphasis on shelf–slope transitions and shelf-edge reefs. The analyses revealed a complex mosaic of benthic megahabitats that are associated to the shelf's morphology, distance offshore, and sediment discharge and transport. The massive and continuous terrigenous sediment input is associated to a smooth muddy deposit along the inner and mid shelf (Regular Continental Shelf megahabitat). The portions of the shelf that are less influenced by riverine sediment accumulation are rougher and characterized by either sand (Irregular Sand Continental Shelf megahabitat) or carbonate-dominated bottom (Irregular Reef Continental Shelf megahabitat). The most notable difference in terms of morphometric analysis and megahabitats can be observed along the outer shelf and shelf break. The shelf–slope transition megahabitat is marked by ridges in the shelf break and by a more acute depth gradient that forms a distinct outer shelf edge. Three different alongshore sectors were explored in order to describe the heterogeneous megahabitat mosaic in terms of slope and bottom morphology. The western-most sector (S3) is remarkable due to an indistinct separation between ridges and the outer shelf edge, as well as for presenting reefs with up to 20 m high, between 110- and 210-m water depths. The central sector (S2) presents no shelf break and lacks ridges, a feature that seems associated with the long-term sediment accumulation associated to the Amazon Fan. The southern-most sector (S1) does not present an outer shelf edge, only ridges, and presents a number of channels incised in the shelf, comprising an erosive area with sediment bypass across the shelf, and carbonate sedimentation. The continental slope is a vastly diverse domain

that may be further divided into a Featured Slope megahabitat with numerous canyons and ravines and a vast area that lacks such features, including a Shallow Gentle Slope megahabitat (<2,000-m water depth), a Steep Slope megahabitat, and a Deep Gentle Slope megahabitat. Our results confirm the usefulness of geomorphometric analyses to define benthic megahabitats and can be used as a starting point in a much-needed marine spatial planning process for the area.

Keywords: Benthic Terrain Modeler, benthic megahabitats, mesophotic reefs, drowned reefs, shelf-edge reefs

INTRODUCTION

The Brazilian Equatorial Margin (BEM) is the widest portion of the Brazilian continental margin and comprises, among others, the Foz do Amazonas Basin, with approximately 360,000 km^2 (Brandão and Feijó, 1994; Silva et al., 1999; Figueiredo et al., 2007). Here, we refer to this part of the BEM as the Amazon Continental Margin (ACM) (Cruz et al., 2019). The modern set of this margin was established at 2.5 Ma (early-Pleistocene) and evolved based on the reshape of the Amazon River due to the Andean uplift event during the Miocene (∼10 Ma) (Hoorn et al., 1995; Campbell, 2005; Figueiredo et al., 2009; Gorini et al., 2014). This event, progressively, gave away the predominance of a mixed and carbonate platform (Neogene Amapá carbonates) to a siliciclastic-dominated shelf, contributing to the development of the Amazon Fan (Milliman et al., 1975; Brandão and Feijó, 1994; Gorini et al., 2014). Cruz et al. (2019) show that mixed carbonate–siliciclastic sedimentation change spatially during the Neogene. An aggrading mixed shelf predominated across the entire Foz do Amazonas shelf during 24 and 8 Ma, with carbonates production giving away to siliciclastic sedimentation along the SE and Central shelves. Carbonate sedimentation was restricted to the NW shelf between 8 and 5.5 Ma. Continuous terrigenous sediment input from the Amazon river progressively buried the inner shelf carbonates, and carbonate sedimentation occurred in the NW outer shelf until 3.7 Ma (Cruz et al., 2019). In addition, low stand sea level during the Miocene was responsible for exposing, karstifying, and eroding carbonate deposits. Later on, from Mid-Pleistocene to Holocene, progradation produced a steeper slope prone to failure. Gravitational tectonics was responsible for mass wasting events, forming large megaslides, or mass-transport complexes that mobilized kilometer-thick deposits, extending for thousands of kilometers in the Amazon Fan (Reis et al., 2016).

Sedimentation along the ACM is highly influenced by the Amazon River, which is responsible for approximately 20% of the global riverine discharge to the ocean (Coles et al., 2013) and a sediment discharge of approximately 10 billion tons per year, developing a fine-grained submerged delta over an area of 3.3×10^5 km^2 (Meade et al., 1979; Kuehl et al., 1986; Nittrouer et al., 1986; Nittrouer and DeMaster, 1996). The Amazon River plume is superficial (25-m maximum depth) and driven by seasonal winds and by the North Brazilian Current (NBC), which flows northwestward into the Caribbean and retroflects eastward during September and October (Nittrouer and DeMaster, 1996). The main depocenter is largely driven by the NBC flow and occurs northwestward of the Amazon River mouth, off Amapá state. This plume and sediment dispersion dynamics is typically interglacial (highstand sea level) (Milliman et al., 1975, 1982; Nittrouer and DeMaster, 1986). During glacial (lowstand), sediment load bypasses the shelf break and is transported to the deep sea through various canyons and channels (Damuth and Fairbridge, 1970; Damuth and Kumar, 1975; Milliman et al., 1975; Damuth and Flood, 1984; Damuth et al., 1988) and may favor the active growth of biogenic carbonate structures on the outer shelf (Barreto et al., 1975; Milliman and Barretto, 1975a,b; Kumar et al., 1977; Moura et al., 2016).

The ACM is a promising area for the oil and gas industry, as part of the "Deep Water Golden Triangle" in the Atlantic Ocean (Brazil, Gulf of Mexico, and West Africa). These geologically similar margins comprise large accumulations of oil with high commercial value (Milani et al., 2001). More than a hundred exploratory blocks have been auctioned by Brazil since 2012, but environmental licensing is still a matter of discussion and concern (e.g., Francini-Filho et al., 2018), largely due to the recently mapped reef system off the Amazon mouth (Cordeiro et al., 2015; Moura et al., 2016).

Since the 1950s, there has been a vast amount of survey effort to characterize the stratigraphy and sediment dynamics of this margin, including the continental shelf (Milliman et al., 1975; Nittrouer et al., 1996) and slope (Reis et al., 2010; Silva et al., 2010; Gorini et al., 2014). However, a regional analysis of the geomorphology within the shelf–slope–rise transition was still lacking. Besides being relevant to understand the distribution of distinct seabed sedimentary features, such as an improved characterization of the benthic habitat mosaic off the Amazon mouth is an essential component for the development of an adequate marine spatial planning framework.

Considering the expansion of the oil and gas industry in the ACM, the occurrence of mesophotic reefs along the shelf and shelf break (Moura et al., 2016), and even the overestimated size of the "Great Amazon reefs" by Francini-Filho et al. (2018), a quantitative terrain characterization is a powerful tool to map potential benthic habitats based on their morphology (Lecours et al., 2016) and to set the stage for marine spatial planning (e.g., Moura et al., 2013). Herein, a quantitative terrain characterization is used to map potential benthic habitats based on their morphology. The objectives of this contribution are (i) to define the potential megahabitats along the equatorial/ACM; (ii) to investigate if spatial changes in geomorphometric patterns along the continental shelf and slope can be used as a proxy for habitats distribution; and

(iii) discuss the presence and potential formation of shelf-edge reefs.

MATERIALS AND METHODS

The ACM is located along the so-called BEM. A general bathymetric map of the study area is shown in **Figure 1**, with the three defined sectors, based on Moura et al. (2016) and Cruz et al. (2019), which were used to describe the changes in seafloor morphology and habitat distribution.

Bathymetric Data Set

The geomorphometric analyses were based on the Benthic Terrain Model (Walbridge et al., 2018), a modeling tool that indicates the potential occurrence of distinct habitats in terms of relief heterogeneity. A regional model was produced with the database from the Diretoria de Hidrografia e Navegação, Marinha do Brasil (LEPLAC Project). This bathymetric database is a compilation from seismic, single beam, multibeam, and remote sensing data acquired from GEODAS (NOAA Geophysical Data System), GEBCO (General Bathymetric Chart of the Oceans from International Hydrographic Organization and the Intergovernmental Oceanographic Commission, UNESCO), PETROBRAS, and ANP (Brazil's National Petroleum Agency). Data from STRM30_Plus V 7.0 (NASA Shuttle Radar Topography Mission) were used to fill regions lacking *in situ* data. Data validation was carried out by a cross-check verification considering control lines as references, using an Oasis Montaj tool, LevTie Line/Intersections and Rangrid GX/Geosoft. Minimum curvature and a cell size of 1,500 m were employed with Equatorial Mercator Projection and the WGS1984 Datum. Raw xyz data were interpolated using ArcGIS IDW method, originating a 2.5-km grid. Although the most used global dataset is GEBCO_2014, with 30-arc-second grids (900-m resolution), we used the LEPLAC project dataset, with 2-km grid but with comparatively greater accuracy at the regional level. We will refer to this regional bathymetric model as Leplac-DTM.

A detailed multibeam dataset was acquired on July 2017 during an oceanographic cruise with the M/V Alucia, using a Reson 7160 echosounder operating at a nominal frequency of 44 kHz. Backscatter data were not recorded. The survey aimed to detail morphological transitions in shelf–slope areas (**Figure 1**). Data were processed with CARIS HIPS and SIPS software to remove noise and adjust for sound velocity in the water column. Multibeam mosaics were built with a 40-m cell grid size and covered three different sectors of the continental slope. A detailed shelf-edge mosaic with 5-m cell grid size was produced for Sector 3, aiming to detail its reef structures.

Seabed Classes

The Leplac-DTM grid, along with its derivate slope and Bathymetric Position Index (BPI), was used to produce the morphometric analysis with the ArcGIS toolbox Benthic Terrain Modeler 3.0 (BTM), a suite of spatial analysis scripts for seabed classification (Walbridge et al., 2018).

Bathymetric Position Index evaluates elevation differences between a focal point and the mean elevation of its surrounding cells in an annulus, a ring shape bounded by two concentric circles that allow for the exclusion of immediately adjacent cells for measuring mean surrounding elevation (Lundblad et al., 2006; Walbridge et al., 2018). The outer radius multiplied by data resolution defines the scale factor, and the most suitable factor for the analysis is defined by trial and error (Erdey-Heydorn, 2008). Intrinsically scale dependent, BPI differentiates benthic features in both fine and broad scales. For example, at a small BPI neighborhood, a large valley would appear as a flat plain, whereas at a scale of several kilometers, the same area will look like a deep canyon. Combining BPI at fine and broad scales allows for the distinction of a variety of nested features. Positive cell values (greater than surrounding cells' mean) define high elevation areas (crests), negative values define low elevation areas (depressions), and near-zero or equal-to-zero values define flat areas (Weiss, 2001).

As spatial data tend to be auto correlated, the raw BPI has to be standardized to allow classification at almost any scale (Lundblad et al., 2006). The fine scale grid was generated with a scale factor of 5,000, and a broad scale grid was generated with a scale factor of 15,000. These scale factors were chosen on the basis that small seascape features are, on average, 5,000 m across. This is based on thorough observation of the bathymetry prior to BPI calculation.

The final step in the BTM analysis is related to the definition of a dictionary that categorizes the bathymetric BPI and the slope grid into user-defined classes that work within a lower and upper bound of grid units designated by the user (**Table 1**). Negative values mean below the standard deviation, whereas positive values mean above it. For example, in order to classify features such as depressions, the upper bound is set as negative values, whereas to classify positive features (e.g., crests), the lower bound is set as a positive value. An angle threshold of 0.1 was set for the classification of the slope (most of the shelf presents smaller values), with steep and gentle gradients falling above and below this threshold, respectively. In terms of depth, the continental shelf was divided into inner shelf (<40-m depth), mid shelf (40–60 m), outer shelf (60–100 m), and outer shelf edge (100–300 m).

Twelve seabed classes (**Table 1**) were defined based on depth (four classes), slope (two classes), and BPI (six classes). Classes based on depth include inner shelf (<40-m water depth), mid shelf (40–60 m), outer shelf (60–100 m), and outer shelf edge (100- to 300-m water depth). Classes based on slope are Gentle Slope (<0.1°) and Steep Slope (>0.1°). Classes based on BPI include Ridge 1 (crest on broad scales and a plateau where the gradient becomes less gentle), Ridge 2 (crest on both broad and fine scale, evidencing the shelf break or depression edges where the gradient is about to get steeper), Edges (crests on fine scale, associated with depression edges), Depression 1 (depression on both broad and fine scales and representing an axial incision associated with the thalweg of broad scale depressions), Depression 2 (axial incision associated with the thalweg of fine scale depressions), and Flanks (depressions on broad scale, related to depression's walls).

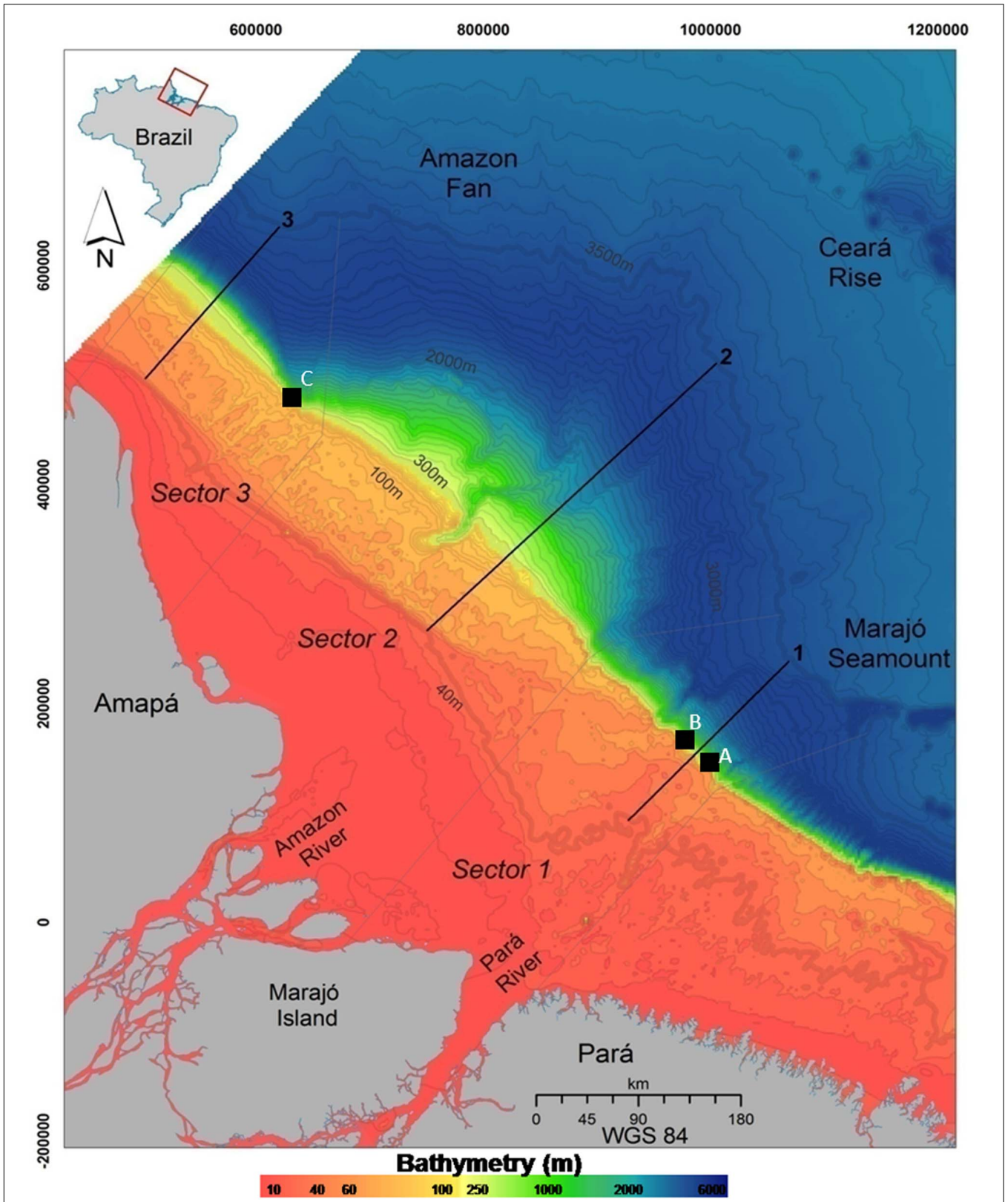

FIGURE 1 | The Brazilian Equatorial Margin (BEM) and the three sectors used in our geomorphometric descriptions. Gray dashed lines are sectors' borders, and black lines correspond to the longitudinal profiles within each sector (from 40- to 3,500-m water depth, thicker isobaths). Isobaths are spaced at each 10 m (up to 300-m water depth) or 100 m (deeper than 300 m). Black squares indicate the location of Multibeam data acquisition. **(A–C)** define the 2017 multibeam survey areas along the shelf edge.

TABLE 1 | BTM dictionary.

	Broad BPI		Fine BPI		Slope		Depth	
	Lower	Upper	Lower	Upper	Lower	Upper	Lower	Upper
(1). Inner shelf	−40	40	−40	40			−40	
(2). Mid shelf	−40	40	−40	40			−60	−40
(3). Outer shelf	−40	40	−40	40			−100	−60
(4). Outer shelf edge	−40	40	−40	40		0.1	−300	
(5). Ridge 1	40		40					
(6). Ridge 2	40		−40	40				
(7). Edges	−40	40	40					
(8). Depression 1		−40		−40				
(9). Flank		−40						
(10). Depression 2				−40				
(11). Gentle slope	−40	40	−40	40		0.1		
(12). Steep slope	−40	40	−40	40	0.1			

Seabed classes were categorized into BPI on both broad and fine scale, slope, and depth using a lower and upper bound. Forty grid units were used, and missing value indicates that the bound is not applicable to the seabed class.

A complementary Aspect Analysis was also carried out in order to analyze the mean orientation of the isobaths. This analysis is also derived from the bathymetric grid and allows for the identification of the downslope direction of the maximum rate of change from each cell to its neighbors, which corresponds to the dipping direction.

Sediment facies were compiled from Dutra's (2018) dataset (based mainly in Kuehl et al., 1996; Moura et al., 2016) and spatially combined in the GIS to produce physical megahabitat classes or seascapes along the ACM.

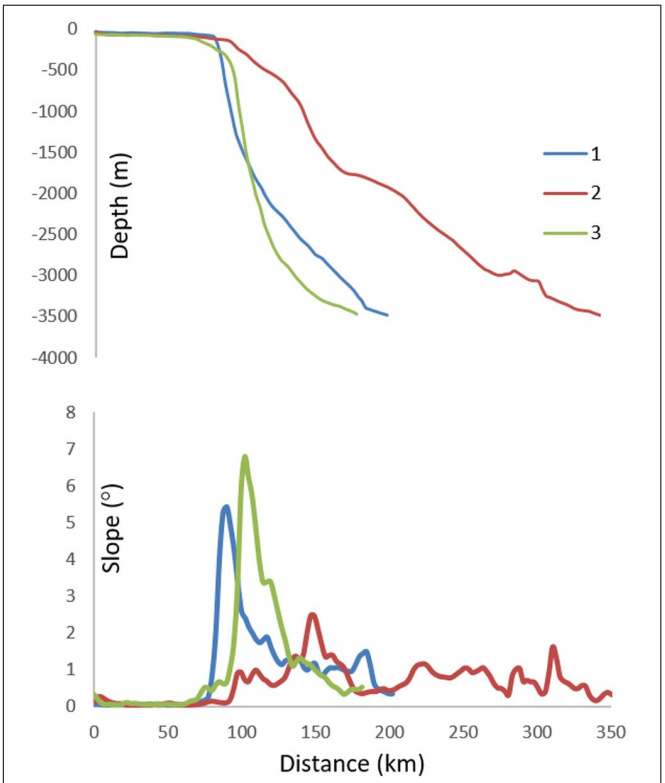

FIGURE 2 | Longitudinal geomorphological profiles from 40- to 3,500-m water depth for each sector (top graph) and corresponding slopes (bottom graph). Sector S1 breaks at approximately 100-m water depth and presents a concave curvature. Sector S2 has no defined break and a convex curvature, and sector S3 breaks at approximately 300-m water depth and shows a sigmoidal curvature.

Shelf–Slope Transitional Features

Features along the transition between the continental shelf and the slope were explored with the Leplac-DTM database and with our primary multibeam data. The Leplac-DTM was used to map individual depressions (canyons and/or incision-like features) on the slope. Classes Depression 1 and Depression 2 were used to set the beginning and the ending of depression features, and isobaths were used to track the axial incisions. Depression metrics were measured using ArcMap 10.1 toolbox and included length (m), sinuosity (length/straight length), area (km^2), minimum depth (m) where canyons start, maximum depth (m) where canyons end, and slope mean (°), this latter a gradient measurement at the canyon thalweg. Slope depressions were classified according to Harris and Whiteway (2011), assuming that canyons are depressions with at least 1000-m depth range, 100-m incision, and heads not deeper than 4,000-m water depth. Canyons can also be categorized as shelf incises or slope-confined canyons. If the feature does not fall within canyon metrics, it was described as a slope-confined depression.

RESULTS

The morphological profiles (**Figure 2**) show the distinct morphological characteristics among the three sectors. Sectors 1 and 3 have an abrupt and well-defined shelf breakpoint, whereas Sector S2 is smoother and lacks a clear shelf breakpoint (**Figure 2**). The distinction between S1 and S3 is related to the depth of the continental shelf break, at 100- and 300-m depth,

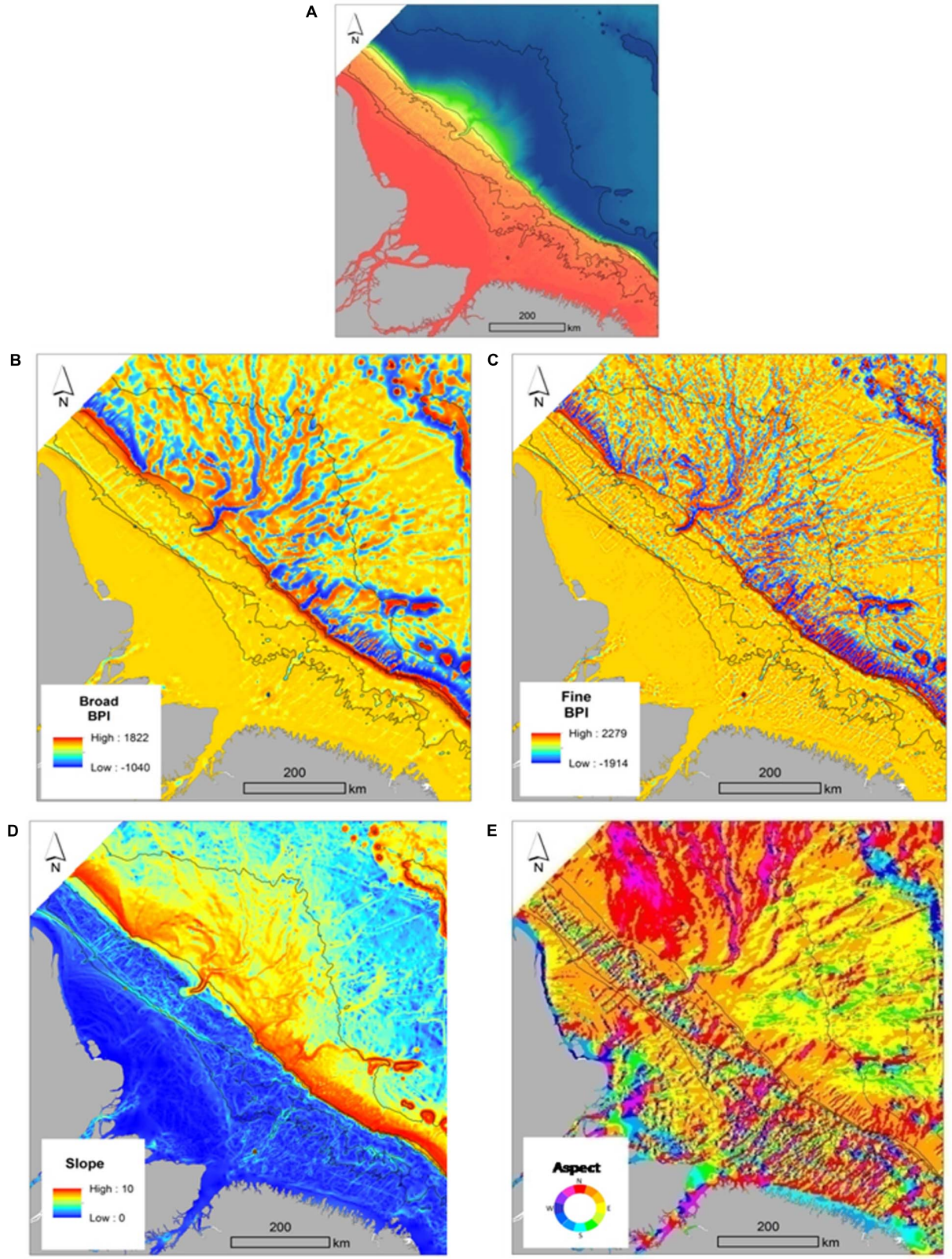

FIGURE 3 | Bathimetric grid **(A)**, Benthic Terrain Model results **(B–D)** and Aspect Grid **(E)**. Inserts **(B)** and **(C)** show the broad and fine BPI, respectively (standardized). Black lines refer to the 40-, 60-, 100-, and 3,500-m water depth isobaths, respectively.

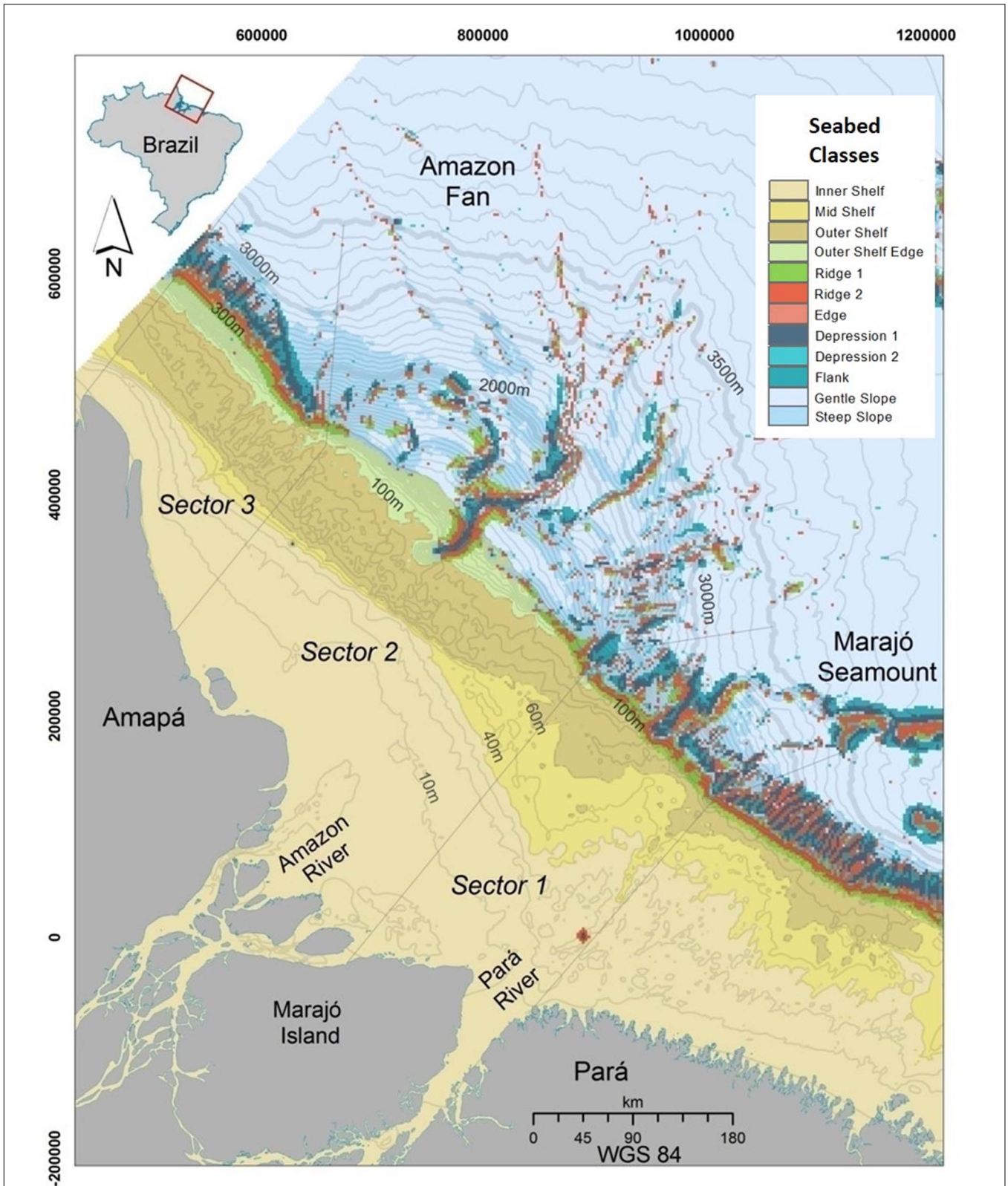

FIGURE 4 | Seabed geomorphometric classes defined with the Benthic Terrain Modeler (BTM). Isobaths are 10-m water depth spaced from the shoreline up to 300 m, and from then on, they are spaced at each 100-m interval (water depth). The thicker isobath represents 300 m, and the last one is set at 3,500 m (water depth).

respectively (**Figure 2**, top graph). Also, the transition in Sector S3 is marked by an outer shelf edge similar to a plateau or terrace, from 100- to 300-m water depth. The continental slope curvatures also differ among sectors, with Sector S1 being convex, S2 concave, and S3 sigmoidal (**Figure 2**, top graph). Slope profiles of Sectors S1 and S3 are flatter on the continental shelf portion and get steeper on the shelf edge, reaching their maximum magnitude at the shelf break zone (<6° for S1, yet >7° for S3), whereas Sector S2 is smooth across its length (<2°; **Figure 2**, bottom graph). Slope is <1° at depths higher than 3,000-m water depth in all sectors (**Figure 2**, bottom graph).

Seabed Classes

The regional bathymetry, together with the BPI models at fine and broad scales, slopes, and Aspect Analysis, results are shown in **Figure 3**, whereas the spatial distribution of the 12 seabed classes derived from the geomorphometric model is shown in **Figure 4**. Crest-related seabed classes are associated with above-mean BPI, depicting the shelf break or depression edges even in steeper regions. Depression-related seabed classes are associated with below-mean BPI, depicting elongated depressions or lower regions. The main attributes of the continental shelf and continental slope at each sector are presented in **Table 2**.

Sector 1

The continental shelf in this southernmost sector is largely flat, apart from valley edges where the slope is steeper but does not exceed 0.21° (**Figure 3C** and **Table 2**). An incise valley from 30- to 60-m depths is a remarkable feature of Sector S1 (**Figure 4**), which also presents a distinct diagonal geometry of isobaths (SE to NW oriented) that ranges from 20- to 40-m water depths. Isobaths are regular in the NW portion of the inner shelf and irregular on its SE portion (**Figure 4** and **Table 2**). Mid Shelf and Outer Shelf isobath geometry also follows the same irregular pattern (**Figure 4** and **Table 2**). Aspect (seabed dipping) on the Inner Shelf is predominantly N–NE, whereas on the Mid Shelf and Outer Shelf, there is no predominant direction (**Figure 3D**). The shelf break is located at ∼100-m water depth and is constituted by a ∼20-km-wide feature that combines seabed classes Ridge 1 and Ridge 2 (**Figure 4**). These same seabed classes form depression edges in deeper areas (**Figure 4**). The 90-km-wide continental slope is steeper (∼7.7°) from 100- to 3,500-m water depth. As depth increases, the slope becomes gentler (<0.1°), with the exception of the Marajó Seamount area (**Figure 3C** and **Table 2**). Seabed dipping orientation is mostly N–NE (**Figure 3D**).

TABLE 2 | Geomorphometric attributes of the continental shelf and continental slope at each sector.

	Sector 1	Sector 2	Sector 3
Continental shelf			
Width	330 km	390 km	230 km
Inner (∼40 m wd)	170 Regular/irregular*	200 Regular*	115 Regular*
Mid (40–60 m wd)	80 Irregular*	10–70** Regular/irregular*	4–20** Regular*
Outer (60–100 m wd)	80 Irregular*	90 Irregular*	80 Irregular*
Outer edge (100–300 m wd)	– Regular*	50 regular*	20 Regular*
Slope range	0–0.21°	0–0.47°	0–0.35°
Shelf break	100 m	No break	300 m
Continental Slope			
Width	90 km	210 km	60 km
Slope range	0.1–7.7°	6.14°	9,1°

*wd, water depth. *Isobaths configuration within the seabed class. **Mid Shelf range width, shown when the wide varies dramatically.*

Sector 2

This sector presents the widest (∼200 km) continental shelf (**Table 2**) and a relatively steep (∼0.47°) slope (**Table 2** and **Figures 3C**, **4**). The Inner Shelf presents a regular isobath geometry and shows the same diagonal pattern as S1 (from SE to NW; **Figure 4** and **Table 2**). The Mid Shelf narrows from 70 to 10 km wide, also from SE to NW (**Figure 4**). The narrower part of the Mid Shelf has a regular geometry, whereas its wider part has an irregular geometry (**Figure 4** and **Table 2**). The Outer Shelf is 90 km wide and depicts an irregular bathymetry pattern (**Figure 4** and **Table 2**). The Outer Shelf Edge (4) is 50 km wide and shows regular isobaths' geometry (**Figure 4** and **Table 2**). Seabed dipping on Sector S2 is similar to that in S1, with a regular N–NE geometry on the Inner Shelf and an irregular geometry with no prevailing direction on the Mid Shelf and Outer Shelf (**Figure 3D**). On the Outer Shelf Edge, the prevailing dipping direction is N–NE. This sector presents no sharp shelf breaking, with the Outer Shelf Edge of the continental slope comprising the 210-km-wide Amazon Fan System, between 300- and 3,500-m water depth. The Amazon Canyon incises at 100-m water depth, and its associated channels can be observed in water depths of up to 3,500 m. The slope varies considerably in this portion of the sector, being steeper on the upper (proximal) end of the fan. While Sector S2 depicts no clear shelf break, Ridge 1 and Ridge 2 seabed classes comprise depressions' edges that combine with seabed class Edges (**Figure 4**). The continental slope seabed orientation is mostly N–NE on the NE side, and N–NW on the NW side (**Figure 3D**).

Sector 3

The continental shelf of Sector S3 is manly flat, with the exception of features recorded on the Mid Shelf and valley edges on the Outer Shelf. The general slope is <0.35° (**Figure 3C** and **Table 2**). Similarly to the other sectors, the Inner Shelf and Mid Shelf seabed classes depict senoidal and parallel isobaths oriented from SE to NW (**Tables 2**, **3**), while the Outer Shelf presents an irregular isobath configuration (**Tables 2**, **3**). The Outer Shelf Edge, together with seabed classes Ridges 1 and 2, represents the shelf break zone at approximately 300-m water depth, being 35 km wide. The continental shelf seabed orientation is mainly N–NE where the isobaths configuration is regular and lacks such a regular orientation in the area with irregular isobaths (**Figure 3D**). The continental slope in Sector S3 is the steepest (9.1°) within the ACM (**Table 2**). Seabed classes

TABLE 3 | Percentage of seabed classes per sector.

	Sector 1		Sector 2		Sector 3	
(1). Inner shelf	38		33		30	
(2). Mid shelf	18		3		4	
(3). Outer shelf	10		10		25	
(4). Outer shelf edge	0.1	66.01%*	3	49%*	6	65%*
(5). Ridge 1	3		2		3	
(6). Ridge 2	4		2		3	
(7). Edges	2	9%*	2	6%*	1	7%*
(8). Depression 1	4		1		4	
(9). Flank	2		1		2	
(10). Depression 2	2	8%*	1	3%*	1	7%*
(11). Gentle slope	10		30		14	
(12). Steep slope	7	17%*	12	42%*	7	21%*

**Sum of above seabed classes.*

Depression 1, Flank and Depression 2 are present but confined to the continental slope. Edge is the only crest-associated seabed class in the continental slope of this sector. Seabed classes Steep Slope and Gentle Slope occur along the continental slope/rise. Seabed dipping orientation is mostly N–NE in the continental slope (**Figure 3**).

Shelf–Slope Transitional Features

A total of 37 depression features were mapped on the Amazon Equatorial Margin (**Figures 5–7** and **Supplementary Table S1**). Sector 1 (**Figure 5** and **Supplementary Table S1**) presented 10 such features, three of which representing shelf incised canyons, one representing a slope-confined canyon, and seven comprising slope-confined depression features. Features 1, 7, and 10 are shelf-incised canyons at 100-m water depth. Canyon 1 is the longest and most sinuous one, reaching more than 3,000-m depth range. Canyon 10 is unique in the ACM for having an associated incising valley (**Figure 4**, inc. valley). At the beginning of Canyons 6 and 7, multibeam data were used to exemplify this shelf slope transition (**Figure 5**). Despite providing different detail levels, both the BTM model and multibeam data detected both the canyon confined at the slope (Canyon 6) and the canyon incising on the continental shelf (Canyon 7).

Sector 2 (**Figure 6** and **Supplementary Table S1**) presented 15 depressions, one of which representing a shelf-incising canyon (Canyon 19). This unique feature is the so-called Amazon Canyon, with 1.840 km^2 and almost 300,000-km length and the only one that cuts the continental shelf. This sector has five slope-confined canyons nearby the Amazon Canyon, whereas the remaining nine canyons are slope confined. Sector 3 (**Figure 7** and **Supplementary Table S1**) presented 12 depressions, one of which represents a slope-confined canyon (Canyon 26). Alongside this canyon, the area mapped with multibeam covered the outer shelf and the continental slope (**Figures 8A,B**) and shows the transition from a gentle (∼0.2°) and irregular outer shelf to a steep (7°) continental slope with gullies and ravines, but lacking major canyons (**Figure 8A**). The irregular features on the Outer Shelf correspond to reef structures between 120- and 200-m water depth, herein represented in five cross-section profiles obtained from the multibeam data (profiles from 1 to 5, **Figure 9**). These structures reached 20 m in height and 450 m in length, occurring in a depth range of 120 to 200 m. Reef structures occurred either as smaller and relatively isolated patches with 10-m heights, generally concentrated in areas shallower than 130-m water depth, or as larger structures that reached 20 m in height and were concentrated in areas deeper than 130-m water depth.

Physical Megahabitats

Although other features (e.g., detailed facies and benthic community) may be considered before a comprehensive megahabitat scheme is proposed for the entire ACM, our results allow for the discrimination of at least eight of such larger compartments, three in the continental shelf, one in the shelf–slope transition, and four within the continental slope.

For the continental shelf, a Regular Mud Continental Shelf megahabitat and an Irregular Continental Shelf, which may be further divided into a Sand and a Reef compartment (**Figure 10**), were defined. The Regular Mud Continental Shelf is composed mainly by flat and irregularly oriented (SE–NW) isobaths in the Inner and Mid Shelf seabed classes, reaching no more than 60-m water depth (**Figure 10**). The Irregular Sand/Reef megahabitat is composed by the rugged parts of the Inner, Mid Shelf, and Outer Shelf seabed classes, in water depths ranging from 20 to 100 m. The slope also indicates greater roughness, and sediment distribution is dominated by sand deposits, rhodolith beds, and reefs (**Figure 10**). Sandy bottom occurs in parts of the Inner Shelf on Sector S1 (eastward of Pará River), on the Mid Shelf on Sectors S1 and S2, and on the Outer Shelf for all sectors (The Mid Shelf in Sector S2 was partially included in the Regular Mud Continental Shelf megahabitat for being part of the Amazon Delta foreset). Conversely, coarse sediments and carbonate structures are frequent on the Outer Shelf.

The shelf–slope transition megahabitat is well defined by the seabed geomorphometric classes that delineate the shelf break (Ridges 1 and 2) at Sectors S1 and S3. Also, the Outer Shelf Edge seabed class plays an important role in the definition of this megahabitat, especially in S3. Even though S2 did not depict a sharp shelf to slope transition, its smoothness could be noticed due to the presence of the Outer Shelf Edge seabed class. This megahabitat is defined by slightly increased slope values, as well as by the regular isobath geometry and N–NE prevailing seabed dipping direction.

Finally, the continental slope was subdivided in terms of the presence/absence of features such as canyons and submarine channels, resulting in four megahabitats: Featured Slope, Shallow Gentle Slope, Steep Slope, and Deep Slope. The Featured Slope megahabitat is defined by the seabed classes associated to depressions (seabed classes Depression 1, Flank, and Depression 2) and crests (Ridge 1, Ridge 2, and Edge seabed classes). The Steep Slope megahabitat occupies the areas surrounding the depressions, where the slope is still higher than 0.1°, whereas the Shallow Gentle Slope megahabitat is found in depths shallower than 2,000 m and the Deep Gentle Slope occurs below 2,000-m depth. Information about sediment facies is scarce for this latter megahabitat.

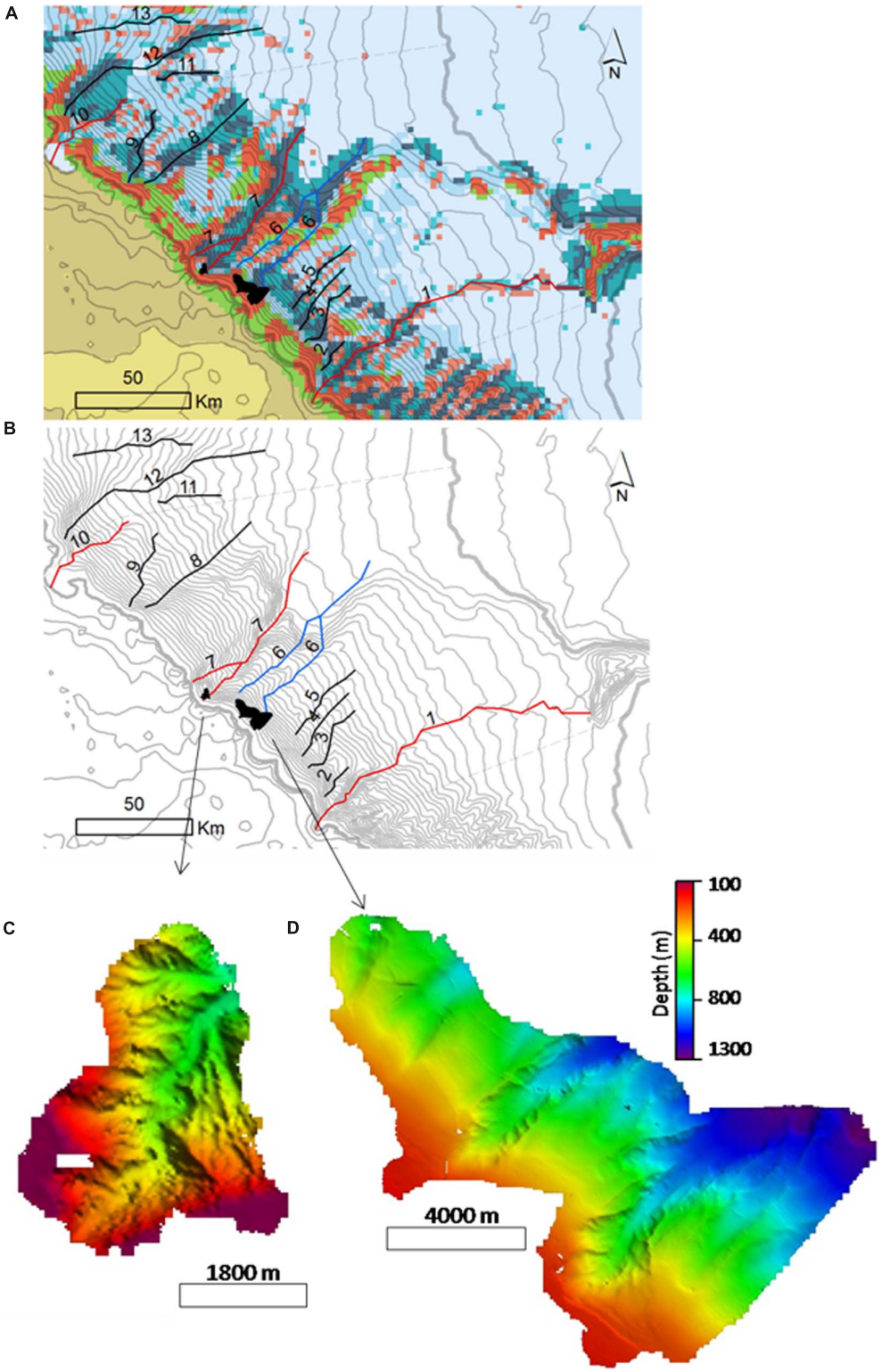

FIGURE 5 | Continental slope depressions in sector S1. Mapping procedures followed the combined methods of delineation by BTM seabed classes thalweg 1 and 2 **(A)**, and the DTM with isobaths spacing each 100-m water depth interval **(B)**. Depression types are distinguished by colors: (1) depressions not classified as canyons and confined at the continental shelf (black lines), (2) slope confined canyons (blue lines), and (3) canyons that incise the continental shelf (red lines). Arrows **(B,C)** show the location of a 40-m resolution multibeam mapped area with examples of canyons incising on the continental shelf **(C)** and canyons confined at the slope **(D)**. Vertical exaggeration 1.

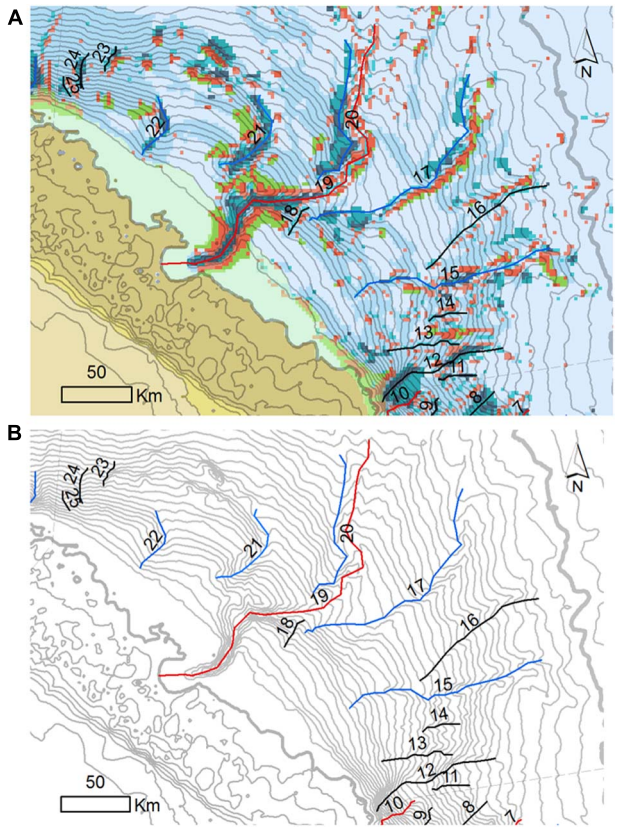

FIGURE 6 | Continental slope depressions in sector S2. Mapping procedures followed the combined methods of delineation by BTM seabed classes thalweg 1 and 2 **(A)**, and the DTM with isobaths spacing each 100-m water depth interval **(B)**. Depression types are distinguished by colors: (1) depressions not classified as canyons and confined at the continental shelf (black lines), (2) canyons that are confined to the continental slope (blue lines), and (3) canyons that incise the continental shelf (red lines).

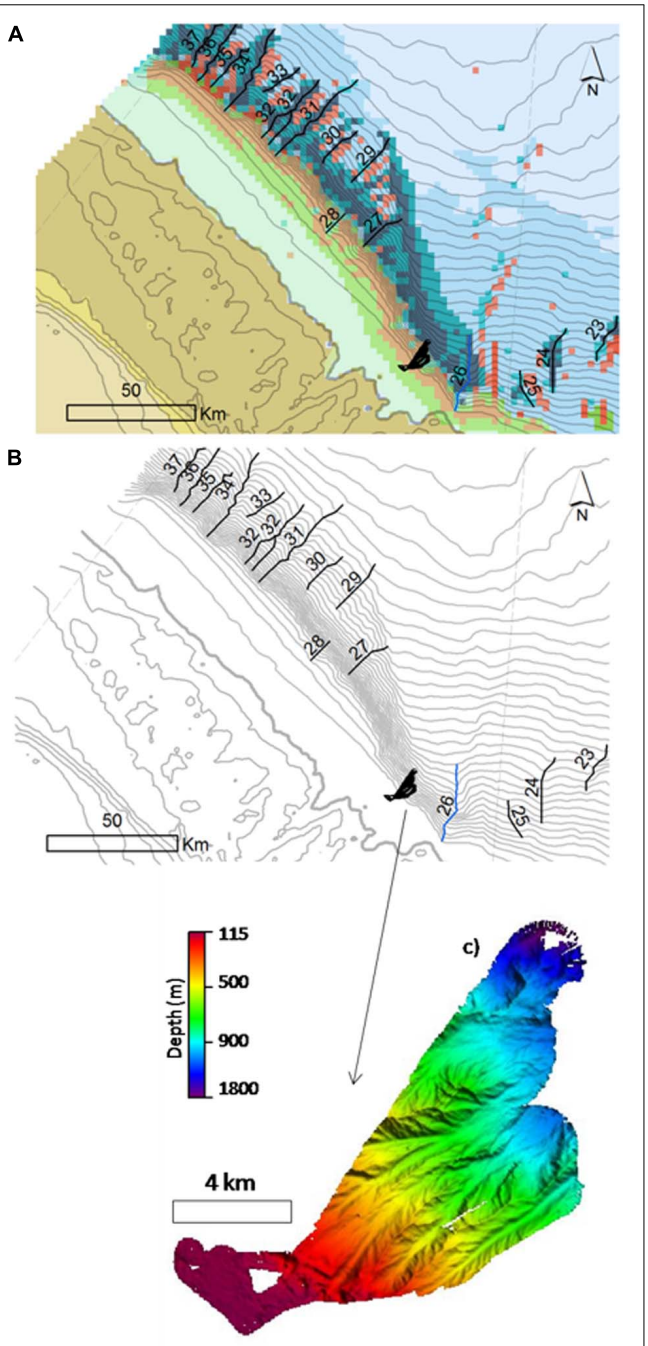

FIGURE 7 | Continental slope depressions in sector S3. Mapping procedures followed the combined methods of delineation by BTM seabed classes thalweg 1 and 2 **(A)**, and the DTM with isobaths spacing each 100-m water depth interval **(B)**. Depression types are discriminated by colors: (1) depressions not classified as canyons and confined at the continental shelf (black lines), (2) canyons that are confined to the continental slope (blue lines), and (3) canyons that incise the continental shelf (red lines). Vertical exaggeration 5.

DISCUSSION

The geomorphometric analysis of a large bathymetric dataset from the ACM allowed for a novel classification of seabed classes and a mosaic of physical benthic megahabitats, that is, large features with dimensions ranging from kilometers to tens of kilometers (Greene et al., 1999). Such seabed heterogeneity is associated to processes and environmental controls acting in different time scales, including mean sea level oscillation, gravity tectonics, and modern sedimentation. Benthic habitat classifications comprise an essential element for the analysis of ecological and fisheries data, once they help organize and describe the environment and its associated biological assemblages in a consistent manner (Costello, 2009).

Megahabitats in the ACM are strongly influenced by the modern sedimentation processes that are largely connected to semidiurnal macrotidal processes, the Amazon River outflow, persistent winds, and the NBC, which is the western boundary geostrophic current that dominates the region (Lentz, 1995; Geyer et al., 1996; Nittrouer and DeMaster, 1996).

In the Inner and Mid Shelf, megahabitats are dominated by muddy sediments (**Figure 10**) and are under a high-energy physical regime that enables unstable benthic habitats

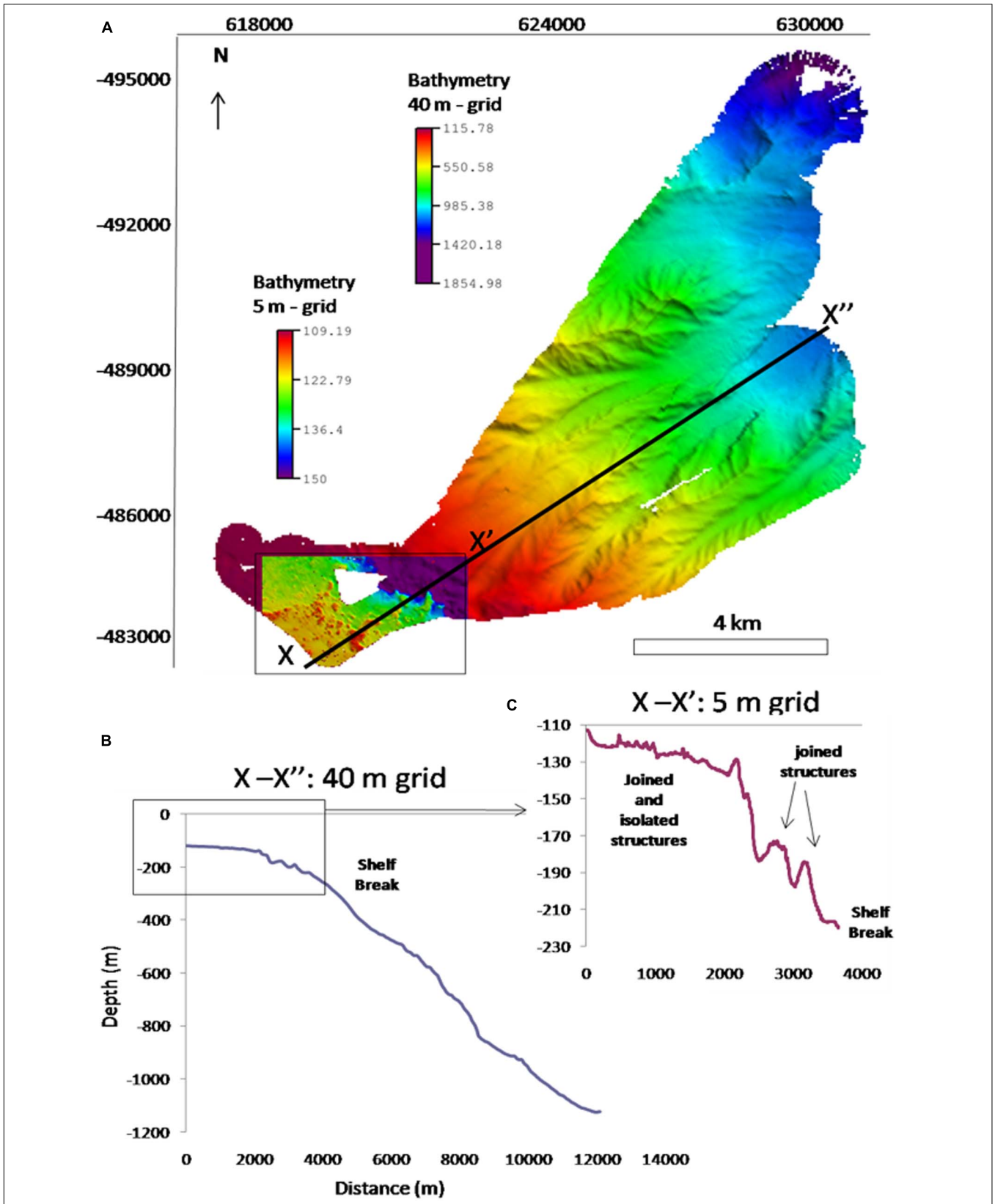

FIGURE 8 | (A) Bathymetric grids from 40- and 5-m resolution, vertical exaggeration of 3; **(B)** longitudinal profiles for the 40-m grid resolution, highlighting the black square—the 5-m grid; **(C)** longitudinal profile showing isolated and joined reefal structures and the shelf break at approximately 250- to 300-m water depth.

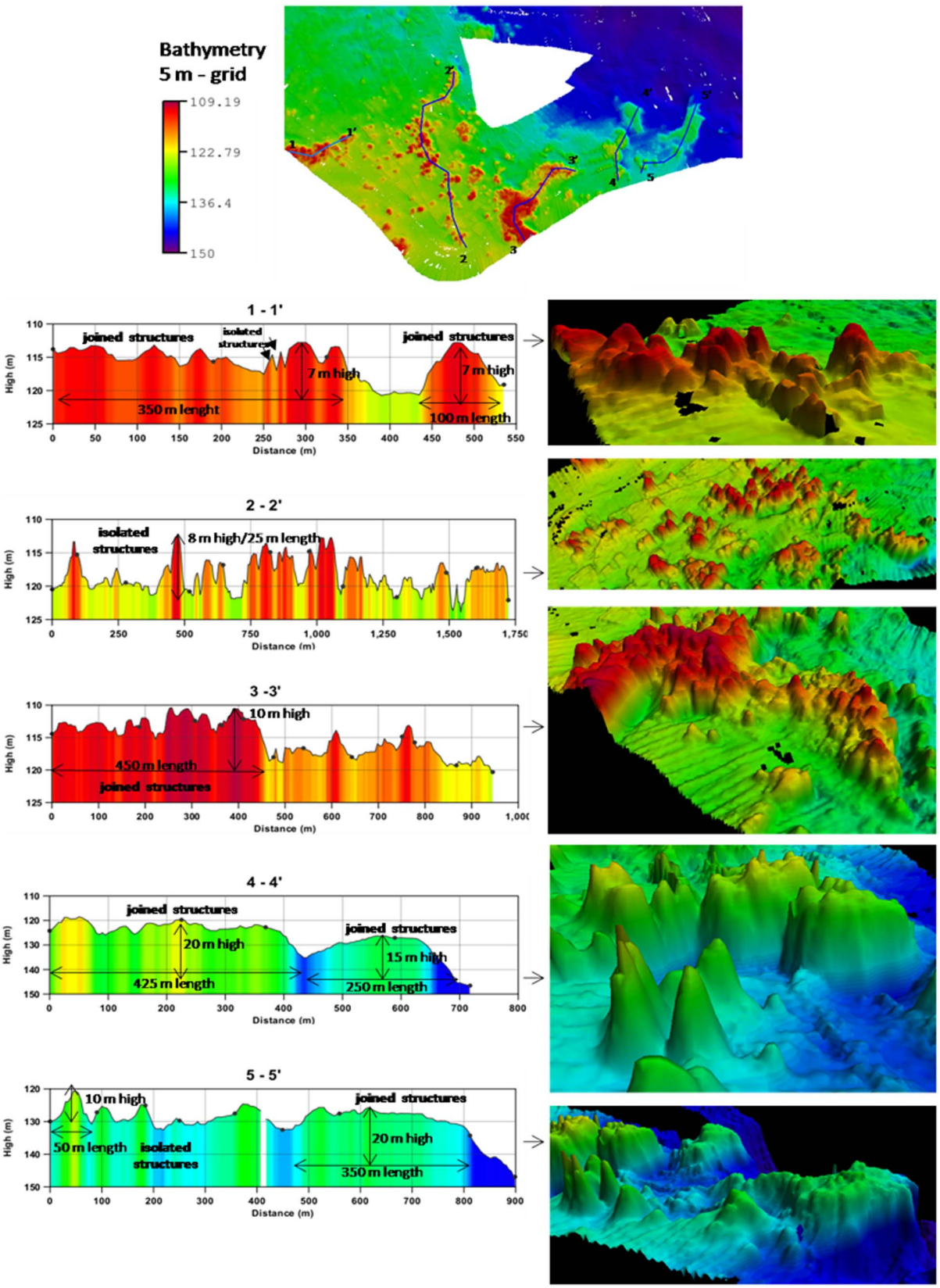

FIGURE 9 | Longitudinal profiles along the 5-m grid (from 1–5).

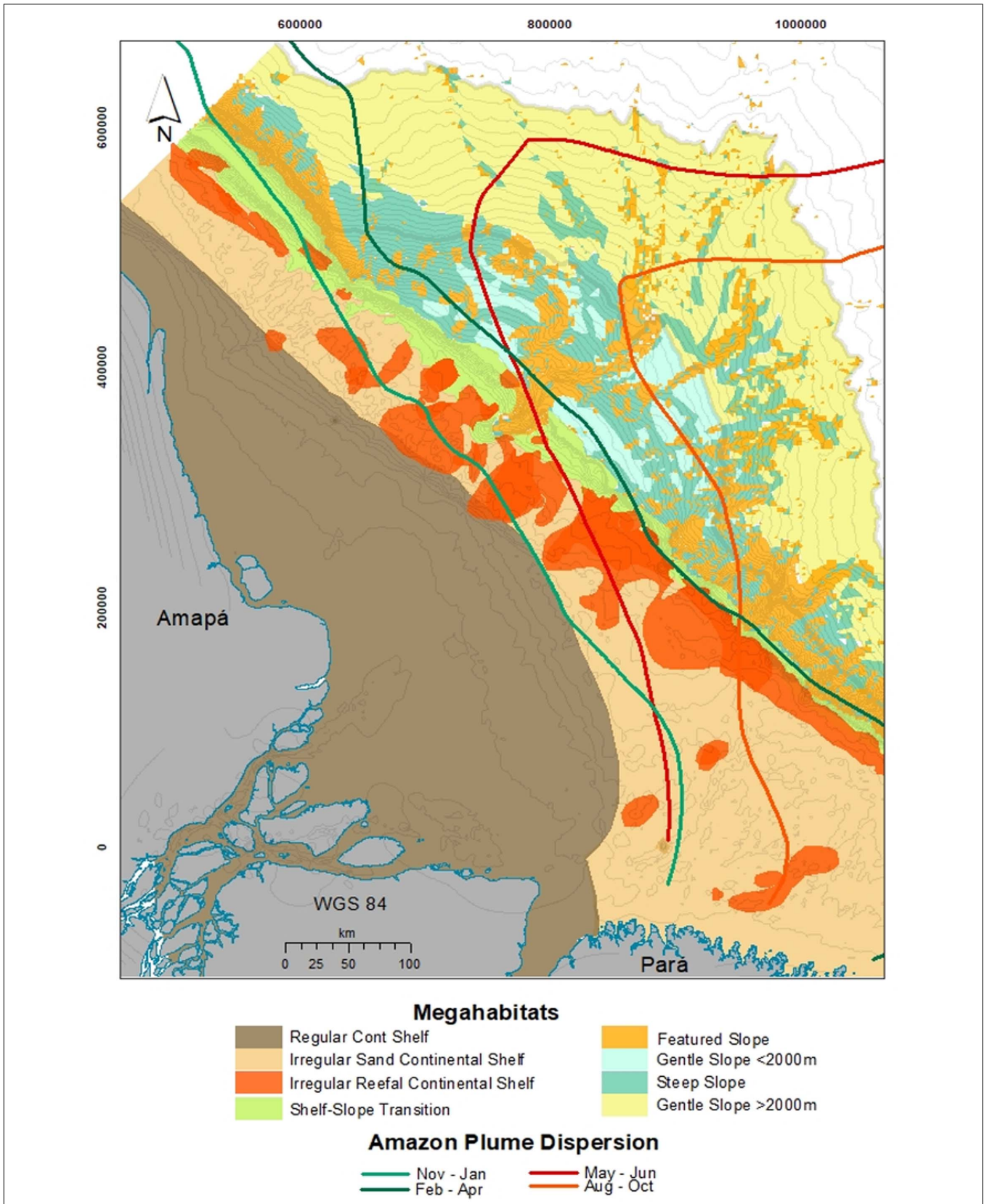

FIGURE 10 | Megahabitats of the Amazon Continental Margin as discriminated by geomorphometric analyzes.

(Nittrouer and DeMaster, 1996). Mass budgets indicate that approximately 6 × 10^6 tons per year of sediment accumulate on the inner shelf, primarily on the outer topset and foreset, at rates exceeding 10 cm/year (Kuehl et al., 1996). The diagonal NW–SE pattern of the sedimentary deposit, which presents a typical clinoform shape of a delta front, is strongly influenced by this complex physical regime (Nittrouer et al., 1996). The isobath configuration of the continental shelf, along with the N–NE prevailing seabed dipping direction, is related to the ongoing development of a clinoform that marks the subaqueous delta, as defined by Nittrouer et al. (1996). The nearly flat Inner Shelf corresponds to the landward portion of a subaqueous Amazon delta (up to 40-m water depth, topset beds), whereas the slightly steeper Mid Shelf on its NW portion, with regular geometry isobaths (S2 and S3 portions, 40- to 60-m water depths), is also part of a submerged delta foreset. The delta bottom set geomorphic feature could be identified in the Outer Shelf seabed class, from 60- to 70-m water depth on Sectors S2 and S3.

The area influenced by the Amazon Plume varies seasonally, with the Regular Continental Shelf megahabitat and part of the Irregular Shelf megahabitat constantly dominated by the Amazon Plume (**Figure 10**). Conversely, the influence of the plume over the Shelf–Slope megahabitat is more seasonal to the east of the Amazon river mouth (Moura et al., 2016). From November to April, the NW flow is associated to the combination of strong trade winds and stronger NBC transport (Geyer et al., 1996), whereas from May to October the plume retroflex eastward due to less trade winds' stress and reduced NBC transport (Geyer et al., 1996). However, 35% of the NBC flow still moves northwestward (Lentz, 1995). As a result of the NBC flow, the Amapá continental shelf (Sector S3) is the greatest sediment depocenter.

The Irregular Sand/Reef megahabitats are under lower influence of sediment input fluvial discharge dominance, together with the strong currents, making this habitat a suitable environment for carbonate occurrence. **Figure 11** shows images of these megahabitats. The outer shelf in Sector S1 is under less influence of the plume, and it is where younger carbonates were observed in comparison to S3, which is under permanent riverine influence (Moura et al., 2016; Vale et al., 2018). The occurrence of carbonate structures in a prevailing turbid environment can be explained by the role played by the NBC (Geyer et al., 1996; Nittrouer and DeMaster, 1996), preventing terrigenous sedimentation from burying reef structures and resulting in the complex hard bottom topography (Moura et al., 2016). Such a low sediment accumulation zone can also be related with a permanent frontal pressure gradient, as well as to Ekman transport associated with the advection of relatively cold and non-turbid waters across the outer and mid shelf (Geyer et al., 1996; Nittrouer and DeMaster, 1996).

The paleovalley observed in Sector S1 is probably associated to Canyon 1 (**Figures 4**, **5A,B**). These features were possibly connected in the last glacial period, when sea level was about 120 m lower than in the present (Milliman et al., 1975). However, the paleovalley associated with the Amazon Canyon (**Figures 4**, **5A,B**; Canyon 19), in Sector S2, is not recognized within our continental shelf dataset. One possible reason for this is related to carbonates' prevalence on S1, which led to the major preservation of paleovalleys. Also, the high sedimentation that subdued this portion of the continental shelf when sea level started to rise (Sommerfield et al., 1995) probably, led to the burial of the channel. In general, the stratigraphic record created on the Amazon shelf is punctuated by hiatuses caused by high-energy conditions and erosional processes occurring at different time scales (Sommerfield et al., 1995; Nittrouer et al., 1996).

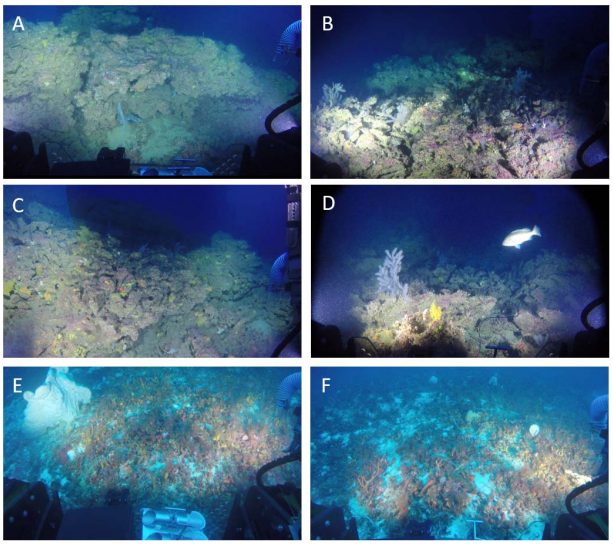

FIGURE 11 | Underwater images **(A–D)** are images from the shelf-edge reef in S3; images **(E,F)** show the rhodolith beds and associated mesophotic community along the mid-outer shelf classes in S1. Photographs taken from a submersible.

The shelf break in the shelf–slope transition varies significantly among sectors, from approximately 100-m water depth at Sector S1 (concave curvature) to 300-m water depth at S3 (sigmoidal), whereas in S2 (convex) there is no defined shelf break. The continental shelf enlargement from Sectors S1 to S3 can be explained by the predominant direction of the Amazon River sediment load. The high load of sediment on Sector S3, since the establishment of the Amazon basin drainage 2.5 Ma BP (Figueiredo et al., 2009; Gorini et al., 2014; Cruz et al., 2019), is associated to its deeper continental shelf (reaching 300-m water depth), whereas the lack of sediment arriving on S1 is associated to a shallower shelf break at approximately 100-m water depth. The shelf–slope transition megahabitat is also dominated by carbonate sedimentation and structures, which are more developed on Sector S1 (Outer Shelf and Shelf-Slope classes) probably due to the lower fluvial dominance. The area mapped with multibeam in Sector S3 showed submerged or drowned structures (**Figures 11A–D**) that possibly constitute an important geological record of sea-level variations and deserve further investigations. Reef building at the edges of continental shelves was common throughout the world during the LGM low stand sea level, with examples in the South Pacific (Flamand et al., 2008), Hawaii (Webster et al., 2004), Caribbean (Blanchon et al., 2002), and Australia (Woodroffe et al., 2010;

Abbey et al., 2011), among others (review in Montaggioni, 2000), and now it is reported in the Equatorial Atlantic margin. The rapid deglaciation process led to high rates of accommodation-space creation, and most of these shelf-edge reefs could not keep up with sea level rise, leaving behind a give-up reef (Neumann and Macintyre, 1985). These reefs are currently distributed from ∼30- to 200-m water depths and are colonized by modern mesophotic benthic assemblages (Hinderstein et al., 2010; Abbey et al., 2011). These reef zones provide structural habitats for a variety of organisms (Hinderstein et al., 2010) and thus are considered by many authors as extensions of shallow reefs and may have biological, physical, and chemical connectivity with the latter, thus having associated communities (Hinderstein et al., 2010; Harris and Whiteway, 2011). In the Great Barrier Reef (GBR), Bridge et al. (2012) showed a depth gradient change in the dominated mesophotic community from photosynthetic organisms in shallower reefs (40 m) to filter feeders dominated in deeper reefs (100 m deep).

In Australia's GBR, Abbey et al. (2013) showed that two generations of mesophotic communities have developed on shelf-edge reefs, one between 13,000 and 10,000 years BP and another from 8,000 years BP to the present. Thus, the reef structures mapped herein at approximately 120 m deep can be interpreted as relict shelf-edge reefs with an associated mesophotic community, as reported by Moura et al. (2016). Although based on a single petrographic analysis from the ACM (Sector S3), Moura et al. (2016) indicated a microfacies of an older grainstone (12,100 ± 30,000 years BP) and composed by filter feeders (polychaetes, foraminifera, barnacles, bryozoans, and mollusks) under a thin veener of coralline algae, which seems to correspond to the situation described by Abbey et al. (2013) for the GBR. The age of the surface of a reef structure at the shelf edge in Sector S3 is 13,382 to 12,749 calibrated years BP (Moura et al., 2016), corresponding to the late stages of the last postglacial maximum transgression. In Sector S1, rhodoliths and calcareous algae reefs are younger, dated from 4,487 calibrated years BP to modern ages (Moura et al., 2016; Vale et al., 2018). This longshore trend shows the shutdown gradient of the reefs, from marginal reef growth and recent shutdown in Sector S1 to a persistent turn off state during thousands of years in Sector S3. Reef growth off the Amazon mouth during the LGM seems to be associated to the bypass of sediments to the deep sea, through an active Amazon Submarine Canyon, and also to the turning off of the muddy channels in the shelf (Gorini et al., 2014; Cruz et al., 2019), enabling shallow water biogenic and oolitic carbonates accumulation off the Amazon River. Considering that there are living mesophotic communities (**Figure 11**), the growth of reef structures is active along part of the ACM but, possibly, with very small growth rates. The reefs, including the rhodolith beds, support highly diverse associated mesophotic communities and relevant ecosystem services (Collette and Rutzler, 1977; Cordeiro et al., 2015; Moura et al., 2016). Indeed, most reef fisheries in the ACM (lobsters and snappers) are carried out in and near these structures (Moura et al., 2016).

In terms of slope-transition habitats, the types of depressions (morphometric features) vary markedly among sectors. Sectors S1 and S3 are erosive, whereas sector S2 is non-erosive. Gravity tectonics was the main driver responsible for shaping the erosive and non-erosive continental slope over the time (Reis et al., 2016). The great amount of sediments that reached the shelf–slope transition through the geological time generates mass movements that lead to steep scarps and mega slides (Silva et al., 2010; Reis et al., 2016). Sediment input is related to the heterogeneous continental slope morphometry among sectors. The slope transition curvature is convex in S2, where most sediment input occurs and where the Amazon Cone was formed. In the erosive part of the region, depressions in S1 begin in shallower waters, approximately 100-m water depth. This is the sector that depicts more canyons incising the continental shelf (Canyons 1, 7, and 10). For instance, depressions in S1 are longer and more sinuous and present lower slope value depressions than those in S3, which begin in deeper water and follow the occurrence of a distinct shelf-edge area in which the shelf breaks at approximately 300-m depth. Depressions in S3 are shorter and less sinuous and present higher slope values than those in S1. In the non-erosive part of the continental slope (Sector S2), the Amazon Canyon is always active during low stand, when the immense amount of sediments caused a turbidity current that was responsible for developing the great canyon (Figueiredo et al., 2009; Gorini et al., 2014). The Amazon Canyon (Canyon 19) is the only depression in S2 that incises the shelf, but five slope-confined canyons are recorded in this sector. Depressions are the most sinuous and present lower slope values. On the NW portion of the Fan, there are fewer and shorter canyons, whereas on the SE portion, canyons are longer. The abrupt distinction of NW and SE portion are associated to N–NW and N–NE seabed dipping orientation, respectively.

The Slope megahabitats comprise a great number of morphometric classes and morphological features associated with canyons and channels, as evidenced in **Figures 4–7**. This makes the ACM Slope classes a potential high-diversity deep-sea habitat, especially when combined with the shelf–slope transition megahabitat. The Features Slope megahabitat (with depressions/canyons) should be prioritized in future assessments targeted at the geobiodiversity of the ACM. The areas where no depressions are observed were classified as the Depression Free Megahabitat. This megahabitat is well defined by the Gentle Slope seabed geomorphometric class. This habitat is in >2,000-m water depth, representing the base of the slope/continental rise and the beginning of the abyssal plain. The deeper areas seem to correspond to the start of sediment accumulation in deep basin (Harris et al., 2014), with gentle slope values and a general lack of other features.

Akin to the continental shelf, which presents a great diversity of facies (Dutra, 2018), the Continental Slope Megahabitat could also be further classified in mesohabitats and macrohabitats if other investigation scales are considered. Considering the important role played by the gravitational tectonics in shaping the seafloor, seafloor higher-resolution data have shown that gravitational collapse is expressed at seabed as ridges formed by paired extensional–compressional belts and thrust faults (Reis et al., 2016; Ketzer et al., 2018). In some areas of the upper slope, gas seeps are observed in association with these faults, which could be another important driver for supporting specific

deep-sea habitats. **Figure 4** depicts a few Steeper Slope Classes in a more distal part of the Amazon Fan. It is possible that changes in slope angle, creating a rough topography, are related to seabed deformation due to the mega mass transport deposits (Reis et al., 2016).

The geomorphometric analysis presented herein revealed novel dimensions of the spatial structuring of megahabitats along cross-shelf and longshore gradients of the ACM. Such marked spatial structuring is largely associated to the interaction of short-mid and long-term geological and oceanographic processes operating in the broad continental shelf and slope off the mouth of the world's largest river. The stronger morphometric heterogeneity found along the Outer Shelf and Outer Shelf Edge megahabitats was also very distinct among the three sectors. Sector S3 is remarkable for presenting the outer shelf edge and ridges together and for encompassing the significant erosive reef structures identified by Moura et al. (2016), which were described herein in greater detail (see **Figures 7–9**, **11**). In a sharp contrast, Sector S2 presents no shelf break and is associated with the long-term sediment accumulation of the Amazon Fan, whereas S1 shows a number of valley incised channels in the shelf, representing an erosive area with main sediment bypass and carbonate sedimentation, especially due to the presence of extensive rhodolith beds. The occurrence of depressions (canyons, ravines, or gullies), especially in Sector S1, adds to the geomorphologic heterogeneity of the shelf–slope transition and the Continental Slope megahabitat, which encompass several macrohabitats.

Besides providing an initial overview of the benthic mosaic of megahabitats in the ACM, our results highlight a number of potential targets for future geodiversity and biodiversity assessments, which are greatly needed for the implementation of a marine spatial planning initiative in this globally relevant region that is under growing pressures from several sectors (oil and gas, fisheries).

CONCLUSION

A digital terrain model allowed us to discriminate eight megahabitats in the ACM: Regular Mud, Irregular Sand, and Carbonate Continental Shelf, Shelf–Slope Transition, Featured Slope, Shallow Gentle Slope (<2,000 m), and Steep Slope, Deep Gentle Slope (>2,000 m). The distribution of these megahabitats is related to distinct geological and oceanographic processes that operate over different time scales.

Megahabitats in the continental shelf are basically controlled by the Amazon River discharge and sediment input, especially the Regular Mud Continental Shelf megahabitat, which comprises the main depocenter in Sector S3. The Irregular Sand/Carbonate Continental Shelf megahabitat is seasonally influenced by the Amazon plume and, along the outer shelf, is influenced by the strong flow of the NBC, which enables carbonate production, the formation of large sand waves, and the persistence of unburied reef structures.

The shelf–slope transition megahabitat varies significantly along the shelf break due to long-term sediment accumulation, river incisions, and gravitational tectonics. The shelf break depth varies among all the sectors from approximately 100-m water depth at Sector S1 down to 300-m water depth at S3, where the outer shelf edge is well defined and the shelf lacks incised valleys. Sector S2 represents the transition to the Amazon fan, which is the most important long-term sediment pathway to the slope and rise.

The Featured Slope megahabitat is formed by channel incisions (canyons, ravines, or gullies) and megaslides. Akin to the shelf–slope transition megahabitat, Sector S2 is very distinct, as it comprises the Amazon Fan and the Amazon deep channel. This is the most diverse habitat and comprises the greatest number of seabed classes defined by the terrain analysis. Megahabitats Shallow Gentle Slope (<2,000 m), Steep Slope, and Deep Gentle Slope (>2,000 m) are less morphologically diverse.

The ACM represents one of the world's most complex and dynamic continental margins, due to its long-term interaction with the Amazon River. In addition, the ACM is under increasing pressure from several sectors (e.g., oil and gas, mining), but comprehensive habitat mapping is still largely incomplete. Our results confirm that geomorphometric analyses comprise a relevant tool to define benthic megahabitats and may be used for triggering a much-needed spatial planning process in the ACM.

DATA AVAILABILITY STATEMENT

The regional bathymetric dataset can be found in the https://www.marinha.mil.br/dhn/q=node/249. The multibeam data is available on request to the corresponding author.

AUTHOR CONTRIBUTIONS

AB, RM, and FM designed the survey and collected the multibeam data. All authors contributed to the writing and review of the manuscript. AL and AB designed the investigation with the BTM. AL conducted the multibeam processing and BTM modeling.

FUNDING

AL had a post-graduate scholarship from CAPES (Ministry of Education, Brazil) to develop this research. Financial support to the acoustic survey and the follow up of AL research was provided by an ANP/Brasoil grant. AB and RM acknowledge CNPq (Ministry of Science, Technology, Innovation and Communications, Brazil) and CAPES/IODP grants. Paulo S. Salomon, Fabio S. Motta, Leonardo M. Neves, and Milton Kampel also provided invaluable field support.

ACKNOWLEDGMENTS

We thank the Brazilian Navy Hydrographic Office for providing the compiled bathymetric dataset. We are also very much thankful to Dalio Philanthropies and OceanX, Woods

Hole Oceanographic Institution and the M/V Alucia Vessel crew for supporting the project and for providing technical assistance with data collection. We dedicate this contribution to the memory of our dear team leader, GA, who passed away in March 2019.

SUPPLEMENTARY MATERIAL

The Supplementary Material for this article can be found online at: https://www.frontiersin.org/articles/10.3389/fmars.2020.00190/full#supplementary-material

REFERENCES

Abbey, E., Webster, J. M., and Beaman, R. (2011). Geomorphology of submerged reefs on the shelf edge of the Great Barrier Reef: the influence of oscillating Pleistocene sea-levels. *Mar Geol.* 288, 61–78. doi: 10.1016/j.margeo.2011.08.006

Abbey, E., Webster, J. M., Braga, J. C., Thorogood, G., Thomas, A. L., Camoin, P. J., et al. (2013). Deglacial mesophotic reef demise on the Great Barrier Reef. *Palaeogeogr. Palaeoclimatol. Palaeoecol.* 392, 473–494. doi: 10.1016/j.palaeo.2013.09.032

Barreto, L. A., Milliman, J. D., Amaral, C. A., and Francisconi, O. (1975). Upper continental margin sedimentation off Brazil, northern Brazil. *Contr. Sedimentol.* 4, 11–43.

Blanchon, P., Jones, B., and Ford, D. C. (2002). Discovery of a submerged relic reef and shoreline off Grand Cayman: further support for an early Holocene jump in sea level. *Sediment Geol.* 147, 253–270. doi: 10.1016/S0037-0738(01)00143-149

Brandão, J. A., and Feijó, F. J. (1994). Bacia foz do amazonas. *Bol. Geoc. Petrobras.* 8, 91–99.

Bridge, T., Beaman, R., Done, T., and Webster, J. (2012). Predicting the location and spatial extent of submerged coral reef habitat in the great barrier reef world heritage area. Australia. *PLoS One* 7:e0048203. doi: 10.1371/journal.pone.0048203

Campbell, A. E. (2005). Shelf-geometry response to changes in relative sea level on a mixed carbonate-siliciclastic shelf in the Guyana Basin. *Sediment. Geol.* 175, 259–275. doi: 10.1016/j.sedgeo.2004.09.003

Coles, V. J., Brooks, M. T., Hopkins, J., Stukel, M., Yager, P., and Hood, R. R. (2013). The pathways and properties of the Amazon river plume in the tropical North Atlantic Ocean. *J. Geophys. Res. Ocean.* 118, 6894–6913. doi: 10.1002/2013JC008981

Collette, B. B., and Rutzler, K. (1977). "Reef fishes over sponge bottoms of the mouth of Amazon River," in *Proceedings of the Third International Coral Reef Symposium*, Miami, FL, 305–310.

Cordeiro, R. T. S., Neves, B. M., Rosa-Filho, J. S., and Pérez, C. D. (2015). Mesophotic coral ecosystems occur offshore and north of the Amazon River. *Bull. Mar. Sci.* 91, 491–510. doi: 10.5343/bms.2015.1025

Costello, M. J. (2009). Distinguishing marine habitat classification concepts forecological data management. *Mar. Ecol. Prog. Ser.* 397, 253–268. doi: 10.3354/meps08317

Cruz, A. M., Reis, A. T., Suc, J. P., Silva, C. G., Praeg, D., Granjeon, D., et al. (2019). Neogene evolution and demise of the Amapá carbonate platform, Amazon continental margin, Brazil. *Mar. Petrol. Geol.* 105, 185–203. doi: 10.1016/j.marpetgeo.2019.04.009

Damuth, J. E., and Fairbridge, R. W. (1970). Equatorial atlantic deep-sea arkosic sands and ice-age aridity in tropical South America. *Geol. Soc. Am. Bull.* 81, 2181–2202. doi: 10.1130/0016-7606197081

Damuth, J. E., and Flood, R. D. (1984). Morphology, sedimentation processes, and growth pattern of the Amazon Deep-Sea Fan. *Geo Mar. Lett.* 3, 109–117. doi: 10.1007/BF02462455

Damuth, J. E., Flood, R. D., Kowsmann, R. O., Belderson, R. H., and Gorini, M. A. (1988). Anatomy and growth pattern of amazon deep-sea fan as revealed by long-range side-scan sonar (GLORIA) and high-resolution seismic studies. *AAPG Bull.* 72:30.

Damuth, J. E., and Kumar, N. (1975). Amazon cone: morphology, sediments, and growth pattern. *Geol. Soc. Am. Bull.* 86, 863–878.

Dutra, L. (2018). *Growing Industrialization Challenges Biodiversity Conservation And Natural Resources Management In The Amazon Shelf Off Brazil*. Dissertação de Mestrado, Universidade Federal do Rio de Janeiro, Brasil.

Erdey-Heydorn, M. (2008). An ArcGIS seabed characterization toolbox developed for investigating benthic habitats. *Mar. Geod.* 31, 318–358. doi: 10.1080/01490410802466819

Figueiredo, J., Hoorn, C., Van der Ven, P., and Soares, E. (2009). Late miocene onset of the amazon river and the amazon deep-sea fan: evidence from the foz do amazonas Basin. *Geology* 37, 619–622. doi: 10.1130/G25567A.1

Figueiredo, J., Zálan, P. V., and Soares, E. F. (2007). Bacia da Foz do Amazonas. *Bol. Geociências Petrob.* 15, 299–309.

Flamand, B., Cabioch, G., Payri, C., and Pelletier, B. (2008). Nature and biological composition of the New Caledonian outer barrier reef slopes. *Mar. Geol.* 250, 157–179. doi: 10.1016/j.margeo.2007.12.002

Francini-Filho, R., Asp, N., Siegle, E., Hocevar, J., Lowyck, K., D'Avila, N., et al. (2018). Perspectives on the great amazon reef: extension. biodiversity and threats. *Front. Mar. Sci.* 5:142. doi: 10.3389/fmars.2018.00142

Geyer, W., Beardsley, R. C., Lentz, S. J., Candela, J., Limeburner, R., Johns, W. E., et al. (1996). Physical oceanography of the Amazon shelf. *Cont. Shelf Res.* 16, 575–616. doi: 10.1016/0278-4343(95)00051-8

Gorini, C., Haq, B. U., dos Reis, A. T., Silva, C. G., Cruz, A. M., Soares, E., et al. (2014). Late neogene sequence stratigraphic evolution of the foz do amazonas basin. Brazil. *Terra Nov.* 26, 179–185. doi: 10.1111/ter.12083

Greene, G., Yoklavich, M., Starr, R., O'Connell, V., Wakefield, W., Sullivan, D., et al. (1999). A classification scheme for deep seafloor habitats. *Oceanol. Acya* 22, 663–678. doi: 10.1016/s0399-1784(00)88957-4

Harris, P. T., Macmillan-Lawler, M., Rupp, J., and Baker, E. K. (2014). Geomorphology of the oceans. *Mar. Geol.* 352, 4–24. doi: 10.1016/j.margeo.2014.01.011

Harris, P. T., and Whiteway, T. (2011). Global distribution of large submarine canyons: geomorphic differences between active and passive continental margins. *Mar Geol.* 285, 69–86. doi: 10.1016/j.margeo.2011.05.008

Hinderstein, L. M., Marr, J. C. A., Martinez, F. A., Dowgiallo, M. J., Puglise, K., Pyle, R. L., et al. (2010). Theme section on "mesophotic coral ecosystems: characterization, ecology, and management." *Coral. Reefs* 29, 247–251. doi: 10.1007/s00338-010-0614-5

Hoorn, C., Guerrero, J., Sarmiento, G., and Lorente, M. (1995). Andean tectonics as a cause forchanging drainage patterns in Miocene northern South America. *Geology* 23, 237–240.

Ketzer, J. M., Augustin, A., Rodrigues, L. F., Oliveira, R., Praeg, D., Pivel, M. A. G., et al. (2018). Gas seeps and gas hydrates in the Amazon deep-sea fan. *Geo Mar. Lett.* 38, 429–438. doi: 10.1007/s00367-018-0546-6

Kuehl, S. A., Nittrouer, C. A., Allison, M. A., Faria, L. E. C., Dakut, D. A., Maeger, J. M., et al. (1996). Sediment deposition, accumulation, and seabed dynamics in an energetic fine-grained coastal environment. *Cont. Shelf Res.* 16, 787–815. doi: 10.1016/0278-4343(95)00047-x

Kuehl, S. A., Nittrouer, C. A., and DeMaster, D. J. (1986). Distribution of sedimentary structures in the Amazon subaqueous delta. *Cont. Shelf Res.* 6, 311–336. doi: 10.1016/0278-4343(86)90066-X

Kumar, N., Damuth, J. E., and Gorini, M. A. (1977). Discussion: relict magnesian calcite oolite and subsidence of the Amazon shelf. *Sedimentology* 24, 143–148. doi: 10.1111/j.1365-3091.1977.tb00124.x

Lecours, V., Dolan, M. F. J., Micallef, A., and Lucieer, V. L. (2016). A review of marine geomorphometry, the quantitative study of the seafloor. *Hydrol. Earth Syst. Sci.* 20, 3207–3244. doi: 10.5194/hess-20-3207-2016

Lentz, S. J. (1995). Amazon Plume inferred from historical hydrographic. *J. Geophys. Res.* 100, 2391–2400.

Lundblad, E., Wright, D., and Miller, J. (2006). Classifying benthic terrains with multibeam bathymetry, bathymetric position and rugosity: Tutuila, American Samoa. *Mar. Geodesy.* 29, 89–111.

Meade, R., Rodrigues, F., Carlos, V., and John, E. (1979). Sediment loads in the Amazon River. *Nature* 278:3. doi: 10.1016/j.zool.2016.07.003

Milani, E. J., Brandão, J. A., Zálan, P. V., and Gamboa, L. A. P. (2001). Petróleo na margem continental brasileira: geologia, exploração, resultados e perspectivas. *Braz. J. Geophys.* 18, 351–396.

Milliman, J. D., and Barretto, H. T. (1975a). Relict magnesian calcite oolite and subsidence of the Amazon shelf. *Sedimentology* 22, 137–145. doi: 10.1111/j.1365-3091.1975.tb00288.x

Milliman, J. D., and Barretto, H. T. (1975b). Upper continental margin sedimentation off Brazil. *Contribut. Sedimentol.* 4, 1–10.

Milliman, J. D., Butenko, J., Barbot, J. P., and Hedberg, J. (1982). Depositional patterns of modern Orinoco/Amazon muds on the northern Venezuelan shelf. *J. .Mar. Res.* 40, 643–657.

Milliman, J. D., Summerhayes, C. P., and Barretto, H. T. (1975). Quaternary sedimentation on the amazon continental margin: a model. *Bull. Geol. Soc. Am.* 86, 610–614.

Montaggioni, L. (2000). Post glacial reef growth. *Earth Planet Sci. Lett.* 331, 319–330.

Moura, R. L., Amado-filho, G. M., Moraes, F. C., Brassileiro, P. S., Salomon, P. S., Mahiques, M. M., et al. (2016). An extensive reef system at the Amazon River mouth. *Sci. Adv.* 2, 1–12. doi: 10.1126/sciadv.1501252

Moura, R. L., Secchin, N. A., Amado-Filho, G. M., Francini-Filho, R. B., Freitas, M. O., Minte-Vera, C. V., et al. (2013). Spatial patterns of benthic megahabitats and conservation planning in the Abrolhos Bank. *Continental. Shelf Res.* 70, 109–117. doi: 10.1016/j.csr.2013.04.036

Neumann, A. C., and Macintyre, I. (1985). "Reef response to sea level rise: keep-up, catch-up or give up," in *Proceedings of the 5th International Coral Reef Congress*, Tahiti, 105–110.

Nittrouer, C. A., and DeMaster, D. J. (1986). Sedimentary processes on the Amazon continental shelf: past, present and future research. *Cont. Shelf. Res.* 6, 5–30. doi: 10.1016/0278-4343(86)90051-8

Nittrouer, C. A., and DeMaster, D. J. (1996). The Amazon shelf setting: tropical, energetic, and influenced by a large river. *Cont. Shelf. Res.* 16, 553–573. doi: 10.1016/0278-4343(95)00069-0

Nittrouer, C. A., Kuehl, S. A., DeMaster, D. J., and Kowsmann, R. O. (1986). The deltaic nature of Amazon shelf sedimentation. *Geol. Soc. Am. Bull.* 97, 444–458.

Nittrouer, C. A., Kuehl, S. A., Figueiredo, A. G., Allison, M. A., Sommerfield, C. K., Rine, J. M., et al. (1996). The geological record preserved by Amazon shelf sedimentation. *Cont. Shelf. Res.* 16, 817–841. doi: 10.1016/0278-4343(95)00053-4

Reis, A. T., Araújo, E., Silva, C. G., Cruz, A., Gorini, C., Droz, L., et al. (2016). Effects of a regional décollement level for gravity tectonics on late Neogene to recent large-scale slope instabilities in the Foz do Amazonas Basin. *Brazil. Mar. Pet. Geol.* 75, 29–52. doi: 10.1016/j.marpetgeo.2016.04.011

Reis, A. T., Perovano, R., Silva, C. G., Vendeville, B. C., Araujo, E., Gorini, C., et al. (2010). Two-scale gravitational collapse in the Amazon Fan: a coupled system of gravity tectonics and mass-transport processes. *J. Geol. Soc. Lond.* 167, 593–604. doi: 10.1144/0016-76492009-035

Silva, C. G., Araújo, E., and Reis, A. T. (2010). "Advances in natural and technological hazards research", in *Submarine Mass Movements and Their Consequences*, eds J. Locat, J. Mienert, and L. Boisvert (Dordrecht: Springer Science), 1–540. doi: 10.1007/978-94-010-0093-2

Silva, S. R. P., Maciel, R. R., and Severino, M. C. G. (1999). Cenozoic tectonics of Amazon Mouth Basin. *Geo Mar. Lett.* 18, 256–262. doi: 10.1007/s003670050077

Sommerfield, C. K., Nittrouer, C. A., and Figueiredo, A. G. (1995). Stratigraphic evidence of changes in Amazon shelf sedimentation during the late Holocene. *Mar. Geol.* 125, 351–371. doi: 10.1016/0025-3227(95)00019-U

Vale, N. F., Amado-Filho, G. M., Braga, J. C., Brasileiro, P. S., Karez, C. S., Moraes, F., et al. (2018). Structure and composition of rhodoliths from the Amazon River mouth. *Braz. J. South Am. Earth Sci.* 84, 149–159. doi: 10.1016/j.jsames.2018.03.014

Walbridge, S., Slocum, N., Pobuda, M., and Wright, D. J. (2018). Unified geomorphological analysis workflows with benthic terrain modeler. *Geosciences* 8:94. doi: 10.3390/geosciences8030094

Webster, J. M., Clague, D. A., Riker-Coleman, K., Gallup, C., Braga, J. C., Potts, D., et al. (2004). Drowning of the - 150 m reef off Hawaii: a casualty of global meltwater pulse 1A? *Geology* 32, 249–252. doi: 10.1130/G20170.1

Weiss, A. D. (2001). "Topographic position and landform analysis (poster)," in *Proceedings of the ESRI User Conference*, San Diego, CA.

Woodroffe, C. D., Brooke, B. P., Linklater, M., Kennedy, C., Jones, B. G., Buchanan, C., et al. (2010). Response of coral reefs to climate change: expansion and demise of the southernmost pacific coral reef. *Geophys. Res. Lett.* 37, 1–6. doi: 10.1029/2010GL044067

Conflict of Interest: The authors declare that the research was conducted in the absence of any commercial or financial relationships that could be construed as a potential conflict of interest.

frontiers in Marine Science

ORIGINAL RESEARCH
published: 24 April 2020
doi: 10.3389/fmars.2020.00213

Distribution and Suitable Habitat of the Cold-Water Corals *Lophelia pertusa*, *Paragorgia arborea*, and *Primnoa resedaeformis* on the Norwegian Continental Shelf

Hanna Sundahl[1], *Pål Buhl-Mortensen*[2]* *and Lene Buhl-Mortensen*[2]

[1] Department of Biological Sciences, University of Bergen, Bergen, Norway, [2] Institute of Marine Research, Bergen, Norway

Cold-water corals are habitat-forming species that are also classified as indicators of vulnerable marine ecosystems (VMEs) due to the threat of various anthropogenic impacts, e.g., fisheries and oil/mineral exploration. To best protect VMEs, knowledge of their habitat requirements and distribution is essential. However, comprehensive sampling of the deep sea is difficult due to access and cost constraints, so species distribution modeling (SDM) is often used to predict overall distributions and ecological preferences of species based on limited data. We used Maximum Entropy (Maxent) modeling to predict the probability of presence of the reef-building scleractinian *Lophelia pertusa* and the octocorals *Paragorgia arborea* and *Primnoa resedaeformis* using a total of 2149 coral presence points and 15 environmental predictor variables. The environmental variables used in the analysis were processed to 176 m resolution and included bathymetry, depth, geomorphometric characteristics [slope, aspect, and bathymetric position index (BPI)], oceanography (temperature, salinity, current directions, and speed), surface chlorophyll a concentration, sediment type, and marine landscape type. Comparing presence points with environmental data showed that the temperature and depth range for *Lophelia* was narrower compared to the gorgonians, and it occurred in shallower, warmer water. Observations showed that *Lophelia* had a broad, bimodal response to Broad BPI, while the predicted model indicated a more narrow response. *Paragorgia* tolerated the greatest range of sloping according to the model. All three species were observed with a bimodal pattern along a wide range of mean current speed, while the models indicated a high response to faster current speed. Jackknife tests showed that sediment type was an important predictor for gorgonian corals, while BPI and minimum temperature were more important for *Lophelia*. The spatial precision of the models could be further increased by applying environmental layers with a higher and uniform spatial resolution. The predicted distribution of corals and their relation to environmental variables provides an important background for prioritizing areas for detailed mapping surveys and will aid in the conservation efforts for these VMEs in Norwegian waters and beyond.

Keywords: cold-water corals, Maxent, species distribution modeling, habitat suitability, vulnerable marine ecosystems, *Lophelia pertusa, Paragorgia arborea, Primnoa resedaeformis*

OPEN ACCESS

Edited by:
Ana Colaço,
Marine Research Institute (IMAR), Portugal

Reviewed by:
Evan Edinger,
Memorial University of Newfoundland, Canada
Lindsay Beazley,
Department of Fisheries and Oceans (Canada), Canada

***Correspondence:**
Pål Buhl-Mortensen
paal.mortensen@hi.no

Specialty section:
This article was submitted to Deep-Sea Environments and Ecology, a section of the journal Frontiers in Marine Science

Received: *21 July 2019*
Accepted: *18 March 2020*
Published: *24 April 2020*

Citation:
Sundahl H, Buhl-Mortensen P and Buhl-Mortensen L (2020) Distribution and Suitable Habitat of the Cold-Water Corals Lophelia pertusa, Paragorgia arborea, and Primnoa resedaeformis on the Norwegian Continental Shelf. Front. Mar. Sci. 7:213. doi: 10.3389/fmars.2020.00213

INTRODUCTION

Cold-water corals, including sea pen communities, gorgonian coral gardens, and coral reefs, are important providers of habitat in the deep sea. Numerous species are associated with these ecosystems, and the species richness and biomass are often orders of magnitude higher here than on the surrounding seabed (Buhl-Mortensen P. et al., 2016). Their complex three-dimensional structures may provide shelter, breeding ground, and feeding space for numerous fish, such as redfish (*Sebastes* spp.), tusk (*Brosme brosme*), ling (*Molva molva*), and ray species, as well as microhabitats for both sessile and mobile epifauna (Husebø et al., 2002; Costello et al., 2005; Buhl-Mortensen et al., 2010; Buhl-Mortensen, 2017). Their skeleton and tissue may also serve as host to various cryptofauna and endoparasites, e.g., crustaceans, nematodes, fungi, and sponges (Buhl-Mortensen P. et al., 2016).

The cold-water corals *Lophelia pertusa* (Linnaeus, 1758), *Paragorgia arborea* (Linnaeus, 1758), and *Primnoa resedaeformis* (Gunnerus, 1763) (denoted herein as *Lophelia*, *Paragorgia*, and *Primnoa*) are common on the Norwegian continental shelf (Buhl-Mortensen et al., 2015b). *Lophelia* is a reef-forming scleractinian that has received much focus within research and management due to its extent, accessibility, and its status as a flagship species for deep-sea conservation (Davies et al., 2007; Davies and Guinotte, 2011). *Primnoa* and *Paragorgia* are sea fans, which are colonies that do not form reefs but may occur in dense aggregations known as "coral gardens" (Buhl-Mortensen P. et al., 2016).

Cold-water corals are long-lived sessile organisms (Druffel et al., 1995; Andrews et al., 2002; Risk et al., 2002; Mortensen and Buhl-Mortensen, 2005). *Lophelia* colonized the Norwegian waters after the last glaciation about 10,000 years ago (Mortensen et al., 2001; Freiwald et al., 2002; Roberts et al., 2009b). Although each individual *Lophelia* polyp has a relatively short life span (<20 years) (Mortensen and Lepland, 2007), the extensive reef structures they build can be of considerable age, with the oldest occurring reefs in Norway dating back to 8600 years before present (Mortensen et al., 2001; López Correa et al., 2012). The gorgonian colonies do not create similarly old habitat structures, but individual colonies may reach an age of several hundred years (Andrews et al., 2002; Mortensen and Buhl-Mortensen, 2005). Thus, these cold-water coral ecosystems are unique biological structures, and because of their slow growth, fragile skeletons, and dependency on suspended food particles, they are also especially vulnerable to anthropogenic disturbances such as bottom trawling, petroleum exploitation, seabed mining, cable laying, and threat of ocean acidification (Davies and Guinotte, 2011; Buhl-Mortensen et al., 2015b). Damage caused by bottom trawling is well documented, where crushed *Lophelia* frameworks are left behind (Fosså et al., 2002; Buhl-Mortensen et al., 2013; Buhl-Mortensen, 2017), but also negative effects of long-lining (Mortensen et al., 2005) and exposure to oil spills (Demopoulos et al., 2016) have been demonstrated. Many countries have therefore made efforts to protect these vulnerable marine ecosystems (VMEs) within their Exclusive Economic Zones, such as Norway (Fosså et al., 2005), Canada (Mortensen et al., 2005; Breeze and Fenton, 2007), and United Kingdom (Huvenne et al., 2016). In addition, the presence of cold-water corals is often considered in the design and establishment of marine protected areas (MPAs) in the Atlantic high seas (UNGA, 2006; O'Leary et al., 2012). In order to establish the most appropriate protected areas, information about the distribution of VMEs is important. Thanks to improved and new technologies (e.g., multibeam echosounders, remotely operated vehicles, autonomous vehicles), the efficiency of seafloor mapping is increasing, providing more information at a higher spatial resolution than previously. However, to obtain a more comprehensive coverage of species distribution, modeled predictions are currently required (e.g., Tittensor et al., 2009; Yesson et al., 2012; Buhl-Mortensen et al., 2015b). Species distribution modeling (SDM) can help us identify locations where VMEs are likely to occur so that conservation efforts can focus on these areas (Anderson and Martínez-Meyer, 2004; Davies and Guinotte, 2011; Ross and Howell, 2012). Similarly, knowledge of their ecological niche is essential for the development of reliable and accurate models that can be useful in area-based management (Phillips et al., 2004).

Several papers have identified various environmental factors that control the distribution of cold-water corals (Mortensen et al., 2001; Wheeler et al., 2007; Davies and Guinotte, 2011), including substrate type, temperature, salinity, currents, and food availability. However, knowledge of their relative importance and how these factors may interact is still limited. Corals have specific tolerance windows for physical parameters (e.g., temperature, salinity, and currents), which may additionally reflect the different water masses and corresponding variation in terms of food quality and abundance. Many of the environmental factors influence each other directly and are therefore correlated; e.g., water mass properties define density and occur at different depths, currents are directed by topography, and near bottom food availability and substrate composition are controlled by current patterns and production in the water column (Mortensen et al., 2001; Dolan et al., 2008). Corals are abundant on elevated topography, where there is stronger continuous or periodic flow (Mortensen and Buhl-Mortensen, 2004; Mohn et al., 2014), and observations show that the part of a *Lophelia* reef and gorgonian coral facing the prevailing current has the highest density of polyps (Mortensen and Buhl-Mortensen, 2005; Buhl-Mortensen P. et al., 2016). Strong and prevailing near bottom currents supply food, disperse larvae, and prevent benthic fauna from being smothered by sediment deposition (Davies et al., 2009). In addition, food from surface productivity can be transported to the seabed by vertical mixing and is thought to be an important factor in the distribution of *Lophelia* (Davies et al., 2008; Roberts et al., 2009a). Moreover, environmental factors may influence the different life stages differently. For example, broad scale current patterns are important for the dispersal of long-lived larvae, whereas substrate is crucial for settling and food supply is critical for the adult stage (Buhl-Mortensen et al., 2015b).

Recently a report on the distribution and threats to VMEs (coral and sponge habitats) in the Nordic waters was provided to aid in spatial management of fisheries (Buhl-Mortensen et al., 2019). Nevertheless, the knowledge of the distribution and importance of cold-water corals off Norway is still limited. The Norwegian national seabed mapping program MAREANO has

to date covered approximately one third of the seabed within the depth range of the three corals within the study area. The density of survey stations is high and systematically distributed within the MAREANO mapping area, whereas in the remaining part of the study area, the historical records of coral occurrence are scarce and geographically biased. Management measures have been implemented for *Lophelia* reefs based on observed hot spot areas (areas with clusters of reefs), but none for the two other species. We believe that this study would be an aid to prioritizing areas in need of special protection.

Davies et al. (2008) modeled the distribution of *Lophelia* on both regional and global scales and noted coarse environmental data as a limiting factor. This study presents for the first time modeled distributions of *Lophelia*, *Paragorgia*, and *Primnoa* in Norwegian waters using high resolution environmental predictors. We use a wide range of predictor variables for training the models: depth, geomorphometric variables [slope, aspect, bathymetric position index (BPI)], oceanographic variables (temperature, salinity, current direction, and current speed), surface chlorophyll a concentration, sediment type, and marine landscape type.

The main objectives of the study were to:

1. Identify environmental variables, among those available as GIS layers, that are most useful for predicting the spatial distribution of *Lophelia*, *Paragorgia*, and *Primnoa* to increase our knowledge about their niches;
2. Develop SDMs with high spatial resolution for these species in Norwegian waters to predict areas with high probability of presence;
3. Explore the effects of differing environmental variable resolution on the accuracy of the predicted distribution.

MATERIALS AND METHODS

Coral Presence Data

The majority of the coral presence data comes from video observations at survey stations of the Norwegian national seabed mapping program, MAREANO (**Figure 1A**). Survey stations were selected based on a combined stratified and random sampling strategy, with the aim to cover the variation in bathymetry, topography, landscapes (e.g., canyons, banks, troughs), and sediment types (indicated by the backscatter). The majority of stations (ca 80%) are distributed randomly within areas of potentially similar environment (identified by unsupervised classification), whereas the remaining 20% are allocated to features of special scientific interests (Buhl-Mortensen et al., 2015a).

The MAREANO dataset contains 21,356 presence observations of *Lophelia*, 449 of *Paragorgia*, and 238 of *Primnoa* from 62°N to 71°N with a geographic precision of ± 5 m (**Figures 1B–D**). The presence points for *Lophelia* represent several observations within individual reefs, and therefore presence points less than 50 m apart were grouped and defined as a "Coral Reef Habitats." A total of 595 such habitats were identified, and the center points of these reef observations were used as the presence points for the study of environmental characteristics and spatial modeling.

To provide a wider geographic coverage, the MAREANO dataset on *Lophelia* was supplemented with that from a database of *Lophelia* records from various sources dating back to the 1930s (Fosså et al., 2002). This dataset added 867 *Lophelia* observations, mainly from the mid-Norwegian coast and shelf, but also included data from western Norway and Skagerrak. Since the original points had variable geographic precision (10–1000 m uncertainty), only records with uncertainty of 100 m or less were included. Database points that were duplicates of the MAREANO video points were removed in ArcGIS 10.5.1 by creating a 50 m radius buffer polygon around the MAREANO points and deleting *Lophelia* database points overlapping the buffer. This, together with the Coral Reef Habitat points, resulted in a final total of 1462 *Lophelia* presence points for this study (**Figure 1B**).

Environmental Data

Twenty environmental raster layers were prepared using ArcMap (**Table 1**). **Figures 2A–F** show six selected environmental layers in the study area. Six digital terrain model (DTM) bathymetry base maps in 1/8 arc minute resolution were downloaded from the European Marine Observation and Data Network (EMODnet) portal for depth and geomorphometric variables. Benthic oceanographic point data were retrieved from the ocean modeling system NorKyst-800 ("Norwegian Coast-800," see references and assessment results in, e.g., Myksvoll et al., 2018), where oceanographic variables are modeled at 800 m resolution along the Norwegian coast from the Swedish border to the Russian coast. The hydrodynamic model produces hourly results, and the ten years from 2005 to 2014 are used in our analysis. The lowermost vertical level in the NorKyst-800 system is assumed to represent the physical conditions near the benthic communities, and this level is approximately 10% of the height of the water level above the sea floor (Albretsen et al., 2011). Fifteen ocean color image rasters (2002–2016) indicating annual average values of sea surface chlorophyll a concentration were obtained from MODIS-Aqua (NASA Goddard Space Flight Center, 2018). Two categorical variables, sediment and marine landscape (**Figures 2E,F**), were obtained as shapefiles from the Geonorge public map catalog.

All environmental variables were processed in ArcMap to final raster layers and made to cover the extent of the coral presence data along the continental shelf (**Figure 2**). The six DTM bathymetry base maps were merged together and then re-projected to WGS84 UTM33, leading to a cell size of ≈176.51 m. This layer was then resampled to the nearest higher resolution integer cell size of 176 m, resulting in the final depth layer. The geomorphometric variables slope, broad and fine BPIs, ruggedness, and statistical aspect (Northness and Eastness) were derived from the depth layer using the Benthic Terrain Modeler (BTM) plug-in for ArcGIS (Walbridge et al., 2018) (**Table 1**). The low-scale raw ruggedness layer produced showed very small values (from 0 to 0.14), so a natural logarithm transformation of the layer, omitting values of 0, was created to separate out the values.

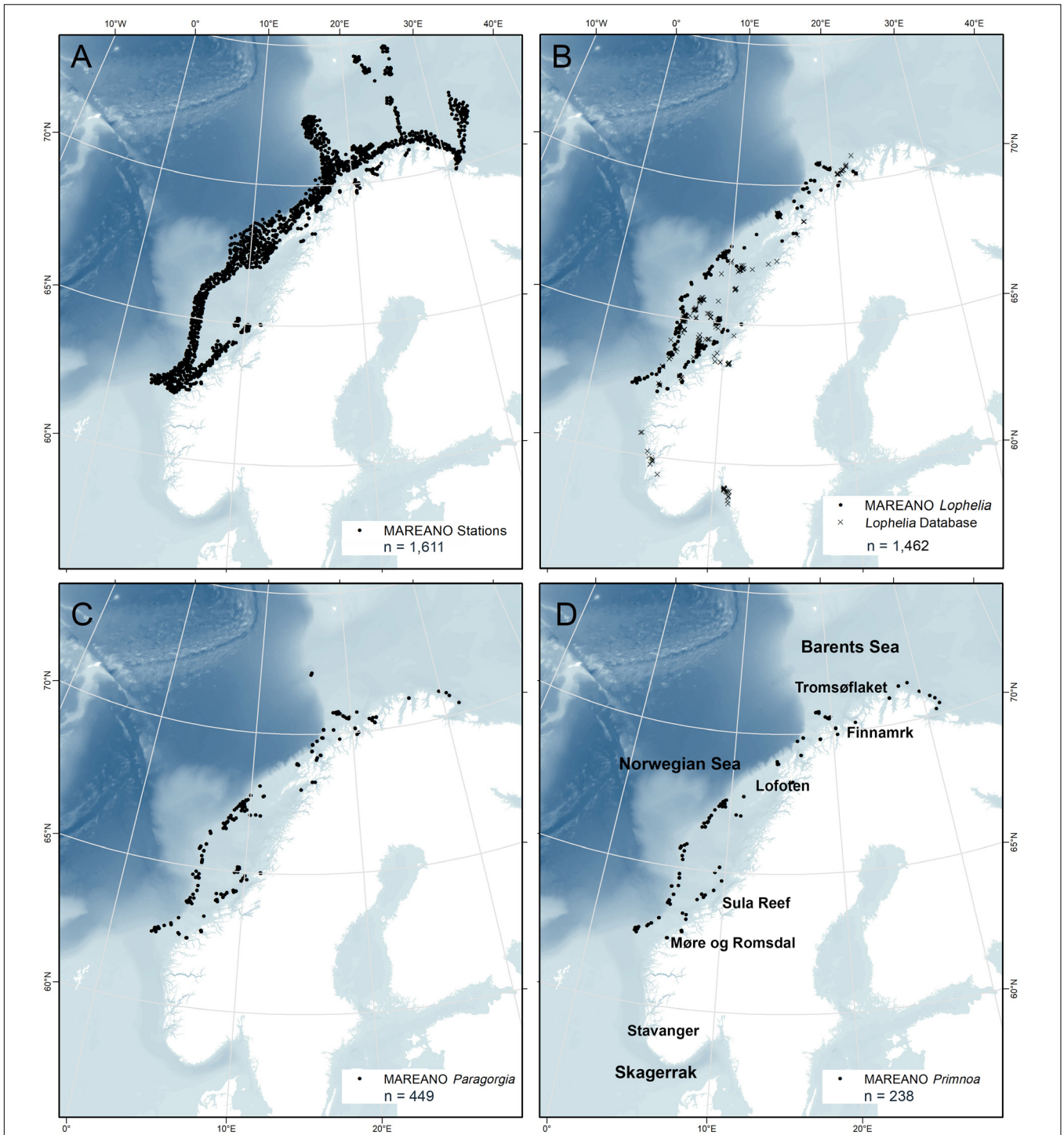

FIGURE 1 | Distribution of all MAREANO video stations **(A)** and all coral presence points for *Lophelia pertusa* **(B)**, *Paragorgia arborea* **(C)**, and *Primnoa resedaeformis* **(D)** on the Norwegian continental shelf. *n* = number of presence points.

The point data collected from the NorKyst-800 model were bottom temperature (mean monthly), salinity (minimum, mean, maximum), current speed (mean, maximum), and current direction. The 3 months with the coldest mean bottom temperature, March through May, were averaged and used as the bottom minimum temperature, and the three warmest months, October through December, were averaged and used as the bottom maximum temperature. The 10th percentile values for minimum salinity and 90th percentile values for maximum salinity and maximum current speed were used to

alleviate errors in the form of extreme values, introduced during Norkyst-800 model processing. The points for each variable were interpolated and then resampled to 176 m (using Inverse Distance Weighted interpolation tool in the Spatial Analyst toolbox) to match the depth and geomorphometric variables. Finally, current direction was decomposed into statistical Northness and Eastness.

To study if the interaction between terrain and currents is a better indicator than each of them separately, we created the variable "Current-Aspect Angle"; the angle between current direction and the heading of the terrain aspect (sloping direction) was used (**Supplementary Figure S1**). This variable was processed with the Raster Calculator and Math tools in the Spatial Analyst toolbox, as follows:

- If Current-Aspect Angle $\leq$ 180°, Current-Aspect Angle = abs (Current° − Aspect°);
- If Current-Aspect Angle $>$ 180°, Current-Aspect Angle = abs [abs (Current° − Aspect°) − 360)].

Angles greater than 180° were matched with the corresponding angle since a 2D surface is measured. Thus, if the Current-Aspect Angle value:

= 0°, the direction of current and aspect are the same (e.g., slope facing North, current heading North);

$<$ 90°, the current is at the same angle and with the same direction as the aspect;

= 90°, the current is perpendicular to the aspect and runs in parallel with the terrain;

$>$ 90°, the current is at an angle opposite to the aspect, and hits the terrain;

= 180°, the direction of the current and aspect are opposite and the current hits the terrain (e.g., slope facing North, current heading South).

For chlorophyll a concentration, the last continuous variable, the 15 ocean color image raster layers were averaged into one (**Figure 2D**). All variables were snapped and resampled to match the final depth and geomorphology layers. **Figure 2** shows maps for the continuous variables broad BPI (**Figure 2A**), minimum temperature (**Figure 2B**), mean current speed (**Figure 2C**), and chlorophyll a (**Figure 2D**).

Finally, the categorical variables sediment type and landscape were processed. Sediment type (**Figure 2E**), as classified by grain size based on Folk (1954), was collated from two sources: (1) "Regional," a detailed layer mapped by MAREANO based on sediment sampling, backscatter, and seismic data, with video observation and bathymetry data to support, and (2) "Continental Shelf," a coarser mapping based on the National Atlas of Norway (Vorren and Vassmyr, 1991). The Continental Shelf layer was used to cover areas outside the Regional layer. The sediment class "Bioclastic material" was removed to avoid circularity since this substrate is part of reefs. Marine landscape (**Figure 2F**) as defined by MAREANO is a large geographical region (can be mapped with a scale of 1:500,000) with a uniform appearance. MAREANO Buhl-Mortensen et al. (2015c) defined this using the parameters (1) relative relief (difference of 50 m in height within a 1 km^2 area is set as a cut-off point), (2) slope angle, (3) terrain variation (e.g., ruggedness), and (4) relative position (BPI). The collated sediment and the marine landscape shapefile layers were then converted to raster layers.

The relationship between the values for all 20 environmental variables and coral presence data points was analyzed.

Modeling

Maximum Entropy (Maxent) version 3.4.1 Java application (Phillips et al., 2004) was used to create an SDM for each species. Maxent modeling is a common method used by many benthic ecologists (see Table 1 in Elith et al., 2011 for an overview) due to its good performance compared to other SDM modeling and its ease of use (Ghisla et al., 2012; Merow et al., 2013; Phillips et al., 2017). Maxent is relatively robust in dealing with variable correlation because regularization makes sure the model does not overfit (Phillips et al., 2006). However, some *a priori* variable selection is good to reduce covariation and better understand individual variable importance (Davies and Guinotte, 2011). The correlation between the continuous environmental variables at the location of coral presence points was evaluated using Spearman's Rank test in the "Scatterplot Matrix for Table" tool in the Marine Geospatial Ecology Tools 0.8a68 (MGET) plug-in (Roberts et al., 2010). An ρ-value of 0.75 was applied as a cut off for pairs of correlated variables of which only one was selected.

As a result of the categorical sediment and marine landscape variables not covering the entire study area, two different models were run (**Table 2**). Model 1 excluded these two categorical terrain variables and is therefore limited by their absence, while Model 2 included these two variables and is therefore limited by a more restricted geographical extent (**Figure 3**). Models 1 and 2 were each run 10 times using cross-validation to test the models. This process involved splitting the presence data into 10 groups, and in each run, one group was left out while the rest of the data was used to train the model. The trained model was then tested with the omitted group (the "test data"), a method that uses all data to test the model (Philips, 2017). The default of 10,000 randomly placed background points was chosen for the comparison with presence data. The regularization multiplier was left as the default of 1, leaving regularization coefficients for the module training at default values.

The default cloglog (computes the complementary log-log transformation, including its inverse and the first two derivatives) output was used because of its higher discrimination power compared to the logistic output. Duplicate coral records within a 176 m cell were removed to reduce location bias. A bias grid was also used by creating a point density map of MAREANO station locations, which does not include sampling effort of the *Lophelia* database.

To gain an understanding of coral niches, a response curve for each modeled environmental variable was produced for each species. The response curves compare values of the environmental variables at coral presence points with values at random background points within the study area, and thus indicate a species' preference to certain environmental values. "Clamping" extrapolation was also done in order to make conservative predictions of variable responses that could happen outside observations made in the study, whether it is geographical

TABLE 1 | List of all obtained environmental variables, with format, resolution, sources, and processing method.

	Variable	Original format	Original resolution	Source	Processing
Terrain	Depth	B1, B2, C1, C2, D1, D2 base maps as ESRI Ascii files	1/8 arc minute, WGS84	EMODnet	1. Merged using Mosaic to New Raster with "Blend" mosaic operator 2. Reprojected to WGS84 UTM33 using Project Raster with "Nearest" resampling (176.51 m res.) 3. Resampled to 176 m
	Slope BPI Fine Broad *Ruggedness (Ln)* Aspect (Stat.) Northness Eastness	Depth variable			Variables derived with BTM plug-in 1. Fine BPI: nine-cell outer radius × 176 m, creating 1584 m search radius. Standardized 2. Broad BPI: 49-cell outer radius × 176 m, creating 8624 m search radius. Standardized 3. Ruggedness: a. 3 × 3 cell neighborhood b. Natural log, ignoring values of 0
Oceanographic	Temperature Min (mean March–May) *Max (mean Oct–Dec)*	Points	800 m, 10 years	NorKyst-800	1. Interpolated with inverse distance weighted interpolation (search points = 1, max search distance = 800 m), creating 800 rasters 2. Resampled to 176 m. 3. Statistical current direction: a. Northness = Cos [current × (math.pi/180)] b. Eastness = Sin [current × (math.pi/180)]
	Salinity *Min (10th perc)* Mean *Max (90th Perc)*				
	Current speed Mean *Max (90th Perc)*				
	Current direction (Stat.) Northness Eastness				
	Current-aspect angle	Current° and aspect° values			Absolute difference between current° and aspect°
Biological productivity	Surface chlorophyll a concentration	Ocean color image raster layers	4 km^2, annual averages 2002–2016	NASA Ocean Biology Processing Group	Averaged with Raster Calculator into one layer
Categorical	Sediment	"Regional" and "Continental shelf" shapefiles	Classification by grain size based off of Folk, 1954	Geonorge public map catalog Original sources: Regional: MAREANO Continental shelf: National Atlas for Norway	1. Combined into one shapefile with Union, ranking "regional" first and "continental shelf" second 2. "Bioclastic material" type removed 3. Converted to raster using Polygon to Raster with "maximum combined area" cell assignment type
	Marine landscape	Shapefile	Large geographical regions (1:500,000), classified by MAREANO	Geonorge public map catalog Original source MAREANO	Converted to raster using Polygon to Raster with "maximum combined area" cell assignment type

The variables are grouped into terrain, oceanographic, biological, and categorical variables. Variables in italic were eliminated after a Spearman's rank correlation test and not used in the modeling.

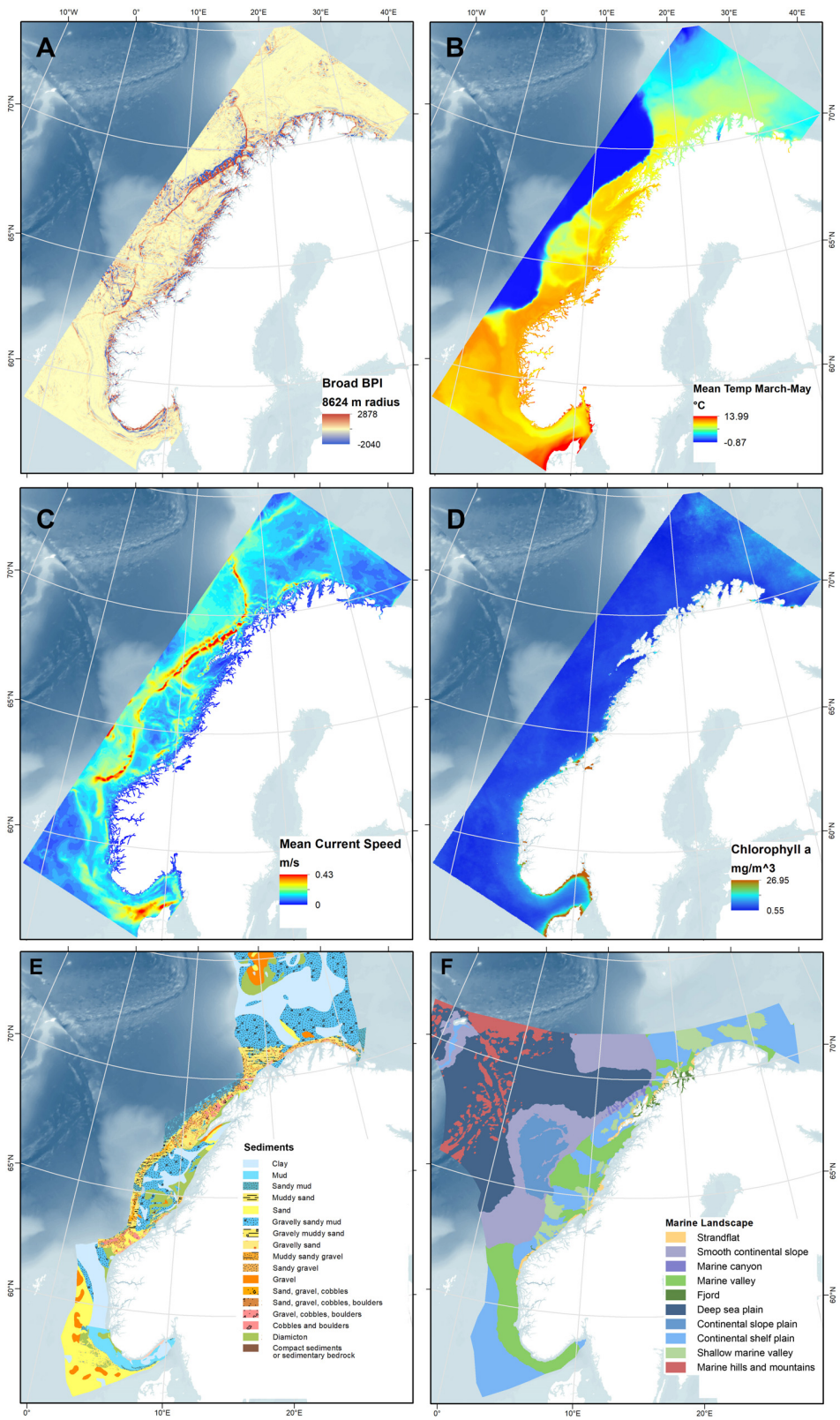

FIGURE 2 | Maps of four selected numerical environmental variables **(A–D)**, and two categorical variables **(E,F)**. **(A)** Broad BPI, **(B)** minimum temperature (mean March through May), **(C)** mean current speed, **(D)** chlorophyll a concentration, **(E)** sediment type (classified by grain size, based on and modified from Folk (1954) combining MAREANO's finer Regional map and the coarser Continental Shelf map from the National Atlas for Norway, 1991), and **(F)** Marine landscape types classified by MAREANO.

TABLE 2 | The two models run in Maxent, with their used variables and limitations.

Model	Description	Variables used	Limitation
Model 1	Full geographical range	Terrain variables: *Depth, Slope, Broad BPI, Fine BPI, Aspect Northness, Aspect Eastness* Oceanographic variables: *Min Temperature, Mean Salinity, Mean Current Speed, Current Northness, Current Northness, Current-Aspect Angle* Biological variables: *Surface chlorophyll a*	Modeling species distribution without the categorical variables
Model 2	With sediment and marine landscape	All of the above, as well as the categorical variables *Sediment, Marine Landscape*	Models restricted by the limiting extent of the categorical variables

or temporal in nature. Linear, quadratic, and hinge variable response features were used.

Each of the 10 model runs produced a "gain," a measure of goodness of fit that gives the likelihood ratio of finding coral points over random background points, using both the training points (training gain) and the test points (test gain). A gain of two means that the average likelihood of presence at a presence point is $e^2 \approx 7.4$ times greater than at a background point (Phillips et al., 2017). Maxent also evaluated each model's discrimination ability with the training and test Area under the receiver operating characteristic (ROC) curve, the AUC, a value giving the ratio of the true positive rate (correctly predicting presence over falsely predicting absence) to the false positive rate (falsely predicting presence over correctly predicting absence), based on a chosen discrimination threshold of misclassification rate.

RESULTS

Observed Environmental Characteristics of Coral Habitats

A summary of environmental variable characteristics at the coral presence points and in the overall study area is shown in **Table 3**. The distribution relative to six selected variables [depth, minimum temperature (March–May), broad BPI, mean current speed, and surface chlorophyll a concentration] per coral species is presented in **Figure 4**. Note that value extremities are grouped together in overflowing bins.

Depth

Corals were present across a wide depth range, from 50 to almost 800 m, while the overall maximum depth within the study area was 3052 m. **Figure 4A** shows that *Paragorgia* and *Primnoa* had a similar depth distribution, with maximum occurrences around 325–350 m. *Lophelia* was more common at shallower depths between 250 and 275 m depth. The two gorgonians also extended deeper than *Lophelia*, with maximum depths of >700 m, compared to 575 m for *Lophelia*. The plots of occurrence versus temperature (**Figure 4B**) reflected similar differences among the species.

Temperature

On average, *Lophelia* occurred in warmer water than *Paragorgia* and *Primnoa* (**Table 3**). For minimum temperature (March–May), *Lophelia* distribution showed a clear peak and clustering around 6–6.5°C, while high gorgonian presence extended widely between 4.5 and 7°C (**Figure 4B**). *Primnoa* peaked at warmer temperatures (6.5–7.0°C) and *Paragorgia* at slightly colder temperatures of around 5.0–5.5°C. *Lophelia* was associated with a higher minimum temperature of 3°C, compared to below 1°C for the other two species.

Salinity

On average, the distribution across the gradient in salinity was similar for all three species (mean salinity: 35.00–35.02 PSU, **Table 3**). The minimum salinity values differed more for the corals with 31.59 PSU for *Lophelia*, 33.79 PSU for *Primnoa*, and 33.80 PSU for *Paragorgia* (**Table 3**). Maximum salinity values were at 35.44 PSU for *Lophelia*, 35.43 PSU for *Primnoa*, and 35.46 PSU for *Paragorgia*.

Slope and BPI

The corals had an overall preference for moderate sloping terrain, with *Lophelia*'s mean slope at 2.15°, *Primnoa* at 3.17°, and *Paragorgia* at 3.35°, despite ranging up to 38.24° for *Lophelia* and 35.00° for the gorgonians. BPI (both broad and fine) and ruggedness (natural log) values had a unimodal distribution, centered around the mean. *Lophelia* was unique by displaying two peaks of high occurrences for broad BPI: one around more level areas similar to that for the gorgonians, and the other in strongly negative values (i.e., troughs) (**Figure 4C**). In general, *Lophelia* had a weak preference to negative BPI values with a broad BPI mean of −39.64 and fine BPI mean of −4.57, indicating occurrences in troughs.

Aspect

The gorgonians had a tendency to occur at north and west-facing slopes as indicated by positive values for Northness and negative values for Eastness, while *Lophelia* tended to occur on south and west-facing slopes due to negative Northness and Eastness values (**Table 3**).

Current Direction

The gorgonians appeared more in areas with north and east-heading currents and *Lophelia* in areas with north and west-heading currents (**Table 3**). The rose diagrams for the Current-Aspect Angle for all species (**Supplementary Figure S2**) show that most coral occurrences were in areas with currents generally flowing over (22.5–67.5°) or passing parallel to (67.5–112.5°) the slope, with slightly fewer occurrences of the current hitting the slope (112.5–157.5°).

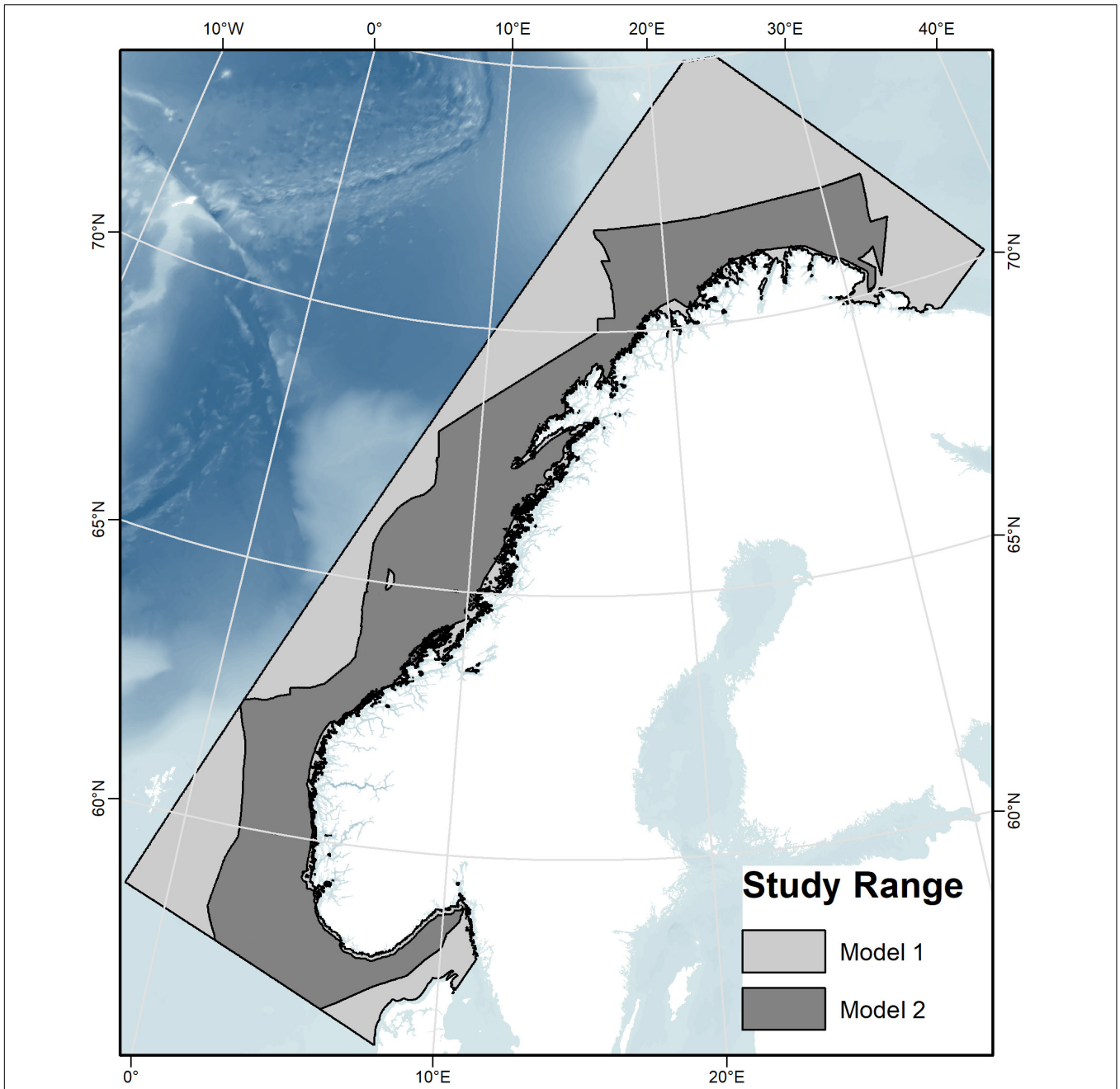

FIGURE 3 | The study area showing the geographic extent of the two models. The light-gray polygon (Model 1) indicates the full study area, without full-areal coverage of the sediment and marine landscape environmental variables, and the dark-gray polygon (Model 2) superimposed on Model 1 indicates the more restricted area with all variables, including sediment and marine landscape.

Current Speed

Corals had a bimodal distribution related to mean current speed, with peaks in occurrence at slow (0.06 m/s) and fast (0.2 m/s) current speeds (**Figure 4D**). The max observed speed of the max current speed was 0.53 m/s for all corals (**Table 3**).

Surface Productivity

Lophelia had a clear peak in occurrence at a surface chlorophyll a concentration of 1.35–1.4m g/m^3 (**Figure 4E**), as well as a large range of 0.87–20.59 mg/m^3, compared to 0.86–4.76 mg/m^3 for the gorgonians (**Table 3**).

Sediment

The bar graphs in **Figure 5** show the relative frequency of sediment types for each coral species using MAREANOs sediment classification. The frequency results obtained from the combined sediment layer are juxtaposed with actual records of sediment type made in the MAREANO coral

TABLE 3 | Summary statistics count (n), mean ($\bar{x}$) ± standard deviation (s), and range (min to max) for the continuous environmental variables for each species and the overall study area.

Environmental variable	*Lophelia pertusa*	*Paragorgia arborea*	*Primnoa resedaeformis*	Overall
Depth (m)	*n* = 1449 $\bar{x}$ = 281.45 ± 77.12 Range = 54.04–715.45	*n* = 449 $\bar{x}$ = 343.50 ± 107.08 Range = 108.11–769.25	*n* = 238 $\bar{x}$ = 339.62 ± 118.04 Range = 88.30–714.87	$\bar{x}$ = 515.12 ± 680.39 Range = 0–3051.67
Slope (°)	*n* = 1441 $\bar{x}$ = 2.15 ± 3.16 Range = 0–38.24	*n* = 449 $\bar{x}$ = 3.35 ± 4.46 Range = 0–35.00	*n* = 238 $\bar{x}$ = 3.17 ± 5.75 Range = 0–35.00	$\bar{x}$ = 0.94 ± 2.39 Range = 0–63.53
Broad BPI	*n* = 1339 $\bar{x}$ = −39.64 ± 180.99 Range = −937.00–700.00	*n* = 412 $\bar{x}$ = 15.17 ± 303.76 Range = −1260.00–1220.00	*n* = 222 $\bar{x}$ = 33.73 ± 145.07 Range = −542.00–448.00	$\bar{x}$ = 0.55 ± 99.80 Range = −2040–2878
Fine BPI	*n* = 1431 $\bar{x}$ = −4.57 ± 134.00 Range = −870.00–1204.00	*n* = 442 $\bar{x}$ = 25.88 ± 180.27 Range = −566.00–1296.00	*n* = 227 $\bar{x}$ = 39.02 ± 158.78 Range = −496.00–739.00	$\bar{x}$ = 0.44 ± 99.88 Range = −2691–5927
Ln ruggedness	*n* = 1334 $\bar{x}$ = −9.95 ± 2.47 Range = −15.94– −3.26	*n* = 444 $\bar{x}$ = −9.54 ± 2.56 Range = −15.94– −4.23	*n* = 233 $\bar{x}$ = −9.81 ± 2.63 Range = −15.94– −4.48	$\bar{x}$ = −12.96 ± 2.72 Range = −15.94– −1.96
Aspect eastness	*n* = 1441 $\bar{x}$ = −0.21 ± 0.7 Range = −1–1	*n* = 449 $\bar{x}$ = −0.14 ± 0.71 Range = −1–1	*n* = 238 $\bar{x}$ = −0.27 ± 0.68 Range = −1–1	$\bar{x}$ = −0.11 ± 0.69 Range = −1–1
Aspect northness	*n* = 1441 $\bar{x}$ = −0.04 ± 0.67 Range = −1–1	*n* = 449 $\bar{x}$ = 0.12 ± 0.68 Range = −1–1	*n* = 238 $\bar{x}$ = 0.20 ± 0.65 Range = −1–1	$\bar{x}$ = 0.11 ± 0.71 Range = −1–1
Min temp (°C) (Mean temp March–May)	*n* = 1462 $\bar{x}$ = 6.12 ± 0.85 Range = 0.62–8.01	*n* = 449 $\bar{x}$ = 5.26 ± 1.61 Range = −0.32–7.43	*n* = 238 $\bar{x}$ = 5.28 ± 1.42 Range = 0.65–7.40	$\bar{x}$ = 4.33 ± 2.78 Range = −0.87–13.99
Max temp (°C) (Mean temp Oct–Dec)	*n* = 1462 $\bar{x}$ = 7.18 ± 1.27 Range = 0.68–11.29	*n* = 449 $\bar{x}$ = 6.00 ± 1.80 Range = −0.27–8.93	*n* = 238 $\bar{x}$ = 6.02 ± 1.63 Range = 1.09–8.93	$\bar{x}$ = 5.17 ± 3.38 Range = −0.82–13.40
Min (10th Perc) salinity (PSU)	*n* = 1444 $\bar{x}$ = 34.86 ± 0.27 Range = 31.59–35.14	*n* = 449 $\bar{x}$ = 34.89 ± 0.21 Range = 33.80–35.14	*n* = 238 $\bar{x}$ = 34.84 ± 0.29 Range = 33.79–35.14	$\bar{x}$ = 34.80 ± 0.44 Range = 18.56–35.25
Mean salinity (PSU)	*n* = 1462 $\bar{x}$ = 35.02 ± 0.17 Range = 33.15–35.26	*n* = 449 $\bar{x}$ = 35.03 ± 0.15 Range = 34.09–35.28	*n* = 238 $\bar{x}$ = 35.00 ± 0.22 Range = 34.08–35.23	$\bar{x}$ = 34.93 ± 0.35 Range = 24.77–36.39
Max (90th Perc) salinity (PSU)	*n* = 1444 $\bar{x}$ = 35.19 ± 0.10 Range = 34.30–35.44	*n* = 449 $\bar{x}$ = 35.17 ± 0.11 Range = 34.28–35.46	*n* = 238 $\bar{x}$ = 35.15 ± 0.17 Range = 34.27–35.43	$\bar{x}$ = 35.09 ± 0.22 Range = 29.12–39.04
Mean current speed (m/s)	*n* = 1462 $\bar{x}$ = 0.14 ± 0.07 Range = 0.01–0.30	*n* = 449 $\bar{x}$ = 0.12 ± 0.06 Range = 0.02–0.29	*n* = 238 $\bar{x}$ = 0.14 ± 0.07 Range = 0.02–0.29	$\bar{x}$ = 0.08 ± 0.04 Range = 0–0.43
Max (90th Perc) current speed (m/s)	*n* = 1444 $\bar{x}$ = 0.26 ± 0.11 Range = 0.02–0.53	*n* = 449 $\bar{x}$ = 0.23 ± 0.11 Range = 0.04–0.53	*n* = 238 $\bar{x}$ = 0.26 ± 0.13 Range = 0.03–0.53	$\bar{x}$ = 0.15 ± 0.07 Range = 0.01–0.81
Current direction eastness	*n* = 1449 $\bar{x}$ = −0.08 ± 0.62 Range = −1–1	*n* = 449 $\bar{x}$ = 0.07 ± 0.64 Range = −1–1	*n* = 238 $\bar{x}$ = 0.16 ± 0.59 Range = −1–1	$\bar{x}$ = 0.16 ± 0.69 Range = −1–1
Current direction northness	*n* = 1449 $\bar{x}$ = 0.55 ± 0.56 Range = −1–1	*n* = 449 $\bar{x}$ = 0.39 ± 0.66 Range = −1–1	*n* = 238 $\bar{x}$ = 0.45 ± 0.66 Range = −1–1	$\bar{x}$ = 0.22 ± 0.67 Range = −1–1
Current-aspect angle (°)	*n* = 1424	*n* = 446	*n* = 238	Range = −1–180
Surface [Chlor *a*] (mg/m^3)	*n* = 1346 $\bar{x}$ = 1.60 ± 2.05 Range = 0.87–20.59	*n* = 420 $\bar{x}$ = 1.39 ± 0.74 Range = 0.86–4.76	*n* = 212 $\bar{x}$ = 1.28 ± 0.49 Range = 0.88–4.75	$\bar{x}$ = 1.50 ± 0.97 Range = 0.55–26.95

video dataset. According to the video observations, the gorgonians had the highest occurrence on *Lophelia* reefs, which was removed in the sediment layer to eliminate redundancy. The sediment types containing gravel were favorable habitats for all three corals. *Lophelia* observations were most common on "gravelly muddy sand" based on the sediment layer, while video observations indicated that it was most common on "gravelly sand," two very similar sediment types. *Primnoa* occurred on muddy, sandy, gravelly sediment types in the interpreted sediment layers, while video observations indicated that "exposed bedrock" was the dominant sediment.

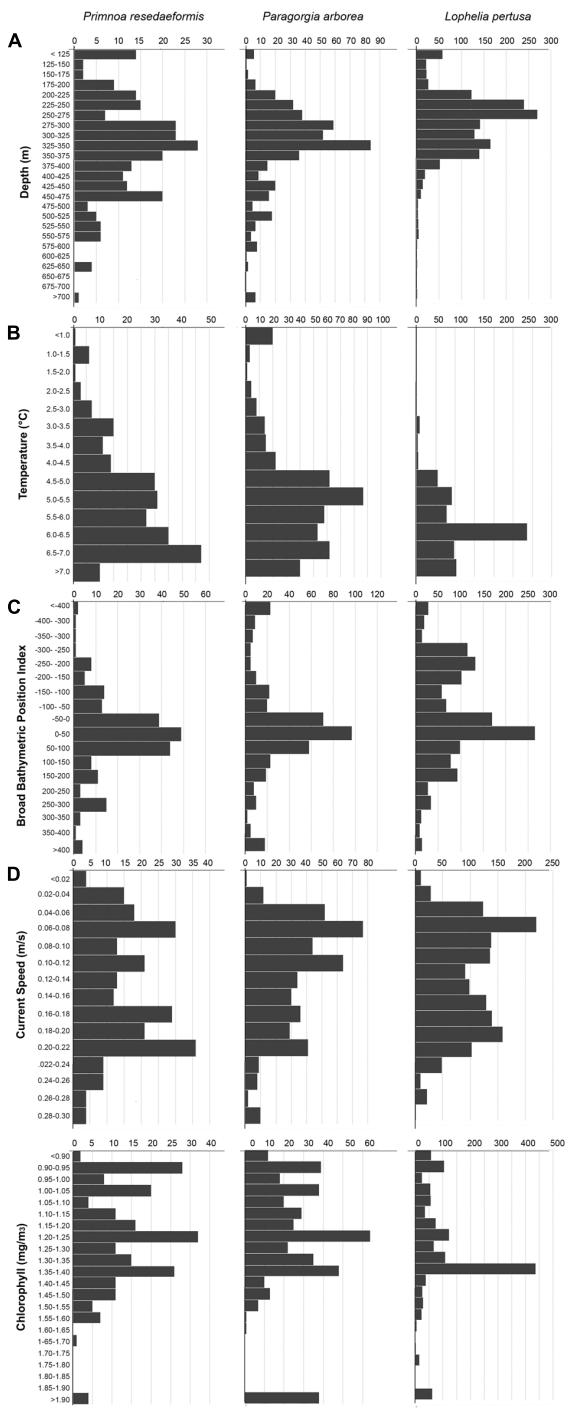

FIGURE 4 | Number of occurrences of *Primnoa*, *Paragorgia*, and *Lophelia* versus depth **(A)**, minimum temperature **(B)**, broad BPI **(C)**, mean current speed **(D)**, and chlorophyll a concentration **(E)**.

Landscape

Based on MAREANO's broad classification of marine landscapes in Norwegian waters (**Figure 6**), *Lophelia* was most frequent in shallow marine valleys, *Paragorgia* in marine valleys, and *Primnoa* on the smooth continental slope. All three species were also frequent on the continental shelf plain and to some degree in fjords. The correlations found for the continuous environmental variables are shown in **Supplementary Figure S3**. Variables eliminated from the model were natural-log ruggedness [$\rho(2011) \geq 0.75$ ($p < 0.01$)], maximum current speed [$\rho(2131) \geq 0.75$ ($p < 0.01$)], maximum salinity [$\rho(2131) \geq 0.75$ ($p < 0.01$)], minimum salinity [$\rho(2131) \geq 0.75$ ($p < 0.01$)], and maximum temperature [$\rho(2149) \geq 0.75$ ($p < 0.01$)]. This resulted in a total of 15 variables used for the modeling stage.

Model Evaluation

The average 10-run test AUC was 0.931 ± 0.005 in Model 1 (excludes categorical terrain variables) and 0.933 ± 0.007 in Model 2 (includes categorical terrain variables) for *Lophelia*, 0.951 ± 0.008 in Model 1 and 0.945 ± 0.012 in Model 2 for *Paragorgia*, and 0.951 ± 0.021 in Model 1 and 0.954 ± 0.025 in Model 2 for *Primnoa*. The high test AUC values for all models show that the models have high discriminatory power between the test points and background data within the study area (see points on interpreting this below in the discussion). Looking at the average test gain from the Jackknife results in **Figure 7** test gain is highest for *Primnoa*, indicating that the model concentrates around the presence points for *Primnoa* the most, owing perhaps to the fact that this species has the fewest presence points out of the three species and/or because this species is more restricted in its distribution.

Modeled Environmental Niches

The individual variable response curves in **Figure 8** show how the Maxent model predicts the environmental niches for the three coral species, based on the values of the environmental variables at coral presence points compared to random background points within the study area. The curves show the mean response (red line) ± one standard deviation (blue shaded area) from 10 replicates for all three species from Model 2. Clamping extrapolation creates the flat predictions at the extremities, conditions that are outside the range found in the study's presence and background points.

The gorgonians appear to prefer slightly deeper, and colder, environments than *Lophelia* overall (**Figures 8A–F**). *Lophelia*'s temperature preference lies roughly between 4 and 7.5°C, peaking around 6.5°C, while for the gorgonians it ranges from 0 to 7°C, with a colder and a warmer peak. *Paragorgia* tolerates a greater range of sloping, and more convex terrain than *Lophelia* and *Primnoa* based on more certain predictions for increasing slope and extreme BPI values (**Figures 8G–L**). None of the corals seem to prefer flat terrain. All species have a strong response to the upper peak for mean current speed of around 0.2 m/s discussed above, as well as a small response to the slower mean current speed peak (**Figures 8M–O**).

In terms of sediment type (Not shown), there is very little response to clay, predominantly muddy sediment types, and gravel. There are strong responses to "gravelly muddy sand," "sand, gravel, cobbles," and various bedrock classifications ("thin sediment cover on bedrock," "exposed bedrock," "compact sediments or sedimentary bedrock"). *Lophelia* and *Paragorgia*

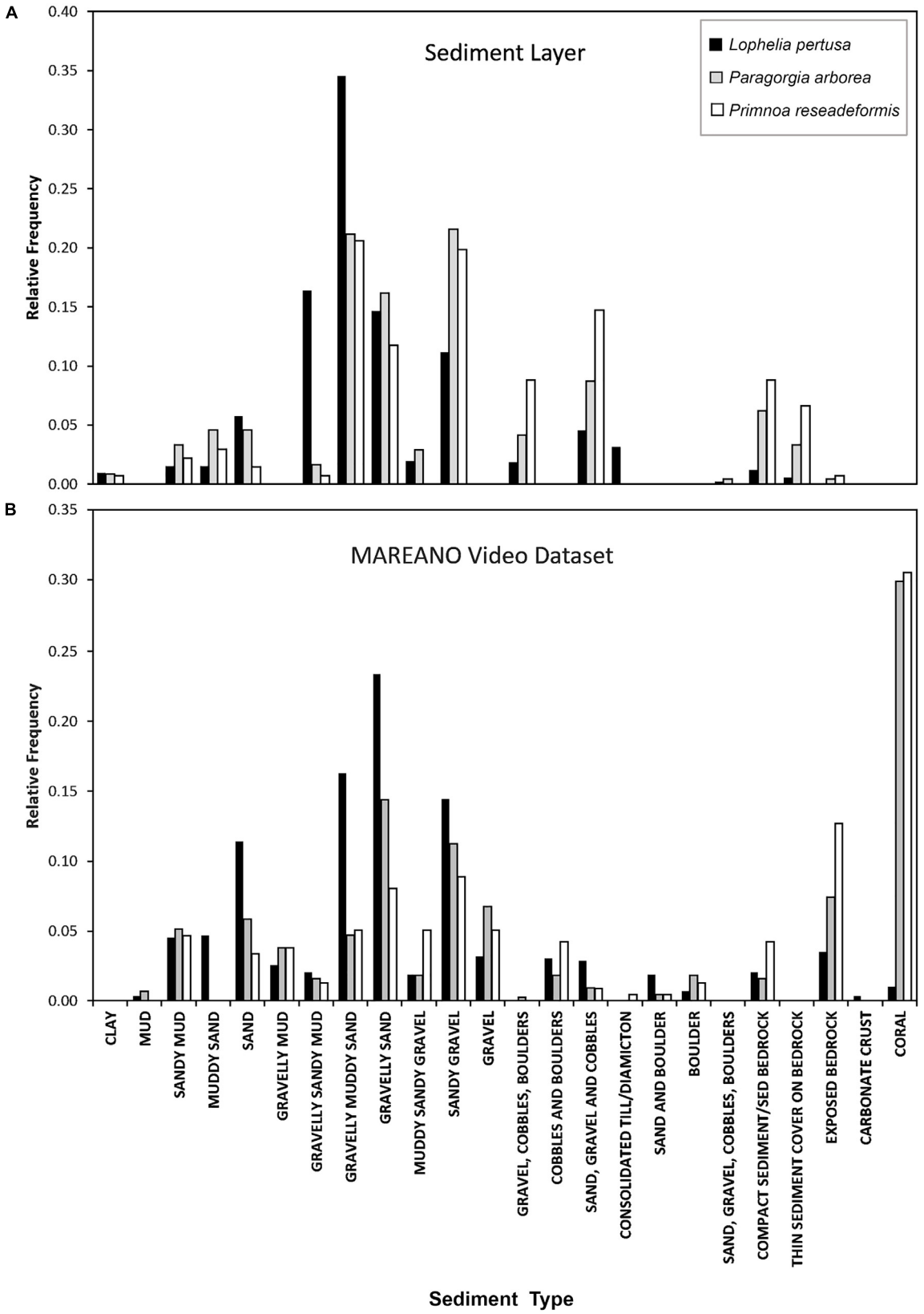

FIGURE 5 | Relative frequency of sediment types for each coral species at their sites of occurrence from the MAREANO sediment layer **(A)**, compared with the observed sediment type from the MAREANO video dataset **(B)**.

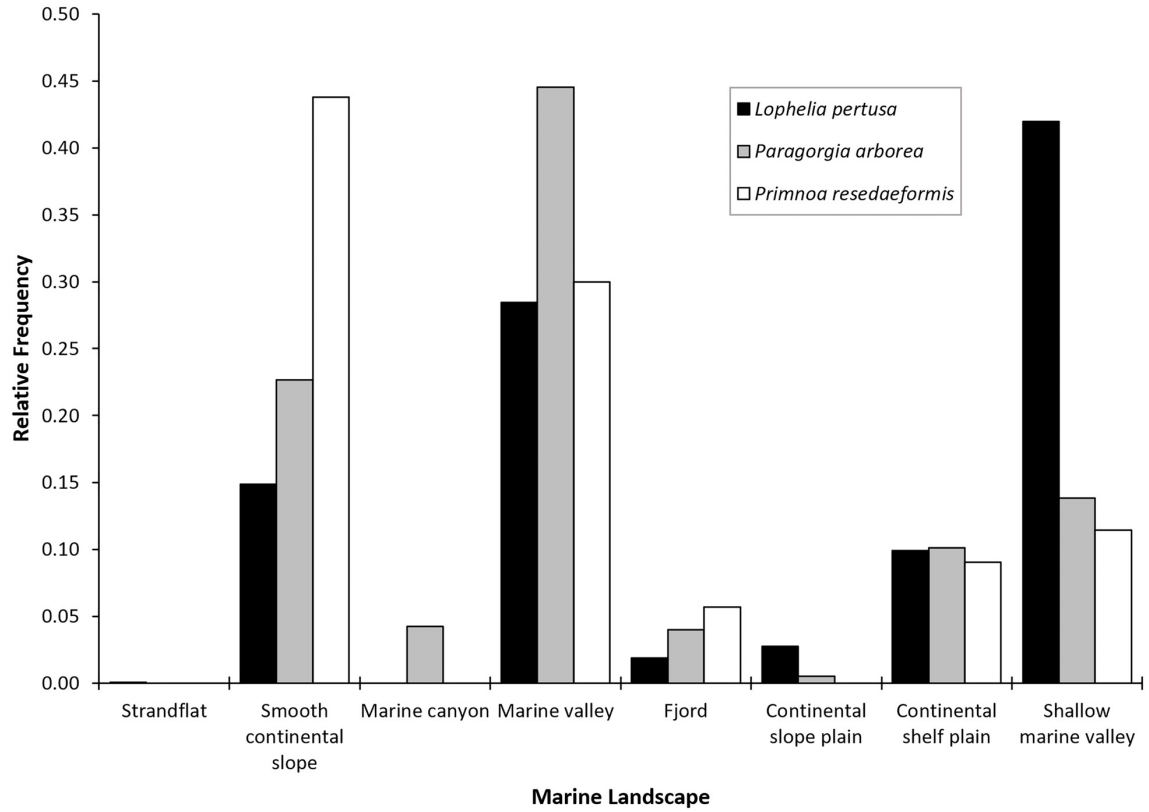

FIGURE 6 | Relative frequency of marine landscape type for each coral species.

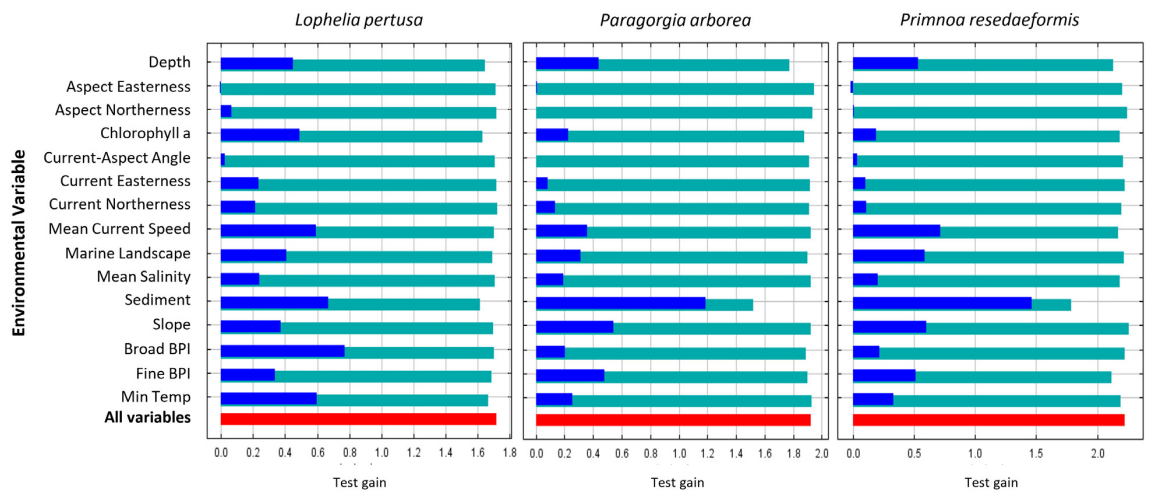

FIGURE 7 | Average Jackknife test gain results from the 10 cross-validation Model 2 runs per species. Red bars indicate the average overall test gain, teal bars the test gain result when one variable is omitted, and blue bars the test gain result when only one variable is used in a model run.

also strongly prefer "sand, gravel, cobbles, boulders." Out of the marine landscape categories (Not shown), *Lophelia* appears to mostly prefer shallow marine valleys and fjords, *Paragorgia* the smooth continental slope and marine canyons, and *Primnoa* the smooth continental slope and marine valleys.

Variable Contribution

The average test gains from Jackknife tests for the 10 Model 2 re-runs are shown in **Figure 7**. The red-colored bar shows the model's average overall test gain. The teal-colored bars indicate the model's test gain when one of the variables is omitted,

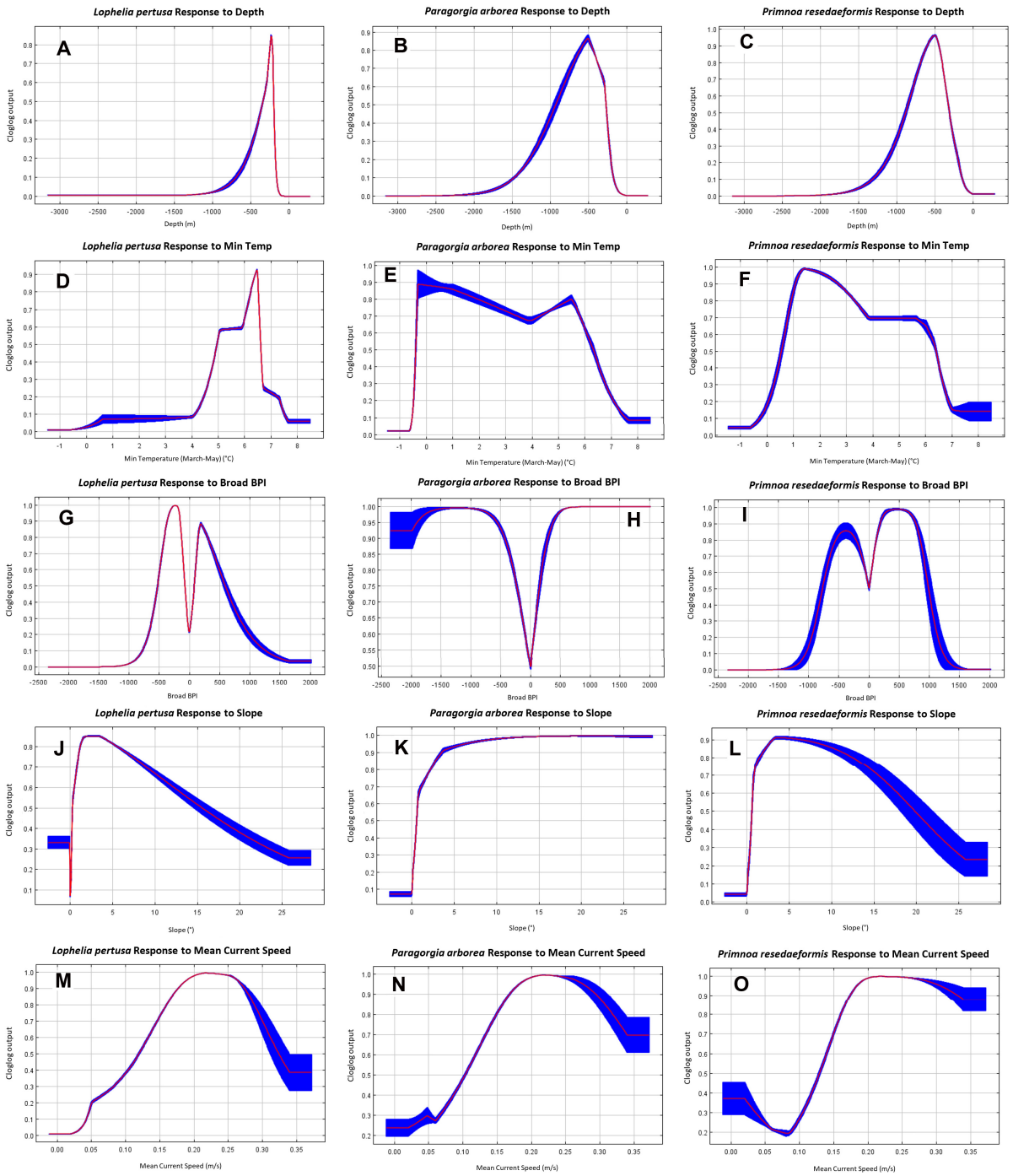

FIGURE 8 | Model 2 individual variable response curves of each species for depth **(A–C)**, minimum temperature **(D–F)**, broad BPI **(G–I)**, slope **(J–L)**, and mean current speed **(M–O)**.

showing which variables have the most unique information for the model that is not present in the other variables. The blue-colored bars indicate the model's test gain when only one variable is used in each rerun, and the models with the least loss in test gain have the most useful information for the overall model (Philips, 2017).

For the *Lophelia* model, broad BPI, sediment, temperature, and current speed are the most useful variables, while sediment, chlorophyll a, and depth have the most unique information. Sediment gave the highest test gain alone for both gorgonians, and the models lost the highest amount of information without this variable. Thus, this variable is important for predicting these

species' distributions. For *Lophelia*, however, the sediment type was less important. The second most useful variables for the gorgonians were slope for *Paragorgia* and current speed for *Primnoa*.

Modeled Species Distribution

Model 1 extends to the full study range because sediment and marine landscape variables with limited geographical extent were not included, while Model 2 includes these two and consequently covers a smaller area. The mean SDMs after 10 model runs for all three species for Model 1 and Model 2 are shown in **Figure 9**.

The predicted probability of presence showed congruency with the presence points used for the model, with presence points often overlaying red areas (highest probability of presence), as shown in **Figure 10**. Note that Model 2 does not cover areas closest to the coast due to the restricted sediment and marine landscape variables, so presence points within fjords are not incorporated into this model for each species. High probability of presence for all corals was predicted along the entire edge of the continental shelf from 62°N to 71°N, extending slightly further north into the Barents Sea for the gorgonians. Other high probability areas included the coastal regions of western Finnmark, the area on the shelf southwest of Lofoten (which includes the Røst Reef), Froan region with the Sula Reef, Iverryggen, in the Boknafjord around Stavanger, and some parts within the Norwegian coastal Skagerrak area. These areas are known to have many *Lophelia* reefs, of which many are protected against bottom trawling. *Lophelia* also has high probability in the Trondheimsfjord, along the western Norway coastal region (including Korsfjorden), and in the Oslo fjord. There is also some probability of presence at the coastal region running along the northern coast toward the Russian border, and the gorgonians have high probability at the most eastern point.

In general, *Lophelia* is more widespread than the gorgonians, with green areas (at least 0.5 probability of presence) around most parts of the middle continental shelf. This becomes more restricted when the sediment and marine landscape variables in Model 2 are added; here, the gorgonians are almost entirely excluded on the continental shelf. Inclusion of the sediment and marine landscape variables overall created more defined SDMs and they were very important in model prediction (**Figures 9D–F**). An interesting artifact of the larger, less precise sediment classification used for the combined sediment layer is that a large chunk along the coast of Western Norway becomes entirely dark blue, especially noticeable for *Lophelia*; this is because this whole area is drawn as clay in the National Atlas from 1991, a sediment type to which all corals responded poorly.

DISCUSSION

Due to limitations of surveying the deep sea, it is hard to gain a comprehensive understanding of cold-water coral distribution and niche. However, SDMs allow us to estimate these in relation to the available environmental conditions within the study area, which helps us to optimize mapping the presence of cold-water corals, such as *Lophelia*, *Paragorgia*, and *Primnoa*. The accuracy and precision of such models depend on the quality and density of predictor variables. Depth and geomorphology are common predictor variables for coral distribution modeling in both local and broad scaled studies (Leverette and Metaxas, 2005; Bryan and Metaxas, 2007; Davies et al., 2008; Dolan et al., 2008; Guinan et al., 2009; Ross and Howell, 2012; Georgian et al., 2014; Guijarro et al., 2016). High resolution bathymetry obtained with multi beam echosounder and interpreted substrate is in general more available at a local scale, whereas oceanographic variables (e.g., currents, temperature, and salinity), and water chemistry variables (e.g., chlorophyll, nutrients, pH) often do not exist at this spatial scale. For broad or global scales, coarse oceanographic variables together with bathymetry from GEBCO or similar data repositories has proven useful to illustrate the general distribution patterns (Davies et al., 2008; Tittensor et al., 2009; Davies and Guinotte, 2011; Yesson et al., 2012, 2017). However, recent development of high-resolution oceanographic models and oceanographic variables have proven more useful for local-scale modeling of coral distributions also at local scales (Georgian et al., 2014; Mohn et al., 2014).

Data Accuracy and Bias

Bias in data may cause inaccurate model predictions. Maxent assumes environmental conditions are represented in proportion to their occurrence within the study area (Merow et al., 2013). With sampling bias of presence points, uncertainty arises on whether predictions are due to species preference for specific environmental conditions or due to an unrepresentative sampling of the environmental conditions within the study area. The MAREANO video stations, the source of the majority of coral records, cover a wide range of geomorphometric, sediment, and marine landscape conditions in Norwegian waters. In terms of oceanographic variables, a broader range in mean temperature and current speed was represented by the oceanographic model compared to what has earlier been observed at locations for these three coral species (Buhl-Mortensen et al., 2015b). However, the range of modeled salinity was considerably smaller than the total range for the study area. This large salinity range is likely due to an area near the Baltic Sea having particularly low salinity. Range of sampled surface chlorophyll *a* concentration was also considerably smaller, due to a small area of high surface productivity in Kattegat (**Figure 2D**). A sampling bias grid was created for the MAREANO stations as a step to account for this bias connected to the choice of sampling areas.

Another potential bias is the clustering of presence points due to uneven sampling, known as spatial auto-correlation, which violates Maxent's assumption of independent sampling (Phillips et al., 2006). Presence points from MAREANO videos are from 700 to 1000 m long transects. Thus, records can be viewed as observation clusters along the transect cluster. Clustering was reduced by grouping individual *Lophelia* video observation points into Coral Reef Habitat points, removing duplicate *Lophelia* points, and generally removing duplicate points for a species within a raster cell.

The number of background points, which can be points at any location within the study area (whether a presence or not), also

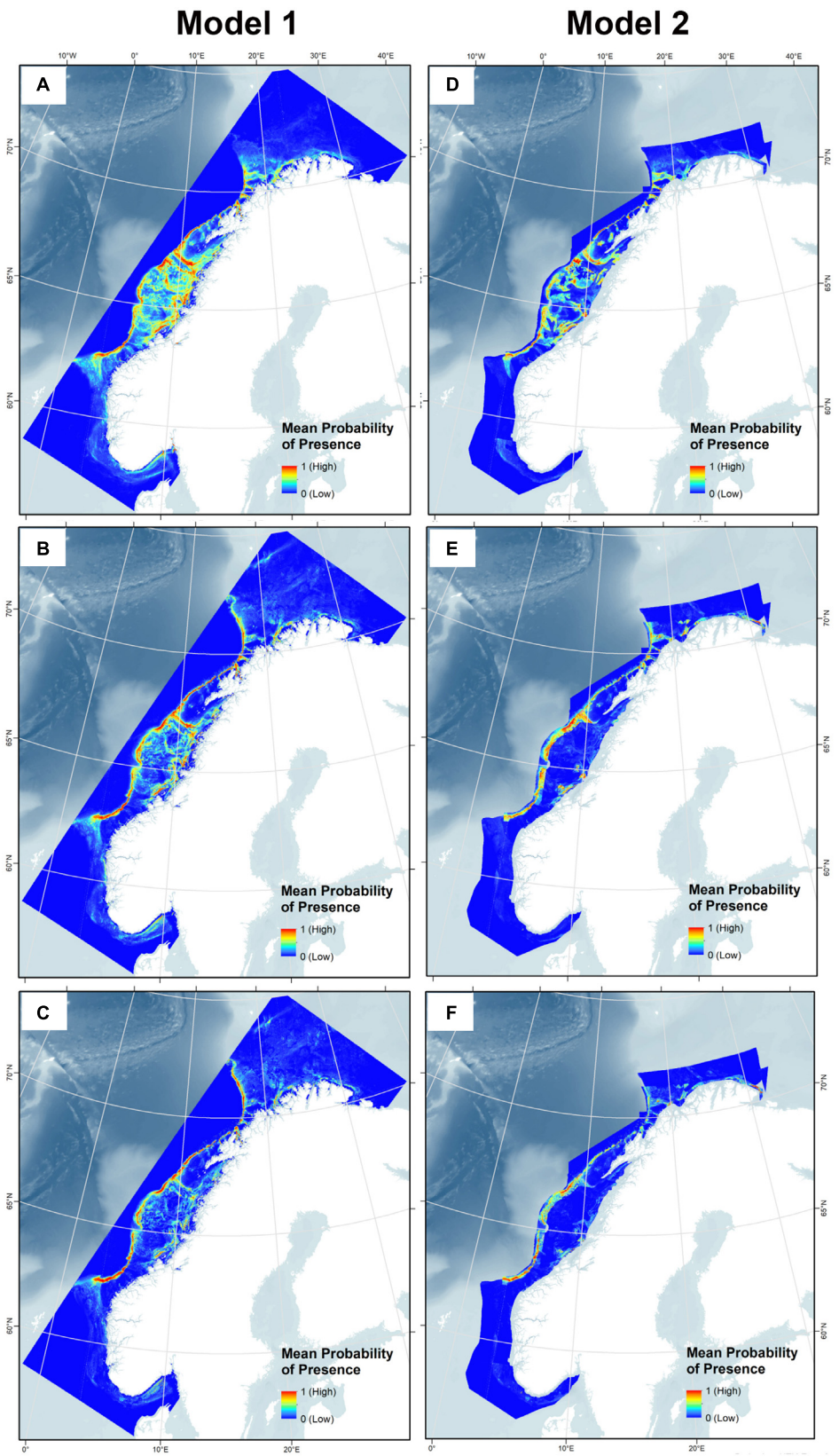

FIGURE 9 | Habitat suitability for *Lophelia pertusa* **(A,D)**, *Paragorgia arborea* **(B,E)**, and *Primnoa resedaeformis* **(C,F)** on the Norwegian continental shelf using Model 1 and 2.

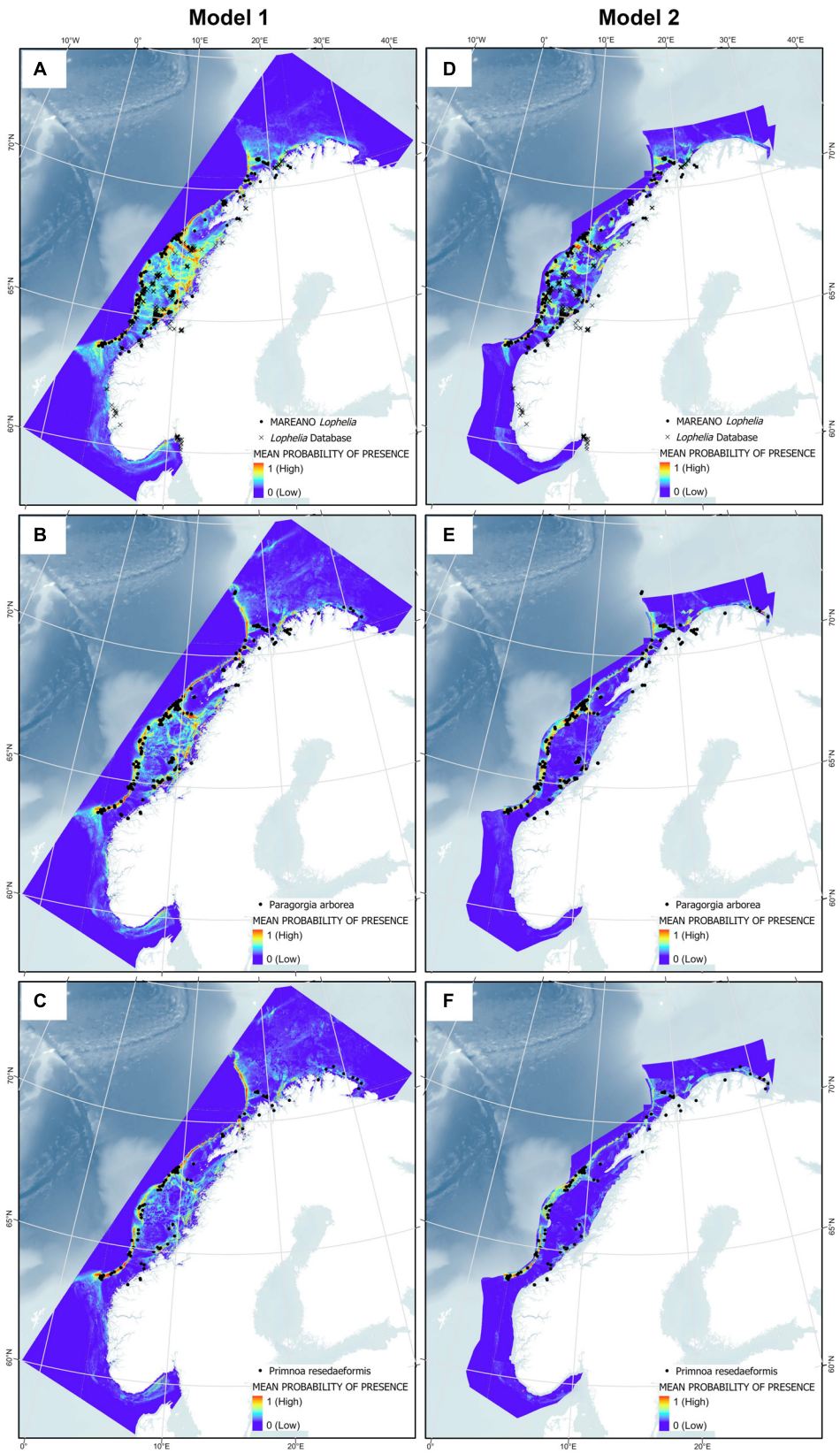

FIGURE 10 | Presence points of *Lophelia pertusa* **(A,D)**, *Paragorgia arborea* **(B,E)**, and *Primnoa resedaeformis* **(C,F)** on the Norwegian continental shelf overlaying the results from Model 1 and 2.

affects the predictive power of the model. Increasing the number increases the AUC because the chance of selecting points that are different from sampled presence locations is larger, and the model will better discriminate between presence and background points (Acevedo et al., 2012). However, this can result in over-prediction (Chefaoui and Lobo, 2008). Like most studies using SDM, the default of 10,000 background points was used here (Fourcade et al., 2014). Finally, for the regularization multiplier, the control on the effect and number of factors used to create coefficients to the model, we used the standard setting of 1. A lower multiplier would result in too many constraints and make the model overfit, while a higher multiplier would give a more diffuse prediction (Philips, 2017).

The quality of the model results is only as good as the quality of the input environmental data. The oceanography data points from Norkyst-800 were 800 m apart and new continuous values was created by interpolation between the original points, which may not reflect actual conditions between the points. This could increase the deviation in temperature and salinity in steep terrain where there is a steep gradient in the relationship between depth temperature, and salinity. Also, converting the sediment and marine landscape shapefiles into rasters using the maximum combined area cell assignment type causes smaller vectors to be eliminated, though it is a small inconvenience as this assignment type chooses the value that covers most of a cell.

The resolution of environmental layers is likewise an important factor to consider. When Davies et al. (2008) modeled with the Ecological Niche Factor Analysis (ENFA), the model indicated temperatures outside of *Lophelia*'s known tolerance range because the grid resolution was not high enough. In this study, some points of *Paragorgia* had temperatures of around −0.3°C, outside its known tolerance; selecting these points in ArcMap indicated they were located on the continental margin. This suggests that large differences present at a short horizontal distance at the continental margin may not be captured within a 176 m grid cell (or the original 800 m for the oceanographic data), potentially assigning the values from the deeper area to the cells where the coral points were.

Broad areas particularly along the western coast had low probability of presence, and these areas matched the extent of clay sediment presence. Clay sediment gave a very low response for all three coral species, too soft a substrate for the corals to settle on. However, these broad sediment categorizations originate from the coarse "Continental Shelf" sediment map used to supplement the more restricted "Regional" sediment map, which in turn gave these coarse predictions. Lastly, the bathymetry map obtained from EMODnet and derived geomorphometric maps have straight lines in some areas that give false terrain variation, which is an artifact of obtaining data from different sources with differing sampling precision (Gunleiksrud and Hodnesdal, 2013).

The geographic precision is within 10 m for the corals observed from the MAREANO mapping. However, many of the historic records of *Lophelia* from the "*Lophelia* database" have an uncertainty of up to 100 m. Compared to the relative broad gridding of the predictor layers, these records are not a great source of uncertainty in the model. Misidentifying the corals in video records may happen, however. This is demonstrated by the occurrence of unusually deep records of *Lophelia* (715 m depth, **Table 3**), in areas where the cold deep water mass is not likely to support live *Lophelia*. These observations could be dead coral skeleton that have been transported down slope from nearby shallower areas.

Predicted Distributions and Niches

Twenty environmental variables were initially considered for analyzing the potential distribution of *Lophelia*, *Paragorgia*, and *Primnoa* on the Norwegian continental shelf, but elimination of some correlating variables resulted in 15 variables used for the actual modeling stage.

The models indicated high probability of presence for all three coral species along the continental margin from Møre og Romsdal up to Tromsøflaket, and along the northern Norwegian coast toward the Russian border. Large areas on the continental shelf southwest of Lofoten also showed high probability, which includes the Røst Reef, the largest known *Lophelia* reef found thus far (Fosså et al., 2005). Other areas of interest near the Norwegian coast were particularly the northern Lofoten/Tromsøflaket region near the continental margin and Lopphavet, and the Froan region with the Sula Reef (Freiwald et al., 2002). Fjords were also areas of high probability, specifically within the Trondheimsfjord (only *Lophelia*), as well as outside the Geirangerfjord, Korsfjorden, and the outer Oslo fjord, for which the environmental data layers do not extend *into*. Overall, the models confirm present species observations. When the sediment and marine landscape variables were included, there were more high probability areas for the gorgonians along the northern coast in the Barents Sea toward the Russian border.

The models confirmed previous observations (Järnegren and Kutti, 2014) of a very distinct coral response to a narrow salinity range close to 35 PSU, and other observations (Brooke and Järnegren, 2013; Buhl-Mortensen et al., 2015b) that *Lophelia* has a shallower preferred depth range (approximately 100–500 m) compared to *Paragorgia* and *Primnoa* (up to 1000 m). Temperature reflected this depth pattern, with a window of approximately 4–7.3°C for *Lophelia*, compared to 0.7–7.3°C for the gorgonians.

Regional maximum depths for *Lophelia* generally reflect different maximum depths of water masses with suitable temperatures for the corals (Frederiksen et al., 1992; Mortensen et al., 2001). Off the Norwegian coast, *Lophelia* reefs are most abundant at depths between 200 and 400 m, and the deepest presence at around 500 m coincides with the shallowest occurrences of the boundary layer between the relatively warm North Atlantic Current and the cold Norwegian Sea (Buhl-Mortensen et al., 2015b). This warm Atlantic water is also found in the basin south of Iceland where *Lophelia* is found down to over 1000 m (mostly dead samples, BIOICE data). The low number of records from Canada and Davis Strait can be explained by the strong Labrador Current from north to south that prevents the warm Gulf Stream from reaching the continental margins, which prohibits further northward colonization of this coral species. Likewise, the distribution of *Paragorgia* in the North Atlantic is connected to the North Atlantic Current, which is

characterized by temperatures generally between 4 and 8°C and stable salinity around 35 PSU (Tendal, 1992). Madsen (1944) regards *Paragorgia* and *Primnoa* as extremely stenothermal requiring temperatures between 5 and 8°C. However, their minimum temperature is colder, down to 2°C (Buhl-Mortensen et al., 2015b). Mortensen and Buhl-Mortensen (2004) found a shallower upper limit for *Primnoa* than for *Paragorgia* off eastern Canada and suggested that the maximum temperature for *Primnoa* is about 2°C higher than for *Paragorgia*. This difference was not indicated in this study, which may be due to local environmental differences other than temperature and salinity, or that the shallower range of the MAREANO mapping area is more poorly represented than deeper locations.

All corals showed preference for exposure to a relatively high mean current speed, especially around 0.20 m/s, confirming the importance of flowing water, for, e.g., feeding and resuspension of sediment deposition (Davies et al., 2009). However, the angle at which the current hits the slope ("current-aspect angle") where corals occur did not indicate a coral specific response. The rose diagrams showing the distribution of current direction observations show that all three species resided mostly on slopes with currents flowing parallel or slightly parallel to the terrain, and fewest observations were made for currents that hit (180°) or pass over (0°) the slope directly. This may indicate that not directly incoming or outgoing currents is a better condition for the corals, or it is simply an artifact of the dynamics of current-slope interaction. However, aspect and current-aspect angle in general were the least useful model predictors for all three corals. The current-aspect angle does not differentiate between currents heading from the land with currents heading toward land, on a broad scale. A modified variable differentiating between these situations could possibly have a greater explanatory power for the coral distribution. Preference for sloped terrain was indicated by species response not dropping with increasing slope, and by a strong response for non-flat terrain. The corals' relation to topographic features reflects a correlation of topography and other factors such as substrate type and food availability. *Lophelia's* preference for negative BPI (troughs) is probably caused by favorable current dynamics bringing food to the reefs. The difference between *Lophelia* and the two gorgonians with respect to aspect may be related to marine landscape-influenced current patterns. *Lophelia* showed a preference for shallow marine valleys and fjords, while the gorgonians preferred the smooth continental slope, marine canyons (*Paragorgia*) and marine valleys (*Primnoa*). Controlled by the Coriolis force and the topography, the currents in marine valleys (troughs) and fjords may differ on the two sloping sides having opposite aspect.

Surface productivity, on the other hand, had a more considerable effect on *Lophelia* presence than for the gorgonians. *Lophelia* has a varied diet, ranging from ingesting copepods to utilizing dead particulate matter, so it can benefit directly from particulate matter brought down to the surface (Frederiksen et al., 1992; Mortensen, 2001; Mortensen et al., 2001). As also indicated by Sherwood et al. (2008), we assume that also the two gorgonians would benefit from enhanced surface production. However, this factor might be of less importance compared with *Lophelia*, or the difference could be due to a stochastic effect related to low number of observation points for the gorgonians compared to *Lophelia*.

The overall AUC values for each species were slightly higher in Model 2 than in Model 1, suggesting that including sediment and marine landscape as predictors allows the model to better discriminate between species presence and absence. Species distribution was more restricted with these two variables included. Sediment type was clearly an important predictor of distribution for all species according to the Jackknife results. This was especially so for the gorgonians, with clear loss to the goodness of fit of the trained model (training gain) and to presence-background discrimination when this variable was omitted (when using test points, i.e., test AUC). Training gain and test AUC also decreased the least for the gorgonians when only sediment type was used, meaning sediment type could predict gorgonian presence well when used alone. *Paragorgia* and *Primnoa* require more solid substrate (boulder and bedrock) than *Lophelia* does, which creates its own substrate (coral skeleton framework) after initially settling on smaller hard substrate, such as pebble. In this study, the gorgonians most frequently occurred on *Lophelia* reefs according to MAREANO's video records; this bioclastic bottom type was removed from the sediment layer. In this case, the substrate of the *Lophelia*-reefs can be regarded as substrate for *Paragorgia* and *Primnoa*. Moreover, *Lophelia* has been observed to grow on oil platforms in the North Sea (Bell and Smith, 1999), indicating that artificial substrates may provide settling opportunities in the absence of natural substrates, when other environmental conditions are suitable.

Study Implications

Evaluating accuracy of SDMs with only AUC should be done with caution, especially if the AUC is very high. If only background points are used when absence data is lacking, there is a higher degree of uncertainty of the probability of absence than there is for presence. False prediction of absences is therefore more likely to occur than false prediction of presences (Lobo et al., 2008), which means the model could potentially be over-predicting. It is better to over-predict slightly than to under-predict, however, since the modeled areas of high probability can be verified further with bottom cameras, for example; such field validation will also further improve model accuracy (Davies and Guinotte, 2011).

The actual realized distribution of corals could also be more limited than predicted due to, e.g., physical barriers that limit potential coral dispersal or bottom trawling that may have destroyed and removed corals from suitable areas (Elith, 2000). Also, climate change may alter the distribution of suitable habitat for coral: changes in sea level and consequently in currents and food delivery may affect the growth and waning of corals, as proposed for coral in the Porcupine Seabright (Rüggeberg et al., 2007).

Future studies could include other variables not used here, such as calcite and/or aragonite saturation state, which were found to contribute greatly to models for octocoral suborders (Yesson et al., 2012) and for *Lophelia* (Davies et al., 2008; Davies and Guinotte, 2011), or oxygen measurement (Yesson et al., 2012; Buhl-Mortensen et al., 2015b). Depth could be left out since, like

in the study of Yesson et al. (2012), many variables utilized the bathymetry layer. Ideally, different regularization values should be explored, too, and the resulting models compared to obtain the best model that is simple and predicts accurately at the same time (Merow et al., 2013).

A combination of threats, from bottom trawling to particles released from the oil and mining industries, to ocean acidification and warming, put cold-water corals under pressure, especially those living near their tolerance threshold. About 30% of all known *Lophelia* occurrences so far are on the Norwegian continental shelf (Järnegren and Kutti, 2014). The threats as well as abundance of cold-water corals give Norway a great responsibility in leading their conservation, but also a head-start. The models created in this study should serve as guidance for further finding, studying, and conserving *Lophelia*, *Paragorgia*, and *Primnoa*.

DATA AVAILABILITY STATEMENT

The datasets generated for this study are available on request to the corresponding author.

AUTHOR CONTRIBUTIONS

HS analyzed data and authored the manuscript. PB-M and LB-M co-authored the manuscript.

ACKNOWLEDGMENTS

The data used were obtained with thanks from MAREANO, the NASA's Ocean Biology Processing Group, EMODnet, Norkyst-800, and data under the Norwegian license for public data (NLOD) made available by Norges geologiske undersøkelse (NGU). Thanks to Jon Albretsen (IMR) and Genoveva Gonzalez-Mirelis (IMR) for constructive help with the manuscript.

SUPPLEMENTARY MATERIAL

The Supplementary Material for this article can be found online at: https://www.frontiersin.org/articles/10.3389/fmars.2020.00213/full#supplementary-material

FIGURE S1 | Current-aspect angle. For same direction as aspect: 0°, toward the aspect: 180°, perpendicular to the aspect: 90°.

FIGURE S2 | Rose diagrams for current-aspect angle (number of occurrences in five sections).

FIGURE S3 | Scatterplot matrix produced with the MGET plug-in for ArcGIS on all coral presence points for all continuous variables. The Spearman's Rank ρ value for each variable pairing is in the upper right half, distribution of each variable in the diagonal, and a scatterplot with a line of best fit in the lower left half. Correlation pairings with $\rho \geq 0.75$ are outlined; variables eliminated for the Maxent analysis are highlighted (from top-left to bottom-right): Max current speed, Ln ruggedness, max salinity, min salinity, and max temperature.

REFERENCES

Acevedo, P., Jiménez-Valverde, A., and Lobo, J. M. (2012). Delimiting the geographical background in species distribution modelling. *J. Biogeogr.* 39, 1383–1390. doi: 10.1111/j.1365-2699.2012.02713.x

Albretsen, J., Sperrevik, A. K., Staalstrøm, A., Sandvik, A. D., Vikebø, F., and Asplin, L. (2011). *NorKyst-800 Report No. 1 - User Manual and Technical Descriptions*. Bergen: Havforskningsinstituttet - Institute of Marine Research.

Anderson, R. P., and Martínez-Meyer, E. (2004). Modeling species' geographic distributions for preliminary conservation assessments: an implementation with the spiny pocket mice (*Heteromys*) of Ecuador. *Biol. Conserv.* 116, 167–179. doi: 10.1016/S0006-3207(03)00187-3

Andrews, A. H., Cordes, E. E., Mahoney, M. M., Munk, K., Coale, K. H., Cailliet, G. M., et al. (2002). Age, growth and radiometric age validation of a deep-sea, habitat-forming gorgonian (*Primnoa resedaeformis*) from the Gulf of Alaska. *Hydrobiologia* 471, 101–110. doi: 10.1023/A:1016501320206

Bell, N., and Smith, J. (1999). Coral growing on North Sea oil rigs. *Nature* 402:601. doi: 10.1038/45127

Breeze, H., and Fenton, D. (2007). Designing management measures to protect cold-water corals off Nova Scotia, Canada. *Bull. Mar. Sci.* 81, 123–133.

Brooke, S., and Järnegren, J. (2013). Reproductive periodicity of the scleractinian coral *Lophelia pertusa* from the Trondheim Fjord, Norway. *Mar. Biol.* 160, 139–153. doi: 10.1007/s00227-012-2071-x

Bryan, T. L., and Metaxas, A. (2007). Predicting suitable habitat for deep-water gorgonian corals on the Atlantic and Pacific continental margins of North America. *Mar. Ecol. Prog. Ser.* 330, 113–126. doi: 10.3354/meps330113

Buhl-Mortensen, L., Aglen, A., Breen, M., Buhl-Mortensen, P., Ervik, A., Husa, V., et al. (2013). Impacts of fisheries and aquaculture on sediments and benthic fauna: suggestions for new management approaches. *Fisken Og Havet* 2:69.

Buhl-Mortensen, L., Buhl-Mortensen, P., Dolan, M. F., and Holte, B. (2015a). The MAREANO programme – A full coverage mapping of the Norwegian offshore benthic environment and fauna. *Mar. Biol. Res.* 11, 4–17. doi: 10.1080/17451000.2014.952312

Buhl-Mortensen, L., Burgos, J. M., Steingrund, P., Buhl-Mortensen, P., Ólafsdóttir, S. H., and Ragnarsson, S. A. (2019). Vulnerable marine ecosystems (VME) Coral and sponge VMEs in Arctic and sub-Arctic waters - distribution and threats. *Temanord* 519:144.

Buhl-Mortensen, L., Hodnesdal, H., and Thorsnes, T. (2015c). *The Norwegian Sea Floor: New Knowledge from MAREANO for Ecosystem-Based Management* (Trondheim: Skipenes kommunikasjon AS), 192.

Buhl-Mortensen, L., Olafsdottir, S. H., Buhl-Mortensen, P., Burgos, J. M., and Ragnarsson, S. A. (2015b). Distribution of nine cold-water coral species (Scleractinia and Gorgonacea) in the cold temperate North Atlantic: effects of bathymetry and hydrography. *Hydrobiologia* 759, 39–61. doi: 10.1007/s10750-014-2116-x

Buhl-Mortensen, L., Vanreusel, A., Gooday, A. J., Levin, L. A., Priede, I. G., Buhl-Mortensen, P., et al. (2010). Biological structures as a source of habitat heterogeneity and biodiversity on the deep ocean margins. *Mar. Ecol.* 31, 21–50. doi: 10.1111/j.1439-0485.2010.00359.x

Buhl-Mortensen, P. (2017). Coral reefs in the Southern Barents Sea: habitat description and the effects of bottom fishing. *Mar. Biol. Res.* 13, 1027–1040. doi: 10.1080/17451000.2017.1331040

Buhl-Mortensen, P., Buhl-Mortensen, L., and Purser, A. (2016). *Trophic Ecology and Habitat Provision in Cold-Water Coral Ecosystems*. Berlin: Springer.

Chefaoui, R. M., and Lobo, J. M. (2008). Assessing the effects of pseudo-absences on predictive distribution model performance. *Ecol. Modell.* 210, 478–486. doi: 10.1016/j.ecolmodel.2007.08.010

Costello, M. J., McCrea, M., Freiwald, A., Lundälv, T., Jonsson, L., Bett, B. J., et al. (2005). "Role of cold-water *Lophelia pertusa* coral reefs as fish habitat in the NE Atlantic," in *Cold-water Corals and Ecosystems*, eds A. Freiwald and J. M. Roberts (Heidelberg: Springer), 771–805. doi: 10.1007/3-540-27673-4-41

Davies, A. J., Duineveld, G. C., Lavaleye, M. S., Bergman, M. J., van Haren, H., and Roberts, J. M. (2009). Downwelling and deep-water bottom currents as food supply mechanisms to the cold-water coral *Lophelia pertusa* (Scleractinia) at the Mingulay Reef complex. *Limnol. Oceanogr.* 54, 620–629. doi: 10.4319/lo.2009.54.2.0620

Davies, A. J., and Guinotte, J. M. (2011). Global habitat suitability for framework-forming cold-water corals. *PLoS One* 6:e18483. doi: 10.1371/journal.pone.0018483

Davies, A. J., Roberts, J. M., and Hall-Spencer, J. (2007). Preserving deep-sea natural heritage: emerging issues in offshore conservation and management. *Biol. Conserv.* 138, 299–312. doi: 10.1016/j.biocon.2007.05.011

Davies, A. J., Wisshak, M., Orr, J. C., and Roberts, J. M. (2008). Predicting suitable habitat for the cold-water coral *Lophelia pertusa* (Scleractinia). *Deep Sea Res. I* 55, 1048–1062. doi: 10.1016/j.dsr.2008.04.010

Demopoulos, A. W. J., Bourque, J. R., Cordes, E., and Stamler, K. M. (2016). Impacts of the Deepwater Horizon oil spill on deep-sea coral-associated sediment communities. *Mar. Ecol. Prog. Ser.* 561, 51–68. doi: 10.3354/meps11905

Dolan, M. F. J., Grehan, A. J., Guinan, J. C., and Brown, C. (2008). Modelling the local distribution of cold-water corals in relation to bathymetric variables: Adding spatial context to deep-sea video data. *Deep Sea Res. I Oceanogr. Res. Pap.* 55, 1564–1579. doi: 10.1016/j.dsr.2008.06.010

Druffel, E. R., Griffin, S., Witter, A., Nelson, E., Southon, J., Kashgarian, M., et al. (1995). *Gerardia*: bristlecone pine of the deep-sea? *Geochim. Cosmochim. Acta* 59, 5031–5036. doi: 10.1016/0016-7037(95)00373-8

Elith, J. (2000). "Quantitative methods for modeling species habitat: comparative performance and an application to australian plants," in *Quantitative Methods for Conservation Biology*, eds S. Ferguson and M. Burgman (New York, NY: Springer), 39–58. doi: 10.1007/0-387-22648-6-4

Elith, J., Phillips, S. J., Hastie, T., Dudík, M., Chee, Y. E., and Yates, C. J. (2011). A statistical explanation of MaxEnt for ecologists. *Divers. Distribut.* 17, 43–57. doi: 10.1111/j.1472-4642.2010.00725.x

Folk, R. L. (1954). The distinction between grain size and mineral composition in sedimentary-rock nomenclature. *J. Geol.* 62, 344–359. doi: 10.1086/626171

Fosså, J. H., Lindberg, B., Christensen, O., Lundälv, T., Svellingen, I., Mortensen, P. B., et al. (2005). "Mapping of lophelia reefs in Norway: experiences and survey methods," in *Cold-Water Corals and Ecosystems. Erlangen Earth Conference Series*, eds A. Freiwald and J. M. Roberts (Berlin: Springer), 359–391. doi: 10.1007/3-540-27673-4_18

Fosså, J. H., Mortensen, P. B., and Furevik, D. M. (2002). The deep-water coral *Lophelia pertusa* in Norwegian waters: distribution and fishery impacts. *Hydrobiologia* 471, 1–12. doi: 10.1023/A:1016504430684

Fourcade, Y., Engler, J. O., Rödder, D., and Secondi, J. (2014). Mapping species distributions with MAXENT using a geographically biased sample of presence data: a performance assessment of methods for correcting sampling bias. *PLoS One* 9:e97122. doi: 10.1371/journal.pone.0097122

Frederiksen, R., Jensen, A., and Westerberg, H. (1992). The distribution of the scleractinian coral *Lophelia pertusa* around the Faroe Islands and the relation to internal tidal mixing. *Sarsia N. Atlant. Mar. Sci.* 77, 157–171. doi: 10.1080/00364827.1992.10413502

Freiwald, A., Hühnerbach, V., Lindberg, B., Wilson, J. B., and Campbell, J. (2002). The sula reef complex Norwegian shelf. *Facies* 47, 179–200. doi: 10.1007/BF02667712

Georgian, S. E., Shedd, W., and Cordes, E. E. (2014). High-resolution ecological niche modelling of the cold-water coral *Lophelia pertusa* in the Gulf of Mexico. *Mar. Ecol. Prog. Ser.* 506, 145–161. doi: 10.3354/meps10816

Ghisla, A., Rocchini, D., Neteler, M., Förster, M., and Kleinschmidt, B. (2012). "Species distribution modelling and open source GIS: why are they still so loosely connected?," in *Proceedings of the 2012 International Congress on Environmental Modelling and Software. Managing Resources of a Limited Planet: Pathways and Visions under Uncertainty, Sixth Biennial Meeting*, Leipzig.

Guijarro, J., Beazley, L., Lirette, C., Kenchington, E., Wareham, V., Gilkinson, K., et al. (2016). Species distribution modelling of corals and sponges from research vessel survey data in the newfoundland and labrador region for use in the identification of significant benthic areas. *Can. Tech. Rep. Fish. Aquat. Sci.* 3171:126.

Guinan, J., Brown, C., Dolan, M. F. J., and Grehan, A. J. (2009). Ecological niche modelling of the distribution of cold-water coral habitat using underwater remote sensing data. *Ecol. Informat.* 4, 83–92. doi: 10.1016/j.ecoinf.2009.01.004

Gunleiksrud, G., and Hodnesdal, H. (2013). *Mer Detaljert Kart Av Terrenget På Havbunnen*. Available online at: http://www.mareano.no/nyheter/nyheter_2012/mer_detaljert_kart_av_terrenget_pa_havbunnen (accessed July 2017).

Gunnerus, J. E. (1763). Om en søevext, allevegne ligesom besat med frøehuuse, Gorgonia resedæformis. *Det Kongelige Norske Videnskabers Selskabs Skrifter*, 2, 321–329.

Husebø, Å, Nøttestad, L., Fossa, J. H., Furevik, D. M., and Jørgensen, S. B. (2002). Distribution and abundance of fish in deep-sea coral habitats. *Hydrobiologia* 471, 91–99. doi: 10.1023/A:1016549203368

Huvenne, V. A. I., Bett, B. J., Masson, D. G., Le Bas, T. P., and Wheeler, A. J. (2016). Effectiveness of a deep-sea cold-water coral marine protected Area, following eight years of fisheries closure. *Biol. Conserv.* 200, 60–69. doi: 10.1016/j.biocon.2016.05.030

Järnegren, J., and Kutti, T. (2014). *Lophelia Pertusa in Norwegian Waters. What Have We Learned Since 2008?*. NINA Report 1028. Trondheim: Norwegian Institute for Nature Research.

Leverette, T. L., and Metaxas, A. (2005). "Predicting habitat for two species of deep-water coral on the canadian Atlantic continental shelf and slope," in *Cold-Water Corals and Ecosystems*, eds A. Freiwald and J. M. Roberts (Berlin: Springer-Verlag), 467–479. doi: 10.1007/3-540-27673-4_23

Linnaeus, C. (1758). *Systema Naturae per Regna Tria Naturae, Secundum Classes, Ordines, Genera, Species, Cum Chararteribus, Differentiis, Synonymis, Locis (Holmiae: Laurentii Salvii)*. Tomus 1: Regnum animale. Stockholm.

Lobo, J. M., Jiménez-Valverde, A., and Real, R. (2008). AUC: a misleading measure of the performance of predictive distribution models. *Glob. Ecol. Biogeogr.* 17, 145–151. doi: 10.1111/j.1466-8238.2007.00358.x

López Correa, M., Montagna, P., Joseph, N., Rüggeberg, A., Fietzke, J., Flögel, S., et al. (2012). Preboreal onset of cold-water coral growth beyond the arctic circle revealed by coupled radiocarbon and u-series dating and neodymium isotopes. *Q. Sci. Rev.* 34, 24–43. doi: 10.1016/j.quascirev.2011.12.005

Madsen, F. J. (1944). Octocorallia (stolonifera–telestacea–xeniidea–alcyonacea–gorgonacea). *Danish Ingolf Exped.* 5, 1–65.

Merow, C., Smith, M. J., and Silander, J. A. (2013). A practical guide to MaxEnt for modeling species' distributions: what it does, and why inputs and settings matter. *Ecography* 36, 1058–1069. doi: 10.1111/j.1600-0587.2013.07872.x

Mohn, C., Rengstorf, A., White, M., Duineveld, G., Mienis, F., Soetaert, K., et al. (2014). Linking benthic hydrodynamics and cold-water coral occurrences: a high-resolution model study at three cold-water coral provinces in the NE Atlantic. *Prog. Oceanogr.* 122, 92–104. doi: 10.1016/j.pocean.2013.12.003

Mortensen, P. B. (2001). Aquarium observations on the deep-water coral *Lophelia pertusa* (L. 1758) (Scleractinia) and selected associated invertebrates. *Ophelia* 54, 83–104. doi: 10.1080/00785236.2001.10409457

Mortensen, P. B., and Buhl-Mortensen, L. (2004). Distribution of deep-water gorgonian corals in relation to benthic habitat features in the Northeast Channel (Atlantic Canada). *Mar. Biol.* 144, 1223–1238. doi: 10.1007/s00227-003-1280-8

Mortensen, P. B., and Buhl-Mortensen, L. (2005). Morphology and growth of the deep-water gorgonians *Primnoa resedaeformis* and *Paragorgia arborea*. *Mar. Biol.* 147, 775–788. doi: 10.1007/s00227-005-1604-y

Mortensen, P. B., Buhl-Mortensen, L., Gordon, D. C. Jr., Fader, G. B., McKeown, D. M., and Fenton, D. G. (2005). Evidence of fisheries damage to deep-water gorgonians in the Northeast channel, Nova Scotia. *Am. Fish. Soc. Symp.* 41, 369–382.

Mortensen, P. B., Hovland, M. T., Fosså, J. H., and Furevik, D. M. (2001). Distribution, abundance and size of Lophelia pertusa coral reefs in mind-Norway in relation to seabed characteristics. *J. Mar. Biol. Assoc. U. K.* 81, 1–17.

Mortensen, P. B., and Lepland, A. (2007). Ecological consequences of exploration drilling on coral reefs in the Træna Deep. *Fisken Og Havet* 7:87.

Myksvoll, M. S., Sandvik, A. D., Albretsen, J., Asplin, L., Johnsen, I. A., Karlsen, O., et al. (2018). Evaluation of a national operational salmon lice monitoring system—From physics to fish. *PLoS One* 13:e0201338. doi: 10.1371/journal.pone.0209949

NASA Goddard Space Flight Center (2018). *NASA Goddard Space Flight Center, Ocean Ecology Laboratory, Ocean Biology Processing Group. Moderate-Resolution Imaging Spectroradiometer (MODIS) Aqua. NASA OB.DAAC*. Greenbelt, MD: NASA.

O'Leary, B. C., Brown, R. L., Johnson, D. E., von Nordheim, H., Ardron, J., Packeiser, T., et al. (2012). The first network of marine protected areas (MPAs) in the high seas: the process, the challenges and where next. *Mar. Policy* 36, 598–605. doi: 10.1016/j.marpol.2011.11.003

Philips, S. J. (2017). *A Brief Tutorial on Maxent*. Available online at: http://biodiversityinformatics.amnh.org/open_source/maxent/ (accessed august 16, 2017).

Phillips, S. J., Anderson, R. P., Dudík, M., Schapire, R. E., and Blair, M. E. (2017). Opening the black box: an open-source release of Maxent. *Ecography* 40, 001–007. doi: 10.1111/ecog.03049

Phillips, S. J., Anderson, R. P., and Shapire, R. E. (2006). Maximum entropy modeling of species geographic distributions. *Ecol. Modell.* 190, 231–259. doi: 10.1016/j.ecolmodel.2005.03.026

Phillips, S. J., Dudík, M., and Schapire, R. E. (2004). "A maximum entropy approach to species distribution modeling," in *Proceedings of the Twenty-First International Conference on Machine Learning*, Banff.

Risk, M. J., Heikoop, J. M., Snow, M. G., and Beukens, R. (2002). Lifespans and growth patterns of two deep-sea corals: *Primnoa resedaeformis* and *Desmophyllum cristagalli*. *Hydrobiologia* 471, 125–131. doi: 10.1023/A:1016557405185

Roberts, J. J., Best, B. D., Dunn, D. C., Treml, E. A., and Halpin, P. N. (2010). Marine geospatial ecology tools: an integrated framework for ecological geoprocessing with ArcGIS, Python, R, MATLAB, and C++. *Environ. Model. Softw.* 25, 1197–1207. doi: 10.1016/j.envsoft.2010.03.029

Roberts, J. M., Wheeler, A. J., Freiwald, A., and Cairns, S. D. (2009a). *3. Biology in Cold-Water Corals - The Biology and Geology of Deep-Sea Coral Habitats*. Cambridge: Cambridge University Press, 67–107.

Roberts, J. M., Wheeler, A. J., Freiwald, A., and Cairns, S. D. (2009b). *4. Reefs and Mounds in Cold-Water Corals - The Biology and Geology of Deep-Sea Coral Habitats*. New York, NY: Cambridge University Press, 108–141.

Ross, R. E., and Howell, K. (2012). Use of predictive habitat modelling to assess the distribution and extent of the current protection of 'listed' deep-sea habitats. *Divers. Distribut.* 19, 433–445. doi: 10.1111/ddi.12010

Rüggeberg, A., Dullo, C., Dorschel, B., and Hebbeln, D. (2007). Environmental changes and growth history of a cold-water carbonate mound (Propeller Mound, Porcupine Seabight). *Intern. J. Earth Sci.* 96, 57–72. doi: 10.1007/s00531-005-0504-1

Sherwood, O. A., Jamieson, R., Edinger, E. N., and Wareham Hayes, W. E. (2008). Stable C and N isotopic composition of cold-water corals from the Newfoundland and Labrador continental slope: examination of trophic, depth and spatial effects. *Deep Sea Res. Part I Oceanogr. Res. Pap.* 55, 1392–1402. doi: 10.1016/j.dsr.2008.05.013

Tendal, O. S. (1992). The North Atlantic distribution of the octocoral *Paragorgia arborea* (L., 1758) (Cnidaria. Anthozoa). *Sarsia* 77, 213–217. doi: 10.1080/00364827.1992.10413506

Tittensor, D. P., Baco, A. R., Brewin, P. E., Clark, M. R., Consalvey, M., Hall-Spencer, J., et al. (2009). Predicting global habitat suitability for stony corals on seamounts. *J. Biogeogr.* 36, 1111–1128. doi: 10.1111/j.1365-2699.2008.02062.x

UNGA (2006). *Resolution 61/105 Sustainable Fisheries, Including Through the 1995 Agreement for the Implementation of the Provisions of the United Nations Convention on the Law of the Sea of 10 December 1982 relating to the Conservation and Management of Straddling Fish Stocks and Highly Migratory Fish Stocks, and Related Instruments*. New York, NY: UNGA.

Vorren, T. O., and Vassmyr, S. (1991). *Kontinentalsokkelen - Overflatesedimenter, 1:3 Mill in Nasjonalatlas for Norge, Karblad 2.3.8*. Hønefoss: Statens kartverk.

Walbridge, S., Slocum, N., Pobuda, M., and Wright, D. J. (2018). Unified geomorphological analysis workflows with benthic terrain modeler. *Geosciences* 8:94. doi: 10.3390/geosciences8030094

Wheeler, A. J., Beyer, A., Freiwald, A., de Haas, H., Huvenne, V. A. I., Kozachenko, M., et al. (2007). Morphology and environment of cold-water coral carbonate mounds on the NW European margin. *Intern. J. Earth Sci.* 96, 37–56. doi: 10.1007/s00531-006-0130-6

Yesson, C., Bedford, F., Rogers, A. D., and Taylor, M. L. (2017). The global distribution of deep-water antipatharia habitat. *Deep Sea Res. II.* 145, 79–86. doi: 10.1016/j.dsr2.2015.12.004

Yesson, C., Taylor, M. L., Tittensor, D. P., Davies, A. J., Guinotte, J., Baco, A., et al. (2012). Global habitat suitability of cold-water octocorals. *J. Biogeogr.* 39, 1278–1292. doi: 10.1111/j.1365-2699.2011.02681.x

Conflict of Interest: The authors declare that the research was conducted in the absence of any commercial or financial relationships that could be construed as a potential conflict of interest.

frontiers in Marine Science

ORIGINAL RESEARCH
published: 30 April 2020
doi: 10.3389/fmars.2020.00271

Classification and Mapping of Benthic Biotopes in Arctic and Sub-Arctic Norwegian Waters

Pål Buhl-Mortensen[1], Margaret F. J. Dolan[2], Rebecca E. Ross[1], Genoveva Gonzalez-Mirelis[1], Lene Buhl-Mortensen[3], Lilja Run Bjarnadóttir[2] and Jon Albretsen[4]*

[1] Benthic Communities and Coastal Interactions Research Group, Institute of Marine Research (IMR), Bergen, Norway, [2] Marine Geology, Geological Survey of Norway, Trondheim, Norway, [3] Marine Research in Developing Countries, Institute of Marine Research, Bergen, Norway, [4] Oceanography Research Group, Institute of Marine Research, Flødevigen, Norway

In this paper, we describe the species composition of biotopes occurring in a wide range of environments and present their geographic distribution based on results from quantitative analyses of video-records collected as part of the Norwegian seabed mapping program MAREANO. We present results from an analysis of annotated video records at 757 stations from an area exceeding 100,000 km^2 in the Barents Sea and Norwegian Sea. A two-way indicator species analyses (TWINSPAN) was used to identify sample groups and species assemblages for biotope classification. Environmental conditions were compared for the station groups identified at different similarity levels to detect environmental drivers behind each division and hence biotopes indicated by the analysis. In total, 27 groups were identified as potential biotopes in the study area giving a geographic resolution suitable for management needs and subsequent predictive modeling. The faunal composition was mainly correlated with water masses (temperature and salinity). The most distinct biotope identified occurred on Spitsbergenbanken, a shallow area (<50 m) with strong bottom currents. The other biotopes formed two main groups characterized by different oceanographic properties: (1) Atlantic Water and Arctic Intermediate Water associated with higher temperatures and stronger current speed and (2) Arctic Water, Atlantic Water, and Norwegian Sea Deep Water (NSDW) associated with both lower temperatures and slower current speeds. The cold-water species occurred both in the shallow (<200 m) Artic Water in the north-eastern part of the study area, and the deep (>600 m) NSDW, separating into two TWINSPAN groups. Further divisions of these groups reflected variations in sediment and terrain attributes. Ten biotopes were characterized by indicators species of vulnerable marine ecosystems (e.g., coral gardens, sea pen communities, and sponge aggregations). Knowledge about megafauna composition and biotopes is poor for deep-water benthic habitats in the Arctic region, and better classification of benthic biotopes will be valuable for management purposes such as design of monitoring program for documenting the effects of climate change on ecosystems.

Keywords: seabed mapping, benthic biotopes, habitat classification, habitat mapping, spatial distribution modeling, Norwegian Sea, Barents Sea

OPEN ACCESS

Edited by:
Daphne Cuvelier, Center for Marine and Environmental Sciences (MARE), Portugal

Reviewed by:
Jaime Selina Davies, University of Plymouth, United Kingdom
Steven Degraer, Royal Belgian Institute of Natural Sciences, Belgium

****Correspondence:***
Pål Buhl-Mortensen
paal.buhl.mortensen@hi.no; paalbu@imr.no

Specialty section:
This article was submitted to Deep-Sea Environments and Ecology, a section of the journal Frontiers in Marine Science

Received: *08 September 2019*
Accepted: *03 April 2020*
Published: *30 April 2020*

Citation:
Buhl-Mortensen P, Dolan MFJ, Ross RE, Gonzalez-Mirelis G, Buhl-Mortensen L, Bjarnadóttir LR and Albretsen J (2020) Classification and Mapping of Benthic Biotopes in Arctic and Sub-Arctic Norwegian Waters. Front. Mar. Sci. 7:271. doi: 10.3389/fmars.2020.00271

INTRODUCTION

An increasing interest in deep-sea resources has brought about a growing number of offshore activities such as industrial fishing, mining, and oil and gas extraction (Ramirez Llodra et al., 2011). These activities cause a wide range of pressures on benthic ecosystems including animal removal, habitat destruction, sedimentation, pollution, etc. The ecological effects of these pressures (i.e., impacts) may include local and global species extinctions, altered food web dynamics, loss of connectivity, decreased ecosystem stability, and altered patterns of biogeochemical cycling (McCauley, 2015). Area-based management is a tool to avoid negative impact on biological communities, habitats, and the environment. In addition, ongoing climate change heightens the need for solid knowledge of marine ecosystems to support appropriate management strategies. Area-based management, however, typically requires spatial ecological data, which is notably difficult to obtain (Steltzenmüller et al., 2013).

The Marine AREAl database for NOrwegian waters (MAREANO) program conducts seabed mapping, as required by the Norwegian government, in order to fill knowledge gaps relevant to the implementation of management plans for different parts of the Norwegian EEZ. The program was launched in 2005 with the goal of obtaining information that can be used as a scientific basis for the regulation of human activities such as those undertaken by the petroleum industry and fisheries. By using a variety of complementary sampling gears (such as towed video, beam trawl, Van Veen grab, and Rothlisberg and Pearcy sledge) to ensure that a broad set of benthic organisms on all types of seabed are represented, MAREANO offers a unique insight into the diversity, biomass, and production of benthic communities. Map products and data from MAREANO include bathymetric and geological maps as well as information on environmental status, species distribution, biological production, biodiversity, habitats, and biotopes. The latter being the focus of this paper.

In this paper, we utilize video data (results from analyses of video records) to define and predict benthic biotopes. Although video observations are mainly documenting epi-benthic megafauna (>c. 5 cm), they provide information on community composition from all substrate types. These observations are therefore useful for characterizing biotopes from a wider range of seabed substrates than is possible with physical sampling tools. By combining the MAREANO data and map products with modeled oceanographic data (temperature, salinity, and currents near the sea floor), the ecological insights that can be gained from the MAREANO data are enhanced.

A biotope can be defined as a combined characteristic species composition and environmental settings. In particular, the physical characteristics of water masses near the seabed, topography, and seabed substrate are often the main determining factors (Barnes and Hughes, 1982; Harris, 2012; in review) shaping benthic communities. These environmental settings can be used to predict biotope distribution in areas without observations using methods common to habitat distribution modeling (HDM).

Biotope maps can display multiple biotopes simultaneously, suggesting the most likely biotope to occur in each area (as shown in this study), or they can display the probability of occurrence of a single biotope, similar to a species distribution model (e.g., Ross and Howell, 2013). The multi-biotope format is better suited for assessing the likely distribution of the biotopes we define in this study compared to a set of individual single biotope maps. Both map types are generated by MAREANO, where the single biotope maps are used for vulnerable marine ecosystems. In this paper, we focus on the identification of biotopes and environmental factors that correlate with their spatial distribution. The aim of this study is: (1) classification of biotopes based on megafaunal composition at observed seabed areas and (2) to relate these biotopes to environmental variables that can be used to predict the distribution of biotopes across the entire mapping area.

MATERIALS AND METHODS

The study area was surveyed over the course of 12 years (2006–2018) collecting video transects at 757 different locations (none of which were repeat visits) within the Norwegian Barents Sea region including shelf areas off Troms and Finnmark counties and north-eastern shelf and slope areas in the Norwegian Sea (**Figure 1**). This area comprises a wide range of environmental conditions over which we know there is a varied distribution of benthic communities. The continental margin offshore North Norway described here is in the area 68°N–77°N and 15°E–37°E.

Geological Setting

The Barents Sea is a shallow (<800 m deep) epicontinental sea. Depths within the study area range from 24 to 1170 m in the Norwegian Sea and to the full depth of the Barents Sea. The seabed in the study area consists mainly of sedimentary rocks from the Mesozoic and Cenozoic (Sigmond, 2002).

The broad-scale seafloor morphology is a result of repeated glaciations throughout the Quaternary (Knies et al., 2009) and is characterized by a landscape of shallow banks, approximately 20–300 m deep, intersected by deeper marine valleys or troughs, approximately 300–800 m deep (**Figure 1B**). The seafloor is covered with sediments deposited either sub-glacially or in a glacimarine environment. The type, distribution, and thickness of the majority of unlithified sediments in the study area are a result of glacial and oceanographic processes during the late Pleistocene and Early Holocene, rather than contemporary processes (e.g., Elverhøi et al., 1993; Bjarnadóttir et al., 2014). Similarly, most of the fine-scale seafloor geomorphic features record processes related to the last deglaciation of the area (e.g., Bjarnadóttir et al., 2014), although some areas have since been reshaped by oceanographic processes (e.g., Bellec et al., 2019). Geomorphic features from broad-scale landscapes (**Figure 1B**) to smaller landforms have been widely documented to be linked to benthic habitat (Harris and Baker, 2011). The modern-day distribution of substrate types (**Figure 1C**) is influenced by bottom currents, and both are expected to have an important effect on the distribution of benthic fauna. The southwestern part of the study area is

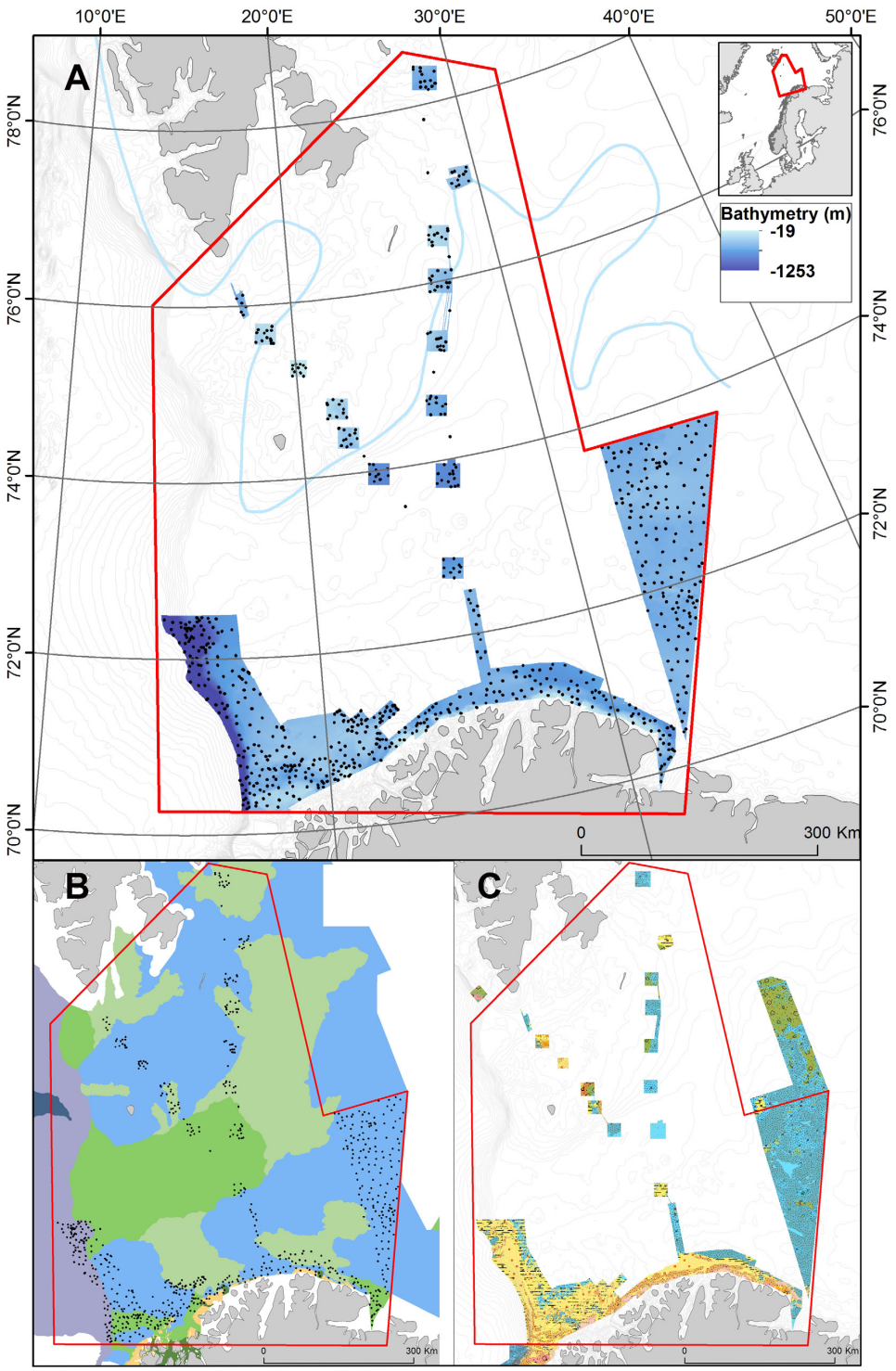

FIGURE 1 | (A) Map of the study area in the Barents Sea. The extent of the study area is indicated in red and MAREANO video stations used in this study area shown as black dots over color shaded bathymetry from Kartverket https://mareano.no/en/maps-and-data/marine-geospatial-data. The approximate location of the polar front is indicated with a line. **(B)** A MAREANO landscape map (broad-scale geomorphology) showing how the area is dominated by continental shelf plain (blue), marine valleys (green), and shallow marine valleys (light green) with areas near the coast comprising strandflat (orange) while deeper areas to the west are classified as smooth continental slope (purple). Full symbology is available at https://www.ngu.no/Mareano/Landscape.html. Landscape mapping procedures are based on Elvenes (2013). **(C)** A MAREANO sediment map showing how the southwestern part of the study area is dominated by sandy and gravelly sediments (yellow, orange) while eastern areas are dominated by muddy sediments (blue). Full symbology available at https://www.ngu.no/Mareano/Grainsize.html.

dominated by sandy and gravelly sediments, while eastern areas are dominated by muddy sediments (**Figure 1C**).

Oceanographic Setting

Four major water masses originating in the Atlantic and Arctic oceans meet in the Norwegian Sea (Hansen and Østerhus, 2000), and the associated currents are of fundamental importance for the global climate. The warm, salty North Atlantic Current (NAC) flows in from the Atlantic Ocean, and the colder and less saline Norwegian Coastal Current (NCC) originates in the North Sea. The Norwegian Atlantic water (NAW) extends down to about 500–600 m and is part of the relatively warm and saline NAC. Below this depth, two cold water masses occur: the Norwegian Sea Arctic Intermediate Water (NSAIW) which flows as a continuation of the East Iceland Current from the Iceland and Greenland Seas and the Norwegian Sea Deep Water (NSDW) from the Greenland Sea. NSAIW has a temperature range between −0.5 and 0.5°C, whereas the NSDW typically shows a temperature range between −0.5 and −1.1°C. The interface between these two water masses typically occurs at around 1300 m off the Norwegian coast in the Norwegian Sea (Blindheim, 1990).

The bottom topography with banks and basins steers the currents and influences the distribution of water masses in the Barents Sea (Loeng, 1991). The Norwegian Atlantic Current splits into two main branches, one flowing into and through the Barents Sea from southwest to northeast, the other flowing around the western and northern flanks of the Barents Sea as the West Spitsbergen Current (Skagseth, 2008; Ingvaldsen and Loeng, 2009; Ozhigin et al., 2011). Cold fresh Arctic waters arrive from the Arctic Ocean, entering the Barents Sea between Nordaustlandet and Franz Josef Land and between Franz Josef Land and Novaya Zemlya. The Polar Front is a prominent feature in the Barents Sea, and it represents the transition zone between the warm and saline Atlantic Water and the cold and less saline Arctic and Polar waters.

Video Recording and Annotation

The seabed was inspected using the towed video platforms, "CAMPOD" (as described in Buhl-Mortensen et al., 2009, 2012) and "Chimaera" (as described in Buhl-Mortensen and Buhl-Mortensen, 2017) equipped with similar High-Definition video cameras systems, tilted forward at an angle of approximately 45°. Video was continuously recorded to harddrive along each transect. The video platform was towed behind the survey vessel at a speed of 0.7 knots and controlled by a winch operator providing a near-constant altitude of 1.5 m above the seabed. Each video transect was planned to cover a distance of 700 m, but in practice, the distance varied between 600 and 800 m. Positioning of the video data is provided by a hydroacoustic positioning system (Simrad HIPAP and Eiva Navipac software) with a transponder mounted on the video platform, giving a position accurate to 2% of water depth. Navigational data (date, UTC time, positions, and depth) are recorded automatically at 10-s intervals using the software CampodLogger developed by the Institute of Marine Research (as described in Buhl-Mortensen et al., 2015a,b).

After the cruise a detailed video analysis was undertaken using a custom-made (Institute of Marine Research) software: VideoNavigator (as described in Gomes Pereira et al., 2016). The output of this software is a text file showing time stamped species names, abundances, substrates, comments, field of view (as measured based on laser points mounted 10 cm apart), and image quality records. These biological annotations were then georeferenced by synchronizing the video timestamps with the navigation data which had undergone cleaning to remove spurious pings. X and Y coordinates were recorded in UTM zone 33 (WGS 1984).

Biological observations were aggregated into sums of species abundance per ∼200 m long annotated video sequences (hereafter referred to as "samples"). Since the actual distance of the full video transects often was not possible to divide into equal long sequences, sequences with lengths less than 20% of the sample length (<160 m) were not included in the material. All organisms were identified to the lowest taxonomic level possible and counted or quantified as percentage of seabed coverage (the latter only in few cases, e.g., for encrusting sponges and similar) following the method described by Mortensen and Buhl-Mortensen (2005). The few organisms that were recorded as percent cover during video annotation were converted to counts before analysis by using the approximate standard size of an individual or colony (from expert knowledge) and the area of the video frame. Abundance data were then standardized as the number of individuals per 100 m^2, where area was calculated based on traveled distance (generally 200 m) and average field width.

Preparation of Biological Community Data

The biological data from the 757 videos were split into 2959 (200 m) samples. Taxa with uncertain identifications or a broad taxonomic resolution (e.g., "sponge" and "fish") were removed before the analysis. Pelagic species were removed, while demersal fish such as saithe and redfish were retained. To include only species that were well documented and videos with enough biological community information (to avoid outliers in the data) only samples with four taxa or more, and taxa occurring in at least four samples were used in the analysis. The final dataset consisted of 2913 video samples and 222 taxa.

Preparation of Environmental Data

A selection of available environmental variables was compiled for analysis of potential drivers behind biotope distribution. Only variables available as complete coverage raster layers were included to allow for subsequent model predictions of biotope distribution.

Terrain and Geological Attributes

In addition to bathymetry data, we generated a suite of terrain attributes (slope angle, rugosity, etc.) which may influence the distribution of benthic communities. For the purposes of this study, existing high resolution (5–25 m horizontal resolution) multibeam bathymetry data were resampled to 200 m resolution using bilinear resampling. The terrain attributes themselves

require a choice of spatial neighborhood size across which to calculate changes in the derived variable. For example, in order to calculate the slope of the bathymetry every focal 200 m pixel needs to be compared to the surrounding pixels to understand its difference in height relative to its surroundings. However, you must choose whether that analysis area refers only to those pixels that are nearest or whether it spans several rings of pixels surrounding that point (the diameter of these rings of analysis is hereafter referred to as "a neighborhood" for analysis). We chose to apply a multi-scale approach (Wilson et al., 2007; Lecours et al., 2016) using neighborhoods of varying size to represent terrain effects on varying scales (i.e., local at 3 × 3 pixels, to broader scale at $n \times n$ pixel neighborhoods). Derivation of accurate terrain attributes is only possible for the portion of data where the neighborhood is entirely full of data (Wilson et al., 2007; Dolan and Lucieer, 2014). MAREANO video surveys are planned to avoid the edges of raster data coverage but nevertheless it has been necessary to limit the broadest scale terrain-derived variables in this study to a maximum neighborhood size of 9 × 9 pixels (on a 200 m grid this represents a comparative neighborhood covering a ground distance of 1800 × 1800 m) to avoid too many video samples falling outside the coverage of terrain attributes. In order to capture initial information representing environmental conditions across large parts of the Barents Sea, MAREANO surveys in much of the northern part of the study area are limited to boxes, including both newly acquired and legacy data. The terrain attributes generated for this study are summarized in **Table 1**. Sediment grain size and landscape maps (Geological Survey of Norway [NGU], 2019a,b) were converted from polygon shape file to a raster dataset and aligned with the terrain variables at 200 m resolution using feature-to-raster conversion tools in ArcGIS.

Oceanographic Model Data

The oceanographic model data used in this study come from a 1-year (2010) model simulation for the Barents Sea using 800 m × 800 m horizontal resolution (**Figure 2**). The model was set up using the bathymetry from IBCAO.v3 (International Bathymetric Chart of the Arctic Ocean, Jakobsson et al., 2012) and was run using the numerical ocean model ROMS (Regional Ocean Modeling System[1], e.g., Shchepetkin and McWilliams, 2005; Haidvogel et al., 2008) which applies a vertical topography-following coordinate system. Our simulation was defined with 35 vertical levels. Along the open boundaries, the model was forced with tidal analysis from TPXO7.2 (Egbert and Erofeeva, 2002) and daily averages of water level, salinity, temperature, and currents from the 4 km-model described in Lien et al. (2014). The atmospheric forcing applied was the ERA-Interim reanalysis provided by the European Centre for Medium-Range Weather Forecasts (ECMWF, see Dee et al., 2011). The model then provided information (maximum, mean, minimum, 90th percentile, standard deviation) on near-bottom temperature, salinity, and current speed. Data were resampled to 200 m using bilinear resampling to match the resolution of the terrain and geological data for onward use in biotope modeling.

[1]http://myroms.org

Additional Variables

A number of variables derived from satellite observed ocean color were downloaded as raster datasets from MODIS-Aqua (Nasa Goddard Space Flight Center, 2018) using the Create Rasters for NASA OceanColor L3 SMI Product utility in the MGET toolbox (Roberts et al., 2010). While ocean color products represent surface conditions, they can have relevance for the seabed environment and have been used in several other seabed habitat mapping studies (e.g., Bryan and Metaxas, 2007; Davies et al., 2008; this issue). These data have a resolution of 4 km and represent annual average conditions. Data were downloaded for the entire time period over which MAREANO video surveys were conducted in this area, i.e., 2006–2017 and averaged over this time to create a single layer for each variable.

Latitude and longitude are not, strictly speaking, environmental variables but could be a proxy for biogeographic gradients or provinces, and may correlate with oceanographic variation, so these were also included in our analysis in the form of UTM33 (WGS84) easting and northing.

Classification Analyses

TWINSPAN

Video samples and species were classified using two-way indicator species analysis (TWINSPAN—Hill, 1979), as part of the software PCord 5.10. TWINSPAN is an algorithm which performs a divisive hierarchical ordination of site and species data. The data are ordered by the first axis of a correspondence analysis and then split near the middle, the location of the split being adjusted by the identification of indicator species with preferential affiliation to one half or the other (hereafter these halves are termed as "groups"). Each group is then iteratively split again using the same process, producing a hierarchical classification of site data with indicator species for each group. TWINSPAN, like detrended correspondence analysis (DCA), has been widely used by ecologists and has the potential to be particularly useful in HDM. The TWINSPAN method was selected also because it provides much clearer groupings of samples in a dataset with a large number of samples. The abundances of taxa in the video samples were square root transformed to down-weight the superabundant species and approximate a normal distribution. The transformed abundances were then placed into five abundance levels (called "pseudo-species" within the TWINSPAN terminology) using the following cut levels: >0–2, 2–5, 5–10, 10–20, and >20. All species that met the criteria described above were included in the analysis, but rare species were down weighted using the corresponding TWINSPAN function (meaning that they would be less likely to be chosen as an indicator species for each group). The TWINSPAN analysis then performs subsequent divisions of the dataset until the statistics are not able to distinguish any further divisions of groups. We applied an additional criterion that the resulting groups could not consist of too few samples. Groups with less than 20 samples were therefore merged with "parent groups" (lifted one division level). Terminal groups adhering to this rule were then considered to be our putative biotopes. As a result, some of the identified terminal groups, where

TABLE 1 | Summary of terrain attributes generated from bathymetry data.

Terrain attribute	Resolution	Analysis window	Method
Slope	200	3, 9	Generated using GRASS module r.param.scale via QGIS
Eastness	200	3, 9	Computed from aspect generated using GRASS module r.param.scale via QGIS.
Northness	200	3, 9	Computed from aspect generated using GRASS module r.param.scale via QGIS.
Profile curvature	200	3, 9	Generated using GRASS module r.param.scale via QGIS
Plan curvature	200	3, 9	Generated using GRASS module r.param.scale via QGIS
Bathymetric position index (BPI)	200	3, 9	Calculated in ArcGIS Spatial Analyst Raster Calculator based on BPI Lundblad 2006 but adapted for a rectangular window and floating point output.
Vector Ruggedness Measure (VRM)	200	3, 9	Calculated using BTM toolbox in ArcGIS (Walbridge et al., 2018)

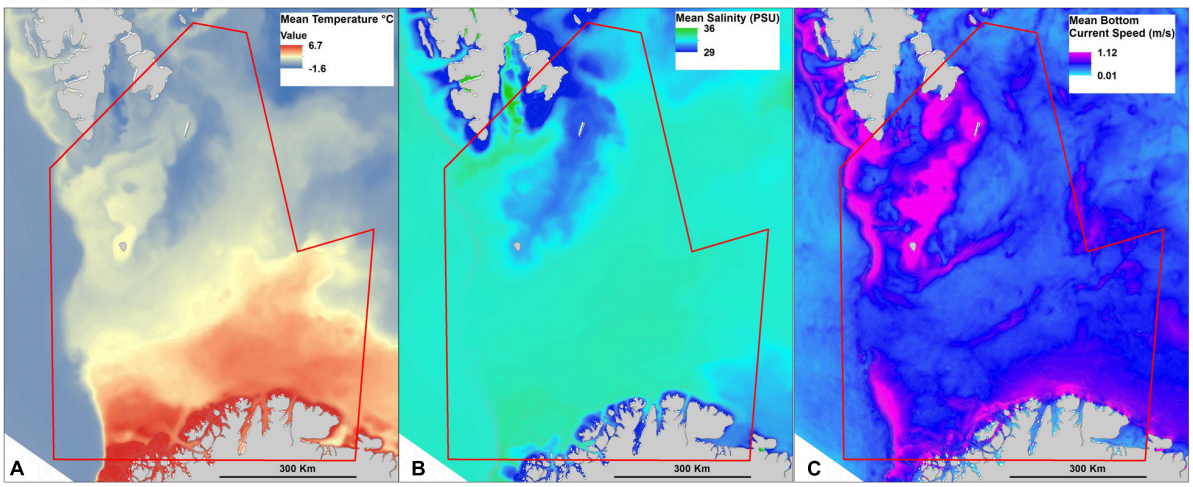

FIGURE 2 | Examples of oceanographic variables indicating the level of detail captured by the Barents 800 model, and spatial variation in seabed oceanographical settings. **(A)** Mean temperature (°C), **(B)** mean salinity (PSU), and **(C)** mean bottom current speed (m/s).

merging with parent groups occurred, may more accurately represent "biotope complexes" which may include more than one distinguishable biotope if there were enough samples to properly define the community and correlated environmental parameters.

The TWINSPAN results also provided an overview of indicator species for each group based on species (and pseudo-species) composition. To refine the TWINSPAN-identified indicator species lists, expert knowledge was used to select those that are both dominant and easily identifiable from video footage. These species were considered to be representative of the new putative biotopes.

Environmental characteristics of TWINSPAN groups

An exploratory analysis was performed upon each TWINSPAN dichotomous split (i.e., pairings of groups) to investigate whether each group was correlated with any environmental variables. Draftsman plots, symbolizing each group in a pair and examining all variables from corresponding samples locations against depth together with key variable pairings such as temperature and salinity, enabled initial explorations of group/environment patterns. Principal component analyses (PCAs), comprising the most likely environmental correlates as identified by the draftsman plots and with points symbolized paired groups, were also used to indicate the dominant eigenvectors at each split (see **Supplementary Information S1** for the main results of these investigations). In addition, forward selection analysis was performed using the software Canoco 5.04 to explore how much of the biological variation the different numerical environmental variables explained while using the biotopes as a categorical response variable. These analyses helped ensure that biologically relevant variables were pre-selected as potential predictor variables for subsequent modeling.

Modeling and Prediction of Spatial Biotope Distribution

To demonstrate the wider distribution of putative biotopes defined by TWINSPAN, a full coverage raster biotope map was produced using random forest models built using the Ranger package in R. This approach allows us to predict the distribution of biotopes between MAREANO stations providing full-coverage information in a format that is more convenient for onward use in management. Environmental predictor selection was decided based on the exploratory analyses described above, and a balance of model performance statistics and visual validation. The final model included the following 15 predictors: longitude, latitude,

TABLE 2 | List of biotopes, with a brief description of their characteristic water mass, landscapes, sediments, and fauna.

Biotope	Landscapes	Substrates	Characteristic fauna
Atlantic water			
F	Strandflat	Hard substrate	Encrusting red algae
G	Shallow continental shelf plain	Coarse substrate	Sea pens and Cauliflower corals
L	Continental shelf plain and marine valley	Gravelly muddy sand	Soft bottom sponge aggregation or *Lophelia* reef
I	–– " ––	Mixed	Cup corals
O	Continental shelf	Muddy	*Liponema* anemones
P	Continental shelf plain and shallow marine valley	Muddy	Bryozoans and filamentous Suberites sponges
N	Continental shelf	Mixed muddy	*Filograna* polychaetes and small sponges
K	–– " ––	Mixed	Sponge garden
M	–– " ––	Mixed sandy	Sea urchins, *Parastichopus* sea cucumber, and *Kukenthalia* tunicate
J	Continental shelf and upper continental slope	Gravelly, sandy	*Reteporella* bryozoan
H	Shallow marine valley	Sandy, muddy	*Asbestopluma* sponges and cup corals
Arctic intermediate water			
B	Continental slope	Sandy, gravelly	Cauliflower corals
C	–– " ––	Sandy, gravelly	Encrusting sponges, tunicates, and cauliflower corals
A	–– " ––	Sandy	Pigtail coral garden
D	–– " ––	Sandy	Tethya and Craniella sponges
E	–– " ––	Sandy	*Phakellia* sponges
Norwegian sea deep water			
X	Continental slope	Mixed sandy	Encrusting sponges
V	–– " ––	Sandy	*Virgularia* sea pens
W	–– " ––	Sandy	*Umbellula* sea pens
Y	–– " ––	Sandy	Cold water sponges and leeches
Z	–– " ––	Sandy	Tube anemones and cold-water sponges
Arctic water			
ZA	Shallow bank	Sandy, gravelly	Sea cucumber (*Cucumaria frondosa*), *Thuiaria hydrozoans*, and *Eucratea bryozoans*
Q	Continental shelf	Mixed	Psolus (holothurian) and Cauliflower corals (*Gersemia rubiformis*)
U	–– " ––	Sandy, gravelly	Iceland scallop aggregations
T	Continental shelf plain	Muddy, sandy	Cauliflower corals and tube anemones (Cerianthidae)
S	Continental shelf plain and marine valley	Muddy, sandy	Cauliflower corals (*Gersemia rubiformis*) and *Porella* bryozoans
R	Continental shelf plain and shallow marine valley	Muddy	Basket star aggregations

depth, average/s.d./max/min temperature, s.d. salinity, average/max/s.d. current speed, average chlorophyll, average POC, sediment, landscape. The model performance was evaluated using Cohen's kappa coefficient which compares observed vs. expected accuracy (the proportion of correct predictions), while accounting for chance, and is a suitable performance statistic for multi-class problems. Further details of the modeling and prediction are beyond the scope of this paper and will be reported separately.

RESULTS

Biotopes and Their Environmental Characteristics

The TWINSPAN analysis of the species data from all video samples split iteratively into groups is shown as a dendrogram in **Figure 3**. The TWINSPAN analysis generated a total of 27 groups adhering to our rule of >20 samples each (the smallest resulting group contained 23 samples). These groups became our putative biotopes (hereafter "biotopes") and are described in **Table 2** and represented by the letters A–Z and ZA in **Figure 3**.

One group of locations at Spitsbergenbanken formed a clear outlier (biotope ZA, **Figure 3**). This biotope, characterized by the holothurian *Cucumaria frondosa*, bryozoan *Eucratea loricata*, and hydrozoan *Thuiaria obsoleta* on a shallow shell sand bank, was found to be distinct from all other groups due to its occurrence in an area of both high average current speeds and highly variable temperature and salinity (**Figure 4**).

The main analysis without the Spitsbergenbanken samples identified an additional 26 biotopes with different species compositions. **Figure 3** also shows information on which of the environmental variables are correlated with each group at each split proceeding down the dendrogram.

The TWINSPAN analysis of the main dataset first divided into two main groups characterized by warm or fast flowing

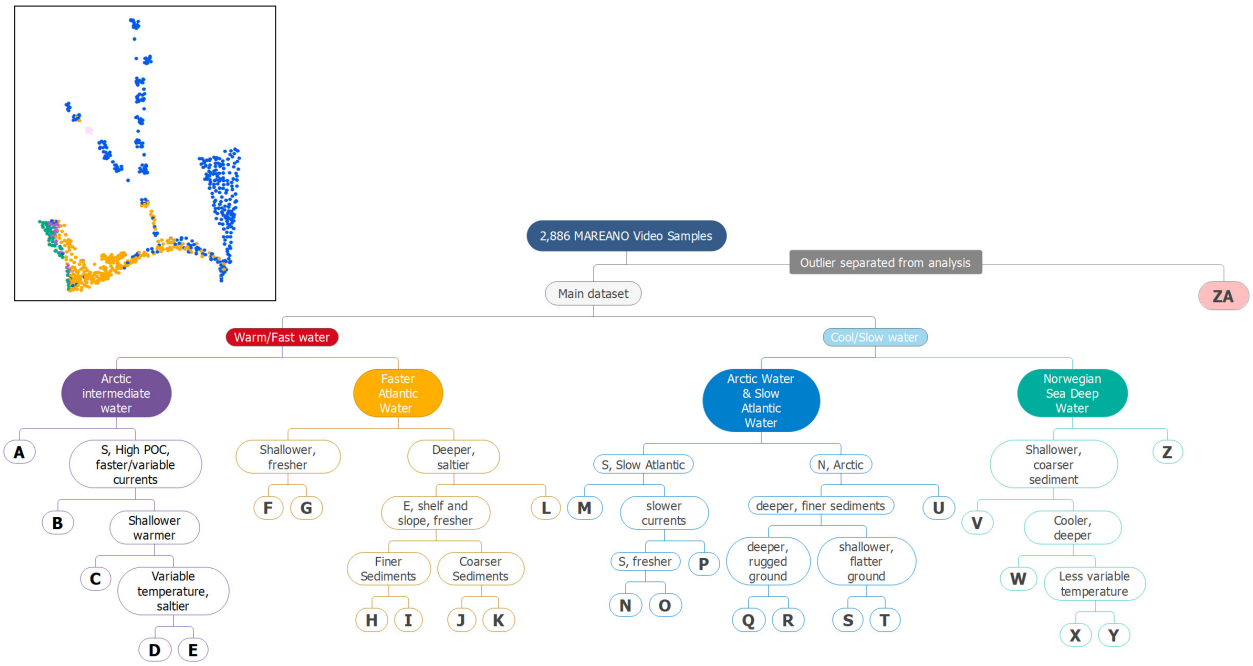

FIGURE 3 | A cluster dendrogram visualizing the TWINSPAN analysis and possible dominant environmental drivers for splits after various ordinations. The letters A–ZA correspond to the putative biotopes described in **Table 2**. The inserted map shows the locations of samples of the five main groups identified at the third division level. The colors on the map correspond to the colors in the dendrogram.

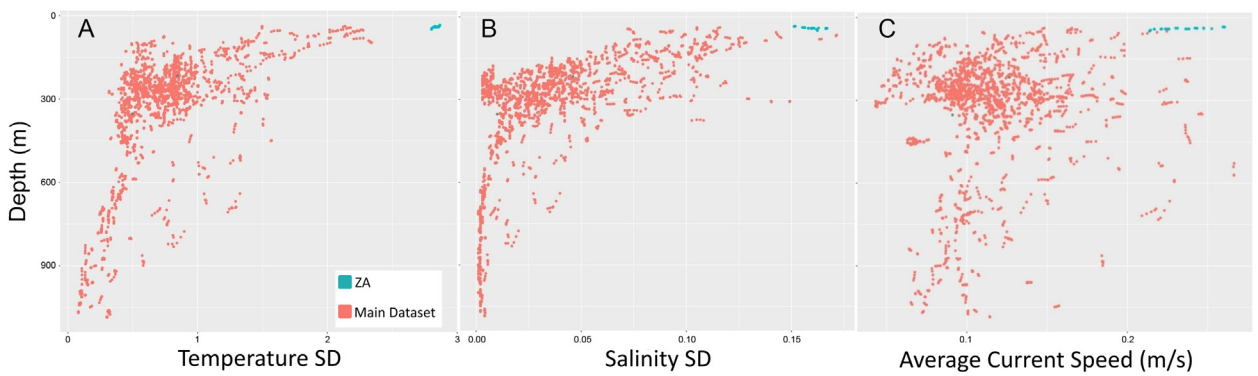

FIGURE 4 | Plots showing the distinct conditions present at the Spitsbergenbanken sample sites (ZA) relative to the main dataset. **(A)** Temperature. **(B)** Salinity. **(C)** Average current speed. Subsequently, the ZA group was removed from the main analysis to better characterize communities found in more typical conditions.

water (NAW and AIW) and cold or slow flowing water (AW and NSDW). An overview of the spatial distribution of these groups and biotope ZA is given in the inset map in **Figure 3** to provide an indication of the spatial relevance of these clusters. Including the outlier, or singleton (Spitsbergenbanken, group ZA), the analysis indicated 12 biotopes in warm water/fast water masses (groups A-L in **Figure 3** and **Table 2**), and 15 in cold/slow (M–Z and ZA). Similar cold-water species occurred both in the NSDW, below ca 700 m, and shallower in the Arctic water of the north eastern part of the study area. The next division level mainly separated deep (groups V–Z) and shallow (M–U) sites within these two cold and slow water groups while slope areas at intermediate depths (500–700 m) in the AIW (groups A–E) were separated from Atlantic shelf areas (F–L). Environmental correlates for biotopes identified by the first two divisions of the TWINSPAN hierarchy are illustrated in **Figure 5**. The colder and slower water masses represented five biotopes in NDSW (groups V–Z), five in Arctic Water (Q–U), and four in slower moving Atlantic water in the Southern Barents Sea (M–P). The warmer and faster water masses contained five biotopes in AIW (A–E), and seven in NAW (F–L). Further divisions reflected environments characterized by different variables including sediment and landscape types.

A summary of the results of the forward selection analyses is presented in **Table 3**. The forward selection identified the

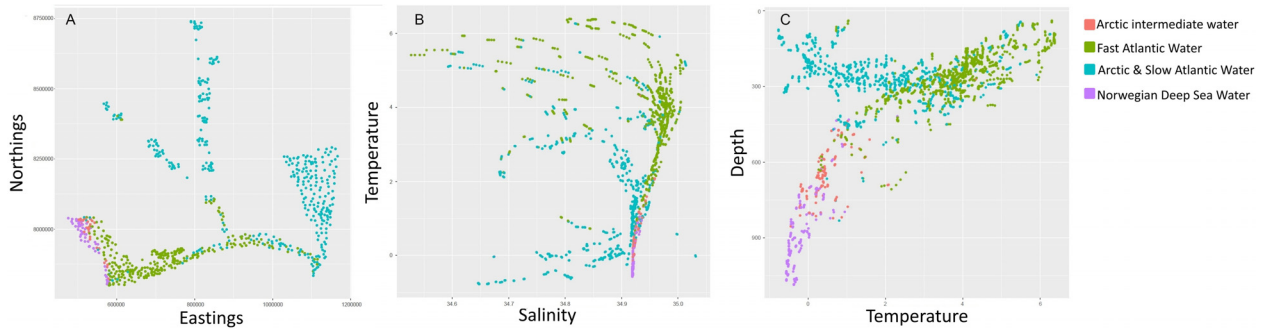

FIGURE 5 | Example of environmental patterns of sample groups identified by the first two divisions of the TWINSPAN of the species dataset with the main clusters indicated in different colors. **(A)** Geographical distribution, **(B)** temperature vs. salinity, and **(C)** Depth vs. temperature.

TABLE 3 | Results from forward selection analysis of environmental data.

Name	Explains %	Contribution %	Pseudo-F	*P*
UTM_Y	4.4	24.0	127	0.002
Bathy	2.2	12.3	66.5	0.002
UTM_X	2.1	11.7	64.5	0.002
Salinity_min	1.2	6.8	38.0	0.002
Temp_mean	1.0	5.6	31.6	0.002
Euph_depth	0.9	4.7	27.1	0.002
Salinity_mean	0.7	3.7	21.2	0.002
Temp_sd	0.5	2.9	16.9	0.002
Salinity_max	0.5	2.6	15.4	0.002
Current_dir	0.4	2.3	13.7	0.002
Current_speed_mean	0.4	2.4	14.1	0.002
Salinity_sd	0.4	2.1	12.1	0.002
Slope	0.4	2.0	11.9	0.002
Chl_a_surfMean	0.4	2.0	11.7	0.002

variables with the highest explanatory power, without being strongly intercorrelated with each other, affecting the variance in TWINSPAN-defined biotope type. Latitude (UTM_Y), longitude (UTM_X) and bathymetry each contributed more than 10% toward the explanation of the variation between the TWINSPAN groups. Various oceanographic variables explained between 2 and 6% of the variation. Average chlorophyll was also among the 14 best variables suggesting a link with surface production. Of the terrain variables, only slope showed any explanatory potential. These results served as a starting point from which to guide the selection of predictors for biotope modeling, in conjunction with other methods.

Taxonomic Composition of the Biotopes

A brief characterization of each biotope is given in **Table 2**, corresponding to letters in the dendrogram in **Figure 3**, with example images of selected contrasting biotopes given in **Figure 6**.

Of the 11 biotopes in Atlantic Water (**Figure 3**, F–P) most of them (seven) occurred on mixed sediment types with occurrence of gravel in mixtures of sand and mud. Many of the characteristic taxa of these biotopes were sessile animals attached to hard substrate in the form of pebbles, cobbles, and shell fragments (e.g., anemones or sponges). In biotope P, although characterized by a predominance of mud, sessile bryozoans were characteristic. In most cases, these bryozoans (mainly Cyclostomatidae) seemed to be attached to fragments of bivalves or other calcareous organisms, but some seemed to occur as unattached colonies lying on the soft sediment. Of the biotopes characterized by hard and coarse bottoms (F and G), encrusting organisms (red algae in the shallow biotope F), and sessile organisms [cauliflower corals (Nephtheidae) in G] were dominant. Group L clearly represents a "biotope complex" and comprises observations of at least two likely biotopes including both soft bottom sponge gardens and *Lophelia pertusa* reefs. However, the latter in particular was represented by insufficient samples within the study area to permit a clear split into its own biotope during this analysis.

In the Arctic Intermediate Water on the continental slope (**Figure 3**, A–E) in the western part of the study area all biotopes represented sandy sediments where two (B and C) also contained gravel dominated, in part, by cauliflower corals. Of the biotopes on substrates dominated by sand: Biotope A was characterized by a pigtail coral (*Radicipes gracilis*). while the others were characterized by the sessile sponges Tethya and Craniella (D), and *Phakellia* sp. (E) attached to the few scattered pebbles or cobbles in the area.

The NSDW biotopes on the lower part of the continental slope in the western part of the study area (**Figure 3**, V–Z) contained mainly sandy sediments. Biotope X had sediment with content of gravel, providing substrate for characteristic encrusting sponges. Two types of sea pen dominated biotopes were found in this water mass (V and W). Biotope V was characterized by *Virgularia* sp. and W by *Umbellula encrinus*. The associated fauna within these sea pen biotopes were also different to each other. For instance, the burrowing amphipod *Neohela monstrosa* was common in the areas with *Umbellula* but was not observed in areas with *Virgularia*. Different Hexactinellid and carnivorous Poecilosclerid sponges characterized biotopes Y and Z.

The six biotopes identified in Arctic Water (**Figure 3**, Q–U and ZA) comprised varying substrates ranging from mud to mixed sediments with gravel (biotope Q). The basket star dominating biotope R was most likely *Gorgonocephalus arcticus*. Cauliflower corals were also characteristic of three of the arctic biotopes (S,

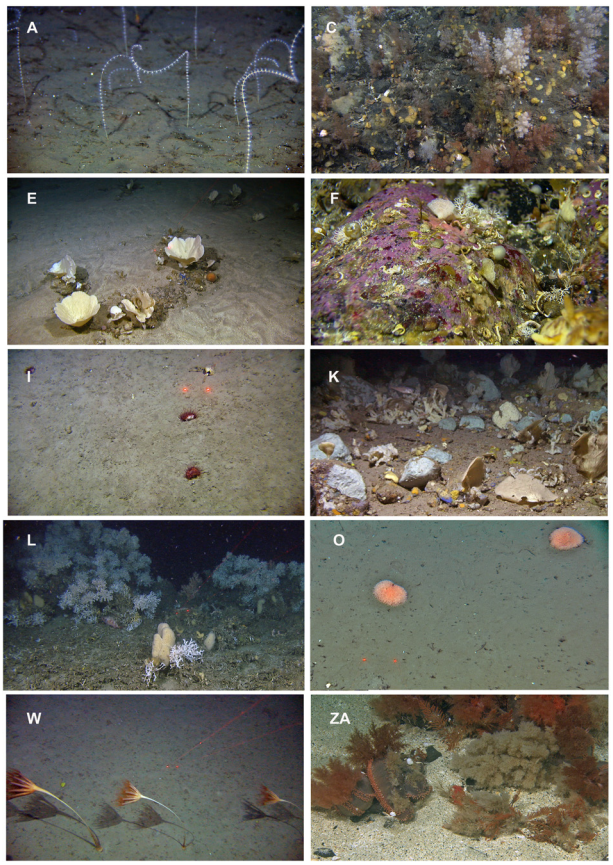

FIGURE 6 | Examples of 10 contrasting biotopes identified by a TWINSPAN analysis of the species data from the video analyses. The letters represent the biotope abbreviation corresponding to **Table 2**. *Arctic Intermediate Water Masses:* **(A)** Soft bottom coral garden dominated by the pigtail coral (*Radicipes gracilis*) on the slope south west of Svalbard. **(C)** Encrusting sponges and tunicates and cauliflower corals on a gravelly bottom. **(E)** Sponge garden on sandy bottom dominated by *Phakellia* sp. and *Axinella* sp. *Atlantic Water:* **(F)** Hard substrates dominated by encrusting red algae in strandflat areas. **(I)** Mixed sediments dominated by cup corals (*Flabellum macandrewi*). **(K)** Sponge garden with a variety of axinellid sponges on mixed bottom. **(L)** Cold water coral reef (*Lophelia pertusa*) in the south western part of the study area. The same biotope complex is also represented by soft bottom sponge aggregations dominated by Geodidae sponges. **(O)** Muddy bottom on the shelf in central parts of the study area dominated by the anemone *Liponema multicornis*. *Norwegian Sea Deep Water:* **(W)** Sandy substrate on the lower slope dominated by the sea pen *Umbellula encrinus*. *Arctic Water:* **(ZA)** Shallow, sandy, gravelly bank dominated by the holothurian *Cucumaria frondosa*, the hydrozoan *Thuiaria obsoleta*, and the bryozoan *Eucratea loricata*.

T, and Q). The cauliflower corals of biotope S were unidentified but did not include *Gersemia rubiformis* which was present in biotopes S and Q. Biotope S and Q differed by dominance of the bryozoan *Porella* in biotope S and the sessile holothurian *Psolus* sp. in biotope Q. Biotope ZA was dominated by great abundances of the sea cucumber *C. frondosa*, the hydrozoan *T. obsoleta*, and the bryozoan *E. loricata*. Biotope U was characterized by the Iceland scallop (*Chlamys islandica*).

Spatial Distribution of Biotopes

All analyzed observation locations and their biotope assignments after TWINSPAN analysis are shown on the map in **Figure 7**. Here we see a detailed view of the biotope distribution following the major splits already indicated in **Figure 3**. Broadly biotope complex L appears to be dominant in the NAW, together with biotopes Y in the NSDW, A in the NSAIW, and Q in the Arctic Water. The arctic biotopes appear to largely sit north of the approximate location of the polar front, highlighting this biogeographic boundary. **Figure 8** shows a map of the predicted distribution of biotopes in the Barents Sea based on models which combine the observed biotopes with the relevant environmental data. The final model had a Kappa value of 0.59 which is at the upper end of a moderate predictive performance across all biotopes—this seems reasonably good given the small percentage of raster pixels containing a biotope observation (<0.2%). We obtained higher (overestimated) performance statistics with standard methods (e.g., out of bag and cross-validation estimates), however, based on Meyer et al. (2018), we chose to use more conservative estimates which account for the ability of the model to predict to new locations.

DISCUSSION

The extensive sampling undertaken by the MAREANO project has allowed this first broadscale assessment of biotope characterization in the Barents Sea region. Our results reflect that this region spans a biogeographic boundary where warmer Atlantic water and related communities meets with Arctic waters and the polar front. This region is highly susceptible to climate change with indications of an "Atlantification" of the Barents Sea region (Barton, 2018; Lind et al., 2018) suggesting that this boundary is likely to move northward due to decreasing southward extension of the sea ice. The effect of this warming can have a severe effect on the arctic benthic communities, which as this study shows, are restricted to the colder and fresher Arctic water mass. The clear influence of water masses found in this study suggests either a dependence upon particular conditions (temperature, salinity, and/or nutrients) or a dispersal restriction imposed by water mass boundaries.

We note that certain biotopes are more restricted with respect to their environmental properties than others, i.e., they exist within a narrower range of conditions. These are generally easier to predict (have a lower rate of false predictions as assessed using the kappa coefficient), compared to those characterized by a wider range of environmental variation. However, the predictive ability is also influenced by the sample number and density within the biotope classes. Work is ongoing to provide a convenient and reliable method for communicating the degree of uncertainty associated with predicted the biotope distributions (map uncertainty), and also by attributing sample points with the certainty of their classification (classification uncertainty).

Due to the need for sufficient observations of each biotope for successful modeling, a few biotopes are less specific than might be desirable. Biotope complex L, which contains both sponge

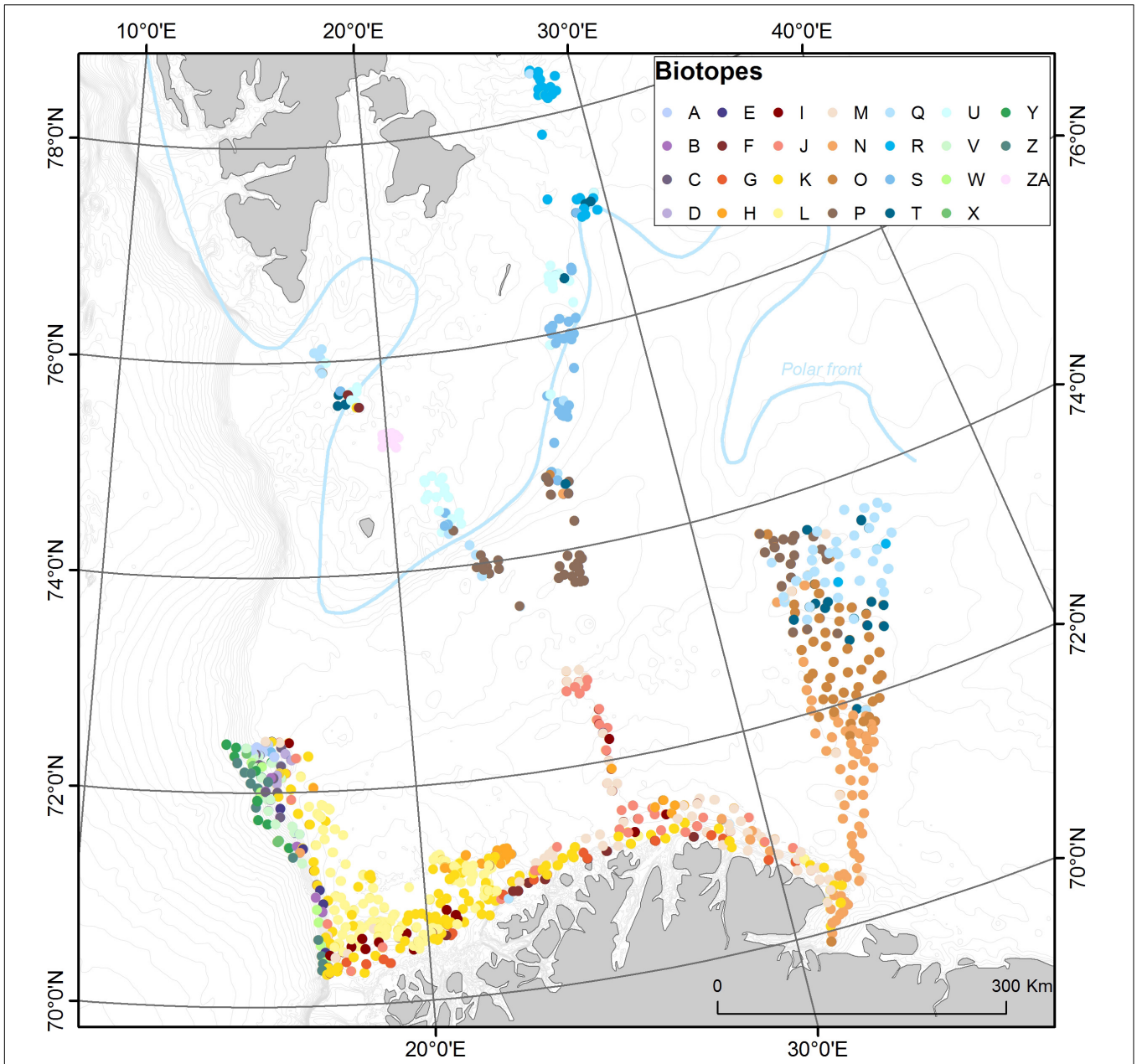

FIGURE 7 | Distribution of video observation locations classified into 27 general biotopes. Colors are roughly grouped according to the water mass splits (greens = NDSW, purples = NSAIW, yellow/browns = NAW, blues = Arctic Water) (cf. **Figure 3**). An approximate location of the polar front is indicated with a blue line.

habitats and cold-water coral reefs, is an example of two distinct biotopes or habitats that have been recognized by numerous studies in the past (e.g., Davies et al., 2008; Ramirez Llodra et al., 2011). These usually distinct biotopes group together in our analyses probably because they (1) share a great number of taxa such as redfish (*Sebastes* spp.), several sponges (e.g., Geodidae and Axinellidae), sea urchins, and sea stars, and (2) that the number of video samples within one of these communities (the coral reefs) is too low. We expect that these classes would separate should they be analyzed together with locations from within the core distribution areas of cold-water corals. Similarly, biotope ZA present on Spitsbergenbanken appears to be unique to this mapped area, and fortunately had sufficient samples to be retained as a distinct biotope class. However, we note that no similar environments have yet been mapped by MAREANO so its extent is as yet unknown. It is possible that there could be other locations with similar conditions where this community could be encountered, most likely on other shallow banks where the Barents Sea and Norwegian Sea meet. Future explorations of the area and/or extended predictions when further data become available may be able to clarify how unique this community is. These examples illustrate how it is important to consider

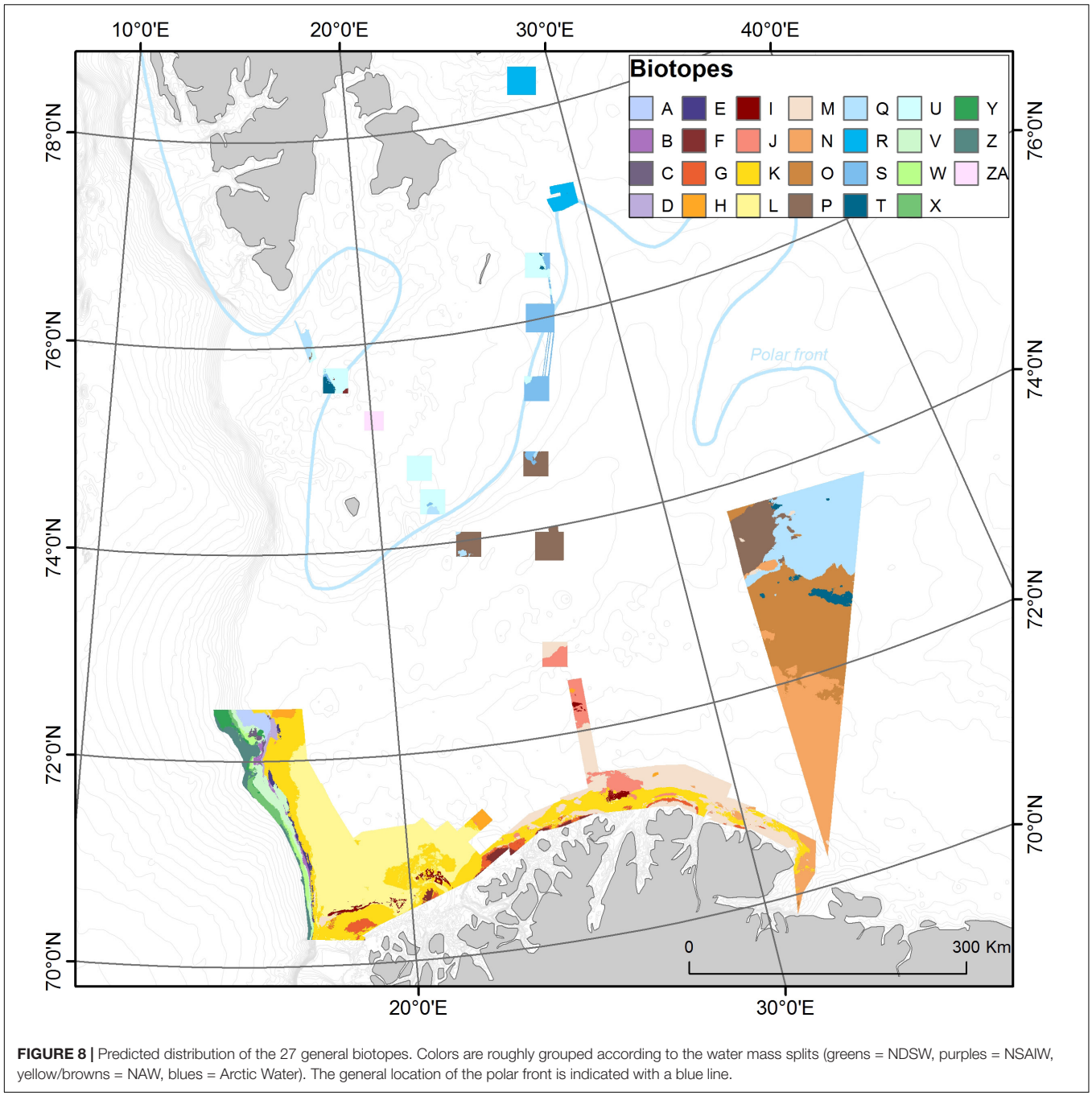

FIGURE 8 | Predicted distribution of the 27 general biotopes. Colors are roughly grouped according to the water mass splits (greens = NDSW, purples = NSAIW, yellow/browns = NAW, blues = Arctic Water). The general location of the polar front is indicated with a blue line.

the limitations of sampling and mapping areas covered when assessing the results of biotope mapping.

Due to the large area mapped and volume of samples used, the methods for defining biotopes and subsequently modeling their distribution have been updated from those used in previous MAREANO biotope maps. The new TWINSPAN approach is well matched to processing larger datasets and will form the basis of updating MAREANO general biotope maps in other areas (all MAREANO map products are available via www.mareano.no). We note that TWINSPAN and other methods may not fully agree in the number of groups defined, and other methods may be better suited when analyzing smaller datasets (Anderson and Clements, 2000), yet the clear environmental correlates with the TWINSPAN splits in this study suggest that this tool is adequate for the purposes of mapping communities in this region.

The environmental variables used to assess the TWINSPAN splits were evaluated at the resolution that would subsequently be used for the modeling. Those variables generated from broader-scale neighborhood analyses may miss some finer scale effects, but also offer some valuable assessment of larger geomorphological influences that would otherwise be overlooked. Although the resampling of the original bathymetric

data to 200 m means that finer-scale terrain variability is lost this resolution still allows us to capture the variations that match the length of video samples (200 m). Early MAREANO biotope maps were produced before oceanographic model data were available, while recent maps including the current study use oceanographic models originating from 800 m resolution. Resampling of model data from 800 to 200 m introduces minimal pseudo-variation from interpolating to a finer scale. Note that the values come from the lowest layer in a surface-optimized multi-layer ROMS model. The values therefore represent conditions spanning meters to tens of meters above the seabed depending on depth, rather than a fixed depth from the seabed. A 200 m scale is also well suited to raster-representation of the geological maps, which are produced at 1:100,000 scale and coarser, and therefore do not contain information on fine-scale variations at sub-200 m scales. In addition, we note that reduction of the bathymetry data to 200 m resolution overcomes certain acquisition-related artifacts associated with the bathymetry data in deeper waters, which are problematic for terrain analysis at finer scales and could produce misleading results when predicting habitat distribution (Lecours et al., 2017).

While the biotope classification (**Figure 3**) and observed spatial distribution (**Figure 7**) represent the main results of this study, the predicted biotope map is presented here (**Figure 8**) to provide a further indication of the varied environment and benthic communities present across the Barents Sea, including many areas previously undocumented at this scale. The results demonstrate that there is a clear biogeographic boundary for benthic communities related to the Polar front. Several cold-water biotopes toward the north and east in the study area are quite distinct from those in Atlantic water or NSDW. Temperature is probably the most important of the factors causing the biotic differences, as it is also a contributor to the strong effects of Latitude (UTM_Y) and Depth (Bathy) in the forward selection (see **Table 2**). However, different larval transport routes associated with the water masses may control the larval supply from different biogeographic and climatic regions. Overall, we note that the influence of major water masses is clearly important in controlling biotope distribution with oceanographic variables being among the most important. Other studies have also found oceanographic variables to be highly influential in models of species distribution (e.g., Yesson et al., 2012). This is likely because terrain variables, while easier to obtain as full coverage datasets, are often acting as a proxy for oceanographic variables such as temperature and current speed, and in some areas inadequately so. The oceanographic variables naturally relate to species tolerance and physiological functioning (e.g., temperature and salinity), as well as conditions that may affect food availability and access (e.g., current speeds).

The continued importance of geographic variables (location) suggests that they act as proxies to more directly influencing factors on benthic communities, and that there are other variables besides those used in the present model that may be more relevant to biotope distribution. In the meantime, the geographic variables appear to provide adequate proxies to capture some of these influences until such time as the relevant data are identified and made available for use in future models. The spatial scale of the response variables (biotope class) should ideally reflect the patchiness of the characteristic species. The scale used for megafauna composition in this study (200 m video sequences) will in many cases capture areas comprising different patches of sub-communities whose distribution reflects local fine scale variation in bottom substrate composition and local topography within the biotope. The biotopes described and modeled in this study may therefore be regarded as "local ecounits" where some represent areas with occurrence of several distinct sub-communities mosaiced due to patchiness. Although some biotopes do commonly occur as patches far larger than the sampling size. For instance, on level soft bottoms with a homogenous substrate composition fields of sea pens, scattered smaller sponges, anemones, or polychaetes may extend continuously over several hundreds of meters.

CONCLUSION

Twenty-seven biotopes were identified by applying TWINSPAN to quantitative species data obtained from analyses of seabed video records. The groups represented different environments with the main clusters related to water mass, landscape, and sediment composition. This enhanced the detection of different biogeographic regions, here likely related to the Polar Front, and provided a basis for better predictive modeling of seabed communities spanning a biogeographic boundary. The classification of benthic habitats in the deep sea has been limited by broad scale information about environmental factors acting at a local scale. The environmental variation is not uniform, and the variation in community composition will reflect this. Thus, biotope mapping of larger areas faces a challenge of representing a multitude of spatial scales. In this study, we have demonstrated that the dominating substrate is not always reflected in the community composition, as sessile organisms may appear as characteristic taxa even with a very low contribution of hard substrate. The oceanographic setting and probably also biological factors such as food availability and larval transport is of great importance for the control of species composition of epibenthic megafauna. Better knowledge of these factors could improve the models of biotope distribution further.

DATA AVAILABILITY STATEMENT

The original contributions presented in the study are included in the article/**Supplementary Material**, further inquiries can be directed to the corresponding author.

AUTHOR CONTRIBUTIONS

PB-M contributed to video analyses, statistical analyses, figures, and writing. MD contributed to modeling, figures, and writing. RR contributed to statistical analyses, figures, and writing. GG-M contributed to statistical analyses and writing. LB-M and LB contributed to writing. JA contributed to oceanographical modeling and writing.

FUNDING

This research was carried out as part of the Norwegian national seabed mapping program MAREANO, funded directly from the Norwegian Government.

ACKNOWLEDGMENTS

We acknowledge the video analysts at IMR for their patient annotations of more than 500 h of seabed video. Thanks to all participants of the MAREANO program (www.mareano.no) for their input to this article. The multibeam data were acquired and supplied by the Norwegian Hydrographic Service (Kartverket). The data are released under a Creative Commons Attribution 4.0 International (CC BY 4.0): https://creativecommons.org/licenses/by/4.0/. The ocean model simulation was performed on resources provided by UNINETT Sigma2—the National Infrastructure for High Performance Computing and Data Storage in Norway. We also thank the two reviewers and our editor, Daphne Cuvelier, for their time and assistance in making this manuscript stronger.

SUPPLEMENTARY MATERIAL

The Supplementary Material for this article can be found online at: https://www.frontiersin.org/articles/10.3389/fmars.2020.00271/full#supplementary-material

INFORMATION S1 | Draftsman plots and PCAs demonstrating the potential environmental drivers behind each TWINSPAN split.

REFERENCES

Anderson, M. J., and Clements, A. M. (2000). Resolving environmental disputes: a statistical method for choosing among competing cluster models. *Ecol. Appl.* 10, 1341–1355. doi: 10.1890/1051-0761(2000)010[1341:redasm]2.0.co;2

Barnes, R. S. K., and Hughes, R. N. (1982). *An Introduction to Marine Ecology*. Oxford: Blackwell Scientific.

Barton, B. I. (2018). Observed atlantification of the Barents Sea causes the polar front to limit the expansion of Winter Sea Ice. *J. Phys. Oceanogr.* 48, 1849–1866. doi: 10.1175/JPO-D-18-0003.1

Bellec, V. K., Bøe, R., Bjarnadóttir, L. R., Albretsen, J., Dolan, M., Chand, S., et al. (2019). Sandbanks, sandwaves and megaripples on Spitsbergenbanken, Barents Sea. *Mar. Geol.* 416:105998. doi: 10.1016/j.margeo.2019.105998

Bjarnadóttir, L. R., Winsborrow, M. C. M., and Andreassen, K. (2014). Deglaciation of the central Barents Sea. *Quat. Sci. Rev.* 92, 2018–2226.

Blindheim, J. (1990). Arctic intermediate water in the Norwegian Sea. *Deep Sea Res.* 37, 1475–1489. doi: 10.1016/0198-0149(90)90138-L

Bryan, T. L., and Metaxas, A. (2007). Predicting suitable habitat for deep-water gorgonian corals on the Atlantic and Pacific Continental Margins of North America. *Mar. Ecol. Prog. Ser.* 330, 113–126. doi: 10.3354/meps330113

Buhl-Mortensen, L., and Buhl-Mortensen, P. (2017). Marine litter in the Nordic Seas: distribution composition and abundance. *Mar. Pollut. Bull.* 125, 260–270. doi: 10.1016/j.marpolbul.2017.08.048

Buhl-Mortensen, L., Buhl-Mortensen, P., Dolan, M. F. J., and Holte, B. (2015a). The MAREANO programme – A full coverage mapping of the Norwegian off-shore benthic environment and fauna. *Mar. Biol. Res.* 11, 4–17. doi: 10.1080/17451000.2014.952312

Buhl-Mortensen, L., Buhl-Mortensen, P., Dolan, M. F. J., and Gonzalez-Mirelis, G. (2015b). Habitat mapping as a tool for conservation and sustainable use of marine resources: some perspectives from the MAREANO Programme, Norway. *J. Sea Res.* 100, 46–61. doi: 10.1016/j.marpolbul.2017.08.04810.1016/j.seares.2014.10.014

Buhl-Mortensen, L., Olsen, E., Røttingen, I., Buhl-Mortensen, P., Hoel, A. H., Lid, S. R., et al. (2012). *Application of the MESMA Framework. Case Study: The Barents Sea*. MESMA report, 138.

Buhl-Mortensen, P., Buhl-Mortensen, L., Dolan, M., Dannheim, J., and Kröger, K. (2009). Megafaunal diversity associated with marine landscapes of northern Norway: a preliminary assessment. *Norw. J. Geol.* 89, 163–171.

Davies, A. J., Wisshak, M., Orr, J. C., and Roberts, J. M. (2008). Predicting suitable habitat for the cold-water coral *Lophelia pertusa* (Scleractinia). *Deep Sea Res. I* 55, 1048–1062. doi: 10.1016/j.dsr.2008.04.010

Dee, D. P., Uppala, S. M., Simmons, A. J., Berrisford, P., Poli, P., Kobayashi, S., et al. (2011). The ERA-Interim reanalysis: configuration and performance of the data assimilation system. *Q. J. R. Meteorol. Soc.* 137, 553–597. doi: 10.1002/qj.828

Dolan, M. F. J., and Lucieer, V. L. (2014). Variation and uncertainty in bathymetric slope calculations using geographic information systems. *J. Mar. Geodesy* 37, 187–219. doi: 10.1080/01490419.2014.902888

Egbert, G. D., and Erofeeva, S. Y. (2002). Efficient inverse modeling of barotropic ocean tides. *J. Atmos. Ocean. Technol.* 19, 183–204. doi: 10.1175/1520-0426(2002)019<0183:eimobo>2.0.co;2

Elvenes, S. (2013). *Landscape Mapping in MAREANO. NGU Report 2013.035.*. Available online at: https://www.ngu.no/upload/Publikasjoner/Rapporter/2013/2013_035.pdf (accessed April 14, 2020).

Elverhøi, A., Fjeldskaar, W., Solheim, A., Nyland-Berg, M., and Russwurm, L. (1993). maximum. *Quat. Sci. Rev.* 12, 863–873.

Geological Survey of Norway [NGU] (2019a). *Marine – Seabed Sediments (Grain Size), Regional*. Available online at: http://geo.ngu.no/download/order?lang=en&dataset=701 (accessed January 7, 2019).

Geological Survey of Norway [NGU] (2019b). *Marine Landscapes*. Available online at: http://geo.ngu.no/download/order?lang=en&dataset=705 (accessed January 7, 2019).

Gomes Pereira, J. N., Auger, V., Beisiegel, K., Benjamin, R., Bergmann, M., Bowden, D., et al. (2016). Current and future trends in marine image annotation software. *Prog. Oceanogr.* 149, 106–120.

Haidvogel, D. B., Arango, W. P., Budgell, B. D., Cornuelle, E., Curchitser, E., Di Lorenzo, K., et al. (2008). Ocean forecasting in terrain-following coordinates: formulation and skill assessment of the regional ocean modeling system. *J. Comp. Phys.* 227, 3595–3624. doi: 10.1016/j.jcp.2007.06.016

Hansen, B., and Østerhus, S. (2000). North Atlantic-Nordic Seas exchanges. *Prog. Oceanogr.* 45, 109–208. doi: 10.1016/s0079-6611(99)00052-x

Harris, P. T. (2012). "Biogeography, benthic ecology, and habitat classification schemes," in *Seafloor Geomorphology as Benthic Habitat: Geohab Atlas of Seafloor Geomorphic Features and Benthic Habitats*, 1st Edn, eds P. T. Harris and E. Baker (Boston: Elsevier), 61–91. doi: 10.1016/b978-0-12-385140-6.00004-9

Harris, P. T., and Baker, E. K. (2011). *Seafloor Geomorphology as Benthic Habitat: GeoHab Atlas of Seafloor Geomorphic Features and Benthic Habitats*. Amsterdam: Elsevier.

Hill, M. O. (1979). *TWINSPAN a Fortran Program for Arranging Multivariate Data in an Ordered Two-Way Table by Classification of the Individuals and Attributes. Ecology and Systematic*. Ithaca, NY: Cornell University.

Ingvaldsen, R., and Loeng, H. (2009). "Physical oceanography," in *Ecosystem Barents Sea. Vol. 2009 Tapir*, eds E. Sakshaug, G. Johnsen, and K. Kovacs (Trondheim: Academic Press).

Jakobsson, M., Mayer, L. A., Coakley, B., Dowdeswell, J. A., Forbes, S., Fridman, B., et al. (2012). The international bathymetric chart of the arctic ocean (IBCAO) version 3.0. *Geophys. Res. Lett.* 39:L12609. doi: 10.1029/2012GL052219

Knies, J., Matthiesen, J., Vogt, C., Laberg, J. S., Hjelstuen, B. O., Smelror, M., et al. (2009). The Plio-Pleistocene glaciation of the Barents Sea-Svalbard region: a new model based on revised chronostratigraphy. *Quat. Sci. Rev.* 10, 1–18.

Lecours, V., Brown, C. J., Devillers, R., Lucieer, V. L., and Edinger, E. N. (2016). Comparing selections of environmental variables for ecological studies: a focus on terrain attributes. *PLoS One* 12:e0167128. doi: 10.1371/journal.pone.0167128

Lecours, V., Devillers, R., Edinger, E. N., Brown, C. J., and Lucieer, V. L. (2017). Influence of artefacts in marine digital terrain models on habitat maps and species distribution models: a multiscale assessment. *Remote Sens. Ecol. Conserv.* 3, 232–246. doi: 10.1002/rse2.49

Lien, V. S., Gusdal, Y., and Vikebø, F. B. (2014). Along-shelf hydrographic anomalies in the Nordic Seas (1960–2011): locally generated or advective signals? *Ocean Dyn.* 64, 1047–1059. doi: 10.1007/s10236-014-0736-3

Lind, S., Ingvaldsen, R. B., and Furevik, T. (2018). Arctic warming hotspot in the northern Barents Sea linked to declining sea-ice import. *Nat. Clim. Change* 8, 634–639. doi: 10.1038/s41558-018-0205-y

Loeng, H. (1991). Features of the physical oceanographic conditions of the Barents Sea. *Polar Res.* 10, 5–18. doi: 10.1111/j.1751-8369.1991.tb00630.x

McCauley, D. J. (2015). Marine defaunation: animal loss in the global ocean. *Proc. Natl. Acad. Sci. U.S.A.* 347:1255641. doi: 10.1126/science.1255641

Meyer, H., Reudenbach, C., Hengl, T., Katurji, M., and Nauss, T. (2018). Improving performance of spatio-temporal machine learning models using forward feature selection and target-oriented validation. *Environ. Model. Softw.* 101, 1–9. doi: 10.1016/j.envsoft.2017.12.001

Mortensen, P. B., and Buhl-Mortensen, L. (2005). "Coral habitats in The Gully, a submarine canyon off Atlantic Canada," in *Cold-water Corals and Ecosystems*, eds A. Freiwald and J. M. Roberts (Berlin: Springer-Verlag), 247–277. doi: 10.1007/3-540-27673-4_12

Nasa Goddard Space Flight Center (2018). *NASA Goddard Space Flight Center, Ocean Ecology Laboratory, Ocean Biology Processing Group*. Greenbelt, MD: MODIS.

Ozhigin, V. K., Ingvaldsen, R. B., Loeng, H., Boitsov, V., and Karsakov, A. (2011). "Introduction to the Barents Sea," in *The Barents Sea. Ecosystem, Resources, Management. Half a Century of Russian-Norwegian Cooperation*, eds T. Jakobsen and V. K. Ozhigin (Trondheim: Tapir Academic Press), 315–328.

Ramirez Llodra, E., Tyler, P. A., Baker, M. C., Bergstad, O. A., Clark, M. R., Escobar, E., et al. (2011). Man and the last great wilderness: human impact on the Deep Sea. *PLoS One* 6:e22588. doi: 10.1371/journal.pone.0022588

Roberts, J. J., Best, B. D., Dunn, D. C., Treml, E. A., and Halpin, P. N. (2010). Marine geospatial ecology tools: an integrated framework for ecological geoprocessing with ArcGIS, Python, R, MATLAB, and C++. *Environ. Model. Softw.* 25, 1197–1207. doi: 10.1016/j.envsoft.2010.03.029

Ross, R. E., and Howell, K. L. (2013). Use of predictive habitat modelling to assess the distribution and extent of the current protection of 'listed' deep-sea habitats. *Divers. Distrib.* 19, 433–445. doi: 10.1111/ddi.12010

Shchepetkin, A. F., and McWilliams, J. C. (2005). The regional ocean modeling system (ROMS): a split-explicit, free-surface, topography-following coordinates ocean model. *Ocean Model.* 9, 347–404. doi: 10.1016/j.ocemod.2004.08.002

Sigmond, E. M. O. (2002). *Geological Map, Land and Sea Areas of Northern Europe, Scale 1:4 Million*. Trondheim: Geological Survey of Norway.

Skagseth, Ø (2008). Recirculation of Atlantic Water in the western Barents Sea. *Geophys. Res. Lett.* 35:L11606. doi: 10.1029/2008GL033785

Steltzenmüller, W., Breen, P., Stamford, T., Thomsen, F., Badalamenti, F., Borja, A., et al. (2013). Monitoring and evaluating of spatially managed areas: a generic framework for implementation of ecosystem based marine management and its application. *Mar. Pollut. Bull.* 37, 149–164. doi: 10.1016/j.marpol.2012.04.012

Walbridge, S., Slocum, N., Pobuda, M., and Wright, D. (2018). Unified geomorphological analysis workflows with benthic terrain modeler. *Geosciences* 8:94. doi: 10.3390/geosciences8030094

Wilson, M. F. J., O'Connell, B., Brown, C., Guinan, J. C., and Grehan, A. J. (2007). Multiscale terrain analysis of multibeam bathymetry data for habitat mapping on the continental slope. *Mar. Geodesy* 30, 3–35. doi: 10.1080/01490410701295962

Yesson, C., Taylor, M. L., Tittensor, D. P., Davies, A. J., Guinotte, J., Baco, A., et al. (2012). Global habitat suitability of cold-water octocorals. *J. Biogeogr.* 39, 1278–1292. doi: 10.1111/j.1365-2699.2011.02681.x

Conflict of Interest: The authors declare that the research was conducted in the absence of any commercial or financial relationships that could be construed as a potential conflict of interest.

frontiers in Marine Science

DATA REPORT
published: 16 October 2020
doi: 10.3389/fmars.2020.536295

High-Resolution Sub-Bottom and Magnetometer Data From Southeastern Brazilian Coast

Daniel Pavani Vicente Alves[1], Eduardo Bomfin Caldato[2], Denise Silva de Moura[3], Roberto P. Zanon dos Santos[3] and Luigi Jovane[1]*

[1] Department of Physical, Chemical and Geological Oceanography, Institute Oceanographic, Universidade de São Paulo, São Paulo, Brazil, [2] Department of Natural Resources and Hydrogeology, Institute of Geosciences, Universidade de São Paulo, São Paulo, Brazil, [3] Department of Geophysics, Institute of Astronomy, Geophysics and Atmospheric Sciences, São Paulo, Brazil

Keywords: reflection seismic, magnetic anomalies, geophysics, oceanography, geologic oceanography

INTRODUCTION

Sub-bottom profilers are used across shallow and deep oceanic waters with several applications, such as sea-level studies (e.g., Bastos et al., 2010; Koša, 2015; Aquino da Silva et al., 2016; Yoo et al., 2016), sedimentation process (e.g., Miller et al., 2013; Alves and de Mahiques, 2019), gas seeps (e.g., Benites et al., 2015; Michel et al., 2017), geomorphology (e.g., Jobe et al., 2011; Gomes et al., 2016), and others. Marine magnetometer data have also been used for most various studies, as archeological (Boyce et al., 2004), environmental (Boyce et al., 2001), engineering (Yu et al., 2007), and geological, mainly for mineral exploration (Dehler and Potter, 2002) and academic purposes (Müller et al., 1997). Combining both techniques enhances considerably the possibilities of geological and oceanographic interpretation, as multi-data surveys in marine environments allow complementary studies (e.g., Kadima et al., 2011; Demir et al., 2012).

The Boqueirão Strait in the northern coast of São Paulo (Southeast Brazil) connects two semi-enclosed bays, allowing water exchange between them (Mahiques and Souza, 1999). Despite its importance to the oceanographic evolution of the region, it has still been poorly studied. Therefore, this new dataset will contribute to future comprehension of the geologic and oceanographic evolution.

DATA COLLECTION

Location and Date

New seismic and magnetometer data were acquired on the region of the Boqueirão Strait during a cruise between November 26 and 30, 2018, onboard R/V Veliger II from Instituto Oceanográfico of Universidade de São Paulo. This 35-m-deep strait is located between 23°31′ S/45°06′ W and 23°32′ S/45°04′ W and is a unique region that separates the shallow areas of Flamengo Bay and the Toninhas Bay on the city of Ubatuba, northern coast of São Paulo State, Brazil (**Figure 1**). The strait also separates the continent from the Anchieta Island, a touristic destiny whose main beaches are located on Palmas Bay (**Figure 1**). The strait was probably formed from an ancient drainage system developed during the Quaternary in the Brazilian coast (Almeida, 1964), and, in fact, Mahiques and Souza (1999) found seismic and sediment evidences of regressive and transgressive surfaces in the area.

The Ubatuba region is characterized by the proximity of the Serra do Mar from the shore (**Figure 1**). The input of terrigenous sediments into the bay is mostly controlled by rainfall, resulting in fine sediments rich in organic matter (Mahiques, 1995). Sediments reaching the Flamengo Bay are characterized by a clockwise transport system. These sediments are reworked by the water that enters the bay from the western sector (Mahiques and Souza, 1999). On the Boqueirão area,

OPEN ACCESS

Edited by:
Vincent Lecours, University of Florida, United States

Reviewed by:
Y. Meriah Arias-thode, Naval Information Warfare Center Pacific, United States
Daniele Maestrelli, National Research Council, Italy

****Correspondence:***
Daniel Pavani Vicente Alves
daniel.alves@usp.br

Specialty section:
This article was submitted to Deep-Sea Environments and Ecology, a section of the journal Frontiers in Marine Science

Received: *13 March 2020*
Accepted: *28 August 2020*
Published: *16 October 2020*

Citation:
Alves DPV, Caldato EB, de Moura DS, dos Santos RPZ and Jovane L (2020) High-Resolution Sub-Bottom and Magnetometer Data From Southeastern Brazilian Coast. Front. Mar. Sci. 7:536295. doi: 10.3389/fmars.2020.536295

circulation is mostly due to SW–NE wind and wave currents that, with appropriate cold fronts influence, can reach up to 0.80 m/s (Tessler, 1988; Mahiques and Souza, 1999).

Seismic Data Collection

High-resolution single-channel seismic data were acquired using a SIG Sparker ELC-1200L coupled to an Energos 300J power supply, operating at 250J with a signature source-frequency of 0.9 kHz and 3.4 ms vertical resolution. Acquisition was performed at a constant vessel speed of 3.5 knots and, for decreasing the effect of vessel noise, the source used a 25-m layback. For data recording, a 4.7-m length SIG Streamer was used, with a single-channel formed by eight hydrophones coupled to a pre-amplifier to increase signal–noise rate. In order to minimize the effect of the vessel's noise on the hydrophones, the streamer used a 35-m layback, therefore spaced 10 m from the seismic source. Both the layback lengths for source and streamer were defined after a testing and calibration period prior to acquisition, in which different lengths were applied and noise decrease was read in the online data view of the acquisition software. More than 30 km of seismic data were collected in the datum WGS84 and UTM 23S projection, in a total coverage of circa 1.6 km^2 (**Figure 1**).

The acquisition of seismic data was performed with the software Meridata MDCS 5.2, which controlled shot and recording settings. The source used a SEG capacitor bank of up to 300 J, which was triggered by MDCS software. Navigation was acquired with a DGPS system Hemisphere Atlas Link, which provides horizontal resolution up to 0.1 m and vertical precision of 0.2 m. Installation offsets were measured on the port.

Magnetometer Data Collection

A magnetometric survey was performed using a SeaSPY 2 magnetometer, from Marine Magnetics, simultaneous to the seismic survey. The SeaSPY has an Overhauser sensor that measures the intensity of the magnetic field vector, regardless of its direction. The resolution is 0.001 nT and the absolute accuracy is 0.1 nT. There is no heading error, temperature drift, or dead zone associated with the measurements.

The magnetometer layback was 30 m to avoid interferences from the vessel, along the same profiles presented in **Figure 1**, adding the maneuver path. The optimal tow-cable length has been defined to be 30 m after several surveys with the research vessel. Prior to acquisition, offsets for the magnetometer and GPS antenna were measured and applied to the acquisition software BOB. The sample rate was 1 Hz, resulting in 13,330 data points distant by 4 m along the profiles.

The diurnal magnetic anomaly was registered by a ground Overhauser magnetometer, a GSM-19 from GEM Systems, located at a shore-based magnetic station, on the Ubatuba base of the Instituto Oceanográfico of Universidade de São Paulo, 5 km apart from the survey area.

DATA DESCRIPTION

Seismic Dataset

After acquisition, seismic data were converted to SGY format (IEEE Float-32 bit) using Meridata REX software and applying the acquisition offsets. Therefore, all seismic data have precise position information (bytes 73 and 77) in WGS84/UTM 23S. Shotpoint (SP) information is located on byte 17. No filters, gain, or any other processing was applied to the data, except for the pre-amplifier on the streamer. Trace length varies between 100 and 150 ms, with sampling interval of 50 μs and positive seabed reflection. Details on the seismic data format are presented on **Table 1**.

Given the proximity of the Serra do Mar formation to the coast in this region, it is possible to interpret the acoustic basement (interpreted in red in **Figures 2A,B**) as the crystalline basement in most of the seismic sections. A detailed view of the survey area shows the basement outcrops near the continent (north) and the Anchieta Island (south). A seismic line N–S oriented (**Figure 2A**) indicates that the basement is much shallower in the southern sector, close to the Anchieta Island, and some sections clearly show the basement outcropping on the seafloor (**Figure 2B**), pointing to the connection between the continent and the island.

Above the basement reflector and the present seafloor multiple (mapped in green in **Figure 2A**), it is possible to notice important reflectors related to ancient oceanographic and possibly sea-level conditions. The "paleo-Boqueirão" represents an ancient configuration of the region, with morphological characteristics much similar to the present. On the flanks of this paleo-depression, a stabilization surface on the northern sector and a ravinement surface on the southern, as well as erosive truncation on the slope, point to structures produced by sea-level variations, as interpreted by Mahiques and Souza (1999).

Magnetometer Dataset

The abnormal spikes were removed from the collected dataset; thereafter, the diurnal magnetic correction was applied using shore-based magnetic station data. Besides the preprocessing described above, no filter or further corrections were applied to calculate the total magnetic field (**Figure 2C**). A NE trending formed by a series of dipoles is highlighted by the magnetic data. The pattern can be related to the basement structure, since the region is located in the Ribeira Belt, a neoproterozoic orogenic belt formed by the accretion of terranes in the NE trending (Heilbron and Machado, 2003).

Data Availability

The seismic and magnetometer data are available in the community at FigShare.com (doi: 10.6084/m9.figshare.11861889). Seismic data are available in SGY format (see detailed description in **Table 1**). SGY files are named following their date: YYYYMMDD_HHMMSS. Magnetometer data are

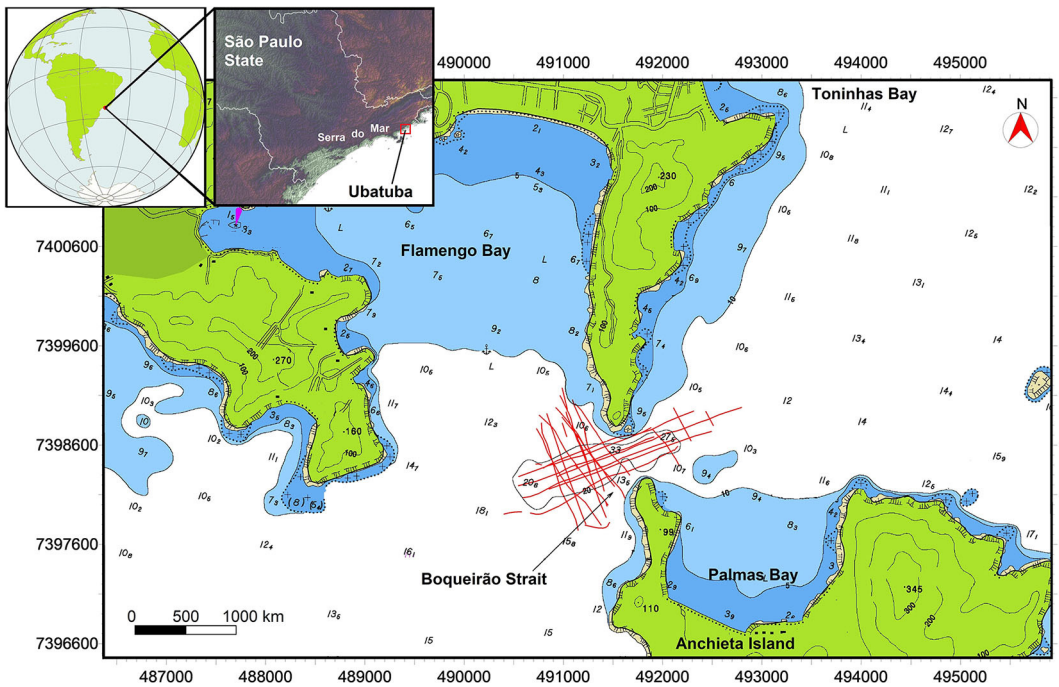

FIGURE 1 | The data were acquired in the Southeastern Brazilian coast, on the north coast of São Paulo state. The seismic and magnetometer acquisitions (red lines) were acquired in the Boqueirão Strait, a narrow passage between the continent and the Anchieta Island. Top left box shows USGS SRTM topography and the position of Serra do Mar (warmer colors represent higher altitudes).

TABLE 1 | Summary of SGY data information.

Name format	DATE_TIME.sgy
Data format	SGY IEEE Float (32 bit)
Position	WGS84/UTM 23S
Gain	No
Filter	No
Pre-amplify	Applied on the streamer
Bytes for X/Y information	73/77
Byte for SP information	17
Trace length	100–150 ms
Sample interval	50 μs
Seafloor reflection	Positive

available on text file format (.XYZ), including navigation. Data also include the shapefile of the seismic acquisition survey.

POSSIBLE APPLICATIONS

Mahiques and Souza (1999) published the seismic stratigraphy of the Boqueirão Strait two decades ago. With the technological advances in seismic acquisition, these new data provide a better tool to enhance the studies on the region. The improvement of data is based on positioning technology evolution, with the use of differential Global Positioning System (GPS), for example, as well as newer seismic source, recorder, and digital/analogic conversion tools. The seismic and paleobathymetry characteristics of this strait can provide important information to the Quaternary evolution of the southern coast of Brazil. With the support of other data such as cores and gravimetric data, more detailed research can be carried out in order to contribute to the still poor sea-level change studies on the region (Klein et al., 2005; Veiga, 2005; Angulo et al., 2006; Alves and de Mahiques, 2019).

This dataset can be used as a guide for sediment sampling. Recent studies question the actual sea-level curve applied to portions of São Paulo coast (Suguio and Martin, 1978; Angulo et al., 2006). Sediment cores would make it possible to date and correlate the seismic surfaces interpreted with sea-level changes during the Quaternary.

For studies focused on tectonics of passive margins, these datasets are oriented to guide data acquisitions in a more regional perspective. Many of the faults found on the seismic data show the same orientation observed on continental outcrops. Authors such as Almeida (1964) and Zalán and Oliveira (2005) offer a different perspective over the evolution of the rift systems found southeast of Brazil. Nonetheless, the lack of information over the continental shelf creates a gap of data between continental and deep marine deposits. This dataset was a first attempt to search for structures that relate tectonics with syndepositional sedimentation.

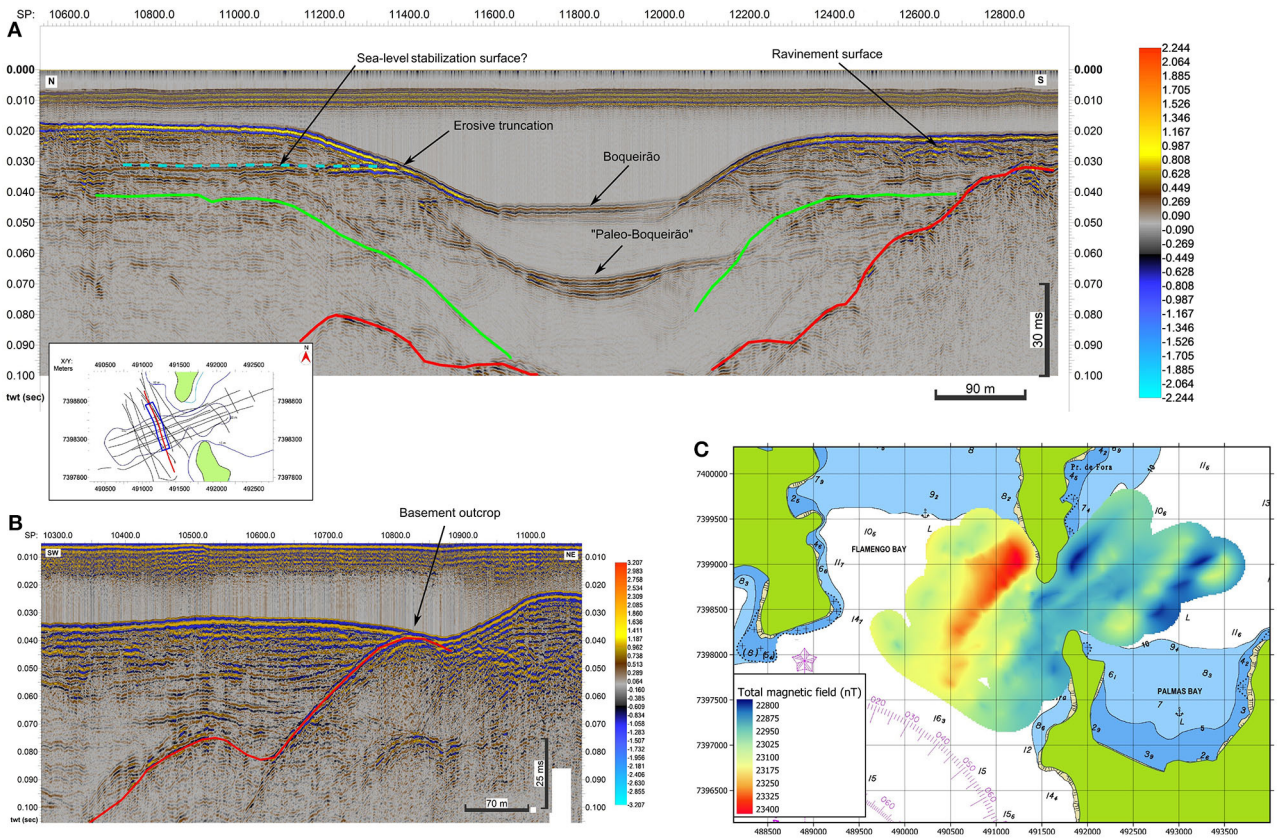

FIGURE 2 | (A) Seismic line N–S oriented, showing the crystalline basement (red mapped reflector), the present seabed, and an ancient position of the seabed. In green, the seabed multiple. Vertical exaggeration of approximately three times; **(B)** seismic line SW–NE oriented, showing the outcrop of the crystalline basement (red mapped reflector) and the divergent reflections onto it. Vertical exaggeration of approximately three times; **(C)** total magnetic field in nT obtained in the Flamengo Bay area.

The magnetic data can be used to distinguish geological structures on the area, as faults and basement features that may complement studies about the formation of the bay, identifying fragile zones and regional patterns.

The uncompleted magnetic anomalies limit the interpretation of the volume and depth of the magnetic sources. Since the anomalies are not completely outlined, the modeling of them is not conclusive.

Limitations

The limitation of this single-channel seismic data is related to the acquisition process in shallow water environments. In such environment and in addition to using a single-channel system, the multiple reflections are present and the removal is difficult (**Figure 2A**). Additionally, as a high-energy source (250 J) was used in order to reach the deepest areas of the basement, the shallowest regions have high-amplitude reflections and multiples.

Recording was maintained even during short crossing lines and owing to that, some seismic lines are very short. Nevertheless, all lines were kept in the dataset.

Finally, the most important limitation is that there are no new sediment cores in the area. Therefore, with this dataset alone, it is not possible to assign sedimentary information and/or ages to the reflectors.

FINAL REMARKS

The north coast of São Paulo state in Southeastern Brazil is a region of great importance due to its natural conservancy and environmental significance. It is fundamental to further develop studies in the regions, especially those related to its formation and evolution of this portion of the Brazilian Margin. Only with this information the scientific community will be able to provide evolution models for the area, better understanding the effects of sea-level and depositional changes during the Quaternary and Holocene. These kinds of studies will contribute to the development of climate change scenarios for coastal zones and aid government mitigatory policies. Therefore, this new geophysical dataset can aid researchers with those goals.

DATA AVAILABILITY STATEMENT

The datasets generated for this study are available on request to the corresponding author and also available at FigShare.com (doi: 10.6084/m9.figshare.11861889).

AUTHOR CONTRIBUTIONS

DA, EC, and DM were responsible for data collection and organization. DA was responsible for writing the manuscript. EC, DM, and RS were responsible for reviewing the manuscript. LJ coordinated the process. All authors contributed to the article and approved the submitted version.

FUNDING

This research was part of the Fundação de Amparo a Pesquisa do Estado de São Paulo (FAPESP) grants 2016/24946-9 and 2011/22018-3 to LJ.

ACKNOWLEDGMENTS

The authors would like to thank SALT–Sea & Limno Technology for the seismic acquisition system and IHS Markit for the Kingdom license. We also thank the Instituto Oceanográfico of Universidade de São Paulo for the research vessel used for the survey and the technicians who helped with the acquisition.

REFERENCES

Almeida, F. F. M. (1964). "Os fundamentos geológicos do relevo paulista," in *Brasil, a terra e o homem* (São Paulo: Companhia Editora Nacional), 55–120.

Alves, D. P. V., and de Mahiques, M. M. (2019). Deposition and sea-level evolution models for Upper Pleistocene/Holocene in the São Sebastião Channel (SE Brazilian coast) inferred from 5th order seismic stratigraphy. *J. South Am. Earth Sci.* 93, 382–393. doi: 10.1016/j.jsames.2019.05.012

Angulo, R. J., Lessa, G. C., and De Souza, M. C. (2006). A critical review of mid- to late-Holocene sea-level fluctuations on the eastern Brazilian coastline. *Quat. Sci. Rev.* 25, 486–506. doi: 10.1016/j.quascirev.2005.03.008

Aquino da Silva, A. G., Stattegger, K., Schwarzer, K., Vital, H., Aquino da Silva, A. G. A. G., Stattegger, K., et al. (2016). Seismic stratigraphy as indicator of late Pleistocene and Holocene sea level changes on the NE Brazilian continental shelf. *J. South Am. Earth Sci.* 70, 188–197. doi: 10.1016/j.jsames.2016.05.001

Bastos, A. C., Vilela, C. G., Quaresma, V. S., and Almeida, F. K. (2010). Mid- to late-Holocene estuarine infilling processes studied by radiocarbon dates, high resolution seismic and biofacies at Vitoria Bay, Espirito Santo, Southeastern Brazil. *An. Acad. Bras. Cienc.* 82, 761–770. doi: 10.1590/S0001-37652010000300022

Benites, M., Alves, D. P. V., de los Santos Maly, M., Jovane, L., Maly, M., de los, S., et al. (2015). Shallow gas occurrence in a Brazilian ría (Saco do Mamanguá, Rio de Janeiro) inferred from high-resolution seismic data. *Cont. Shelf Res.* 108, 89–96. doi: 10.1016/j.csr.2015.08.022

Boyce, J., Pozza, M., and Morris, B. (2001). High-resolution magnetic mapping of contaminated sediments in urbanized environments. *Lead. Edge* 20, 886–895. doi: 10.1190/1.1487301

Boyce, J. I., Reinhardt, E. G., Raban, A., and Pozza, M. R. (2004). Marine magnetic survey of a submerged Roman harbour, Caesarea Maritima, Israel. *Int. J. Naut. Archaeol.* 33, 122–136. doi: 10.1111/j.1095-9270.2004.00010.x

Dehler, S. A., and Potter, D. P. (2002). Determination of nearshore geologic structure off western Cape Breton Island, Nova Scotia, using high-resolution marine magnetics. *Can. J. Earth Sci.* 39, 1299–1312. doi: 10.1139/e02-057

Demir, D., Bilim, F., Aydemir, A., and Ates, A. (2012). Modelling of Thrace Basin, NW Turkey using gravity and magnetic anomalies with control of seismic and borehole data. *J. Pet. Sci. Eng.* 86–87, 44–53. doi: 10.1016/j.petrol.2012.03.013

Gomes, M. P., Vital, H., Stattegger, K., and Schwarzer, K. (2016). Bedrock control on the Assu Incised Valley morphology and sedimentation in the Brazilian Equatorial Shelf. *Int. J. Sediment Res.* 31, 181–193. doi: 10.1016/j.ijsrc.2015.04.002

Heilbron, M., and Machado, N. (2003). Timing of terrane accretion in the Neoproterozoic–Eopaleozoic Ribeira orogen (SE Brazil). *Precambr. Res.* 125, 87–112. doi: 10.1016/S0301-9268(03)00082-2

Jobe, Z. R., Lowe, D. R., and Uchytil, S. J. (2011). Two fundamentally different types of submarine canyons along the continental margin of Equatorial Guinea. *Mar. Pet. Geol.* 28, 843–860. doi: 10.1016/j.marpetgeo.2010.07.012

Kadima, E., Delvaux, D., Sebagenzi, S. N., Tack, L., and Kabeya, S. M. (2011). Structure and geological history of the Congo Basin: an integrated interpretation of gravity, magnetic and reflection seismic data. *Basin Res.* 23, 499–527. doi: 10.1111/j.1365-2117.2011.00500.x

Klein, D. A. (2005). *Registros de variações ambientais no Canal de São Sebastião (Estado de São Paulo), durante o Último Ciclo Glacial.* São Paulo: University of São Paulo.

Koša, E. (2015). Sea-level changes, shoreline journeys, and the seismic stratigraphy of Central Luconia, Miocene-present, offshore Sarawak, NW Borneo. *Mar. Pet. Geol.* 59, 35–55. doi: 10.1016/j.marpetgeo.2014.07.005

Mahiques, M. M. (1995). Dinâmica sedimentar atual nas enseadas da região de Ubatuba, Estado de São Paulo. *Bol. Inst. Ocean.* 43, 111–122. doi: 10.1177/001316447403400221

Mahiques, M. M., and Souza, L. A. P. (1999). Shallow seismic reflectors and upper Quaternary sea level changes in the Ubatuba region, São Paulo State, Southeastern Brazil. *Rev. Bras. Oceanogr.* 47, 1–10. doi: 10.1590/S1413-77391999000100001

Michel, G., Dupré, S., Baltzer, A., Ehrhold, A., Imbert, P., Pitel, M., et al. (2017). Pockmarks on the South Aquitaine Margin continental slope: the seabed expression of past fluid circulation and former bottom currents. *Compt. Rendus Geosci.* 349, 391–401. doi: 10.1016/j.crte.2017.10.003

Miller, K. G., Sugarman, P. J., Browning, J. V., Sheridan, R. E., Kulhanek, D. K., Monteverde, D. H., et al. (2013). Pleistocene sequence stratigraphy of the shallow continental shelf, offshore New Jersey: Constraints of integrated ocean drilling program Leg 313 core holes. *Geosphere* 9, 74–95. doi: 10.1130/GES00795.1

Müller, R. D., Roest, W. R., Royer, J. Y., Gahagan, L. M., and Sclater, J. G. (1997). Digital isochrons of the world's ocean floor. *J. Geophys. Res. Solid Earth* 102, 3211–3214.

Suguio, K., and Martin, L. (1978). "Quaternary marine formations of the State of São Paulo and southern Rio de Janeiro," in *1978 International Symposium Coastal Evolution in the Quaternary,* Special Publication no. 1 (São Paulo), 55.

Tessler, M. G. (1988). *Dinâmica sedimentar quatemária no litoral sul paulista.* São Paulo: University of São Paulo.

Veiga, F. A. (2005). *Processos morfodinâmicos e sedimentológicos na plataforma continental rasa paranaense.* Curitiba: Federal University of Paraná.

Yoo, D. G., Chang, T. S., Lee, G. S., Kim, G. Y., Kim, S. P., and Park, S. C. (2016). Late Quaternary seismic stratigraphy in response to postglacial sea-level rise at the mid-eastern Yellow Sea. *Quat. Int.* 392, 125–136. doi: 10.1016/j.quaint.2015.07.045

Yu, B., Liu, Y., Zhai, G., Bian, G., and Xiao, F. (2007). Magnetic detection method for seabed cable in marine engineering surveying. *Geo. Spat. Inf. Sci.* 10, 186–190. doi: 10.1007/s11806-007-0085-1

Zalán, P., and Oliveira, J. A. B. (2005). Origin and structural evolution of the Cenozoic Rift System of Southeastern Brasil [Origem e evolução estrutural do Sistema de Rittes Cenozóicos do Sudeste do Brasil]. *Boletim Geociencias Petrobras* 13, 269–300.

Conflict of Interest: The authors declare that the research was conducted in the absence of any commercial or financial relationships that could be construed as a potential conflict of interest.

frontiers in Marine Science

ORIGINAL RESEARCH
published: 05 January 2021
doi: 10.3389/fmars.2020.496688

Modeling the Distribution of Habitat-Forming, Deep-Sea Sponges in the Barents Sea: The Value of Data

Genoveva Gonzalez-Mirelis, Rebecca E. Ross, Jon Albretsen and Pål Buhl-Mortensen*

Institute of Marine Research, Bergen, Norway

The use of species occurrence as a proxy for habitat type is widespread, probably because it allows the use of species distribution modeling (SDM) to cost-effectively map the distribution of e.g., vulnerable marine ecosystems. We have modeled the distribution of epibenthic megafaunal taxa typical of soft-bottom, Deep-Sea Sponge Aggregations (DSSAs), i.e., "indicators," to discover where in the Barents Sea region this habitat is likely to occur. The following taxa were collectively modeled: *Hexadella* cf. *dedritifera*, *Geodia* spp., *Steletta* sp., *Stryphnus* sp. The data were extracted from MarVid, the video database for the Marine AREAl database for NOrwegian waters (MAREANO). We ask whether modeling density data may be more beneficial than presence/absence data, and whether using this list of indicator species is enough to locate the target habitat. We use conditional inference forests to make predictions of probability of presence of any of the target sponges, and total density of all target sponges, for an area covering a large portion of the Norwegian Barents Sea and well beyond the data's spatial range. The density models explain <31% of the variance, and the probability models have high classificatory power (AUC > 0.88), depending on the variables/samples used to train the model. The predicted surfaces were then classified on the basis of a probability threshold (0.75) and a density threshold (13 n/100 m^2) to obtain polygons of "core area" and "hotspots" respectively (zones). The DSSA core area comprises two main regions: the Egga shelf break/Tromsøflaket area, and the shelf break southwest of Røst bank in the Træna trench. Four hotspots are detected within this core area. Zones are evaluated in the light of whole-community data which have been summarized as taxon richness and density of all megafauna. Total megafaunal density was significantly higher inside the hotspots relative to the background. Richness was not different between zones. Hotspots appeared different to one another in their richness and species composition although no tests were possible. We make the case that the effectiveness of the indicator species approach for conservation planning rests on the availability of density data on the target species, and data on co-occurring species.

Keywords: species distribution modeling, vulnerable marine ecosystems, deep sea sponge aggregations, soft bottom sponges, ostur, VME indicators, marine management, marine conservation

OPEN ACCESS

Edited by:
Paul E. Renaud,
Akvaplan-niva, Norway

Reviewed by:
Philippe Archambault,
Laval University, Canada
Benjamin Merkel,
Akvaplan-niva, Norway

****Correspondence:***
Genoveva Gonzalez-Mirelis
genoveva@hi.no

Specialty section:
This article was submitted to Deep-Sea Environments and Ecology, a section of the journal Frontiers in Marine Science

Received: *08 September 2019*
Accepted: *23 November 2020*
Published: *05 January 2021*

Citation:
Gonzalez-Mirelis G, Ross RE, Albretsen J and Buhl-Mortensen P (2021) Modeling the Distribution of Habitat-Forming, Deep-Sea Sponges in the Barents Sea: The Value of Data. Front. Mar. Sci. 7:496688. doi: 10.3389/fmars.2020.496688

INTRODUCTION

Classifying the variability of nature into habitat types and furthermore, projecting those habitats onto geographic space, represents a leap toward ecosystem-based management, which is now widely recognized as the best way to manage natural resources and ensure economic prosperity (Murawski, 2007). Habitat mapping has thus become a pillar of nature conservation (Hooftman and Bullock, 2012).

In the marine, benthic realm, one approach toward habitat mapping is to use species occurrence as a proxy for the realization of a habitat type (Howell et al., 2016; Buhl-Mortensen et al., 2019). Under this approach, a central requirement is a checklist of one or more (typically species-level) taxa. These are often referred to as "indicators," albeit not in the sense of ecological indicators but rather, defined as the species/taxa of epibenthic megafauna which are typical for an ecosystem or habitat. This checklist can comprise structure-forming (i.e., habitat-forming) species, associated fauna, or simply, easy-to-identify species which are constituents of the assemblage. Given the appropriate environmental data, these benthic taxa can become the object of Species Distribution Modeling (SDM, *sensu* Elith and Leathwick, 2009; Franklin, 2010). The (spatial) predictions from such models are used to discern the distribution of the marine ecosystem or habitat in question. Distribution maps of vulnerable marine ecosystems (VMEs), red-listed habitats etc., are thus cost-effectively produced, even for areas that have never been sampled or observed.

Deep-sea sponge aggregations (DSSAs) are one such conservation-relevant habitat (OSPAR, 2008). Deep-sea sponges are known to be ecosystem engineers. Some DSSAs can alter the characteristics of the surrounding muddy sediment by creating dense mats of spicules. Spicule mats have been found to increase biodiversity and abundance of fauna, whether of epibenthic megafauna (Beazley et al., 2013) or macrofauna (Bett and Rice, 1992) depending on the species composition of the sponge community. DSSAs filter large quantities of water and may play a key role in nutrient recycling, benthopelagic coupling and the silicon cycle (Maldonado et al., 2005) among other ecosystem functions.

DSSAs first became a habitat of concern for marine conservation policy when they were included by the Oslo-Paris (OSPAR) Convention for the Protection of the Marine Environment of the North East Atlantic in their List of Threatened and/or Declining Species and Habitats (OSPAR, 2008). Later, OSPAR published a separate document with a more detailed definition, as well as assessment of the habitat to better support mapping efforts throughout the OSPAR region (OSPAR, 2010).

Recently, Buhl-Mortensen et al. (2020) analyzed extensive occurrence data from Arctic and subarctic waters and proposed a classification of DSSAs (among other marine ecosystems) with specific lists of indicators. One of the classes they proposed was named "soft bottom sponge aggregations" which, besides being characterized by the dominance of mud in the sediment, is further defined by the following indicators: *Geodia* spp., *Stryphnus* sp., and *Steletta* spp., all of which are tetractinellid sponges. These sponges are large, can be found in high densities, and modify their environment by creating mats of spicules (Maldonado et al., 2016), and they are considered habitat-forming species; they provide habitat to mobile filter-feeders and smaller mega- and macro-fauna. This habitat also corresponds with the habitat sometimes referred to as "boreal ostur" (e.g., Howell et al., 2016).

In Norway, soft-bottom sponge aggregations are known to occur in large patches across some areas of the northern Norwegian shelf from fishing by-catch observations (Klitgaard and Tendal, 2004; Mortensen, 2005). Howell et al. (2016) predict that the core distribution area of soft-bottom DSSAs at the continental scale is located largely in Norwegian waters. Fisheries and management authorities alike are therefore interested in knowing the exact locations and boundaries of these patches so that they can be sustainably managed and have requested distribution maps to support, among other things, the recent revision of the Barents Sea Management Plan. Distribution modeling of soft-bottom DSSA indicator species was quickly chosen as a basis to provide such maps. This choice of approach was also driven by the fact that Norway has an extensive database of epibenthic megafauna georeferenced records, which are collected and curated by the Marine AREAl database for NOrwegian waters (MAREANO) Programme.

The majority of benthic SDMs are built using presence-only or presence/absence data due to the cost associated with the collection of geospatial, quantitative data on benthic communities, or the issues with combining datasets from different time periods and sampling equipment (e.g., Pearce and Boyce, 2006; Howard et al., 2014; Hao et al., 2019). One of the major benefits of the MAREANO video database (MarVid) is that all records have been collected using a standardized method since 2006. Consequently, reliable abundance data (here translated into densities) are available over a large area, allowing us to make a comparison between models built using density data and those built using presence/absence data.

Also, we are interested to explore whether the presence of pre-selected species (as per a list of indicators, e.g., Burgos et al., 2020) is enough to isolate the target habitat, and we use the greater MarVid data to assess this question. Just what are these indicators indicative of, in terms of ecosystem structure and function? We start to investigate patterns of epibenthic megafaunal taxon richness (as a proxy for biodiversity), and total abundance of epibenthic megafauna (as a proxy for productivity) in relation to the predicted distribution of soft-bottom, deep-sea sponges. As, arguably, the most valuable locations would have high biodiversity and productivity, these data can act as a proxy for assessing the conservation value of model predicted hotspots.

We model the distribution of soft-bottom, deep-sea, habitat-forming species of sponges using environmental variables ranging in resolution from 800 m to 4 km. The modeling area covers a large portion of the Norwegian Barents Sea so that the results can be used to inform the revision process of the Barents Sea management plan. We compare the use of presence/absence data with abundance data to assess the benefits and weaknesses of both types of data for the purpose of informing

marine management. We then provide additional context using the greater MarVid dataset to differentiate between predicted DSSA hotspots and their relative conservation value. With a view to improving the way we define and map marine ecosystems, going beyond presence of indicators, this paper addresses the two following questions: (1) Does density data (rather than presence/absence data) provide an advantage when predicting DSSA hotspots? (2) Are predictive maps which are based on lists of indicator species enough to find places of conservation interest, or are there benefits of using data from other members of the epibenthic community?

DESCRIPTION OF DATA, AND DATA PROCESSING

Faunal Data

Data describing the composition of epibenthic megafauna were derived from video footage, which was in turn captured with an underwater camera under the MAREANO Programme. At each station, an underwater camera platform (*Campod* or *Chimera*) is towed along a 700 m, to 1,000 m-long, straight survey path at an approximate altitude of 1.5 m off the seabed. The platform is equipped with two video cameras, one for navigation, and a high-definition, forward-looking, color video camera (Sony HDC-X300) for visual data collection. Underwater positioning is provided by a hydroacoustic USBL (Ultra-short baseline) system (Simrad HIPAP and Eiva Navipac software) with a transponder mounted on the camera platform. This system provides positions accurate to about 2% of the water depth. A pair of laser pointers is used to estimate the width of the field of view.

Routinely, post-cruise video analysis is carried out on all video footage captured with the high-definition camera. During playback, all organisms are named (using standard taxonomic nomenclature whenever possible), counted, timestamped, and later, with the aid of cleaned navigation data, linearly georeferenced. When it is not feasible to count all individuals of a given, identifiable taxon, their abundance is estimated by percent cover. Values in percent cover units are subsequently converted to pseudo-counts by using the approximate (or average) surface area of one single individual or typical colony, derived from expert knowledge, and the area of the field of view. Species indicative of vulnerable habitats and other taxa of special interest are typically identified by their scientific name, and at a taxonomical level no higher than Family (e.g., "*Paragorgia arborea*," "Axinellidae"). Most organisms are, however, identified as morphospecies (e.g., "Porifera egg-shaped"), or custom-made, morpho-taxonomical units (e.g., "Actiniaria, buried"). All of these data are collated and stored within the MarVid database. For this study, the dataset was restricted to all organisms in view which are larger than 5 cm in their longest dimension. This size filter was applied in advance of all data extractions. Henceforth, every time we use terminology like "whole-community" or "all records," etc., we refer to this section of the community, i.e., the epibenthic megafaunal community.

The spatial domain of the dataset is the southwestern part of the Barents Sea, on Norway's continental shelf and slope (**Figure 1** and **Supplementary Figure S1**). The boundaries of the areas surveyed under the MAREANO Programme respond to natural features, management areas for the oil and gas industry, and other factors, not least geopolitical (e.g., the Norwegian-Russian border). Along the large transects between continental Norway and Svalbard, designed to cross the Polar Front, stations are laid out within square boxes rather than along long lines (e.g., data from 2010, **Figure 1**). This design responds to the ultimate purpose of the data collection, which is to make biotope maps (Buhl-Mortensen et al., 2014). Within these boundaries (henceforth, the MAREANO area) video stations are relatively evenly spaced, with a target sampling density depending on the topographic and environmental heterogeneity of each survey area. Depth spans from 40 to 2,500 m, with most stations within the 100–600 m range. The field surveys were carried out during years 2006–2017, with 61% of stations taken in the months of August, September and October but none taken in January or February.

In line with Burgos et al. (2020) the following species were used as indicators of soft-bottom DSSAs in the study area: *Hexadella* cf. *dedritifera*, *Geodia atlantica*, *Geodia barretti*, *Geodia macandrewii*, *Geodia* sp., *Steletta* sp., and *Stryphnus* sp. This community of sponges has also been recognized in other North Atlantic regions (Klitgaard and Tendal, 2004; Murillo et al., 2011; Beazley et al., 2013; Cárdenas et al., 2013; Maldonado et al., 2016) providing additional support to the ecological coherence of the chosen taxa. We will refer to this set of soft-bottom, deep-sea sponges as the target taxa.

From the MarVid database, we first pulled all records on any of the target taxa. Then, total abundance was pooled for the whole survey line. Total density was calculated using the average width of the field of view to calculate the total area of the surveyed strip and given in number of individuals or colonies per 100 m^2. Total density as well as presence/absence (derived from density) were then used as response variables.

We do not use year, or month of survey in our analyses. As far as the former is concerned, we assume we can safely ignore this information because all the target taxa are long-lived. No data points come from the winter months, where the Barents Sea may present more severe stratification. This is not necessarily a problem because neither of these organisms shows seasonal fluctuations in its distribution. Nevertheless, it is worth noting that our response data represents the mild season better than the winter season.

Subsequently, taxon richness and total abundance of all taxa were also calculated for each survey line, providing proxies for diversity and productivity to cross reference with predictions.

Environmental Data

Environmental data can be divided into four main groups: (1) bathymetric/terrain variables, (2) geological variables, (3) oceanographic variables, and (4) ocean surface (satellite-derived) variables, all of which have been found to be drivers of benthic biological composition to varying degrees (Levin et al., 2001; McArthur et al., 2010; Selkoe et al., 2010; Harris and Baker, 2019), although not necessarily of sponge distribution.

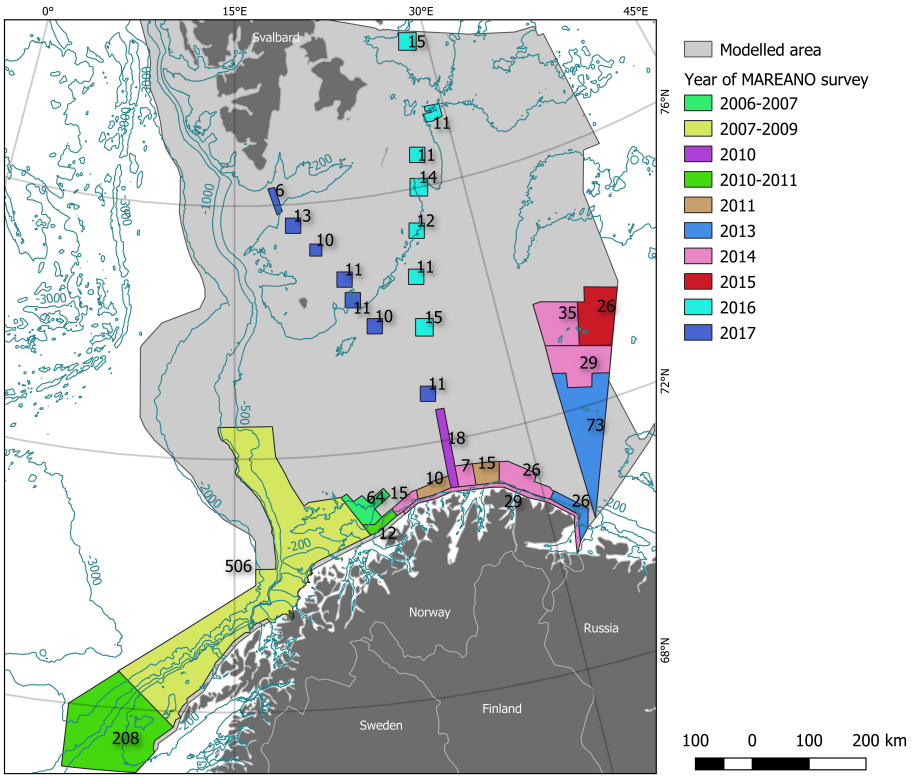

FIGURE 1 | The faunal data used in this study were collected under the Marine AREAl database for NOrwegian waters (MAREANO) Programme. Under this government-funded, data collection programme, benthic sampling is conducted according to predefined survey areas. In this figure, we illustrate the number of video stations per survey area (labels on the map), as well as the year when the sampling was carried out (see legend for details), for the surveys that were used in this study in the Barents Sea. Also shown are bathymetric contour lines (dark blue) and land masses with political boundaries (gray). The scale on this map (scale bar) is 1:5,745,500.

Bathymetry and Terrain Analyses

Bathymetry data for the southwest Barents Sea was downloaded from the EMODnet bathymetry portal[1] on October 2018 (i.e., after the 2018 data became available). The resolution of the Digital Terrain Model hosted by EMODnet was 1/16 × 1/16 arc minutes (circa 500 × 500 m at this latitude) (EMODnet Bathymetry Consortium, 2018). All downloaded tiles were mosaicked into one single raster layer and gridded at 800 m on a UTM projected grid (zone 33N).

We calculated: slope, terrain ruggedness index (TRI), roughness, and vector ruggedness measure (VRM, Sappington et al., 2007) in R using the **raster** (Hijmans, 2020), and **spatialEco** (for VRM, Evans, 2020) packages using default neighborhoods.

We also derived: topographic position index (TPI) using two neighborhood sizes, aspect using three analysis window sizes, and type of geomorphological feature using three analysis window sizes. TPI was also calculated in R using the **raster** package. Aspect and feature were calculated using GRASS 7.8 (**rgrass7**, Bivand, 2019) in R. See **Table 1** for a summary and additional details of this part of the data processing.

The latter six layers, namely the three for aspect and three for geomorphology, as well as current direction (see below) were further processed before entering the model. They were put through a classification procedure and were converted to a single categorical variable, henceforth named terrain class. This classification was achieved by applying Random Forests

TABLE 1 | Summary of multiscale analyses performed on bathymetric data.

Procedure (function and/or parameters)	Output	How used in the model
Neighborhood = 5 pixels, i.e., 1,000 m (function terrain, option tpi)	Fine TPI*	As is
Neighborhood = 15 pixels, i.e., 3,000 m (custom-made function)	Broad TPI*	As is
Analysis window = 3 pixels, i.e., 600 m (function r.param.scale)	Fine Aspect, and geomorphological feature	Used in a supervised classification together with *u* and *v* components of current direction (categorical layer with 8 classes)
Analysis window = 19 pixels, i.e., 3,800 m (function r.param.scale)	Intermediate-scale Aspect, and geomorphological feature	
Analysis window = 33 pixels, i.e., 6,600 m (function r.param.scale)	Broad Aspect, and geomorphological feature	

**TPI, Topographic Position Index.*

[1]https://portal.emodnet-bathymetry.eu/

in a supervised framework. First, 10,000 points were sampled at random. Then we used the CLARA (Clustering Large Applications) algorithm in R (available through the **cluster** package, Maechler et al., 2019) to classify cells into eight classes, followed by the **randomForest** function (and package, Liaw and Wiener, 2002) to predict class for all unsampled cells and thus generate a full coverage, categorical layer. This way we generated a new predictor variable which summarizes current direction, aspect, and feature type information. The goal was to reduce the number of (potentially correlated) predictors without losing predictive power.

Geological Data

Landscape type was also used as predictor in our SDM exercise. This spatial dataset shows a division of all Norwegian waters into different marine landscapes, defined as major features of the seabed topography (Norges geologiske undersøkelse, 2014). Examples of marine landscape types in Norwegian marine areas are fjords, marine valleys, continental slopes and deep-sea plains. The data was downloaded on 2019/08/28 as a categorical map from the Norwegian Geological Survey portal[2]. The maximum scale of the downloaded map was 1:100,000 and it was subsequently rasterized to the appropriate resolution (800 m).

Oceanographic Data

Ocean model outputs describing the physical properties of the near-seabed environment were also included as predictors (Pearman et al., 2020). The data were derived from two separate oceanographic models known as the NorKyst-800 m (NK800) model and Barents Sea-800 m (B800) model, each covering a different part of our SDM model area (see **Supplementary Figure S2**). Both 800 × 800 m ocean models are based on the Regional Ocean Modeling System (ROMS, e.g., Shchepetkin and McWilliams, 2005; Haidvogel et al., 2008[3], but had different external forces, and simulated different periods. The NK800 model is explained in detail in Asplin et al. (2020). The B800 model is not yet documented, but the configuration is comparable to the NK800 model and it is the best resolved regional oceanographic model available in the area. It is run and disseminated by the Institute of Marine Research, Norway but is not yet publicly available. Meanwhile, the NK800 model is well established and daily forecasts are produced by the Norwegian Meteorological Institute[4].

From the NK800 model we were able to obtain data derived from a simulation based on years 2013–2015, and for an area which encompassed approximately the Exclusive Economic Zone around continental Norway. From the B800 model instead, the data we obtained was from a 1-year simulation (year 2010), while the area covered was more centered around the Norwegian Barents Sea. Both these simulations, although financed by MAREANO, had been ordered for purposes going beyond the objectives of this study, hence the discrepancy between the time and space coverage in relation to the video data.

[2]http://geo.ngu.no/download/

[3]http://myroms.org

[4]https://thredds.met.no

Maximum, minimum, mean, and standard deviation of salinity, temperature, and current speed were obtained from each model, as well as the mean u and v component of current direction, giving a sum of fourteen fields. These fields were extracted from the bottom layer of either model, although neither model was bottom-optimized. For NK800, salinity and temperature statistics are based on daily values, while current speed and direction are based on hourly values. For B800, hourly fields of temperature, salinity and current speed and direction were used. The resulting fields were then interpolated to an 800 × 800 m regular grid defined in UTM33 coordinates using a nearest grid point-interpolation.

Fourteen pairs of raster layers were then blended with each other to yield a total of fourteen complete predictor layers covering our entire model area (**Supplementary Figure S2**). Blending for each combination of variable and summary statistic was generally carried out through the following steps: create intersection rasters, create points around overlapping area, calculate distances to points in overlapping area, sum distance rasters, create distance weighted rasters, and merge rasters (Wueest et al., 2012). While the seam between the two models did not fully disappear, artifacts were absent from the SDM predictions.

Sea Surface Data

The NASA Goddard Space Flight Center, Ocean Ecology Laboratory, Ocean Biology Processing Group provides ocean color data with worldwide coverage. We downloaded data on chlorophyll *a*, particulate organic carbon and maximum euphotic depth for use within this study from https://oceancolor.gsfc.nasa.gov/cgi/l3. They are 4 km data, resampled to 800 m. The downloaded data were pooled to a 10 years average from 2006 to 2017, in alignment with the period of MAREANO observations. All predictor layers were aligned to the bathymetry layer in terms of extent, origin, and resolution.

MODELING AND ADDITIONAL ANALYSES

Modeling Method

We used a Conditional Inference Forest (CIF, Hothorn et al., 2006b) as the modeling framework. CIF is a recursive partitioning and ensemble method for discovering patterns in multiple-predictor, complex datasets that has been found not to be biased toward variables with many values (Strobl et al., 2007). Their application in ecology remains low relative to other fields (e.g., psychology, Martin, 2015; safety, Das et al., 2009; engineering Sardá-Espinosa et al., 2017). Ecological applications include (Müller et al., 2009; Hothorn and Müller, 2010) and only a handful concern SDM (Pottier et al., 2014; Gonzalez-Mirelis and Buhl-Mortensen, 2015) despite the suitability of the method to the SDM problem, and the typically noisy ecological data.

CIFs belong to the family of Machine Learning Algorithms. The base learner of a CIF is a Conditional Inference Tree. The method for building trees is based on a well-defined theory of permutation tests, whereby splitting (i.e., partitioning) is

performed based on measured correlations between predictor variables and the response. First, a global null hypothesis of independence between the response and all predictors is tested. A correlation coefficient (e.g., Pearson's or other depending on the data), with a corresponding *p*-value is calculated for each variable's association with the response. If no *p*-value is below the pre-selected alpha level after accounting for multiple significance tests, the global null hypothesis is not rejected, and the algorithm terminates. Otherwise, the predictor with the strongest association with the response is selected for splitting. The best split within this predictor is selected, and the training set is partitioned on this value. Finally, these steps are iteratively repeated until the global null hypothesis can no longer be rejected in all subsections (Martin, 2015).

Machine Learning algorithms have been designed to be robust in the face of correlated predictors (e.g., Nicodemus and Malley, 2009): if two of the variables provide the same child node purity the model simply selects one. This effect is controlled by the *mtry* parameter, which determines the number of variables tried at each split. This is one of the features that help machine learning applications excel at predicting (Shmueli, 2010).

Multicollinearity does become an issue when the goal is to interpret the patterns learned by the model. While ecological inference is not the focus of this paper, our study provides an opportunity to describe and/or validate species-habitat relationships. We therefore trained another set of models where colinear predictors (as measured by their variance inflation factors) had been eliminated so as to gain an opportunity to illustrate variable importance. Variance Inflation Factors were calculated using the **usdm** R library (Naimi et al., 2014).

Eight models were built in total, for all the three-way combinations of the following parameters: response variable (density, or probability of presence), number of predictors (all available, or a selected subset of non-correlated variables), and finally, number of observations (all available, or just 70% of them, reserving a set of 30% for validation purposes, see below). We conducted model training in R by means of the **party** package (Hothorn et al., 2006a). Additional arguments used include number of trees in the CIF (*ntree* = 1,000), and the number of variables tried at each split (*mtry* = 3).

The four density models were tested by means of the statistic developed in Li (2017): Variance Explained by Cross-Validation (VEcv). VEcv is a measure of model accuracy for continuous data that is independent of unit or scale, data mean, and data variance, and it unifies other measures of error, including the commonly used mean absolute error and root mean square error. It was calculated using the **spm** R package (Li, 2019).

The four probability models (effectively, binary classifiers) were assessed by means of the Area Under the Curve (AUC) statistic, which measures the area under the so-called Receiver Operating Characteristic (ROC) curve. The ROC curve is a plot of the true positive rate against the false positive rate over all possible threshold values of an automatic classifier and is commonly used in SDM applications using presence/absence data. AUC ranges from 0.5, when the model does no better than a random guess, and 1 when the model can discriminate perfectly between presence and absence. We further tested the significance of this value through the DeLong's test for two ROC curves, where the null curve used for comparison was that obtained by randomly shuffling the response variable. For these tests we used the **pROC** R package (Robin et al., 2011).

Data Model

The total number of samples was n = 1,142. This set included survey lines of varying length. The mean line length was 738.16 m, with standard deviation 174.22 m. The average nearest neighbor distance was 6764.85 m. We used a prediction grid of 800 × 800 m covering an area of 614,376 km^2. We ignored the position of the survey lines relative to grid cells and assumed the data observed along each line to be representative of the entire cell containing the centroid of the line.

The two models used for spatial prediction were those where all variables and all observations were used for training. Henceforth these will be referred to as "the density model" and "the probability model."

Additional Analyses

To compare the predictions between the density model and the probability model we first calculated the Pearson correlation coefficient (r) between each pair of predictions, pixel-wise, for the whole study area. We then calculated Pearson correlation between predicted density values and predicted probability values within a running window of size approximately 41 by 41 km (more precisely 51 by 51 grid cells) using the **SpatialEco** package (Evans, 2020). This window size captured areas big enough to display variation in the predictions within, while still showing local patterns of correlation.

Hotspots (high-density areas) and core area (high-probability areas) were defined by applying a threshold to the density and the probability predictions, respectively. Areas below the thresholds are hence forth referred to as background. The threshold for density was determined visually. The threshold for probability was conservatively derived from the True Skill Statistic (TSS), also called Youden's J, defined as the average of the net prediction success rate for present sites and that for absent sites (Liu et al., 2009). The three obtained zones thus represent a gradient of likelihood of presence of a soft-bottom, deep-sea sponge (vulnerable) marine ecosystem.

We compared mean total taxon richness and mean total abundance of megafauna between all zones (i.e., along the gradient). There was a total of 13 observations within the hotspots, 174 observations within the core area, and 955 observations in the background zone. To achieve a balanced design, we sampled 13 observations from the core area and the background zone and used only those in the test. Furthermore, these 13 observations were stratified by the range of the variable being tested (richness, or abundance). The strata were created in each case by discretizing the variable into three classes using Jenks breaks as cut points.

We also looked at patterns of richness and abundance within the high-density zone (i.e., between hotspots). For this comparison we had very few samples available and no statistical tests were performed.

RESULTS

Model Predictions

With this data set, spanning a vast area and collected over many years, and this set of environmental layers, most of which are themselves the outcome of other models, we were able to account for between 15 and 31% of the spatial variation in density of soft-bottom, deep-sea sponges, depending on the training data. The classificatory power of all four probability models was consistently high (**Table 2**). Model predictions are displayed as continuous rasters in **Figure 2**.

The following variables were eliminated from the twenty-four initial ones: slope, roughness, maximum temperature, standard deviation of current speed, standard deviation of salinity, and mean temperature. **Supplementary Figure S3** ranks the remaining variables by their importance and shows that temperature (minimum), salinity (mean, minimum and maximum), and depth are the most important predictors for the target set of species. Variance Importance is reported from the density model because this is the model that had access to the most information. A look at variance importance from the probability model revealed that minimum temperature dropped by one position, ranking third instead of second; additionally, Chlorophyll *a* raised to position number five. The remaining top predictors were consistent. This plot can be easily generated if needed with the R Notebook provided with this paper.

The relationship between the responses and the top two predictors (namely mean salinity, and minimum temperature) can be visualized by means of partial dependence plots, in **Supplementary Figure S4**. When predicting abundance, the models indicate a preference of the target sponges for a mean salinity above 34.9 ppt and a temperature which does not drop below −0.5°C at any time of year. The curve for probability of presence is slightly different in the case of minimum temperature, where the probability remains low (but not zero) beyond −0.5°C and it becomes 0 at −2.0°C. The combinations of salinities and temperatures indicate that the maximum response is observed within Atlantic water.

The overall Pearson's r between predicted densities and predicted probabilities was 0.79. Locally (at scales 10–100 km) the two models largely agreed with each other (82% of model domain with $r > 0.2$, blue in **Figure 3**), while lack of correlation, or discrepancy (16% r between −0.2 and 0.2) and disagreement (0.01% $r < -0.2$) between the two models also occurred. This correlation is illustrated in **Figure 3** in relation to the data range, where we show the areas of disagreement in more detail than those were agreement occurred, as they provide a more useful backdrop to interpret model results. It is, however, worth mentioning that twenty-four percent of the model domain had very high (>0.7) correlation values; for a look at where those areas are located you may use the R Notebooks provided.

To decide on a threshold for the probability model we looked first at the TSS, which was 0.41. This threshold would classify as soft-bottom DSSA core area a very large region (notice the area depicted in dark green and dark blue in **Figure 2A**) which we deemed unpractical from the management point of view; it would also be difficult to defend a probability threshold that is below 50%, no matter the management application intended. Therefore, we raised the threshold from 0.41 to 0.75. At this level, two main regions remain: the Egga shelf break and Tromsøflaket area, as well as the area around the Røst bank and Træna Trench (see **Figure 4** for reference). At 0.85 the area at Egga/Troms is reduced to a few small kernels while the size of the Træna trench area is hardly affected. Ultimately, we decided to use 0.75 as a threshold value for probability. For density, we used 13 n /100 m^2, which was chosen visually to mimic the main patterns in **Figure 2B**. We subsequently digitized the boundaries around all pixels with value above the threshold, on each layer.

Four hotspots can be identified if we ignore the small gaps between nearby features: one elongated patch at Tromsøflaket, two minor ones along the Egga shelf break, and a fourth one along the shelf margin west and south of Røst bank, in the Træna trench. These hotspots are all wholly contained within the identified core area (**Figure 4**).

Tromsøflaket had the highest observed (210 n/100 m^2) and predicted densities of the whole study area. The overall (observed) mean density was 2 n/100 m^2.

Patterns of Richness and Abundance of All Megafauna

Figure 5 illustrates the differences in total taxon richness and total abundance of epibenthic megafauna between zones, namely, the background, the core area, and the hotspots. There was no conclusive evidence for a difference in taxon richness between zones ($p = 0.08$). In contrast, we found a difference in the mean total abundance of epibenthic megafauna ($p = 0.008$). A *post hoc* Tukey's test revealed that only one two-way comparison was significant, and it was between the background and the high-density zone (extremes in the gradient).

The comparison between hotspots (bottom plots in **Figure 5**) gave us further insight into the ecosystem structure and function of these areas in relation to each other. The hotspot at Træna had much higher taxon richness than Tromsøflaket. It is less clear whether there are real differences in total abundance between hotspots because of the large variation between samples,

TABLE 2 | Model evaluation statistics.

	Observations	All (n = 1,142)	All (n = 1,142)	70% (n = 800)	70% (n = 800)		
	Variables	All (24 vars)	Selected (18 vars)	All (24 vars)	Selected (18 vars)		
Response	**Probability**	0.95 (p-value∼0)	0.95 (p-value∼0)	0.88 (p-value∼0)	0.88 (p-value∼0)	AUC	**Statistic**
	Density	31.28%	30.58%	28.51%	15.38%	VEcv	

AUC, Area Under the Curve; VEcv, Variance Explained by Cross-Validation.

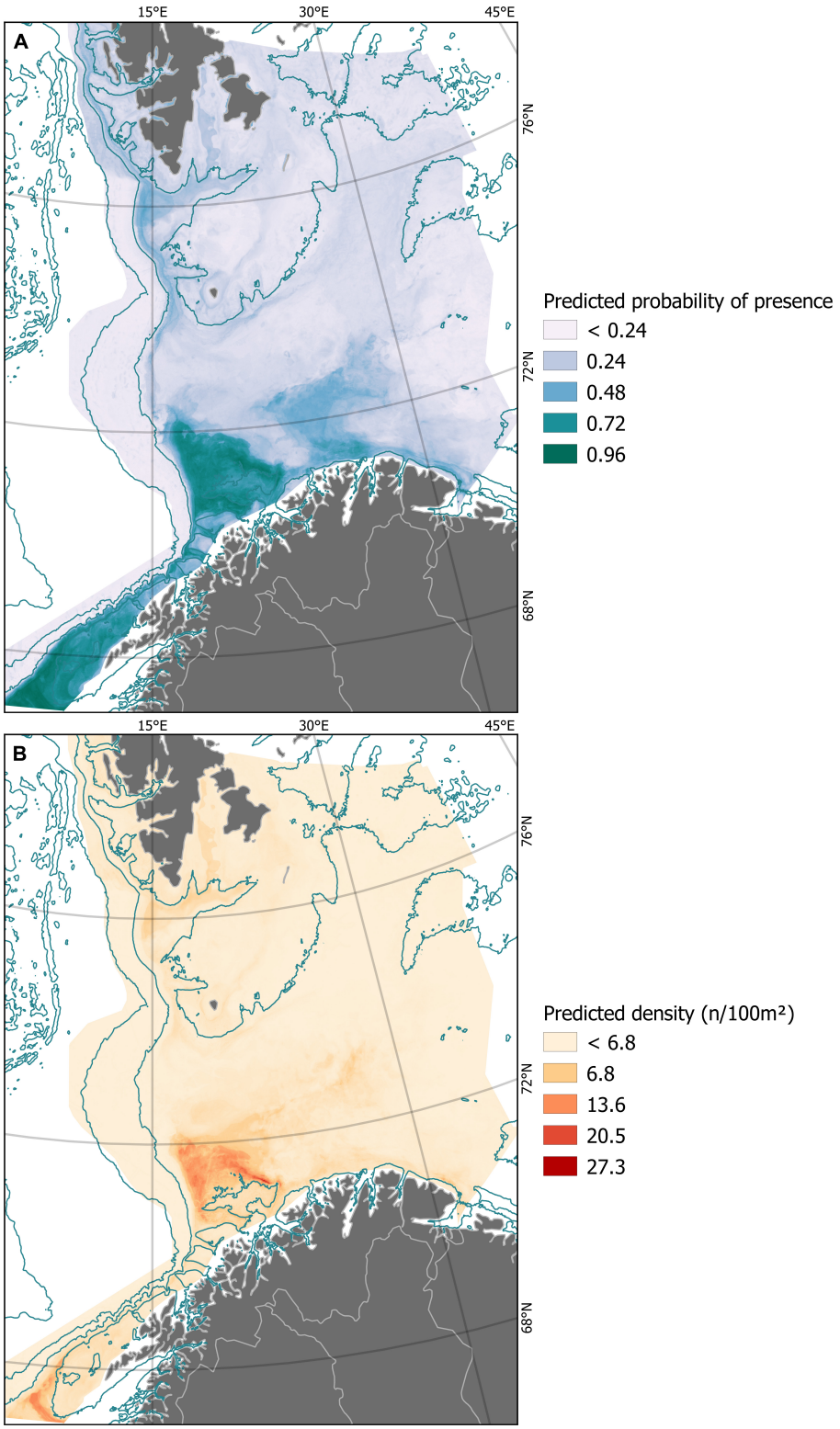

FIGURE 2 | Model predictions of probability of presence **(A)** and density **(B)** of soft-bottom, deep-sea sponges across the Norwegian Barents Sea as modeled using conditional inference forests and multiple environmental predictors. Also shown are selected bathymetric contour lines (dark blue) and land masses with political boundaries (gray), about which more details can be found in **Figure 1**. For scale, refer also to **Figure 1**.

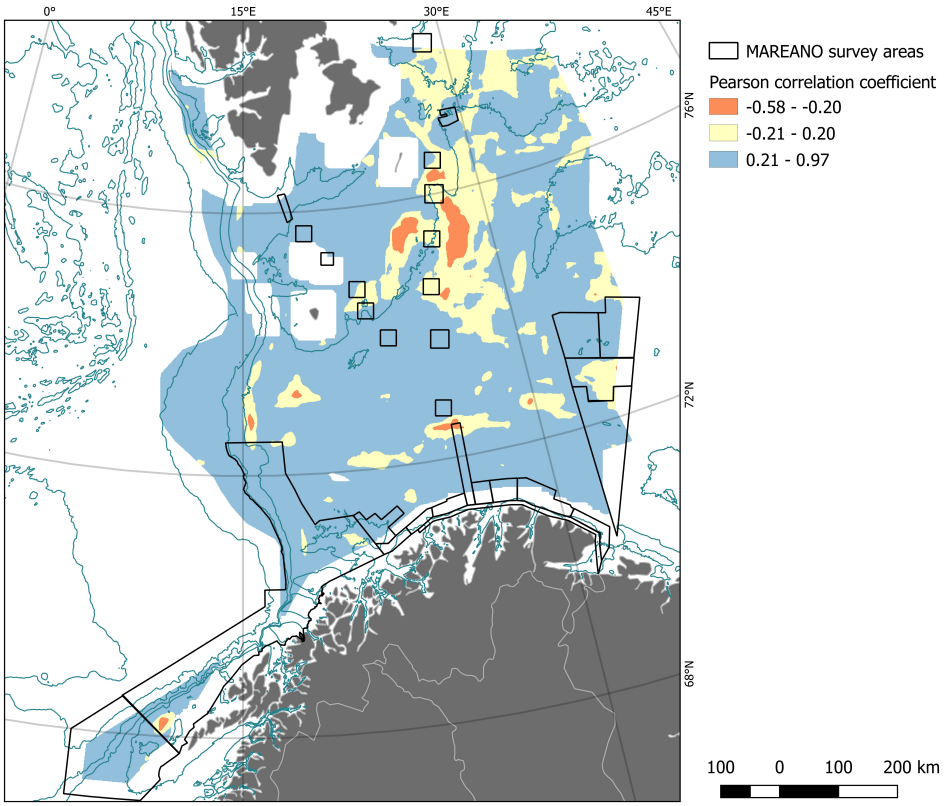

FIGURE 3 | Pearson correlation between predicted density and predicted probability of presence of soft-bottom, deep-sea sponges for each pixel was calculated within a running window of size 41 km by 41 km. In this figure we illustrate the areas where the correlation coefficient was most negative (red, see legend for coefficient values). In yellow are shown all areas where the correlation between the two models was around zero, meaning there was no correlation between the two models. Areas of model agreement are shown in blue. The black outline overlaid is the extent of the training data coverage. Also shown are selected bathymetric contour lines (dark blue) and land masses with political boundaries (gray), about which more details can be found in **Figure 1**.

particularly at Træna and Tromsøflaket. There are nevertheless very few samples to draw conclusions.

The high abundance at Tromsøflaket was accounted for by the presence of brachiopods, which are in the limit of what can be considered "mega" fauna.

DISCUSSION

This study aimed to discover the distribution of soft-bottom DSSAs in the Barents Sea region, identify the benefits of using density data over presence/absence data for this community, and explore whether the "indicator-species list" collective modeling approach is adequate to highlight conservation-relevant hotspots for this community.

In agreement with other authors (e.g., Howard et al., 2014; Dallas and Hastings, 2018) we find that predicted probability maps based on presence/absence data may be adequate to highlight regions of interest, but are insufficient to determine particular areas that may require management attention, for example because they harbor high densities of megafauna. We shall be more specific: it would be virtually impossible (for, let's say, a fisheries manager) to delineate the boundaries of what we have termed the Tromsøflaket patch (whose existence is known from by-catch data, see Mortensen, 2005, and whose conservation value is undisputed) using the probability map alone as a supporting tool. Depending on the threshold they used, they would come up with either a huge, unmanageable area, or with a tiny, irrelevant one; no single probability threshold even approximates the boundaries the Tromsøflaket patch.

Predictive modeling of density has enabled us, in contrast, to detect specific locations of conservation interest and more importantly, of reasonable size, even if delineating their boundaries required some "visual" calibration and is admittedly, hardly reproducible. Should there be any dispute, though (let's say between fisheries managers and conservation practitioners), this can easily be settled by looking at the stability of the boundaries in relation to thresholds. Indeed, the boundary around Tromsøflaket was very stable, while the Træna patch completely disappears raising the threshold by 1 unit! Therefore, the evidence suggests that Tromsøflaket patch should be put forward as an area where management action can help protect DSSAs.

Very few studies have looked at biological differences *within* the predicted range of a species or habitat of interest, although some (e.g., Hui and McGeoch, 2008; Boulangeat et al., 2012)

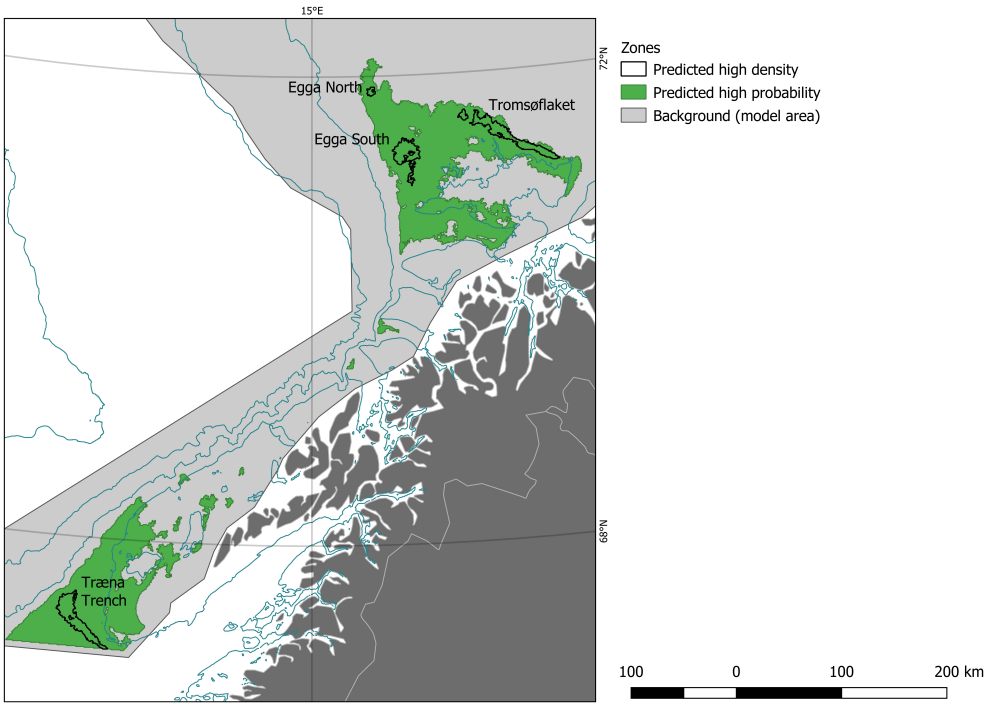

FIGURE 4 | The areas referred to as "predicted high probability" are those where the model predicted a probability of presence of soft-bottom, deep-sea sponges larger than 0.75 (green), whereas the areas referred to as "predicted high density" enclose the pixels where the model predicted a density of the target species above 13 colonies/100 m^2 (outlined in black). For reference we have also plotted the extent of the model area (light gray). Also shown are selected bathymetric contour lines (dark blue) and land masses with political boundaries (gray), about which more details can be found in **Figure 1**. Here, we can identify four main high-density patches, or hotspots (labels).

have suggested that looking at species co-occurrence and/or biotic interactions is beneficial to model species distributions. The use of whole, epibenthic community data has enabled us to validate the indicator species approach from the point of view of total abundance of epibenthic megafauna and we provide evidence that areas of increased biomass can be detected by modeling the density of these species of soft-bottom, deep-sea sponges. But it has also called into question whether the locations detected are equivalent to one another as far as their species assemblage. We have found that there can be substantial variation between locations (keep in mind the bottom plots of **Figure 5**), even when they have been modeled using the same dataset and the same model. While this result is intriguing and raises interesting ecological and management-related questions (some of which will be discussed in the paragraphs that follow), it is not yet clear how dependent it is on the chosen thresholds. Further work is planned to analyze the data in a framework that is free from binning the predictions into zones but rather, are used as a continuous variable.

Modeling a collective of species rather than a single one is a good strategy from the point of view of the model because one quickly increases the number of presences in the data. But even with a list of co-occurring species, it may be that other species are in fact dominant in the result, or that mosaics are present. Indeed, the community observed at Træna consisted of many types of sponges, not only those modeled here but also taxa such as Axinellidae (including species of *Phakellia* and *Axinella*), and *Antho dichotoma*. It follows from our results that our knowledge on the structure and function of this marine ecosystem is still poor, and equally, that work must continue to develop indicators that point to some homogenous entity (one may even add, worthy of the name "indicator") to ensure that detected locations are representative of each other.

On the other hand, it may be that DSSAs and probably other marine ecosystems as well, are a case of a fuzzy category, meaning that there is no list of attributes (species) that can unambiguously define the category (Levitin, 2014). From this point of view, one could only say that something *is* a DSSA when it looks *similar* to a declared DSSA, thereby doing away with the whole approach where species are used as a proxy for the presence of the habitat (the indicator species approach).

Much more work is needed to make this approach operational. For comparison, notice that an "ecological indicator" is a variable that is measured in order to derive (i.e., directly and without the need for additional data) the status of some other variable which is really the variable of interest but which itself is unfeasible to measure. Notoriously, the VME literature shows that the presence of VME indicators (or even their known density) cannot tell us whether the location should or should not be

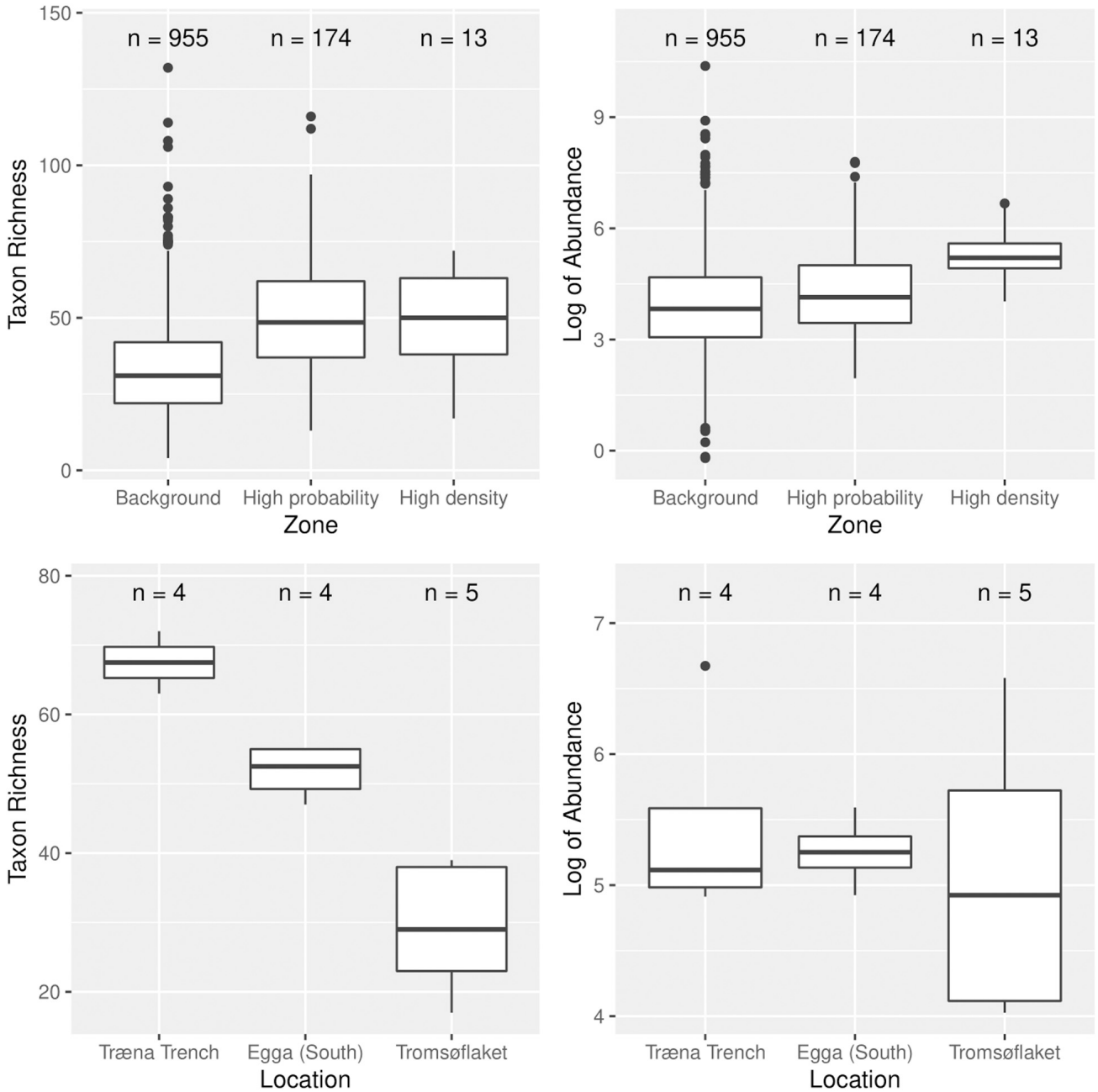

FIGURE 5 | Boxplots illustrating patterns in epibenthic megafaunal taxon richness, and total abundance of epibenthic megafauna (which was log-transformed) in relation to the predicted distribution of soft-bottom, deep-sea sponges. On the top plots we compare these parameters (namely richness and abundance) in relation to a "gradient" toward the areas of highest predicted sponge density. The three zones compared are "background" (low probability and low density), "high probability" (probability above 0.75 and density below 13 n/100 m^2) and "high density" (the four identified hotspots). On the bottom plots we compare richness and abundance among three of the four hotspots (one of them did not have any sampling stations within). Also included are the number of stations in each group. Note that the bottom plots represent the variation among the 13 samples in the high-density zone (see the plot above).

declared a VME. This is epitomized by an ongoing search for universally applicable density thresholds for VME indicators, threshold values which are proving more than a little elusive (e.g., Baco-Taylor et al., 2020). The MarVid database offers a rare opportunity to ascertain the assumptions that are implicit in using SDMs as a basis for mapping VMEs and offering conservation advice, as well as to develop new approaches more aligned with the concept of fuzzy categories which may prove easier to operationalize.

We must not forget that the (density) model accounted for less than 31% of variation in the response data. Similarly, our model may be incurring some degree of overfitting, particularly

given (a) the existence of mass occurrences in the area and (b) the extent to which we have extrapolated our predictions. Therefore, model predictions should be assessed with a generous dose of skepticism.

The partial dependence plots of the top two contributing variables showed intuitive minimum values, encountered within the study region, while a maximum value was not encountered. This suggests that the model may be adequate within the survey area but should be re-trained with data from elsewhere in the Barents Sea, and particularly from the areas of model disagreement (yellow and red, in **Figure 3**) to increase confidence. Considering this, we would not recommend making any policy decisions based solely on the predictions that are completely outside the data range.

While additional training data would certainly improve the model, so would adjustments in the predictor variables. Let us discuss first the aspects that worked, before we move onto potential improvements.

The variables used as predictors within this study highlighted temperature and salinity, together with depth as being important for locating soft-bottom DSSAs in the Barents Sea region. All terrain and geological variables were less important. This aligns well with the findings of other studies (e.g., Beazley et al., 2015; Pearman et al., 2020) that oceanographic variables are more important than terrain variables for defining benthic species distributions. This points to a more mechanistic relationship existing between oceanographic conditions and benthic species composition (described in Young et al., 1996 for the case of sponges), which is emerging thanks to the fact that oceanographic models are becoming more accessible to researchers engaged in benthic SDM, while previous studies utilized only topographic variables and were relying upon the terrain characteristics as proxies for the oceanographic parameters (Wilson et al., 2006).

Variable importance in our model(s) reflected this very well, but not so the partial response curves, where a bell-shaped curve would have been a better diagnostic than one where a drop follows a peak. We have already discussed the degree to which model overfitting may be responsible for this, but equally, there could have been misrepresentations in the oceanographic layers. Let's not forget that the resolution of the models is 800 m and may be missing spatial variation of temperatures and salinities occurring over the varied topography often associated with shelf break landscapes (e.g., canyons and throughs).

Similarly, our oceanographic models may not necessarily be representative of the period when the data were collected, particularly the B800 model which only ran for 1 year, and furthermore, that the Barents Sea may be experiencing broad scale climatic/oceanographic changes (Lind et al., 2018).

In addition to aligning the time period better, our ability to quantify the relationship between soft-bottom, deep-sea sponges and oceanographic descriptors may be much increased by letting the ROMS models simulate the same months where our species were observed, or in other words, exclude all the values from January and February. These factors undoubtedly limit the degree of trust we can place in the model predictions.

Among the clearly missing variables from our set of potential predictors of soft-bottom DSSAs is sediment type. The MAREANO project does routinely produce sediment maps which have coverage across the MAREANO area (Norges geologiske undersøkelse/MAREANO, 2015), but, as this study predicts beyond the range of the MAREANO area, we have strayed into areas with less reliable/non-existent sediment maps as potential model inputs. It is therefore possible that a future predictive model will be able to better refine were the soft-bottom DSSA hotspots lie, filtering out areas with non-suitable sediment types. It should be acknowledged that these soft-bottom sponges often originally settle on a small piece of gravel or stone that later becomes embedded in the adult colony's base. Calling these species a "soft-bottom" community is therefore a slight misnomer, and indeed many of these species are found on rocks in fjord areas. However, the soft-bottom DSSA does tend to aggregate on a predominantly soft bottom, so models including sediment type may be able to improve our predictions. It is also possible that such a model may be able to identify the mosaicked hard-bottom and soft-bottom sponge community from the Træna area without a deeper examination of species lists. However, in that event we would still suggest a deeper exploration of the whole-community data to consider what other differences may be being missed by the indicator-species-only models being built.

In summary, we have produced new maps which may be useful for the identification of potential conservation-relevant hotspots for soft-bottom DSSAs in the Barents Sea. We would primarily advocate the use of probability models for identifying areas to study further. However, we would recommend using abundance or density models to try and highlight the potential conservation-relevant hotspots in a region. Lastly, we believe it is important to undertake a deeper exploration of the associated fauna, beyond only the indicator species used to build conservation-relevant models. This data can provide marine managers with more nuanced base from which to make conservation decisions, especially if there is a need to choose between hotspots when designing conservation efforts.

DATA AVAILABILITY STATEMENT

The data used in this study are available for download at: https://zenodo.org/record/4302591. The source code needed to reproduce the results reported in this paper is available at this repository: https://github.com/GeOnoveva/fmars.2020.496688/releases/tag/v0.1.

AUTHOR CONTRIBUTIONS

PB-M and GG-M proposed the concept. GG-M conducted the data analysis. GG-M and RR wrote the manuscript. JA provided access to, and information about the oceanographic data. All authors contributed to the article and approved the submitted version.

FUNDING

Funding for this work came in full from the MAREANO Programme (Norway).

ACKNOWLEDGMENTS

We would like to acknowledge the contributions by Margaret Dolan (who helped provide the satellite-derived data), Kjell Bakkeplass (who helped process some of the bathymetric data), Audun Ronesen (for technical support), and Gjertrud Jensen, Yngve Klungseth Johansen, and Anne Kari Sveistrup for their continued excellence and patience performing video analyses. Thanks are due also to Henning Wehde for a much-needed push at a critical time.

SUPPLEMENTARY MATERIAL

The Supplementary Material for this article can be found online at: https://www.frontiersin.org/articles/10.3389/fmars.2020.496688/full#supplementary-material

REFERENCES

Asplin, L., Albretsen, J., Johnsen, I. A., and Sandvik, A. D. (2020). The hydrodynamic foundation for salmon lice dispersion modeling along the Norwegian coast. *Ocean Dyn.* 70, 1151–1167. doi: 10.1007/s10236-020-01378-0

Baco-Taylor, A., Ross, R., Althaus, F., Bridges, A., Brix, S., Colaço, A., et al. (2020). "A community consensus on designating vulnerable marine ecosystems from imagery," in *Proceedings of the Ocean Science Meeting Oral Presentation, 16-21 February 2020*, San Diego, CA.

Beazley, L. I., Kenchington, E. L., Murillo, F. J., and Sacau, M. M. (2013). Deep-sea sponge grounds enhance diversity and abundance of epibenthic megafauna in the Northwest Atlantic. *ICES J. Mar. Sci.* 70, 1471–1490. doi: 10.1093/icesjms/fst124

Beazley, L. I., Kenchington, E. L., Yashayaev, I., and Murillo, F. J. (2015). Drivers of epibenthic megafaunal composition in the sponge grounds of the Sackville Spur, northwest Atlantic. *Deep Sea Res. I Oceanogr. Res. Pap.* 98, 102–114. doi: 10.1016/j.dsr.2014.11.016

Bett, B., and Rice, A. L. (1992). The influence of hexactinellid sponge (Pheronema carpenteri) spicules on the patchy distribution of macrobenthos in the Porcupine Seabight (Bathyal NE Atlantic). *Ophelia* 36, 217–226. doi: 10.1080/00785326.1992.10430372

Bivand, R. (2019). *rgrass7: Interface Between GRASS 7 Geographical Information System and R. R package version 0.2-1*.

Boulangeat, I., Gravel, D., and Thuiller, W. (2012). Accounting for dispersal and biotic interactions to disentangle the drivers of species distributions and their abundances. *Ecol. Lett.* 15, 584–593. doi: 10.1111/j.1461-0248.2012.01772.x

Buhl-Mortensen, L., Buhl-Mortensen, P., Dolan, M. J. F., and Gonzalez-Mirelis, G. (2014). Habitat mapping as a tool for conservation and sustainable use of marine resources: some perspectives from the MAREANO Programme, Norway. *J. Sea Res.* 100, 46–61. doi: 10.1016/j.seares.2014.10.014

Buhl-Mortensen, L., Burgos, J. M., Steingrund, P., Buhl-Mortensen, P., Ólafsdóttir, S. H., and Ragnarsson, S. Á (2019). Vulnerable marine ecosystems (VME): coral and sponge VMEs in Arctic and sub-Arctic waters - Distribution and threats. *Nord. Council Ministers* 2019:519. doi: 10.6027/TN2019-519

Buhl-Mortensen, P., Dolan, M. F. J., Ross, R. E., Gonzalez-Mirelis, G., Buhl-Mortensen, L., Bjarnadóttir, L. R., et al. (2020). Classification and mapping of benthic biotopes in arctic and sub-arctic Norwegian waters. *Front. Mar. Sci.* 7:271. doi: 10.3389/fmars.2020.00271

Burgos, J. M., Buhl-Mortensen, L., Buhl-Mortensen, P., Ólafsdóttir, S. H., Steingrund, P., Ragnarsson, S. Á, et al. (2020). Predicting the distribution of indicator taxa of vulnerable marine ecosystems in the arctic and sub-arctic waters of the Nordic Seas. *Front. Mar. Sci.* 7:131. doi: 10.3389/fmars.2020.00131

Cárdenas, P., Rapp, H. T., Klitgaard, A. B., Best, M., Thollesson, M., and Tendal, O. S. (2013). Taxonomy, biogeography and DNA barcodes of Geodia species (Porifera, Demospongiae, Tetractinellida) in the Atlantic boreo-arctic region. *Zool. J. Linn. Soc.* 169, 251–311. doi: 10.1111/zoj.12056

Dallas, T. A., and Hastings, A. (2018). Habitat suitability estimated by niche models is largely unrelated to species abundance. *Glob. Ecol. Biogeogr.* 27, 1448–1456. doi: 10.1111/geb.12820

Das, A., Abdel-Aty, M., and Pande, A. (2009). Using conditional inference forests to identify the factors affecting crash severity on arterial corridors. *J. Saf. Res.* 40, 317–327. doi: 10.1016/j.jsr.2009.05.003

Elith, J., and Leathwick, J. (2009). Species distribution models: ecological explanation and prediction across space and time. *Annu. Rev. Ecol. Evol. Syst.* 40, 677–697. doi: 10.1146/annurev.ecolsys.110308.120159

EMODnet Bathymetry Consortium (2018). *EMODnet Digital Bathymetry (DTM)*. Oostende: EMODnet Bathymetry Consortium.

Evans, J. S. (2020). *spatialEco_. R package version 1.3-1*.

Franklin, J. (2010). *Mapping Species Distributions: Spatial Inference And Prediction*. Cambridge, MA: Cambridge University Press.

Gonzalez-Mirelis, G., and Buhl-Mortensen, P. (2015). Modelling benthic habitats and biotopes off the coast of Norway to support spatial management. *Ecol. Inform.* 30, 284–292. doi: 10.1016/j.ecoinf.2015.06.005

Haidvogel, D., Arango, H., Budgell, W., Cornuelle, B., Curchitser, E., Lorenzo, E. D., et al. (2008). Ocean forecasting in terrain-following coordinates: formulation and skill assessment of the Regional Ocean Modeling System. *J. Comput. Phys.* 227, 3595–3624. doi: 10.1016/j.jcp.2007.06.016

Hao, T., Elith, J., Guillera-Arroita, G., and Lahoz-Monfort, J. (2019). A review of evidence about use and performance of species distribution modelling ensembles like BIOMOD. *Divers. Distrib.* 25, 839–852. doi: 10.1111/ddi.12892

Harris, P. T., and Baker, E. K. (eds) (2019). *Seabed Geomorphology as Benthic Habitats: GeoHab Atlas of Seabed Geomorphic Features and Benthic Habitats*, 2nd Edn. Amsterdam: Elsevier.

Hijmans, R. J. (2020). *raster: Geographic Data Analysis and Modeling. R package version 3.1-5*.

Hooftman, D. A. P., and Bullock, J. M. (2012). Mapping to inform conservation: a case study of changes in semi-natural habitats and their connectivity over 70 years. *Biol. Conserv.* 145, 30–38. doi: 10.1016/j.biocon.2011.09.015

Hothorn, T., Buehlmann, P., Dudoit, S., Molinaro, A., and Van Der Laan, M. (2006a). Survival ensembles. *Biostatistics* 7, 355–373. doi: 10.1093/biostatistics/kxj011

Hothorn, T., Hornik, K., and Zeileis, A. (2006b). Unbiased recursive partitioning: a conditional inference framework. *J. Comput. Graph. Stat.* 15, 651–674. doi: 10.1198/106186006X133933

Hothorn, T., and Müller, J. (2010). Large-scale reduction of ungulate browsing by managed sport hunting. *For. Ecol. Manag.* 260, 1416–1423. doi: 10.1016/j.foreco.2010.07.019

Howard, C., Stephens, P. A., Pearce-Higgins, J. W., Gregory, R. D., and Willis, S. G. (2014). Improving species distribution models: the value of data on abundance. *Methos Ecol. Evol.* 5, 506–513. doi: 10.1111/2041-210X.12184

Howell, K. L., Piechaud, N., Downie, A. L., and Kenny, A. (2016). The distribution of deep-sea sponge aggregations in the North Atlantic and implications for their effective spatial management. *Deep Sea Res. I Oceanogr. Res. Pap.* 115, 309–320. doi: 10.1016/j.dsr.2016.07.005

Hui, C., and McGeoch, M. A. (2008). Does the self-similar species distribution model lead to unrealistic predictions. *Ecology* 89, 2946–2952. doi: 10.1890/07-1451.1

Klitgaard, A. B., and Tendal, O. S. (2004). Distribution and species composition of mass occurrences of large-sized sponges in the northeast Atlantic. *Prog. Oceanogr.* 61, 57–98. doi: 10.1016/j.pocean.2004.06.002

Levin, L. A., Etter, R. J., Rex, M. A., Gooday, A. J., Smith, C. R., Pineda, J., et al. (2001). Environmental influences on regional deep-sea species diversity. *Annu. Rev. Ecol. Syst.* 32, 51–93. doi: 10.1146/annurev.ecolsys.32.081501.114002

Levitin, D. J. (2014). *The Organized Mind: Thinking Straight in The Age of Information Overload*. New York, NY: Dutton.

Li, J. (2017). Assessing the accuracy of predictive models for numerical data: not r nor r2, why not? Then what? *PLoS One* 12:e0183250. doi: 10.1371/journal.pone.0183250

Li, J. (2019). *spm: Spatial Predictive Modeling. R package version 1.2.0*. Available online at: https://CRAN.R-project.org/package=spm

Liaw, A., and Wiener, M. (2002). Classification and regression by randomForest. *R News* 2, 18—-22.

Lind, S., Ingvaldsen, R. B., and Furevik, T. (2018). Arctic warming hotspot in the northern Barents Sea linked to declining sea-ice import. *Nat. Clim. Change* 8, 634–639. doi: 10.1038/s41558-018-0205-y

Liu, C., White, M., and Newell, G. (2009). "Measuring the accuracy of species distribution models: a review," in *Proceedings of the 18th World IMACS / MODSIM Congress* (Cairns).

Maechler, M., Rousseeuw, P., Struyf, A., Hubert, M., and Hornik, K. (2019). *cluster: Cluster Analysis Basics and Extensions. R package version 2.1.0*.

Maldonado, M., Aguilar, R., Bannister, R. J., Bell, J. J., Conway, C. W., Dayton, P. K., et al. (2016). "Sponge grounds as key marine habitats: a synthetic review of types, structure, functional roles, and conservation concerns," in *Marine Animal Forests: The Ecology of Benthic Biodiversity Hotspots*, eds S. Rossi, L. Bramanti, A. Gori, and C. Orejas Saco del Valle (Switzerland: Springer).

Maldonado, M., Carmona, M. C., Velásquez, Z., Puig, A., Cruzado, A., López, A., et al. (2005). Siliceous sponges as a silicon sink: an overlooked aspect of benthopelagic coupling inthe marine silicon cycle. *Limnol. Oceanogr.* 50, 799–809. doi: 10.4319/lo.2005.50.3.0799

Martin, D. P. (2015). *Efficiently Exploring Multilevel Data with Recursive Partitioning*. Charlottesville, VA: University of Virginia.

McArthur, M. A., Brooke, B., Przeslawski, R., Ryan, D. A., Lucieer, V. L., Nichol, S., et al. (2010). On the use of abiotic surrogates to describe marine benthic biodiversity. *Estua. Coast. Shelf Sci.* 88, 21–32. doi: 10.1016/j.ecss.2010.03.003

Mortensen, P. B. (2005). "Koraller og andre sårbare bunnhabitater. Vols. Fisken og havet, særnummer 1-2005," in *Havets Ressurser Og Miljø*, eds P. B. Mortensen, I. Dommasnes, A. Føyn, L. Haug, T. Iversen, S. A. Røttingen, et al. (Bergen: Havforskningsinstituttet), 61–63.

Müller, D., Schröder, B., and Müller, J. J. (2009). Modelling habitat selection of the cryptic Hazel Grouse *Bonasa bonasia* in a montane forest. *J. Ornithol.* 150, 717–732. doi: 10.1007/s10336-009-0390-6

Murawski, S. A. (2007). Ten myths concerning ecosystem approaches to marine resource management. *Mar. Policy* 31, 681–690. doi: 10.1016/j.marpol.2007.03.011

Murillo, F. J., Muñoz, P. D., Cristobo, J., Ríos, P., González, C., Kenchinton, E., et al. (2011). Deep-sea sponge grounds of the Flemish Cap, Flemish Pass and the Grand Banks of Newfoundland (Northwest Atlantic Ocean): distribution and species composition. *Mar. Biol. Res.* 8, 842–854. doi: 10.1080/17451000.2012.682583

Naimi, B., Hamm, N., Groen, T. A., Skidmore, A. K., and Toxopeus, A. G. (2014). Where is positional uncertainty a problem for species distribution modelling. *Ecography* 37, 191–203. doi: 10.1111/j.1600-0587.2013.00205.x

Nicodemus, K. K., and Malley, J. D. (2009). Predictor correlation impacts machine learning algorithms: implications for genomic studies. *Bioinformatics* 25, 1884–1890. doi: 10.1093/bioinformatics/btp331

Norges geologiske undersøkelse (2014). *Marine Landskap*. Trondheim: Norges geologiske undersøkelse.

Norges geologiske undersøkelse/MAREANO (2015). *Bunnsedimenter (kornstørrelse), regionalt*. Trondheim: Norges geologiske undersøkelse.

OSPAR (2008). *List of Threatened and/or Declining Species and Habitats. Reference Number 2008-06*. London: OSPAR.

OSPAR (2010). *Background Document for Deep-Sea Sponge Aggregations*. London: OSPAR.

Pearce, J. L., and Boyce, M. S. (2006). Modelling distribution and abundance with presence-only data. *J. Appl. Ecol.* 43, 405–412. doi: 10.1111/j.1365-2664.2005.01112.x

Pearman, T. R. R., Robert, K., Callaway, A., Hall, R., Lo Iacono, C., and Huvenne, V. A. I. (2020). Improving the predictive capability of benthic species distribution models by incorporating oceanographic data – Towards holistic ecological modelling of a submarine canyon. *Prog. Oceanogr.* 184:102338. doi: 10.1016/j.pocean.2020.102338

Pottier, J., Malenovskı, Z., Psomas, A., Homolová, L., Schaepman, M. E., Choler, P., et al. (2014). Modelling plant species distribution in alpine grasslands using airborne imaging spectroscopy. *Biol. Lett.* 10:20140347. doi: 10.1098/rsbl.2014.0347

Robin, X., Turck, N., Hainard, A., Tiberti, N., Lisacek, F., Sanchez, J.-C., et al., (2011). pROC: an open-source package for R and S+ to analyze and compare ROC curves. *BMC Bioinformatics* 12:77. doi: 10.1186/1471-2105-12-77

Sappington, J. M., Longshore, K. M., and Thomson, D. B. (2007). Quantifying landscape ruggedness for animal habitat analysis: a case study using Bighorn Sheep in the Mojave desert. *J. Wildlife Manag.* 71, 1419–1426. doi: 10.2193/2005-723

Sardá-Espinosa, A., Subbiah, S., and Bartz-Beielstein, T. (2017). Conditional inference trees for knowledge extraction from motor health condition data. *Eng. Appl. Artif. Intellig.* 62, 26–37. doi: 10.1016/j.engappai.2017.03.008

Selkoe, K. A., Watson, J. R., White, C., Horin, T. B., Iacchei, M., Mitarai, S., et al. (2010). Taking the chaos out of genetic patchiness: seascape genetics reveals ecological and oceanographic drivers of genetic patterns in three temperate reef species. *Mol. Ecol.* 19, 3708–3726. doi: 10.1111/j.1365-294X.2010.04658.x

Shchepetkin, A. F., and McWilliams, J. C. (2005). The regional oceanic modeling system (ROMS): a split-explicit, free-surface, topography- following-coordinate oceanic model. *Ocean Model.* 9, 347–404. doi: 10.1016/j.ocemod.2004.08.002

Shmueli, G. (2010). To explain or to predict? *Stat. Sci.* 25, 289–310. doi: 10.1214/10-STS330

Strobl, C., Boulesteix, A.-L., Zeileis, A., and Hothorn, T. (2007). Bias in random forest variable importance measures: illustrations, sources and a solution. *BMC Bioinformatics* 8:25. doi: 10.1186/1471-2105-8-25

Wilson, M. F. J., O'Connell, B., Brown, C., Guinan, J. C., and Grehan, A. J. (2006). Multiscale terrain analysis of multibeam bathymetry data for habitat mapping on the continental slope. *Mar. Geodesy* 30, 3–35. doi: 10.1080/01490410701295962

Wueest, R., Racine, E. B., and Hijmans, R. J. (2012). *rdrr.io. November*. Available at: https://rdrr.io/rforge/raster/src/R/blend.R (accessed January 23, 2019).

Young, C. M., Tyler, P. A., and Gage, J. D. (1996). Vertical distribution correlates with pressure tolerances of early embryos in the deep-sea asteroid *Plutonaster Bifrons*. *J. Mar. Biol. Assoc. U.K.* 76, 749–757. doi: 10.1017/S002531540003143X

Conflict of Interest: The authors declare that the research was conducted in the absence of any commercial or financial relationships that could be construed as a potential conflict of interest.

Advantages of publishing in Frontiers

OPEN ACCESS
Articles are free to read for greatest visibility and readership

FAST PUBLICATION
Around 90 days from submission to decision

HIGH QUALITY PEER-REVIEW
Rigorous, collaborative, and constructive peer-review

TRANSPARENT PEER-REVIEW
Editors and reviewers acknowledged by name on published articles

Frontiers
Avenue du Tribunal-Fédéral 34
1005 Lausanne | Switzerland

Visit us: www.frontiersin.org
Contact us: frontiersin.org/about/contact

REPRODUCIBILITY OF RESEARCH
Support open data and methods to enhance research reproducibility

DIGITAL PUBLISHING
Articles designed for optimal readership across devices

FOLLOW US
@frontiersin

IMPACT METRICS
Advanced article metrics track visibility across digital media

EXTENSIVE PROMOTION
Marketing and promotion of impactful research

LOOP RESEARCH NETWORK
Our network increases your article's readership